Altérations hydrothermales associées aux zones de fractures à l'interface de la couverture sédimentaire et du socle cristallin dans le Fossé rhénan supérieur : application aux forages géothermiques de Rittershoffen (Alsace, France)

Jeanne Vidal

UNIVERSITÉ DE STRASBOURG

École doctorale des Sciences de la Terre et de l'Environnement (ED 413)

Institut de Physique du Globe de Strasbourg (UMR 7516)

THÈSE présentée par :

Jeanne Vidal

soutenue le **21 septembre 2017**

pour obtenir le grade de : **Docteur de l'Université de Strasbourg**

Discipline / Spécialité : Sciences de la Terre / Géologie

Altérations hydrothermales associées aux zones de fractures à l'interface de la couverture sédimentaire et du socle cristallin dans le Fossé rhénan supérieur.

Application aux forages géothermiques de Rittershoffen (Alsace, France)

THÈSE dirigée par :

M Jean Schmittbuhl	Directeur de Recherche, Université de Strasbourg
M Hubert Whitechurch	Professeur, Université de Strasbourg

RAPPORTEURS :

Mme Béatrice Ledésert	Professeure, Université de Cergy-Pontoise
M Benoît Valley	Professeur Assistant, Université de Neuchâtel

---

EXAMINATEURS :

Mme Patricia Patrier	Professeure, Université de Poitiers
Mme Chrystel Dezayes	Ingénieure, BRGM
M Albert Genter	Directeur Général Adjoint, ES-Géothermie

UNIVERSITÉ DE STRASBOURG

École doctorale des Sciences de la Terre et de l'Environnement (ED 413)

Institut de Physique du Globe de Strasbourg (UMR 7516)

THÈSE présentée par :

Jeanne Vidal

soutenue le **21 septembre 2017**

pour obtenir le grade de : **Docteur de l'Université de Strasbourg**

Discipline / Spécialité : Sciences de la Terre / Géologie

Altérations hydrothermales associées aux zones de fractures à l'interface de la couverture sédimentaire et du socle cristallin dans le Fossé rhénan supérieur.

Application aux forages géothermiques de Rittershoffen (Alsace, France)

THÈSE dirigée par :

M Jean Schmittbuhl	Directeur de Recherche, Université de Strasbourg
M Hubert Whitechurch	Professeur, Université de Strasbourg

RAPPORTEURS :

Mme Béatrice Ledésert	Professeure, Université de Cergy-Pontoise
M Benoît Valley	Professeur Assistant, Université de Neuchâtel

---

EXAMINATEURS :

Mme Patricia Patrier	Professeure, Université de Poitiers
Mme Chrystel Dezayes	Ingénieure, BRGM
M Albert Genter	Directeur Général Adjoint, ES-Géothermie

INVITE :

M Philippe Laplaige	Ingénieur, ADEME

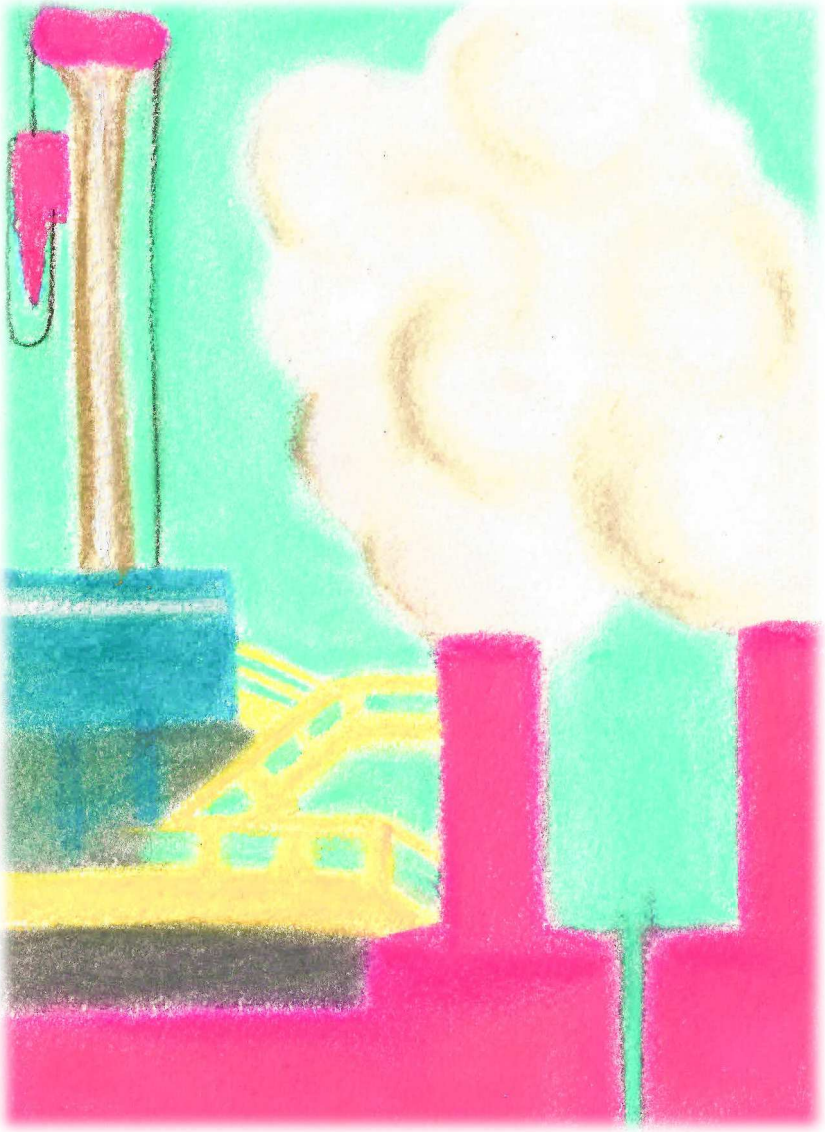

Site de Rittershoffen - 2014

Avant-propos

Cette thèse a bénéficié d'un cofinancement de l'Agence De l'Environnement et de la Maîtrise de l'Energie (ADEME) et de l'Agence Nationale de la Recherche (ANR) au titre du programme « Investissement d'avenir » et du projet Laboratoire d'Excellence G-EAU-Thermie Profonde. Le LabEx G-EAU Thermie Profonde est un partenariat académie-industrie entre l'Université de Strasbourg, l'Electricité de Strasbourg et le GEIE Exploitation Minière de la Chaleur.

Ce travail de recherche s'appuie sur les données de sous-sol du projet industriel de Rittershoffen dont ES-Géothermie est propriétaire. La doctorante a suivi la réalisation des deux forages profonds de Rittershoffen, l'acquisition des données d'imageries acoustiques et les essais de circulations inter-puits.

En parallèle de l'encadrement académique de l'Institut de Physique du Globe de Strasbourg (UMR7516) à l'Université de Strasbourg, la doctorante a travaillé en collaboration avec l'Institut de Chimie des Milieux et Matériaux de l'Université de Poitiers pour la partie analytique sur les cuttings.

Les travaux de thèse ont été présentés aux European Geothermal Workshops 2014 et 2015 (partenariat entre l'Institut de technologie de Karlsruhe et de l'Ecole et Observatoire des Sciences de la Terre de Strasbourg), aux Geothermal Workshops de l'Université de Stanford en 2016 et 2017, au World Geothermal Congress à Melbourne en 2015, à l'European Geothermal Congress à Strasbourg en 2016 et à l'American Geophysical Union à San Francisco en 2016.

Les résultats ont été publiés ou soumis dans 6 articles dont 5 en 1er auteur dans les revues à comité de lecture ; Journal of Geophysical Research, Geophysical Journal International, Geothermal Energy Journal, Geothermics et Journal of Volcanology and Geothermal Research.

Ce mémoire de thèse est structuré sur la base de la production scientifique des trois années de thèse.

Remerciements

En 2009, j'ai été reçue par Albert Genter et Jean-Jacques Graff au GEIE Exploitation de Minière de la Chaleur à Soultz-sous-Forêts dans le cadre d'un projet de recherche de première année de Licence. C'est presque un coup de foudre pour la géothermie. Huit ans plus tard, après plusieurs expériences avec la Soultz Team, puis trois années de thèse aussi éprouvantes qu'enrichissantes, voici l'heure d'apposer la touche finale de ce manuscrit. L'aboutissement de cette thèse n'aurait pas été possible sans le soutien et la collaboration de nombreuses personnes, qui ont joué, de près ou de loin, un rôle dans sa réussite et j'aimerais les remercier chaleureusement.

Je tiens tout d'abord à exprimer ma profonde gratitude à Albert. Tu m'as initiée à ce beau métier de géologue géothermicienne. J'ai été très touchée par ton attitude à mon égard tant au niveau humain que scientifique. Merci pour ton optimisme à toutes épreuves, ta patience et ton investissement durant cette thèse.

Merci à l'Agence de l'Environnement et de Maîtrise de l'Energie et à Philippe Laplaige de m'avoir fait confiance pour mener à bien ce beau projet.

Je souhaiterais également remercier les membres de mon jury Béatrice Ledésert, Benoît Valley, Chrystel Dezayes et Patricia Patrier d'avoir accepté d'évaluer cette thèse.

Un immense merci à tous les chercheurs que j'ai pu rencontrer durant mes passages à Soultz de 2009 à 2013. J'ai beaucoup appris à votre contact et vous avez sans aucun doute participé à mon envie de persévérer dans la recherche.

Merci à mes collègues d'ES-Géothermie avec qui j'ai pu collaborer durant ma thèse et avant. Merci à Jean-Jacques pour ton soutien constant depuis tant d'années. Je voudrais également remercier Emmanuelle et Muriel pour votre aide précieuse durant toutes mes démarches administratives, toujours avec votre bonne humeur. Une petite pensée pour Guillaume et les soirées cocktails qui ont

parfois contribué à ce que je ne baisse pas les bras. Egalement, une pensée pour Abigaëlle qui est bien plus qu'une collègue.

Je tiens à remercier Patricia et les chercheurs de l'équipe Hydrasa de Poitiers qui ont accueilli et initié la non argileuse que j'étais avec beaucoup de bienveillance.

Merci aux copains de thèse, j'ai de très beaux souvenirs à vos côtés durant ces trois dernières années. J'ai une pensée plus particulière pour Médéric et son obsession de la décroissance, pour Jean-Michel et son humour, pour Jeanne, une précieuse amie qui me supporte depuis plusieurs années, pour Charlotte, si intelligente et si douce, et enfin pour Francis, Pierre, Alexis, et leurs canettes.

Je voudrais également remercier mes amis que j'ai pu rencontrer durant mes années d'études : Valentin, David, Yann, Hugo, Patric, Mickaël, Charlotte, Sandrine, Marie-Eva, Joseph, Marc, Camille, Jérémy, Vincent… « Rares sont les amis dont nous pouvons nous dire qu'ils ont changé notre vie, avec cette certitude étrange que, sans eux, notre vie tout simplement n'aurait pas été la même »

J'ai une pensée émue pour ma mère qui m'a ouvert tellement de voies sur les plans moral, intellectuel et humain. Tu es ce modèle extraordinaire que j'ai toujours regardé et que je n'ai eu qu'à suivre.

Romane, ma petite sœur, merci pour ton énergie débordante et ton amour !

Enfin, merci à Quentin, la force tranquille de cette thèse. Je suis profondément reconnaissante de ta présence à mes côtés durant ces trois dernières années et de tout ce que tu m'as apporté.

Extended Abstract

The continental crust below Western Europe experienced several stages of brittle deformation since Devonian-Carboniferous times which lead to the development of a multi-scale fracture network. This interconnected system of fractures ranges in sizes from microcracks of few millimeters to large scale fault zone of several kilometers, and is host to hydrothermal circulations. Exploitation of these deep hydrothermal circulations (>2 km depth), situated notably in Tertiary basins, expanded rapidly with the development of geothermal power plants. In France, several thousands of km^2 located in the Rhine Graben, Rhone corridor and Valencia Graben have been the focus of major exploration and deep well drilling projects to exploit the natural heat from their geothermal resource. Geothermal potential of these Tertiary basins is either located within their Carboniferous crystalline basement or at the base of clastic sediments, known to cause high thermal. High geothermal gradient are interpreted as upwelling of hot geothermal resource through the natural fracture network. However, even though geological conditions might be favorable to produce the necessary temperature, permeability of the fracture network needs to be considered for any geothermal exploitation. In the Upper Rhine Graben (URG), Alsace, a pioneering project to exploit the thermal potential of the region was initiated at Soultz-sous-Forêts. The goal was to develop a deep heat exchanger in the crystalline basement of the basin. To this end, five deep wells were drilled to attain the deep granitic reservoir at 5 km depth. This reservoir bare natural hydrothermal circulations, which are channelized along altered and fractured zones or faulted sectors. The hydraulic yield of these altered and fractured zones are inherently linked to their internal organization, but also depend on the presence of secondary mineral deposits. Hydraulic well tests reveal a general decrease of permeability from the top to the deep granitic basement with depth. Upper and intermediate granitic reservoirs above 3.5 km depth show higher permeability than the deeper granitic reservoir at 5 km depth. Hence to increase the hydraulic yield, application of Enhance Geothermal System (EGS) technology, which consists of hydraulic and chemical stimulations of altered and fractured zones, has shown to improve poor hydraulic connections between wells and the reservoir.

The recent industrial project at Rittershoffen is located less than 10 km eastward of Soultz-sous-Forêts. It directly benefited from the experience gained from the former Soultz project. In 2012, the first geothermal well GRT-1 was drilled at 2.6 km depth, intersecting the local fault of Rittershoffen vertically. The Rittershoffen fault is a normal fault striking N-S, dipping westward and with a vertical offset of 200 m. Hot geothermal resources higher than 160°C is captured inside the fault zone. Connection between the well and the fault zone was however too low for industrial exploitation, which lead to thermally, chemically and hydraulically (TCH) stimulation of GRT-1 in 2013. After a 2D seismic campaign, the second well GRT-2 was drilled in 2014 with a trajectory highly deviated to the North. More than 3 km length were drilled with an inclination of 37°. It presents an excellent permeability and thus did not necessitate any stimulation. Since June 2016, the Rittershoffen geothermal power plant delivers 24 MW_{th} of geothermal energy to the nearby bio-refinery complex at Beinheim, 15 km away.

A major issue for geothermal exploitation and development of the fractured reservoir in the URG is related to the poor knowledge on the natural fracture network and hydrothermal circulations of the crystalline basement. This PhD project aims to better understand the thermal convection cells at the base of the sedimentary basin and within the crystalline basement. Understanding these convection cells at the borehole scale is fundamental for any future exploitation of geothermal resource in Alsace. This study will predominantly look at the geometrical structure of convective cells, their stability through time, affinity with geological structures (local faults, lithologies...), internal permeability organization, secondary hydrothermal deposits and relationship to stress fields. It is mainly based on data from Rittershoffen wells collected over the period of 2012 to 2015. It comprises acoustic image logs, temperature profiles, standard geophysical logs and cuttings. The focus of the study are the hard and fractured sandstones at the base of the sedimentary cover and the upper hundreds of meters of altered and fractured granitic basement, as this reservoir presents a high geothermal potential.

This PhD thesis is structured into three main parts – Introduction, Data analysis and Interpretation, and Conclusion and outlook –, which are further divided into nine chapters.

First part: Introduction

The **first chapter** provides a general introduction to the geothermal development in France, with an emphasis on the URG.

The **second chapter** presents a literature review on the tectonic history of the URG from the Variscan (~360 Ma) to present times. It outlines pioneering studies of hydrothermal circulations and natural fracture network at the sediment-basement interface. These studies are mainly based on the scientific experience gained from Soultz.

The **third chapter** describes the geological context of Rittershoffen and summarizes previous works conducted at this site. This chapter lays out the frame of the PhD.

The **fourth chapter** outlines main issues and goals of the PhD thesis to conclude the first part.

Second part: Data Analysis and Interpretation

The **fifth chapter** begins with a presentation of the methods and data used in this study, such as acoustic image logs, temperature profiles, standard geophysical logs and mud logging data. A detailed description on the methodology to characterize clay minerals in cutting samples is further provided. These tools and data provide information on the geometry of fractures and their permeability at borehole scale. Additionally, they are valuable to evaluate the impact of GRT-1 stimulation at borehole scale. This chapter is concluded with an example of comparison of pre- and post-acoustic image logs and temperature profiles in well GRT-1. This study was published in the peer-reviewed journal *Geophysical International Journal.* It evaluates the impact of TCH stimulation in GRT-1 well at the borehole scale. Comparison of acoustic image logs show dissolution of secondary minerals deposits (carbonates and sulfates) in fractures after chemical stimulation that could enhance permeability of the reservoir. In

addition, no shearing of fractures at the borehole scale after hydraulic stimulation was identified.

The **sixth chapter** gives an overview of deep geothermal sites in the URG. It is outlined as a submitted article to *Geothermics*. Fifteen wells from eight projects in France, Germany and Switzerland were investigated in terms of geology, temperature profiles and hydraulic yield. The confidentiality of these projects renders the collection of original data difficult. Geological, temperature and hydraulic data were compared in hard fractured sandstones, in the hydrothermally altered and fractured granite and in the deep poorly fractured granite from each project. The results show that most permeable fractures in the reservoir were intersected in the first hundred meters of the hydrothermally altered and fractured granitic basement. In addition, temperature profiles present the same pattern in each well, denoting an abrupt decrease of the geothermal gradient at the top of the fractured sandstones, with the exception of the Soultz wells. In Soultz, geothermal gradient in the wells shows a slow decrease between the top of the Triassic sediments and the top of the granitic basement. A particular interest is given to the thermal signature at the base of the sedimentary cover in Soultz wells.

The chapter concludes with an article published in the peer-reviewed journal *Geothermal Energy Journal* that investigates fracture zones in the Triassic sediments of Soultz. Unlike the granitic basement that was the target of the industrial geothermal project, Triassic sediments were poorly investigated at Soultz. Hence, old geophysical logs were re-interpreted in order to identify fracture zones. Permeable fracture zones in limestones from the Middle Trias and sandstones from the Early Trias channelized hydrothermal circulations in a zone of transition between conduction above and convection below.

The **seventh chapter** is devoted to the thermal signature of permeable fracture zones in Rittershoffen wells. In a first instance, the structure of the natural fracture network in sandstones and granitic basement is shown and is based on an extended abstract presented at the *European Geothermal Congress 2016*. Most of natural fractures were observed in the hydrothermally altered granitic basement in GRT-1 and GRT-2. However, lithology does not influence orientation of these fractures. Overall, the main fracture orientation in GRT-1 is

N10°E to N20°E dipping westward. In GRT-2, the main fracture orientation is N160°E to N-S dipping either eastward or westward. The pattern of these orientations are similar to the ones observed for the Soultz wells. Horizontal joints observed at the top of the granitic basement at Soultz have not been discovered at Rittershoffen. This is probably due to the lower resolution of acoustic image logs compared to core samples, making the imaging of tiny fractures difficult. Acoustic image logs were correlated to temperature profiles and mud logging (mud losses and gas survey) to identify permeable fracture zones. Less than 2% in GRT-1 and 3% in GRT-2 of fractures present natural permeable indication at borehole scale.

The second part of the chapter is structured as a published article in the peer-reviewed journal *Journal of Geophysical Research* and presents a detailed study of permeable fracture zones. One originally permeable (OP) fracture zone was observed in the granite of GRT-1. In GRT-2, four OP fracture zones are observed in the granite, and two in sandstones. All OP fractures are associated with positive temperature anomaly. The positive anomalies are interpreted as circulation of geothermal hot water through the permeable fracture. The negative ones are interpreted as the cooling of a porous, altered and fractured zone around the permeable fracture after drilling operations. In granite, these OP fracture zones present an asymmetric internal organization of permeability with several open fractures inside a large porous and altered granitic zone. These open fractures act as fluid conducts. The level of permeability of fractures seems to be closely linked to secondary mineral deposits resulting from paleo-circulations. Sealed fractures have been identified in GRT-1 whereas density of open fractures increase in OP fracture zones of GRT-2. This likely explains the connection between GRT-2 and the reservoir and hence its higher natural permeability compared to GRT-1. Spatial correlation of OP fracture zones between both wells is not trivial because they are separated by more than 1 km at the bottom hole. The geometrical fracture model along the wellbore suggests that the inclined trajectory of GRT-2 increases the connection between the borehole and the nearly vertical fracture network, which is associated to the local fault of Rittershoffen.

The **eighth chapter** describes the clay signature of permeable fracture zones in Rittershoffen wells. First, a preliminary mineralogical study was conducted for the uppermost top section of the granitic basement collected from exploration well EPS-1 at Soultz. Findings were presented in an extended abstract submitted to the *41st Workshop on Geothermal Reservoir Engineering* at Stanford University. At the top of the granitic basement (150 m), low magnetic susceptibility correlates with highest radiogenic heat productivities measured on core samples from Soultz wells. Though this narrow horizon seems attractive for geothermal exploitation, intersected fracture zones in the well does not show natural permeability. Investigations of a fracture from core samples in EPS-1 indicate close relationship between secondary quartz, carbonates and illitic minerals. Illitic minerals are ubiquitous and seem to seal all other secondary minerals, plugging residual permeability inside the fracture. Secondary minerals are the product of a multi-stage history of dissolution-precipitation processes after various hydrothermal fluid events through these fractures. Fracture alteration induced by hydrothermal circulations are superimposed to strong paleo-weathering of the upper section of the granitic basement. This preliminary study lead to an increased appraisal of the role of clay minerals in OP fracture zones in Rittershoffen wells.

Clay minerals are highly reactive to hydrothermal alteration and can therefore be used as an indicator for past and present circulations. Crystal structure and chemical properties of clay minerals were analyzed from cuttings samples in GRT-1 and GRT-2 wells. This study has been summarized in an article submitted in *Journal of Volcanology and Geothermal Research*, and is structure in this chapter as such. Cuttings were preferentially sampled around OP fracture zones described in chapter 7. Observations from the clay fraction reveal that occurrences of illite-smectite mixed layers (<10% of smectite) are promising to identify OP fracture zones which control the present circulation of geothermal fluids in the Rittershoffen wells. Multi-stage paleo-circulations could lead to abundant heterogeneous and fine-grained illitic minerals that obstruct the fracture system such as the one observed in GRT-1. Chlorite is still observed into the OP fracture zones of GRT-2, indicating less intense alteration. Primary minerals from the granitic cutting samples in GRT-2 are less intensively replaced by secondary

illitic minerals, while the natural permeability is much higher in GRT-2 than in GRT-1.

The structural and mineralogical study at the boreholes scale evidenced permeable fracture zones that channelized hydrothermal circulations in GRT-1 and GRT-2 wells.

Third part: Conclusion and outlook

The **ninth chapter** lays out the main conclusions from the previous chapters. Structural and mineralogical studies in Rittershoffen wells reveal several OP fracture zones with highest permeability in the hydrothermally altered granitic basement. OP fracture zones present an asymmetric internal organization of permeability with open fractures that act as conduct for fluid circulation. Open fractures are associated with positive anomalies in temperature profiles whereas the surrounding porous and altered granitic basement is associated with negative anomalies. Geothermal fluid circulations lead to argillic alteration and occurrences of heterogeneous and fine-grained illitic minerals are identified in all OP fracture zones from both wells. The pioneering well GRT-1 intersects the fracture network associated with the Rittershoffen fault vertically. Its hydraulic behavior seems mainly controlled by one major OP fracture zone. However, intense illitisation of this OP fracture zone plugged fluid pathways and reduces natural permeability of the host rock. To improve the connectivity between the well and the geothermal reservoir, TCH stimulation was carried out on GRT-1. The highly deviated trajectory of the second well GRT-2 is collinear to the Rittershoffen fault and intersects on multiple occasions its fracture network. Hydraulic behavior seems controlled by several OP fracture zones and the illitisation is less intense than in GRT-1. The natural permeability was high enough to allow industrial exploitation, which did not require the well to be stimulated. GRT-2 is therefore qualified as a hydrothermal well. The learned experience from Rittershoffen reveals that an optimal trajectory towards the natural fracture network prevent the use of EGS technology.

The **tenth chapter** outlines the perspectives that could be investigated. The objectives of the PhD project are limited to the scale of the borehole. Interpretation of trace of the Rittershoffen fault at the top of the granitic basement

remains unclear from 2D seismic data. The low section of GRT-2 trajectory lies within a zone which is poorly imaged by the 2D seismic data. Possible scenarios are that the well intersects a complex fault termination or relay ramp between two segments of faults. Re-interpretation of 2D seismic or Vertical Seismic Profile data could provide new insights in the relationship between drilled wells and the Rittershoffen fault. 3D seismic data could provide more reliable imaging at the top granitic basement where the fracture network records highest permeability. The idea to intersect fracture corridors that are formed by large clusters of natural fractures with high permeability without significant offset, and thus not observed in 2D seismic, should also be further investigated. Using micro-seismicity in order to image the inter-well domain is promising in GRT-1 but need to be extended around GRT-2. A correlation of all these data could lead to a deterministic 3D geological model at the reservoir scale.

For a better understanding of the geothermal system, further reflection about hydrothermal alteration is required. Current observations on secondary mineral deposits suggest the overlapping of several hydrothermal events. However, relative dating of hydrothermal events remains challenging in cutting samples. Existing methods do not allow to separate illitic phases from the matrix in order to date the individual hydrothermal events. The geochemical model at Rittershoffen remains also incomplete. Finally, understanding convective cells in the deeper layers of a basin requires more knowledge on the natural velocity of hydrothermal fluids, which stresses the need for further investigations on temperature profiles.

Résumé Étendu

En Europe de l'Ouest, la croûte fragile en raison de son évolution géodynamique a subi une histoire tectonique polyphasée depuis le Dévonien-Carbonifère jusqu'à l'Actuel. Cette histoire tectonique a développé des réseaux de fractures multi-échelles, depuis l'échelle des failles régionales de plusieurs kilomètres jusqu'à celle des microcracks de quelques millimètres. Ces réseaux représentent des conduits privilégiés pour des circulations hydrothermales profondes. Il en résulte un essor particulier du développement de la géothermie profonde (>2km) avec la réalisation de centrales électrogènes et/ou de chaleur dans des grabens tertiaires. De ce fait, plusieurs milliers de km² en France métropolitaine, notamment dans le Fossé rhénan, le Fossé rhodanien ou encore le Fossé de Valence, font l'objet de travaux d'exploration et de forages profonds pour exploiter la chaleur contenue dans des fluides profonds. Le potentiel géothermique de ces bassins d'extension tertiaires se localise dans leur socle cristallin tardi-varisque et à la base des remplissages sédimentaires clastiques où des forts gradients thermiques sont rencontrés. Ces gradients sont associés à une remontée de fluides chauds dans un réseau de fractures naturelles dense au sein de la croûte terrestre amincie. Cependant, si les conditions géologiques sont favorables pour atteindre les niveaux de température requis, la quantité de chaleur extraite du sous-sol dépend directement de la perméabilité des réservoirs fracturés associés. Dans le Fossé rhénan, les études menées en Alsace sur le projet pilote de Soultz-sous-Forêts avaient pour objectif de développer un échangeur granitique profond. Les forages profonds réalisés à 5 km de profondeur dans le socle, ont révélé la présence de circulations naturelles avec des chemins d'écoulement très localisés qui sont associés à des zones altérées et fracturées ou des zones faillées. Leurs caractéristiques hydrauliques sont intimement liées à l'organisation géométrique interne de ces zones altérées et fracturées mais également à la nature de leurs remplissages minéralogiques. Les tests hydrauliques montrent que la perméabilité naturelle du granite diminue avec la profondeur entre le toit du socle et la partie la plus profonde des puits. La technique *Enhanced Geothermal System* (EGS) a permis d'augmenter les perméabilités naturelles des fluides circulant dans les zones altérées et

fracturées notamment par la mise en œuvre de méthodes de stimulations hydrauliques et chimiques.

Le récent projet géothermique de Rittershoffen, situé à moins de 10 km à l'Est du projet de Soultz-sous-Forêts, est directement basé sur les leçons scientifiques tirées du projet de Soultz-sous-Forêts. Le premier puits GRT-1 a été foré en 2012 jusqu'à 2.6 km de profondeur de façon à recouper verticalement la faille locale dite de Rittershoffen au toit du socle granitique. Il s'agit d'une faille normale orientée N-S avec un fort pendage ouest et un rejet vertical apparent de 200 m. Cette faille et le réseau de fractures naturelles associé sont le siège de circulations de ressources géothermales à 160°C. Bien que le puits ait recoupé la cible géothermale, la perméabilité du premier puits n'étant pas suffisamment élevée pour le projet industriel, le puits a été stimulé thermiquement, chimiquement et hydrauliquement (TCH) en 2013. Après une campagne vibrosismique, le second puits GRT-2 a été foré en 2014 avec une trajectoire déviée vers le nord. Ce puits montre une excellente perméabilité et n'a nécessité aucune opération de stimulation. Après une phase de tests de circulations interpuits, la centrale de Rittershoffen délivre une puissance thermique de 24 MW_{th} pour un usage industriel.

L'un des obstacles majeurs au développement des réservoirs fracturés comme celui de Rittershoffen est la faible connaissance des réseaux de fractures naturelles et des chemins de circulations empruntés. L'objectif de cette thèse est de mieux comprendre la structure et le fonctionnement des circulations naturelles qui forment de véritables boucles de convection. La compréhension de ces boucles à l'échelle des puits permettra d'améliorer la connaissance du sous-sol alsacien dans l'optique de l'optimisation de l'exploitation future de son potentiel géothermique. Il s'agit notamment d'étudier leur caractère thermiqueprograde ou rétrograde, leur stabilité dans le temps, leurs relations avec des objets géologiques tels que la présence de failles locales, l'organisation des fractures, la lithologie, la nature des dépôts hydrothermaux ou encore leur relation avec le champ de contrainte. Les principales sources de données sont issues d'un doublet de forage dans le socle. Il s'agit principalement des imageries de paroi acoustiques, des profils de température, des diagraphies géophysiques et des cuttings le long des deux forages de Rittershoffen. Le caractère innovant réside

en la spécificité de la zone d'étude c'est-à-dire la base de la couverture sédimentaire et les premières centaines de mètres du socle granitique qui ont été peu étudiées pour leur potentiel géothermique favorable.

Le manuscrit est divisé en trois parties, Etat de l'Art et Objectifs de la thèse, Analyse et Interprétation des données, Conclusions et Perspectives, subdivisées en dix chapitres.

Partie 1 : ÉTAT DE L'ART ET OBJECTIFS DE LA THÈSE

Le **premier chapitre** propose une introduction générale à la géothermie en France et plus particulièrement dans le Fossé rhénan supérieur.

Le **deuxième chapitre** présente l'état de l'art des connaissances sur les circulations hydrothermales et le réseau de fractures naturelles à l'interface de la couverture sédimentaire et du socle cristallin. Une revue bibliographique de l'histoire tectonique du Fossé rhénan depuis l'héritage tardi-varisque du Dévonien-Carbonifère jusqu'à l'Actuel permet d'établir le contexte géologique. Les travaux scientifiques issus des puits profonds de Soultz seront également détaillés.

Le **troisième chapitre** présente le site de Rittershoffen et les études déjà menées sur le réservoir fracturé.

Les problématiques et les objectifs de thèse sont exposés dans le **quatrième chapitre** qui conclut cette partie.

Partie 2 : ANALYSE ET INTERPRÉTATIONS DES DONNÉES

Le **cinquième chapitre** expose les méthodes utilisées dans cette thèse pour caractériser les zones de fractures et leur perméabilité à l'échelle du puits. Les données originales acquises dans les puits profonds de Rittershoffen, telles que les imageries acoustiques, renseignent sur la géométrie in situ du réseau de fractures ainsi que sur l'importance du colmatage hydrothermal à l'échelle du puits. Elles ont été corrélées à des diagraphies géophysiques telles que celles qui mesurent la radioactivité naturelle, la porosité neutron, la densité et la géométrie du puits. La perméabilité des fractures a été évaluée à partir de l'analyse du profil de température à l'équilibre ainsi que les indices de circulations hydrothermales tels que les pertes de boue, les venues d'eau géothermale et de

gaz lors des opérations de foration. Enfin la minéralogie des argiles permet d'étudier les paléo-circulations et circulations actuelles le long du puits. Pour conclure ce chapitre, un exemple d'utilisation des imageries de paroi pour l'étude de l'impact de la stimulation sur les fractures naturelles est présenté sous forme d'article publié dans la revue *Geophysical Journal International*. Il s'agit d'une comparaison des imageries de paroi acoustiques ante- et post-stimulation dans le puits GRT-1 qui permet d'évaluer l'impact de la stimulation TCH à l'échelle du puits. L'étude comparative, présentée sous forme d'une publication scientifique, montre la dissolution du remplissage minéral secondaire qui colmatait un cluster de fractures dans les grès triasiques suite à la stimulation. A l'échelle du puits, la trace de mouvements de cisaillement n'ont pas été observés après l'injection hydraulique.

Le **sixième chapitre** est une étude géologique sur la perméabilité des réservoirs sédimentaires et granitiques du Fossé rhénan. La première partie du chapitre est présentée sous forme d'un article soumis à la revue *Geothermics*. Elle propose une synthèse bibliographique sur les réservoirs fracturés de géothermie profonde dans le Fossé rhénan. Les données géologiques, thermiques et hydrauliques de 15 puits profonds issus de huit projets en France, en Allemagne et en Suisse ont été comparées. Le principal frein à la collecte de ces données est leur caractère confidentiel. Les données de puits montrent que les zones de fractures les plus perméables ont été recoupées dans les 500 premiers mètres du socle granitique hydrothermalement altéré. Les zones de fractures recoupées dans les sédiments triasiques n'ont pas la même signature thermique dans tous les sites du Fossé rhénan et une attention particulière a été portée sur les zones de fractures des puits de Soultz. Cette deuxième partie de chapitre est présentée sous forme d'un article publié à la revue *Geothermal Energy Journal* et propose une réinterprétation d'anciennes données diagraphiques corrélées aux indices de perméabilité dans les puits. Si le réseau de fractures affectant le granite de Soultz a été largement étudié, les connaissances du réseau de fractures perméables dans les sédiments triasiques restent peu approfondies. L'étude a permis d'identifier des fractures perméables dans les grès triasiques mais également dans les calcaires du Muschelkalk. Elles

sont associées à une zone de transition entre un milieu dominé par la conduction et un milieu dominé par la convection

Le **septième chapitre** est consacré à l'étude de la signature thermique des zones de fractures perméables dans les puits de Rittershoffen. Premièrement, une étude structurale de la fracturation naturelle de la base de la couverture sédimentaire et du socle granitique a été réalisée à partir des imageries de paroi acoustiques. Cette première partie de chapitre se base sur un résumé étendu présenté à la conférence *European Geothermal Congress 2016*. Plusieurs centaines de fractures naturelles continues sur la paroi du puits ont été observées dans les sections ouvertes des forages. La lithologie ne semble pas influencer l'orientation des fractures. Elles sont principalement orientées N10°E à N20°E avec un fort pendage ouest dans le puits GRT-1 et N160°E à N-S avec un fort pendage est ou ouest dans le puits GRT-2. Ces orientations sont similaires à celles observées dans les puits de Soultz. Les joints horizontaux observés au toit du socle granitique sur les carottes de Soultz ne sont pas systématiquement observés sur les imageries acoustiques de Rittershoffen bien que la densité de fractures au toit du socle soit plus élevée que dans le granite profond. Le relevé structural a été corrélé aux profils de températures, aux indications de pertes de boue durant le forage et de venues de gaz afin d'identifier les zones de fractures perméables. Moins de 2% des fractures sont perméables dans le puits GRT-1 et 3% dans le puits GRT-2.

La deuxième partie du chapitre se concentre sur ces zones perméables. Elle est présentée sous forme d'un article publié au *Journal of Geophysical Research.* Une zone de fractures perméables a été intersectée dans le socle granitique du puits GRT-1, tandis qu'aucune fracture perméable n'est observée dans les grès après les opérations de forage. Le puits GRT-2 a recoupé quatre zones de fractures perméables dans le socle granitique et deux zones dans les grès triasiques et permiens. Elles sont toutes associées à une anomalie de température positive ou négative visible sur les profils thermiques à l'équilibre. Elles présentent une organisation asymétrique de la perméabilité avec des fractures ouvertes à l'échelle du puits qui pourraient drainer les circulations au sommet ou à la base de zones altérées poreuses. Le remplissage minéralogique de ces fractures a une influence sur leur degré de perméabilité naturelle. Le puits

GRT-2 semble contrôlé par plusieurs zones de fractures ayant développé une forte densité de fractures ouvertes et un remplissage minéralogique secondaire moins important que GRT-1 ce qui expliquerait sa très bonne connexion au réservoir. La corrélation spatiale des zones de fractures entre les deux puits n'est pas triviale car ils sont séparés par une distance horizontale de plus de 1 km au fond des puits. La modélisation géométrique 3D le long des puits suggère que la trajectoire inclinée de GRT-2 favorise les connexions entre le puits et le réseau de fractures verticales associées à la faille de Rittershoffen.

Le **huitième chapitre** est dédié à la signature argileuse des zones de fractures perméables des puits de Rittershoffen. Une étude pétro-minéralogique préliminaire dans la partie supérieure du toit du socle altéré oxydé dans le puits d'exploration EPS-1 de Soultz est présentée sous forme d'un résumé étendu présenté aux *41st Workshop on Geothermal Reservoir Engineering* de l'Université de Stanford. Les 150 premiers mètres du granite sont associés à une susceptibilité magnétique très faible et une production radiogénique très élevée d'après les mesures sur carottes. Cette zone pourrait donc avoir un fort potentiel géothermique. Cependant, les fractures intersectées ne présentent pas de perméabilité dans cet horizon. Les analyses d'une lame mince d'une fracture scellée ont mis en évidence la présence de veines remplies par du quartz, des carbonates et scellées par de l'illite. L'argilisation des fractures et de leurs épontes pourrait expliquer conjointement l'absence de perméabilité résiduelle au toit du socle dans les puits de Soultz et la forte radioactivité naturelle du toit du socle, contributeur de l'anomalie thermique. Ces travaux ont permis de soulever des questionnements sur le rôle des minéraux argileux dans les zones de fractures perméables dans les puits de Rittershoffen

La deuxième partie se focalise sur les propriétés structurales et chimiques des argiles autour des zones de fractures perméables identifiées dans le septième chapitre. Elle est présentée sous forme d'un article soumis à la revue *Journal of Volcanology and Geothermal Research*. L'étude de la fraction argileuse <5 µm a été réalisée dans une cinquantaine d'échantillons. La présence de minéraux illitiques hétérogènes de type interstratifiés illite-smectite (<10% de smectite) est corrélée aux zones de fractures perméables dans le socle granitique des puits GRT-1 et GRT-2. Elle pourrait être un bon guide pour

prospecter les zones de circulations actuelles et passées. L'abondance de ces minéraux illitiques hétérogènes peut entraîner un colmatage partiel ou total de la zone de fracture et réduire sa perméabilité naturelle. Dans les zones de fractures du puits GRT-2, la chlorite ferreuse est encore observée ce qui suggère une illitisation moins intense des minéraux que dans le puits GRT-1. Cela pourrait expliquer la perméabilité naturelle bien supérieure du puits GRT-2.

L'étude structurale et pétro-minéralogique à l'échelle du puits ont permis de localiser les zones de fractures perméables qui drainent les circulations hydrothermales dans les puits GRT-1 et GRT-2.

Partie 3 : CONCLUSION ET PERSPECTIVES

Le **neuvième chapitre** expose les principales conclusions des chapitres précédents. Les travaux structuraux et minéralogiques dans les puits de Rittershoffen montrent que les zones de fractures qui contrôlent la perméabilité à l'échelle du puits sont localisées dans le socle granitique altéré. Les zones de fractures présentent une organisation asymétrique de la perméabilité avec des fractures ouvertes qui contrôlent les circulations de fluides. Ces fractures ouvertes sont associées à des anomalies de température positives observées sur les profils à l'équilibre tandis que les zones granitiques altérées poreuses sont associées à des anomalies de température négatives. Les circulations de fluides entraînent des altérations hydrothermales à dominante argileuse. Les minéraux illitiques hétérogènes de type interstratifiés illite-smectite sont observés dans toutes les zones de fractures perméables du socle granitique dans les deux puits. Le premier puits GRT-1 recoupe verticalement le réseau de fractures associé à la zone de faille de Rittershoffen. Son comportement hydraulique semble contrôlé principalement par une zone de fractures perméables dans le socle granitique altéré. L'illitisation intense colmate cette zone de fractures perméables et réduit la perméabilité naturelle. Des opérations de stimulation TCH ont été réalisées pour améliorer les connexions existantes entre le puits et le réservoir. Le second puits GRT-2 a une trajectoire parallèle à la faille de Rittershoffen mais le réseau de fractures naturelles associé à la faille a été recoupé plusieurs fois dans les grès et dans le socle granitique. Le comportement hydraulique du puits est contrôlé par plusieurs zones de fractures perméables dont l'illitisation est moins intense

que dans le puits GRT-1. La perméabilité naturelle était suffisante pour l'exploitation industrielle et aucune opération de stimulation n'a été réalisée. Cette étude géologique permet de faire évoluer le concept du puits hydrothermal pour lequel la trajectoire du puits est optimisée en fonction du réseau de fractures naturel afin de ne pas avoir recours à la technologie EGS.

Le **dixième chapitre** discute des perspectives qui pourraient compléter les résultats de ce travail de thèse. Les travaux structuraux de cette thèse sont limités à l'échelle du puits. L'interprétation de la trace de la faille de Rittershoffen avec les données de sismique 2D actuelle est incertaine. La trajectoire du puits GRT-2 recoupe une zone peu imagée en sismique 2D. Le puits pourrait recouper une zone de relai complexe entre deux terminaisons de failles. La réinterprétation des données de sismique 2D et du Profil Sismique Vertical pourrait donner des informations supplémentaires sur la relation entre les puits et la faille de Rittershoffen. Les données de sismique 3D pourraient également imager de façon plus précise les structures perméables au toit du socle. La possibilité que le puits GRT-2 recoupe une structure du type *fracture corridors* avec une perméabilité très grande pourrait être envisagée. Ce type de structure ne présente pas de rejet et ne peut donc pas être observé en sismique 2D. Une campagne de terrain permettrait de faire évoluer les concepts de structures perméables dans le Fossé rhénan. Pour imager le domaine inter-puits, la microsismicité dans le puits GRT-1 semble être un outil prometteur mais devrait être approfondi atour du puits GRT-2. Une corrélation de toutes ces données pourrait mener à un modèle géologique 3D à l'échelle du réservoir.

Pour améliorer la connaissance du système géothermal, les réflexions sur l'altération hydrothermale doivent être approfondies. Les observations des minéraux secondaires suggèrent une superposition de plusieurs évènements hydrothermaux. La datation relative de ces évènements hydrothermaux à partir des échantillons de cuttings est compliquée. Les méthodes actuelles ne permettent pas de séparer les minéraux illitiques des différents évènements. Le modèle géochimique de Rittershoffen doit également être perfectionné. La compréhension du système de cellules de convection pourrait être améliorée par des travaux supplémentaires sur les vitesses de circulations naturelles du fluide géothermal ou sur les équilibres thermiques dans les puits.

Sommaire

Liste des Figures

Liste des Tableaux

Acronymes

4550	Old petroleum well deepened for the Soultz geothermal project
BHTV	BoreHole TeleViewer
DITFs	Drilling Induced Tensile Fractures
EDS	Energy Dispersive X-ray Spectrometry
EGS	Enhanced Geothermal System
EPS-1	Old petroleum wells deepened and cored for the Soultz geothermal project
GPIT	General Purpose Inclinometry Tool
GPK-1, -2, -3, -4	Names of the deep boreholes of the Soultz geothermal project
GR	Gamma Ray
GRT-1, -2	Names of the deep boreholes of the Rittershoffen geothermal project
HDR	Hot Dry Rock
MD	Measured Depth
NP FZ	Newly Permeable Fracture Zone
NPHI	Neutron Porosity
OP FZ	Originally Permeable Fracture Zone
ROP	Rate of Penetration
SEM	Scanning Electron Microscopy
TCH	Thermal, Chemical and Hydraulic
TVD	True Vertical Depth
UBI	Ultrasonic Borehole Image
URG	Upper Rhine Graben
VSP	Vertical Seismic Profile
WOB	Weight on Bit
XRD	X-Ray Diffraction

PARTIE 1 : ÉTAT DE L'ART ET OBJECTIFS DE LA THÈSE

Sommaire de la Partie 1

1 Introduction générale

1.1 Une problématique énergétique corrélée à une problématique climatique

La problématique énergétique est au cœur des politiques de développement économique mondial. La dépendance énergétique en Europe et dans le monde est identifiée depuis la première Guerre mondiale avec des besoins énergétiques qui ne cessent d'augmenter depuis la première Révolution industrielle. La préoccupation de l'épuisement des énergies fossiles est amorcée à la fin du XIXe siècle avec la crise charbonnière puis avec la première crise pétrolière de 1973. De plus, l'utilisation de ces énergies fossiles a entraîné un accroissement considérable des gaz à effet de serre (GES). A la forte croissance de la consommation énergétique mondiale et l'incertitude des politiques énergétiques, s'ajoutent désormais les menaces du changement climatique. Les nations industrialisées et en développement se tourne alors vers les énergies renouvelables qui ont l'avantage de renforcer l'indépendance énergétique tout en limitant les émissions de GES. Parmi elles, l'hydroélectricité, l'énergie éolienne, la biomasse, l'énergie photovoltaïque ou encore la géothermie offrent un approvisionnement en énergie compétitif et peu polluant.

La géothermie, du grec ancien « gê » : Terre et « thermos » : chaleur, puise l'énergie thermique du sous-sol soit pour un usage direct de la chaleur soit pour la production d'électricité. L'Homme utilise la chaleur affleurant naturellement depuis plusieurs millénaires, notamment avec le thermalisme très largement démocratisé dans l'Antiquité. En Europe, la première production électrogène géothermique remonte à 1904 à Larderello (Toscane, Italie). La capacité installée de ce champ atteint 800 MW_e en 2014 [*Bertani*, 2015]. En 2014, en Islande, la géothermie, avec une capacité installée de 650 MW_e, représente la quasi-totalité de la production de chaleur du pays et 1/3 de sa production électrogène [*Bertani*, 2015]. Ces exemples très prometteurs exploitent des contextes magmatiques situés en bordure de plaques tectoniques, présentant un flux géothermique particulièrement élevé et favorable. Cependant, les contextes géologiques en

Europe ne sont pas partout aussi favorables, hormis dans le Bassin pannonien, qui présente des températures élevées à relativement faible profondeur.

1.2 Le développement de la géothermie en France

A partir de 2007, dans ce contexte de prise de conscience mondiale, la France organise des rencontres et des débats réunissant tous les acteurs concernés qui ont conduit aux lois Grenelle 1 et 2 et à la loi relative à la transition énergétique pour la croissance verte (TECV). Adoptée à l'Assemblée nationale en 2014, la loi relative à la TECV envisage une réduction de 40% des GES entre 1990 et 2030 ainsi qu'une part de 32% des énergies renouvelables dans la consommation énergétique d'ici 2030. La France a donc engagé une politique volontariste pour soutenir le développement de la filière géothermie à toutes les échelles avec notamment une simplification du cadre réglementaire pour la géothermie de très basse énergie, des aides à l'investissement, un soutien à la production d'électricité renouvelable, des fonds de garantie géothermie et un soutien à la recherche et à l'innovation en géothermie profonde. Cette loi s'est également concrétisée par un tarif d'achat de l'électricité d'origine géothermale de 0.25€/kWh environ.

Quatre types de géothermie sont observés, de l'échelle domestique à urbaine et industrielle :

- A faible profondeur, la géothermie très basse énergie (température du fluide <30°C) est utilisée à l'échelle domestique pour le chauffage individuel ou la climatisation via un système de pompe à chaleur (Figure 1.1).
- La géothermie basse énergie (température du fluide entre 30°C et 90°C) est utilisée pour le réseau de chauffage urbain, le chauffage de serres, la pisciculture, le thermalisme… (Figure 1.1). Elle concerne des aquifères profonds dans des bassins sédimentaires présentant un gradient géothermique normal. Cette ressource géothermique est exploitée via des forages profonds à 2 km de profondeur dans le Bassin parisien depuis une trentaine d'années et alimente 500 000 logements en 2015.

- La géothermie de moyenne énergie (température comprise entre 90 et 150°C) permet de produire de l'électricité en utilisant la technique du cycle binaire (Figure 1.1). Comme pour la géothermie basse énergie, le fluide géothermal circule dans des formations sédimentaires profondes. Ce type de géothermie est notamment développé dans le Bassin molassique au Sud de l'Allemagne [*Schellschmidt et al.*, 2010].
- La géothermie haute énergie (température supérieure à 150°C) est utilisée pour la production de chaleur et d'électricité à l'échelle industrielle (Figure 1.1). Elle concerne des réservoirs fracturés profonds dans des formations cristallines. Elle est associée à un gradient géothermique anormalement élevé.

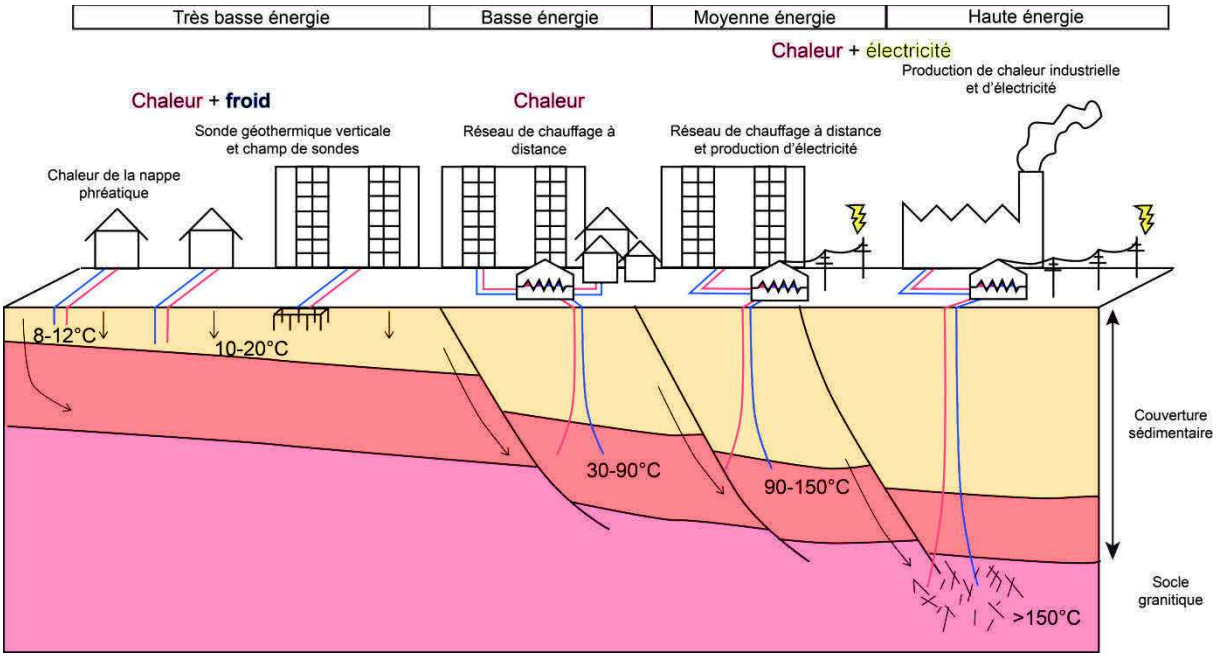

Figure 1.1 Systèmes géothermiques courants de l'échelle domestique à l'échelle urbaine et industrielle (modifié d'après *CREGE c/o CHYN*)

En territoire d'Outre-Mer français, le contexte volcanique est plutôt favorable à la production d'électricité avec des fluides circulant à plus de 250°C dans un réservoir entre 500 et 1000 m de profondeur [*Boissier et al.*, 2010]. La concession de Bouillante sur l'île de la Guadeloupe s'étend sur 24 km^2 et englobe 6 forages profonds et deux centrales produisant 15 MW_e (puissance installée). Un Permis Exclusif de Recherche de 120 km^2 est également en cours de validité dans la région de Vieux-Habitants au Sud-Ouest de l'île de la

Guadeloupe. Un PER est en cours d'instruction également sur l'île de La Réunion (60 km^2).

En métropole, des gradients anormalement élevés (supérieurs à 100°C/km) sont observés dans des bassins d'extension tertiaires (Fossé rhénan, Fossé rhodanien et Fossé de Valence). Cependant l'exploitation industrielle de ces anomalies géothermiques requiert un réservoir fracturé suffisamment perméable pour atteindre des débits suffisants. Le développement de la géothermie en métropole nécessite donc une phase d'exploration conséquente afin de minimiser les risques géologiques. En 2016, 15 PER étaient en cours de validité en France métropolitaine. Ils sont concentrés en Alsace (6), dans les Pyrénées (2), dans le Massif Central (5) et dans la vallée du Rhône (2) et couvrent une superficie totale cumulée de 8750 km^2 (Figure 1.2). Plusieurs autres demandes de PER sont en cours d'instruction ou en demande de prolongation. Ils couvrent une superficie supplémentaire de 2100 km^2.

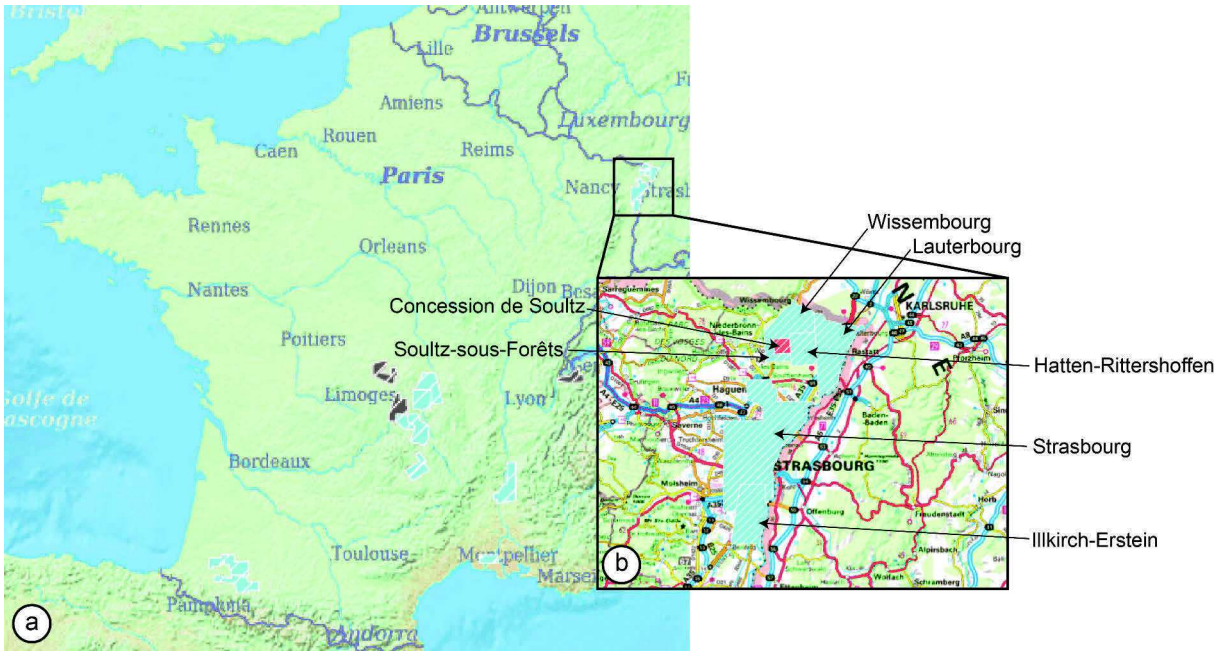

Figure 1.2 Carte des Permis Exclusifs de Recherche en cours d'exploitation (bleu), en cours d'instructions (gris) et concession (rouge) a) en France métropolitaine et b) dans le Bas-Rhin (d'après *Geoportail Minergies*)

On constate donc un réel engouement pour le développement de la géothermie profonde et les objectifs dans le cadre de la loi relative à la TECV sont d'atteindre une puissance installée de 8 MW$_e$ en 2018 et 53 MW$_e$ en 2023.

1.3 L'Alsace, région pionnière en géothermie profonde

Le Fossé rhénan supérieur est marqué par une anomalie géothermique élevée avec des températures proches de 200°C à 5 km de profondeur. A la fin des années 90, sous l'impulsion de la Communauté Européenne et des ministères de l'Energie et de l'Environnement français, allemand et britannique, la mise en œuvre du projet pilote de géothermie profonde à Soultz-sous-Forêts en Alsace avait pour objectif d'exploiter cette anomalie géothermique et de développer un échangeur de chaleur profond [*Gérard and Kappelmeyer*, 1987] (Figure 1.3). Plus de 30 années de recherches par forages profonds jusque dans le granite (3 puits à 5 km et 1 puits à 3,6 km de profondeur et de nombreuses expériences de stimulations et circulations inter-puits, ont révélé un réseau de fractures naturelles dense dans les grès à la base de la couverture sédimentaire mais surtout dans le socle granitique sous-jacent. Dans ce réseau, les circulations d'une saumure entre 150 et 200°C sont à l'origine de l'anomalie géothermique. La perméabilité des zones de fractures et de failles n'étant pas toujours suffisante, la technique Enhanced Geothermal System (EGS) a été développée dans les réservoirs profonds [*Gérard et al.*, 2006]. Basée sur des traitements chimiques et hydrauliques des réservoirs granitiques, elle permet d'augmenter ses capacités hydrauliques de ces derniers. En 2008, la centrale pilote produit les premiers mégawatts (1,5 MW_e). En 2015, le projet évolue vers une exploitation industrielle et la nouvelle centrale est inaugurée en septembre 2016 avec une puissance installée de 1,7 MW_e.

En 2008, le premier projet à vocation industrielle est initié à Rittershoffen, à 8 km de Soultz [*Baujard et al.*, 2017] (Figure 1.3). Ce projet est directement basé sur les expériences et les enseignements tirés du projet pilote de géothermie [*Genter et al.*, 2015]. Les deux forages profonds à 2,5 km de profondeur exploitent la ressource géothermique à plus de 160°C à l'interface entre la couverture sédimentaire et le socle granitique [*Baujard et al.*, 2017]. La centrale avec une puissance installée de 24 MW_{th} est inaugurée en juin 2016 et alimente en chaleur la bioraffinerie Roquette Frères localisée à Beinheim à 15 km.

Du côté allemand du Fossé, de nombreux projets sont également développés à Bruchsal, à Landau et à Insheim (Figure 1.3).

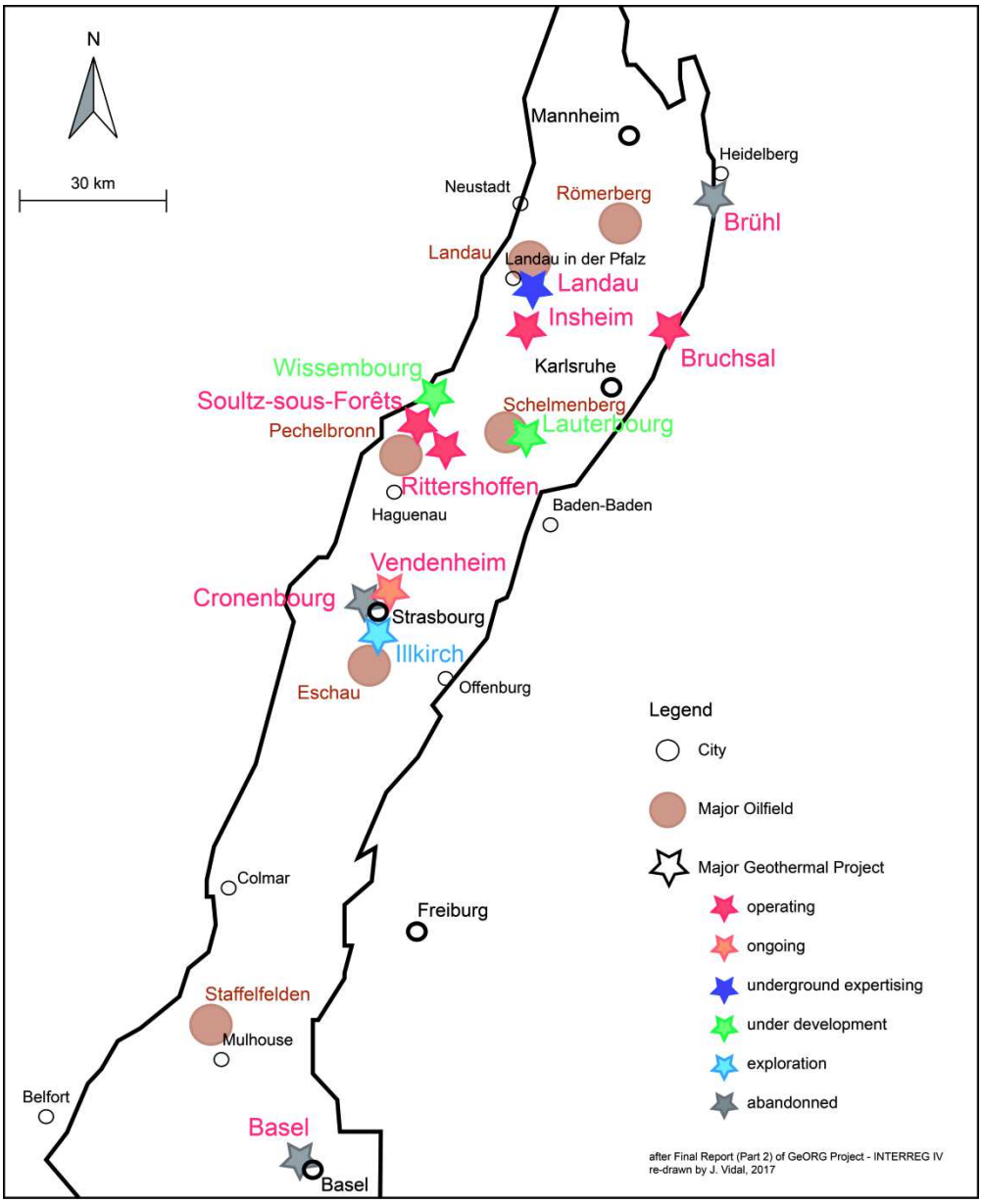

Figure 1.3 Carte des sites de géothermie profonde en exploration, en exploitation, en cours de forage ou abandonnés d'après *Equipe du projet GeORG*, 2013.

L'Alsace est donc une région très attractive pour le développement de la géothermie. En plus de la concession de Soultz de 24 km^2, six PER soit 1250 km^2 répartis entre cinq acteurs principaux (Tableau 1.1). De nombreux projets sont en cours d'exploration ou de développement dans le Nord de l'Alsace (Wissembourg et Lauterbourg) (Figure 1.2). La phase de forage du projet de Vendenheim a démarré en 2017. Le projet d'Illkirch au Sud de Strasbourg est prévu pour 2018.

Tableau 1.1 Surface, pétitionnaires et date de validité des Permis Exclusifs de Recherche et Concessions dans le département Bas-Rhin en juin 2017. La date de validité des PER de Lauterbourg et Wissembourg lors de l'instruction pour prolongation.

Nom	Type	Pétitionnaire(s)	Superficie (km^2)	Date de validité
Soultz-sous-Forêts	Concession	GEIE (Exploitation Minière de la Chaleur)	23	
Soultz-sous-Forêts	PER	GEIE (Exploitation Minière de la Chaleur)	56	05/10/2017
Hatten-Rittershoffen	PER	Electricité de Strasbourg, Roquette Frères	79	23/06/2020
Lauterbourg	PER	Electricité de Strasbourg, Geopetrol	213	03/12/2016
Wissembourg	PER	Electricité de Strasbourg	116	03/12/2016
Strasbourg	PER	Fonroche	575	23/06/2018
Illkitch-Erstein	PER	Electricité de Strasbourg	170	23/06/2018

Malgré les résultats très prometteurs à Soultz, à Rittershoffen, et en Allemagne, le développement des futurs réservoirs géothermiques profonds dans le Fossé rhénan supérieur n'en reste pas moins incertain. Le principal frein à ce développement reste les coûts importants des forages et les risques géologiques associés à l'incertitude de la phase d'exploration du sous-sol. Les opérations de stimulations sont susceptibles de générer une microsismicité induite ou d'utiliser des traitements chimiques. La composante environnementale est donc à prendre en considération pour le développement et l'acceptabilité de ce type de projet. Il est donc nécessaire de mieux connaître le fonctionnement des réservoirs fracturés profonds. Cette thèse s'inscrit directement dans la problématique d'amélioration des connaissances du réseau de fractures naturelles et des circulations hydrothermales associées à l'interface de la couverture sédimentaire et du socle granitique altéré du Fossé rhénan supérieur.

2 Présentation de la zone d'étude

2.1 Le Fossé rhénan supérieur

Le site de Rittershoffen se situe dans le Fossé rhénan supérieur, appartenant au système de rifts ouest européens, également appelé ECRIS (European Cenozoic Rift System) formé à l'âge cénozoïque [*Ziegler*, 1992] (Figure 2.1). Le Fossé rhénan supérieur s'étend sur 300 km de longueur, de Bâle (Suisse) au Sud à Mayence (Allemagne) au Nord selon un alignement SSW-NNE et sur 30 à 40 km de largeur [*Illies*, 1965] (Figure 2.2).

Les bordures orientales et occidentales du Fossé rhénan supérieur ont un comportement symétrique en termes d'orientation et de hauteur. Au Sud, la bordure occidentale du bassin est formée par le massif cristallin paléozoïque des Vosges et la bordure orientale par le massif cristallin paléozoïque de la Forêt Noire. Au Nord, la bordure occidentale est formée par les séries sédimentaires mésozoïques des Vosges du Nord et du Pfälzerwald et la bordure orientale par le massif cristallin paléozoïque de l'Odenwald. Les massifs nord et sud sont séparés par la dépression de Kraichgau.

Cependant cette symétrie n'est pas observée pour le remplissage sédimentaire. Au Nord de Strasbourg, le remplissage est plus épais à l'Est du Fossé (Figure 2.3) tandis qu'au Sud, l'inverse est observé. L'interprétation des profils sismiques de *Brun et al.*[1992] montre une asymétrie de la structure profonde également avec la présence de zones de cisaillement le long de failles listriques coïncidant avec une zone de détachement horizontale dans la croûte inférieure ductile (Figure 2.3). Pour *Brun et al.* [1992], la structure et le remplissage du Fossé rhénan supérieur sont contrôlés par la Faille rhénane occidentale. La bordure occidentale, est marquée par la Faille rhénane occidentale et la Faille vosgienne [*Illies*, 1972; *Sittler*, 1992]. Ces deux failles bordières encadrent le champ de fractures occidental, situé au pied du Massif vosgien. Sur la bordure orientale, la Faille schwartzwaldienne et la Faille rhénane orientale séparent le champ de fractures oriental du massif bordier d'un côté et de la plaine du Rhin de l'autre (Figure 2.2).

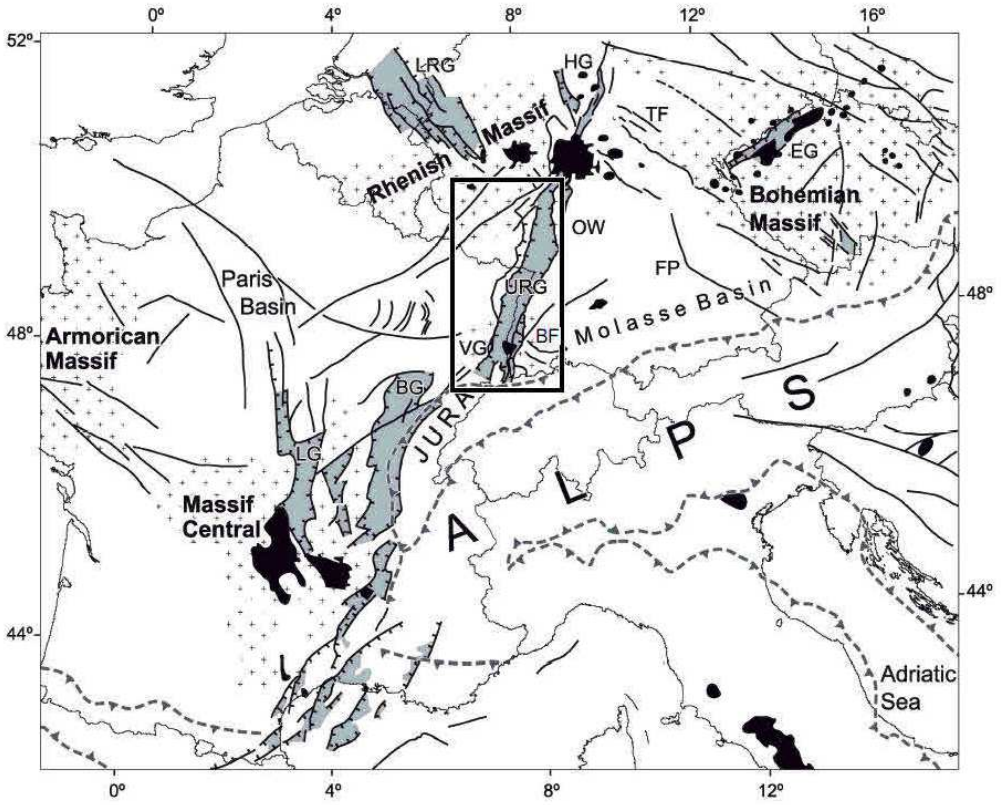

Figure 2.1 Carte du système de rifts européens d'après *Dèzes et al.* [2004] Le cadre noir représente la carte Figure 2.2. Les lignes noires représentent le système de failles cénozoïques, la couleur grise symbolise les bassins sédimentaires, la couleur noire symbolise le volcanisme, le figuré croix symbolise le socle et la ligne pointillée grise représente le front de la poussée alpine. BF = Black Forest, BG = Bresse Graben, EG = Eger (Ohre) Graben, FP = Franconian platform, HG = Hessian Graben, LG = Limagne Graben, LRG = Lower Rhine Graben, URG = Upper Rhine Graben, OW = Odenwald, VG = Vosges

Le site de Rittershoffen est localisé à 15 km de la Faille rhénane occidentale, à une latitude où la faille est orientée N45°E (Figure 2.3). Le socle paléozoïque est situé à 2.2 km en dessous de la couche sédimentaire. La base de la couverture sédimentaire et le socle présente une fracturation intense qui est le résultat d'une histoire tectonique multiphasée complexe dans le Fossé rhénan supérieur. L'exploitation géothermique des réservoirs gréseux et granitique dépend directement de cette fracturation.

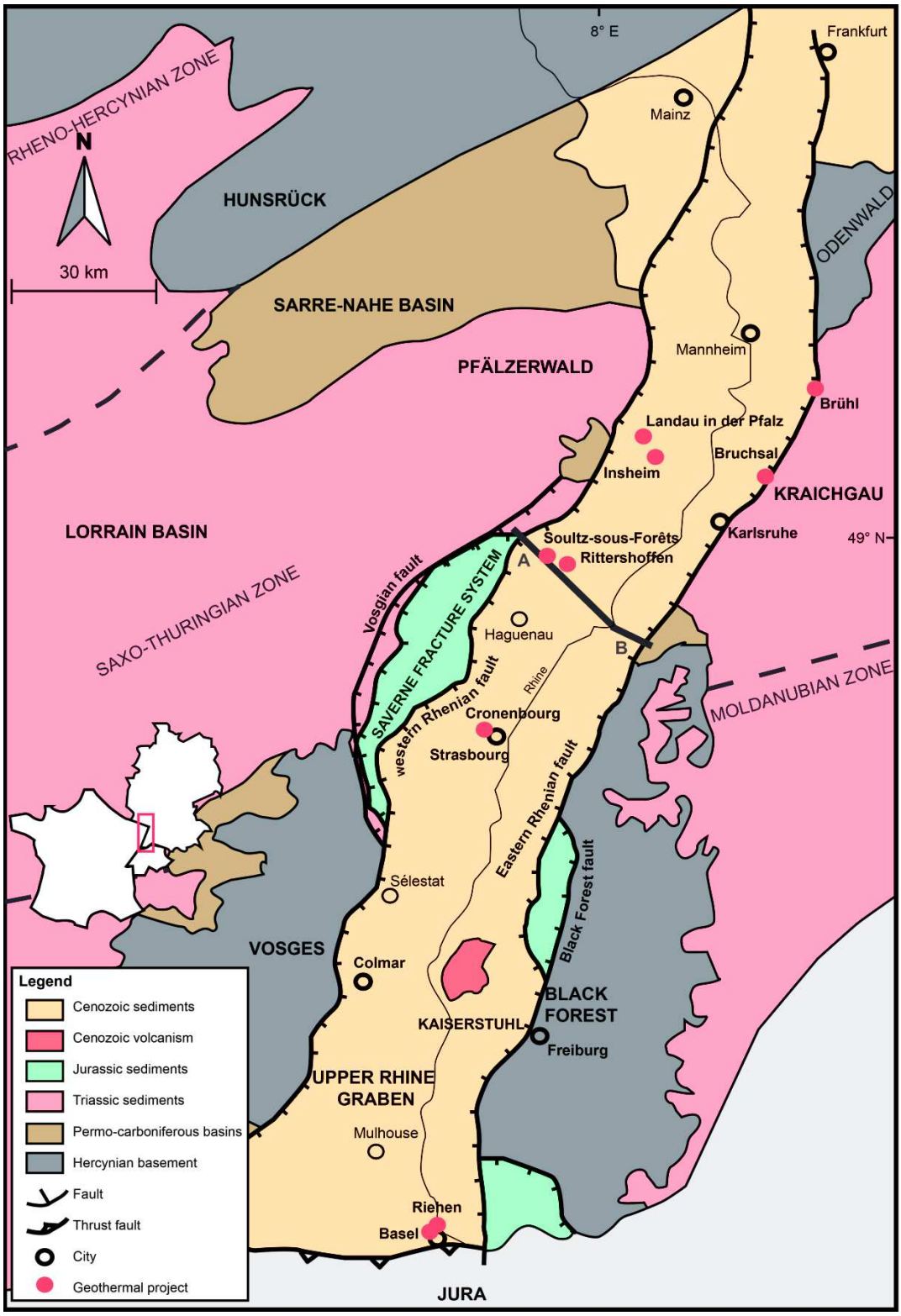

Figure 2.2 Carte du Fossé rhénan supérieur d'après *Dezayes* [1995]. La section AB représente la trace de la coupe Figure 2.3

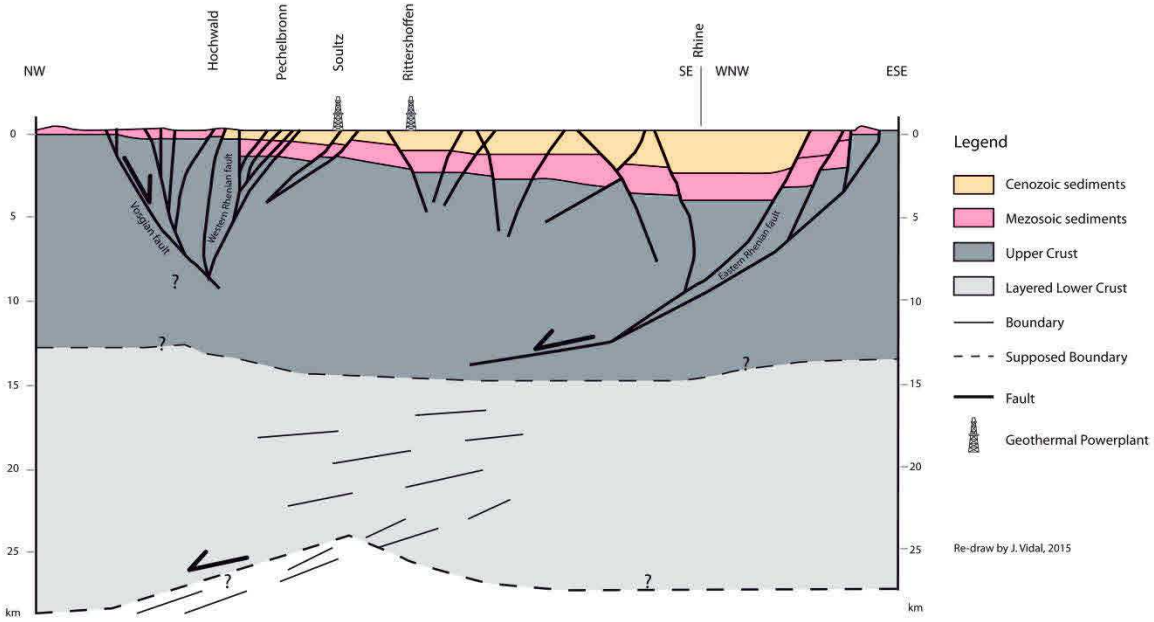

Figure 2.3 Coupe géologique à travers le Fossé rhénan à la latitude de Soultz d'après *Kappelmeyer et al.* [1992]. La localisation de la coupe est représentée sur la Figure 2.2. L'interprétation de la croute profonde est faite à partir des études de *Brun et al.* [1992] et est très schématique.

2.2 Evolution géodynamique du Fossé rhénan supérieur du Paléozoïque à l'Actuel

La structuration du Fossé rhénan supérieur est directement liée à l'orogenèse varisque puis alpine. L'histoire tectonique du Fossé rhénan supérieur est largement décrite dans la littérature. Dans cette section, l'histoire tectonique régionale sera résumée en s'appuyant sur les observations faites dans les massifs des Vosges et de l'Odenwald mais également en périphérie du Fossé rhénan, dans les bassins de Lorraine et de la Sarre d'après les travaux *Schneider* [1984], *Bergerat*, [1985], *Villemin* [1986], *Krohe and Willner* [1995] et *Schumacher* [2002]. Sur la base d'une caractérisation géophysique, ces régions n'appartiennent pas forcément à la même unité tectonique que Rittershoffen. Dans la section suivante, elle sera comparée aux observations faites dans les forages profonds de Soultz d'après les travaux de *Genter* [1989] et complétés par *Dezayes* [1995] et *Valley* [2007].

2.2.1 Cycle varisque

Le socle du Fossé rhénan supérieur résulte de la subduction et de la collision de trois microcontinents orientés ENE-WSW à NE-SW : le domaine Rhénohercynien, le domaine Saxothuringien et le domaine Moldanubien [*Matte*, 1986; *Franke*, 2000; *Matte*, 2001; *Edel and Schulmann*, 2009] (Figure 2.4). Les limites entre ces trois domaines sont des chevauchements ou des sutures [*Franke*, 2000; *Edel and Schulmann*, 2009].

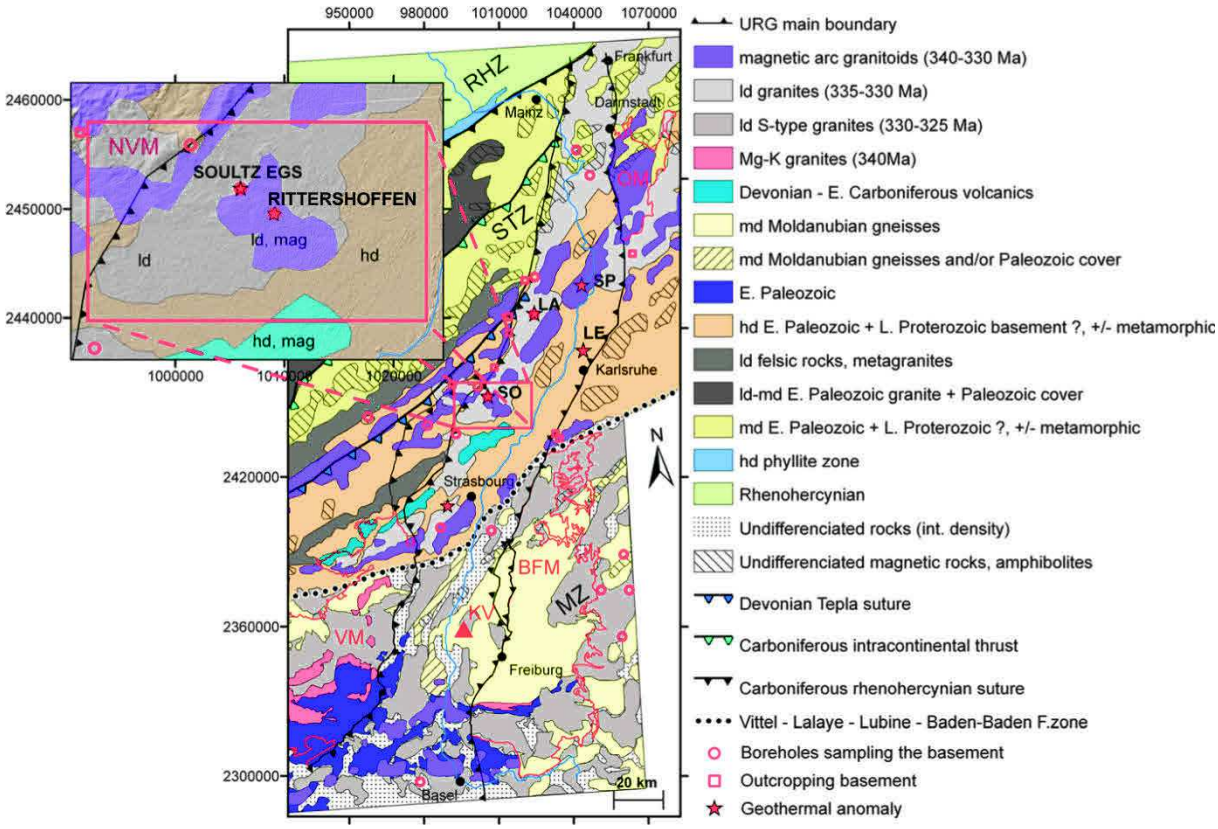

Figure 2.4 Carte des principales unités et discontinuités géologiques sous la couverture du Carbonifère supérieur-Permien d'après les interprétations des données magnétiques et gravimétriques de *Edel and Schulmann* [2009] et *Baillieux et al.* [2014]. Hd = Densité élevée, md = densité moyenne, ld = densité faible, RHS = suture rhénohercynienne, MoS = suture de Morhange, TS = suture de Tepla, LLF = faille de Lalaye-Lubine, BBF = faille de Baden-Baden, URSZ = zone cisaillante du Rhin supérieur, SSF = Soultz-sous-Forêts.

Par exemple la suture de Tepla, au Nord du site de Rittershoffen, correspondrait à la subduction du domaine Saxothuringien durant le Dévonien [*Schulmann et al.*, 2009] et les failles de Lalaye-Lubine et de Baden-Baden seraient une relique

de la subduction du domaine Saxothuringien sous le Moldanubien [*Franke*, 2000]. C'est dans ce contexte de subduction que les arcs magmatiques se mettent en place entre 340 et 330 Ma selon la direction NE-SW [*Altherr et al.*, 1999, 2000]. Les anomalies magnétiques de ces intrusions granitiques sont observées dans les Vosges du Nord et dans l'Odenwald sous les sédiments [*Edel and Schulmann*, 2009]. Des corps granitiques sont mis en place dans des zones de faiblesse orientées NNE-SSW à NE-SW jusque dans le Permien [*Lagarde et al.*, 1992].

Les domaines océanisés auraient totalement disparus au Viséen. La structuration de la chaîne varisque commence lors de la phase principale d'orogenèse, appelée phase Sudète, une compression N-S est à l'origine de la formation de failles de décrochement sénestres NE-SW et dextres NW-SE observées dans les Vosges centrales [*Schneider*, 1984] (Figure 2.5). Au Nord, dans le massif de l'Odenwald, un cisaillement sénestre NE-SW est probablement suivi par une phase d'extension NNE-SSW [*Schneider*, 1984; *Krohe and Willner*, 1995]. L'extension est également observée dans les bassins de Lorraine et de Sarre avec un réseau de failles normales N110° à N140°. Le rejeu de ce réseau de failles se poursuit jusqu'au Permien où la relaxation de l'orogène s'intensifie. La phase de compression finale, appelée la phase Saalique, est marquée par des chevauchement NE-SW associés à des failles décrochantes sénestres NW-SE et dextres E-W [*Burg et al.*, 1994]. La fin du Permien est associée à des extensions N-S à NNE-SSW qui entraîne la formation de bassins qui s'individualisent le long des failles orientées NE-SW à ENE-WSW [*Villemin*, 1986; *Schumacher*, 2002; *Ziegler et al.*, 2006]**.** Ils présentent un remplissage sédimentaire essentiellement clastique et proximal en raison de l'érosion des reliefs qui subissent une altération supergène [*McCann et al.*, 2006].

Figure 2.5 (page suivante) Synthèse des phases tectoniques modifiée d'après *Genter* [1989]. Les données des bassins de Lorraine, de Sarre, de l'ouest du graben sont issues de *Bergerat* [1985] et *Villeminn* [1986]. Celles des Vosges centrales et sud sont issues de *Schneider* [1984] et celles de l'Odenwald sont issues de *Krohe et Willner* [1995]. Les failles normales sont en bleu, les failles décrochantes sénestres en rouge et dextres en vert. Les familles de fractures du socle granitique de Soultz sont d'après *Valley* [2007].

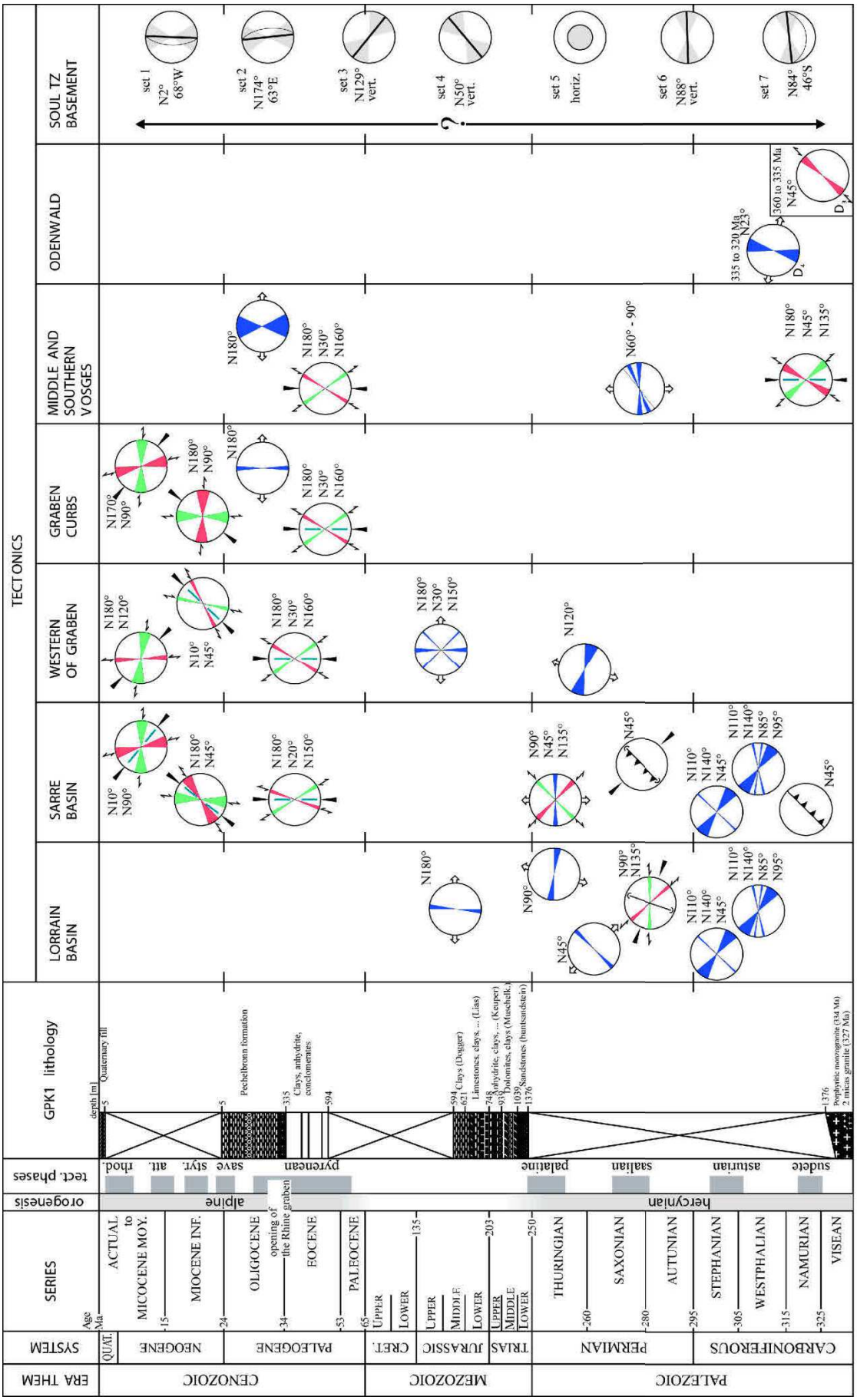
TECTONICS
SOUL TZ BASEMENT
ODENWALD
MIDDLE AND SOUTHERN VOSGES
GRABEN CURBS
WESTERN OF GRABEN
SARRE BASIN
LORRAIN BASIN
GPK1 lithology
tect. phases
orogenesis
SERIES
SYSTEM
ERA THEM
CENOZOIC
MESOZOIC
PALEZOIC
NEOGENE
PALEOGENE
CRET.
JURASSIC
TRIAS
PERMIAN
CARBONIFEROUS
QUAT.
ACTUAL to MIOCENE MOY.
MIOCENE INF.
OLIGOCENE
EOCENE
PALEOCENE
UPPER
LOWER
MIDDLE
THURINGIAN
SAXONIAN
AUTUNIAN
STEPHANIAN
WESTPHALIAN
NAMURIAN
VISEAN
alpine
hercynian
thod.
att.
styr.
save
pyrenean
palatine
saalian
asturian
sudete
set 1 N2° 68°W
set 2 N174° 63°E
set 3 N129° vert.
set 4 N50° vert.
set 5 horiz.
set 6 N88° vert.
set 7 N84° 46°S
335 to 320 Ma N23°
360 to 335 Ma N45°
Quaternary fill
Pechelbronn formation
Clays, anhydrite, conclomerates
Clays (Dogger)
Limestones, clays, ... (Lias)
Anhydrite, clays, ... (Keuper)
Dolomites, clays (Muschelk.)
Sandstones (buntsandstein)
Porphyritic monzogranite (334 Ma)
2 micas granite (327 Ma)

2.2.2 Evolution mésozoïque

A la fin du Trias et jusqu'au Jurassique, une extension E-W affecte le bassin de Lorraine et la périphérie ouest du Fossé [*Villemin*, 1986]. Les séries mésozoïques (Trias et Jurassique) remplissent en discordance les séries permo-carbonifères de manière homogène en faciès et en épaisseur. La paléogéographie et les séries sédimentaires triasiques sont décrites par *Sittler* [1985]. Au Trias inférieur, les séries gréseuses du Buntsandstein se déposent dans un vaste contexte fluviatile (Buntsandstein inférieur) qui évolue vers un contexte fluvio-marin avec l'apparition de mers peu profondes (Buntsandstein supérieur) annonçant la transgression marine du Muschelkalk. Les séries calcaires du Muschelkalk inférieur et supérieur sont formées par des dépôts marins et encadrent les dépôts évaporitiques du Muschelkalk moyen. Au Keuper, les connexions marines dans le Fossé rhénan sont progressivement fermées, conduisant à la mise en place de milieu lagunaire associé à des dépôts évaporitiques.

A la fin du Jurassique, la surrection du Fossé débuterait suite au phénomène de flambage lithosphérique [*Bourgeois et al.*, 2007] et/ou de panache mantellique directement lié à la poussée alpine [*Illies*, 1975; *Ziegler*, 1994; *Bourgeois et al.*, 2007]. Elle entraîne l'émersion et l'érosion des formations jurassiques supérieures qui sont affectées par une karstification et dont les produits de l'altération se retrouvent dans les formations sédimentaires de l'Eocène [*Sittler*, 1985; *Berger et al.*, 2005a, 2005b]. Cette surface d'érosion des sédiments mésozoïques est marquée par des flexures NE-SW et ENE-WSW, de longueur d'onde déca-kilométrique et d'amplitude diminuant vers le Nord, associées à la poussée alpine [*Sittler*, 1985; *Schumacher*, 2002]. Les séries du Crétacé ne sont pas observées dans le Fossé rhénan [*Sittler*, 1985]. Les hypothèses de la lacune de sédimentation ou de leur érosion sont encore discutées.

2.2.3 Rifting cénozoïque

L'évolution du Fossé rhénan supérieur au Cénozoïque est aujourd'hui encore controversée. *Illies* [1965] propose un modèle en deux étapes avec un régime de contrainte extensif stable. Ce modèle est complété par *Behrmann et al.* [2003] et *Lopes Cardozo and Behrmann* [2006].

Bergerat [1985], *Villemin* [1986] et *Villemin and Bergerat* [1987] ont proposé une évolution plus réaliste en quatre étapes associées à des régimes de contraintes successifs d'après l'analyse des tectoglyphes sur les plans de failles (Figure 2.6). Ce modèle est complété par des données tectono-stratigraphiques par *Schumacher* [2002] qui met en avant l'importance de la réactivation des structures varisques préexistantes (Figure 2.7). Dans cette section, seules les formations sédimentaires du Nord du Fossé rhénan supérieur seront décrites.

- À l'Eocène inférieur, la compression N-S influencée par les poussées alpine et pyrénéenne réactivent les structures héritées ENE-WSW et NNE-SSW qui jouent un rôle primordial dans l'initiation de la phase de rifiting [*Villemin and Bergerat*, 1987; *Ziegler*, 1992; *Schumacher*, 2002; *Dèzes et al.*, 2004]. L'initiation de la phase de rifting entraîne la formation de bassins lacustres isolés alignés selon l'axe du futur Fossé rhénan, et dans lesquels se déposent les formations fluviatiles et lacustres en discordance sur les formations mésozoïques (Figure 2.6a, Figure 2.7a).
- De l'Eocène supérieur (Priabonien) à l'Oligocène inférieur (Rupélien), la phase principale de rifting est dominée par une extension E-W chez *Villemin et Bergerat* [1987] (Figure 2.6b). Chez *Schumacher* [2002], le Priabonien est marqué par une rotation de la compression NNE-SSW et la formation de deux sous-bassins principaux de type pull-apart oblique à l'axe du futur Fossé sous l'influence de la réactivation sénestre de bassins permo-carbonifères (Figure 2.7a). Les dépôts marneux et évaporitiques (Formation de la Zone Dolomitique) témoignent de la connexion entre le bassin et le milieu marin péri-alpin [*Sittler*, 1965; *Sissingh*, 1998]. Puis le Rupélien, une extension ESE-WNW domine tandis que les deux sous-bassins principaux fusionnent à l'ouest le long de la faille bordière occidentale. La zone de faille de Lalaye-Lubine-Baden-Baden joue le rôle de transfert sénestre entre les deux sous-bassins [*Brun et al.*, 1992; *Chorowicz and Deffontaines*, 1993]. L'activité des failles normales N-S à NNE-SSW permet le dépôt des sédiments avec dans le sous-bassin nord, la formation des séries pétrolifères de Pechelbronn (Figure 2.7b). Au Rupélien supérieur le dépocentre principal commence à se former dans le segment central (Figure 2.7c). Cette phase d'extension n'est pas

observée, dans le bassin de Sarre ou en périphérie ouest du Fossé rhénan supérieur.

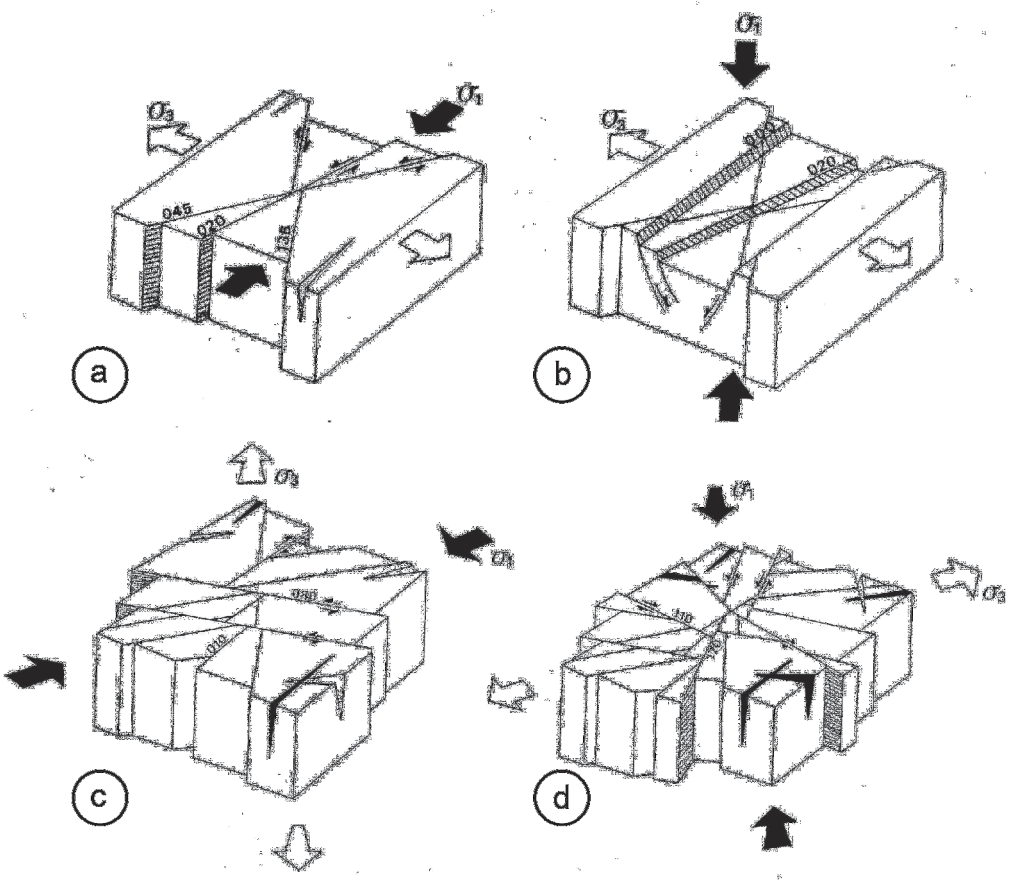

Figure 2.6 Permutation des axes des contraintes et déformation associée durant le rifting Cénozoïque du Fossé rhénan supérieur a) compression N-S à l'Eocène, b) extension E-W à l'Oligocène, c) compression NE-SW, d) compression NW-SE d'après *Villemin and Bergerat* [1987]

- À l'Oligocène supérieur (Chattien), la compression NE-SW est attribuée à la réactivation du système de failles bordières selon un mouvement cisaillant dextre [*Villemin and Bergerat*, 1987; *Schumacher*, 2002] (Figure 2.6c, Figure 2.7d). Les connexions marines sont interrompues comme en témoignent les dépôts fluvio-lacustres (Couches de Niederroedern). Cette compression NE-SW est également observée en bordure du Fossé et dans le bassin de Sarre [*Villemin and Bergerat*, 1987].
- Au Miocène inférieur, une compression orientée NW-SE s'installe, influencée par la poussée pyrénéenne (Figure 2.6d, Figure 2.7e) [*Villemin and Bergerat*, 1987; *Schumacher*, 2002; *Michon and Merle*, 2005]. Le

Fossé devient une zone de cisaillement [*Bergerat*, 1985; *Lopes Cardozo and Behrmann*, 2006; *Rotstein and Schaming*, 2008]. Ce changement de régime de contraintes s'accompagne d'un soulèvement du Sud du Fossé déjà mis en évidence par *Illies and Greiner* [1979] ainsi que de l'activité volcanique du Kaiserstuhl [*Sittler*, 1985]. Un dépocentre principal se distingue au Nord du Fossé et semble contrôlé par la faille bordière occidentale. Les formations au Nord du Fossé témoignent d'une sédimentation marine qui indique une connexion avec le bassin de la Mer du Nord se retirant progressivement [*Bergerat*, 1985; *Berger et al.*, 2005a]. La surrection des massifs cristallins liée à la poussée alpine entraîne un aplanissement érosif des épaules du rift et donc un apport significatif de produits d'érosion venant des Vosges et de la Forêt Noire au Miocène moyen [*Sittler*, 1985; *Berger et al.*, 2005a]. Au Quaternaire, le régime des contraintes est inchangé et le Fossé rhénan supérieur est toujours une structure cisaillante sénestre avec deux sous-bassins de type pull-appart séparés par le segment central surélevé [*Illies*, 1977; *Villemin and Bergerat*, 1987; *Schumacher*, 2002]. Le dépocentre nord est asymétrique et contrôlé par la faille bordière occidentale orientée N-S tandis que le dépocentre sud est orienté Nord à NNW dans un sous-bassin orienté NNE [*Schumacher*, 2002] (Figure 2.7f).

Le Fossé rhénan est actuellement encore régit par la poussée alpine avec une contrainte maximale horizontale orientée N150°E [*Baumann*, 1981]. Les mécanismes au foyer des séismes les plus forts indiquent des mouvements décrochants le long de failles N-S et NE-SW formées au cours des évènements varisques et tertiaires [*Edel et al.*, 2006]

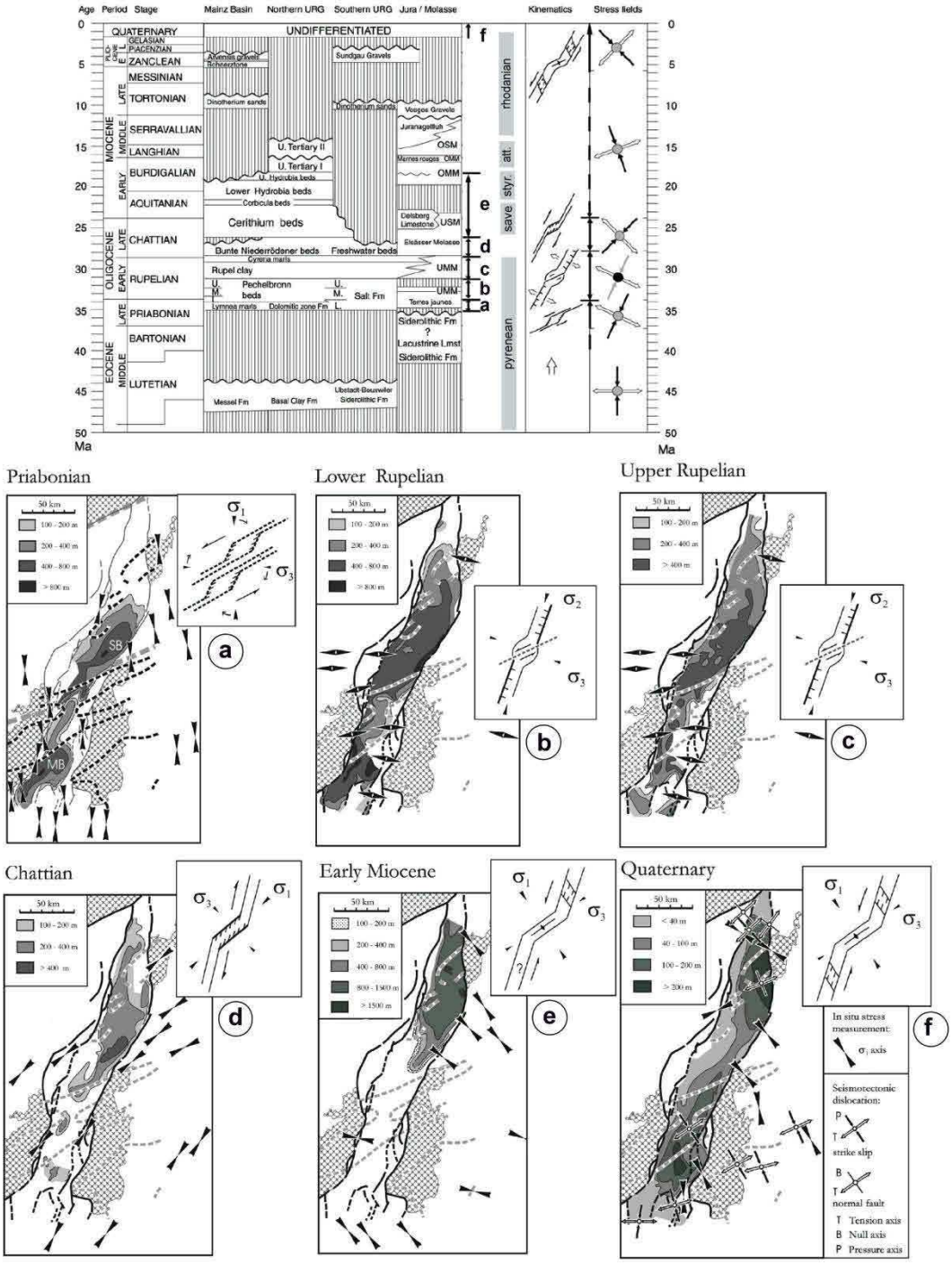

Figure 2.7 Evolution du Fossé rhénan au Cénozoïque. Le diagramme du haut représente la stratigraphie des sédiments cénozoïques dans le Fossé rhénan et les régions voisines. Pour les champs de contraintes, noir = contrainte maximale, gris = contrainte intermédiaire et blanc = contrainte minimale. Les cartes a) b), c), d), e), f) représentent les paléo-contraintes, l'activation des failles et les remplissages sédimentaires d'après *Schumacher* [2002].

2.2.4 Récapitulatif sur la structuration régionale

Trois directions structurales principales sont observées dans le Fossé rhénan supérieur (Figure 2.8) ;

- La direction ENE-WSW à NE-SW, dite Erzebirgienne, qui correspond aux sutures varisques lors de l'accrétion de continents et microcontinents. Elle est activée en décrochement sénestre au Carbonifère. Le plutonisme varisque et la formations de bassins au Permien se font dans une direction NE-SW et ENE-WSW à NE-SW. C'est également la direction des flexures de grande longueur d'onde à la surface des sédiments mésozoïques. Enfin, ces structures sont réactivées en décrochement lors de la poussée alpine.
- La direction NNE-SSW, dite Rhénane, qui comme la direction Erzebirgienne est activée en décrochement au Carbonifère. Des failles NNE-SSW et N-S jouent également un rôle d'accommodation lors de l'extension tertiaire.
- La direction NW-SE accomode des décrochements dextres lors de l'évolution tardi-varisque puis lors de la poussée alpine.

2.3 Etat des connaissances sur les réservoirs fracturés d'après les puits de Soultz-sous-Forêts

La caractérisation des réservoirs fracturés à Soultz-sous-Forêts s'appuie sur 5 forages profonds. Un ancien puits pétrolier, renommé EPS-1, a été approfondi jusqu'à 2,2 km de profondeur dans le socle granitique. Lors de cet approfondissement, le puits a été entièrement carotté sur une longueur de presque 1300 m, comprenant les sédiments du Muschelkalk, du Buntsandstein, du Permien et le socle granitique altéré. Un autre ancien puits pétrolier, nommé 4550, a été approfondi jusqu'à 1.5 km de profondeur. Le forage d'exploration, GPK-1 a été foré jusqu'à 3,6 km de profondeur. Les trois forages profonds, GPK-2, -3 et GPK-4 ont atteint une profondeur de 5 km.

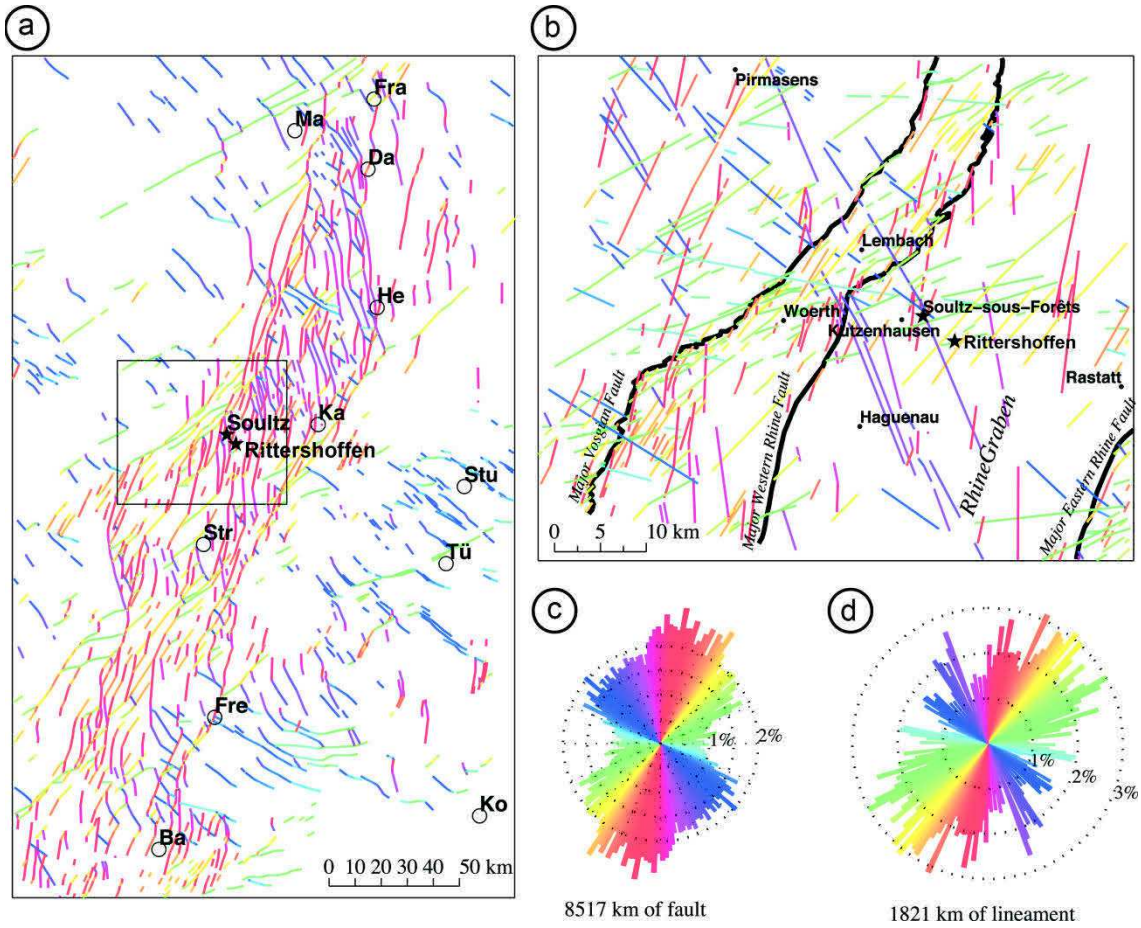

Figure 2.8 Compilation de failles et de linéaments (d'après Valley 2007). La couleur des segments correspond à l'orientation de leur azimuth a) Carte des failles dans le Fossé rhénan supérieur. Les failles bordières sont d'après *Illies* [1972] et les failles dans le Fossé sont d'après *Illies and Greiner* [1979]. (c). Le cadre noir correspond à la carte (b). Ba: Basel; Da: Darmstadt; Fra: Frankfurt; Fre: Freiburg; He: Heildelberg; Ka: Karlsruhe; Ko: Konstanz; Ma: Mainz; Str: Strasbourg; Stu: Stuttgart; Tu: Tubingen. b) Carte des linéaments sur image satellite d'après *Genter* [1989]. c) Rosace avec les azimuts des failles de la carte (a) pondérés par leur longueur d) Rosace avec les azimuts des linéaments de la carte (a) pondérés par leur longueur.

2.3.1 Le socle granitique

A Soultz-sous-Forêts, deux granites ont été recoupés par les forages profonds ; un monzogranite porphyroïde daté à 334.0+3.8/3.5 Ma et un granite à deux micas plus jeune daté à 327+/-7 Ma [*Stussi et al.*, 2002; *Cocherie et al.*, 2004]. Le monzogranite est un granite mélanocrate avec une couleur sombre en raison de

la présence de biotite tandis que le granite à 2 micas est un granite leucocrate avec une couleur claire. Ces deux âges qui correspondent au Viséen montrent que les granites sont mis en place avant la phase sudète et sont donc affectés par la fracturation naturelle décrite dans la section précédente. La cristallisation du monzogranite porphyroïde se fait probablement en deux temps avec une cristallisation profonde à 12 km (350 MPa et 755 à 790°C) et une à plus faible profondeur à 5 km de profondeur environ (150 MPa et 655 à 715°C) [*Stussi et al.*, 2002]. La fabrique cristallographique du monzogranite porphyroïde montre une élongation NE des biotites et des feldspaths parallèlement à l'élongation NE du pluton lors de sa remontée [*Schulmann et al.*, 1997]. Ces stades précoces de refroidissement sont associés à une altération pervasive sur l'ensembe du socle granitique. Cette altération est marquée par une modification des minéraux primaires, plagioclases et biotites, et par la précipitation d'épidote, de chlorite ferromagnésienne et de séricite.

La partie supérieure du socle granitique (150 premiers mètres) est affectée par une altération supergène ou rubéfaction liée à la surrection du socle au Permo-Trias [*Genter and Traineau*, 1996; *Hooijkaas et al.*, 2006]. Elle est affectée par des fractures sub-horizontales à remplissage d'oxydes [*Genter and Traineau*, 1996]. Ces fractures sont interprétées comme des joints de relaxation lors de la surrection par *Genter and Traineau* [1996]. *Wyns* [2012] interprète ce profil d'altération comme un profil latéritique avec une arène très altérée (50 m) au sommet d'un horizon marqué par une importante fissuration à dominante horizontale (100 m). Cet horizon connait un colmatage important suite aux circulations de fluides hydrothermaux lors de l'enfouissement.

Dans le puits EPS-1, le relevé structural a permis de reconstituer l'histoire tectonique tertiaire du socle granitique (Figure 2.9). Les failles et les stries observées par *Dezayes* [1995] sur les carottes de 1400 m à 2200 m de profondeur ont révélé quatre grandes phases :

- Une compression orientée N20°E qui activent des failles décrochantes orientées N50°E avec un fort pendage NW à N150°E avec un fort pendage est. Cette phase est probablement associée à la compression N-S à la fin de l'Eocène décrite par *Villemin and Bergerat* [1987].

- Une extension orientée N95°E qui activent des failles N-S avec un pendage de 60° à 70° à l'est ou à l'ouest. Cette phase est probablement associée à l'extension E-W à l'Oligocène décrite par *Villemin and Bergerat* [1987].

- Une compression N70°E qui activent des failles décrochantes dextres orientées NNE-SSW et sénestres orientées ENE-WSW. Cette phase est probablement associée à la compression NE-SW au début du Miocène décrite par *Villemin and Bergerat* [1987].

- Une compression N122°E qui active des failles décrochantes N-S dextres avec un fort pendage et E-W sénestres avec un pendage nord. Cette phase est probablement associée à la compression NW-SE à la fin du Miocène décrite par *Villemin and Bergerat* [1987].

Les observations structurales du réseau de fractures naturelles ont été étendues dans le socle granitique de tous les puits de Soultz à partir de carottes ou d'imageries de paroi selon les puits (Figure 2.10). Dans la partie supérieure du socle granitique, la densité de fracture est très élevée dans les puits EPS-1 et GPK-1 à élevée dans GPK-3 et GPK-4. En profondeur, la densité de fracture diminue dans GPK-3 et GPK-4 et devient faible sous 4600 m MD dans le granite à deux micas.

Le puits GPK-2 présente lui une très forte densité de fracture dans le granite porphyroïde avec altération hydrothermale. L'orientation des fractures naturelles est relativement homogène dans les puits de Soultz avec une famille de fracture prépondérante N-S +/-02° et un fort pendage. Elles sont associées aux failles normales qui ont accommodé l'extension Oligocène du Fossé. Elles sont essentiellement observées dans le granite porphyroïde à altération hydrothermale. D'autres familles NW-SE et NE-SW sont également observées plutôt dans le granite peu altéré et sont associées à l'évolution tardivarisque du socle granitique [*Genter and Traineau*, 1996; *Valley*, 2007]. Une famille E-W moins bien exprimée est également observée dans les puits. L'analyse des fractures induites à l'échelle des puits a montré une contrainte horizontale maximale principalement orientée N170°E et non NW-SE comme l'orientation

régionale [*Cornet et al.*, 2007; *Valley and Evans*, 2007]. Cette orientation est favorable à l'activation des fractures N-S.

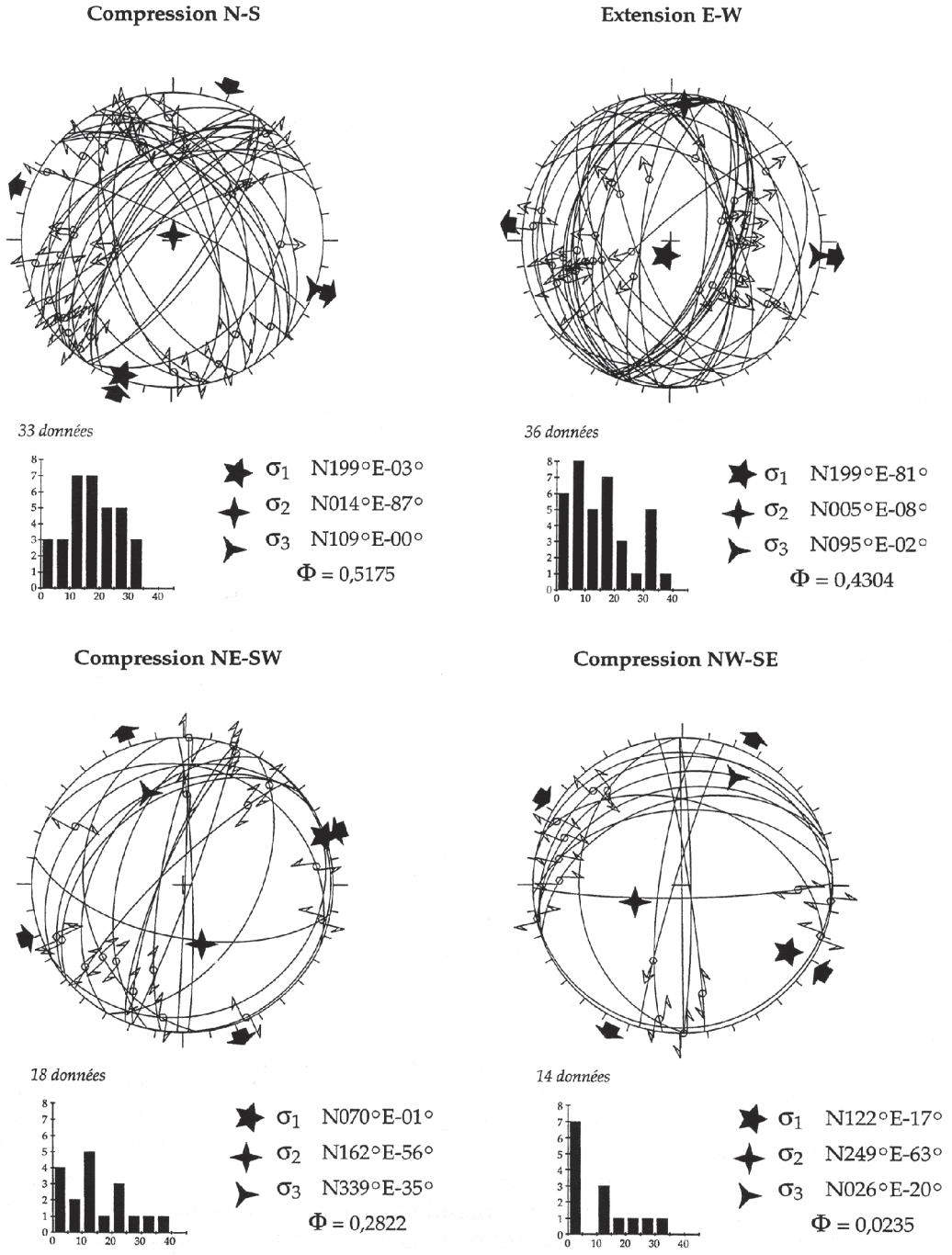

Figure 2.9 Les quatre phases tectoniques tertiaires d'après l'inversion des données de failles et de stries du forage carotté EPS-1 d'après *Dezayes* [1995]. Projections de Schmidt, hémisphère inférieur.

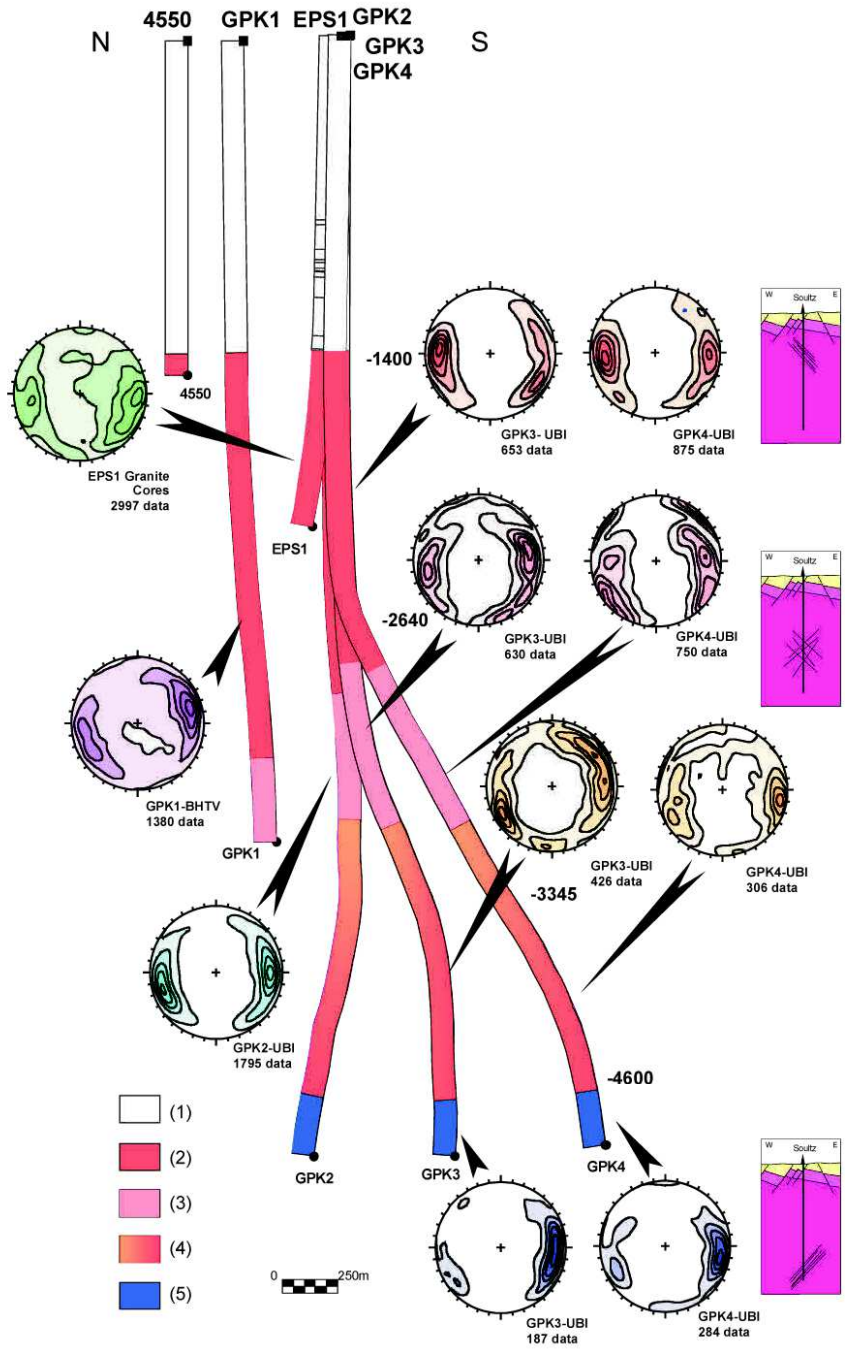

Figure 2.10 Orientation des fractures dans les puits de Soultz-sous-Forêts à partir de l'analyse des carottes et d'images de paroi *Dezayes et al.* [2010a]. Lithologie : (1) couverture sédimentaire, (2) monzogranite porphyroïde, (3) monzogranite porphyroïde avec altération fillonienne intensive, (4) granite riche en amphibole et en biotite évoluant progressivement vers un monzogranite porphyroïde, (5) granite à deux micas et granite riche en biotite. Les profondeurs sont données par rapport au niveau de la mer.

En effet, ce réseau de fractures naturelles chenalisent les circulations à deux échelles ; un large réseau de perméabilité composé de petites fractures auquel se superpose un réseau de perméabilité plus local composé d'épaisses fractures ouvertes [*Sausse and Genter*, 2005]. Ces structures perméables majeures sont appelées Hydrothermally Altered Fracture Zones (HAFZ) [*Genter*, 1989; *Genter et al.*, 2000] (Figure 2.11).

Elles sont marquées par le lessivage des minéraux primaires et la précipitation de carbonates, d'hématite, de chlorite ferreuse ou encore d'illite. Ces zones qui peuvent s'étendre sur plusieurs centimètres à mètres font la transition entre le cœur cataclasé de la fracture et le protolithe granitique peu fracturé. L'intensité de l'altération hydrothermale diminue en s'éloignant du coeur de la fracture. L'argilisation intense peut engendrer des valeurs de porosité atteignant 10%. Cependant malgré ces porosités élevées, les tests hydrauliques de puits révèlent que 95% du fluide circulent dans le cœur de la fracture où la densité de fracture est forte [*Evans et al.*, 2005a]. Ces zones sont associées à la précipitation de veines de quartz qui colmatent la porosité.

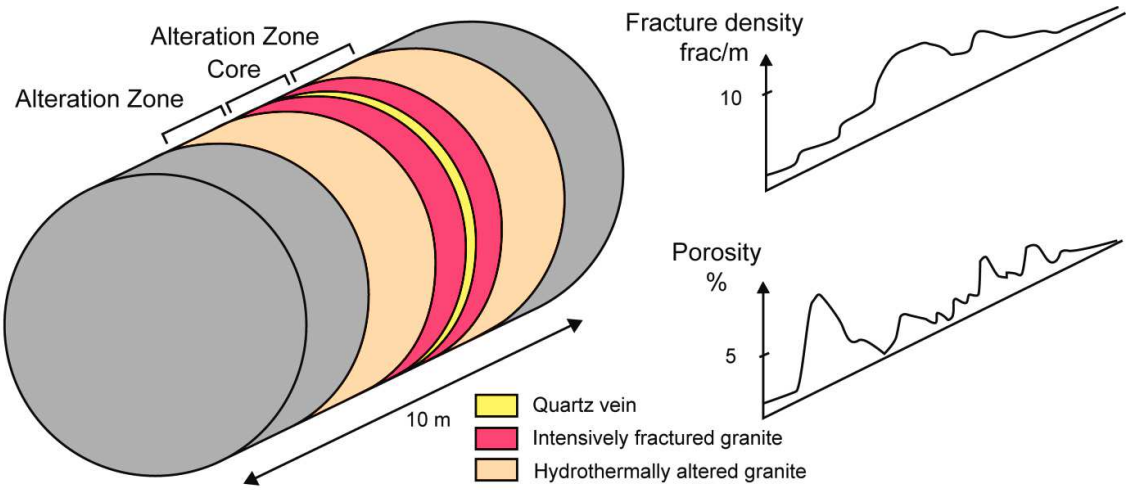

Figure 2.11 Schéma d'une zone de fractures altérée hydrothermalement (Hydrothermally Altered Fracture Zone) d'après *Genter et al.* [2000].

2.3.2 Les grès du Permo-Trias

La base de la couverture sédimentaire est composée par les formations gréseuses du Permien (254 à 251 Ma) et du Buntsandstein (251 à 245 Ma). Les grès permiens sont des arkoses à feldspaths argilisés et des arènes granitiques à peine remaniées. Les grès d'Annweiler (Buntsandstein inférieur) sont des grès fins et argileux moyennement micacés avec des intercalations d'argiles silteuses. Le Buntsandstein moyen est caractérisé par les grès vosgiens qui sont des grès moyens à grossiers voire conglomératiques avec des passées argileuses fréquentes. Les Couches intermédiaires sont des grès dont la taille des grains est plus importante et où les passées argileuses diminuent. Les grès à Voltzia sont un faciès gréseux argileux et micacé très fin qui marque le toit de la formation du Buntsandstein.

Le relevé structural de la fracturation naturelle dans les grès du puits EPS-1 montre un réseau conjugué N170°E, parallèle à la direction Rhénane, avec un pendage de 75°W ou E [*Genter et al.*, 1995]. Entre 1170 et 1215 m MD, dans les grès vosgiens, le puits recoupe une zone d'intense fracturation interprétée comme la faille de Soultz [*Vernoux et al.*, 1995]. L'abondance de dépôts hydrothermaux tels que la calcite, l'illite, le quartz et la barytine, suggère une paléo-perméabilité. Un puits d'observation sismique, 4550, voisin à EPS-1 recoupe dans les grès vosgiens une zone de faille perméable orientée N170°E avec un pendage de 75°W à 1260 m MD [*Genter et al.*, 1995]. Cette zone est associée à des pertes de 30 m^3/h durant la foration.

2.4 Les anomalies thermiques dites de Soultz et de Rittershoffen

2.4.1 Anomalies thermiques du Fossé rhénan supérieur

A l'échelle régionale, une série d'anomalies thermiques locales est très marquée comme dans les régions de Soultz-sous-Forêts et Rittershoffen en Alsace, ou Landau et Insheim dans le Bade-Wurtemberg avec des températures supérieures à 150°C à 2000 m de profondeur [*Schellschmidt and Clauser*, 1996; *Baillieux et al.*, 2013] (Figure 2.12). Ces phénomènes très locaux montrent que la distribution de la température n'est pas homogène dans le Fossé rhénan

supérieur. Ils sont principalement situés dans la partie ouest du Fossé, à des latitudes où la faille rhénane est orientée N45°E [*Dezayes et al.*, 2015].

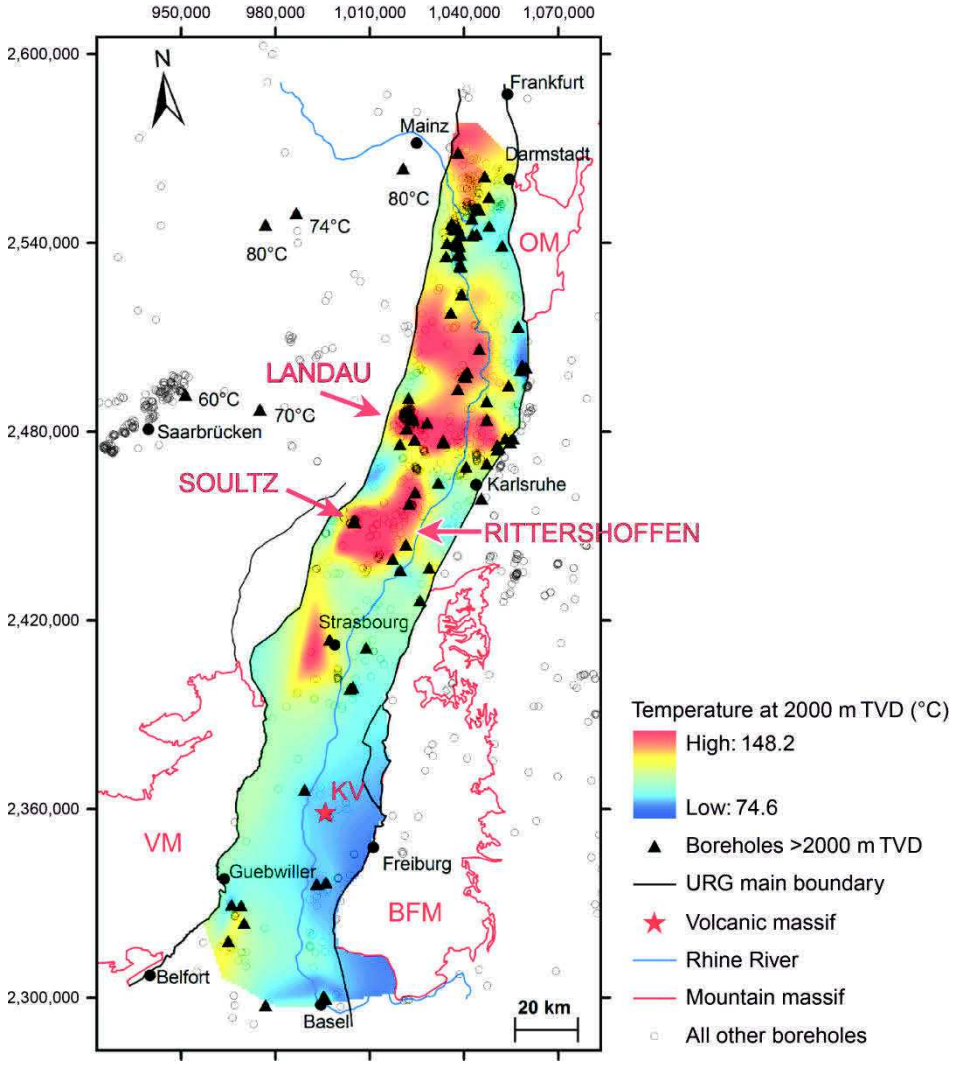

Figure 2.12 Carte des températures à 2000 m de profondeur dans le Fossé rhénan supérieur à partir des données de températures de plus de 1600 puits de la région d'après *Pribnow and Schellschmidt* [2000], *Agemar et al.* [2012] et *Baillieux et al.* [2013]. Les triangles noirs indiquent les puits de plus de 2000 m de profondeur TVD. VM, Vosges Mountains; BFM, Black Forest Mountains; OM, Odenwald Mountains; KV, Kaiserstuhl volcanic massif. Coordonnées Lambert II.

Dans les sédiments, l'anomalie dite de Soultz a été mise en évidence depuis le début du XXe siècle. La foration de plus de 5000 forages pétroliers dans le champ de Pechelbronn-Merkwiller avant les années 70 a permis de recueillir 500 mesures thermométriques dans les sédiments. A partir de ces mesures, *Haas and Hoffmann* [1929] élaborent une carte des isothermes à 400 m de profondeur.

Les isothermes corrélés aux connaissances structurales du bassin pétrolifères [*Schnaebele et al.*, 1948] montrent un allongement N20°E correspondant à la direction des grandes failles normales dans les sédiments qui délimitent les structures de horst et de graben (Figure 2.13).

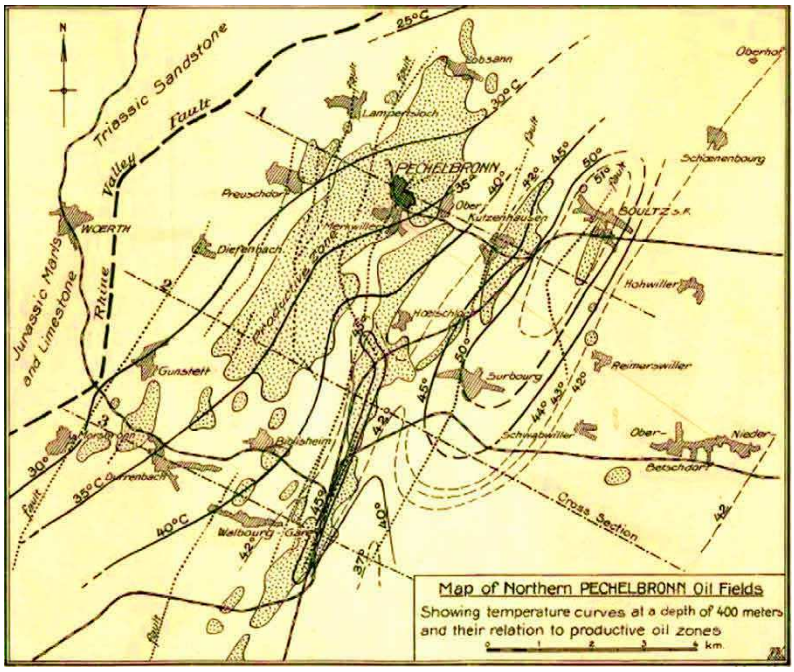

Figure 2.13 Document historique montrant la carte des températures à 400 m de profondeur, établie à partir de mesures réalisées dans des forages pétroliers dans le secteur de Pechelbronn-Soultz, d'après *Haas and Hoffmann* [1929]. Les surfaces hachurées représentent les villages et en pointillés les zones productrices de pétrole.

Au toit du socle cristallin, les mesures thermométriques de plus de 100 puits révèlent des températures >100°C au toit du socle à Soultz mais également à Rittershoffen (Figure 2.14). Localement, ces anomalies apparaissent comme des zones concentriques chaudes le long des tracés des failles de Soultz et de Rittershoffen orientées approximativement N30°E pour le segment de la faille de Soultz et N170°E pour celui de Rittershoffen. Elles sont interprétées comme des circulations hydrothermales verticales per ascensum [*Benderitter et al.*, 1995; *Pribnow and Clauser*, 2000; *Pribnow and Schellschmidt*, 2000]. Environ deux tiers de l'anomalie thermique peut être attribuée au phénomène de convection, le tiers restant étant associé à la production radiogénique du socle granitique [*Baillieux et al.*, 2013]. Le socle granitique à Soultz montre une production

radiogénique variable le long des puits. Les mesures sur carottes dans GPK-1 montrent une production radiogénique très forte (5-6 µW/m^3) au toit du socle dans l'horizon paléo-altéré [*Rummel et al.*, 1988]. Des mesures de diagraphies géophysiques dans le puits GPK-2, indiquent des valeurs de production radiogéniques atteignant 7 µW/m^3, observées entre 3700 et 3800 m MD et autour de 5060 m MD et correspondant à des zones de fractures perméables [*Pribnow*, 2000; *Grecksch et al.*, 2003].

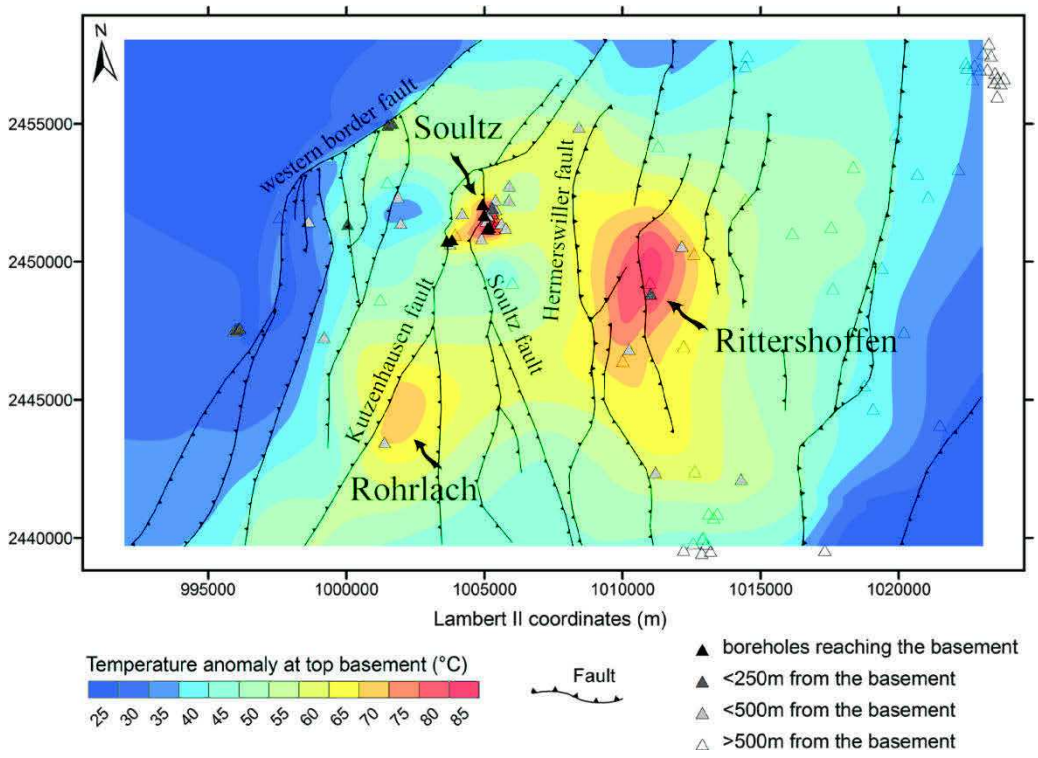

Figure 2.14 Anomalies de températures dites de Soultz et de Rittershoffen et traces des failles locales. La carte des anomalies est obtenue en soustrayant un gradient géothermique de 39.2°C/km (le plus faible gradient de la région) aux températures de la région d'après *Pribnow and Schellschmidt* [2000], *Agemar et al.* [2012] et *Baillieux et al.* [2013]. Coordonnées Lambert II.

Les données magnétotelluriques à Soultz et Rittershoffen montrent une altération hydrothermale principalement localisée sur les failles à pendage ouest qui seraient donc le siège de circulations hydrothermales intenses [*Baillieux et al.*, 2014] (Figure 2.14). Des infiltrations d'eaux météoritiques dans les failles bordières semblent être à l'origine de ces fluides géothermaux [*Pribnow and Clauser*, 2000; *Pribnow and Schellschmidt*, 2000] (Figure 2.15). Au sein du réservoir de Soultz, les inclusions de fluides dans les zones de fractures

montrent un mélange non homogène entre une saumure sédimentaire très salée et un fluide moins salé légèrement plus chaud [*Cathelineau and Boiron*, 2010].

Cette relation entre les structures géologiques et les anomalies thermiques est observée à l'échelle du Fossé également. Les anomalies thermiques sont souvent liées à des structures de horst [*Illies*, 1965; *Schill et al.*, 2009]. Les données géochimiques de l'ensemble des fluides du Fossé indiquent un mélange entre les eaux météoritiques et des eaux marines très salées venant des horizons sédimentaires [*Sanjuan et al.*, 2016a].

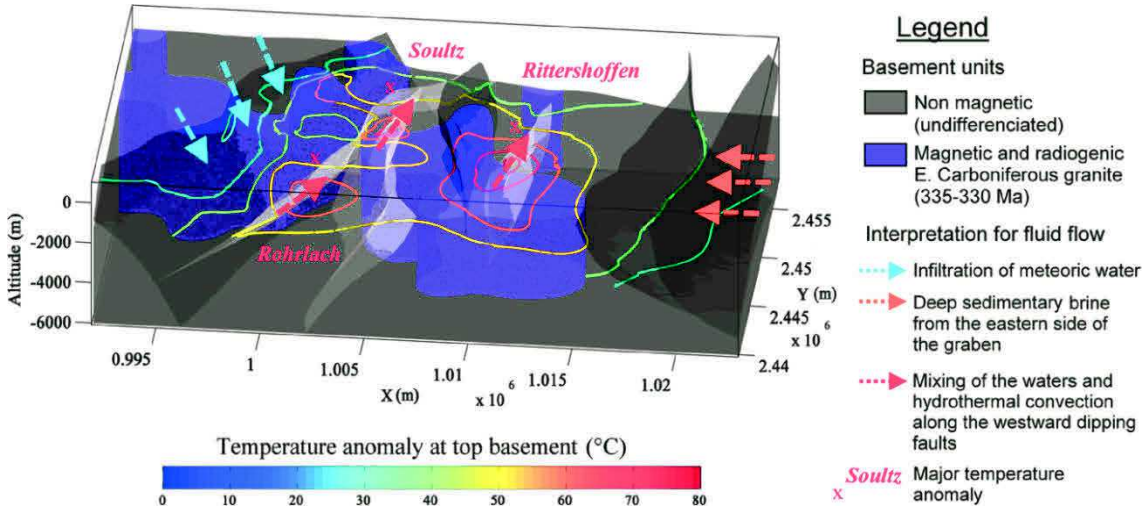

Figure 2.15 Modèle conceptuel 3D des circulations hydrothermales au sein des champs géothermiques de Soultz et de Rittershoffen d'après *Baillieux et al.* [2014]. Coordonnées en Lambert II.

2.4.2 Profils thermiques dans les puits de Soultz

L'effet de la convection hydrothermale est également visible sur le profil thermique des puits de Soultz. Il peut être divisé en trois parties :

- une unité supérieure de 0 à 1 km composée de formations sédimentaires du Tertiaire et du Secondaire (Jurassique, Trias supérieur) avec un gradient thermique de 110° C/km, qui indique un régime de transport de la chaleur de type conductif caractérisé par une droite. Cette unité géologique agit comme un cap rock c'est-à-dire une formation relativement imperméable qui recouvre le système hydrothermal sous-jacent (Figure 2.16);

- une unité de 1 à 3,3 km intégrant les formations du fond de bassin et celles du toit du socle (grès triasiques et permiens et socle granitique carbonifère) avec un gradient thermique très faible de 5 °C/km qui indique un phénomène de convection (Figure 2.16);
- une unité profonde uniquement cristalline après 3,3 km où le gradient redevient linéaire avec la profondeur et d'environ 30° C/km qui indique un retour au régime de conduction (Figure 2.16).

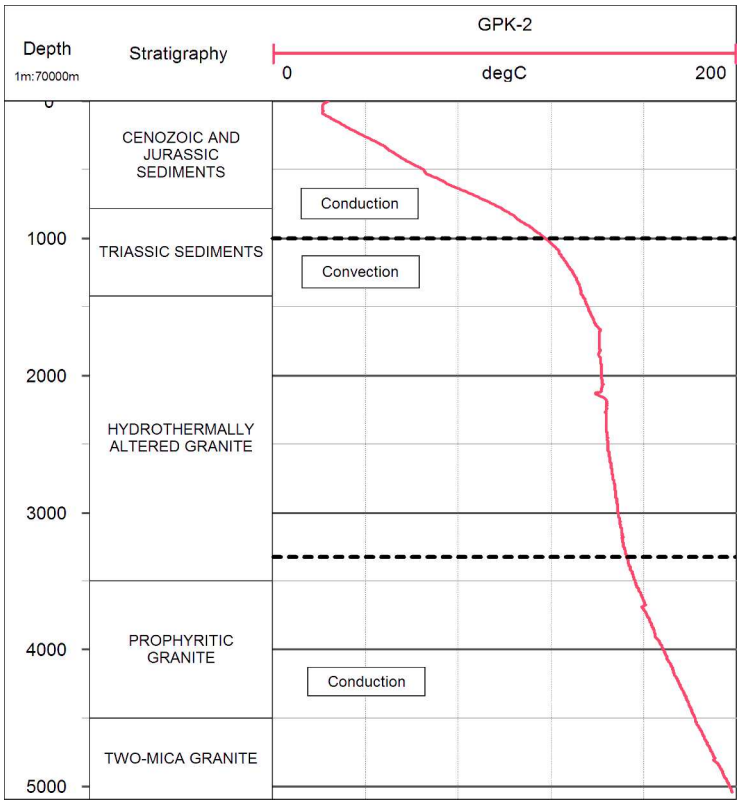

Figure 2.16 Profil de température réalisé à l'équilibre plusieurs mois après la fin du forage dans le puits GPK-2 de Soultz (données collectées par LIAG Hanovre, Allemagne). Les principales unités géologiques sont présentées en fonction de la profondeur.

Sur ce profil thermique et notamment sur la deuxième unité, des zones refroidies sont visibles. Elles correspondent géologiquement à des zones fracturées altérées, généralement perméables pendant la foration [*Genter et al.*, 2010]. Elles ont donc pu être refroidies par l'envahissement de la boue de forage ou par l'injection massive d'eau pendant les opérations de stimulations hydrauliques.

Les fractures dans le socle granitique ont donc une signature thermique visible même plusieurs mois après les opérations hydrauliques.

Bien que les anomalies négatives associées à des zones de fractures perméables soient visibles uniquement dans le socle granitique, des fractures perméables dans lesquelles circulent le fluide géothermal ont également été mises en évidence dans les sédiments triasiques moyens et inférieurs [*Vidal et al.*, 2015]. Ces fractures dans les sédiments triasiques n'ont donc pas la même signature thermique que dans le socle granitique où elles sont associées à une anomalie locale. La formation du Buntsandstein (Trias inférieur) correspond à la transition du régime conductif au régime convectif. Le toit des cellules de convection est la cible des projets de géothermie car elle indique la présence de la ressource géothermique associée à une température qui n'augmentera plus de façon significative avec la profondeur.

3 Le projet géothermique de Rittershoffen

Le projet ECOGI de Rittershoffen est issu d'un partenariat entre Roquette Frères S.A, Electricité de Strasbourg S.A et la Caisse des dépôts et consignations qui avait pour finalité d'utiliser la chaleur géothermique pour alimenter le site de Roquette à Beinheim [*Baujard et al.*, 2017]. L'objectif énergétique de ce projet est de récupérer une puissance thermique de 24 MW_{th} du sous-sol via un doublet de forages et de les transporter jusqu'à la bioraffinerie Roquette Frères (Figure 3.1).

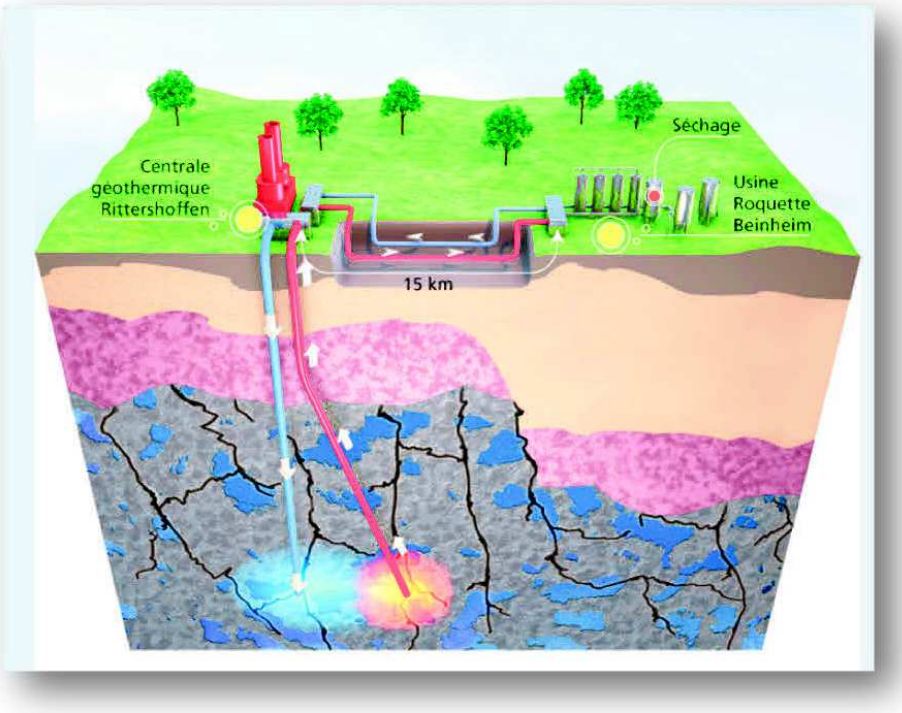

Figure 3.1 Schéma du projet géothermique de Rittershoffen [*ECOGI*]. Après extraction de la chaleur en profondeur, un cycle secondaire transporte la chaleur sur 15 km dans des conduites enterrées jusqu'à Beinheim.

3.1 Etude préliminaire du site

Une étude préliminaire de faisabilité a été réalisée en 2006 à partir des données de forages pétroliers de la région et complétée en 2007 et 2008 par le retraitement et la réinterprétation de profils de sismique réflexion enregistrés par les sociétés pétrolières depuis les années 80. Ces études ont mis en évidence une tectonique en blocs basculés avec la présence d'une zone moins effondrée.

Les couches sédimentaires de cette structure de horst montrent un fort pendage monoclinal vers l'Est délimitées par des failles antithétiques à pendage ouest (faille de Rittershoffen, faille de Betschdorf) [*Dezayes et al.*, 2009]. Les grandes structures faillées à fort rejet vertical pourraient être les drains potentiels d'une ressource géothermale importante à moins de 2500 m de profondeur et expliqueraient l'anomalie thermique. La cible choisie est la structure faillée dite de Rittershoffen qui se décompose depuis la surface en deux branches délimitant le horst en question : la faille occidentale qui limite la remontée de socle et présente un rejet apparent en faille normale estimé à environ 200 m (Figure 3.2).

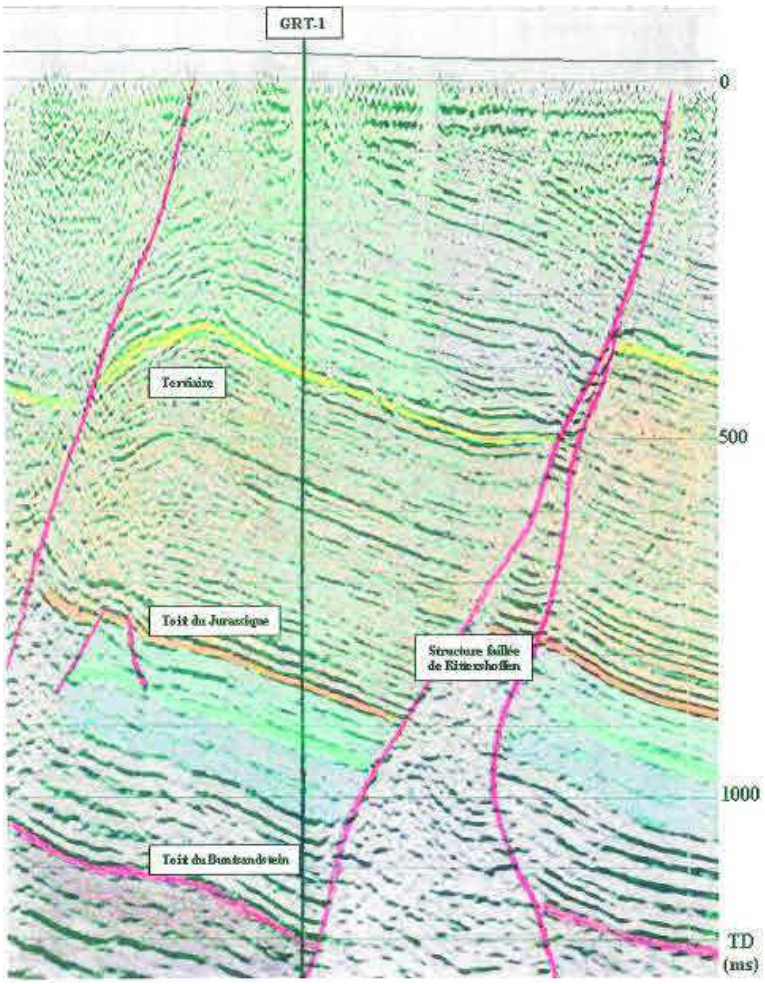

Figure 3.2 Implantation du forage GRT-1 sur l'interprétation de la ligne sismique PHN84N [*Dezayes et al.*, 2009]

La seconde faille constitutive du horst c'est-à-dire celle à regard est présente une géométrie plus complexe avec une vergence ouest dans les sédiments entre la surface et la base du Jurassique. Plus profondément, la faille se verticalise dans

le Muschelkalk puis la vergence de la faille évolue vers l'Est dans les formations compétentes du Buntsandstein. La branche ouest de la faille de Rittershoffen est orientée globalement N-S (Figure 3.3). Il est difficile d'apprécier le jeu décrochant horizontal de cette structure mais on ne peut exclure qu'il existe. Dans le Tertiaire, ces deux structures sont confondues et forment la structure faillée de Rittershoffen (Figure 3.2).

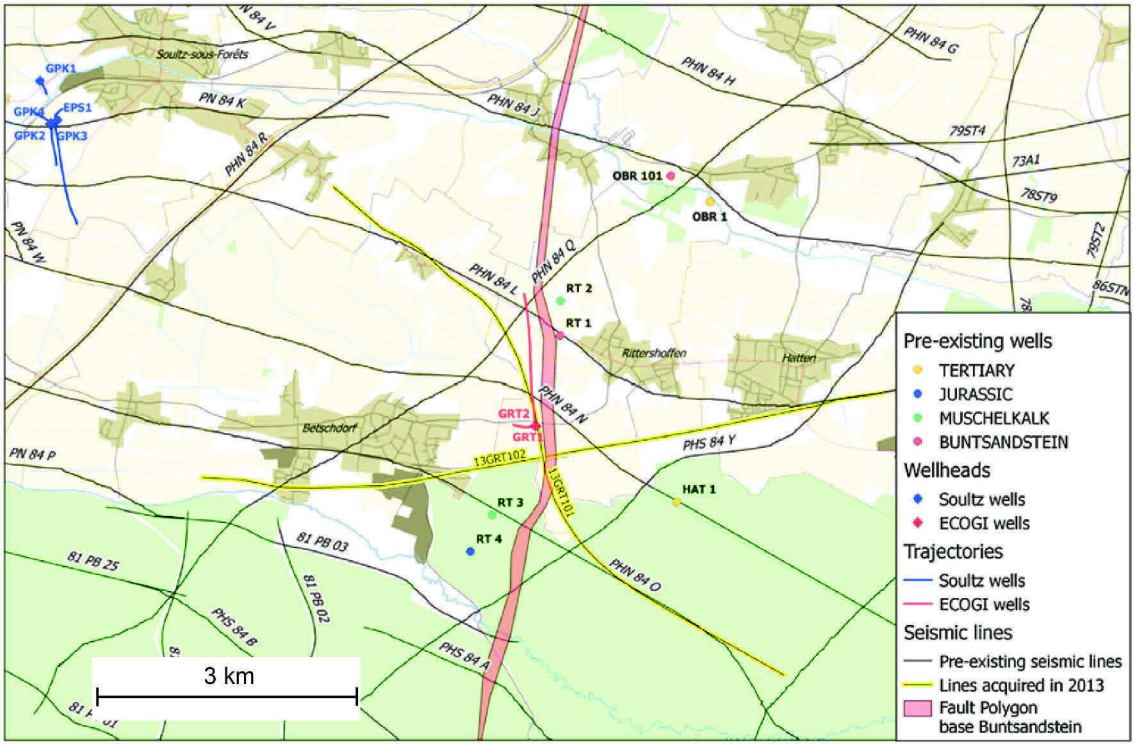

Figure 3.3 Carte des puits profonds de géothermie de Rittershoffen et de Soultz-sous-Forêts, des anciens puits pétroliers, des données de sismique réflexion acquise par les compagnies pétrolières et plus récemment pour le projet Rittershoffen d'après *Baujard et al.* [2017]. Le polygone de faille à la base des grès triasiques est la cible géothermique du projet. Fond carte issu d'Open Street Maps.

Les forages pétroliers forés dans les années 70 et 80 à Rittershoffen et Oberoedern traversent la couverture sédimentaire jusqu'au grès du Buntsandstein pour certains. Les forages pétroliers RT-1 et OBR-101 situés au Nord du site ont révélé des températures de 159°C à 1771 m et 157°C à 1778 m au toit du Buntsandstein (Figure 3.3).

La modélisation thermique 3D des cellules de convection à partir de méthode géostatistiques de *Guillou-Frottier et al* [2013], révèle une montée de fluide géothermal plus chaude à Rittershoffen qu'à Soultz-sous-Forêts.

Les données de production des forages pétroliers semblent indiquer que la faille à vergence ouest est plus favorable d'un point de vue débit [*Munck et al.*, 1979]. Le socle cristallin n'a pas été recoupé par les forages pétroliers proches mais l'anomalie magnétique suggère que le même batholite granitique qu'à Soultz est présent [*Edel and Schulmann*, 2009; *Baillieux et al.*, 2014].

3.2 Forage et développement du doublet géothermique

Le forage premier forage GRT-1 a débuté fin septembre 2012. Il est implanté à l'ouest de la structure de horst (Figure 3.2). Il recoupe la branche occidentale de la faille de Rittershoffen dans le socle cristallin avec une trajectoire légèrement déviée vers l'Ouest [*Baujard et al.*, 2017] (Figure 3.3). Il présente une profondeur développée de 2580 m et une profondeur verticale de 2565 m.

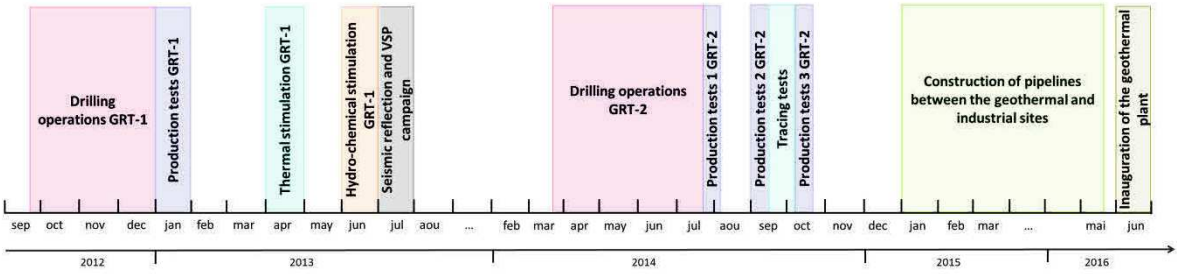

Figure 3.4 Chronologie des opérations de forage, de développement des puits, d'acquisition sismique, de tests de circulations et de construction de la centrale jusqu'à la mise en service de la centrale de Rittershoffen.

A l'issu des opérations de forage et des essais de puits début janvier 2013 (Figure 3.4), le forage ne présente pas une injectivité naturelle suffisante (0.45 L/s/bar) pour l'exploitation industrielle. Il fait l'objet d'un programme de développement spécifique ou stimulation Thermo-Hydro-Chimique (THC) entre avril et juin 2013 dans la partie en trou ouvert du puits [*Vidal et al.*, 2016a; *Baujard et al.*, 2017]. Les conditions de ces opérations de stimulation et l'impact de cette stimulation THC seront détaillées dans la section 5.6. Suite à l'ensemble de cette phase de développement, l'injectivité résultante a été améliorée par 5 (2.5 L/s/bar) [*Recalde Lummer et al.*, 2014; *Baujard et al.*, 2017].

Une campagne vibrosismique ainsi qu'un profil VSP dans le puits GRT-1 ont été réalisés en juillet 2013 afin d'acquérir de nouvelles données sur le sous-sol et ainsi mieux définir la trajectoire du second puits (Figure 3.4). Le second forage GRT-2 a été réalisé entre mars et juillet 2014. Ce forage dévié d'un angle de 37° atteint une longueur forée de 3196 m et une profondeur verticale de 2715 m (Figure 3.5). Il est situé à 8 m du premier puits en surface et à 1200 m en fond de puits. Contrairement au premier puits, la productivité naturelle du puits était suffisante (3.5 L/s/bar) et aucune opération de stimulation n'a été nécessaire [*Baujard et al.*, 2017].

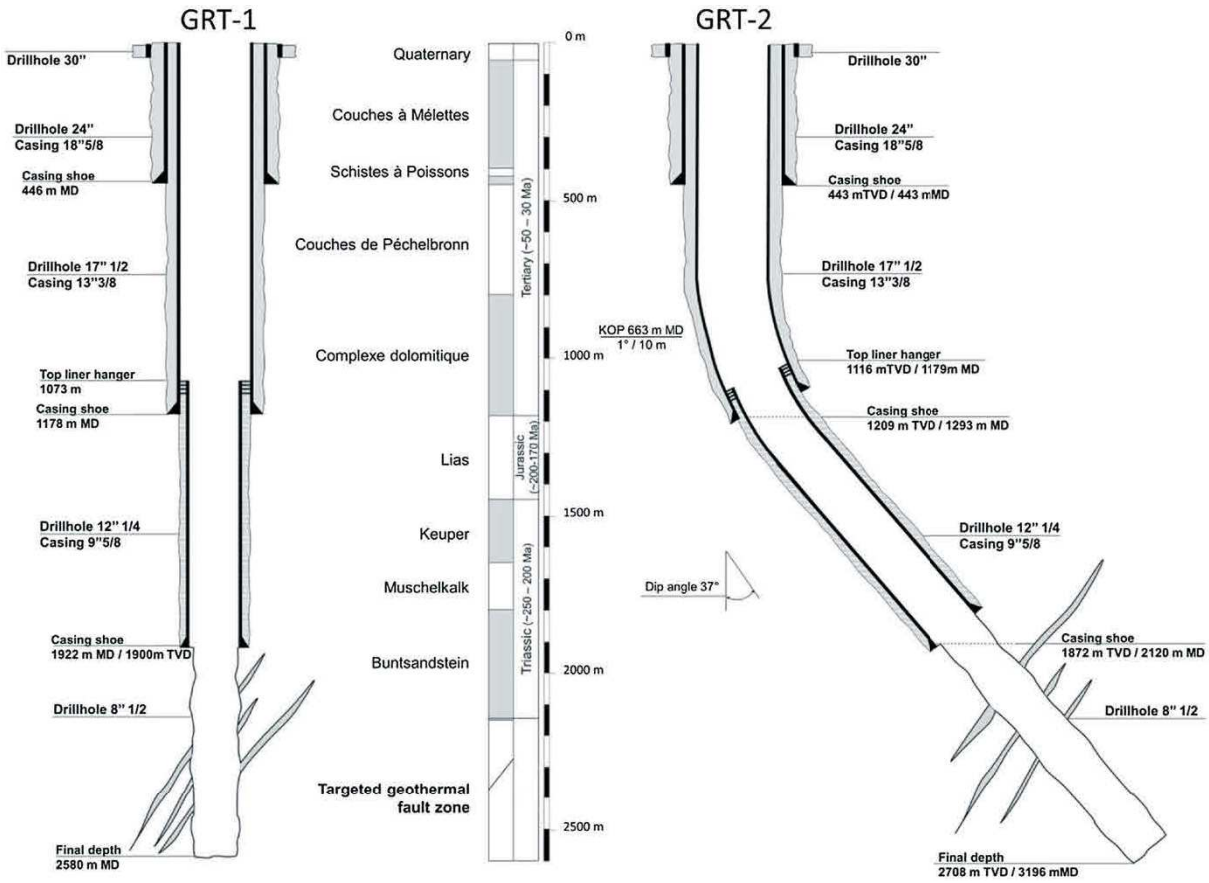

Figure 3.5 Coupe technique des puits géothermiques GRT-1 et GRT-2 (complétion et stratigraphie) d'après *Baujard et al.* [2017]. Les profondeurs sont données par rapport à la surface. GRT-1 est légèrement incliné de 8° vers l'Ouest tandis que GRT-2 est déviée de 37° vers le Nord.

Les tests de circulation entre les deux puits montrent une connexion hydraulique entre les deux puits, bien que d'après le test de traçage elle semble plus faible que celle observée dans ceux de Soultz [*Sanjuan et al.*, 2016b]. Le fluide

géothermal de Rittershoffen présente une composition géochimique similaire à celui de Soultz. Ce fluide est une saumure, avec une salinité supérieure à 100 g/L, et un pH de 6.27. Suite au développement de cet échangeur profond, puis à la construction d'un échangeur en surface et de conduites sur 15 km pour alimenter la bioraffinerie à Beinheim, la centrale a été inaugurée en juin 2016 (Figure 3.4). Depuis décembre 2016, la centrale produit 24 MW_{th} avec un débit production entre 50 et 80 L/s et de réinjection de 40 à 70 L/s ainsi qu'une température de 168°C à la production et 80-90°C à la réinjection. Après 50 ans de circulations selon ses paramètres, la modélisation 3D du réservoir suggère un front de refroidissement qui se propage de 700 m autour de GRT-1 dans la direction de la faille de Rittershoffen [*Sosio et al.*, 2016].

3.3 Le réservoir fracturé de Rittershoffen

Les deux puits ont recoupé les sédiments cénozoïques, jurassiques et triassiques puis l'interface sédiments-socle située à 2200 m TVD [*Aichholzer et al.*, 2016]. Les sédiments cénozoïques et jurassiques sont associés à un gradient géothermique de 95°C/km indiquant une zone de conduction [*Baujard et al.*, 2017] (Figure 3.6). Au toit du Muschelkalk, vers 1600 m TVD, le gradient diminue fortement à 0°C/km dans GRT-1 et 18°C/km dans GRT-2 indiquant une convection dominante (Figure 3.6). Cette zone correspond au réservoir géothermique fracturé à l'interface sédiments-socle.

L'étude structurale à partir des imageries de paroi acoustiques dans le puits GRT-1 a montré un réseau de fractures naturelles denses dans les calcaires du Muschelkalk, dans les grès du Buntsandstein et dans le granite altéré [*Dezayes et al.*, 2013a].

Les calcaires du Muschelkalk sont affectés par des fractures orientées N175°E à N40°E avec un pendage principalement ouest (Figure 3.7). Les grès du Buntsandstein présente une densité de fracture de 0.16 fract/m dans la partie supérieure puis 0.53 fract/m dans la partie inférieure. Les fractures présentent également des orientations très homogènes N0°E à N40°E avec des pendages majoritairement ouest de 60° à 80°(Figure 3.7). Ces orientations sont également

observées dans les grès du Permien où la densité de fracture augmente jusqu'à 0.95 fract/m.

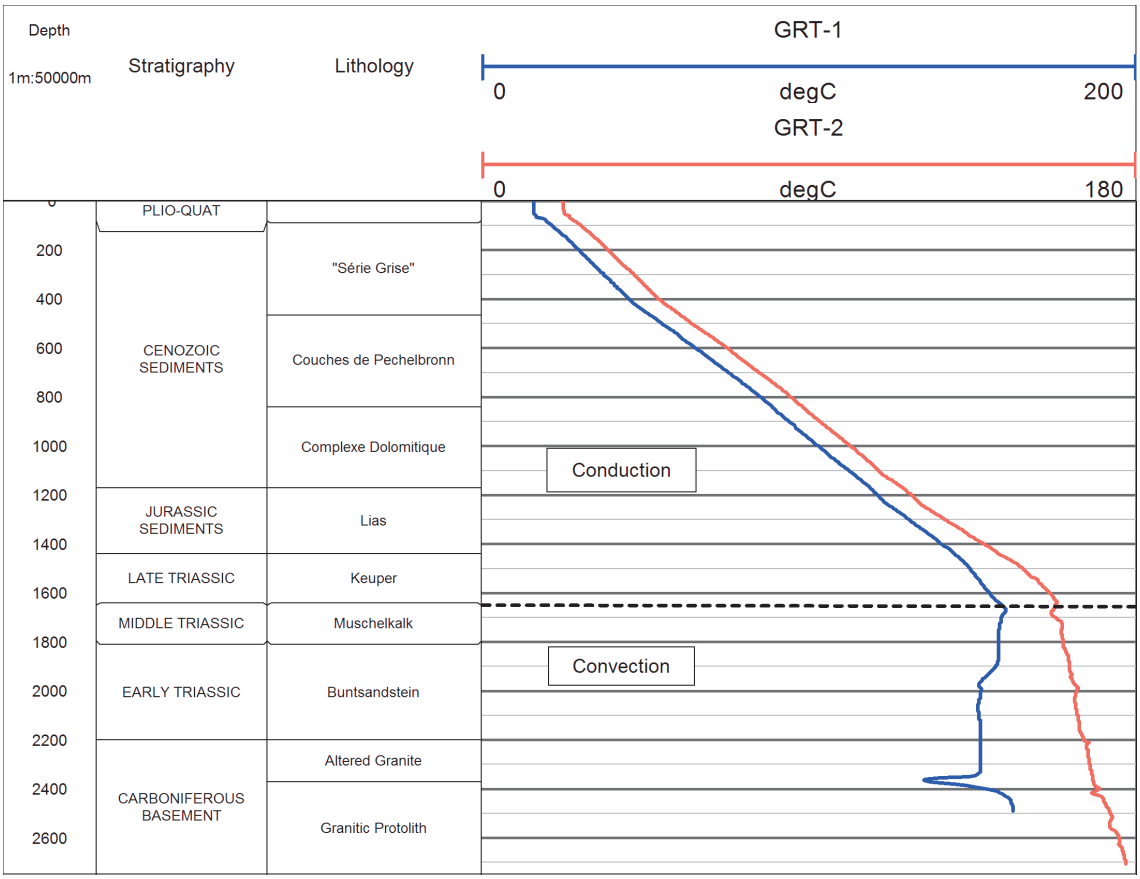

Figure 3.6 Profils de température acquis à l'équilibre thermique dans les puits GRT-1 et GRT-2 d'après *Baujard et al.* [2017]. Les limites des formations géologiques sont indiquées à +/- 30 m selon le puits géothermique. La profondeur est en True Vertical Depth.

Dans le socle granitique, la densité de fractures naturelles est élevée (1.78 fract/m) dans la partie supérieure jusqu'à 2240 m mais diminue jusqu'au fond du puits (0.7 fract/m). Les fractures naturelles montrent des orientations homogènes avec des directions principales entre N140°E et N30°E et des inclinaisons fortes, entre 45° et 90°, majoritairement ouest (Figure 3.7). Quelques fractures E-W sont observées également. La contrainte horizontale maximale est orientée N160°E à 170°E dans le granite profond d'après les relevés de fractures induites en tension [*Hehn et al.*, 2016]. Les fractures naturelles sont donc colinéaires à la contrainte horizontale maximale ce qui favorise leur réactivation soit par cisaillement soit en tension. La contrainte horizontale maximale est

orientée N40°E au toit du socle granitique puis N20°E à N40°E dans les sédiments triasiques [*Hehn et al.*, 2016]. Dans les sédiments triasiques, l'orientation de la contrainte horizontale maximale est perturbée par la présence de grandes fractures naturelles.

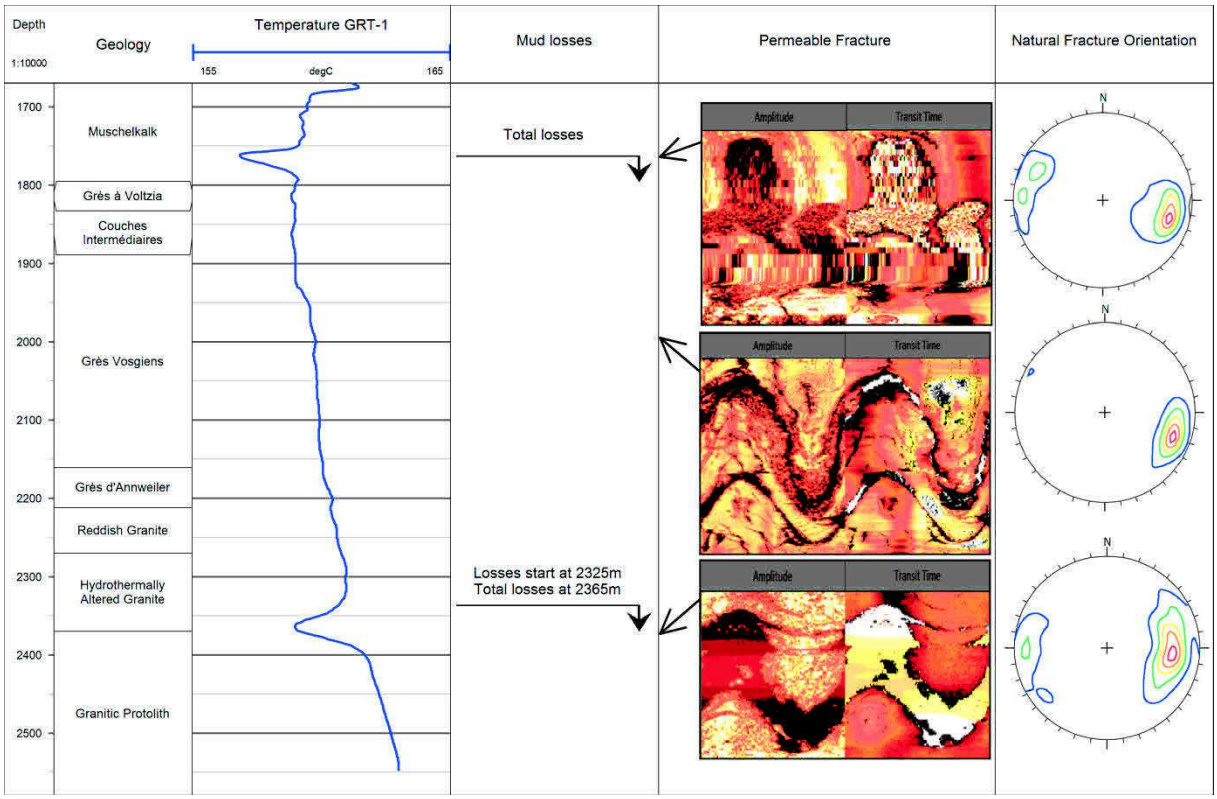

Figure 3.7 Profil de température à l'équilibre thermique dans GRT-1 entre le toit du Muschelkalk et le fond du socle granitique, les pertes de boue et les zones de fractures majeures sur les imageries de paroi acoustiques. Les orientations des fractures naturelles dans le Muschelkalk, le Buntsandstein et dans le granite sont d'après *Dezayes et al.* [2013a]. La profondeur est en Measured Depth. Le puits étant vertical, la profondeur exprimée en True Vertical Depth est très proche de celle en Measured Depth.

Ce réseau de fractures naturelles chenalise les circulations du fluide géothermal. Le fluide collecté dans le puits GRT-1 est très similaire au fluide de Soultz. Dans le puits GRT-1, des zones de fractures perméables ont été recoupées dans les calcaires du Muschelkalk, dans les grès du Buntsandstein et dans le granite altéré. Dans le Muschelkalk, une zone de fractures perméables associée à des pertes totales durant la foration a été recoupée à 1760 m MD [*Dezayes et al.*,

2013a; *Dalmais et al.*, 2015]. Les imageries de paroi acoustiques montrent des fractures N20°E avec des forts pendages ouest [*Dezayes et al.*, 2013a] (Figure 3.7). Elles sont corrélées à une importante anomalie de température négative sur le profil de température. Dans le Buntsandstein, un cluster de fractures partiellement scellées a été recoupé à 1995 m MD. Dans le granite altéré, une zone de fractures majeure a été recoupée de 2325 à 2370 m MD. Elle présente un remplissage minéralogique secondaire de quartz, d'illite, de carbonates et d'anhydrite qui témoigne de paléo-circulations [*Deiller*, 2013; *Dezayes et al.*, 2013a]. De nombreuses fractures ouvertes sont observées dont la principale est localisée à 2368 m MD et présente une orientation N170°E avec un pendage de 65°W (Figure 3.7). Elle est associée à des pertes durant la phase de foration et une large anomalie de température négative sur le profil de température. Elle contrôle les 2/3 du débit dans le puits GRT-1 et symbolise une interface entre un granite hydrothermalement très altéré au-dessus et peu altéré en dessous [*Dezayes et al.*, 2013a]. Elle pourrait être interprétée comme la trace de la zone de faille de Rittershoffen cependant l'extension de cette zone de fractures au-delà du puits est difficilement estimable. Le profil VSP acquis en juillet 2013 dans le puits GRT-1 montre une structure recoupée à 2350 m environ pouvant être une faille [*ECOGI, données sous-sol confidentielles*]. Les données de sismique réflexion 2D imagent peu les failles dans le socle granitique. L'intersection du puits GRT-1 avec la prolongation de la trace de la faille de Rittershoffen à la base du Buntsandstein dans le socle granitique ne semble pas correspondre aux observations de puits [*Baujard et al.*, 2017]. Lors des opérations de stimulation du puits GRT-1, plusieurs centaines d'évènements microsismiques ont été détectés [*Maurer et al.*, 2015].

Le nuage sismique montre une direction de propagation N25°E sur 1 km au Nord de GRT-1 [*Lengliné et al.*, 2017]. La relocalisation du premier évènement sismique a été réalisée à partir de l'observation structurale du puits. Enfin le profil magnétotellurique passant par GRT-1 montre la présence d'un niveau conducteur qui s'étend horizontalement sur 2 km de chaque côté du puits [*Abdelfettah et al.*, 2016]. Le toit de cet horizon est à 2.2 km TVD. Il pourrait correspondre au réservoir fracturé et altéré hydrothermalement.

4 Problématique du sujet de thèse

La synthèse bibliographique proposée sur la base des observations faites à Soultz-sous-Forêts montre que le réseau de fractures qui affecte les sédiments gréseux de la base de la couverture sédimentaire et le socle cristallin est le siège de circulations hydrothermales. Ce réseau est multi-échelle, depuis les microcracks jusqu'aux failles locales à régionales. Deux principales échelles de perméabilité se superposent ; 1) un réseau de micro à méso-fractures de taille millimétrique à centimètrique qui affecte l'ensemble du réservoir et 2) un réseau de fractures de quelques dizaines de centimètres à quelques mètres jusqu'aux zones fracturées ou zones de failles hectométriques à kilométriques qui est plus localisé dans le réservoir. Les zones fracturées, ou zones de fractures, sont définies comme des clusters ayant développé une forte densité de fractures individuelles entourées de halos d'altérations hydrothermales [*Caine et al.*, 1996 ; *Faulkner et al.,* 2010 ; *Genter et al.*, 2000]. Elles sont souvent affectées par un colmatage partiel à total.

Ce travail s'intéresse plus spécifiquement à l'échelle du puits et de la perméabilité associée en s'appuyant sur une connaissance de la fracturation naturelle et des dépôts des minéraux de l'altération hydrothermale (Figure 4.1).

Le sujet de thèse s'inscrit dans une volonté d'améliorer les connaissances sur les circulations hydrothermales dans les zones profondes du Fossé rhénan supérieur. Les anomalies de températures observées à l'échelle du Fossé rhénan supérieur sont la résultante de ces circulations hydrothermales dans le réseau de fractures naturelles à la base de la couverture sédimentaire et dans le socle granitique.

À Rittershoffen, le socle granitique est caché sous une épaisse couverture sédimentaire de plus de 2 km. L'imagerie des zones profondes de faille d'échelle hectométrique à kilométrique dans le socle granitique est peu contrainte spatialement par les techniques standard de type sismique réflexion. La résolution des méthodes magnétotelluriques ne permet pas de caractériser des structures centimétriques à métriques. Enfin, l'absence de relocalisation absolue

des évènements microsismiques nécessite une bonne connaissance structurale à l'échelle du puits et des lois de vitesse en 3D.

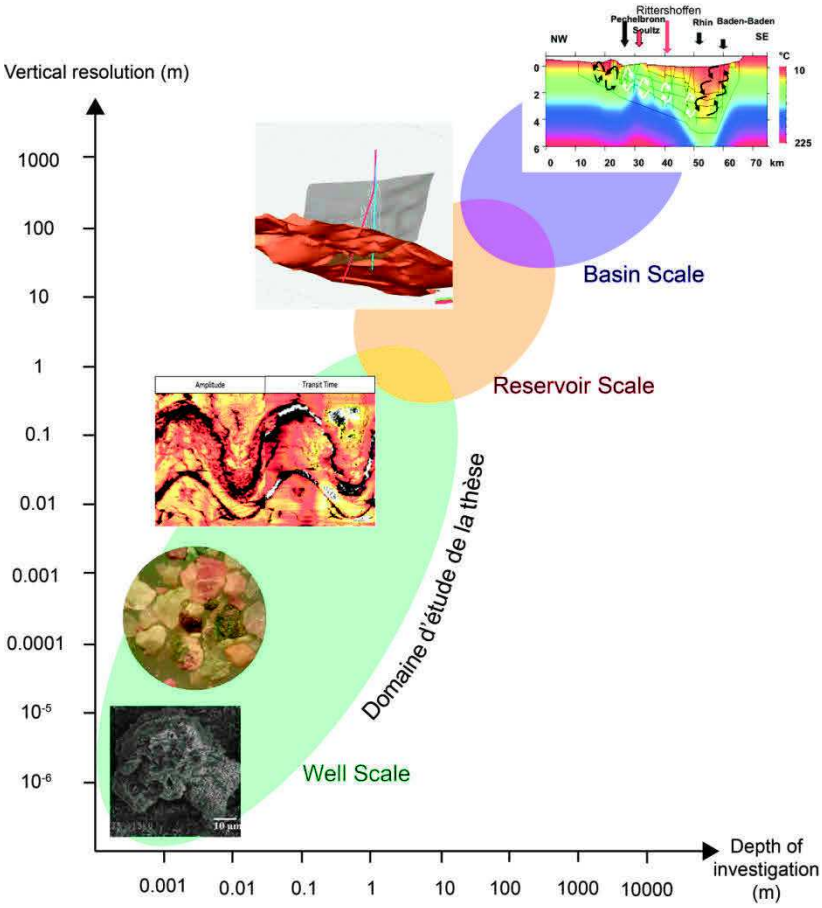

Figure 4.1 Echelles d'investigation des réservoirs. Photographie au Microscope à Balayage Électronique d'un feldspath séricitisé d'après *Baldeyrou et al.* [2003], extrait du modèle géologique 3D de Rittershoffen d'après *Baujard et al.* [2017], coupe extraite du modèle numérique d'après *Le Carlier et al.* [1994].

Avant le démarrage de ces travaux de thèse, peu d'informations géologiques, structurales ou minéralogiques étaient disponibles. La connaissance structurale à l'échelle du puits se limitait au puits GRT-1. Son comportement hydraulique semblait contrôlé par une zone de fractures majeure dans le socle granitique (Figure 4.2). Les altérations hydrothermales associées étaient peu caractérisées tout comme l'impact de la stimulation TCH sur les zones de fractures. Le puits GRT-2 était peu caractérisé alors qu'il présentait une excellente perméabilité naturelle (Figure 4.2). La compréhension de cette différence de perméabilité entre les deux puits est au cœur de cette thèse. Elle cherche à répondre aux questions suivantes :

Quelle est la géométrie du réseau de fractures naturelles à l'échelle du puits ? Quelle est la contribution hydraulique des fractures dans le puits ? Ont-elles un rôle de drain ou de barrière ? Quelles altérations hydrothermales sont associées aux circulations de fluides ?

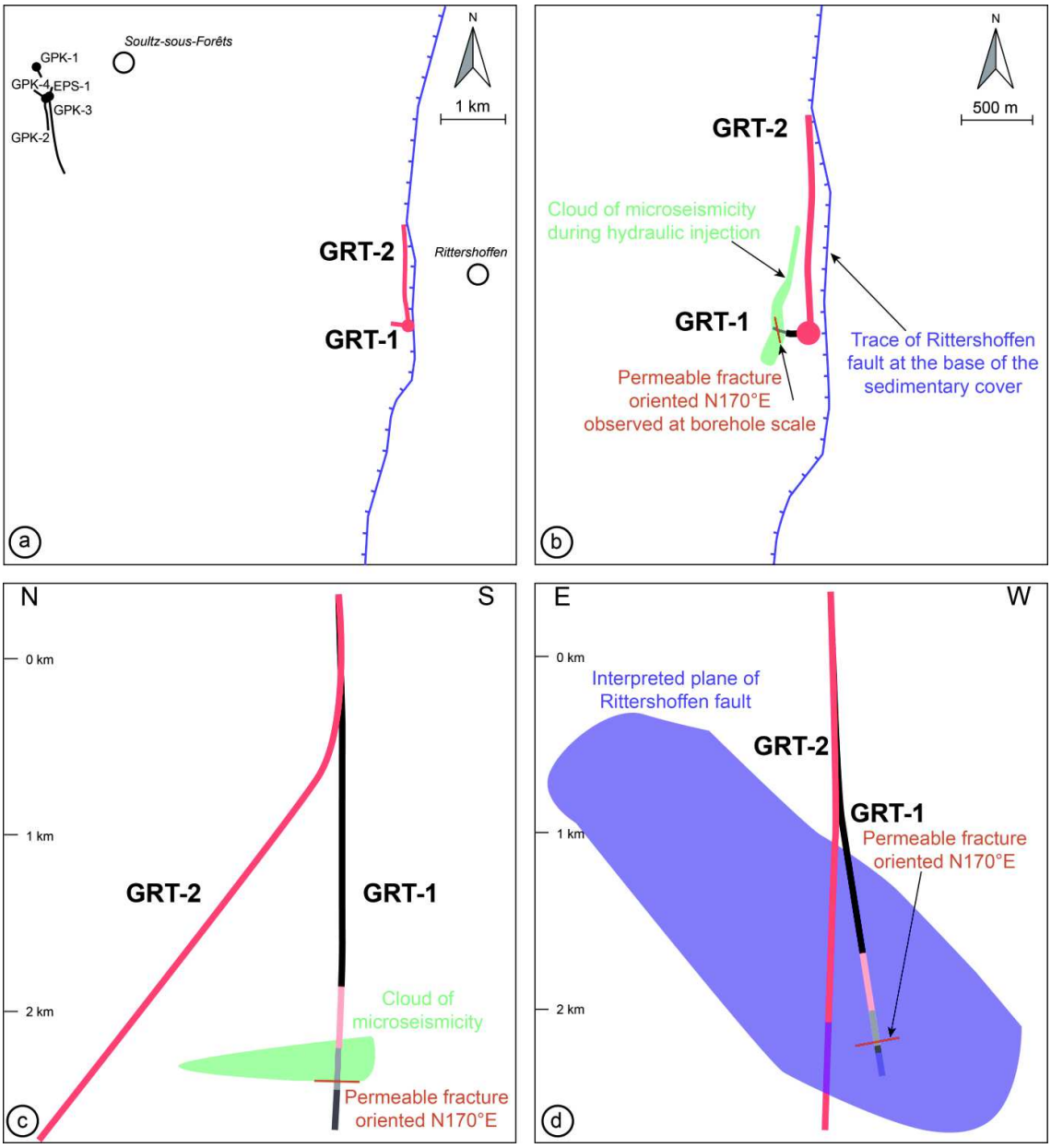

Figure 4.2 Etat des connaissances le long du puits GRT-1 et dans le réservoir de Rittershoffen avant les travaux de thèse. Traces de failles locales à l'échelle sismique [*GeORG Team*, 2017] et des données de microsismicité [*Lengliné et al.*, 2017], de structurale [*Dezayes et al.*, 2013a] et d'observations pétrographiques des cuttings [*Deiller*, 2013] dans le puits GRT-1 sous forme de cartes (a) et (b) et de coupes N-S (c) et E-W (d).

La caractérisation du réseau de fractures naturelles à l'échelle du puits est primordiale pour envisager une interprétation du réservoir à plus grande échelle. Elle se focalisera sur les grès à la base de la couverture sédimentaire et le socle granitique et se basera sur deux types de données :

- Les données de diagraphies standard qui mesurent la radioactivité naturelle, la porosité neutron et la forme du puits mais également les données d'imageries acoustiques. Elles informent sur l'orientation des fractures et permettent d'estimer la présence d'éventuels halos d'altération (Figure 4.3).
- Les données de cuttings qui renseignent sur la pétrographie et la minéralogie des roches constituant le réservoir, sur la nature et sur le degré d'altération hydrothermale (Figure 4.3).

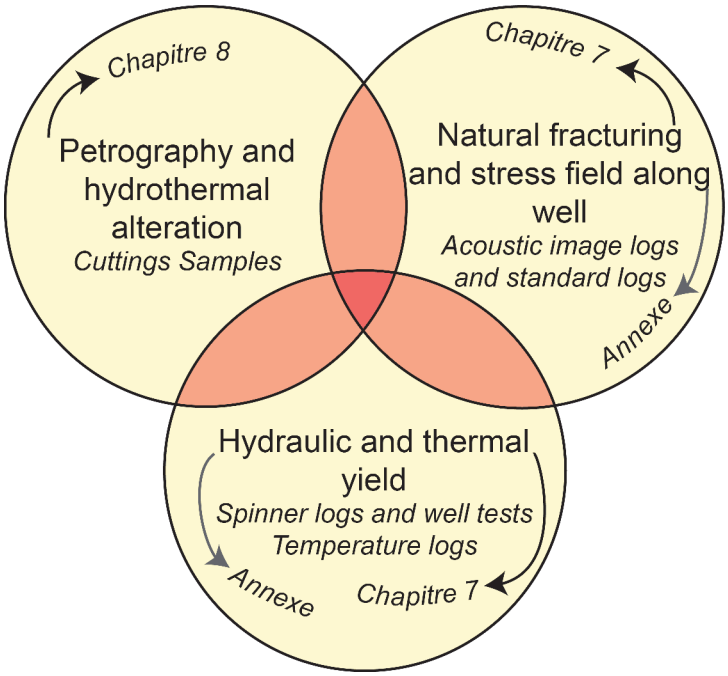

Figure 4.3 Représentation schématique des données de puits dans GRT-1 et GRT-2 traités dans ces travaux de thèse. Le centre rouge représente la connaissance optimale à l'échelle du puits.

A partir de ces données originales, les travaux de thèse tenteront d'identifier la signature thermique des fractures à partir de la corrélation des imageries de paroi acoustiques et des profils de température (Chapitre 7) et également une signature argileuse à partir de l'étude minéralogique des cuttings (Chapitre 8)

(Figure 4.3). Les imageries de paroi acoustiques informent de manière précise sur la position des fractures dans le puits mais leur géométrie 3D loin du puits est mal contrainte. En effet, ces données ne permettent pas de mesurer l'extension des zones de fractures au-delà du puits. Les études de Soultz ont montré la difficulté de corréler les fractures entre deux puits [*Valley*, 2007; *Sausse et al.*, 2010]. Le domaine inter-puits ne sera donc pas traité dans ces travaux. L'objectif est d'évaluer les circulations à l'échelle des puits. Les deux puits de Rittershoffen ont été explorés dans les grès de la base de la couverture sédimentaire et dans le socle granitique (Figure 4.4). Une attention particulière a été portée aux données de température dans la partie sédimentaire des puits de Soultz également, jusqu'alors peu étudiée (Chapitre 6.2).

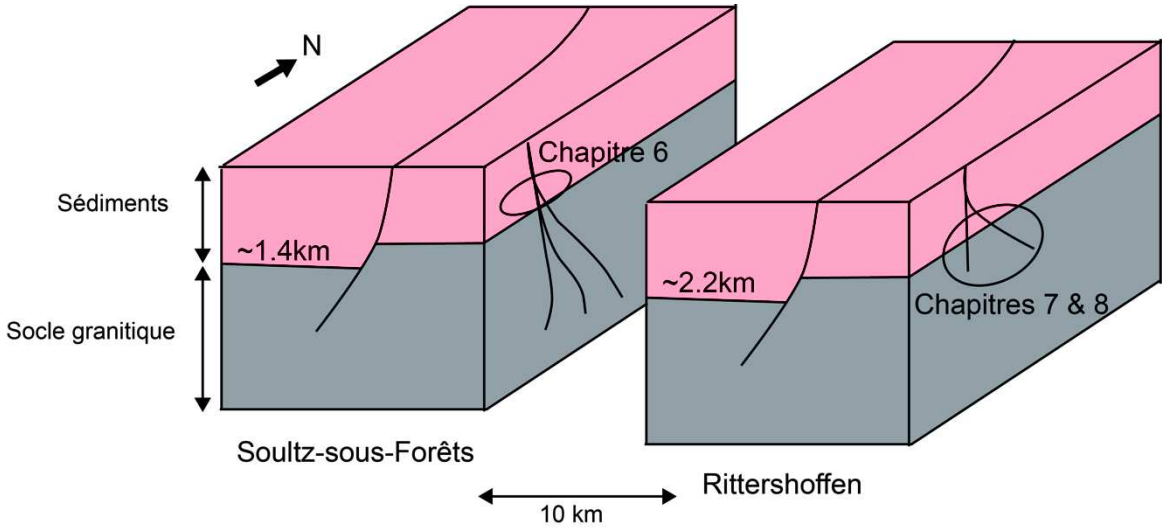

Figure 4.4 Représentation des domaines d'étude des chapitres de la thèse. La trajectoire des puits est projetée schématiquement.

PARTIE 2 : ANALYSE ET INTERPRÉTATION DES DONNÉES

Sommaire de la Partie 2

5 Méthodes utilisées pour caractériser les zones de fractures perméables

5.1 Résumé

Ce chapitre présente les différentes méthodes utilisées durant les travaux de thèse. Il décrit les imageries de paroi acoustiques, les diagraphies différées standard, les diagraphies instantanées puis le protocole pour caractériser les minéraux argileux dans les échantillons de cuttings. L'interprétation des diagraphies différées et des observations pétrographiques des cuttings pour la détection des zones de fractures dans le granite a été largement utilisée dans les puits de Soultz. Dans le cas du puits GRT-1 à Rittershoffen, la comparaison des imageries pre- et post-stimulation mais également des profils de température a permis également d'évaluer l'impact de la stimulation sur le puits. Ce cas d'étude sera présenté dans la dernière section de ce chapitre comme un exemple d'utilisation de ces données d'imagerie. Cette étude est présentée sous forme d'article publié à la revue *Geophysical Journal International*.

Les imageries de paroi acoustiques de type Ultrasonic Borehole Image (UBI) sont les données principalement utilisées dans la thèse. Elles renseignent sur la géométrie des zones de fractures et sur la présence de remplissage secondaire. Elles sont présentées de manière plus détaillée dans la première section de ce chapitre. Elles ont été acquises dans le puits GRT-1 sur toute la section ouverte en 2013 avant la stimulation, en décembre 2013 après la stimulation, ainsi qu'en juillet 2015. Dans le puits GRT-2, des imageries de paroi acoustiques ont été également acquises en juillet 2015. Cependant la qualité de ces données est affectée par la trajectoire du puits pouvant montrait une forte inclinaison importante du puits et la présence de zones de fractures. Dans la section en trou ouvert qui a fait l'objet de logging, 120 m n'ont pas été imagés. Des données de diagraphies standard de type gamma ray, caliper et porosité neutron ont permis d'apporter une information dans les zones où les imageries acoustiques n'ont pas été acquises. Dans ce manuscrit, le caractère perméable d'une zone de fractures est estimé à l'échelle du puits à partir des anomalies observées sur les

profils de température. Plusieurs profils de température ont été acquis dans le puits GRT-1 suite aux opérations de stimulation et un profil post-forage a été acquis dans le puits GRT-2. Les anomalies de température sont corrélées aux données de diagraphies instantanées acquises durant le forage telles que les pertes de boue ou les venues de gaz. Les diagraphies instantanées sont réalisées en cours de forage. Elles sont essentiellement destinées à suivre et à guider la déviation du puits mais apportent également des informations sur la perméabilité des zones de fractures recoupées. Elles seront présentées dans la quatrième section de ce chapitre. Bien que les halos d'altérations hydrothermales autour des fractures puissent être identifiés d'après les diagraphies différées et diagraphies instantanées, l'étude pétrographique des cuttings est indispensable pour la détermination des faciès d'altération. Les travaux de thèse se sont essentiellement focalisés sur les altérations argileuses.

5.2 Les imageries de paroi acoustiques

Les premières sondes d'imageries de paroi acoustiques sont commercialisées sous le nom de BoreHole TeleViewer (BHTV) en 1969 par la compagnie Mobil Oil pour l'inspection interne des tubages [*Zemaneck et al.*, 1970]. Ces outils de diagraphies différées permettent d'obtenir une cartographie orientée de la paroi du puits sous la forme d'un cylindre déroulé et ainsi d'analyser les fractures naturelles et induites et d'étudier la stabilité du puits. La nouvelle génération de BHTV numérique développée par Schlumberger en 1990 sont les Ultrasonic Borehole Imager (UBI). Le principe de l'outil est basé sur un transducteur rotatif qui émet une onde acoustique en direction de la paroi et qui enregistre l'amplitude et le temps de transit de l'onde après sa réflexion sur la roche (Figure 5.1). Ces outils couvrent 100% de la circonférence du puits avec une résolution dépendante de la vitesse d'enregistrement et de l'échantillonnage. A une fréquence de mesure de 250 kHz et avec une vitesse d'acquisition de 800 ft/h, la résolution verticale est de 0.4 in (environ 1 cm) et la résolution azimutale de 2 degré angulaire. L'acquisition de l'UBI se fait avec un outil GPIT (General Purpose Inclinometry Tool) qui permet d'orienter l'image à partir d'un inclinomètre et d'un magnétomètre mesurant la déviation, l'azimut et la position relative de l'UBI.

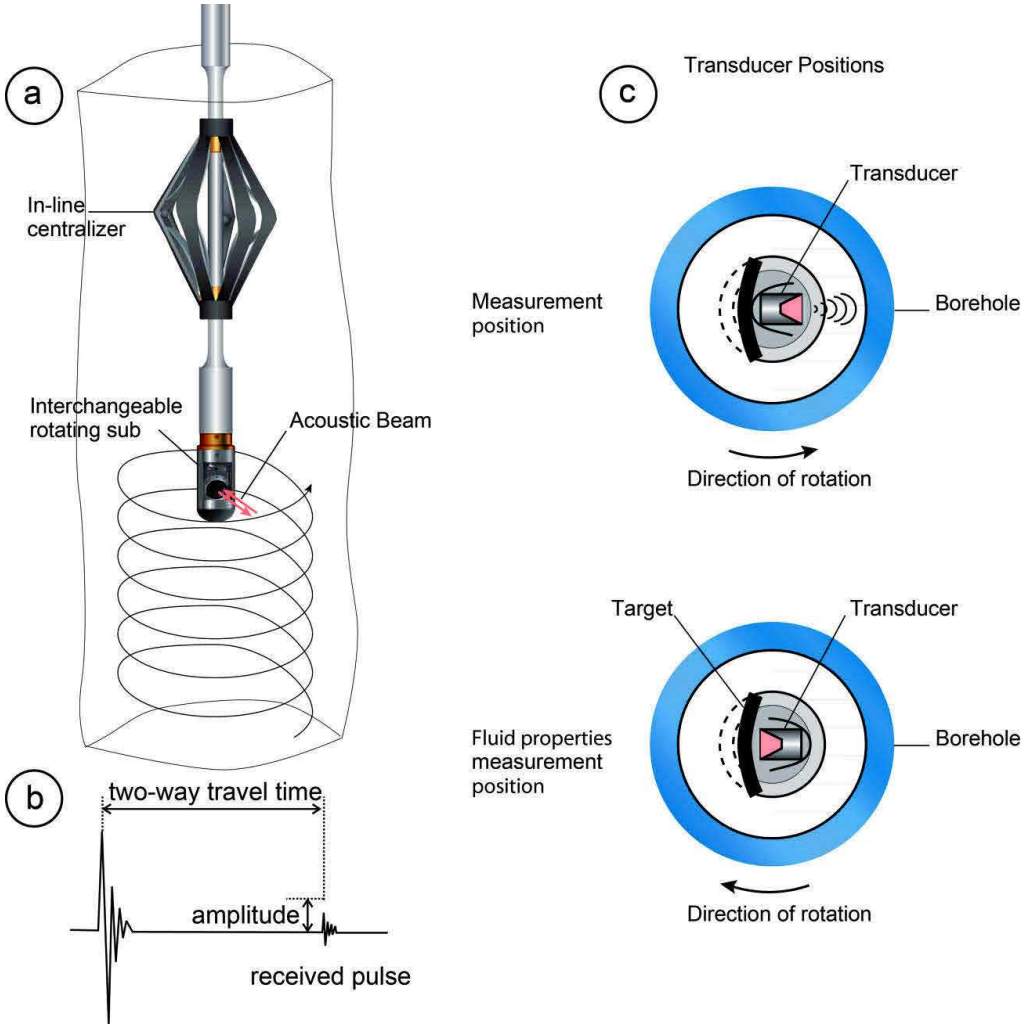

Figure 5.1 Principe de l'outil d'imagerie acoustique de paroi UBI d'après brochure *Schlumberger* [2002]. a) mesure le long du puits à une vitesse variable selon la résolution souhaitée. b) chaque point de mesure consiste à l'émission d'une onde acoustique émise par le transducteur et dont la réflexion contre la paroi du puits est également enregistrée par le transducteur. c) position du transducteur qui mesure les propriétés du fluide à la descente lorsqu'il est orienté vers une cible interne et les propriétés du puits à la montée lorsqu'il est orienté vers la paroi.

Les UBI sont très sensibles aux rugosités qui affectent la paroi du puits et aux variations de diamètre [*Serra and Serra*, 2000]. L'amplitude (en dB) est utilisée pour obtenir des informations sur la qualité de la paroi ; une roche saine et compétente réfléchie l'onde avec une forte énergie et apparait de couleur jaune-orange tandis qu'une formation géologique altérée est représentée en noire (Figure 5.2a). Le temps de transit (en µs) mesure la distance entre l'outil et la paroi et renseigne donc sur la géométrie du puits. Les couleurs jaune-orange

sont associées à un diamètre nominal non affecté par des fractures et les couleurs sombre et noire indiquent un élargissement du puits.

Les imageries de paroi permettent d'évaluer la géométrie de la fracturation naturelle à l'échelle du puits. Les fractures naturelles qui recoupent le puits apparaissent sous forme d'une sinusoïde noire sur la piste de l'amplitude de l'imagerie UBI (Figure 5.2b). Outre la mesure de l'orientation et du pendage, il est également possible de mesurer l'épaisseur acoustique de la fracture en mesurant la différence d'altitude entre les deux épontes de la fracture observées sur l'imagerie de paroi. L'ouverture acoustique de la fracture, également appelée ouverture libre, désigne la partie non scellée à l'échelle du puits (Figure 5.2c). Si une fracture est visible sur la piste de temps de transit, elle est ouverte, du moins dans un champ proche du puits, sinon elle est scellée par un dépôt secondaire et apparait de la même couleur que matrice [*Serra and Serra*, 2000]. Il se peut également que la sinusoïde observée ne soit que partielle. Ce type de fracture ne sera pas pris en compte dans les travaux car ils se concentrent sur le réseau de fractures ouvertes principales qui concentre la majorité des circulations au sein du puits.

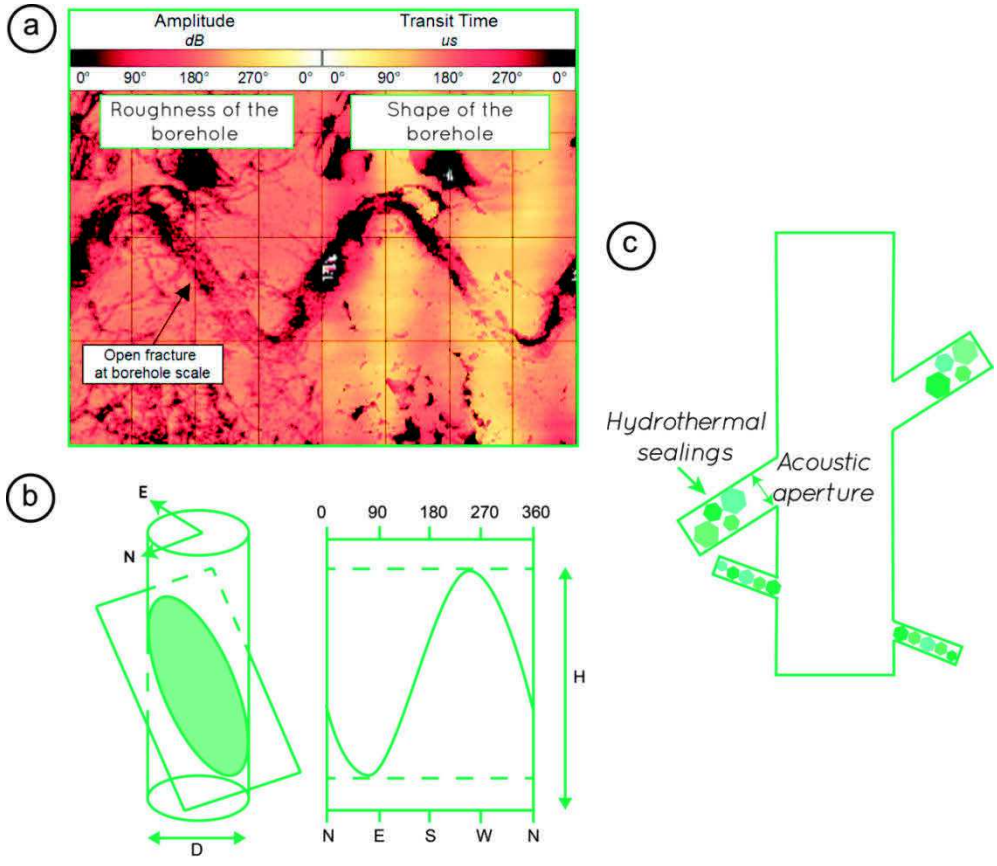

Figure 5.2 (page précédente) Observation d'une fracture naturelle à l'échelle du puits à partir de l'imagerie de paroi. a) exemple d'une fracture ouverte à l'échelle du puits sur l'imagerie de paroi acoustique dans GRT-1. b) vue schématique d'une fracture naturelle qui recoupe le puits sur une image de paroi déroulée pour la mesure de son orientation et de son pendage. c) vue schématique de fractures naturelles partiellement ou totalement scellées qui recoupent le puits.

5.3 Les diagraphies différées standard

Les diagraphies différées sont acquises après les opérations de forage à la sortie des tiges. Elles sont également appelées diagraphies au câble (wireline logging) car elles mesurent des paramètres physiques à l'aide de sondes descendues au bout d'un câble dans le forage. Elles sont acquises avec un échantillonnage d'une mesure tous les 15 cm.

Lorsque les données d'imageries acoustiques de paroi ne sont pas disponibles, il est possible d'utiliser le caliper, terme américain équivalent de diamétreur. Il mesure le diamètre du trou à l'aide d'un à six bras articulés et symétriques. Cette mesure du diamètre de ce puits est donnée en pouce (inch en anglais) qui équivaut à 2,54 cm. Le diamètre du trou dépend essentiellement de la lithologie et de la réaction mécanique de la roche pendant le forage mais également de l'état de fracturation et de contrainte de la roche. Dans une zone de fracture, le trou perd sa forme circulaire et est souvent élargi (Figure 5.3). Il s'agit dans ce cas du terme cave qui est classiquement utilisé. En juillet 2015, le caliper à six bras a été acquis avec un GPIT dans les deux puits de Rittershoffen ce qui permet de mesurer la direction et le pendage des fractures.

Le gamma ray (GR) est l'enregistrement de la radioactivité naturelle émise par les formations traversées par le forage. Les radioisotopes responsables de l'émission des rayons gamma sont le potassium K, le thorium Th et l'uranium U. Le gamma ray, mesuré en gAPI (g signifie giga, API, American Petroleum Industry), informe donc sur la mesure de radioactivité naturelle totale dépendant de la proportion respective de ces trois éléments radioactifs dans la formation. Les variations de GR peuvent être liées aux phénomènes d'altérations qui entraînent l'appauvrissement ou l'enrichissement en éléments U, K, Th. Dans une roche granitique, le lessivage des minéraux primaires suite aux altérations

hydrothermales entraîne une chute du GR. Les chutes de GR très locales sont souvent associées à la présence de veines de quartz dans les puits de Soultz (Figure 5.3). L'altération hydrothermale favorise la formation de phases illitiques qui ont une teneur en potassium élevée et donc entraîne une augmentation du GR. L'utilisation du GR pour détecter les faciès d'altération et les zones de fractures dans le socle granitique s'est révélée très efficace dans les puits de Soultz [*Hooijkaas et al.*, 2006].

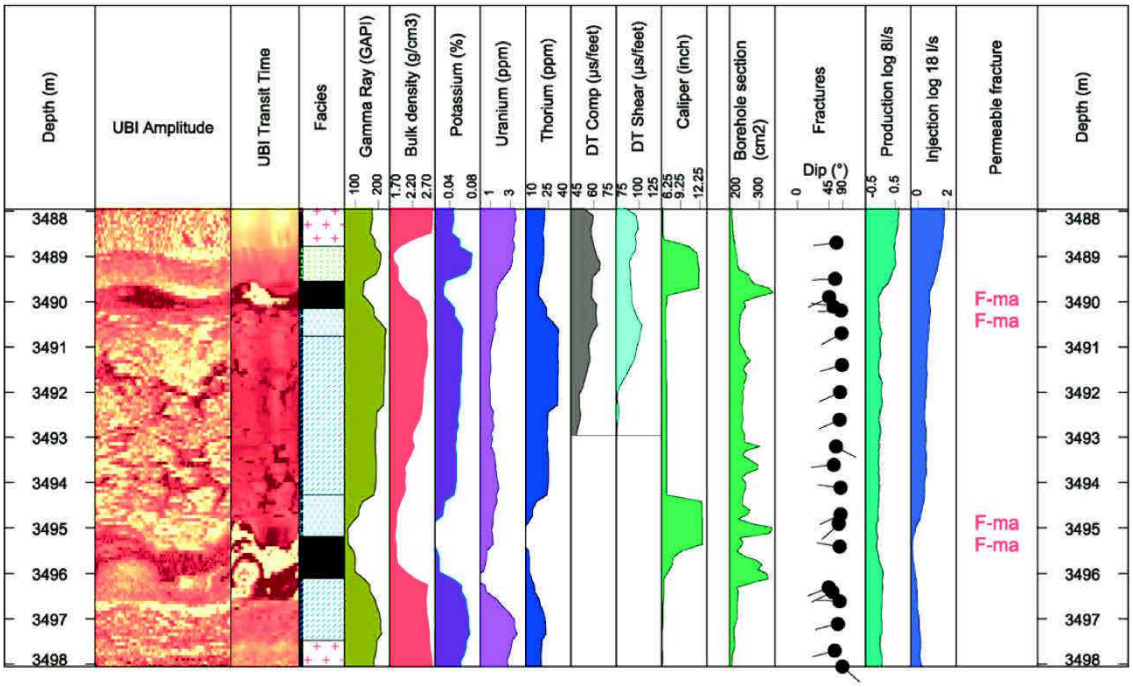

Figure 5.3 Exemple de signatures d'une zone de fracture perméable en imageries acoustiques et en diagraphies dans le puits GPK-1 de Soultz d'après *Dezayes et al* [2010b]. croix rouges : granite porphyroïde ; croix vertes : granite à deux micas ; hachures vertes : granite altéré ; hachures bleues : granite cataclasé ; croix bleues : granite bréchifié ; noir : veine de quartz.

La porosité neutron renseigne sur la porosité de la formation. Elle mesure le ralentissement et l'absorption des neutrons émis par une source radioactive qui entrent en collision avec les atomes d'hydrogène de la roche. La présence d'atomes d'hydrogène peut être fonction de la quantité de fluide présent mais également de la composition minéralogique de la roche. Les minéraux d'altération du granite (chlorite et phases illitiques) mais également les minéraux primaires (biotite) sont riches en groupements hydroxyles et influence la mesure de la porosité neutron. L'altération des minéraux primaires du granite et la

présence de minéraux argileux favorisent l'augmentation de la porosité neutron. En revanche, la recristallisation de veines de quartz au sein de la zone de fracture a tendance à diminuer la valeur de la porosité neutron.

Le GR et la porosité neutron renseignent sur les halos d'altérations autour des zones de fractures et donc sur les paléo-circulations. Les profils de température eux renseignent sur la perméabilité des zones de fractures à l'échelle du puits. Les anomalies de température négatives sont interprétées comme le refroidissement des zones fracturées et poreuses suite aux invasions de boue durant le forage et aux injections hydrauliques durant les stimulations [*Barton et al.*, 1995; *Davatzes and Hickman*, 2005a; *Genter et al.*, 2010; *Bradford et al.*, 2013]. Plusieurs mois après le forage, ces zones sont toujours marquées par des anomalies négatives.

5.4 Les diagraphies instantanées

Les diagraphies instantanées sont réalisées en cours de forage. Elles sont essentiellement destinées à suivre et à guider la déviation du puits mais apportent également des informations sur la perméabilité des zones de fractures recoupées.

Lors de la foration, de la boue aqueuse circule dans le forage. Il s'agit d'eau ou de saumure dans laquelle des argiles de type bentonite sont en suspension. Les débits sont mesurés en sortie et en entrée du forage. Lorsqu'une zone de fractures perméables est recoupée par le forage, des pertes de boue pouvant aller jusqu'à la perte totale de circulation sont observées. En présence d'une boue moins dense que le fluide géothermal, des arrivées de fluide géothermal peuvent être observées. Tout comme pour le débit, les variations brutales de température de la boue peuvent indiquer une venue d'eau chaude géothermale et donc une zone de fractures perméables. Un suivi d'analyse en continu de l'hélium, du dioxyde de carbone et des alcanes est classique en géothermie profonde [*Vuataz et al.*, 1990]. Ces venues de gaz sont également un indicateur des zones de fractures perméables.

Le taux de pénétration (rate of penetration ou ROP) est la vitesse de l'outil de forage mesurée en m/h. L'outil fore le puits avec une vitesse moyenne d'environ

4.5 m/h dans le granite dans le puits GRT-1 [*Baujard et al.*, 2017]. Lorsque le ROP est élevé et notamment lorsqu'il dépasse les 7 m/h, cela peut être interprété comme la présence d'une zone de fracture. Il ne renseigne pas sur la perméabilité de la zone. Lorsque l'outil de forage rencontre généralement des formations géologiques moins résistantes mécaniquement, il avance plus vite pendant la foration. Le ROP est dépendant du poids sur l'outil (weight on bit ou WOB) qui est la masse appliquée sur l'outil de forage en tonnes. Cela correspond au poids du train de tiges qui exerce une pression verticale sur l'outil de forage. Lorsque le ROP devient trop élevé, le foreur peut retenir une partie ou tout le poids sur l'outil afin de ramener un taux de pénétration plus adapté.

5.5 La caractérisation des minéraux argileux de l'altération hydrothermale

L'étude des minéraux argileux dans les systèmes géothermiques de haute enthalpie a montré qu'ils permettent d'identifier les zones perméables mais également la nature des fluides et leurs propriétés géochimiques [*Browne*, 1978; *Reyes*, 1990; *Flexser*, 1991; *Beaufort et al.*, 1992; *Patrier et al.*, 1996]. Les propriétés structurales, cristallochimiques et texturales des minéraux argileux sont intimement liées à l'histoire hydro-thermo-dynamique du champ géothermique. La température a une grande influence mais également la chimie des roches et des fluides ou encore le rapport eau/roche. Si l'étude des minéraux argileux a été développée dans plusieurs champs géothermiques haute enthalpie comme à Okaaki Boradlands [*Browne and Ellis*, 1970] et à Wairakei [*Harvey and Browne*, 1991] en Nouvelle-Zélande, à Milos en Grèce [*Papapanagiotou et al.*, 1993], à Ahuachapan au Salvador [*Beaufort et al.*, 1996], à Sumikawa au Japon [*Inoue et al.*, 1999] et à Bouillante en Guadeloupe [*Mas et al.*, 2006], elle est peu appliquée dans les champs géothermiques du Fossé rhénan. A Soultz, les altérations hydrothermales des zones de fractures du granite de Soultz, ont tendance à favoriser les dépôts de phases illitiques mais également de chlorite [*Genter*, 1989; *Ledésert et al.*, 1999; *Jacquemont*, 2002]. Le terme de phases illitiques décrit une association minérale issue du processus d'altération appelé illitisation. Elle comprend une dominante d'illites plus ou moins bien cristallisées et associées à des proportions mineures et variables d'interstratifiés illite-

smectite. Des interstratifiés chlorite/smectite de type tosudite ont également été vus dans une zone de fracture perméable du puits EPS-1 [*Ledésert et al.*, 1999].

Les minéraux argileux sont des phyllosilicates constitués d'un empilement de feuillets tétraédriques et octaédriques (Figure 5.4). La combinaison d'un empilement des feuillets tétraédriques et octaédriques différencie les minéraux argileux. L'identification des minéraux argileux et de leurs propriétés microstructurales est réalisée à partir de la méthode de la Diffraction des Rayons X (DRX) sur lame orientée. Cette méthode est basée sur la connaissance de la distance réticulaire (001) qui sépare la surface d'un feuillet avec celle du feuillet suivant. La lame orientée permet de renforcer les réflexions (001) en orientant les particules selon le plan (001).

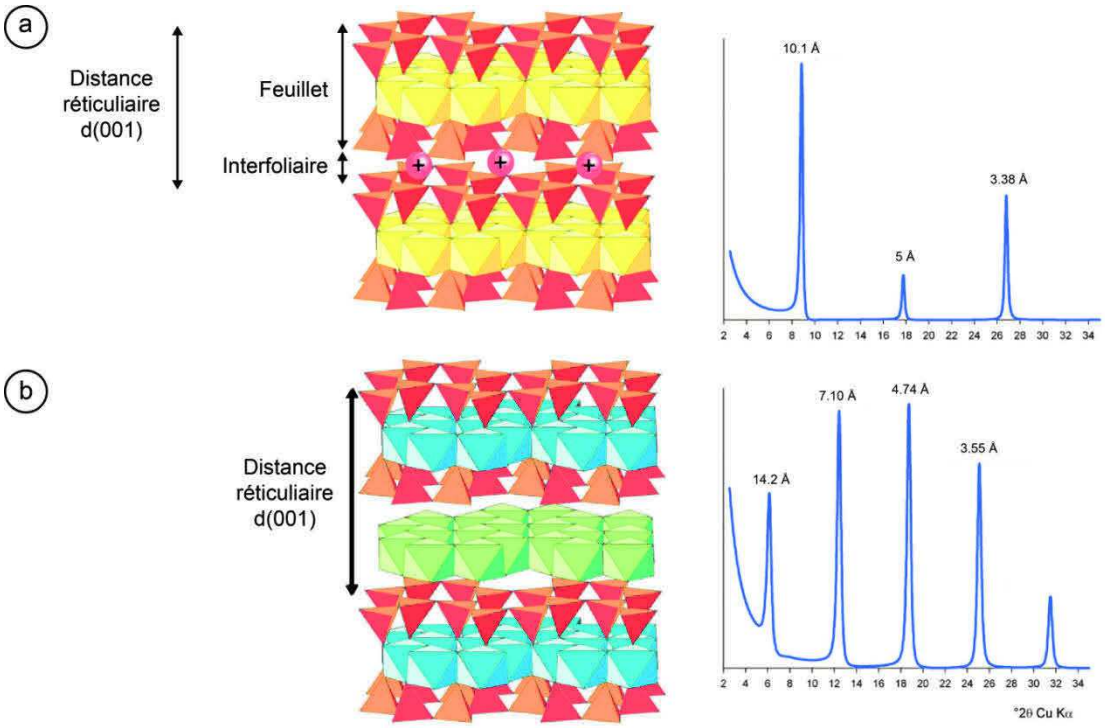

Figure 5.4 Structures des argiles et diagrammes de diffraction des lames orientées d'après *Caner* [2011]. a) l'illite présente une couche interfoliaire occupée par des cations. Le pic de réflexion (001) localisé à 10,1 Å est caractéristique de l'illite. b) la chlorite est composée d'une couche interfoliaire octaédrique. Le pic de réflexion (001) localisé à 14,2 Å est caractéristique de la chlorite.

Pour réaliser les lames orientées, les cuttings sont dispersés dans de l'eau distillée à l'aide d'un canon à ultrasons sans être broyés au préalable.

L'extraction de la fraction argileuse à partir d'une suspension dans l'eau est basée sur la loi de Stokes. En prélevant la fraction de la suspension qui correspond à une granulométrie théorique <5 µm, on élimine la plus grande partie des minéraux non argileux qui ont une morphologie plus proche de la sphère et une densité supérieure aux minéraux argileux (quartz, feldspaths, minéraux lourds, ...). La goutte de suspension est déposée sur la lame et lors du séchage, il se produit une sédimentation selon le plan 001 des minéraux argileux. Les distances réticulaires (001) ou de leurs harmoniques (002), (003), etc… sont mesurables par DRX selon la loi de Bragg et permettent d'identifier le minéral (Figure 5.4). Le diffractomètre utilisé est le Bruker D8 Advance (radiation CuKα, 40 kV, 40 mA). Un diagramme de DRX est enregistré à partir de la lame séchée à l'air. C'est le diagramme de référence pour juger des déplacements de raies occasionnées par les traitements à l'éthylène-glycol. Les lames sont placées une nuit en atmosphère d'éthylène-glycol ce qui fait "gonfler" les smectites puis le diagramme de DRX est acquis à partir de la lame saturée. La saturation entraîne une augmentation de la distance réticulaire des smectites et les pics de diffraction sont modifiés.

Les compositions chimiques des minéraux argileux sont analysées au microscope éléectonique à balayage SEM JEOL 5600 LV équipée avec un BRUKER XFlash 4030 SSD.

5.6 Exemple d'utilisation des imageries de paroi acoustiques pour évaluer l'impact de la stimulation TCH dans le puits GRT-1

Cette section est publiée dans la revue Geophysical Journal International sous la référence : Vidal J., Genter A. and Schmittbuhl J. (2016). Pre- and post-stimulation characterization of geothermal well GRT-1, Rittershoffen, France: insights from acoustic image logs of hard fractured rock, *Geophys. J. Int, 206*(2), 845-860, doi: 10.1093/gji/ggw181.

Les imageries de paroi acoustiques sont classiquement utilisées pour identifier la géométrie des fractures à l'échelle du puits. Cet article montre un exemple d'utilisation des imageries de paroi acoustiques pour évaluer l'impact de la

stimulation à l'échelle du puits. Ce type d'étude est peu réalisé dans les puits car les imageries de paroi acoustiques sont rarement acquises avant et après la stimulation. A Soultz, une partie du granite dans le puits GPK-1 avait fait l'objet d'une étude similaire [*Cornet et al.*, 1997]. Cet article apporte donc des éléments nouveaux à partir de données originales pour évaluer l'augmentation de la perméabilité suite à la stimulation TCH dans les grès et le granite.

5.6.1 Résumé

Le puits géothermique GRT-1 a été foré jusqu'à 2,6 km de profondeur en 2012. Il présente une section en trou ouvert de grès triasiques et permiens et de socle granitique altéré. Suite à la stimulation thermique, chimique et hydraulique du puits GRT-1 en 2013, l'injectivité du puits est multiplié par 5. La stimulation thermique consiste en l'injection de fluide froid dans le puits chaud dans l'objectif de créer des microcracks sur les matrices silicatés et les quartz hydrothermaux. La stimulation chimique consiste en l'injection d'agents chélatants biodégradables afin de dissoudre les carbonates et les sulfates. La stimulation hydraulique s'apparente plutôt à une injection hydraulique à faible pression afin de nettoyer le puits. Suite à ces stimulations, la comparaison des imageries de paroi acoustiques révèle des modifications, sur toutes les zones de fractures du puits. Cependant, les profils de température montrent que seules deux zones sont perméables. Dans les grès, une zone de fracture montre une érosion chimique et mécanique des fractures associées à une anomalie de température positive et localisée sur le profil de température post-stimulation. La zone de fracture perméable principale dans le socle granitique est une zone de cave très large dont le diamètre est plus grand que le champ d'acquisition de l'outil d'imagerie de paroi utilisé. Les modifications de cette zone ne peuvent donc pas être imagées par cette méthode. En revanche, la comparaison des profils de température montre une augmentation de l'amplitude de température négative associée à cette zone ce qui suggère une augmentation de la perméabilité. Les observations macroscopiques de cuttings indiquent la présence importante de quartz hydrothermaux. Les phénomènes de « thermal microcracking » à l'échelle des veines de quartz et des matrices silicatées suite à la stimulation thermique pourraient être à l'origine de l'augmentation de la perméabilité [*Hosni et al.*, 2003; *Heap et al.*, 2013]. Aucun mouvement de cisaillement n'est observé à l'échelle du

puits mais la possibilité d'érosion mécanique suite aux injections hydrauliques de faible pression n'est pas exclue. Les tests hydrauliques ont montré une augmentation par un facteur 2 de l'indice d'injectivité après la stimulation thermique, de 1,70 après la stimulation chimique et de 1,50 après la stimulation hydraulique. Cependant, les modifications observées à l'échelle du puits ne peuvent pas être directement reliées aux augmentations d'injectivité. L'acquisition des imageries acoustiques en juillet 2015 montrent les mêmes modifications que celles de décembre 2013. Les fractures modifiées ou non après la stimulation étant majoritairement orientée N-S +/-10°. La contrainte horizontale maximale étant relativement stable dans la section en trou ouvert du puits, elle ne semble pas être le facteur principal de la réactivation des fractures durant la stimulation. La nature du remplissage minéralogique et notamment la présence de sulfates et de quartz hydrothermaux, semble avoir une influence majeure sur les réactivations de fractures naturelles.

5.6.2 Article publié dans Geophys. J. Int.

Pre- and post-stimulation characterization of geothermal well GRT-1, Rittershoffen, France: insights from acoustic image logs of hard fractured rock

Jeanne Vidal[1], Albert Genter[2] and Jean Schmittbuhl[1]

[1] IPGS, University of Strasbourg/CNRS, Strasbourg, France
[2] ES-Géothermie, Schiltigheim, France

5.6.2.1 Abstract

Geothermal well GRT-1 (Rittershoffen, Alsace) was drilled in 2012. Its open-hole section (extending down to a depth of 2.6 km) penetrated fractured sandstones and granite. In 2013, the well was subjected to Thermal, Chemical and Hydraulic (TCH) stimulation, which improved the injectivity index fivefold. The goal of the study was to assess the impact of the stimulation by comparing pre- and post-stimulation well-logging (acoustic and temperature [*T*] logs) and mud-logging data. This comparison revealed modifications of almost all the natural fractures. However, not all of these fractures are associated with permeability enhancement, and the poststimulation *T* logs are important for characterizing this

enhancement. Chemical alteration due to mechanical erosion at the tops and bottoms of the fractures was observed in the sandstones. These zones display indications of very small new permeability after the TCH stimulation.

Because a major fault zone caved extensively where it crosses the borehole, it was not imaged in the acoustic logs. However, this originally permeable zone was enhanced as demonstrated by the *T* logs. Based on the natural injectivity of this fault zone, hydraulic erosion and thermal microcracking of its internal quartz veins are associated with this permeability enhancement. Although local changes in the borehole wall observed in the acoustic images cannot be directly linked to the improved injectivity index, the comparison of the acoustic image logs allows for identification of fracture zones impacted by the TCH stimulation.

Key words: Downhole methods; Hydrothermal systems; Permeability and porosity; Fracture and flow; Fractures and faults; Europe.

5.6.2.2 Introduction

In the Upper Rhine Graben (URG), several deep geothermal projects, such as those in Soultz-sous-Forêts, Landau and Insheim, exploit local geothermal reservoirs trapped in the fracture network in Triassic sediments and the underlying granitic basement [*Genter et al.*, 2000; *Baumgärtner and Lerch*, 2013; *Hettkamp et al.*, 2013]. These projects are based on the Enhanced Geothermal System (EGS) technology. The principle underlying this technology consists of increasing the low initial natural hydraulic performance of pre-existing natural fractures in the geothermal reservoir via hydraulic and/or chemical stimulation [*Schulte et al.*, 2010]. An EGS project located at Rittershoffen (Alsace, France) was initiated in 2011 by the company ECOGI, a partnership between the companies Groupe Electricité de Strasbourg and Roquette Frères and the French public financial institution La Caisse des Dépôts et Consignation. The project is based on a geothermal doublet that produces geothermal heat from the reservoir at the sediment-basement interface [*Baujard et al.*, 2015]. The heat will be used for industrial processes at the Roquette Frères biorefinery at Beinheim, located 15 km west of the drill site. The first vertical geothermal well, well GRT-1, was drilled to a depth of approximately 2.6 km in 2012. The open-hole section penetrated fractured Triassic sandstones, Palaeozoic hydrothermally altered

granite and fresh granite. After hydraulic testing, the injectivity was insufficient for future industrial exploitation, and the well was therefore Thermally, Chemically and Hydraulically (TCH) stimulated in 2013. After the TCH treatments, the injectivity of well GRT-1 increased fivefold. To identify the physicochemical processes responsible for this hydraulic improvement, we compared pre- and post-stimulation data sets obtained from well GRT-1. In this paper, first, the geologic setting and the TCH stimulation operations at the Rittershoffen site are presented. Then, methods used to compare the pre- and post-acoustic image logs and to correlate observations in these logs and indications of permeability based on temperature profiles are described. Last, the results regarding post-stimulation modified fracture zones and permeability enhancement in the well are discussed. On the whole, the stimulation is generating only one newly permeable zone, and enhanced one originally permeable zone.

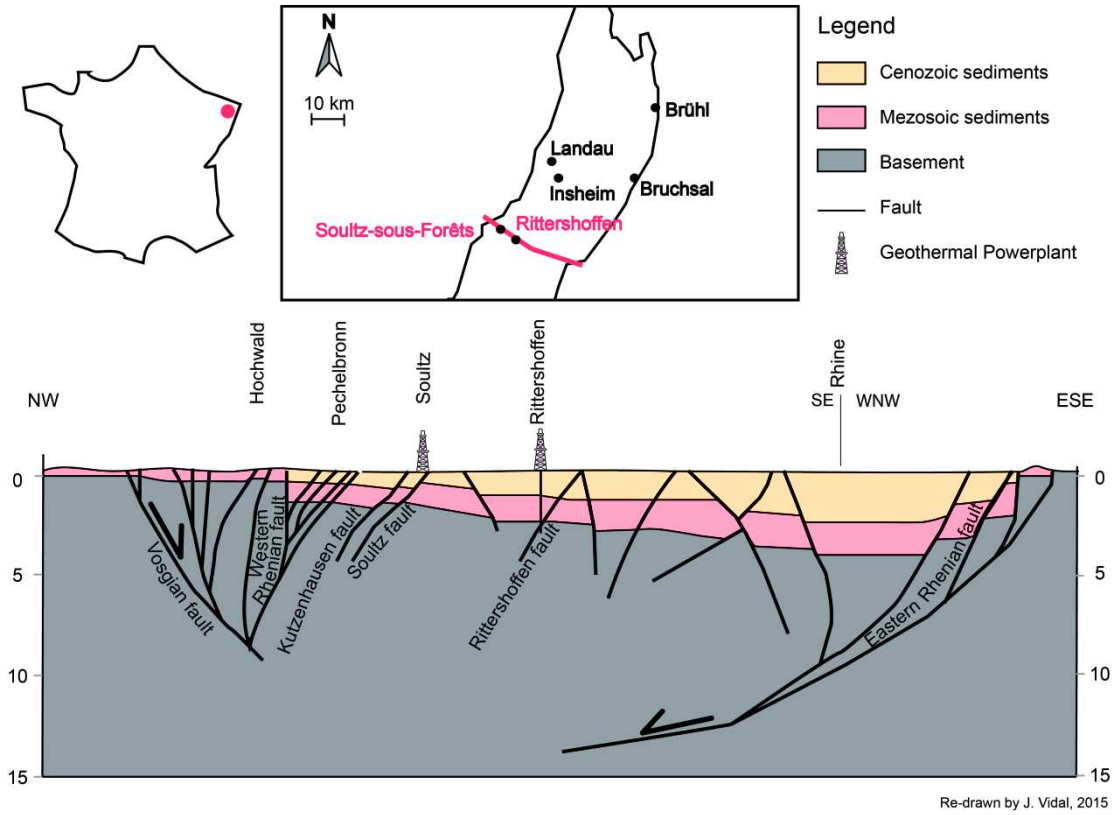

Figure 5.5 Location of the Rittershoffen geothermal site and geological cross-section through the Upper Rhine Graben at the latitude of Rittershoffen. The cross-section was modified after *Kappelmeyer et al.* [1992] and the interpretation below 4 km depth is done by analogy to the cross-section of *Brun et al.* [1992]

and is highly speculative. An interpretative trajectory of GRT-1 crosses the Rittershoffen fault.

5.6.2.3 The Rittershoffen site

5.6.2.3.1 Geological setting

The Rittershoffen site is located in the URG, which is a Cenozoic rift structure belonging to the European Cenozoic Rift System [*Ziegler*, 1992]. The first geothermal well drilled the site is located at 7.939°E and 48.897°N above the so-called Rittershoffen fault. This fault is located approximately 15 km east of the Western Rhenian border fault and is oriented N45°E (Figure 5.5). This project takes advantages of the lessons learned from the Soultz geothermal pilot project located less than 10 km to the north-west of Rittershoffen. For example, mud-logging and well-logging data in the sedimentary cover of the geothermal boreholes at Soultz-sous-Forêts indicated the presence of permeable fractures in the Muschelkalk and Buntsandstein's formations [*Vidal et al.*, 2015] and in the basement [*Genter et al.*, 2000; *Evans et al.*, 2005b; *Dezayes et al.*, 2010b]. The initial target of the Soultz geothermal pilot project was the fracture network in the deep granitic basement, but it was observed that the fracture network at the sediment-basement interface is more permeable. Exploration geothermal well GRT-1 penetrates geologic units similar to those encountered in the Soultz wells. Fractures of similar permeability were expected, and the target of well GRT-1 was a geothermal reservoir at the sediment-basement interface. Its open-hole section penetrates approximately 300 m of sediments and 350 m of granitic basement. The lower portion of the sedimentary cover is composed of the Buntsandstein and Permian's sandstones. The Palaeozoic granitic basement, encountered at a depth of approximately 2210 m, is divided into three units: 50 m of reddish granite, 100 m of hydrothermally altered granite and 200 m of fine-grained fresh granite. The Paleozoic granitic basement was affected by pre-Cenozoic tectonics, particularly the Hercynian orogeny. The top of the granitic basement was affected by post-orogenic exhumation and subsequent palaeoweathering causing sub-horizontal jointing and a general reddish colour of the granite matrix respectively. Uplift of the top basement involved an uploading of the rock mass and the formation of horizontal fractures called jointing. Despite

the high fracture density, the reddish granitic section of the top basement is not an aquifer as it was demonstrated by a packer test in GPK-1 between 1375 and 1395-m depth. Residual permeability in the granite is intimately linked to Hydrothermally Altered Fractured Zones showing a cluster organization deeper in the granitic basement [*Genter et al.*, 2000]. Well GRT-1 was drilled at the south-east of the horst to intersect the so-called Rittershoffen fault at the top of the basement (Figure 5.5). Based on a seismic reflection section, this fault strikes N–S, dips westwards and displays a vertical offset of approximately 200 m. These Rhenish-oriented fractures are Hercynian structures [*Illies*, 1972, 1975] that were reactivated during the Oligocene opening of the URG [*Villemin and Bergerat*, 1987].

5.6.2.3.2 Drilling and stimulation operations

Well GRT-1 was drilled from September to December 2012 (Figure 5.6). Subsequent production tests indicated that a major permeable structure controlling 2/3 of the flow was intersected at the 2368-m depth. However, the initial injectivity of the well was low and insufficient for industrial exploitation. The natural permeability of the sedimentary and granitic parts was very low due to the poor hydraulic connectivity between the well and the fracture network and needed to be increased via TCH stimulation. Stimulation of well GRT-1 consisted of three phases: thermal stimulation, chemical stimulation and hydraulic stimulation.

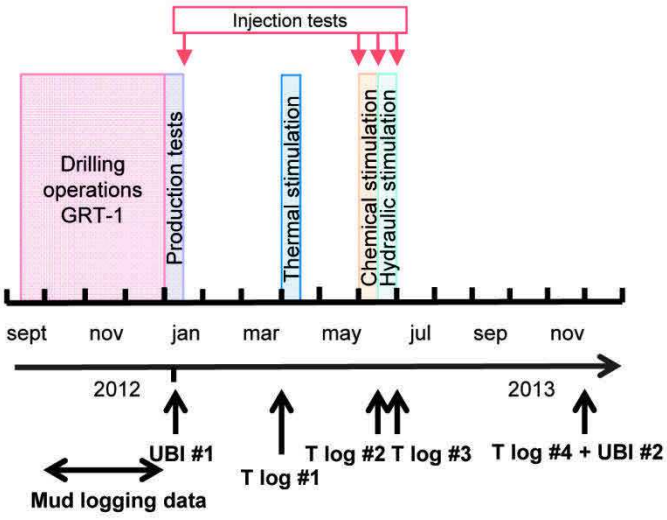

Figure 5.6 Chronology of stimulation and well-logging operations in well GRT-1

The thermal stimulation consisted of cold-water injection from the wellhead 4 months after the drilling. During a time span of more than 60 hr, 4200 m_3 of water at surface temperatures was injected into the hot reservoir to encourage thermal microcracking along the wellbore, thereby increasing connectivity with the reservoir. More precisely, this cold-water injection caused microcracking of the quartz grains in the silicate matrix and fracture fillings [*Griffiths et al.*, 2015]. Thermoelastic effects reducing the normal stress on fractures and thus promoting fracture opening could be also envisaged [*Dempsey et al.*, 2014]. THM modelling of stimulated permeable fracture zones after cold-water injection into the granite rock reservoir of Soultz-sous-Forêts suggested the creation of a halo of alteration of thermos-mechanical origin and microcracking of surrounding quartz veins [*Hosni et al.*, 2003]. Microcracking in secondary quartz is ubiquitous within fractures and the coalescence of microcracks would improve fracture permeability. Thermal stimulation is typically performed to enhance the near-well field permeability, which may have been reduced by drilling (cuttings and mud clogging feed zones), and thus this stimulation is generally performed immediately following the drilling [*Schulte et al.*, 2010; *Grant et al.*, 2013]. This technique is not usually applied to EGS geothermal wells in the URG but has produced satisfactory results in high-temperature systems in volcanic environments [*Tulinius et al.*, 2000; *Axelsson et al.*, 2006]. Following the thermal treatment of well GRT-1, an injection test is performed two months later (Figure 5.6) and the injectivity index was increased twofold (Table 5.1).

Table 5.1 Increase in injectivity index of well GRT-1 following the TCH stimulation and expected radius of influence of each operation. Radius of influence of stimulations are from *Schulte et al.* [2010].

Stimulation	**Increase in injectivity index after stimulation**	**Radius of influence**
Thermal	x2	Near-well field
Chemical	x1.70	
Hydraulic	X1.50	Far-well field

All permeability increases given in this paragraph are considered as permanent and calculated from injection tests performed when the well was at the thermal equilibrium. Hydraulic data and injectivity calculations are not detailed in this

manuscript. The chemical stimulation was performed two months after the thermal operation. The chemical stimulation consisted of injecting an acid fluid to dissolve materials around the wellbore such as cuttings from the drilling and hydrothermal minerals plugging the fracture zones. This technology, which was developed and used by the oil and gas industry for more than a century [*Economides and Nolte*, 1989], has been adapted to deep geothermal wells during the previous 20 yr to enhance the fracture network, particularly in EGS projects [*Rose et al.*, 2007; *Nami et al.*, 2008; *Portier et al.*, 2009].

The chemical stimulation of well GRT-1 targeted minerals that plugged the fracture zones. The stimulated zones and targeted minerals were identified from the cuttings and the post-drilling well-logging data from well GRT-1. The stimulation was performed using the biodegradable chelating agent GLTA (glutanic acid N, N–diacetic acid) to dissolve carbonates (calcite, dolomite, ankerite) and sulphates [*Recalde Lummer et al.*, 2014]. This environmentally friendly fluid does not dissolve alumino-silicates (clay minerals, quartz), is effective up to 200 °C and penetrates more deeply into the rock mass than conventional stimulation fluids. To avoid losing a large volume of acid fluid into the major permeable structure in well GRT-1 at the 2368-m depth, a single packer connected to coiled tubing was installed at three depths to concentrate the fluid treatment in specific intervals. Three intervals were chemically stimulated: one in the unaltered deep granite, one in the hydrothermally altered fractured granite of the upper basement and one in the Buntsandstein sandstones (Figure 5.7). First, to treat the deepest zone, a single packer was installed at the 2368-m depth, and 120 m^3 of the stimulation fluid was injected below. Then, to treat the intermediate zone, a single packer was installed at the 2340-m depth, and 43 m^3 was injected. During the injection through the coiled tubing, the pressure injection is controlled and considered as sustainable. Assuming the chemical fluid penetrates uniformly the rock mass and considering the volume of chemical fluid injected and the volume of the well at the stimulated zone, the height of the stimulated zone is estimated to 40 m above 2340-m depth. Finally, to treat the shallowest zone, a single packer was installed at the 2010-m depth, and 87 m^3 of stimulation fluid was injected up to the casing shoe at

the 1924.5-m depth. After the chemical treatments, the injectivity index increased by a factor of 1.70 (Table 5.1).

Two days afterward, the hydraulic stimulation was applied to the open section of the well to physically reactivate existing fractures. Hydraulic stimulation typically consists of injection of a large amount of water at a high flow rate to increase the pore pressure within the rock mass, which reduces the effective stress and promotes shearing of existing weak fractures in friction mode or the creation of new fractures either in shear mode if a significant natural differential stress (i.e. $\sigma_1 - \sigma_3$) exists or in mode I tension when the in-situ shear stresses are very small and the fluid pressure is very high [*Pine and Batchelor*, 1984; *Cornet*, 1987; *Schmittbuhl et al.*, 2014]. It was demonstrated that this technology is efficient in both sedimentary and crystalline reservoirs [*Baumgärtner et al.*, 2005; *Huenges et al.*, 2007; *Häring et al.*, 2008; *Schindler et al.*, 2010] but might generate significant induced seismicity [*Majer et al.*, 2007; *Cuenot et al.*, 2008; *Bromley and Majer*, 2012; *Mukuhira et al.*, 2013]. At Soultz-sous-Forêts, high-precision mapping of the induced seismicity delineated the great extent of hydrothermally altered zones where permeability enhancement primarily occurred [*Evans et al.*, 2005a]. Most of the flow entered the cores of the major permeable fault zones, whereas clusters of new permeable fractures indicate the zone of damage to the fault [*Evans et al.*, 2005b]. A comparison of borehole image logs before and after the hydraulic stimulation indicated that all the permeable fractures had undergone mechanical damage and that major flowing fractures displayed dislocations of millimetres to centimetres. Some of these deformations at the centimeter scale in the deep reservoir of Soultz are slow deformations associated with aseismic events [*Cornet*, 1987; *Schmittbuhl et al.*, 2014]. Thus, induced microseismicity is not always a good indication of the efficiency of the hydraulic stimulation and permeability enhancement. During the hydraulic operation in well GRT-1, a moderate volume (3250 m^3) of water was injected from the wellhead by increasing the flow rate in steps from 10 L s^{-1} to 80 L s^{-1} and then stepping down the flow rate to 10 L s^{-1}. No proppant or packer was used during the hydraulic stimulation, and the injectivity index was improved by a factor of 1.50. After the TCH treatments, the injectivity of well GRT-1 increased fivefold. Only a few significant microseismic events were recorded during the thermal stimulation,

approximately a couple of hundred events were detected by the automatic detection system during the hydraulic stimulations based on data from the real-time seismic monitoring network deployed during the stimulation, and none occurred during the chemical simulation. Due to the low wellhead pressure during the stimulation operations, no events were felt by nearby residents [*Maurer et al.*, 2015].

5.6.2.3.3 Well logging and mud logging

During all drilling operations, mud-logging data were recorded. Cuttings were collected from the drilling mud every 3 or 4 m of advancement, and their analysis provided a lithostratigraphic survey of the well. It also indicated where the well intersected major fractures based on the presence of secondary quartz and hydrothermal minerals and higher calcite content (Figure 5.7). Investigation of the rock cuttings was an efficient method for identifying hydrothermally altered zones in the granite [*Dezayes et al.*, 2010b; *Meller et al.*, 2014]. To evaluate the geometry of these fractures, an acoustic image log was acquired following the drilling operations in December 2012 (Figure 5.6). The present study is based on these acoustic image logs, which were produced by Schlumberger and are referred to as Ultrasonic Borehole Images (UBIs). This logging was performed using a transducer that emits an ultrasonic pulse towards the borehole wall and records the first echo [*Zemaneck et al.*, 1970]. The amplitude and transit time of the reflected signal generate two unwrapped borehole images (Figure 5.8). The amplitude data correspond to the energy of the reflected signal, that is, the reflectivity of the borehole wall. The transit time of the pulse from the transducer to the wall and its return is related to the geometry of the borehole and the acoustic velocity in the wellbore mud. The transducer is rotated as it advances, which allows it to create a complete map of the wall as the tool travels a spiral trajectory. An orientation tool consisting of a three-axis inclinometer and a three-axis magnetometer is added to the probe to orient the images with respect to magnetic north [*Serra*, 2008]. It is thereby possible to map the fracture orientations along the well [*Davatzes and Hickman*, 2005b]. Natural fractures intersecting the well appear as continuous sinusoidal traces. The amplitude and phase of these traces provide quantitative estimates of their orientations (Figure 5.8). If this sine wave is also visible in the transit time image, then the fracture is

interpreted as an open structure at least at the borehole scale. If not, then the fracture is assumed to be completely or partly filled with secondary deposits.

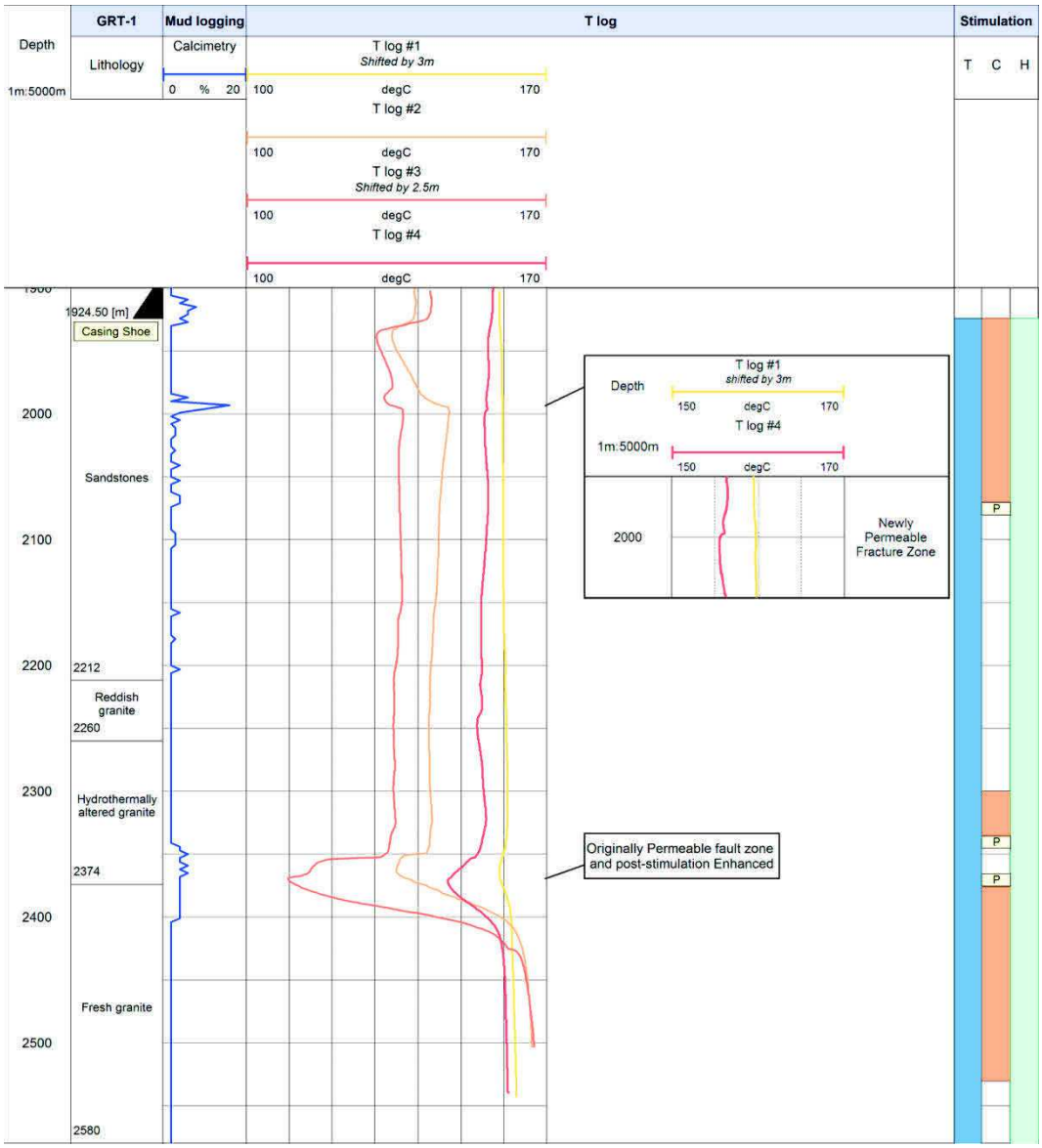

Figure 5.7 Composite log of well GRT-1. Calcimetry was measured by the mud-logging company. T logging operations were performed before the stimulations (*T* log #1), during the hydrochemical stimulation (*T* logs #2 and #3) and following the stimulations (*T* log #4). Stimulation zones are indicated.

Acoustic image logs are also commonly used to identify borehole breakouts and drilling induced tensile fractures (DITFs), which are important indicators of the stress state around the borehole[*Valley and Evans*, 2007; *Tingay et al.*, 2008]. DITFs are narrow, sharply defined features (Figure 5.8) that are produced when

the tensile stress around the wellbore exceeds the tensile strength of the formation [*Brudy and Zoback*, 1999]. They are created along the azimuth of the maximum horizontal stress, that is, perpendicular to the breakout direction. They also appear in pairs 180° apart and are typically vertical in a near-vertical well (Figure 5.8). Characteristics of DITFs are sensitive to the mud weight and to thermal stresses induced by the cooling of the borehole wall during circulation of drilling fluids. The lithology can also be identified in acoustic image logs.

For example, in Figure 5.8, the Permian sandstones are affected by DITFs, and the contact with the underlying basement, which is cut by natural fractures with low dips, is well defined. The sediment-basement interface is difficult to identify based on mud logging primarily because the cuttings from both formations are very similar: the cuttings from reddish sandstone containing clasts of altered granite are difficult to distinguish from cuttings from reddish altered granite. The pre-stimulation acoustic image logs of well GRT-1 were acquired at a vertical resolution of 1 cm and an azimuthal resolution of 2°. The inclinometer provided vertical deviations accurate to +/- 2°, and azimuthal measurements accurate to +/- 0.5° at the latitude of Paris.

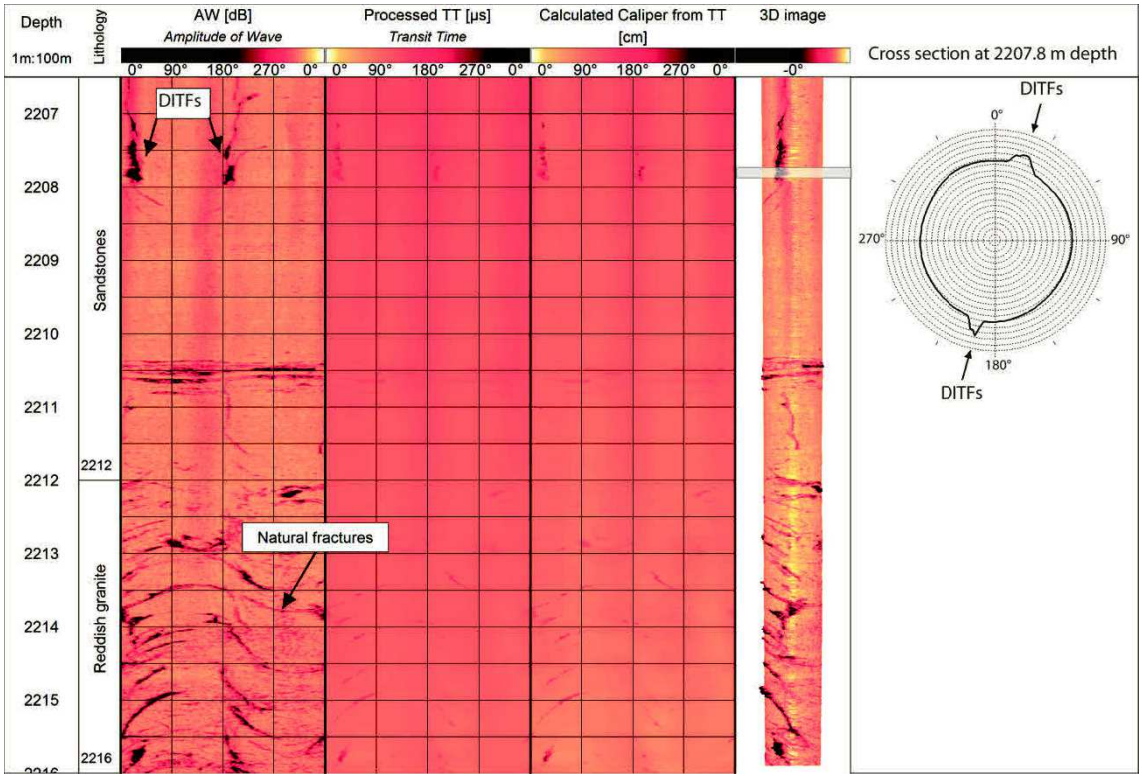

Figure 5.8 Example of acoustic image logs at the sediment-basement interface in well GRT-1. An image of the diameter (cm) was developed from the processed transit time data (μs), and a 3-D image of the well was constructed. The colour scale applies to the amplitude data (dB). An averaged cross-section was drawn through the 2207.77–2207.83-m depth interval (grey frame in the 3-D image of the well). On the cross-section, the concentric patterns are spaced 1 cm apart, and the thick line denotes the wellbore.

The temperature (*T*) logs obtained during the stimulation were a cost-effective way of assessing the stimulation success. Specifically, local variations in the *T* logs typically reflect remnant cooling of permeable fractures following the stimulation injections. Four *T* logging operations were performed in well GRT-1 in 2013 (Figure 5.6 and Figure 5.7). *T* log #1 was the pre-stimulation *T* log and was obtained four months after the drilling but before the thermal stimulation. The well was not disturbed during this period following the acidification in January. The sampling resolution of *T* log #1 was 0.10 m. The second log, *T* log #2, was the post-C-stimulation *T* log, which was obtained after the chemical stimulation and thus was highly affected by the fluid injection. The third log, *T* log #3, was the post-H-stimulation *T* log and was obtained after the hydraulic stimulation, that is, two days following the chemical treatment. The sampling resolution of *T* logs #2 and #3 was 0.20 m. The last log, *T* log #4, was the post-stimulation *T* log and was obtained five months later under thermal equilibrium conditions. The sampling resolution of *T* log #4 was 0.15 m. In December 2013, a second acoustic image log of well GRT-1 was obtained (Figure 5.6) with a vertical resolution of 1 cm and an azimuthal resolution of 2°. Acoustic imaging surveys are a very useful method for assessing the fracture network enhancement based on a comparison of pre- and post-stimulation data [*Cornet et al.*, 1997]. This technique is not commonly used in EGS project. The goal of the present study was to assess the information by comparing the pre- and post-stimulation data sets and to answer questions such as the following: What modifications may be discerned by comparing two acoustic image logs? What is the resolution of the comparison? Does the comparison between pre- and post-stimulation acoustic image logs contribute significantly to the assessment of the stimulation compared to *T* logs?

5.6.2.4 Methodology

5.6.2.4.1 Data processing of acoustic image logs

The acoustic image logs were processed using the software program WellCAD (ALT). First, the amplitude (AW) data and transit times (TT) in the image logs recorded in 2012 were reoriented with respect to magnetic north based on the azimuths acquired by the orientation tool. In 2013, unfortunately, the orientation tool was missing during the acquisition. Thus, the 2013 images were reoriented manually by visually superimposing 2013 images on the 2012 images. The manually reoriented images were rotated clockwise by an angle that varied with depth based on the rotation of the acoustic tool during the up-hole acquisition. The variation in the offset angle is important, and uniform rotation by a fixed angle in a long vertical section is not possible. This manual correction method is adequate for a localized zone, and the choice of the offset angle is well defined where natural fractures exist and is approximate where few patterns are present in the images. Depth mismatches were observed locally; these were due to cable expansion related to the temperature increase along the well or to a decrease in the acquisition speed related to abnormal borehole wall roughness associated with cavities. Depth corrections were applied to the image logs and data set of 2013 when depth differences exceeded 6 cm.

Table 5.2 Error bars (calculated from standard deviation) for the diameters measured in 2012 and 2013.

Tool calibration	Diameter (cm)	Erro Bar (cm)
Casing	22.05	
2012 measurement	22.17	0.011
2013 measurement	21.95	0.017
Massive zone in sandstones		
2012 measurement	22.01	0.095
2013 measurement	20.8	0.084

Once the transit time images were reoriented, they were corrected for decentralization effects that are negligible in GRT-1 with the average eccentering value of 0.38 cm in 2012 and 0.56 cm in 2013. They were also smoothed to remove spikes that are typically related to erroneous data recordings. The

smoothing method consisted of a cut-off based on 3 × 3 window analysis. One cut-off high level (75%) and one cut-off low level (25%) were applied. If the data value exceeded the cut-off, it was replaced with the cut-off value.

The processed transit time data were used to develop a 3-D image of the borehole based on the slowness of the acoustic wave in the mud measured using the acoustic tool in the well (Figure 5.8). In 2012, the acoustic tool used for acquisition was appropriate to image well-diameter in the range of 20–22.6 cm. In 2013, the acoustic tool used for acquisition was appropriate to image well-diameter between 18.6 and 20 cm. Measurements outside the pre-defined ranges are possible, but errors are expected to be large. For this study, we performed a posteriori calibration to estimate error bars of the acoustic borehole diameter measurements. The standard deviation was estimated from the transit time in 2012 and 2013 for different average diameter. We used the casing of well GRT-1 as a fixed reference that did not vary with depth or time. Its internal diameter given by the manufacturer is 22.05 cm. We then measured this casing diameter using the acoustic tool both in 2012 and 2013. The average diameter estimated from the transit time in 2012 was 22.17 cm +/- 0.011, which indicates a systematic error of +1.2 mm with respect to the reference value (Table 5.2). Accordingly, all the calculated diameter data obtained in 2012 were then reduced by 1.2 mm. The average diameter estimated from the transit time in 2013 was 21.95 cm +/- 0.017, and the acoustic tool measurements obtained in 2013 were reduced accordingly by 1 mm. The source of error between measurements in 2012, 2013 and the given value of the internal diameter is assumed to be governed by the error on the internal diameter given by the constructor. When the acoustic tools encountered cavities in the borehole wall, the diameters exceeded the acquisition range, and null data were recorded. In these instances, the transit time data appear as saturated zones, that is, white spots, in the images.

A 3-D image of the well was constructed bymapping the acoustic image onto the geometry provided by the transit times and using the amplitude data to create the colour palette in the 3-D image (Figure 5.8). From this 3-D image, cross-sections of the well were prepared. Another technique was developed to assess error bars of the diameter data in the sandstones. A massive zone (one not cut by fractures) was identified between depths of 2208 and 2210.5 m (Figure 5.8). The rms of this

zone was +/- 0.095 cm in 2012 and +/- 0.084 cm in 2013 (Table 5.2). Thus, for each cross-section, the thickness of the line in Figure 5.8, which is on the order of 1 mm, incorporates the error bars of the acoustic diameter.

Based on the acoustic diameter data set, a transverse cross-section was developed for each centimetre of depth. Nevertheless, because vertical mismatches between the 2012 and 2013 images were as much as approximately 6 cm, the cross-sections developed in this study represent 6-cm-thick slices to ensure that individual geologic structures could be identified and matched in the images of both years. Thus, a cross-section at a given depth is a representation of the average of slices on an interval ranging from 3 cm above to 3 cm below the given depth. The same types of corrections were applied to the amplitude data. Based on these corrected acoustic image logs and associated cross-sections, modifications of the fracture zones and mechanical movements of the wellbore were interpreted. Accuracies of the fracture attitudes are important for the comparison of the 2012 and 2013 images. In this study, the primary source of error in the fracture dip direction and dip angle arose from the ability of the interpreter to pick dipping planes consistently. To quantify the accuracy of measurements from the acoustic image log in the openhole section of well GRT-1, a series of tests were performed. These tests involved three acoustic image interpreters who hand-measured strikes and dips independently in the hydrothermally altered granite section. The reproducibility error was +/-3.85◦ for the strikes and +/-1.04◦ for the dips. The overall error considering the inclinometer accuracy and the reproducibility error may be regarded as very low.

The colour scale of the amplitude and transit time data were adjusted visually. The amplitude and transit time values are comparable in the internal diameter of the casing and assumed as a fixed reference in 2012 and 2013. Thus, this reference zone was used to determine the colour scale in order to compare the rest of the open-hole section with uniform colour scales.

5.6.2.4.2 Data processing of mud-logging data and *T* logs

To maintain a single depth reference for all thewell data in the study, the gamma ray log obtained during the pre-stimulation acoustic logging was used as the baseline. Detailed mud-logging data (rate of penetration (ROP), gas content,

drilling parameters) were not processed in this study. All *T* logging operations were performed downhole at a constant velocity of tool advancement. They were performed, however, by different loggers. *T* log#1was shifted downwards by 3 m to obtain a match with the gamma ray log (Figure 5.7). *T* logs #2 and #3 were obtained without the use of the gamma ray probe, and thus they were adjusted based on the position of a negative anomaly between depths of 1924.5 and 1994.5 m in *T* log #2 and 1921.5 and 1995 m in *T* log #3. This negative anomaly is well known from geothermal wells in Soultz and Landau and corresponds to fractures below the casing shoe that are zones initially affected by the cold-water injections [*Schindler et al.*, 2010]. The image logs show the casing shoe at the 1924.5-m depth. *T* log #2 was not shifted, and *T* log #3 was shifted downwards by 3 m to ensure a match between the distances from the top of the anomaly and the position of the casing shoe. The temperature probe used to acquire *T* logs #2 and #3 experienced technical problems during the acquisition. The bottom hole temperature in *T* log #1, considered to be the temperature under conditions of thermal equilibrium, was 163 °C. The bottom hole temperatures in *T* logs #2 and #3 exceeded 166 °C, although the well was supposedly cooled by the chemical and hydraulic treatments. These technical problems during the acquisition may have affected the data to an unknown extent. However, although the temperature data in *T* logs #2 and #3 may be inaccurate in absolute terms, the major anomalies were taken into account in relative terms. *T* log #4 was not shifted.

5.6.2.4.3 Evaluation of permeability enhancement

To evaluate the impact of the TCH stimulation in well GRT-1, the pre- and post-acoustic image logs were correlated and compared with the *T* logs. The mud-logging survey indicates that the natural fractures are filled with carbonates and sulphates. Any modifications of this fracturing in the post-stimulation UBI amplitude data indicate that mineral dissolution occurred with the chemical treatments. Chemical alteration is localized around fracture zones and is observed in the UBI amplitude data and in the transverse cross-sections. A reopening of the natural fractures in the post-stimulation cross-section may also be associated with hydromechanical impacts due to the hydraulic stimulation. Re-activation of an existing fracture could be interpreted in several ways. One is dip

slip along the fracture (Figure 5.9), in which case this displacement needs to be evaluated. The mean borehole cross-section is assumed to be circular before slip has occurred, and the centre of this circular cross-section is the centre of the well. If displacement has occurred, then the mean borehole cross-section does not match the initial one, and the centre of the post-stimulation well will appear to have shifted. The relative displacement along the fracture can be defined by a vector between two points on either side of the fracture. The displacement is the projection of this vector onto the cross-section through the well. Another possible interpretation is erosion of the wall at the intersection with the fracture plane because the fracture is a zone of weakness (Figure 5.9).

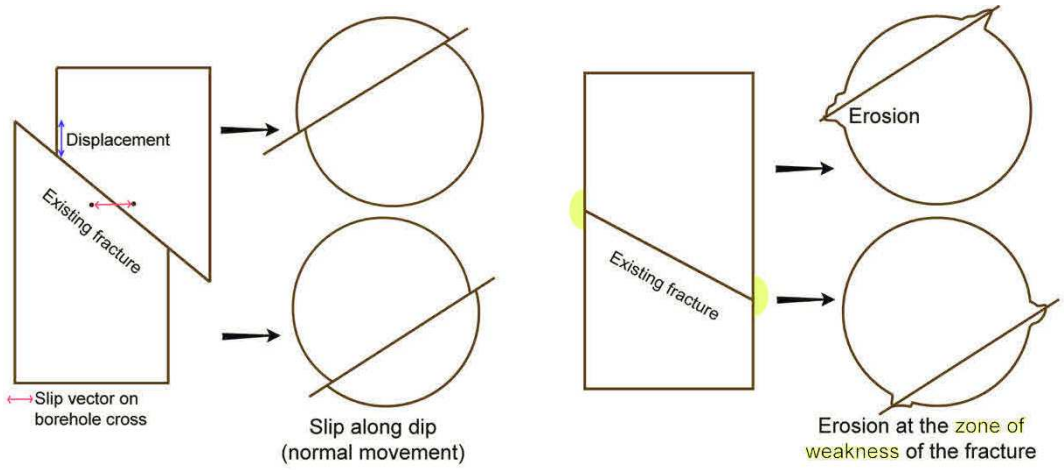

Figure 5.9 Dip slip along an existing fracture and erosion at the intersection between the fracture and the borehole wall.

Because the acoustic image logs represent only conditions before and after all the TCH stimulations, the *T* logs yield additional information about the permeability enhancement along natural fractures between each stimulation operation. Negative anomalies on the *T* logs are the thermal signature of permeable fractures that were cooled by the drilling and massive hydraulic injections. Negative anomalies on the *T* logs indicate circulation of cold water through permeable fracture zones. To quantify the permeability enhancement if a negative anomaly, that is, colder after an injection, appears, parameters used during injection have to be taken in account such as the temperature of the injected fluid, the flow rates, the duration of the injections, and the pressure of the injection. Positive anomalies on the *T* logs indicate circulation of hot geothermal

fluid through a permeable fracture zone. Moreover, *T* logs yield information about major fracture zones that were not imaged by the acoustic tool, for example, in instances of saturation.

A certain amount of saturation of the acoustic tools may also appear where the borehole is affected by significant breakouts and cavities. The appearance and deepening of a breakout on a poststimulation image log are not necessarily associated with stimulation operations butmay be a consequence of stress relaxation around the wellbore.

When evaluating the impact of the TCH stimulation on well GRT-1, the logs have been analysed for the following three patterns:

1) no modification is visible in comparisons of the pre- and poststimulation acoustic image logs;
2) modifications are visible in comparisons of the pre- and poststimulation acoustic image logs, but there is no corresponding temperature anomaly, which indicates the presence of an impermeable fracture zone;
3) modifications are visible in comparisons of the acoustic image logs, and there are corresponding temperature anomalies. If the temperature anomaly is visible on the pre-stimulation *T* log and is cooler after the stimulation, then the fracture zone is classified as originally permeable and post-stimulation enhanced (OPE). If the temperature anomaly appears only on the post-stimulation *T* log, then the fracture zone is classified as newly permeable (NP).

5.6.2.5 Results

All results established on the basis of well-logging and mud-logging data are given in Measured Depth.

5.6.2.5.1 Unmodified fracture zones

Unmodified zones were very rare based on the comparison of the pre- and post-stimulation data sets. The fresh granite below the major fault zone at the 2368-m depth was thermally, chemically and hydraulically stimulated. Fracture zones at substantial depths in the open-hole section were less affected by the thermal and hydraulic stimulations, which were performed either from the wellhead or from the

packer at the 2368-m depth. The fracture zone in the 2518.8–2520.5-m depth interval consists of five primary natural fractures with a mean dip direction of N56°E and a mean dip of 83°E (Figure 5.10). The post-stimulation amplitude and transit time images were shifted downwards by 0.22 m and rotated by 320° clockwise to match the oriented pre-stimulation image. The comparison between the pre- and post-stimulation amplitude images does not show evident modification around the fractures or in the granitic matrix. The same lack of modification was observed in the transit time images. In addition, the cross-sections show an unvarying well diameter in this interval.

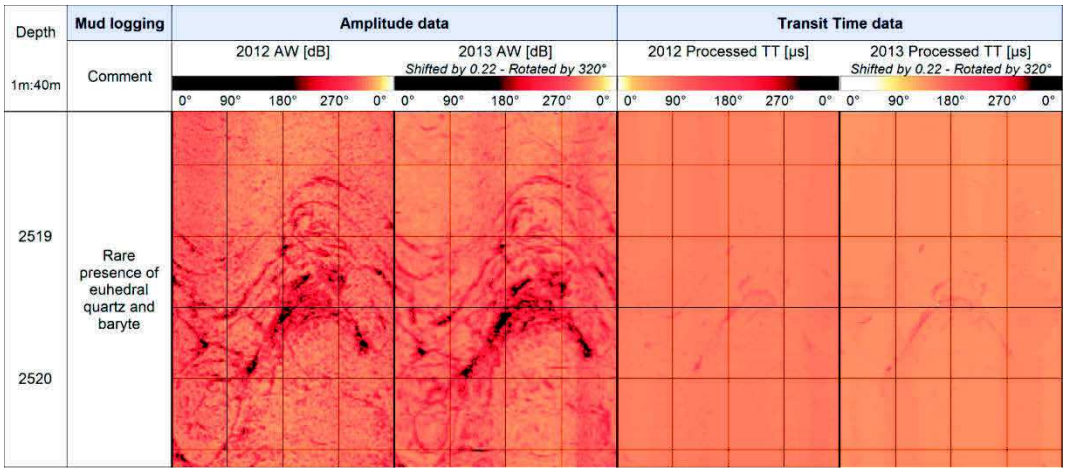

Figure 5.10 Comparison of acoustic image logs before and after the TCH stimulations showing a post-stimulation unmodified zone in the fresh granite. Amplitude data are expressed in dB, and transit time data in µs.

5.6.2.5.2 Modified fracture zones with no permeability evolution

A few fracture zones in the uppermost fresh granite were affected by the TCH stimulation, for example the zone in the 2396–2400-m depth interval. This zone is dominated by DITFs strikingN10°E and N190°E with one natural fracture at the 2399.3-m depth that strikes N24°E and dips 80°E (Figure 5.11). The post-stimulation images were manually shifted upwards by 0.1 m and rotated by 200°E to match the oriented pre-stimulation image. In the pre-stimulation amplitude image, the fracture at the 2398.5-m depth is barely visible. The percentage of calcite is very low in this section, and the mud-logging survey indicates the presence of rare quartz and carbonates in the cuttings. In the post-stimulation amplitude image, the shape of the fracture is better defined, and traces of

alteration are visible around the fracture. DITFs observed in the pre-stimulation amplitude data are more pronounced and wider in the post-stimulation amplitude data. Following the hydraulic injection, the DIFTs are wider. They may act as hydraulic connections between isolated fractures, but they are not associated with any perturbations in the thermal logs, which suggest that their involvement in the permeability enhancement is negligible. The natural fractures and DITFs are not visible in the transit time data, and no diameter anomaly is observed, and thus they are interpreted as superficial structures with no lateral penetration into the rock mass. This observation is valid below the top of the fresh granitic section, where there are tiny natural fractures more visible in the amplitude data that are increasingly less visible with depth.

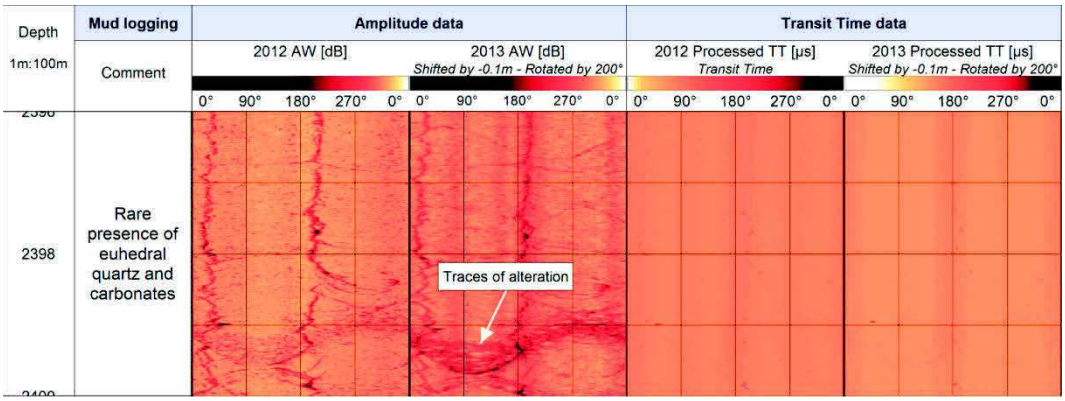

Figure 5.11 Comparison of acoustic image logs before and after the TCH stimulations showing a post-stimulation modified fracture with no permeability indication in the fresh granite. Amplitude data are expressed in dB, and transit time data in µs.

5.6.2.5.3 Modified fracture zones with permeability evolution

Newly permeable fracture zone in sandstones

The section of sandstone under the casing shoewas thermally, chemically and hydraulically stimulated. The pre-stimulation acoustic image log in the 1988–2010-m depth interval presents a cluster of 16 fractures with a mean strike of N21°E and a mean dip of 86°W Schmidt diagram in Figure 5.12). The calcimetry shows peaks of 6 per cent calcite at the 1988-m depth, 16 per cent at the 1993-m depth and 10 per cent at the 1996-m depth (Figure 5.7). This high calcite content in this zone is related to the fracture filling. Carbonates, barite and euhedral

quartz were also observed in cuttings from this zone. The core of the cluster in the 1994–1997-m depth interval is shown in Figure 5.12. Manual orientation of the post-simulation image of this zone to match the oriented pre-stimulation image was complex because the vertical and azimuthal shifts are not consistent. A schematic diagram of the zone is shown in Figure 5.13. Point A is located at 1994.19m at N208°E on the pre-stimulation image, and point A' is located at the 1994.23-m depth at N186°E. Point C is located at the 1996.41-m depth at N90°E, and point C' is located at the 1996.46-m depth at N104°E.

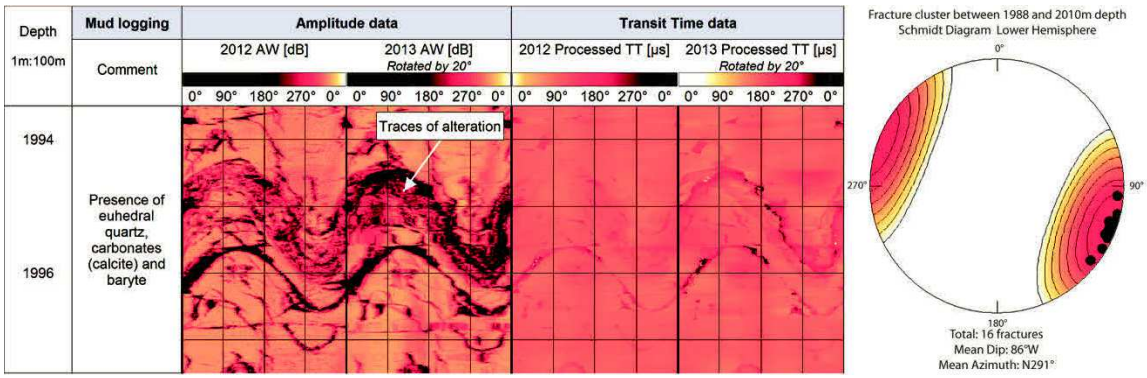

Figure 5.12 Comparison of acoustic image logs before and after the TCH stimulations in a newly permeable fracture zone in sandstones. The Schmidt diagram indication in the fresh granite. Amplitude data are expressed in dB, and transit time data in µs.

The vertical and azimuthal shifts differ between the top and the bottom of the zone. Point B (1995.61 m, N118°E) and B' represent the intersection between the base of the stratigraphic layer (in pink) and the top of the fracture F2 (in blue). The position of the stratigraphic layer was confirmed based on the FMI data and serves as a good reference because it was not modified by the TCH stimulation. The post-stimulation image was rotated by 20° to achieve a match between points B' and B, although this correction may not yield a match throughout the zone. No vertical shift was applied.

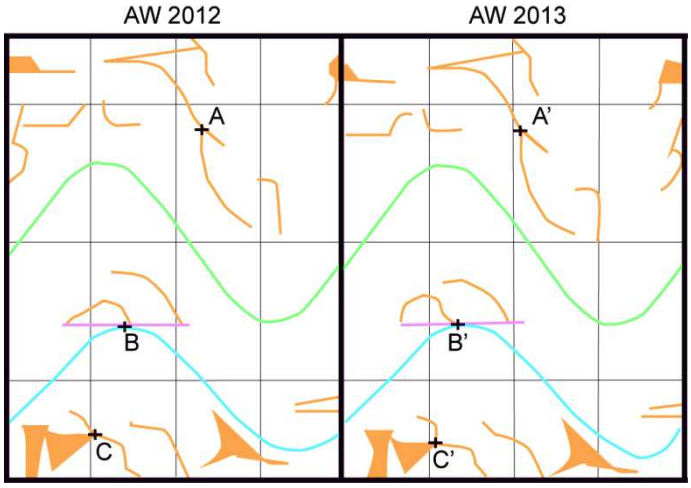

Figure 5.13 Schematic drawing of the fracture zone shown in Figure 5.12

To compare the same geologic structures on the cross-sections in Figure 5.14, the cross-sections are averages of 6-cm vertical intervals because the vertical shift never exceeds 6-cm. The core of the cluster contains two main fractures. One, designated F1, is located at the 1995.00-m depth, strikes N14°E and dips 85°W (Figure 5.14). It is shown in green in Figure 5.14. Another, designated F2, is located at the 1996-m depth, strikes N50°E, dips 83°W and has an aperture of 6 mm (Figure 5.12). It is shown in blue in Figure 5.13.

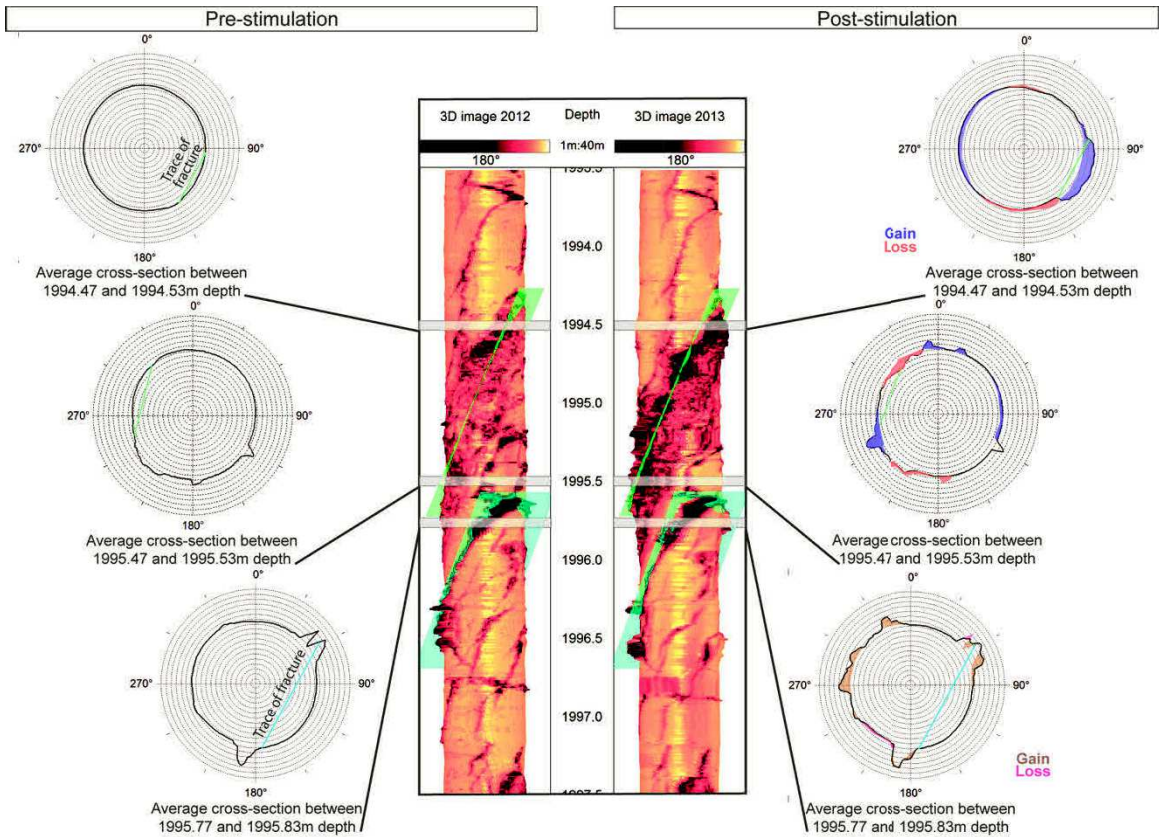

Figure 5.14 Average transverse cross-sections at the 1994.48- and 1994.52-m depths, at the 1995.48- and 1995.52-m depths and at the 1995.78- and 1995.82-m depths through stimulated fracture zones in the sandstones. The left and right cross-sections show conditions before and after the TCH stimulations, respectively. They are denoted by a grey frame in the 3-D image of the well. In the cross-section, the concentric patterns are spaced 1 cm apart, and the thick line denotes the wellbore.

Fracture F1 displays lower amplitudes in the post-stimulation amplitude image than in the pre-stimulation image. A comparison of the pre- and post-stimulation cross-sections at the 1994.5-m depth indicates significant azimuthal enlargement (between 0.5 and 2.5 cm) from N40°E to N150°E (Figure 5.14). The maximum enlargement of 2.5 cm is located between N80° and N150°, which corresponds to the trace of fracture F1 at this depth. Enlargements as wide as approximately 0.8 cm are also visible between N240°E and N330°E. Azimuthal shrinkages between 0.3 and 0.8 cm are also observed between N150°E and N220°E and between N330°E and N20°E. The post-stimulation cross-section at the 1995.50-m depth shows the bottom of fracture F1. Shrinkage between N300°E and N350°E corresponds to the intersection of the fracture trace with the well. Enlargements as wide as 3.5 cm at N250°E, 2 cm at N355° E and 1 cm at N20°E are associated with reactivation of another fracture near fracture F1. As in the cross-section at the 1994.5-m depth, small shrinkages as wide as 1 cm are observed between N190°E and N220°E, and enlargements as wide as 0.5 cm are observed between N60°E and N110°E.

To interpret the observed morphology change of the borehole, we followed the procedure of *Cornet et al.* [1997]. In the pre-stimulation cross-sections at depths of 1994.5 m (top of F1) and 1995.5 m (bottom of F1), circles with similar radii (12 cm) at both depths were searched for one that best fit both borehole traces at each depth (pink circle in Figure 5.15). At the 1995.5-m depth, the orange and the green circles with similar radii also fit the cross-section. The uncertainty in the circle's centre position is 2 cm. On the post-stimulation cross-sections at the 1994.5-m depth, a blue circle with a radius of 12 cm fits the zone not affected by fractures between N180°E and N0°E. At the 1995.5-m depth, a red circle corresponding to the zone not affected by fractures between N90°E and N180°E

was drawn on the post-stimulation cross-section. After the centres of the blue and red circles were plotted, a displacement vector of 2 cm between the centres was noted. Because this displacement is of the same magnitude as the uncertainty in the circle centre location, the displacement between the top and the bottom of fracture F1 is not considered significant.

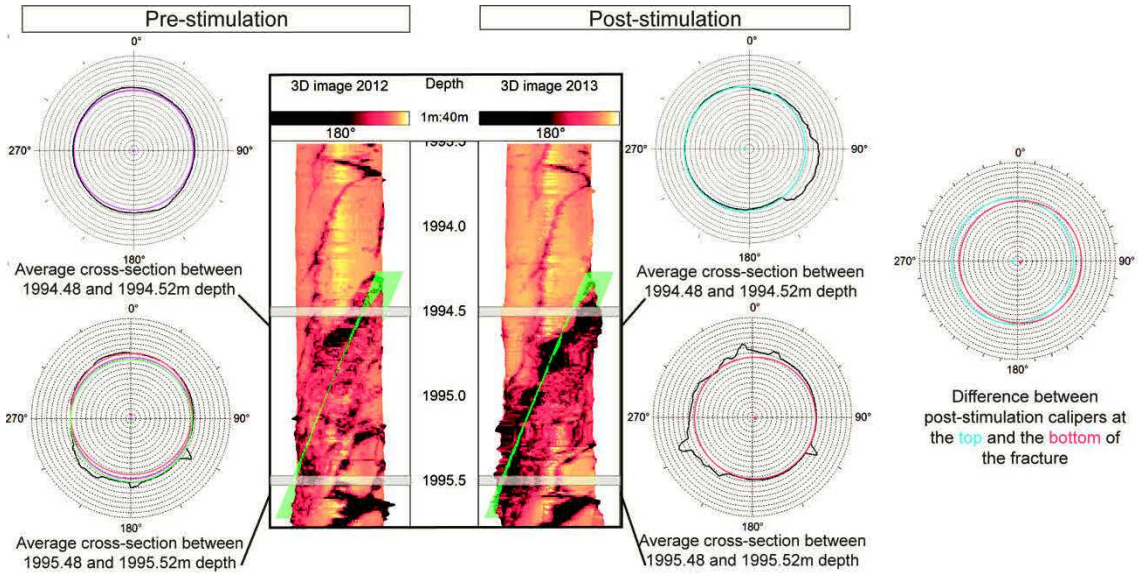

Figure 5.15 Determination of hydromechanical displacement along fracture F1. The pink circle denotes the theoretical 12-cm-diameter circle that fits in the pre-stimulation borehole at the 1994.5-m depth (top of F1). The orange and green circles denote theoretical 12-cm-diameter circles that fit the pre-stimulation borehole at the 1994.5-m depth (bottom of F1). The blue circle denotes the theoretical 12-cm-diameter circle that fits the post-stimulation cross-section at the 1994.5-m depth (top of F1), and the red circle denotes the theoretical 12-cm-diameter circle that fits the post-stimulation cross-section at the 1995.5-m depth (bottom of F1).

Fracture F2 does not display distinct modifications in the poststimulation amplitude image, whereas the top of the fracture is clearly visible in the post-stimulation transit time image (Figure 5.11). A cross-section was drawn at the 1995.8-m depth based on the prestimulation diameter data, thereby allowing for observation of the trace and penetration of fracture F2 (Figure 5.14). One branch of F2 that penetrates 4 cm into the rock mass is observed at N190°E, and a second branch that penetrates 3.5 cm into the rock mass consists of two peaks at N50°E and N60°E. The post-stimulation cross-section at that same depth shows

enlargement and shrinkage of both peaks of 0.5 to 3 cm. Enlargements of 0.5 cm to 2.5 cm between N265°E and N300°E and N330°E and N355°E correspond to re-activation of the bottom of a fracture near fracture F1.

The post-stimulation *T* log indicates circulation of hot geothermal fluid through this fracture zone based on a positive *T* anomaly of +1 °C at the 1995.5-m depth that was not observed in the pre-stimulation *T* log (Figure 5.7). Traces of alteration were observed in the post-stimulation amplitude data, fracture enlargements and shrinkages were observed in the diameter data, and a permeability enhancement was observed after comparing the pre- and post-stimulation *T* logs. Thus, this fracture zone is classified as a newly permeable fracture zone.

Originally permeable and post-stimulation enhanced fracture zone in granite

The pre-stimulation acoustic image log at the 2368-m depth shows a major structure at the base of the hydrothermally altered granitic section that strikes N175°E, dips 65°W and has an aperture of 24 cm (Figure 5.16). This structure is interpreted as a branch of the Rittershoffen fault where it was crossed by the well. The hanging wall of this fault zone consists of hydrothermally altered granite, whereas the foot wall consists of fresh granite. The fault is originally permeable as indicated by mud losses of 8 to 10 m^3/h during the drilling (Figure 5.16) and the negative *T* anomaly on the pre-stimulation log (Figure 5.7). Abundant euhedral quartz was observed in the cuttings from this zone: this material is interpreted as a quartz vein within the fault zone based on findings from the Soultz-sous-Forêts boreholes [*Genter et al.*, 2000]. To enhance the permeability of the fault zone, it was thermally and hydraulically stimulated. The transit time data from this zone are not useable and are saturated in the pre- and post-stimulation images (Figure 5.16) because the well diameter exceeded the range of the acoustic tools. The drill bit penetration rate in the 2368-m depth was double the mean rate in the granitic section, which indicates that the fault zone is borehole enlargement [*Traineau et al.*, 1992]. The post-stimulation acoustic image log was manually shifted downwards by 0.3 m and rotated by N240°E to match the oriented pre-stimulation image log (Figure 5.16). Although quartz veins are not observed in the amplitude image, quartz veins in the fault probably also underwent thermal microcracking because the *T* logs suggest permeability

enhancement following the water injections. A comparison of the *T* logs yields information about the permeability enhancement. The pre-stimulation *T* log shows a negative anomaly of −1°C in the 2350–2375-m depth interval and a temperature of 158°C at the 2365-m depth. Following the chemical injections, the *T* log shows a negative anomaly of −5°C between the 2350- and 2370-m depths.

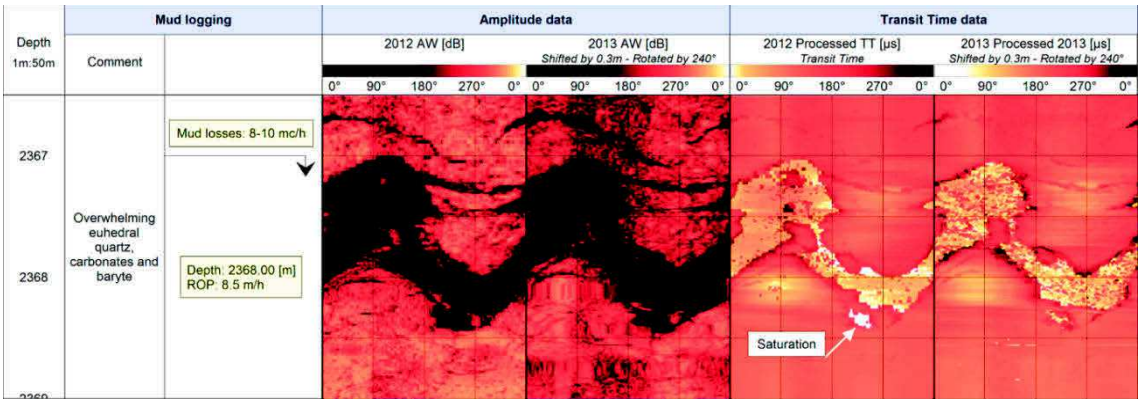

Figure 5.16 Comparison of acoustic image logs before and after the TCH stimulations showing an originally permeable and post-stimulation enhanced fault zone in the hydrothermally altered granite. Amplitude data are expressed in dB, and transit time data in µs.

Following the hydraulic injections, the *T* log shows a negative anomaly of −15°C between the 2355- and 2365-m depths and a small peak of 109°C at the 2370-m depth. In the post-stimulation *T* log, the negative anomaly spans the 2352–2395-m depth interval and shows a small peak of 147°C at the 2372-m depth. This *T* anomaly corresponding to the fault zone is the largest anomaly in the *T* logs (Figure 5.7). The increase of the temperature anomaly following the TCH stimulation can be interpreted as fluid circulation through the fault zone and could correspond to a permeability enhancement. Although no modifications are visible in a comparison of the acoustic image logs, the pre-stimulation acoustic image log, the mud-logging data and the comparison of the *T* logs indicate that this fault zone is classified as originally permeable and post-stimulation enhanced.

5.6.2.6 Discussion

5.6.2.6.1 Insights from the pre-stimulation data set

The acoustic image log is one of the few well-logging tools that provides in-situ orientation of the fracture network and stress field. It is also useful in characterizing the stratigraphy of the sedimentary units and altered facies in the granite. The sediment-basement interface is well constrained based on the acoustic image of well GRT-1, which is of better resolution than the mud-logging data (Figure 5.8). The hydrothermally altered zones in the granite are clearly shown in the acoustic image in terms of their thicknesses, orientations, apertures, and dips. The high reflectivity of quartz allows for identification of quartz veins. The pre-stimulation acoustic image log combined with the mud-logging data (e.g. the calcimetry) allows for characterizing the geometry of the major permeable fault zone crossing the well, identifying the potential zone for the TCH stimulation and designing the TCH stimulation. The pre-stimulation *T* log shows a nearly constant temperature profile with depth (Figure 5.7) that is typical of convective systems in high-enthalpy geothermal fields [*Arnórsson*, 1995; *Guillou-Frottier and Jaupard*, 1995; *Ikeuchi et al.*, 1998; *Guillou-Frottier*, 2003; *Magnenet et al.*, 2014; *Ratouis and Zarrouk*, 2016]. Our interpretation is that the geothermal fluid circulates vertically in the bulk rock through a dense, diffuse network of permeable fractures at the sediment-basement interface next to the major fault zone. The TCH stimulation of well GRT-1 was performed to enhance the permeability of this fracture network.

5.6.2.6.2 Insights from the post-stimulation data set

The comparison of the pre- and post-stimulation acoustic image logs reveals several modifications of the well following the TCH stimulation throughout the open-hole section except for the deepest part. These modifications can be classified as chemical and thermos hydro-mechanical damage (Figure 5.17). Note that the damage is not characterized as mechanical evolution of the material properties related to microfracture propagation but as a generic description of the impact of the stimulation on the formation. All natural fractures except a few in the deep part of the borehole that were not affected by injection display visible modification in the post-stimulation acoustic image, although this modification does not necessarily impact the permeability of the well.

The chemical alteration consists of local impacts around or within fracture zones and a halo of dissolution following their sinusoidal traces. In the sandstones, a high density of fractures in the 1988–2010-m depth interval without major displacement was observed. The entire sandstone formation in GRT-1 is 400-m thick which corresponds to the standard thickness of this formation in Northern Alsace [*Ménillet et al.*, 2015]. These fractures do not show natural permeability but do contain a high amount of calcite. The dissolution of carbonates and the opening of natural fractures F1 and F2 at the core of this cluster (Figure 5.11) were observed in the amplitude data from the post-stimulation image logs. Specifically, the reflected amplitudes are lower in the post-stimulation amplitude data and cross-sections are enlarged in the post-stimulation data. In the crosssections, fracture F1 in the sandstone displays enlargements at the 1994.5-m depth and shrinkage at the 1995.5-m depth. Erosion of fracture F2 is evident in the post-stimulation cross-section. This reopening of fractures could be the result of mineral dissolution after the chemical stimulation or erosion at the zone of weakness at the intersection with the fracture plane highly dipping and sub-vertical to the boreholewall. Mechanical erosion of the top and the bottom of the fracture occurred with the hydraulic injection. This fracture zone is associated with a small *T* anomaly in the post-stimulation *T* log (Figure 5.7), which indicates a small local post-stimulation permeability enhancement, although the contribution is minor.

Haloes of chemical alteration were also observed along isolated natural fractures in the fresh granite (Figure 5.10). Tiny pre-existing fractures are clearly more visible in the fresh granite after the TCH stimulation, but thermomechanical impacts are responsible for these fracture modifications because the cold water injection was performed from the well-head and the intensity of the fracturemodification decreased with depth (Figure 5.17). Microcracking in the fresh granite might have occurred in the matrix, and the post-stimulation amplitude image is slightly darker locally than the pre-stimulation image (Figure 5.10), whereas in the hydrothermally altered granite, the thermal microcracking occurred preferentially in quartz veins within major altered fracture zones.

The major fault zone at the 2368-m depth controls the flow rate in the well. Unfortunately, acoustic borehole imaging is not very appropriate for large

diameter fluctuations associated with deep cavities, and the acoustic measurements saturated in this zone (Figure 5.16). Considering the high natural injectivity of the fault, water penetrated the structure and the permeability was enhanced during the hydraulic stimulations as indicated by the *T* anomalies (Figure 5.7). Hydraulic erosion during the water injection and thermal microcracking of quartz veins are associated with this permeability enhancement (Figure 5.17). This fault displays a substantial offset, probably with a normal sense of motion, based on its position along the western edge of the horst. The size of the offset is difficult to estimate. Microseismicity in an area around the fault zone was recorded during the TCH stimulation. These microseismic events were localized in the crystalline basement, but they extend across an area several hectometres wide, and thus their locations are too imprecise to be attributed to this specific fault zone [*Maurer et al.*, 2015]. Even if the permeability enhancement is regarded as a direct consequence of the fracture reactivation, it cannot be simplistically linked to the microseismicity.

The acoustic image logs show modifications of the borehole wall resulting from the TCH stimulation of the sandstones, hydrothermally altered granite and fresh granite at a high resolution. Several tiny fractures, tensile fractures, alterations of fracture zones, and quartz veins are clearly visible in the acoustic image. These modifications would not be discernible using only *T* logs, whereas the combined post-stimulation acquisitions (*T* log and acoustic image log) allows for identification of modified zones associated with permeability enhancement.

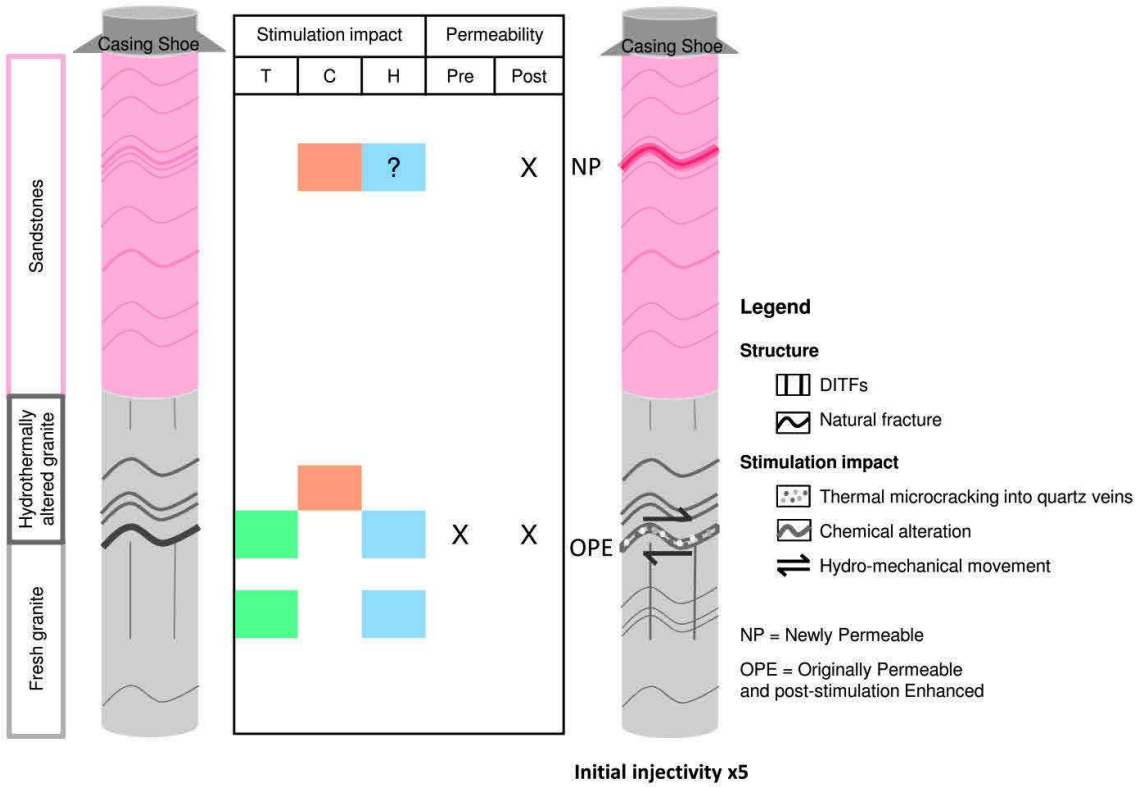

Figure 5.17 Schematic sketch of major modifications after the TCH stimulation of well GRT-1.

5.6.2.6.3 Permeability enhancement after the TCH stimulation in well GRT-1

This comparison of pre- and post-stimulation acoustic images is a technique that is rarely performed. Slow and aseismic deformations were observed by *Cornet et al.* [1997] in well GPK-1. In the open-hole section, several permeable altered fracture zones affect the granite. All permeable fractures and impermeable ones are critically stressed [*Evans*, 2005]. This statement implies that critical stressing is a necessary, but not a sufficient, condition for permeability development. *Meller and Kohl* [2014] demonstrated that on a reservoir scale, clay-rich zones foster the occurrence of aseismic movements on fractures. The permeability enhancement could be favoured by the presence of complex network of fracture partly filled by illite, secondary quartz and calcite in hydrothermalized zones. At Soultz and Rittershoffen, reservoirs are both fracture and fault dominated and stimulation operations targeted sealed fracture zones.

The open-hole section of GRT-1 is composed by sandstones and granite. The hydraulic properties of GRT-1 are controlled by the single fault of high natural

permeability at the base of the altered granitic section. This permeable zone is a porous, altered and fractured zone composed by illite, quartz, calcite and sulphides. After TCH stimulation, the majority of the permeability enhancement was localized in this zone. In GRT-1, chemical stimulation attacks calcite filling fractures in sandstones and granitic basement by dissolving those minerals in a similar way. Thermal and hydraulic stimulations could more impact fracture zones in the granitic basement because no induced seismicity was observed in sandstones during and after these operations. The higher fracture permeability in the granitic basement may be explained by the fracture roughness as it was investigated at Soultz by *Neuville et al.* [2010] and also by the presence of larger damage zone around the fractures.

Zones located in sandstones at 1995-m depth, filled by carbonates and quartz, and in the deep granite in the 2396–2400-m depth interval were impacted by the chemical and thermal stimulations. They display little or no permeability enhancement. The chemical and thermal modifications increased the connectivity between the well and the near-well field, contributed to cleaning of the open-hole section after the drilling and allowed for significant effectiveness of the low-rate hydraulic stimulation, thereby minimizing the microseismicity during the operations. The hydraulic stimulation affects only the fault zone located at 2368-m depth and improves the connectivity between the well and the far-well field. During and after hydraulic stimulation, induced microseismicity is observed. After the TCH stimulations, connectivity between the well and the near-well and far-well fields are improved based on the fivefold increase in the injectivity of well GRT-1.

5.6.2.7 Conclusion

The impact of the TCH stimulation on geothermal well GRT-1 was assessed based on the comparison between the pre- and post-acoustic image logs combined with the temperature logs. Local changes observed in the acoustic images are attributed to chemical and thermo-hydro-mechanical impacts. A fracture zone in the sandstones displays surrounding chemical alteration related to mineral dissolution. The chemical modifications are associated with mechanical erosion along the tops and bottoms of the fractures subparallel to the

well. A comparison of the *T* logs indicates a very small permeability enhancement. The major permeable fault zone crossing the well was not well represented in the acoustic images, but the *T* logs indicate that the initial permeability was greatly enhanced. Thermal microcracking of quartz veins and hydraulic erosion during the stimulation are probably associated with this enhancement. Below the major fault zone, in the fresh granite, a few isolated fractures were chemically altered. DITFs and small fractures were widened by the thermo-mechanical impacts on the well. The well behaviour after the TCH stimulation is controlled primarily by the fault, although almost all the natural fractures displayed evidence of modification in the acoustic logs. The *T* logs indicate significant permeability enhancement localized in and around the fault zone at the 2368-m depth.

5.6.2.8 Acknowledgments

This work was based on data from the ECOGI EGS project at Rittershoffen, France. A part of the work was performed in the framework of the LabEx G-Eau-Thermie Profonde, which is co-funded by the French government under the program ‘Investissements d’Avenir’. The manuscript was prepared as a contribution to the PhD thesis of Jeanne Vidal, co-funded by ADEME (French Agency for Environment and Energy). A part of this work was done in the framework of the H2020 DESTRESS Eu project which has received funding from the European Union Framework Programme for Research and Innovation under grant agreement No. 691728. The authors would like to kindly thank two anonymous reviewers for their contributions and manuscript improvement.

6 Réservoirs fracturés naturels et perméables du Fossé rhénan supérieur

6.1 Résumé

Ce chapitre s'appuie essentiellement sur la réinterprétation de données de puits de géothermie profonde dans l'ensemble du Fossé rhénan. Cette étude comparative permet de définir un cadre harmonisé pour les projets du Fossé. Il se décompose en deux parties.

La première partie du chapitre se présente sous forme d'un article soumis à la revue Geothermics. Il présente une synthèse géologique, thermique et hydraulique des réservoirs fracturés profonds dans le Fossé rhénan supérieur. Depuis les années 80, plus de 15 puits géothermiques ont été forés dans le Fossé rhénan supérieur, soit plus de 60 km de forage. L'étude s'appuie sur les puits des projets de Cronenbourg à Strasbourg, Soutlz-sous-Forêts et Rittershoffen en France, Bruchsal, Landau, Insheim et Brühl en Allemagne et Bâle en Suisse. L'ensemble des fiches descriptives des projets sur lesquelles s'appuie cette étude, sont réunies dans l'Annexe 1. Les projets pionniers reposaient sur le concept de porosité matricielle dans les grès ou encore sur le concept Hot Dry Rock dans les réservoirs granitiques profonds. Les forages ont démontré les circulations de la ressource géothermale piégée dans le réseau de fractures naturelles à l'interface entre la couverture sédimentaire et le socle granitique altéré. Les données géologiques, hydrauliques et thermiques issues des forages géothermiques ont été analysées afin d'étudier les zones de fractures naturelles qui chenalisent les circulations hydrothermales. Des zones de fractures perméables ont été recoupées par les forages de Soultz-sous-Forêts, Rittershoffen et Cronenbourg à Strasbourg en France, de Bruchsal, de Landau, d'Insheim et de Brühl en Allemagne. Des zones de fractures perméables ont également été recoupées au toit du socle granitique altéré par les forages de Soultz-sous-Forêts et de Rittershoffen en France et de Landau et d'Insheim en Allemagne. Enfin, des zones de fractures perméables ont également été recoupées dans le socle granitique profond pourtant peu altéré à Soultz-sous-Forêts en France et à Bâle en Suisse. La perméabilité des zones de fractures

semble dépendante de la lithologie avec un maximum de perméabilité atteint au toit du socle granitique altéré. Ces zones sont composées d'épaisses fractures ouvertes entourées d'une large zone poreuse et altérée. Elles sont marquées par des dépôts hydrothermaux secondaires suite aux paléo-circulations. La présence de zones de fractures perméables est souvent associée à des gradients très faibles qui marquent la convection. L'ensemble des profils de température acquis dans les puits montre un gradient géothermique élevé d'environ 100°C/km dans la couverture sédimentaire jusqu'au toit des grès triasiques. Les grès triasiques et permiens et le socle granitique sont associés à un régime convectif dans la majorité des puits avec des gradients géothermiques inférieurs à 10°C/km. Les profils des puits de Soultz indiquent une zone de transition entre la conduction et la convection dans les sédiments triasiques avec des gradients géothermiques intermédiaires entre 100°C/km et 5°C/km. Cette zone de transition n'est pas observée sur les profils dans d'autres puits géothermiques du Fossé rhénan supérieur.

Cette zone de transition est la cible de l'étude proposée dans la seconde partie du chapitre. Elle se présente sous forme d'un article publié dans Geothermal Energy Journal sous la référence Vidal J., Genter A., Schmittbuhl J. (2015). How permeable fractures in the Triassic sediments of Northern Alsace characterize the top of hydrothermal convective cells? Evidences from Soultz geothermal boreholes (France), *Geotherm. Energy*, Special Issue: Characterization of Deep Geothermal Systems, *3*(1), doi:10.1186/s40517-015-0026-4.

L'article détaille les données de diagraphies instantanées et différées disponibles dans les puits de Soultz GPK-2, GPK-3 et GPK-4 dans la couverture sédimentaire. Neuf zones de fractures sont identifiées d'après la corrélation des données de diagraphies dans les calcaires du Muschelkalk et les grès du Buntsandstein. La présence de pertes de boue totales ou partielles permet de qualifier les zones de fractures de perméables ou non. Aucun indice de perméabilité n'est observé au-dessus de la formation du Keuper. La partie supérieure de la couverture sédimentaire, jusqu'à 900 m de profondeur, agit probablement comme un cap rock imperméable qui isole les cellules de convection circulant dans les sédiments à la base de la couverture sédimentaire

(Trias inférieur et moyen) et dans le socle granitique. Contrairement aux zones de fractures perméables dans le socle granitique, celles du Muschelkalk et du Buntsandstein ne sont pas associées à des anomalies de température négative. La corrélation des zones de fractures entre les puits GPK-2, -3 et -4 n'est pas triviale bien que les puits ne soient séparées que de 6 m à ces profondeurs. Elle est réalisée à partir des anomalies de caliper qui indiquent la profondeur des zones de fractures. Toutes les zones de fractures ne sont pas recoupées par chacun des puits. Ces zones sont probablement reliées à un réseau de fractures naturelles plus large et connecté à la faille locale de Soultz dont la trace a été identifiée sur les carottes du puits d'exploration EPS-1.

Le socle granitique a fait l'objet de nombreuses études à Soultz tandis que la base de la couverture sédimentaire est moins connue. En raison de son dense réseau de fractures naturelles, elle représente un réservoir géothermique potentiel. Des zones de fractures perméables ont été recoupées dans les calcaires du Muschelkalk par les forages des Hélions, d'Insheim, et de Rittershoffen et dans les grès du Buntsandstein par les forages des Hélions à Preuschdorf, de Cronenbourg à Strasbourg, de Bruchsal, d'Insheim, de Rittershoffen et de Brühl. L'étude détaillée de ces zones de fractures perméables contribue à la compréhension des boucles de convection car elles coïncident avec le toit des circulations hydrothermales. Les fractures perméables sub-verticales dans les sédiments triasiques et dans le granite semblent contrôler les remontées et les descentes des boucles de convection tandis que les sédiments imperméables au toit des sédiments triasiques, qui forment un cap rock, semblent contrôler les circulations horizontales des boucles. La base des boucles de convection pourrait être contrôlée par le changement de régime de contrainte dans le socle granitique profond, sous 3000 m de profondeur [*Evans*, 2005].

D'après les données de puits du Fossé, les 500 premiers mètres du socle granitique altéré semblent cependant correspondre au réservoir naturel le plus perméable.

6.2 Perméabilité naturelle des réservoirs gréseux et granitiques à partir des données de puits géothermiques du Fossé rhénan supérieur (Article soumis dans Geothermics)

Overview of naturally permeable fractured reservoirs in the central and southern Upper Rhine Graben: insights from geothermal wells

Jeanne VIDAL[1*] and Albert GENTER[2]

[1] IPGS, University of Strasbourg, 1 rue Blessig, 67084 Strasbourg Cedex, France
[2] ES-Géothermie, Bâtiment Belem, 5 rue de Lisbonne, 67300 Schiltigheim, France

6.2.1 Abstract

Since the 1980's, more than 15 geothermal wells have been drilled in the Upper Rhine Graben, which represent more than 60 km of drill length. Although some early concepts were related to purely matrix-porosity reservoirs or Hot Dry Rock systems, geothermal projects are currently exploiting the geothermal resources that are trapped in fracture networks at the base of the sedimentary cover and in the granitic basement. Permeable fractures in Triassic sediments have been observed during drilling operations at Soultz-sous-Forêts, Rittershoffen, Cronenbourg (France), Landau, Insheim, Bruchsal and Brühl (Germany). Permeable fractures in the uppermost altered granitic basement have been observed at Soultz-sous-Forêts, Rittershoffen (France), Landau and Insheim (Germany). Permeable fractures in the deepest granitic basement are intersected at Soultz-sous-Forêts (France) and Basel (Switzerland). Fracture permeability appears to be different in the lithologies with a maximum at the top of the hydrothermally altered granite. An analysis of geologic, hydraulic and thermal data from 15 geothermal wells in the Upper Rhine Graben suggests that the highest permeability could be associated with fracture zone at the top of the hydrothermally altered granitic basement. They are composed of thick open fractures surrounded by a large porous and altered damage zone.

Keywords: fracture permeability, geothermal resources, geothermal systems, Upper Rhine Graben

6.2.2 Introduction

The Upper Rhine Graben (URG) is a part of the European Cenozoic Rift System. This graben is characterized by a series of thermal anomalies that are interpreted as the signature of large-scale natural advection and convection inside a nearly vertical multi-scale fracture system that cross-cut both deep-seated Triassic sediments and Paleozoic crystalline basement [*Schellschmidt and Clauser*, 1996; *Pribnow and Schellschmidt*, 2000a; *Baillieux et al.*, 2013]. The sedimentary formations of the URG host oil fields that have been widely exploited in the past and are still exploited in Germany [*Sittler*, 1985]. They exhibit exceptionally high temperature gradients up to 100°C/km. Over the last 35 years, geothermal projects have been developed in France, Germany and Switzerland to exploit deep geothermal energy.

Geothermal systems in the URG are all deep fracture-controlled circulation systems. Deep sedimentary systems in Triassic and Permian sandstones at the bottom of the sedimentary cover are affected by natural fracture clusters, which exhibit higher natural fracture permeability than matrix permeability. The exploitation of granitic systems was initially developed based on the *Hot Dry Rock* (HDR) concept. The HDR concept was initiated in Los Alamos (USA) and Cornwall (UK) to exploit the vast energy resources that reside as heat in the low-permeability rocks that underlie most continental regions at practically drillable depths [*Schulte et al.*, 2010]. The Soultz-sous-Forêts pilot project was initially based on the HDR technology to create artificially a heat exchanger in the deep crystalline rocks. All wells that intersected the deep sedimentary cover and the granitic basement exhibit at least one permeable natural fracture zone. However, the natural permeability of these fracture zones are weak and need to be stimulated to reach the permeability required for industrial project. These deep reservoirs are more associated with *Enhanced Geothermal System* (EGS) technology whose are based on stimulation of existing fractures in order to improve their low initial permeability [*Ledru and Guillou-Frottier*, 2010]. Recent geothermal projects are directly based on lessons that have been learned from Soultz projects. Projects have targeted fracture networks at sediment-basement interfaces to exploit geothermal resources at shallower depths in the URG. Indeed, the temperature of the geothermal fluid is lower but the flowrate is higher

than that in deeper reservoirs. Fracture zones that channelized the hydrothermal circulations are organized as clusters and not require stimulation treatments systematically. They are described as *hydrothermal* systems with large natural reservoir permeability.

Geomechanical properties of the reservoir are influenced by the lithology [*Meixner et al.*, 2014] as well as the degree of hydrothermal alteration in the granitic basement [*Meller and Kohl*, 2014]. The hydraulic yield of geothermal reservoirs is mainly controlled by fracture zones in the Upper Rhine Graben. In this paper, we will compare the permeability of fractures zones with the lithology of geothermal reservoirs based on temperature data and hydraulic yield in several wells. Sometimes hydraulic yield are not available for each reservoirs and temperature data are a good indicator of first-order fluid circulations [*Evans et al.*, 2005a; *Genter et al.*, 2010; *Vidal et al.*, 2017]. After a presentation of fractured system and hydrothermal circulations in the Upper Rhine Graben, deep geothermal projects of the central and southern Upper Rhine Graben will be detailed. The geothermal project of Soultz-sous-Forêts will be used as a frame to compare geological properties, hydraulic yield and thermal data. These data will be described for each reservoir in each geothermal site and then relation among fracture zones, in-situ stress field, lithology and hydrothermal circulations will be discussed.

6.2.3 Structural evolution of the URG

The Upper Rhine Graben (URG) forms the central, most conspicuous segment of the ECRIS [*Illies*, 1965], which extends over a distance of more than 1000 km from the North Sea to the Mediterranean (Figure 6.1). The NNE-trending URG, which is limited by the Rhenish Massif to the north and the Jura Mountains to the south, has a length of some 300 km and a width of 30 to 40 km. This geological setting will focus on the structural inheritance of the crystalline basement and the evolution of fractured system from Variscan to late Alpine.

The Variscan crystalline basement of the URG is characterized by three major tectonic terranes, oriented NE to NNE, from north to south, the Rhenohercynian, the Saxothuringian and the Moldanubian that present major lithological differences [*Ziegler*, 1990; *Edel and Weber*, 1995; *Edel and Schulmann*, 2009].

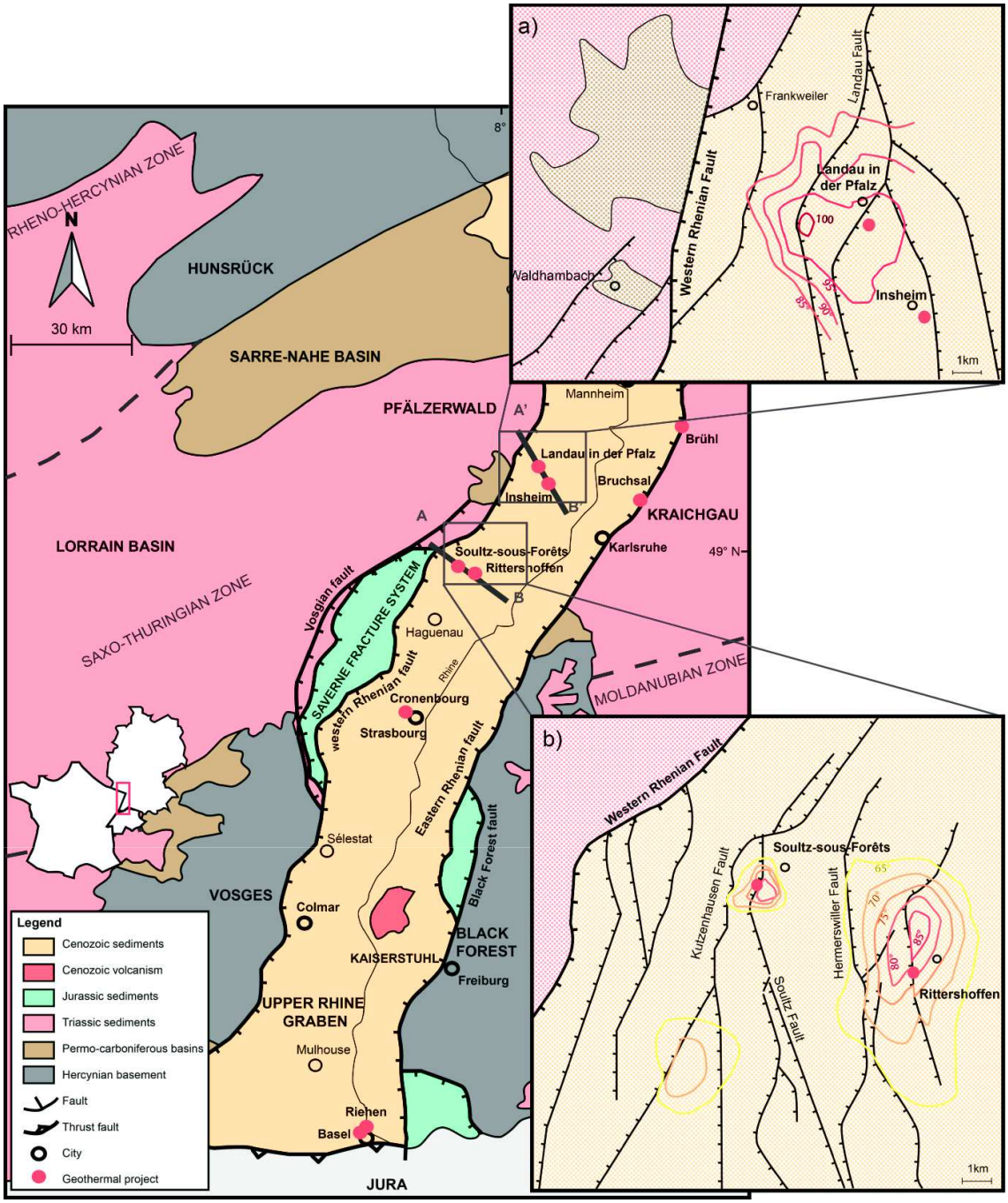

Figure 6.1 Geological map of the Upper Rhine Graben. Temperature anomaly at the top of the basement of a) Soultz-sous-Forêts and Rittershoffen [*Baillieux et al.*, 2014] and b) Landau and Insheim (thermal isotherms are from *Eisbacher and Fielitz* [2010] and geological data are from *GeORG Team* [2017]. Sections AB and A'B' are represented in Figure 6.2.

They are intruded by carboniferous granitoid (340 Ma (Visean) and 270 Ma (Permian)) that exhibit a large petrological and geochemical diversity of crystalline rocks, which are related to a variety of active deep magmatic sources

and different petrogenetic mechanisms.[*Lagarde et al.*, 1992; *Altherr et al.*, 1999, 2000]. These granitoids are emplaced following a NE to NNE direction according to main weakness zones such as collisional or shear zones. These inherited Hercynian NE to NNE-striking crustal weakness were reactivated to the URG formation under compressional stresses during Alpine and Pyrenean collisions [*Illies*, 1965, 1972; *Villemin and Bergerat*, 1987; *Schumacher*, 2002; *Dèzes et al.*, 2004; *Edel et al.*, 2007]. Mesozoic platform sediments of Triassic (Buntsandstein, Muschelkalk and Keuper) and Jurassic (Lias and Dogger) times that results from eroded Variscan belt are also affected by structural evolution during Cenozoic rifting. [*Villemin and Bergerat*, 1987] and [*Villemin and Bergerat*, 1987; *Schumacher*, 2002] proposed a Cenozoic rifting of the URG divided into four brittle deformation phases, which were accompanied by different stress regimes from the late Eocene rifting to the late Miocene. The first phase (middle to late Eocene) was characterized by an N–S compressive regime. During the second phase (late Eocene to late Oligocene), major E–W extension resulted in the greatest rifting and the development of thick sedimentary sequences in the URG [*Doebl*, 1967]. These events included two marine transgressions, which induced the deposition of the carbon-rich Pechelbronn layers and salt layers in the southern area of the graben, among others. During the early Miocene, the stress regime changed to an NE–SW-oriented compressive phase. This episode was characterized by the uplift of the upper mantle and crust, as suggested by the up-doming Moho and the beginning of volcanism at the Vogelsberg and Kaiserstuhl volcanos [*Fuchs et al.*, 1987]. The prevailing stress regime in the URG from the late Miocene to the present has been a compressional regime with an NW–SE orientation, as observed over much of central Europe, which resulted in a left-lateral transcurrent motion [*Illies and Greiner*, 1979; *Bergerat*, 1985].

6.2.4 Thermal settings and fractured system

In the URG, the underground temperature distribution is spatially heterogeneous, and a series of local anomalies with temperatures above 140°C at 2-km depth. Most of them are mainly concentrated on the western side of the URG, where the direction of the border fault rotates from N20°E to N45°E, such as at Soultz-sous-Forêts (France), Landau (Germany), or Mainz (Germany) [*Schellschmidt and Clauser*, 1996; *Baillieux et al.*, 2013, 2014; *Dezayes et al.*, 2015]. Temperature

data from various oil and geothermal wells revealed a concentration of hot zones along large-scale faults such as the Soultz fault, Rittershoffen fault and Landau fault zone (Figure 6.1a and b) [*Benderitter et al.*, 1995; *Pribnow and Clauser*, 2000; *Pribnow and Schellschmidt*, 2000a; *Bächler et al.*, 2003; *Baillieux et al.*, 2013]. These geothermal anomalies at the local scale are attributed to buoyancy-induced hydrothermal circulation in fractures within the crystalline basement and sandstones. The isotherms have been very disturbed by the presence of sub-vertical normal faults (Figure 6.2). The up-flow of thermal water occur mainly along westward dipping normal faults [*Baillieux et al.*, 2014]. The so-called 'Soultz geothermal anomaly' is one of the most important temperature anomalies and has been the subject of numerous studies. Hydrothermal convection may explain 75-85% of the anomaly [*Baillieux et al.*, 2013]. The radiogenic heat production due to the crystalline composition of the basement may explain the remaining 15-25%. The highest radiogenic productions are associated to hydrothermally altered zones. In the deep geothermal well GPK-1, the highest measurements of radiogenic production in core samples (from 5.5 to 6.5 $\mu W/m^3$) are localized from 1400and 1550 m MD [*Rummel et al.*, 1988]. Continuous logging of the deep geothermal well GPK2 revealed values of radiogenic production up to 7 $\mu W/m^3$ between 3700 and 3800 m depth and at 5060 m depth that correspond to permeable levels [*Pribnow*, 2000; *Grecksch et al.*, 2003].

Fractured system within the crystalline basement and sandstones channelized hydrothermal circulations. All the geothermal fluids collected in deep geothermal wells result from a mixing of primary marine brine (seawater evaporation at least up to the halite precipitation stage) and water of meteoric origin [*Pauwels et al.*, 1993; *Aquilina et al.*, 1997; *Sanjuan et al.*, 2010, 2014]. They are Na-Cl type fluid with a high salinity values, approximately 100 g/L, and a pH value close to 5 [*Sanjuan et al.*, 2014, 2016]. Both fossil and present-day hydrothermal circulations in the fracture system have resulted in a strong dissolution of the primary minerals such as biotite and plagioclase as observed in the granitic basement of Soultz, and a significant deposition of some altered minerals such as clay minerals (illite, tosudite), calcite, secondary quartz and sulfides [*Genter and Traineau*, 1993]. Circulation ages have been estimated from fracture filling dating at Soultz. Illites from fracture veins revealed ages from the Permian,

Cretaceous, Miocene and earlier [*Schleicher et al.*, 2006; *Bartier et al.*, 2008]. Hydrothermal circulations might have been linked to major volcanic events in the URG during the Permian [*Lorenz and Nicholls*, 1976], Cretaceous and Miocene [*Illies*, 1972]. Mineralogical studies of assemblages in fracture fillings indicate a complex polyphaser circulation system [*Smith et al.*, 1998; *Dubois et al.*, 2000].

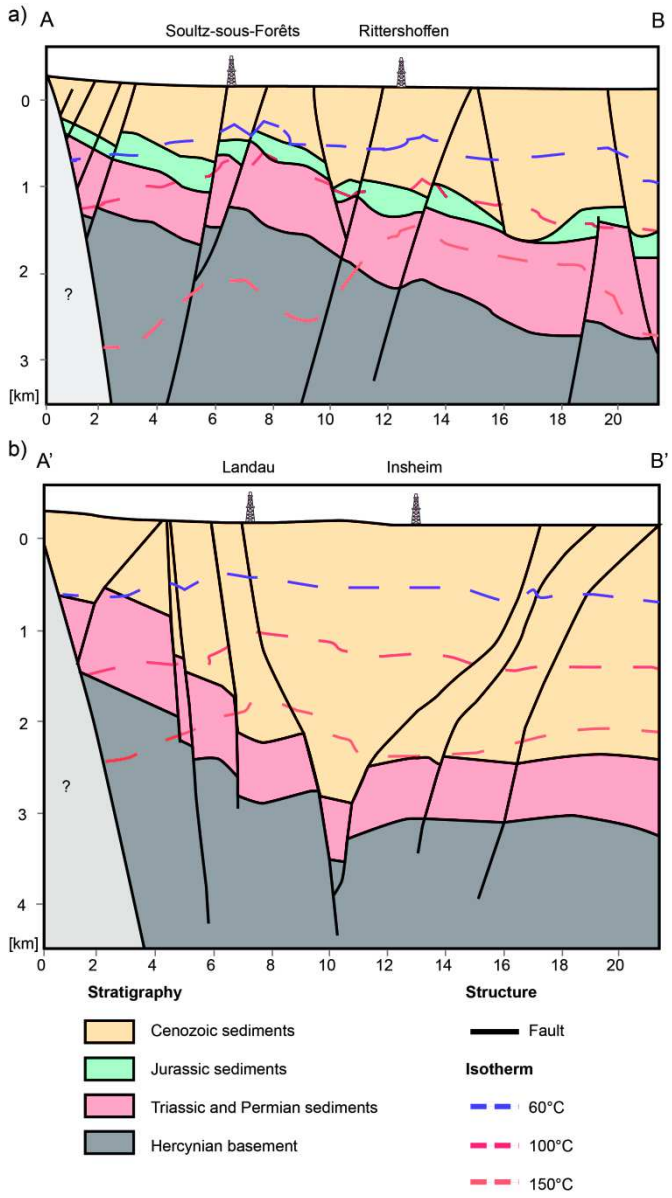

Figure 6.2 a) Geological cross section and isotherms between Soultz and Rittershoffen, which are indicated as AB in Figure 6.1 b) Geological cross section and isotherms between Landau and Insheim, which are indicated as A'B' in Figure 6.1 (after *GeORG Team* [2017]).

6.2.5 Presentation of geothermal sites

The geothermal well GCR-1 was drilled in 1984 at **Cronenbourg** (Alsace, France) to explore the geothermal potential of the sandstones in Buntsandstein (Lower Triassic) (Figure 6.3, Table 6.1) [*Housse*, 1984]. The well was drilled vertically in a tilted block that was intersected by a normal fault that strikes NE-SW and dips westward (Figure 6.4). The productivity of the well was too low to set an economically viable geothermal loop, but hydraulic testing showed that the natural permeability was higher in localized fracture zones than in the matrix. Accordingly, the matrix permeability concept was shown not to be effective for deep geothermal exploitation in the URG.

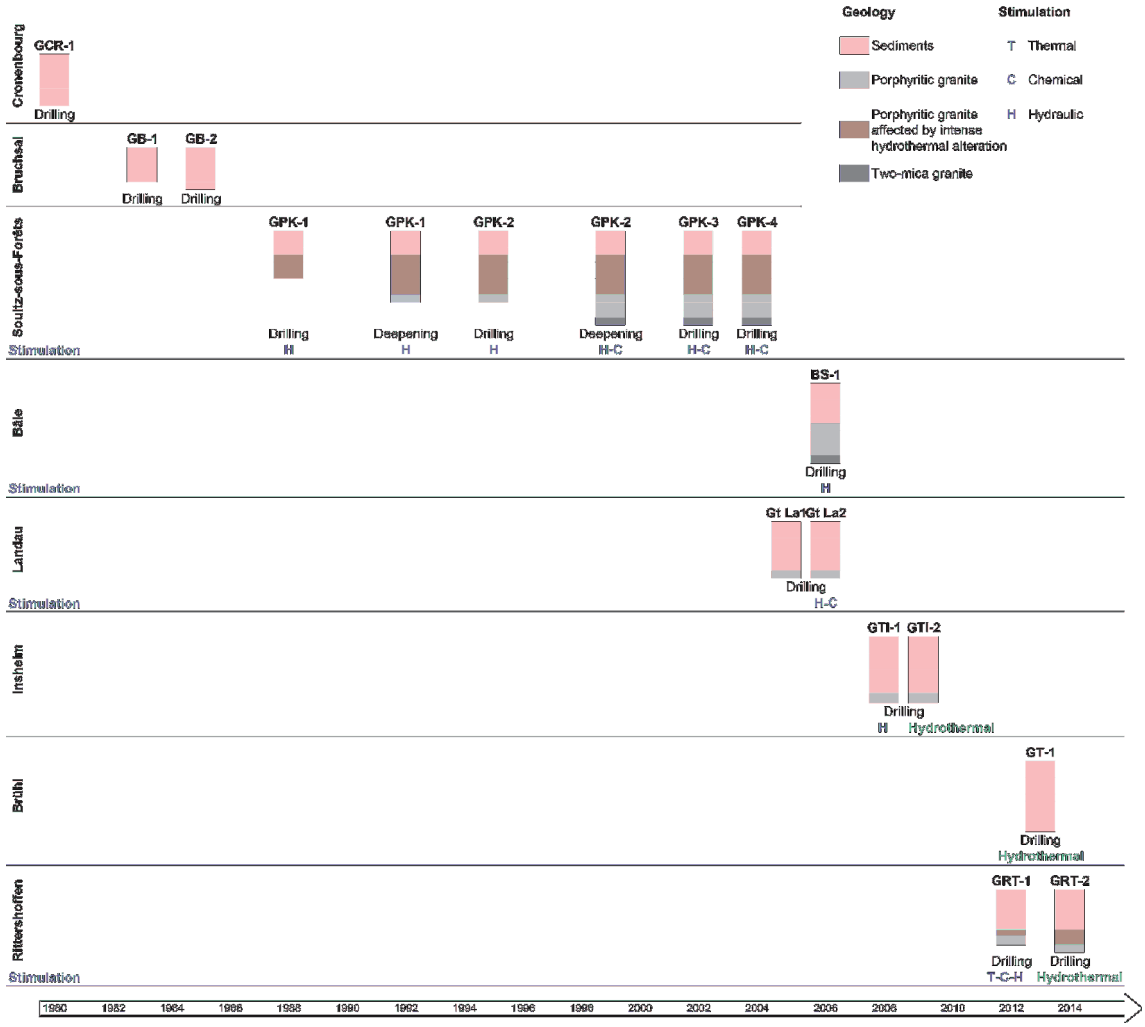

Figure 6.3 Chronology of the deep geothermal projects and their associated wells in the URG. For each well, lithologies of open-hole are represented in depths along the borehole and stimulation treatments are detailed.

Since 1983, the geothermal project of **Bruchsal** (Germany) has exploited geothermal resources with two wells, namely, GB-1 and GB-2, which were drilled into the Buntsandstein sandstone reservoir (Figure 6.3, Table 6.1) [*Herzberger et al.*, 2010]. Geothermal wells were drilled nearly vertically into tilted blocks (Figure 6.4). Normal faults within the accommodation zone strike N-S to N10°E and dip westward [*Meixner et al.*, 2016].

The pilot geothermal project of **Soultz-sous-Forêts** (Alsace, France) was the first project in the URG to create a deep granitic reservoir based on the Hot Dry Rock (HDR) concept [*Gérard and Kappelmeyer*, 1987]. In order to produce electricity, without the use of binary plant technology, the minimum required temperature was 200°C. The initial goal was to monitor the micro-seismicity during the heat exchanger creation to ensure the effectiveness of the hydraulic operations. In 1987, the exploration well GPK-1 was drilled down to 2000 m depth (Figure 6.3, Table 6.1). Geothermal well was drilled vertically in a horst that is bordered by the complex Soultz fault system (Figure 6.4) [*Sausse et al.*, 2010]. At the top of the basement, the main branch of the normal fault strikes N170°E and dips westward. The exploration well reveals brine circulating into hydrothermally altered fracture zones at the top of the basement and was deepened in order to find “dry” rocks and higher temperatures. Three other wells, namely, GPK-2, GPK-3 and GPK-4, were drilled down to 5000 m depth between 1992 and 2004 (Figure 6.3, Table 6.1) [*Dezayes et al.*, 2005]. The deep granitic reservoir showed a lower fracture density with a low productivity index, which was not improved by the performed hydraulic operations. At Soultz, more than 20 km of drilled length into the sedimentary cover and the granitic basement reveals that the natural fracture network acts as a natural heat exchanger with geothermal resources circulations. All the five wells exhibit at least one permeable fracture zone but the natural permeability may be too weak for industrial exploitation. The stimulations operations performed in wells have not sufficiently taken into consideration the presence of fracture zones. The scientific challenge became the stimulation of these pre-existing fractures according to the EGS technology. The following projects developed in the URG were based on lessons learned from Soultz and EGS technology.

In 2006, the first well of a planned doublet, namely, BS-1, was drilled in **Basel** for the Deep Heat Mining project (Figure 6.3, Table 6.1) [*Häring et al.*, 2008]. The deep granitic section of the well was hydraulically stimulated, and an induced seismic event that was felt on surface in this urban area interrupted the project (M=3.4) [*Häring et al.*, 2008]. Future projects targeted the sediment-basement interface and not the deep granitic basement.

At **Landau** (Baden-Württemberg, Germany), the geothermal doublets Gt La1 and Gt La2 were drilled at in 2005 (Figure 6.3, Table 6.1). Geothermal wells targeted local normal faults within a horst/graben system that strikes N-S and dips eastward (Figure 6.4) [*Schad*, 1962]. The first well was deviated 33° westward and the second one 25° eastward [*Baumgärtner*, 2007]. The geothermal reservoir at Landau was developed on a multi-reservoir concept (Triassic and Permian sandstones - Altered granite) (Table 6.1) [*Hettkamp et al.*, 2007].

At **Insheim** (Baden-Württemberg, Germany), the geothermal doublets GTI-1 and GTI-2 were drilled in 2008 (Figure 6.3, Table 6.1). The geothermal target was a normal fault oriented N-S and dipping westward in a horst/graben system (Figure 6.4) [*Baumgärtner et al.*, 2013]. Both wells intersected this fault with a deviated trajectory to the NW and SE [*Baumgärtner et al.*, 2013]. The geothermal reservoir at Insheim was also developed on a multi-reservoir concept (Muschelkalk-Rotliegendes-Altered granite) [*Baumgärtner and Lerch*, 2013]. The second well was hydraulically and chemically stimulated, whereas a sidetrack and a hydraulic stimulation were achieved within the first well at Insheim to reach the expected flowrate (Figure 6.3, Table 6.1) [*Schindler et al.*, 2010].

At **Rittershoffen** (Alsace, France), the geothermal doublet GRT-1 and GRT-2 was drilled in 2012 and 2014 to exploit the geothermal resources at the sediment-basement interface (Figure 6.3, Table 6.1) [*Baujard et al.*, 2017]. They targeted the Rittershoffen normal fault that bordered the graben system (Figure 6.4) [*Baujard et al.*, 2017]. This fault strikes N10°W to N10°E and dips westward. The first well intersects the fault vertically and the second one is deviated 37° to the North [*Baujard et al.*, 2017]. Only the first well was thermally, chemically and hydraulically stimulated (Figure 6.3, Table 6.1) [*Recalde Lummer et al.*, 2014; *Vidal et al.*, 2016a]. Recent stimulation treatments were based on a combined stimulation (thermal-chemical-hydraulic) and environmentally friendly solution,

packer utilization to isolate treated zones, and low-pressure hydraulic injection [*Recalde Lummer et al.*, 2014].

At **Brühl** (Rhine Palatinate, Germany), the first well of the project, namely, GT-1, was drilled in 2013 and reached the Buntsandstein formation (Figure 6.3, Table 6.1) [*Lotz*, 2013]. The geothermal well was drilled into an accommodation zone and targeted a normal fault that is oriented N170°E to N-S and dips westward (Figure 6.4) [*Lotz*, 2013; *Reinecker et al.*, 2014]. The well was deviated of less than 30° to the SE (Table 6.1) [*Lotz*, 2013].

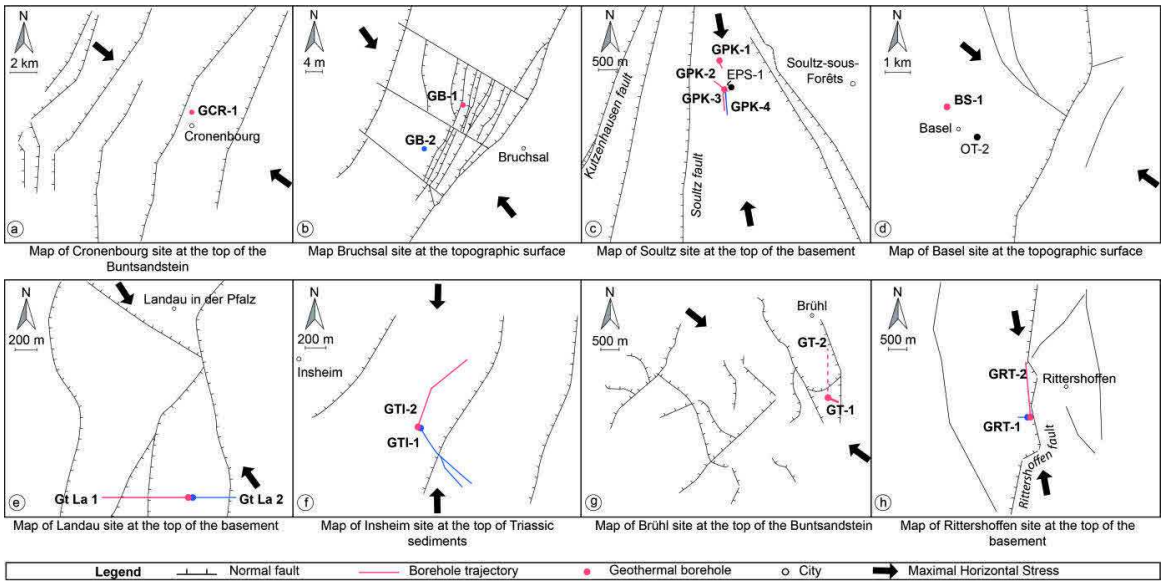

Figure 6.4 Maps of geothermal sites with fault traces and well trajectories a) at the top of the Buntsandstein at Cronenbourg, b) at the topographic surface at Bruchsal, c) at the top of the basement at Soultz-sous-Forêts, d) at the topographic surface at Basel, e) at the top of the basement at Landau, f) at the top of the Triassic sediments at Insheim, g) at the top of the Buntsandstein at Brühl, and h) at the top of the basement at Rittershoffen. Maximum horizontal stress in open-holes are oriented N142°E at Bruchsal [*Meixner et al.*, 2014], N170°E at Soultz [*Valley*, 2007], NNW-SSE at Landau [*Ritter et al.*, 2014], N-S at Insheim [*Baumgärtner et al.*, 2013], N140°E at Brühl [*Reinecker et al.*, 2014] and N170°E at Rittershoffen [*Hehn et al.*, 2016]. Regional maximum horizontal stress is indicated for Cronenbourg and Basel.

Table 6.1 Properties of geothermal wells in the URG at Cronenbourg [*Housse*, 1984; *Pauwels et al.*, 1993], at Bruchsal [*Herzberger et al.*, 2010; *Kölbel*, 2010; *Meixner et al.*, 2016; *Sanjuan et al.*, 2016a], at Soultz-sous-Forêts [*Dezayes et al.*, 2005; *Genter et al.*, 2010; *Sanjuan et al.*, 2014; *Schill et al.*, 2017], at Basel [*Häring et al.*, 2008; *Ladner and Häring*, 2009], at Landau [*Schindler et al.*, 2010; *Sanjuan et al.*, 2016a], at Insheim [*Baumgärtner et al.*, 2013; *Baumgärtner and Lerch*, 2013; *Sanjuan et al.*, 2016a], at Rittershoffen [*Sanjuan et al.*, 2016a; *Baujard et al.*, 2017] and at Brühl [*Melchert et al.*, 2013; *Sanjuan et al.*, 2016a]

Name	Location	Year of drilling	Trajectory	Drilled Length (m MD)	Top of the Open-Hole (m MD)	Lithology of the OH	*Initial* hydraulic yield **Post-stimulation** (L/s/bar)		Stimulation	T_{Bottom} (°C)	pH	TDS (g/L)
GCR-1	Cronenbourg	1980	Sub-Vertical	2870	2664	Sandstones (Buntsandstein)	*0.12*		-	140	6.70	104
GB-1	Bruchsal	1983	Sub-Vertical	1932	1573	Sandstones (Buntsandstein)	-		-	120	5.06	121
GB-2	Bruchsal	1984	Sub-Vertical	2542	2350	Sandstones (Buntsandstein)	*0.7*		-	134	-	-
GPK-1	Soultz-sous-Forêts	1987 Deepening in 1992	Sub-Vertical	3590	2850	Hydrothermally Altered Granite (Carboniferous)	upper granitic reservoir	*0.1*	Hydraulic stimulation	160	-	-
							intermediate granitic reservoir	*0.07* **0.1**				
GPK-2	Soultz-sous-Forêts	1994 Deepening in 1999	Sub-Vertical and deviated to the NW	5060	4440	Granite (Carboniferous)	intermediate granitic reservoir	*0.06* **1.5**	Hydraulic and chemical stimulation	200	4.98	100
							deep granitic reservoir	*0.02* **0.5**				
GPK-3	Soultz-sous-Forêts	2002	Sub-Vertical and highly deviated to the South	5110	4592	Granite (Carboniferous)	deep granitic reservoir	*0.2* **0.4**	Hydraulic and chemical stimulation	200	-	-
GPK-4	Soultz-sous-Forêts	2003	Sub-Vertical and highly deviated to the South	5270	4767	Granite (Carboniferous)	deep granitic reservoir	*0.01* **0.4**	Hydraulic and chemical stimulation	200	-	-
BS-1	Basel	2006	Sub-Vertical	5000	4629	Granite (Carboniferous)	*$2.5x10^{-3}$*		Hydraulic stimulation	190	-	-
Gt La-1	Landau	2005	33°W	3300	2100	Granite (Carboniferous)	**-**		-	160	4.96	106
Gt La-2	Landau	2006	25°E	3170	2200	Granite (Carboniferous)	*0.25* **>1**		Hydraulic and chemical stimulation	170	-	-

Name	Location	Year of drilling	Trajectory	Drilled Length (m MD)	Top of the Open-Hole (m MD)	Lithology of the OH	*Initial* hydraulic yield **Post-stimulation** (L/s/bar)	Stimulation	T_{Bottom} (°C)	pH	TDS (g/L)
GTI-1	Insheim	2008	Highly deviated to SE	3850	3620	Sandstones (Permian) Granite (Carboniferous)	*0.9*	Hydraulic stimulation and drilling of a sidetrack	165	5.23	107
GTI-2	Insheim	2009	Highly deviated to NE	3850	2980	Sandstones (Buntsandstein and Permian) Granite (Carboniferous)	-	-	-	-	-
GRT-1	Rittershoffen	2012	Sub-Vertical	2580	1925	Sandstones (Buntsandstein) Hydrothermally Altered Granite (Carboniferous)	*0.5* **2.5**	Thermal, hydraulic and chemical stimulation	160	6.27	101
GRT-2	Rittershoffen	2014	37°to the North	3200	2120	Sandstones (Buntsandstein) Hydrothermally Altered Granite (Carboniferous)	*3.5*	-	180	-	-
GT-1	Brühl		30°SE	2542	3155	Sandstones (Buntsandstein)	*3.5*	-	170	-	100

6.2.6 The pilot geothermal site of Soultz-sous-Forêts

In this section, geologic, hydraulic and thermal properties of geothermal reservoirs at Soultz will be detailed. Data are issues from deep geothermal wells. They represent a frame for comparison with other geothermal data in section 6 and 7. Permeable fracture zones described have been detected during drilling operations with important mud losses and were naturally permeable prior to any stimulation operations.

6.2.6.1 Geothermal reservoirs of Soultz-sous-Forêts

The deep granitic basement of **Soultz-sous-Forêts** corresponds to the open-hole section from 4500 to 5230 m. This section consists of a grey fine-grained two-mica granite (327 +/- 7 Ma) [*Stussi et al.*, 2002; *Cocherie et al.*, 2004]. The porosity of the two-mica granite is around 0.5% [*Géraud et al.*, 2010]. The fracture density in GPK-3 and GPK-4 is approximately from 0.8 to 0.9 fract/m below 4.5 km Measured Depth (MD) and decreases to 0.25 fract/m in the last 150 m of GPK-3 [*Valley*, 2007]. The fractures mainly strike N-S and dip to the west. A major fault zone intersected the GPK-3 well between 4755 and 4780 m MD and controls 70% of the flowrate in the well [*Dezayes et al.*, 2010a]. This zone consists of 7 individual fractures with a cumulative altered granite thickness of 15 m. No residual permeability was observed in the other wells in the deep granitic basement prior to stimulation operations. The deep granitic reservoir (>4.5 km TVD) showed an initial injectivity index of $1x10^{-2}$ L/s/bar in GPK-4, $2x10^{-2}$ L/s/bar in GPK-2 and $1x10^{-1}$ L/s/bar in GPK-3 [*Schill et al.*, 2017]. After hydraulic and chemical stimulation, injectivity index is 0.5 L/s/bar in GPK-4 and -2, and 0.4 L/s/bar in GPK-3. In 2010, during circulation experiment for almost a year, GPK-2 showed a production index of 1 L/s/bar. In 2013, during circulation experiment for six months, GPK-3 and GPK-4 showed an injection index of 1.3 L/s/bar and 1.5 L/s/bar [*Schill et al.*, 2017]

A grey porphyritic monzogranite (334 +/- 4 Ma) was encountered above a fine-grained two mica granite [*Stussi et al.*, 2002; *Cocherie et al.*, 2004]. In GPK-3 and GPK-4, the fracture density is approximately 0.5 to 0.6 fract/m according to acoustic image logs in this section [*Valley*, 2007]. In GPK-2 and GPK-1, the fracture density is around 0.4 to 0.5 fract/m between 2100 and 3500 m MD

according to acoustic image logs [*Genter et al.*, 1997a]. This value increases until 1.3 fract/m between 1600 and 2100 m MD. According to EPS-1 cores, the density is around 0.8 fract/m within the same depth section. The fractures are oriented N-S to NNE-SSW with a steep dip (>60°) eastward or westward. In this section, the residual permeability is intimately linked to Hydrothermally Altered Fracture Zones that affect the monzogranite. These zones consist of a fault core, highly fractured, which is surrounded by an altered, porous and fractured damage zone [*Genter et al.*, 2000]. The damage zone is characterized by strong alteration with the leaching of primary minerals and the precipitation of secondary minerals (quartz, clays, carbonates, hematite, and sulfides) [*Genter and Traineau*, 1996]. These minerals are related to the early pervasive alteration stage that affected the granite on a large scale and later vein alteration stage that was controlled by the fracture network. Quartz, illite and carbonates are located within the main fracture zones, and barite, galena and pyrite occur sporadically. Chlorites, epidote and carbonates are found in tiny natural fractures in massive granite. Quartz veins observed in core samples or in cuttings correspond to a localized decrease of the gamma ray (Figure 6.5a). Quartz veins which are mainly localized into the fault core correspond to the precipitation of silica-rich fluids derived from the dissolution of primary silicates minerals during the vein alteration. They are associated with a high reflectivity into a dark mottled zone in acoustic image (Figure 6.5a). In EPS-1, the acoustic image presents a low quality. The surrounded damage zone is highly hydrothermalized and clay-rich zone associated with an increase of the gamma ray (Figure 6.5a). The porosity of the damage zone is higher than in the fault core (Figure 6.5a). The highest porosity of this fracture zone is around 25% in the damage zone [*Ledésert et al.*, 1999]. The main permeable fracture zones were intersected between 2155 and 2190 m MD in EPS-1, between 1810 and 1825 m MD in GPK-1 and between 1970 and 2110 m MD in GPK-2 [*Dezayes et al.*, 2010a]. These regions exhibit more than 100 fractures with a cumulative fracture zone thickness of 10 to 15 m. The major permeable drains are 10 m thick [*Genter et al.*, 1997b]. In GPK-1, the pre-stimulation injectivity that is associated with this fault zone is estimated to be 3 L/s/bar [*Jung*, 1992]. The pre-stimulation injectivity associated with the permeable fracture zone in GPK-2 is higher. However this injectivity should be considered with caution because, the upper granitic reservoir (1.4-2 km TVD)

shows an initial injectivity of $9x10^{-2}$ L/s/bar in GPK-1 [*Schill et al.*, 2017]. In the intermediate granitic reservoir (2.5-3.5 km TVD), GPK-1 shows an initial injectivity of $7x10^{-2}$ L/s/bar that is increased to $1x10^{-1}$ L/s/bar after stimulation. In the intermediate reservoir of GPK-2, the initial injectivity is $6x10^{-2}$ L/s/bar and is increased to 1.5 L/s/bar after stimulation [*Jung and Weidler*, 2000; *Schill et al.*, 2017]. HAFZ were hydraulically and chemically stimulated [*Nami et al.*, 2008; *Portier et al.*, 2009; *Schill et al.*, 2017]. Hydraulic fracture stimulation, or hydro-shearing, does not require proppants inside the stimulated fractures to maintain a higher resulting permeability. Hydraulic stimulation causes an irreversible increase in the permeability by release of the shear stress operating in the vicinity of the stimulated fractures. The effectiveness of hydro-shearing which induced a microseismicity activity, is linked to the initial low planarity and high roughness of the natural fracture surfaces. The post-stimulation behavior of reactivated fractures allows a self-propping and a permeability increase which is sustainable during exploitation. During hydraulic stimulation, induced seismicity is less intense in the intermediate granitic reservoir than in the deep reservoir [*Cuenot et al.*, 2008] probably due to the presence of secondary clay minerals [*Meller and Kohl*, 2014].

The top of the granitic basement consists of a 150 m-thick reddish granitic layer, which was observed in all the geothermal wells. This section was affected by a superimposed paleo-weathering alteration event because of paleo-emersion during the Permian. The bulk porosity in this section is between 2% and 7% [*Géraud et al.*, 2010]. Primary magnetic and ferromagnetic minerals such as magnetite and biotite were leached, decreasing the magnetic content, as measured on a continuous Soultz core [*Rummel*, 1992]. From a structural perspective, sub-horizontal joints that were probably related to the granite's uplift during the Permian were superimposed by sub-vertical fractures. The fracture density is 9 fract/m [*Genter et al.*, 1997a]. Sub-horizontal joints strike N120°E and dip 10°-40°S. Despite the high fracture density and high porosity of this granitic formation, no permeability was observed during drilling operations. This lack of permeability was confirmed by hydraulic tests that were performed in GPK-1 [*Herbrich*, 1988]. The fractures were mainly sealed by hematite, carbonates and clays [*Genter and Traineau*, 1996].

The transition between the granitic basement and the sedimentary cover is located at approximately 1400 m depth. The base of the sedimentary cover consists of Permian coarse-grained to microconglomeratic sandstones that are 10 m thick. Annweiler sandstones are the first sandstones from Triassic formation [*Vernoux et al.*, 1995]. Thus, the 50 m-thick formation is argillaceous red sandstone.

This formation shows an erosive contact with the Vosgian sandstones, which consist of typical medium-grained to conglomeratic continental sandstones with clay formations. After the so-called Intermediate beds, which are 40-m-thick large-grained sandstones, the 10-m-thick Voltzia sandstones include fine-grained sandstones with interbedded clays that overlie the Buntsandstein formation. The porosity reaches 20% in the Vosgian sandstones and around 10% in the Intermediate beds and Annweiler sandstones [*Vernoux et al.*, 1995; *Haffen et al.*, 2013; *Griffiths et al.*, 2016]. The fracture system is conjugated and strikes N170°E with a dip of 75°W or 75°E [*Vernoux et al.*, 1995]. The fracture density is 0.8 fract/m, and the fractures are mainly filled by barite and calcite. Galena, pyrite, quartz and hematite were also observed as fracture fillings alongside organic materials and oil impregnation. The major permeable fault zone intersects between 1170 to 1215 m MD in EPS-1. This zone consists of more than 50 fractures with a maximum individual thickness that reaches 5 cm. The fault zone was also intersected at 1220 m MD in GPK-1 [*Dezayes et al.*, 2010a] and at 1265 m MD in a peripheral Soultz well called 4550. The intersected fault zone produces 30 m^3/h with a natural post-drilling productivity estimated to be 1 L/s/bar [*Degouy et al.*, 1992]. This value is estimated from a Drill Stem Test that is not exactly representative from the hydraulic yield of a geothermal well.

The Middle Triassic formation is called Muschelkalk and is 150 m thick. This formation consists of fossil-rich sandstones at the base, marly dolomites that were invaded by anhydrite, and massive limestones at the top [*Aichholzer et al.*, 2015]. A permeable fracture zone intersects at around 950 m MD in the Middle Muschelkalk of the EPS-1 well, around 1000 m MD in GPK-1, and around 950 m MD in GPK-2, -3, and -4 [*Vidal et al.*, 2015]. EPS-1 core samples indicate the presence of hydraulic breccia at around 950 m MD in this layer.

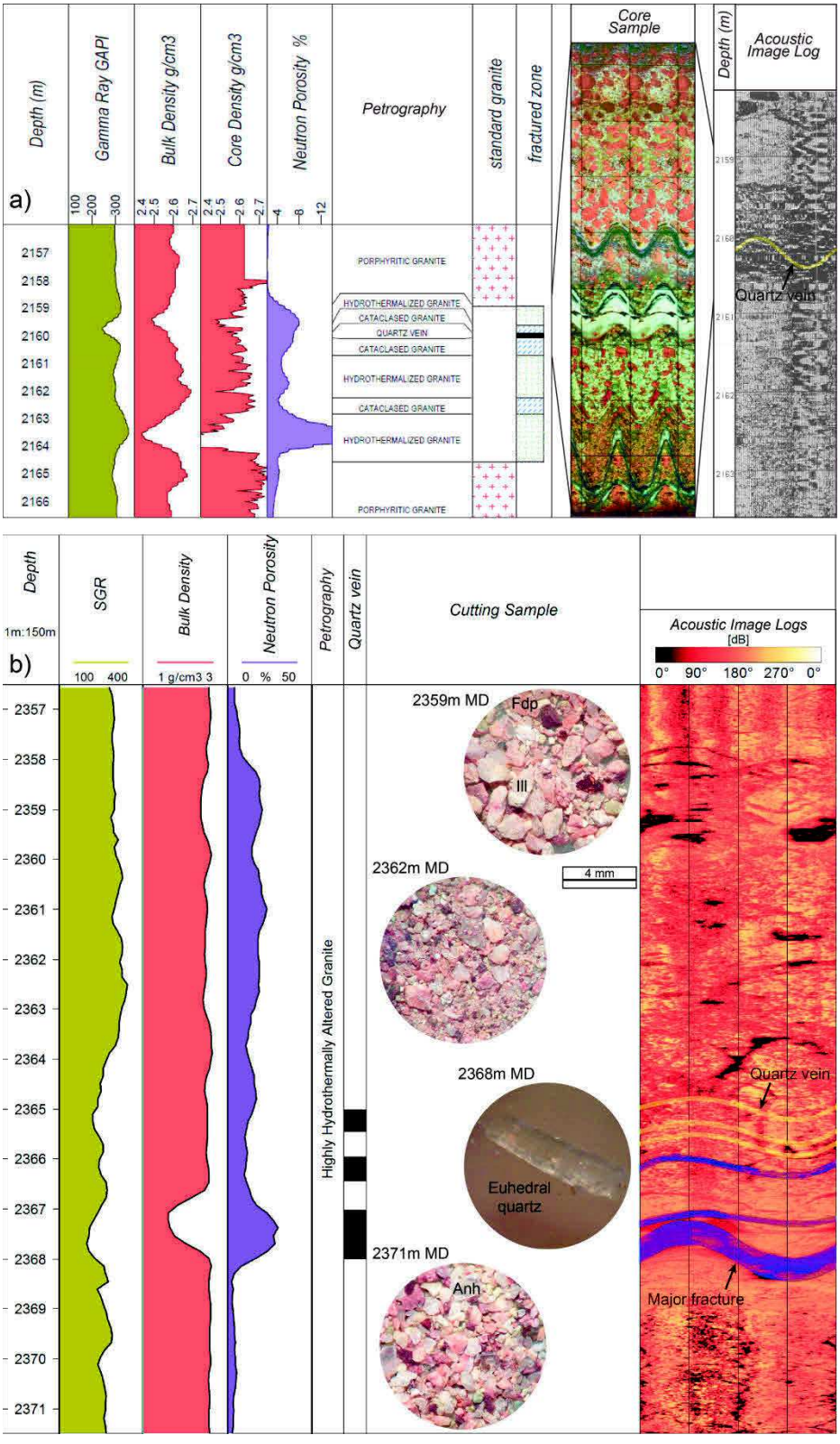

Figure 6.5 Composite logs of major permeable fracture zones a) in EPS-1 well at Soultz-sous-Forêts and b) in GRT-1 well in Rittershoffen. Well logs in EPS-1 well are from [*Dezayes et al.*, 2010a]. The hydrothermal alteration is linked to the fracture and thus interfaces between levels of alteration are highly dipping.

6.2.6.2 Thermal profiles in Soultz wells

The typical thermal profile in the URG can be divided into two major sections (Figure 6.6). The uppermost region consists of sedimentary formations from the Tertiary and Mesozoic (Jurassic and Upper Triassic) and features a high geothermal gradient (up to 100°C/km), which indicates a conductive heat transport mechanism [*Pribnow and Schellschmidt*, 2000]. This geological section acts as a cap rock, i.e., an impermeable layer that insulates an active hydrothermal system below. This hydrothermal system is associated with deep sedimentary formations and granitic basement. In the Muschelkalk limestones, Buntsandstein and Permian sandstones, a zone of transition between conduction and convection is observed with intermediate geothermal gradients between 100°C/km and 10°C/km [*Vidal et al.*, 2015]. In the hydrothermally granitic basement, the very low geothermal gradient (lower than 10°C/km) indicates the presence of a convection process (Figure 6.6). The deep granitic basement is associated to a geothermal gradient of 30°C/km associated to a conduction process (Figure 6.6). Thermal profiles are locally disturbed by fracture zones. Negative anomalies on the temperature logs are the thermal signature of altered, porous and fractured zones that were cooled by drilling, massive hydraulic injections and the circulation of cold water [*Genter et al.*, 2010]. In GPK-3, the permeable fracture zone from 4755 to 4780 m MD is associated to a local negative temperature anomaly. In GPK-2, the permeable fracture zone from 1970 to 2110 m MD is associated to a local negative anomaly (Figure 6.6). However, permeable fracture zones observed in the Muschelkalk limestones and Buntsandstein sandstones are not associated to thermal anomalies.

The bottom hole temperature reached at 5 km depth is 200°C (Figure 6.6). The temperature in the hydrothermally altered granitic reservoir is between 160°C and 170°C.

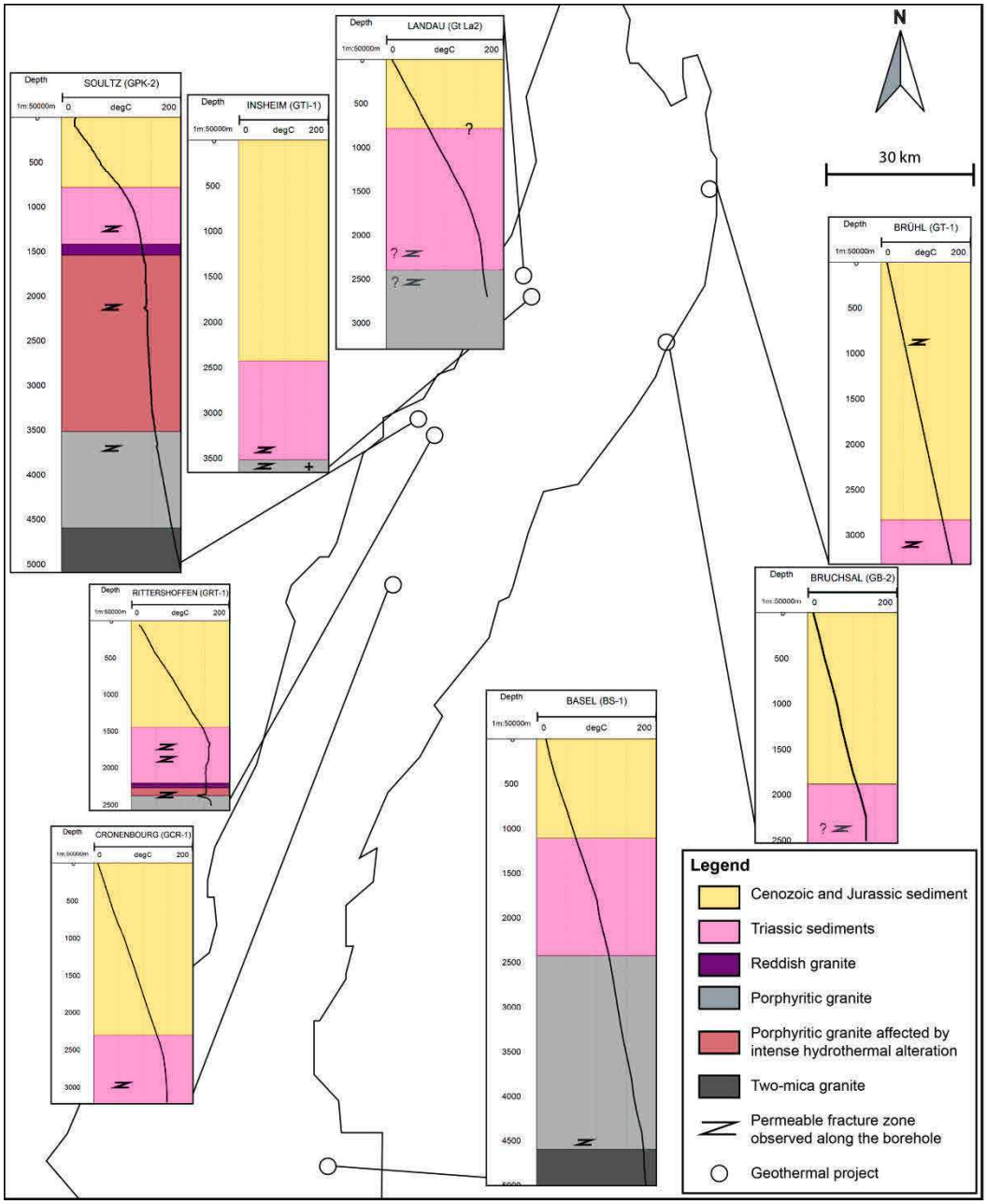

Figure 6.6 Thermal profiles that are associated with the geology and permeable fracture zones in geothermal wells in the URG. The depths are given in "measured depth". At Soultz, thermal profiles were acquired at the thermal equilibrium in GPK-2 in January 1999 [*Genter et al.*, 2010]. At Cronenbourg, thermal profile in GCR-1 was acquired at the thermal equilibrium in December 1981 [*Housse*, 1984]. The deepest part below 2700 m MD is extrapolated. At Bruchsal, thermal profile in GB-2 was acquired at the thermal equilibrium [*Herzberger et al.*, 2010]. At Basel, the deepest part of the geothermal profile in BS-1 is approximated [*Ladner and Häring*, 2009]. At Landau, the thermal profile in Gt La2 is extrapolated [*Schindler et al.*, 2010]. At Insheim, the thermal profile is

not published [*Baumgärtner and Lerch*, 2013]. At Insheim, only the bottom hole temperature is published. At Rittershoffen, thermal profiles were acquired at equilibrium in GRT-1 and GRT-2 in July 2015 [*Baujard et al.*, 2017]. At Brühl, the thermal profile was acquired in September 2013 [*Melchert et al.*, 2013].

6.2.7 Comparison with geothermal reservoirs of other geothermal sites

6.2.7.1 Deep granitic reservoir

A comparative study of hydraulic data in the URG in Germany and France reveals a mean hydraulic conductivity of 9.6×10^{-7} m/s in granitic basement [*Stober and Jodocy*, 2009].

The deep granitic basement of **Basel** consists of hornblende-biotite-rich and quartz-poor granitoid rocks below 4600 m MD [*Käser et al.*, 2007]. The fractures strike NW-SE to NNW-SSE with steep dips, and the fracture density is around 0.2-0.3 fract/m. Two cataclastic fracture zones intersected BS-1 at 4700 and 4835 m MD, and the cuttings exhibit significant amounts of anhydrite and illite. Their initial permeability was very low and the well BS-1 showed an initial injectivity index of 2.5×10^{-3} L/s/bar which is increased after hydraulic stimulation [*Ladner and Häring*, 2009].

6.2.7.2 Hydrothermally altered granitic reservoir

At **Basel**, a hornblende-biotite monzogranite forms the upper portion of the granitic reservoir [*Käser et al.*, 2007]. The fracture density is 0.95 fract/m. The fracture orientation is the same as in the deepest section. No permeability was observed in this granitic section in BS-1.

At **Rittershoffen**, the bottom holes of GRT-1 and GRT-2 consist of hydrothermally altered granite, similar to those at Soultz. The fracture density is around 0.6 and 1 fract/m at the top and decreases with depth to 0.3 fract/m [*Vidal et al.*, 2016b]. The fractures strike N165°E to N-S and dip 65°W or E. The GRT-1 well exhibits one major permeable fault zone that intersects between 2325 and 2370 m MD [*Vidal et al.*, 2017] and controls 70% of the flowrate [*Baujard et al.*, 2017]. The main permeable fracture is 24 cm thick at 2368 m MD and is surrounded by quartz veins. These quartz veins are associated with localized

decrease of the gamma ray and a high reflectivity in acoustic image (Figure 6.5b). Acoustic image present a very good quality in GRT-1 but only cutting samples are available and the petrographic and structural interpretation is less accurate than with core samples. The damage zone above consists of 50 fractures with a cumulative individual thickness that reaches 25 cm. The damage zone is associated to a high porosity (until 30%) due to the primary minerals dissolution (Figure 6.5b). The increase of gamma ray associated to this zone indicates the secondary illitization of the zone also observed in cutting samples (Figure 6.5b). Mineralogical investigations indicated that the first hundreds of meter of the granitic reservoir are illitized because of the hydrothermal alteration [*Vidal et al.*, 2017]. The GRT-2 well exhibits four permeable fracture zones in this section, and the main fault zone intersects at 2765 and 2800 m MD [*Vidal et al.*, 2017]. This zone consists of 30 fractures with a cumulative individual thickness that reaches 17 cm. The initial injectivity was less 0.5 L/s/bar in GRT-1 and 2.5 L/s/bar after thermal, chemical and hydraulic stimulation, and the initial productivity was around 3.5 L/s/bar in GRT-2 [*Baujard et al.*, 2017].

At **Landau**, granite was encountered at approximately 2400 m MD [*Schindler et al.*, 2010]. Its petrography was not published but is probably similar to the Soultz and Rittershoffen granitic basement because these areas are also located in the Saxothuringian domain. Water-bearing fractures surely control the flowrate in the granitic reservoir according to the shape of the thermal profile (Figure 6.6) [*Hettkamp et al.*, 2007; *Schindler et al.*, 2010]. The injection well Gt La2 showed an injectivity of approximately 0.25 L/s/bar before stimulation and higher than 1 L/s/bar after hydraulic and chemical stimulation [*Schindler et al.*, 2010]. The initial productivity of Gt La1 is not published.

At **Insheim**, granite was encountered at approximately 3500 m MD [*Baumgärtner et al.*, 2013]. Permeable fracture zones were intersected between GTI-1 and GTI-2 [*Baumgärtner et al.*, 2013]. The productivity in GTI-1 was 0.9 L/s/bar before hydraulic stimulation and increased after side-track operation [*Baumgärtner et al.*, 2013]. The initial productivity of GTI-2 is not published.

6.2.7.3 Reddish granitic reservoir

At **Rittershoffen**, the reddish granite is less than 100 m thick in GRT-1 and exhibits the same petrography as in Soultz. The fracture density is 2.5 fract/m [*Vidal et al.*, 2016b]. The fractures are very scattered but mainly strike N15°E and dip 50°W. The neutron porosity that was measured from geophysical well logs was 2% on average [*Vidal et al.*, 2016c]. Open fractures on borehole images did not exhibit permeability during drilling operations.

6.2.7.4 Sandstone reservoir

A comparative study of hydraulic data in the URG in Germany and France reveals a mean hydraulic conductivity of 2.4×10^{-7} m/s in Buntsandstein sandstones [*Stober and Jodocy*, 2009].

At **Rittershoffen**, the lithostratigraphy sedimentary cover is similar to that in Soultz [*Aichholzer et al.*, 2015]. The neutron porosity is 3% on average in GRT-1 and GRT-2 and higher when clays are present in the formation [*Vidal et al.*, 2016c]. The fracture density is 0.25 fract/m in GRT-1 and 0.4 fract/m in GRT-2 [*Vidal et al.*, 2016b]. Fractures in the sandstones are oriented N20°E and dip 70°W in GRT-1 and N170°E with a dip 85°E in GRT-2. Two major clusters with initial permeability intersect through GRT-2 and are approximately 20 m and 10 m thick.

At **Landau**, the Permian formation is thicker than that in Soultz and Rittershoffen and is called Rotliegendes [*Eisbacher and Fielitz*, 2010]. This sequence consists of coarse clastics (continental conglomerates), fluvial and aeolian sandstones, shales and some evaporites. Triassic sandstones overlie Permian sandstones. Permeable fractures were intersected in the multi-horizon geothermal reservoir [*Hettkamp et al.*, 2007].

At **Insheim**, the Rotliegendes sandstones and Buntsandstein sandstones are approximately 500 m thick and exhibit permeable fractures in both wells [*Baumgärtner et al.*, 2013].

At **Cronenbourg**, the base of the sedimentary cover in the GCR-1 well consists of Permian sandstones that are overlaid by Triassic sandstones (465 m-thick) [*Housse*, 1984]. The porosity is between 5 and 10%. The main permeable zone is located between 2870 m and 2880 m MD, which coincides with fractured

sandstones, whereas sandstones with silica-rich cement are porous but not permeable. The productivity of the sandstone reservoir is estimated to be 0.12 L/s/bar.

At **Bruchsal**, the exploited geothermal reservoir consists of the Buntsandstein sandstones in GB-1 (>200 m-thick) and the Buntsandstein and Rotliegendes sandstones in GB-2 (between 150 and 200 m thick for both formations) [*Herzberger et al.*, 2010]. Water-bearing fractures control the permeability in the sandstone reservoir [*Meixner et al.*, 2016]. The injectivity of the well GB-2 is 0.7 L/s/bar [*Kölbel*, 2010]. The initial productivity of GB-1 is not published.

At **Brühl,** the targeted geothermal reservoir consists of the Buntsandstein sandstones. The fractures are oriented N170°E with an eastward sub-vertical dip [*Reinecker et al.*, 2014]. The permeable fault zone intersects between 3150 and 3200 m MD [*Melchert et al.*, 2013]. The injectivity index of GT-1 is 3.5 L/s/bar and the well was not stimulated [*Melchert et al.*, 2013].

6.2.7.5 Limestone reservoir

A comparative study of hydraulic data in the URG in Germany and France reveals a mean hydraulic conductivity of 2.0×10^{-6} m/s in Muschelkalk limestones [*Stober and Jodocy*, 2009].

At **Rittershoffen,** the Muschelkalk formation is similar to that at Soultz. The fractures are oriented N20°E and dip steeply westward in GRT-1 [*Dezayes et al.*, 2014]. These fractures are filled by calcite, quartz and anhydrite. A major permeable fracture zone with drilling mud losses intersects at 1760 m MD in the Middle Muschelkalk in GRT-1 [*Baujard et al.*, 2017].

In the Middle Muschelkalk, permeable zones were also observed in some geothermal wells, including Les Hélions I, II and III at Preuschdorf, which are less than 10 km westward from Soultz [*BRGM*, 1971, 1993].

At **Insheim**, Muschelkalk is also described as a reservoir, and fracture zones were intersected.

6.2.8 Comparison with thermal profiles in wells of other geothermal sites

At **Cronenbourg**, the thermal profile shows a high geothermal gradient of 55°C/km above 2600 m MD (Figure 6.6). The Early Muschelkalk limestones, Buntsandstein and Permian sandstones are associated to a lower geothermal gradient of 15°C/km. The deep fractured sediments are associated to a convection process. The temperature reaches 150°C at 3200 m MD [*Housse*, 1984].

At **Bruchsal**, the thermal profile shows a high geothermal gradient of 50°C/km above 2300 m MD (Figure 6.6). The Buntsandstein and Permian sandstones are associated to null geothermal gradient that indicates a convection process. The temperature reaches 135°C at 2500 m [*Herzberger et al.*, 2010].

At **Basel**, the thermal profile shows a geothermal gradient of approximately 40°C/km until 4400 m MD (Figure 6.6). In the deepest granitic part, the thermal gradient decreases below 20°C/km. The transition between conduction or convection zone is not clear. The temperature reaches 200°C at 5000 m MD [*Ladner and Häring*, 2009].

At **Landau**, the thermal profile shows a geothermal gradient of 75°C/km above 2000 m MD (Figure 6.6). Below 2000 m MD, the decrease of the geothermal gradient to approximately 20°C/km indicates a convection process. The temperature reaches 160°C at 2600 m MD [*Schindler et al.*, 2010].

At **Insheim**, the temperature reaches 160°C at 3600 m MD but the thermal profile is not published [*Baumgärtner and Lerch*, 2013].

At **Rittershoffen**, the thermal profile shows a high geothermal gradient of 95°C/km from 0 to 1650 m MD in GRT-1 and from 0 to 1850 m MD (i.e. 0 to 1650 m True Vertical Depth(TVD)) in GRT-2 (Figure 6.6) [*Baujard et al.*, 2017]. This uppermost part is associated to conduction process. The deepest part from 1650 to 2600 m MD (i.e. 1650 to 2600 m TVD) exhibits a null geothermal gradient in GRT-1 that indicates a dominant convection process [*Baujard et al.*, 2017]. In GRT-2, from 1850 to 3200 m MD (i.e. 1650 to 2700 m TVD), the geothermal gradient is low, 18°C/km. This deepest part is composed of Buntsandstein and Permian sandstones and of the hydrothermally altered granitic basement. In

GRT-1, the main permeable fracture zone from 2325 to 2370 m MD is associated to a major negative anomaly in the hydrothermally altered granitic basement (Figure 6.6). This negative anomaly is interpreted as the cooling of the hydrothermally altered and porous zone of the fracture zone after mud invasion during drilling operations. In GRT-2, all permeable fracture zones (two in sandstones and four in the hydrothermally altered granitic basement) are associated to positive or negative anomalies [*Baujard et al.*, 2017]. Positive anomalies suggest circulations of hot geothermal fluid through the permeable fracture zone. The temperature reaches 175°C at 2700 m MD [*Baujard et al.*, 2017].

At **Brühl**, the thermal profile shows a geothermal gradient of 45°C/km (Figure 6.6). The convective regime is not clearly evidenced from this thermal profile. The reservoir temperature is 160°C [*Melchert et al.*, 2013].

6.2.9 Relationship among fracture zones, hydrothermal circulations and borehole trajectories

In the URG, large-scale normal faults strike N10°W to N20°E. With their relatively important vertical displacement (>200 m), these faults are potential permeable drains for geothermal resources. Hot geothermal fluid upwelling is mainly observed through west-dipping faults [*Baillieux et al.*, 2014]. Hydrothermal circulations in the deep sedimentary cover and in the hydrothermally altered granitic basement are visible on thermal profiles from several geothermal wells in the URG. High geothermal gradients are associated to conductive regime and the decrease of geothermal gradients indicates a convective regime. At Soultz, the transition between conduction and convection occurs in the Muschelkalk limestones, Buntsandstein and Permian sandstones (Figure 6.6) [*Vidal et al.*, 2015]. The geothermal gradient decreases slowly from 110°C/km to less than 10°C/km. In other geothermal sites the transition between conduction and convection is more distinct with an abrupt slope of the geothermal gradient located mainly at the top of the Muschelkalk formation for Cronenbourg and Rittershoffen and at the top of the Buntsandstein formation for Bruchsal (Figure 6.6). At Landau, the top of the convection is located deeper in the hydrothermally altered granite (Figure 6.6). At Basel and Brühl, the transition to a convection

regime is not clearly evidenced in thermal profiles (Figure 6.6). At Soultz as well as at Rittershoffen, permeable fracture zones are associated to a thermal signature that is not obviously identified in other geothermal sites. The intersection between wells and the fracture system that channelized the hydrothermal circulations is crucial for geothermal projects and thus, local normal fault zones are the main targets during regional exploration. As fault zones are steeply dipping, vertical wells have a low probability to intersect them. The most recent wells that were drilled in the URG were deviated in order to intersect fractured system associated to fault zone (Landau, Insheim, Rittershoffen, Brühl). These deviated wells show high hydraulic yield that suggest a good connection between open-hole section and fractured system (Figure 6.7).

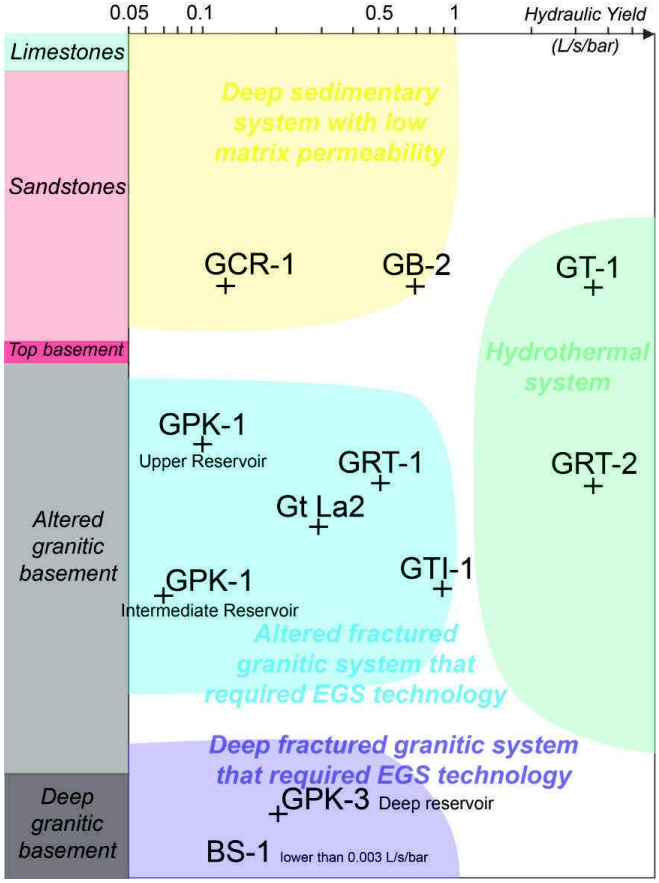

Figure 6.7 Hydraulic yield of geothermal wells in the URG expressed in L/s/bar [*Housse*, 1984; *Ladner and Häring*, 2009; *Kölbel*, 2010; *Schindler et al.*, 2010; *Baumgärtner et al.*, 2013; *Melchert et al.*, 2013; *Baujard et al.*, 2017; *Schill et al.*, 2017]). Hydraulic yields are before stimulation treatments if there is one. Lithology is from Soultz. Depths for other projects are not at scale. Varieties of reservoirs are from [*Ledru and Guillou-Frottier*, 2010].

6.2.10 Relationship between permeable fracture zones and lithology

The architecture of permeable fracture zones is derived from correlation between core samples, cutting observations, acoustic image logs and standard geophysical logs (caliper, gamma ray, neutron porosity…) (Figure 6.5) [*Genter et al.*, 1992; *Genter and Traineau*, 1993; *Traineau et al.*, 1992; *Dezayes et al.*, 2010b]. The permeability at borehole scale is estimated from anomaly on temperature logs, flow logs, mud losses and gas occurrences [*Davatzes and Hickman*, 2005a; *Mas et al.*, 2006; *Dezayes et al.*, 2010b; *Genter et al.*, 2010; *Bradford et al.*, 2013].

Permeable fractures were intersected in deep granite in the deepest sections of the Soultz and Basel wells. At Soultz, a fault plane intersected through GPK-3 [*Sausse et al.*, 2010]. The fault zone is approximately 25 m thick. The fault core is composed by main permeable drains that are approximately 10 cm to 20 cm thick. The damage zone is composed by 7 individual fractures. At Basel, the fracture zones are very localized and poorly connected.

Permeable fracture zones were intersected through hydrothermally altered granite at Soultz, Rittershoffen and probably Insheim and Landau. At Soultz, these zones are approximately 25 to 40 m thick. They are composed by a fault core with a high fracture density and main permeable drains that are 10 cm thick [*Genter et al.*, 2000]. Main permeable drains are partly sealed with geodic quartz (Figure 6.8). The surrounded damage zone is highly altered and porous and composed by more than 100 tiny fractures that are probably connected at the borehole scale (Figure 6.8). Despite the high porosity values in the damage zone, well tests reveal that 95% of the flow entered the rock mass at only 10 discrete flow points that correspond to main opened fractures observed on acoustic image logs [*Evans et al.*, 2005a]. At Rittershoffen, a branch of the Rittershoffen fault probably intersected through GRT-1 and GRT-2 [*Baujard et al.*, 2017]. At borehole scale, this fault zone is 40 m thick. In GRT-1, the main permeable drain is 25 cm thick and is topped by a damage zone that consists of 50 fractures in GRT-1 (Figure 6.8). In GRT-2, several thick permeable drains are surrounded by a lot of tiny fractures. At Insheim, permeable fracture zones are 10-15 m thick.

The top of the granitic basement is a clay-rich, altered and fractured formation that acts as a tight reservoir because of secondary mineral precipitation and therefore is not considered to be permeable [*Vidal et al.*, 2016c].

Permeable fracture clusters were intersected through sandstones at Bruchsal, Cronenbourg, Rittershoffen and probably Insheim. These clusters exhibit a thickness between 10 and 20 m with no obvious displacement observed. At Soultz, a branch of the Soultz fault intersects EPS-1 and GPK-1 in the Vosgian sandstones [*Sausse et al.*, 2010]. The fault zone is approximately 50 m thick. The fault core is composed by main permeable drains that are 5 cm thick [*Vernoux et al.*, 1995]. The damage zone consists of more than 50 individual fractures. At Brühl, a local fault zone was also intersected through sandstones that is up to 100 m thick [*Melchert et al.*, 2013; *Reinecker et al.*, 2014].

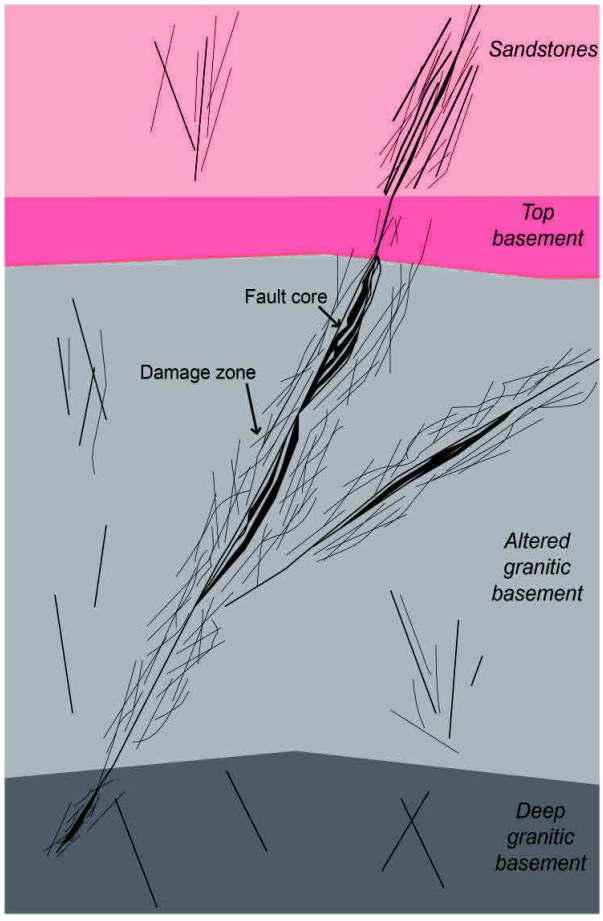

Figure 6.8 Fault zone architecture in sandstones, hydrothermally altered granite and deep granite. FZ = Fault Zone, FC = Fault Core, DZ = Damage Zone.

Deep sedimentary reservoirs and deep granitic reservoirs show lower permeability than altered granitic reservoirs (Figure 5). This difference in permeability could be explained by a structural difference in the architecture of fault zones in sediments, hydrothermally altered granite and deep granite. A high density of macro-scale fractures favors intersection and, thus, connectivity. This highly clustered organization could sustain permeability. The fault zones in the hydrothermally altered granite consist of a thick fault core that is characterized by a high fracture density and a porous, altered and fractured damage zone (Figure 9). This large damage zone could extend several dozen meters around the fault core; thus, several fault zones are well-connected to the large-scale fracture network. The permeability of fault zones is a first-order permeability that responds locally and quickly [*Sausse and Genter*, 2005]. However thick permeable fractures are connected to a wide and regular network of small-scale fractures affecting the whole granitic batholith and responding to a larger scale of permeability. The fault zones in the deep granite are more localized. Even if the fault cores are thick, the fracture density in the damage zone is less important, so the connectivity in the fracture network is poorer. The fault zones in deep sediments exhibit thinner fault cores than those in granite and a large damage zone, where fracture clusters promote permeability. These zones are less prevalent in sediments than in granite.

6.2.11 Concluding remarks

The Soultz-sous-Forêts project was an important scientific contribution for the deep geothermal development in the Upper Rhine Graben. The permeability is supported by the major fracture network. Drilling more than 20 km at Soultz in the sedimentary cover and in the granitic basement reveals geothermal brine circulating into the natural fracture network. This convection system leads to the thermal anomaly. Soultz experience makes the HDR technology, which aims to create a deep geothermal reservoir into low-permeability crystalline rocks, obsolete. It demonstrated the feasibility of the EGS technology in the URG. It aims to reactivate and connect preexisting fractures into a large-scale fractured reservoir by thermal, chemical and hydraulic treatments. Soultz experience revealed that the first 500 m of the granitic basement, highly fractured and hydrothermally altered, is a higher potential reservoir. Fault zones present a

higher permeability into the hydrothermally altered granitic basement than into hard fractured sandstones or poorly altered deep granitic basement probably because of their intense fracture density into the fault core and their larger damage zone that allows connection with the reservoir. The larger roughness of fracture surface in the granite is also a key for explaining the self-propping of fracture after the stimulation. Soultz sedimentary reservoir and deep sedimentary wells (GCR-1, Les Hélions, GT-1) demonstrated that permeability is supported by fracture zones and not by porous matrix. The porosity associated to fractures in the sediments is lower than in the hydrothermally altered granitic basement. Following industrial projects (Landau, Insheim, Rittershoffen, Brühl) are based on the Soultz lesson learned. For most of these project the permeability of fracture zones is higher in the hydrothermally altered granitic reservoir.The permeability is intimately linked to the sub-vertical fault zone in the URG that strikes N-S and dips westward. Wells target local fault zones at the sediments-basement interface. Depths of geothermal wells were divided by two compared to Soultz and the flowrate was increased more than twice. Development of reservoir in the top of the hydrothermally altered granitic basement is economically more interesting. Inclined trajectory allows a higher connection between the well and the sub-vertical fault zone and thus, a higher natural permeability. If the well trajectory is correctly technically designed according to the fault zone's geometry, geothermal wells exhibit sufficient hydrothermal permeability for industrial exploitation and do not need to be stimulated as observed at Rittershoffen (GRT-2), Brühl (GT-1) or Insheim (GTI-2). These recent geothermal wells are qualified as hydrothermal wells. The absence of stimulation is a substantial advantage in terms of environmental purposes for the public acceptance of future geothermal projects. However, the localization of faults at the top of the granitic basement at the seismic scale is also less uncertain. Two-dimensional seismic profiles imaged the sedimentary cover and but poorly, the top of the basement [*Sausse et al.*, 2010]. Major faults at the seismic scale that cross-cut the sedimentary cover in seismic interpretations are extended downwards into the deep basement. The future geothermal projects require technical innovation in exploration methods to accurately characterize the fractured system at the top of the basement. Experience with 3D seismic profiles for the geothermal project in Brühl showed

promising results to identify the geometry of faults at the sediment-basement interface [*Lotz*, 2013].

6.2.12 Acknowledgments

This work was performed in the framework of the LabEx G-Eau-Thermie Profonde which was co-funded by the French government under the program “Investissements d’Avenir”, and as a contribution to the PhD thesis of Jeanne Vidal, who was co-funded by ADEME (French Agency for Environment and Energy). A portion of this work was conducted in the framework of the EGS Alsace project, which was co-funded by ADEME and ES. The authors are grateful to GEIE EMC (Soultz) and ECOGI (Rittershoffen) for accessing to geological and geophysical data. Dr Chrystel Dezayes from BRGM and Dr Clément Baujard from ES-Géothermie are also acknowledged for their support.

6.3 Signature thermique des zones de fractures perméables des sédiments triasiques dans les puits de Soultz (Article publié dans Geotherm. Energy)

How do permeable fractures in the Triassic sediments of Northern Alsace characterize the top of hydrothermal convective cells? Evidence from Soultz geothermal boreholes (France)

Jeanne Vidal[1], Albert Genter[2,3] and Jean Schmittbuhl[1]

[1] IPGS, University of Strasbourg/CNRS, Strasbourg, France
[2] GEIE, Exploitation Minière de la Chaleur, Kutzenhausen, France
[3] ES-Géothermie, Schiltigheim, France

6.3.1 Abstract

Background: The thermal regime of the Upper Rhine Graben (URG) is characterized by a series of anomalies near Soultz-sous-Forêts (France), Rittershoffen (France), and Landau (Germany). These temperature anomalies are associated with groundwater circulation in fractures and faults distributed in the Cenozoic and Mesozoic sedimentary cover associated with and connected to fractures originating deep within the Paleozoic basement. The present study helps to understand the convective cell structure in order to optimize geothermal borehole trajectories.

Methods: The work concentrated on a detailed interpretation of the geophysical and geological logs from Soultz geothermal wells mainly from the topographic surface to the Triassic formations, at between 800- and 1,400-m depth above the deep granitic basement.

Results: The analysis of drilling mud logging data and geophysical well logging data from the deep Soultz geothermal wells (GPK-2, GPK-3, GPK-4) reveals the occurrence of nine fracture zones situated at depths greater than 900 m in the limestones of the Muschelkalk (Middle Trias) and the sandstones of the Buntsandstein (Lower Trias). Based on indications of total or partial mud losses, these fracture zones have been classified as permeable or impermeable.

Conclusions: Permeable fractures between circa 900-m depth and 1,400-m depth are connected to a large-scale fault and control the top of the convective

cells. There is no indication of permeability in the formations above the Keuper layer, and the uppermost part of the sedimentary cover acts as a cap rock, insulating the convective regime in the Triassic sediments and the granitic basement.

Keywords: Triassic sediments; Well logging; Fracture zones; Permeability; Convection; EGS

6.3.2 Background

The thermal regime of the Upper Rhine Graben (URG) is characterized by a series of geothermal anomalies near Soultz-sous-Forêts (Alsace, France), Rittershoffen (Alsace, France), and Landau (Rhine-Palatinate, Germany). These areas reveal local thermal gradients up to 100°C/km in the uppermost part of the sedimentary cover. These gradients are attributed to hydrothermal convective cells circulating inside a nearly vertical fracture network in the granite basement and in the fractured Triassic sediments above it [*Schellschmidt and Clauser*, 1996; *Pribnow and Clauser*, 2000; *Pribnow and Schellschmidt*, 2000]. The interpretation of seismic reflection profiles identifies major large-scale faults extending across the Cenozoic and Mesozoic sedimentary cover and originating in the Paleozoic fractured basement (Figure 6.9) [*Cautru*, 1988]. Hydrothermal pathways in the sub-vertical fault network within the granitic basement are confirmed by thermo-hydraulic modeling [*Le Carlier et al.*, 1994; *Kohl et al.*, 2000; *Bächler et al.*, 2003]. The thermal profile of the deep Permo-Triassic sediments and the crystalline basement is dominated by a convective regime with a thermal gradient of 5°C/km. This part is characterized by the occurrence of negative thermal anomalies corresponding to zones of natural fractures [*Genter et al.*, 2010]. These cooled zones, due to drilling or stimulation operations, may be interpreted as a thermal expression of faults. However, they are not noticeable in the sedimentary cover between 0- and 1-km depth, where the dominating thermal regime remains highly conductive. The present paper focuses on the transitional zone located between 0.8- and 1.2-km depth (Figure 6.10). This depth segment lies between the uppermost conductive zone (0- to 1.0-km depth) and the underlying convective zone (1.0- to 3.5-km depth).

The sediment-basement interface is clearly very attractive for industrial exploitation due to the heat carried by the geothermal fluid circulating within natural fractures. Several enhanced geothermal system (EGS) projects in the URG target geothermal reservoirs at this depth between the bottom of the sedimentary cover and the top of the granitic basement, corresponding to the top of the convective cells. For example, geothermal wells were drilled in the fractured Muschelkalk layer in Southern Germany (at Offenbach) and in Switzerland (at Riehen) to produce brine with acceptable temperatures for local energy use [*Kreuter et al.*, 2003; *Stober and Jodocy*, 2009, 2011]. Other projects at Cronenbourg and Rittershoffen in France and at Landau, Insheim, and Bruchsal in Germany demonstrate the quality of the resource at the fractured sediment-basement interface for geothermal uses [*Housse*, 1984; *Baumgärtner and Lerch*, 2013; *Hettkamp et al.*, 2013; *Villadangos*, 2013; *Meixner et al.*, 2014].

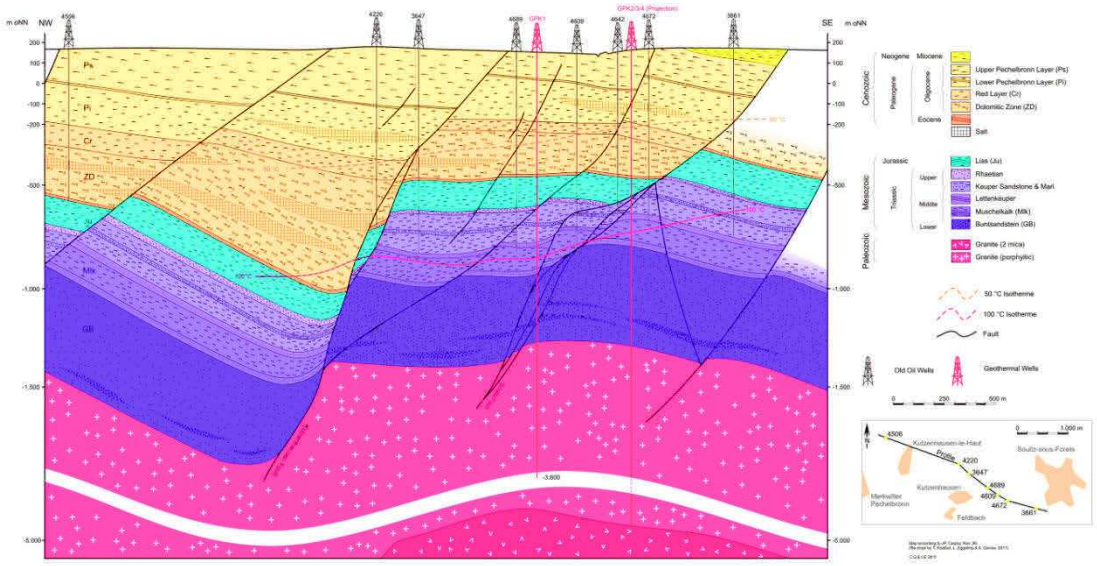

Figure 6.9 Geological cross section based on seismic reflection profiles. Numerous large-scale crustal faults originate in the basement and cross the sedimentary cover. Oil wells and the geothermal boreholes GPK-1, GPK-2, GPK-3, and GPK-4 are projected onto the cross section [*Cautru*, 1988].

The aim of this study is to significantly contribute to a better understanding of the geological structure of the convective cells. The authors based our geological analysis of the sediment-basement interface on drilling, geological, and geophysical data available for the Soultz geothermal wells. The work

concentrated on a detailed interpretation of the geophysical and geological logs from the Soultz geothermal wells GPK-1 (3.6 km), GPK-2 (5 km), GPK-3 (5 km), and GPK-4 (5 km), which extend mainly from the topographic surface to the Triassic formations between 0.8- and 1.4-km depth. The available drilling data include the lithology, rate of penetration of the drill bit, weight on bit, evidence of natural outflow (partial and total mud losses), occurrence of gas (helium and methane), and mud temperature variations. Additional well logging data, such as temperature, gamma ray, and caliper logs, were correlated with the drilling data. The methodology was extended to peripheral wells (EPS-1 and 4550) of the Soultz field in which borehole images were available for sediments. Based on these well logging data, the location in the sedimentary cover of the fracture zones and their permeability were used to estimate the impact of the fracture system on the thermal regime. Properties of the fracture system itself limit hydrothermal circulation, and the authors tried to identify a sedimentary layer that could limit the upper part of the convective cells. Spatially correlating the fracture zones between different geothermal boreholes was an important focus of this study in order to explore the heterogeneity of the permeability of a given fault that crosses several wells at depth.

Following a presentation of the geothermal reservoirs at the Soultz site and a description of the geological and thermal background, the well logging data from the Soultz geothermal boreholes are evaluated to highlight fracture zones in the sedimentary cover. Then, the temperature profiles are analyzed to assess the thermal expression of fracture zones in the conductive region. Finally, a schematic conceptual model of the convective cell structure will be proposed.

6.3.3 Presentation of the EGS site of Soultz-sous-Forêts

6.3.3.1 The so-called ‘Soultz geothermal anomaly’

At the regional scale, the underground temperature distribution is spatially heterogeneous, and a series of local anomalies with temperatures above 140°C at 2-km depth are mainly concentrated on the western side of the URG, such as Soultz-sous-Forêts (France), Landau (Germany), or Mainz (Germany) [*Schellschmidt and Clauser*, 1996; *Baillieux et al.*, 2013]. The temperature anomalies in the URG are controlled by three thermally relevant mechanisms:

variability in the radiogenic heat production, convection, and conduction. The so-called 'Soultz geothermal anomaly' is one of the most important temperature anomalies and has been the subject of numerous studies. Soultz granites exhibit a maximum variation in radiogenic production of 5.5 to 6.5 $\mu W/m^3$ measured in core samples from GPK-1 [*Rummel et al.*, 1988] and a more important vertical variation of 2 to 7 $\mu W/m^3$ in GPK-2 [*Pribnow and Schellschmidt*, 2000b]. However, this radiogenic production is insufficient to explain the geothermal anomalies [*Stussi et al.*, 2002]. Temperature data from various oil and geothermal wells reveal a concentration of hot zones along Soultz or Kutzenhausen normal faults [*Benderitter and Elsass*, 1995; *Pribnow and Clauser*, 2000; *Pribnow and Schellschmidt*, 2000b].

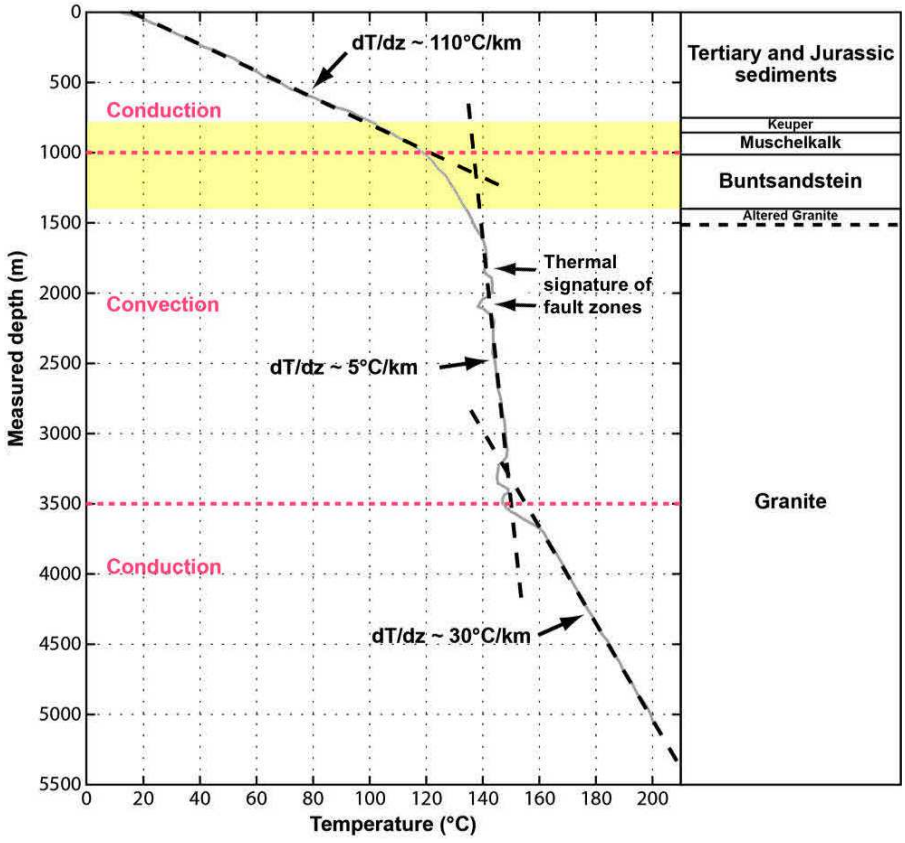

Figure 6.10 Equilibrium temperature profile obtained from GPK-2. The equilibrium temperature profile was obtained several monts after drilling operation was finished (data from LIAG-Hannover, Germany). Main geological units are presented versus depth. The yellow rectangle indicates the zone of the top of the convection, the target of the study.

These geothermal anomalies at the local scale are attributed to buoyancy-induced hydrothermal circulation within the crystalline basement and the sandstones. To explain the Soultz anomaly, various hydrothermal modeling studies have focused on the Soultz horst region [*Kohl et al.*, 2000] and on several vertical cross sections perpendicular to the graben axis [*Person and Garven*, 1992; *Le Carlier et al.*, 1994; *Guillou-Frottier et al.*, 2013].

The typical thermal profile in the 5-km-deep wells features a temperature of 200°C at 5-km depth (Figure 6.10). The profile was measured several months after the drilling operations, and the thermal conditions are considered to be at equilibrium. This profile can be divided into three parts. The uppermost part from 0- to 1.0-km depth is composed of sedimentary formations from Tertiary and Mesozoic (Jurassic and Upper Trias) and features a geothermal gradient of 110°C/km, which indicates a conductive heat transport mechanism [*Pribnow and Schellschmidt*, 2000]. This geological section acts as a cap rock, i.e., an impermeable layer that insulates the hydrothermal system active below.

The part from 1.0- to 3.5-km depth is composed of deep sedimentary formations (Buntsandstein and Permian sandstones) and granitic basement and features a very low geothermal gradient of 5°C/km, which indicates the presence of a convection process. This second thermal unit is locally disturbed by cold fractured zones, for example at 1.6-km depth or 2.1-km depth, which can be interpreted as the remnants of formation cooling induced by drilling and from massive hydraulic injections [*Genter et al.*, 2010]. Permeable fractured and altered zones are cooled by the invasion of drilling mud or fresh water during hydraulic stimulation operations. Fractures in the granitic basement have a negative thermal signature visible even several months after hydraulic operations.

Finally, the deepest part of the profile, greater than 3.5-km depth, is composed only of crystalline formations and features a linear gradient of approximately 30°C/km, indicating a return to a conduction-dominated regime.

6.3.3.2 Soultz reservoirs

The target of the Soultz project was the development, the hydraulic testing, and the modeling of two EGS heat exchangers developed within the granitic

basement at depths of 3.5- and 5-km depth [*Gérard et al.*, 2006; *Dezayes et al.*, 2010a]. The different phases of the Soultz project have provided a rich and diverse database on the granitic basement (Figure 6.11). However, knowledge of the 1.4 km of overlying Cenozoic and Mesozoic sediments is much poorer. Despite intensive investigations in the uppermost depth range during the oil production of the Merkwiller-Pechelbronn oil field, geothermal exploration has focused on the granitic basement. Four geothermal boreholes were drilled into the crystalline basement: GPK-1, GPK-2, GPK-3, and GPK-4 (Figure 6.11). Geothermal water is pumped from the production well (GPK-2) and re-injected at lower temperatures into the injection wells (GPK-3 and GPK-4) after delivering geothermal energy through a heat exchanger to a binary power plant [*Genter et al.*, 2013]. At Soultz, three other proximal wells penetrated the granitic basement and thus its sedimentary cover, and these wells provided extra information. These additional wells include the pilot geothermal borehole GPK-1; EPS-1, a renamed former petroleum well that has been deepened to 2.2-km depth and fully cored for use as an exploration well, and another former petroleum well 4550 that has been extended to 1.5-km depth and used as a micro-seismic monitoring well [*Degouy et al.*, 1992].

Below the sediments, the crystalline basement is encountered at 1.4- to 5.0-km depth (Figure 6.9) and exhibits several indications of convection associated with the fracture system that ranges from micro-cracks to local faults. From core analyses and interpretations of well logs, natural fractures within the granite are thought to be clustered in hydrothermally altered and fractured zones [*Genter et al.*, 2000]. Moreover, the natural fracture system directly controls the zones that produce geothermal fluid and the zones of drilling mud loss [*Vuataz et al.*, 1990; *Evans et al.*, 2005a]. Strong hydrothermal alteration is evidence of paleo-circulation, which has resulted in the dissolution of primary minerals, such as biotite and plagioclase [*Genter*, 1989; *Genter et al.*, 2000]. However, fracture zones present both permeability and sealing related to the deposition of hydrothermal minerals, such as secondary quartz, clay minerals, calcite, and sulfides (Figure 6.12) [*Genter and Traineau*, 1993, 1996; *Genter et al.*, 1997a]. Traces of organic matter in a fracture zone from EPS-1 reveal hydraulic communication between the basement and sediments [*Ledésert et al.*, 1996].

A detailed analysis of image logs, standard geophysical logs, petrographic logs, and flow logs reveals a clear spatial relationship between the occurrence of natural permeability and hydrothermally altered and fractured zones in the granite [*Evans et al.*, 2005a; *Dezayes et al.*, 2010b]. Natural brine circulates within a sub-vertical fracture system between the deepest crystalline water-bearing zones and those in the lower sedimentary layers. This paper focuses on a detailed analysis of various borehole data (mud logging and geophysical logs) from the formations between 0.8- and 1.2-km depth.

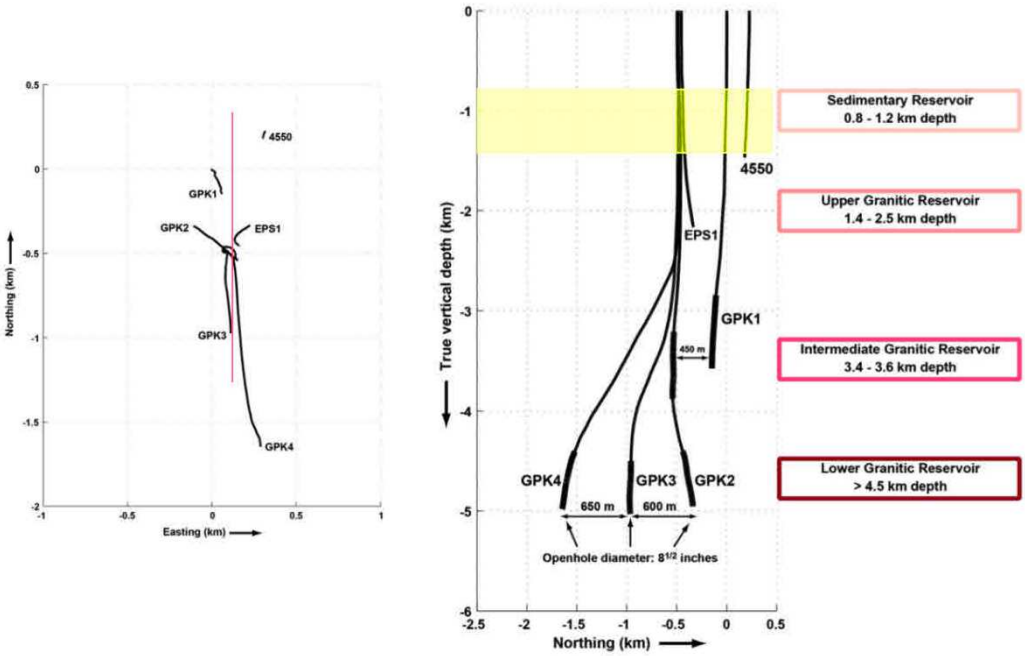

Figure 6.11 Local map view of the Soultz site and north-south vertical cross section. The view shows the trajectories of the deep geothermal wells GPK-2, GPK-3, and GPK-4, as well as the exploration wells GPK-1 and EPS-1 and the seismic well 4550. The vertical cross section (trace in red on the map) shows the location of the different sedimentary and granitic reservoirs. Depths are expressed in True Vertical Depths (TVD).

6.3.3.3 Geology of the sedimentary cover

In GPK-2, the Tertiary sediments extend from the topographic surface down to 623-m depth. The uppermost part is composed of clays and marls in the Pechelbronn oil formations of Oligocene age (316-m depth) (Figure 6.9) [*Ménillet*, 1976; *Cautru*, 1988]. The Eocene formations are divided into two types of marl:

the ferruginous marlstones of the Red Layer (353-m depth) and the marlstones interbedded with dolomite layers of the Dolomitic Zone (601-m depth). At its base, there is a thin layer of dark claystones dated to the late Eocene. This Tertiary section features an erosional contact with the Jurassic formations. The Dogger formations are dark-grey clays with calcareous shale (653-m depth), and the Lias formations are grey silty calcareous claystones (763-m depth). The lowest part of the sedimentary cover is a typical Germanic Triassic sequence with Upper Triassic dolomites, anhydrite and clays for layers: the Keuper formation extends down to 853-m depth and the Lettenkohle formation down to 873-m depth. The stratigraphy of the Muschelkalk and Buntsandstein can be specified thanks to core samples from EPS-1. The stratigraphic series of the typical Germanic Triassic sequence indicates rather constant thicknesses through all the URG, and all formations can be easily correlated between boreholes, even if separated by several kilometers. The top of the Upper Muschelkalk is composed of massive limestones rich in Terebratula over marly calcareous formations that extend over 35 m before giving way to massive crinoidal limestone beds. These high carbonate content limestone beds are the most competent rocks of the sedimentary cover. They are approximately 14-m thick and mark the transition to the Middle Muschelkalk. The central section of the Muschelkalk is composed of marly dolomites invaded by anhydrite (circa 50-m thick). The Upper Muschelkalk begins at a depth of approximately 980 m and is divided into two parts: the upper part is marly calcareous dolomites and the lower part is fossil-rich sandstones to a depth of 1,021 m. The sedimentary cover ends with the Buntsandstein sandstones that extend to a depth of 1,405 m. At the top of the formation, the Voltzia sandstones are fine-grained sandstones with interbedded clays and are over 10-m thick. The so-called Intermediate Layers are sandstones with a larger grain size and are approximately 40-m thick. The Middle Buntsandstein is represented by the Vosgian sandstones, typical medium-grained to conglomeratic continental sandstones with clay formations. The last 50 m of the formation is composed of the Annweiler sandstones, an argillaceous red sandstone. The transitional layer of Permian sandstones is visible in core samples from the EPS-1 well but hardly distinguishable in cuttings. The evaluated porosity of the Buntsandstein is quite low (10% at the top of the formation and 20% for the Vosgian sandstones [*Vernoux et al.*, 1995]. Petrophysical studies of

the core samples note the role of the matrix permeability, which controls the geothermal fluid circulation through these sandstones [*Haffen et al.*, 2013].

Figure 6.12 Core sample from a sandstone in the Buntsandstein at 1,204-m depth in the well EPS-1. The core sample exhibits a part of a fracture zone (1) and its damage zone (2). Barite and galena fill the hydraulic breccia. The diameter of the core sample is 8 cm.

6.3.4 Methods

6.3.4.1 Fracture zone definition

The authors conducted a comprehensive borehole data analysis of the Soultz geothermal boreholes. The data collected during the drilling operations included drilling mud losses, natural outflow, gas content, and the rate of penetration (ROP). Geophysical well logs, such as caliper, gamma ray (GR), bulk density, neutron porosity, and borehole wall images, were used and compared to the mud logging data. The depth match interval of −4 m between the drilling mud logging data and the geophysical well logging data must be taken into account. To avoid moving these data sets artificially upward or downward, it was decided to leave the data in their own separate depth reference frames.

Because the Soultz geothermal project mainly focused on deep crystalline reservoirs, only a few of the geophysical well logs have been collected properly. For example, the GR and caliper logs were systematically collected in all the

geothermal wells, whereas the bulk density, neutron porosity, and image logs were less frequently collected. For GPK-2, GPK-3, GPK-4, EPS-1, and 4550, the temperature logs were obtained behind the casing at thermal equilibrium conditions, whereas for GPK-1, one temperature log was obtained just a few hours after the end of drilling operations. For each geothermal well, the available borehole data were correlated spatially with depth to highlight any physical variations that might be interpreted as indication of fracture zones. Three types of fracture zones have been outlined:

- A permeable fracture zone is defined by the occurrence of drilling mud losses, natural outflow, or helium gas content. The best permeability indicator during drilling operations is total mud loss. Generally, in such conditions, calipers and ROP increase simultaneously at the same depth.
- A sealed fracture zone is defined by absence of obvious mud losses or natural outflow. However, a fracture zone can be defined by caliper enlargement, porosity increase, ROP increase, or bulk density decrease.
- A partially sealed fracture zone possesses an intermediate set of properties between a permeable and a sealed fracture zone. In some cases, there is a clear indication of fracture zone occurrence (caliper or ROP increases), but permeable indicators are poorly constrained. For example, mud logging data are mainly qualitative, and this fact introduces a certain amount of uncertainty to the permeability range. Very small temperature variations are also a criterion, which might cause a given fracture zone to be re-qualified as only partially permeable.

Fracture geometry has been evaluated only in EPS-1 and 4550 in certain localized fracture zones where image logs were available. Thus, this methodology has only been applied to data collected from boreholes drilled specifically for exploration and research.

6.3.4.2 Typology of the data

Even if sedimentary cover was not the main target of the geothermal exploration at Soultz, a series of well logs has been collected from the geothermal wells (GPK-2, GPK- 3, and GPK-4), the exploration wells (GPK-1 and EPS-1), and one of the micro-seismic monitoring wells (4550).

The first group of well logging data consists of instantaneous well logs, such as the ROP, which records the speed at which the drill bit penetrates the rock, usually reported in m/h. Normally, the speed of the drill bit decreases as the drill bit bores into denser formations. At Soultz, the mean speed is 8 m/h in soft sediments (above 1-km depth), 5 m/h in hard sediments (below 1-km depth) and just 2 m/h in the granite. When the ROP is higher than the mean value, the occurrence is generally interpreted as the effect of a localized fracture zone. In such a case, the driller is obliged to reduce the weight on the bit (WOB) to drill in stable drilling conditions. The WOB is the mass of the tool string that applies a vertical load on the drill bit and ranges, in the Soultz case, from 11 tons in soft sediments to 15 tons in hard Triassic sediments or granite. If the WOB is reduced by the driller, the ROP is artificially low but could nevertheless indicate a fracture zone.

Flow variations represent the amount of mud circulation and can be interpreted as a loss (outflow). Mud, also called drilling fluid, refers to fluids that contain a significant proportion of suspended solids in aqueous solution. When the drill bit crosses a permeable fracture zone, the well records a partial decrease in the outflow or even a total loss of mud circulation. Variations in the mud temperature, recorded in degrees Celsius, suggest mixing between hot geothermal fluid and cold drilling mud. As is the case for a natural outflow, the permeable fractures bearing hot fluid could induce drastic variations in the drilling mud temperature.

Mud logging also includes the monitoring of natural gas emissions. This classic method for fracture zone detection has already been demonstrated at Soultz, where helium gas anomalies are associated with permeable fractures at 1,810-m depth in the granite part of GPK-1 [*Vuataz et al.*, 1990]. A content of hydrocarbon gas, such as methane, could be interpreted as indicating fluid circulation in local fracture zones or as an indicator of matrix permeability. For reference, the contents of helium, methane, and ethane in the atmosphere are approximately 5.24 ppm, 1.75 ppm, and 0.50 ppm, respectively.

The second group of well logging data consists of wireline logs, measured continuously while the tool is pulled upward from the bottom of the borehole. The measurements are transmitted continuously via the wireline to the surface. For this study, standard geophysical wireline logs were used to measure the gamma

ray of natural radioactivity in the geological formations in the borehole and reported in gAPI. At Soultz, the spectral gamma ray measurement was a significant proof of hydrothermally altered and fractured zones in the granite [*Hooijkaas et al.*, 2006]. It is more difficult to use this method to identify fracture zones in Triassic sediments due to their lower content of radioisotopes. In the Lettenkohle and the Upper Muschelkalk, the local GR minima are associated with the marly calcareous formations. In the Buntsandstein, clay layers (less than 2 m thick) correspond to isolated and localized GR peaks. Peaks associated with fracture zones with hydrothermal alteration halos show a larger GR variation than those induced by sedimentary clay layers.

In a fracture zone, the caliper no longer measures a simple cylindrical borehole diameter. The drillhole is no longer circular but rather resembles a 'cave'. The borehole image log, also called the BoreHole TeleViewer (BHTV) log, is very useful in evaluating the fracture geometry. If the fracture is visible in both the amplitude and transit time data, the fracture is open at least on the borehole scale. If fractures are visible in the amplitude data but not in the transit time data, the fractures are sealed by mineral deposition. Because these tools are oriented according to the magnetic North, stratification or fracture geometry (dip and dip direction) can be estimated with the borehole image logs. In the Soultz wells, BHTV logs in the depth ranges of interest here were only available in sandstones from the Buntsandstein in EPS-1 and 4550. Other standard geophysical measurements, such as the bulk density of the rock formation (recorded in g/cm^3), neutron porosity (measured in percent), or resistivity (expressed in ohm/m), are commonly used to characterize fracture zones and were already widely available from Soultz granite [*Genter and Traineau*, 1993].

6.3.4.3 Fracture zone location in the wells

Fracture zone locations were first evaluated in the wells GPK-2, GPK-3, and GPK-4 from mud logging, calipers, and GR data [*Baumgärtner et al.*, 1995, 2000; *Hettkamp et al.*, 2004; *Baumgärtner et al.*, 2005]. Because the wellheads are very close (less than 15 m apart) and because the wells are sub-vertical in the same sedimentary section, we spatially correlated certain fracture zones. To compare the fracture zones in the wells, a similar terminology and labeling for fracture

zones has been used for the three geothermal wells. A given fracture zone is not necessarily visible in all the wells.

Fracture zone locations have also been investigated in the pilot geothermal/exploration borehole GPK-1, the exploration/research well EPS-1, and the micro-seismic monitoring well 4550 [*Degouy et al.*, 1992]. In GPK-1, the density, porosity, GR, and resistivity logs were available [*Herbrich*, 1988]. Additional geophysical measurements, such as BHTV, were available for EPS-1 and 4550, and continuous core samples collected in EPS-1 have proved to be very useful for correlating mud losses with depth.

In this analysis, a fracture zone could be defined as a steeply dipping single fracture. It is clearly visible on caliper data or BHTV logs when available. However, a fracture zone is generally a rather complex geometric structure composed of several individual fractures, spatially concentrated within a cluster. When BHTV logs are also available, a fracture zone is easily interpreted in terms of geometry and depth location. With standard geophysical logs, such as that obtained with a six-arm caliper, several individual peaks visible on each curve are very helpful in characterizing a given fracture zone (Figure 6.13, zone 1). In some cases, the depth of an ROP increase agrees with a caliper enlargement, reinforcing indications of the presence of a fracture zone.

6.3.5 Results and discussion

6.3.5.1 Characterization of the fracture zones in the wells

Well GPK-2

The synthetic log of GPK-2 shown in Figure 6.13 contains lithology, stratigraphy, GR, and caliper data. The caliper was a three-arm tool with three diameters that correspond to C14, C25, and C36 data. The nominal diameter of the well is 12.25 inches when the wellbore is not affected by caving or ovalization. ROP is locally absent because digital data were only available for the granite section. The log in Figure 6.13 also presents two permeability indicators: mud losses and helium or methane enrichment.

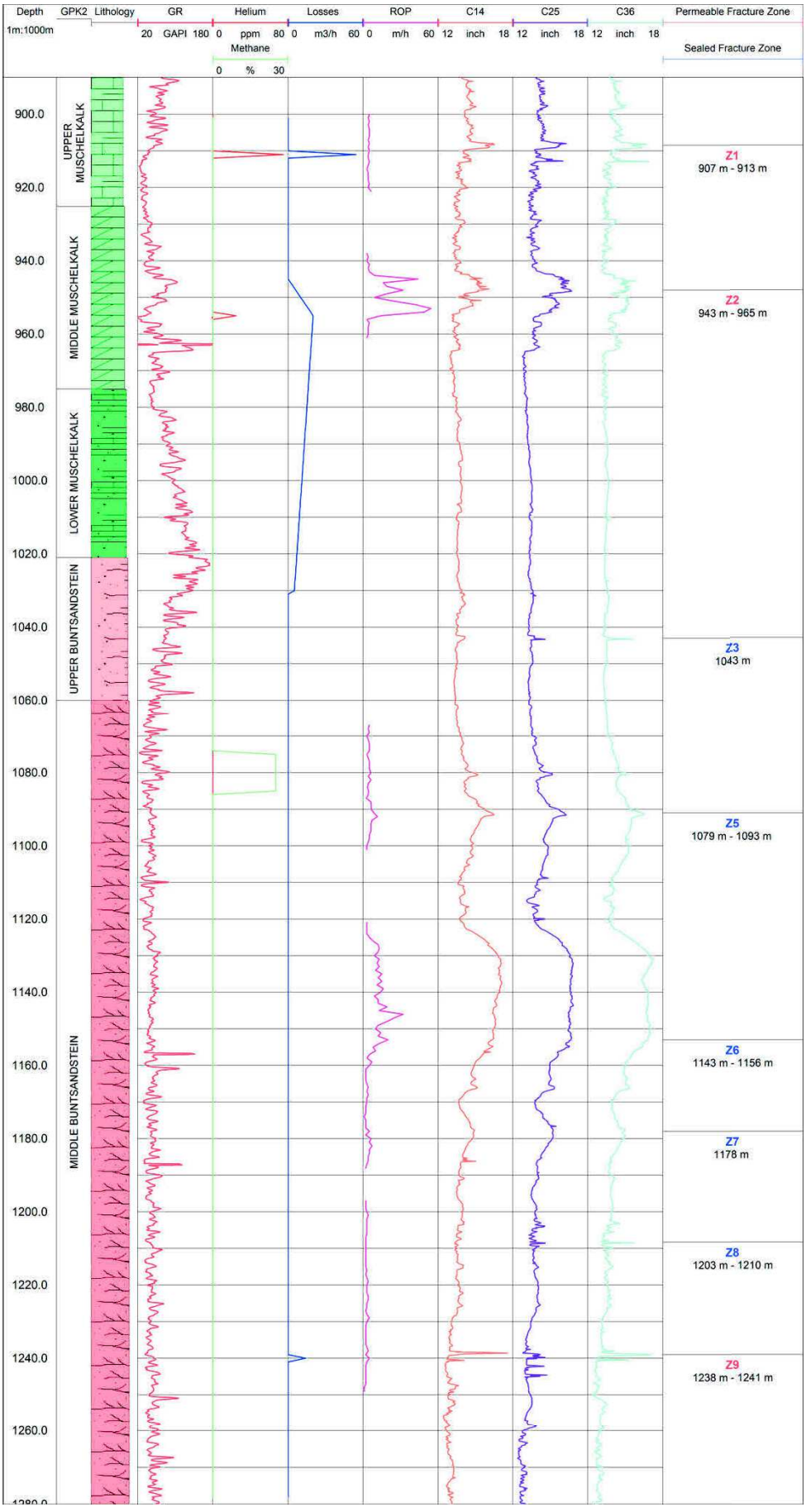
Depth
1m:1000m
GPK2
Lithology
GR
20 GAPI 180
Helium
0 ppm 80
Methane
0 % 30
Losses
0 m3/h 60
ROP
0 m/h 60
C14
12 inch 18
C25
12 inch 18
C36
12 inch 18
Permeable Fracture Zone
Sealed Fracture Zone
UPPER MUSCHELKALK
MIDDLE MUSCHELKALK
LOWER MUSCHELKALK
UPPER BUNTSANDSTEIN
MIDDLE BUNTSANDSTEIN
900.0
920.0
940.0
960.0
980.0
1000.0
1020.0
1040.0
1060.0
1080.0
1100.0
1120.0
1140.0
1160.0
1180.0
1200.0
1220.0
1240.0
1260.0
Z1
907 m - 913 m
Z2
943 m - 965 m
Z3
1043 m
Z5
1079 m - 1093 m
Z6
1143 m - 1156 m
Z7
1178 m
Z8
1203 m - 1210 m
Z9
1238 m - 1241 m

Figure 6.13 (previous page) Synthetic log of GPK-2. The synthetic log shows the lithology, mud losses, GR, gas occurrences (helium and methane), ROP, and caliper (C14, C25, C36) data. Fracture zones are indicated: Z1, Z2, Z3, Z5, Z6, Z7, Z8, and Z9. Permeable zones are in red and sealed zones are in blue. Depths are expressed in measured depth.

The depth range covered by the synthetic log was focused on the sedimentary part, where permeability indicators were detected, for example between the 890- and 1,280-m depth (Figure 6.13). In this depth section, eight fracture zones have been highlighted from well logging data. Zones Z1, Z2, and Z9 are deduced from mud loss information and helium emissions correlated spatially with local caliper enlargement. Zones Z3, Z5, Z6, Z7, and Z8 are hypothesized from local caliper or ROP variations. Thus, they are interpreted as sealed fractures or fracture zones with no indications of permeability during drilling.

Zone Z1 is permeable and featured total mud loss. Several individual peaks are visible in the caliper data from 907- and 913-m depth, with a maximum of 16.60 inches for C36 at 908-m depth. Because of the nominal diameter of 12.25 inches at this depth, the well diameter is wider by 4.45 inches in zone Z1. Helium concentrations reach 73 ppm at 911-m depth, which is 14 times higher than the atmospheric helium value. Zone Z1 clearly shows the depth match of circa −4 m between the drilling mud logging data and the geophysical well logging data (Figure 6.13). The helium peak visible at 911 m fits with the caliper anomaly visible at 908-m depth. Surprisingly, the ROP is stable. Zone Z1 is a complex permeable fracture zone.

Zone Z2 is a complex structure extending vertically from 943- to 965-m depth. The caliper data indicate a large perturbation zone with a maximum C25 diameter of 16.60 inches at 948 m, an enlargement of 4.45 inches. The ROP values are higher than 50 m/h at 953-m depth and fit spatially with helium concentrations of 25 ppm. Persistent mud losses are recorded between 955 m (20 m^3/h) and 1,030 m (5 m^3/h). The relatively high GR values (104.34 gAPI and 223.25 gAPI at depths of 945 m and 963 m, respectively) are interpreted as a brecciated fault zone filled with clays in the Middle Muschelkalk. Hence, zone Z2 is a complex fracture zone with obvious permeability indicators.

Caliper variations in zone Z3 are very local, featuring a sharp peak on three calipers with a maximum of 15.56 inches for C36 at 1,043-m depth. This fracture zone is a single, non-permeable fracture.

Zone Z4 is not visible on GPK-2 but is visible in GPK-3 and GPK-4.

Zone Z5 is characterized by noticeable positive anomalies on the three caliper curves between 1,079- and 1,093-m depth. The maximum caliper variation of 16.18 inches for C25 at 1,091 m fits with a ROP positive anomaly of 11.50 m/h at 1,092 m. A depth interval stretching from 1,075 to 1,089 m features a substantial methane content. Because the methane variation is larger than the discrete caliper peaks, the methane could be related to the presence of organic compounds in the matrix sandstones. Thus, zone Z5 corresponds to a sealed complex fracture zone.

Caliper variations in zone Z6 extend from 1,143- to 1,156-m depth. This zone represents the greatest enlargement found in the sedimentary part of GPK-2 (5.25 inches at 1,130-m depth). It is most likely related to the lithologic nature of the formations. The ROP positive anomaly features a maximum of 32.40 m/h at 1,146-m depth. Because there is no evidence of mud loss or helium anomalies, zone Z6 is classified as a sealed fracture zone.

Zone Z7 features a caliper variation in all three curves. For C25, a maximum of 15.46 inches occurs at 1,176-m depth. There is no anomaly in the mud logging data; hence, zone Z7 is an individual sealed fracture.

Zone Z8 is considered as complex because calipers present several individual peaks between 1,203- and 1,210-m depth. As in the case of Z7, there is no evidence of permeability indicators; thus, Z8 has been interpreted as a complex sealed fracture zone.

The last zone, Z9, is characterized by mud losses of 14 m^3/h recorded at a depth of 1,240 m. The caliper values match the depths of several peaks and a major anomaly of 16.80 inches at 1,238-m depth. Zone Z9 is therefore classified as a complex permeable fracture zone.

Well GPK-3

The synthetic log of GPK-3 presented in Figure 6.14 contains lithology, GR, ROP, natural inflow and outflow, temperature inflow and outflow, and six-arm caliper (radii RD1 to RD6) data. Between 890- and 1,280-m depth, the nominal diameter is 17.50 inches. For GPK-3, helium and methane surveys were performed only in the granitic section of the well, i.e., below 2-km depth. Mud loss data come from daily drilling reports from Socomine (dark blue curve) and from *Hettkamp et al.* [*Hettkamp et al.*, 2004] (light blue section).

Zones Z1, Z2, Z4, and Z9 have been highlighted by mud losses recorded by the drilling company. Zones Z3, Z6, Z7, and Z8 are based on significant variations in at least two well log parameters (Figure 6.14).

In GPK-3, mud losses are observed at 904-m depth. Zone Z1 features a series of caliper variations visible on the six radii recorded by the six-arm tool between 894- and 914-m depth and is characterized by a clear positive anomaly visible in the ROP data (11.77 m/h at 914-m depth). Z1 is interpreted as a complex permeable fracture zone.

Zone Z2 is a complex structure with several positive anomalies visible in the ROP curve with a maximum of 42.52 m/h at 950 m, which correlates with mud losses of approximately 32.40 m^3/h at the same depth. The GR value of 98.97 gAPI at 950-m depth is an additional indication of a fracture zone with clay deposition. The caliper data also feature the values 13.94 inches for RD4 at 951-m depth and 13.18 inches for RD5 at 952-m depth. These values correspond to a diameter of 24.60 inches, thus an enlargement of 7.10 inches. As mud losses are observed, Z2 is classed as a complex permeable fracture zone.

Figure 6.14 (next page) Synthetic log of GPK-3. The synthetic log shows mud losses from daily report (dark blue curve) and from Hettkamp et al. (2004) (light blue section), GR, ROP and caliper (RD1, RD2, RD3, RD4, RD5, RD6) data. The lithology is the same as GPK-2. Fracture zones are indicated: Z1, Z2, Z3, Z4, Z6, Z7, Z8, and Z9. Permeable zones are in red and sealed zones are in blue. Depths are expressed in measured depth.

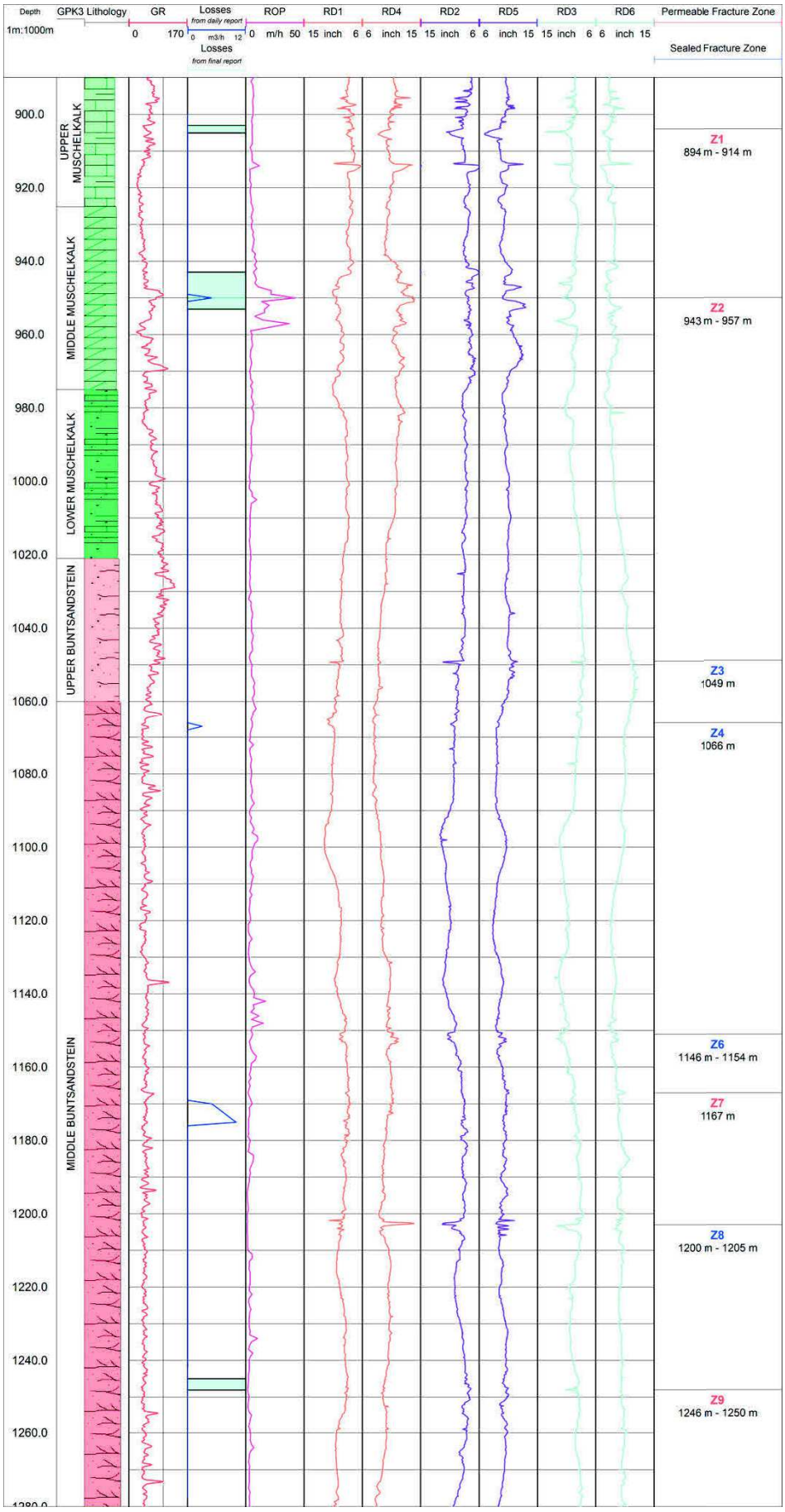
Depth
1m:1000m
GPK3 Lithology
GR
0
170
Losses
from daily report
0 m3/h 12
Losses
from final report
ROP
0 m/h 50
RD1
15 inch 6
RD4
6 inch 15
RD2
15 inch 6
RD5
6 inch 15
RD3
15 inch 6
RD6
6 inch 15
Permeable Fracture Zone
Sealed Fracture Zone
UPPER MUSCHELKALK
MIDDLE MUSCHELKALK
LOWER MUSCHELKALK
UPPER BUNTSANDSTEIN
MIDDLE BUNTSANDSTEIN
900.0
920.0
940.0
960.0
980.0
1000.0
1020.0
1040.0
1060.0
1080.0
1100.0
1120.0
1140.0
1160.0
1180.0
1200.0
1220.0
1240.0
1260.0
Z1
894 m - 914 m
Z2
943 m - 957 m
Z3
1049 m
Z4
1066 m
Z6
1146 m - 1154 m
Z7
1167 m
Z8
1200 m - 1205 m
Z9
1246 m - 1250 m

Zone Z3 features a sharp positive variation in caliper data, with values of 10.35 inches for RD1, 11.52 inches for RD2, and 9.22 inches for RD3 at a depth of 1,049 m. Zone Z3 is a sealed individual fracture.

Zone Z4 represents a small variation in the caliper data (11.22 inches at 1,066 m on RD1) and in the ROP data (6.68 m/h at 1,072 m). Z4 features several permeability indicators from the mud logging. Mud losses of 3 m^3/h are recorded at 1,067-m depth. Clear evidence from the mud logging data have led to Z4 being interpreted as a permeable single fracture.

Zone Z5 is not clearly visible in GPK-3.

Zone Z6 is characterized by several positive variations visible from the readings of the six-arm caliper between 1,146- and 1,154-m depth. The maximum of caliper anomaly is 11.62 inches for RD4 at 1,152-m depth. The ROP also presents several positive variations, with a maximum of 15.17 m/h at 1,148-m depth. Zone Z6 is a sealed fracture zone.

Zone Z7 is characterized by variations in both the caliper data (10.50 inches at 1,167-m depth) and ROP data (5.38 m/h at 1,169-m depth). Mud losses of 5 m^3/h are observed at 1,169-m depth and increase to 10 m^3/h at 1,175 m. Zone Z7 is a permeable fracture.

Zone Z8 is visible on the radius readings of the six-arm caliper (13.94 inches for RD4 at 1,202-m depth). The ROP is constant, but this fact could be explained by the zero WOB at this depth. Zone Z8 is a complex sealed fracture zone with a vertical extent from 1,200- to 1,205-m depth.

Zone Z9 is characterized by mud losses at 1,245-m depth and caliper variations, with a maximum of 10.84 inches at 1,248-m depth. Surprisingly, the ROP is flat. Z9 is a permeable fracture zone extending vertically from 1,246- down to 1,250-m depth.

Well GPK-4

The synthetic log of GPK-4 in Figure 6.15 presents lithology and ROP data, as well as methane and ethane occurrences monitored by the driller and a service company in the sedimentary part of the well. The caliper and GR data were collected between the surface and the top of the basement. The caliper was a

two-orthogonal-arms tool with two measurements, CAL1 and CAL2. The nominal diameter between 890- and 1,280-m depth was 17.50 inches.

As was the case for GPK-2 and GPK-3, it was possible to correlate zone Z2 in GPK-4 due to the mud loss data. Zones Z4, Z6, and Z9 are thought to be present due to significant variation in at least two well logging data sets (Figure 6.15).

Zone Z1 is not visible in GPK-4.

Zone Z2 is a complex structure with several peaks visible between 945- and 957-m depth in the ROP data (124.86 m/h at 954-m depth) and caliper data (21.91 inches on CAL2 at 952-m depth). Zone Z2 is permeable because 4 m^3/h losses were recorded between 956-m and 1,012-m depth. The clear shift to 80.30 gAPI in the GR curve from 948- to 955-m depth is also a permeability indication. Z2 is a complex permeable fracture zone.

Zone Z3 is not visible in GPK-4.

In zone Z4, caliper readings show a moderate variation to 18.87 inches at 1,069-m depth, the outflow data feature a strong negative anomaly with a total loss at 1,069-m depth. At 1,066-m depth, the ROP value reaches 43.17 m/h, even when the WOB is reduced to 5.30 tons at the same depth. At a depth of 1,065 m, mud outflow becomes zero, suggesting a loss of mud in a permeable structure, but this information is of uncertain value because the mud inflow data are missing. Gas contents increase to 72.13 ppm for methane and to 11.12 ppm for ethane, both at 1,069-m depth. However, it is rather difficult to attribute this gas content increase to fracture permeability and not to matrix permeability. Z4 is therefore classified as a partly sealed fracture.

Zone Z5 is not visible on GPK-4.

Zone Z6 is characterized by several anomalies between 1,138- and 1,155-m depth. These anomalies affect the caliper data (18.69 inches for CAL2 at 1,141-m depth) and ROP data (18.99 m/h at 1,147-m depth). The temperature data also display large variations in the same depth section. Zone Z6 is a complex sealed fracture zone.

Zone Z7 is not noticeable on GPK-4.

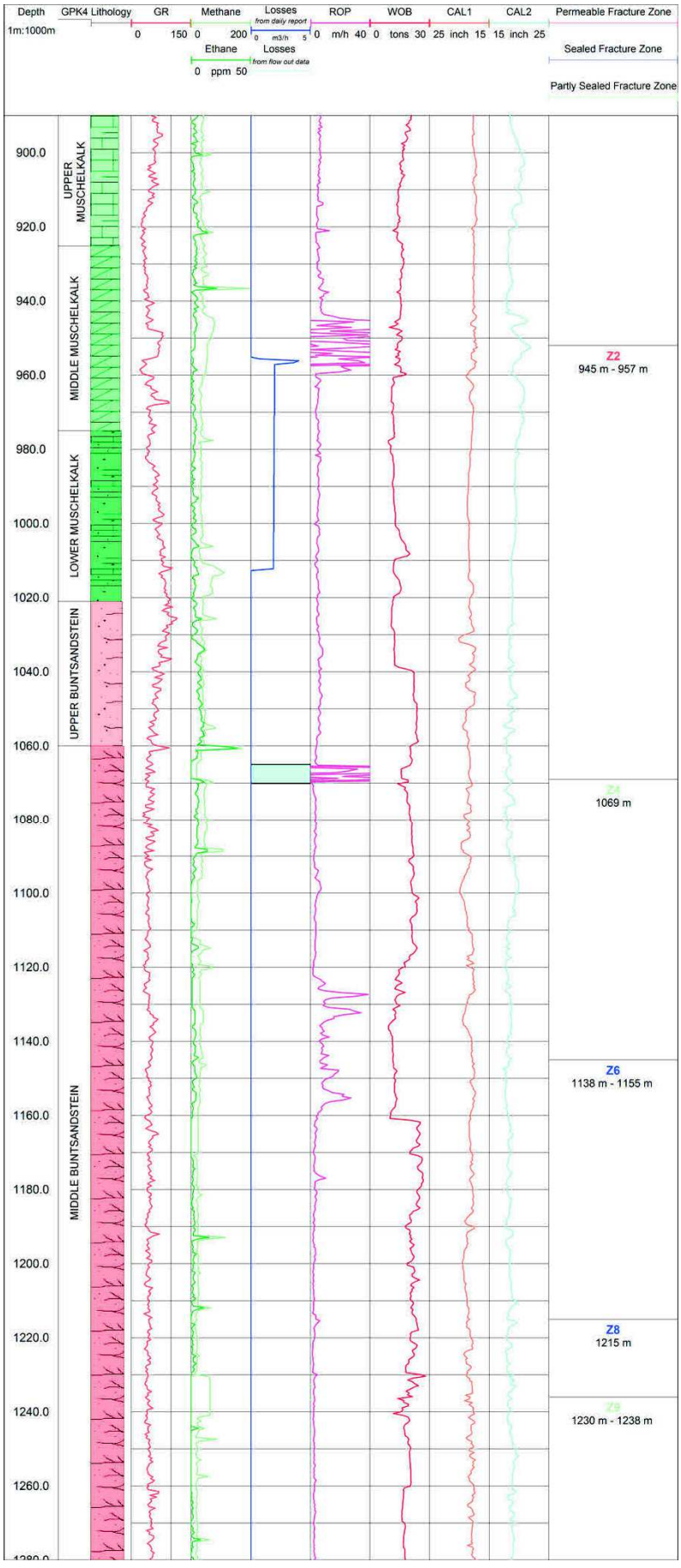
Depth
1m:1000m
GPK4 Lithology
GR
0 150
Methane
0 200
Ethane
0 ppm 50
Losses
from daily report
0 m3/h 5
Losses
from flow out data
ROP
0 m/h 40
WOB
0 tons 30
CAL1
25 inch 15
CAL2
15 inch 25
Permeable Fracture Zone
Sealed Fracture Zone
Partly Sealed Fracture Zone
UPPER MUSCHELKALK
MIDDLE MUSCHELKALK
LOWER MUSCHELKALK
UPPER BUNTSANDSTEIN
MIDDLE BUNTSANDSTEIN
900.0
920.0
940.0
960.0
980.0
1000.0
1020.0
1040.0
1060.0
1080.0
1100.0
1120.0
1140.0
1160.0
1180.0
1200.0
1220.0
1240.0
1260.0
Z2
945 m - 957 m
Z4
1069 m
Z6
1138 m - 1155 m
Z8
1215 m
Z9
1230 m - 1238 m

Figure 6.15 (previous page) Synthetic log of GPK-4. The synthetic log shows mud losses from daily report (dark blue curve) and from outflow data (light blue section), GR, occurrences of gas (methane and ethane), ROP, and caliper (CAL1 and CAL2) data. The lithology is the same as GPK-2. Fracture zones are indicated: Z2, Z4, Z6, Z8, and Z9. Permeable zones are in red, partly sealed zones are in green and sealed zones are in blue. Depths are expressed in measured depth.

Zone Z8 is apparent at 1,215-m depth with a CAL2 value of 19.66 inches and a positive ROP anomaly of 6.37 m/h at the same depth. Because there are no significant variations in the mud logging, Z8 is interpreted as a sealed, localized fracture.

Zone Z9 features a slight caliper enlargement between 1,230- and 1,238-m depth, with a maximum of 19.47 inches for CAL2 at 1,233-m depth. The ROP is abnormally flat in this depth range. The methane curve exhibits a large jump of 100 ppm, suggesting some permeability. Zone Z9 is a partly sealed fracture zone.

Well GPK-1

For GPK-1, the lithology is slightly different from that for GPK-2, GPK-3, and GPK-4 because its wellhead is located approximately 450 m to the North of the deeper triplet (Figure 6.11). The correlation of fracture zones between GPK-1 and the other geothermal wells is not possible in this 1D study; thus, the labeling of fracture zones is different for GPK-1. Mud logging data are composed of descriptions of cuttings composition, spot coring samples, variations in mud temperature, and ROP. The mud logging data are indicated on the master log but are not available in digital format. A temperature log was measured in the well but not under thermal equilibrium conditions, as was the case in GPK-2, GPK-3, and GPK-4. Because this thermal profile is plotted in its own depth reference framework, there is a depth matching shift of +2 m between the thermal profile and the other well log curves (Figure 6.16). The wireline logging data collected in the sedimentary part of GPK-1 are GR, bulk density, neutron porosity. The caliper was a two-orthogonal-arm tools with two measurements, CAL1 and CAL2. The nominal diameter for this depth section was 12.25 inches.

Six fracture zones were observed in the sedimentary part of GPK-1 between 740- and 1,300-m depth (Figure 6.16).

Only zone F7 featured mud losses. The existence and locations of zones F1 to F6 were deduced from the presence of variations in at least two well log parameters. Zone F1 presents a clear negative thermal anomaly of −3°C at 750 m, which correlates with a cave only visible on CAL1 between 747- and 754-m depth and with an increase in the ROP. This zone is the only fracture zone with a sharp caliper variation. Deeper in the sedimentary cover, the caliper curves are smooth, and it is rather difficult to observe peaks associated with fracture zones. Zone F1 is a partly sealed fracture zone located in the Upper Keuper formation, which is composed of fine, colored clays in the uppermost part and fine-grained sandstones at the base.

A small temperature anomaly is visible at 981-m depth, which correlates with a small anomaly in the density log. The size of this anomaly is too small to assume that a fracture zone is present.

Zone F2 is characterized by a small negative temperature variation (−1°C) at a depth of 1,003 m, which matches the depth of a weak caliper variation for both CAL1 (11.12 inches) and CAL2 (12.84 inches). The GR data include a peak of 99.37 gAPI over a 2-m-thick zone at 1,003-m depth. At the same depth, the neutron porosity reaches 20.50%, and bulk density decreases to 2.53 g/cm^3. F2 is a single, partly sealed fracture.

Between 1,042- and 1,049-m depth, several caliper peaks are visible for CAL1 (12.97 inches at 1,048 m) and CAL2 (12.82 inches, also at 1,048 m). These peaks match the depths of variations in the neutron porosity (28.67% at 1,048 m) and bulk density variation (1.65 g/cm^3 also at 1,048 m). At 1,046-m depth, the thermal profile obtained after drilling features a cooled zone (−1.00°C) due to mud invasion. F3 is a complex, partly sealed fracture zone.

In zone F4, a cave occurrence is clearly visible in the CAL2 data, 13.93 inches at 1,107-m depth, which is associated with a temperature variation of −2°C at 1,105 m. There is no indication of permeability; thus, F4 is a single, partly sealed fracture.

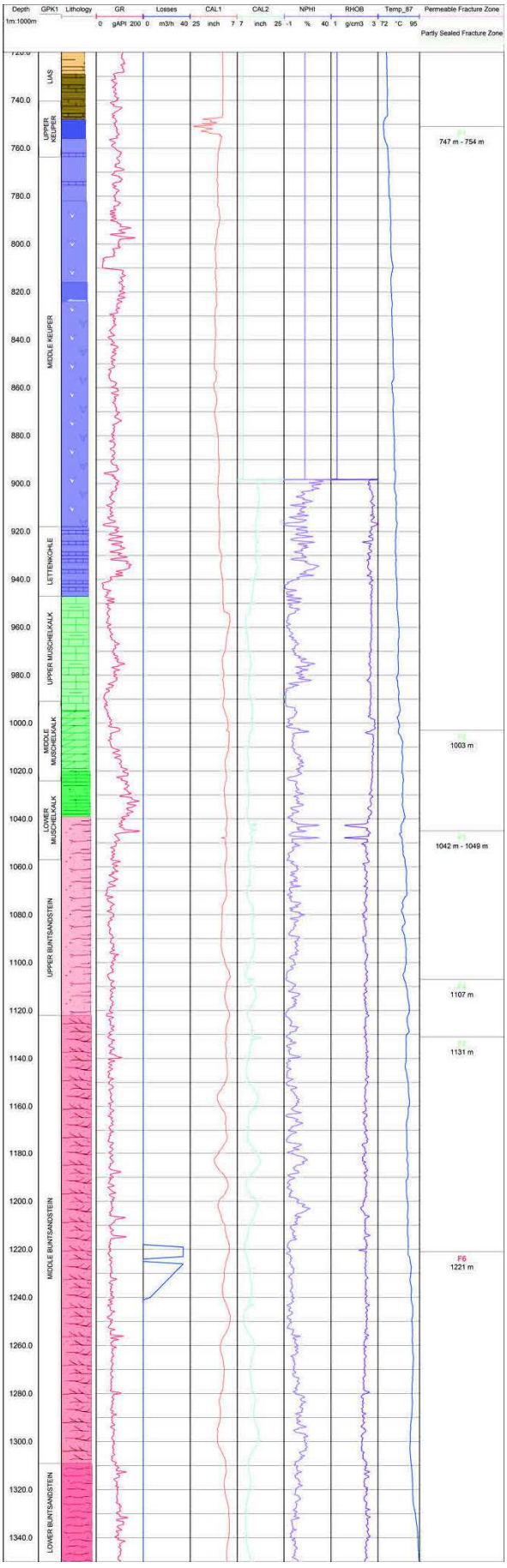
Depth
1m:1000m
GPK1
Lithology
GR
0 gAPI 200
Losses
0 m3/h 40
CAL1
25 inch 7
CAL2
7 inch 25
NPHI
-1 % 40
RHOB
1 g/cm3 3
Temp_87
72 °C 95
Permeable Fracture Zone
Partly Sealed Fracture Zone
LIAS
UPPER KEUPER
MIDDLE KEUPER
LETTENKOHLE
UPPER MUSCHELKALK
MIDDLE MUSCHELKALK
LOWER MUSCHELKALK
UPPER BUNTSANDSTEIN
MIDDLE BUNTSANDSTEIN
LOWER BUNTSANDSTEIN
740.0
760.0
780.0
800.0
820.0
840.0
860.0
880.0
900.0
920.0
940.0
960.0
980.0
1000.0
1020.0
1040.0
1060.0
1080.0
1100.0
1120.0
1140.0
1160.0
1180.0
1200.0
1220.0
1240.0
1260.0
1280.0
1300.0
1320.0
1340.0
747 m - 754 m
1003 m
1042 m - 1049 m
1107 m
1131 m
F6
1221 m

Figure 6.16 (previous page) Synthetic log of GPK-1. The synthetic log shows lithology, mud losses, GR, neutron porosity (NPHI), bulk density (RHOB), calipers (CAL1 and CAL2), and temperature data (Temp87). Fracture zones are indicated: F1 to F6. Permeable zones are in red and partly sealed zones are in green. Depths are expressed in measured depth.

Zone F5 is visible on both calipers at 1,131-m depth, where a small variation in CAL1 (11.49 inches) and a strong variation in CAL2 (16.34 inches) are associated with a positive anomaly of +1°C on the thermal profile at 1,129-m depth. Similar to F4, there is no mud logging variation, and F5 is a single, partly sealed fracture.

Mud loss was total at 1,221-m depth and decreased slowly with increasing depth. The ROP shows several positive peaks, but caliper variations are not clearly visible. After drilling operations, the thermal profile reveals small variations. Zone F6 is a single permeable fracture.

Well EPS-1

For older oil wells, the interpretation of mud logging and geophysical logs is much more challenging because the drilling data are not always available. However, the continuous coring of EPS-1, in particular for the interval from 930- to 1,417-m depth, provides a direct view of the natural fractures in the sedimentary part. Based on the continuous core survey in the Buntsandstein formations, a structural analysis of the fracture network has been performed. Fracture location, typology, nature of hydrothermal filling, and the fracture thickness data sets were collected [*Vernoux et al.*, 1995; *Genter et al.*, 1997b]. The longest naturally fractured zone is located between 1,170- and 1,215-m depth and is characterized by euhedral barite, galena, pyrite, and geodic quartz. The location of this zone matches perfectly with mud losses observed from the drilling survey [*Degouy et al.*, 1992]. Partial mud losses were observed at approximately 1,204-m depth in EPS-1 in the Intermediate Buntsandstein formations. At the same depth, borehole image logs indicate that the orientation of this main permeable fracture strikes N-S and dips westward (Figure 6.17). The core sample indicates that barite and galena have filled the fracture zone (Figure 6.12) [*Genter et al.*, 1997b].

The thermal profile available in the sedimentary part of EPS-1 has been obtained from within the casing. The thermal gradient presents the same trend as in the other Soultz wells. In the uppermost part, it is on the order of 100°C/km, revealing a conduction regime. Below 1 km, it decreases to 5°C/km. However, in this convection dominated part, there is no impact of the fracture zone at 1,204-m depth behind the casing or any other perturbations related to the geological formations.

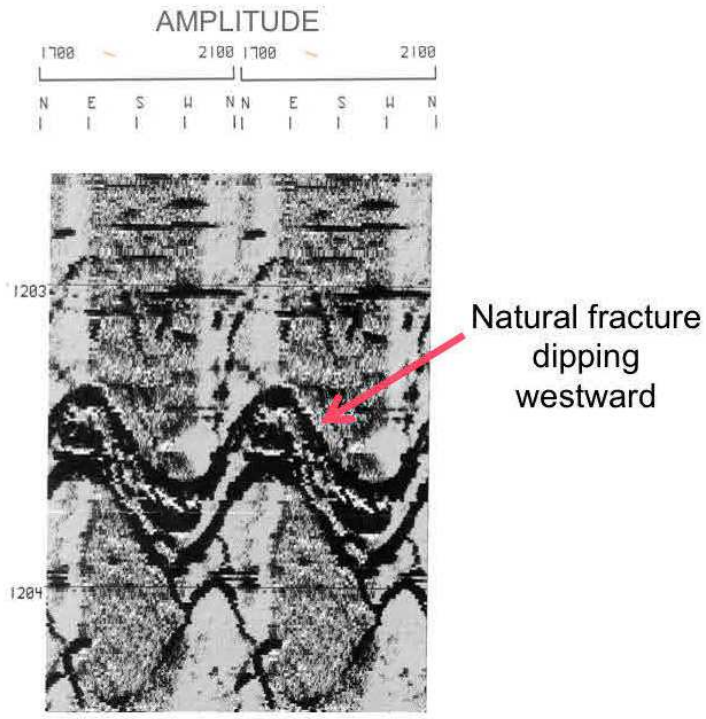

Figure 6.17 Detailed BHTV image at 1,204-m depth in the well EPS-1. The BHTV shows a fracture oriented N-S and dipping westward (data from DMT-Institute for Geophysics, Germany).

Well 4550

For the seismic well 4550, a BHTV log was the only geophysical well log available to correlate with mud losses recorded by the driller. A total loss was recorded at 1,280-m depth in the Intermediate Buntsandstein. A fracture zone, dipping westward and composed of a conjugate fracture system, is clearly visible on the BHTV log, as well as on a caliper log with the occurrences of well enlargement (caving) (Figure 6.18) [*Dezayes et al.*, 2010a]. This fracture zone could have been produced by artesian flow of approximately 30 m^3/h at 125°C

with a natural productivity approximately 30 L/s/bar [*Degouy et al.*, 1992]. The thermal profile in the 4550 well shows an upper part dominated by conduction with a thermal gradient of 105°C/km. Below the depth of 800 m, the thermal gradient decreases to 30°C/km, corresponding to a convective regime. At 1,280-m depth, the occurrence of a sharp negative thermal anomaly is clearly visible and fits with the permeable fracture zone location (Figure 6.19).

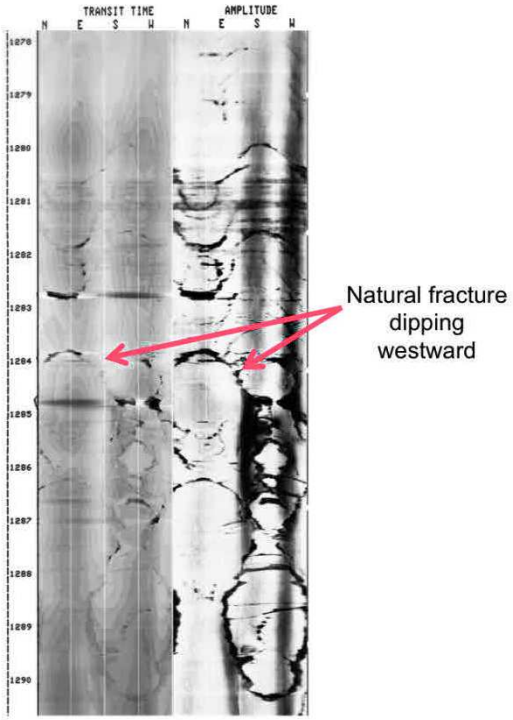

Figure 6.18 Detailed BHTV image at 1,280-m depth in the well 4550. The BHTV shows a conjugate fracture system with a major structure dipping westward (data from GEIE EMC, France).

Sausse et al. (2010) analyzed the same fracture zones in the sedimentary cover for the wells GPK-1, EPS-1, and 4550 but only from a geometrical point of view. Their locations in the different wells are roughly located at the same depth.

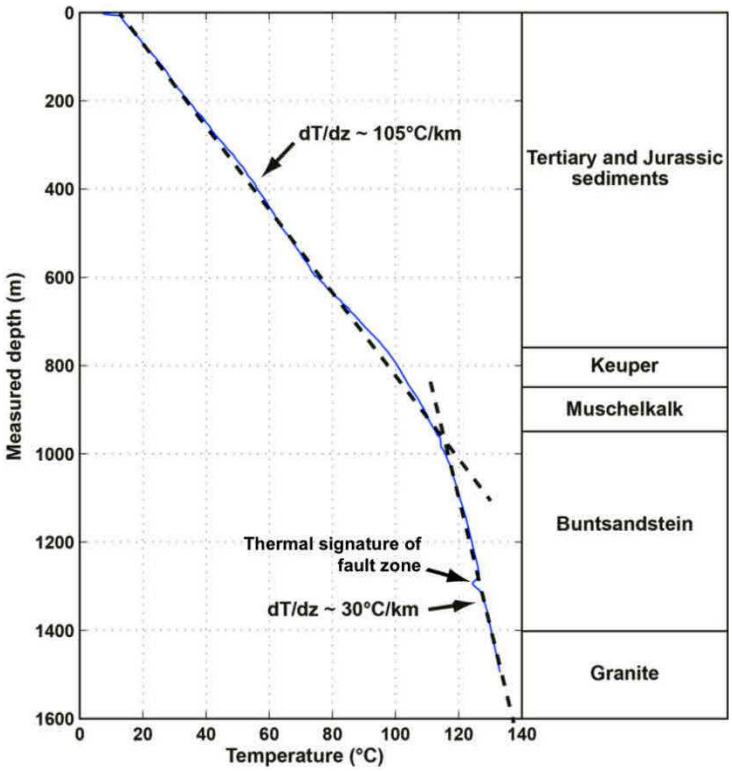

Figure 6.19 Equilibrium temperature profile from 0- to 1,500-m depth in the well 4550. The equilibrium temperature profile was obtained several months after drilling operation was finished (data from LIAG-Hannover, Germany).

6.3.5.2 Correlation of permeability between the wells

Fracture zone correlation between the Soultz wells has already been investigated but only in the granitic basement [*Valley*, 2007; *Sausse et al.*, 2010]. By using various geometric correlation methods, *Valley* [*Valley*, 2007] demonstrated that the extrapolation of a given fracture zone visible in one well is rather difficult to identify in a second spatially close well. In this study, the authors made spatial correlations of fracture zone permeability in the sedimentary part of the geothermal boreholes GPK-2, GPK-3, and GPK-4. In total, nine fracture zones have been identified with and without permeability indications (Table 6.2). Two zones have been located in the Muschelkalk formations with indications of permeability (Figure 6.20). These two zones represent a complex structure with an apparent thickness between 5 and 20 m (Figure 6.13, Figure 6.14 and Figure 6.15). They are composed of many individual fractures that are partly filled with hydrothermal deposits.

Table 6.2 Permeability properties of fracture zones detected in the Muschelkalk and Buntsandstein formations

	GPK-2	GPK-3	GPK-4
	Muschelkalk		
Z1	Permeable	Permeable	
Z2	Permeable	Permeable	Permeable
Z3	Sealed		
	Buntsandstein		
Z4		Sealed	Partly Sealed
Z5	Sealed		
Z6	Sealed	Sealed	Sealed
Z7	Sealed		Permeable
Z8	Sealed	Sealed	Sealed
Z9	Permeable	Permeable	Partly Sealed

Zone Z1 intercepts GPK-2 and GPK-3, whereas zone Z2 crosses all three wells. As image logs have not been acquired in the Muschelkalk, it is rather difficult to derive a 3D organization of those thick structures visible at the same depth in closely spaced vertical boreholes.

Seven fracture zones have been interpreted in the Buntsandstein formations. Four zones do not show clear permeability indications (Z3, Z5, Z6, and Z8), whereas Z9 is a complex permeable fracture zone observed in three wells with evidence of natural outflow in GPK-2 and GPK-3. Zone Z4 is permeable only in GPK-3 and zone Z7 is permeable in GPK-3 and GPK-4. Sealed fracture zones correspond to both single fractures (Z3, Z4, and Z7) and complex structures (Z5, Z6, and Z8). Zone Z6 is the only sealed fracture zone that intercepts all three wells (Figure 6.20). All other sealed fracture zones in the Buntsandstein are visible in two wells, with the exception of Z5, which is only visible in GPK-2.

Fracture zones derived from mud logging and geophysical data in the Muschelkalk and Buntsandstein are not observed in the thermal profile obtained under thermal equilibrium conditions (Figure 6.10).

Six fracture zones have been outlined in GPK-1: in the Upper Keuper (F1), in the Muschelkalk (F2) and in the Buntsandstein (F3 to F6). All of them are associated with thermal variations, but only F6 correlates with mud losses (Figure 6.16).

In EPS-1, only one complex fracture zone (at a depth of 1,204 m) correlates with mud losses.

In Buntsandstein formations, the complex permeable fracture zone Z9, visible in GPK-2, GPK-3, and GPK-4, could be correlated with zone F6 in GPK-1 and the permeable zone in EPS-1 (Figure 6.20). This fracture zone could fit with a branch of the Soultz fault visible at the local scale (Figure 6.9).

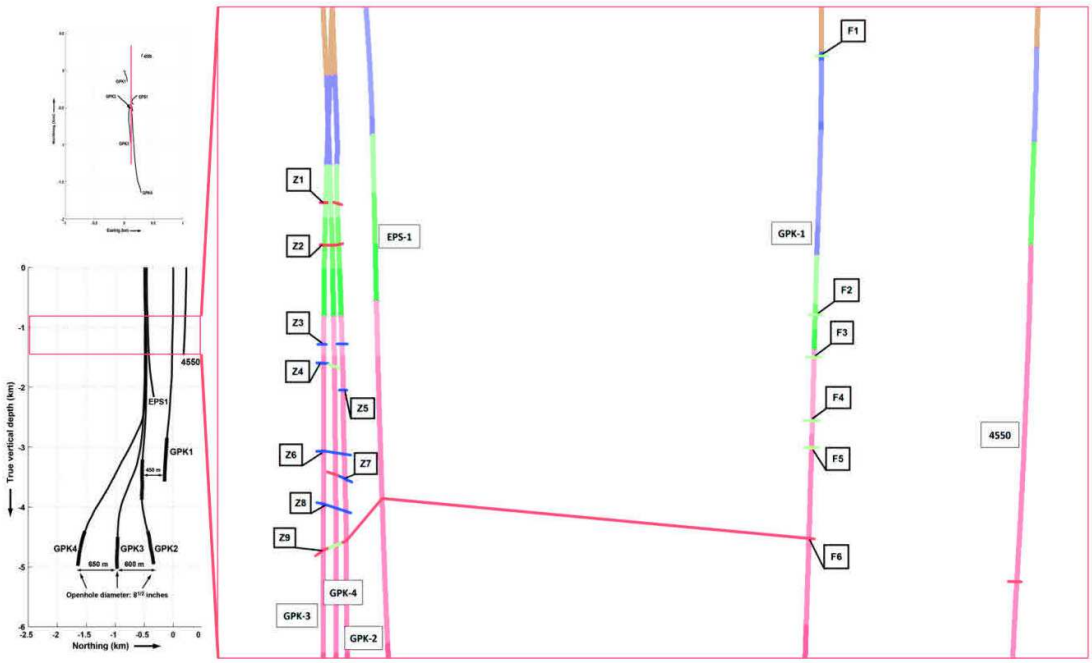

Figure 6.20 North-South cross section through the Soultz site showing the fracture zones in the Soultz wells. Fracture zones are located on GPK-1 (F1 to F6), GPK-2, GPK-3, GPK-4 (Z1 to Z9), EPS-1, and 4550. Permeable zones are in red, partly sealed zones are in green and sealed zones are in blue. Vertical and horizontal scales are 1/5000.

6.3.5.3 Interpretation of thermal profile and convective cells

Under thermal equilibrium conditions, a conduction regime is dominant in the Tertiary, Jurassic, and the top of the Triassic sedimentary formations (0- to 800-m depth). Within the deepest Mesozoic sedimentary formations (Muschelkalk and Buntsandstein) and in the top of the granitic basement, the heat transport process is dominated by convection. The depth section 880 to 1,000 m, i.e., the base of the Muschelkalk and the top of Buntsandstein, contains permeable fracture zones and corresponds to a transition from a conduction to a convective

thermal regime. This indication suggests that this zone is the top of the convective cells and that fluids cannot move upward within the fractures located above the Muschelkalk formations. The horizontal bounding layer at the top of the convective cells could correlate with the Keuper formation (Upper Triassic). Convection arises in the granitic section.

Based on various borehole data sets, we propose a conceptual model of the convective cell structure at the sediment-basement interface (Figure 6.21). Fracture zones in the Muschelkalk and in the Buntsandstein have been highlighted in GPK-2, GPK-3, and GPK-4 at Soultz. Above these formations, i.e., between the Tertiary formations and the lower part of the Upper Triassic (Keuper), there is no obvious evidence of permeable or sealed fractures from the mud logging and well logging data except in GPK-1, where two permeable fracture zones were found in the Keuper formation. Below the Triassic formations, in the granitic basement, the permeable or sealed fracture zones are widely documented. Natural permeability in the granite is related to hydrothermally altered fracture zones. This permeability is evidenced by brine occurrences (the formation fluid has 100 g/L of dissolved solids) [*Vuataz et al.*, 1990]. The highest drilling mud losses have been observed in the granitic basement and are clearly related to fracture zones [*Evans et al.*, 2005a; *Dezayes et al.*, 2010b]. This fracture network controls the convection, especially between 1,400- and 3,500-m depth in the granite (Figure 6.10). At the scale of the Soultz site, the lower part of the convective cells initiates at approximately 3.5-km depth in the fractured and altered granite at 160°C. Hydrothermal fluids percolate through the sub-vertical fault system. During its ascent, the formation fluids precipitate minerals, primarily quartz and carbonates and more locally sulfates and sulfides (Figure 6.21). Based on a fluid inclusion study of quartz and carbonate veins, *Dubois et al.* [*Dubois et al.*, 2000] demonstrated that the minerals precipitated in the same temperature-pressure range and under conditions similar to the present day conditions. This study shows that the ascending fluids are recent and sealed the fracture system. Due to the structural history of this area, the fracture system is also well developed in the sedimentary pile overlying the granite, including small-scale fractures and large-scale faults. For example, at the seismic scale, steeply dipping normal faults intersect both the

granitic basement and its sedimentary cover (Figure 6.9). During its ascent and after passing out of the crystalline basement, hydrothermal fluids could circulate in fractures in the Lower Triassic sandstones (Buntsandstein) and then in the Middle Triassic limestones (Muschelkalk). In the sandstones, similar hydrothermal mineral assemblages precipitated and partly plugged the vertical fracture system [*Vernoux et al.*, 1995]. In those layers, the temperature is lower, decreasing from 140°C to 90°C in the section ranging from 1,400- to 1,000-m depth. In the limestones, the main hydrothermal deposits are anhydrite and carbonates (Figure 6.21). The Upper Triassic formation (Keuper) is the shallowest sedimentary fractured layer with permeability indicators. The vertical fluid circulation could transition towards a horizontal circulation under the Tertiary and the Jurassic sediments. This interface could govern the top of the convection cells, and it is characterized by lateral flow and most likely temperature decreases. The heat carried by the hydrothermal fluid is most likely dissipated vertically to the overlying sediments. It generates the conductive section with the high geothermal gradient of 110°C/km. At the top of the permeable reservoir, fluids must flow out laterally and may descend again in the natural fracture system from the Triassic sediments to the granitic basement, due to their increasing density upon cooling. Occurrences of organic matter inside the deep fractured and altered granitic zone demonstrate communication with the sediments [*Ledésert et al.*, 1996]. This convective cell structure indicates ancient and recent fluid circulation across the sediment-basement interface. This conceptual model does not take into account time and size constraints, but hydrothermal circulation is clearly at the root of the geothermal anomaly.

Various borehole data collected in the Soultz wells outline permeable fractures in both the sediments and the basement. During the fluid's ascent, the temperature decreases; consequently, the high salinity fluid precipitates minerals. Therefore, permeability decreases vertically, whereas the fracture sealing increases. Thus, the top of the convective cells could fit with reduced permeability in the brittle sedimentary layers. The top boundary layers made of late Jurassic and Tertiary sedimentary deposits have a low permeability and a low thermal conductivity due to occurrences of clay-rich formations.

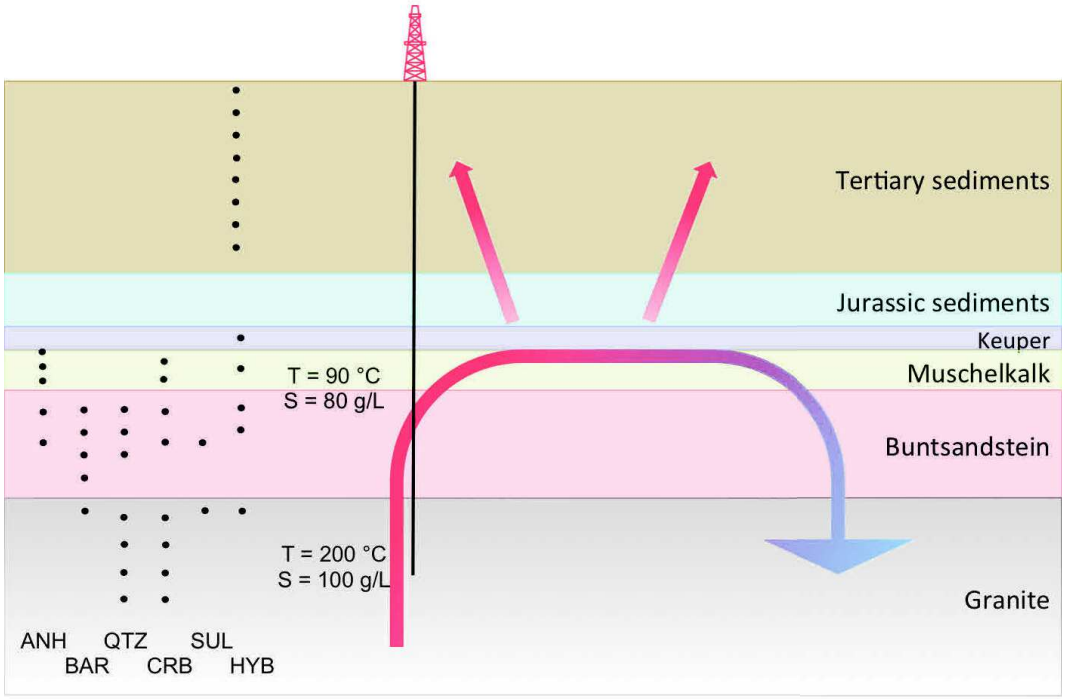

Figure 6.21 Schematic section through the convective cells in the sedimentary and granitic reservoirs. Geothermal fluid circulations are controlled by the fracture network in the Muschelkalk, Buntsandstein, and crystalline basement. During circulation, secondary mineral deposits occur in the fractures (ANH=Anhydrite, QTZ=Quartz, SUL=Sulfides, BAR=barite, CRB=Carbonates). On the sketch, the black dots indicate the vertical evolution of hydrothermal minerals. The uppermost part of the sedimentary cover remains largely conductive and insulates the convective system below. Hydrocarbons (HYB) are mostly located in the Triassic sediments. Temperature values and the salinity of the brine are from the Soultz geothermal wells.

This cap rock, which consists of the uppermost sedimentary section down to the depth of 800 m insulates the more brittle underlying formations and underlines the contrast of the mechanical properties of the two units. In the soft sediments of the cap rock, brittle deformation is rather limited and faults do not exhibit permeability. In the brittle formations below a depth of approximately 1 km, natural fractures are developed over geological time, allowing circulation of hydrothermal fluids (permeability) and deposition of secondary minerals (sealing).

The competition between the natural permeability and the mineral deposition characterizes the fractures located at the top of the convective cells.

6.3.6 Conclusions

The combined analysis of mud logging and well logging data from the sedimentary cover of several geothermal wells at the Soultz site in the URG reveals the presence of fracture zones in the Triassic sedimentary formations. These fracture zones are made of individual or complex structures. The complex structures most likely represent faulted zones crosscutting the deepest sediments of the Tertiary basin. Based on mud loss occurrences, it has been shown that fracture permeability is associated mainly with complex fracture zones located in the Middle Muschelkalk limestones and Middle Buntsandstein sandstones. At the borehole scale, many fracture zones are sealed due to the occurrence of secondary precipitated mineral, which most likely reduce the permeability.

The natural permeability in the sub-vertical fracture zone reveals the geothermal fluid pathways. A schematic conceptual model of the top of a convective cell has been proposed : hot natural fluids move upward under buoyancy from the top of the crystalline basement into the Triassic sediments and then migrate laterally before circulating downward. The top of the convection is characterized by reduced permeability due to partial hydrothermal seals. There, complex permeable fracture zones are most likely connected to large-scale faults and small-scale fracture networks at the sedimentbasement interface and control the top of the thermal convection loop.

Authors' contributions

JV and AG did the data analysis, comparison, and interpretation. JV, AG, and JS contributed to the conceptual model. All the authors read and approved the final manuscript.

6.3.7 Acknowledgements

A part of this work was conducted in the framework of the Labex G-Eau-Thermie Profonde, which is co-funded by the French government under the program 'Investissements d'Avenir'. The manuscript was performed as a contribution to the PhD thesis of Jeanne Vidal co-founded by ADEME (French Agency for

Environment and Energy). The authors acknowledge the GEIE EMC and the LIAG for providing Soultz boreholes data and Dr. Nicolas Cuenot and Dr. Thomas Koelbel for support. Finally, the authors would like to kindly thank Robert Hopkirk for his full check of the English language and the anonymous reviewers for their contributions and manuscript improvement.

7 Signature thermique des zones de fractures perméables

7.1 Résumé

Ce chapitre s'appuie sur les données de diagraphies instantanées et différées dans les sections en trou ouvert des puits GRT-1 et GRT-2. L'objectif est d'évaluer la structure du réseau de fractures majeur qui chenalise les circulations à l'échelle du puits. Il se décompose en deux parties.

La première partie du chapitre s'appuie sur un résumé étendu présenté à la conférence European Geothermal Congress 2016 à Strasbourg. Il est disponible sous la référence : Vidal J., Genter A., Chopin F., Dalmais E. (2016). Natural fractures and permeability at the geothermal site Rittershoffen, France, *European Geothermal Congress*, September 19 - 26 2016, Strasbourg, France. Les calculs d'espacement entre les fractures (section 7.2.5.4) ont été ajoutés au manuscrit de thèse mais ne figurent pas dans le résumé étendu initial.

Le réseau de fractures majeur a été observé à partir des imageries de paroi acoustiques dans les sections en trou ouvert de GRT-1 et GRT-2. Seules les fractures continues sur les imageries ont été prises en compte car elles chenalisent la majorité des circulations et contrôlent la perméabilité du premier ordre des puits. Si une fracture continue a une épaisseur acoustique de 1 cm ou plus, elle est qualifiée de majeure, sinon elle est qualifiée de mineure. Le relevé structural détaillé est consultable en Annexe 2. Dans le puits GRT-1 ; les fractures sont orientées principalement N15°E à N20°E avec un pendage de 80°W. Dans le puits GRT-2, la famille principale est orientée N155°E à N175°E avec un pendage de 80°E à 90°E dans les grès. La famille conjuguée présente un pendage de 50°E à 60°E. Dans le puits GRT-1, les fractures sont orientées principalement N-S +/-10°E avec un pendage de 60°W dans le granite. Dans le puits GRT-2, l'orientation des fractures principale est identique mais les familles de fractures sont plus dispersées. La densité de fractures est maximale au toit du socle granitique. Ces fractures sont principalement orientées selon la direction Rhénane comme dans les puits de Soultz. Elles correspondent à des failles

normales d'héritage varisque réactivée sous la compression pyrénéenne à l'Eocène [*Villemin and Bergerat*, 1987]. A l'échelle du puits, seules 1% des fractures sont perméables dans le puits GRT-1 et 5% dans le puits GRT-2. La différence de perméabilité entre ces deux puits sera le sujet d'étude de la seconde partie de ce chapitre.

La seconde partie de ce chapitre est présentée sous forme d'article accepté dans la revue Journal of Geophysical Research sous la référence : Vidal J., Genter A. and Chopin F. (2017). Permeable fracture zones in the hard rocks of the geothermal reservoir at Rittershoffen, France, *J. Geophys. Res*. *Solid Earth*, *122*, doi: 10.1002/2017JB014331.

Cet article se concentre sur les zones de fractures qui chenalisent les circulations de fluide dans le réservoir géothermal. La faille locale de Rittershoffen, identifiée comme le siège de circulations hydrothermales, est la cible du projet. Cette faille normale est orientée N-S avec un pendage de 60°W. L'intersection entre la trajectoire des puits et le réseau de fractures naturelle associé à la faille de Rittershoffen a été évalué d'après les imageries de paroi acoustiques corrélées aux diagraphies différées standard (profil de température, gamma ray, porosité neutron et caliper) et aux diagraphies instantanées (cuttings, pertes de boue et venues de gaz). La structure interne des zones de fractures (ouverture des fractures et halos d'altération) est observée à partir des imageries de paroi acoustiques, du caliper lorsque ces dernières ne sont pas disponibles, du gamma ray et de la porosité neutron. Si cette zone de fractures est associée à une anomalie de température sur le profil, à des pertes de boue ou à une venue de gaz, elle est qualifiée de perméable à l'échelle du puits. La typologie Originally Permeable (OP) pour une zone de fractures lorsque les indices de perméabilité sont observés après les opérations de forage, introduite dans l'article présenté dans la section 5.6.2, est conservée dans ce chapitre. Les zones de fractures qualifiées Newly Permeable (NP) lorsque la perméabilité n'est observée qu'après les opérations de stimulations ne sont pas traitées dans cette article.

Dans le puits GRT-1, une zone de fractures OP est observée à la base du granite altéré. Dans le puits GRT-2, quatre zones de fractures OP sont observées dans le granite altéré et deux dans les grès triasiques et permiens. Elles sont toutes

associées à des anomalies de températures positives ou négatives. Dans la littérature, les anomalies de températures négatives sont interprétées comme le refroidissement des zones poreuses suite aux invasions de boue durant le forage et aux injections hydrauliques massives durant les stimulations [*Barton et al.*, 1995; *Davatzes and Hickman*, 2005a; *Genter et al.*, 2010; *Bradford et al.*, 2013]. Plusieurs mois après le forage, ces zones sont toujours associées à des anomalies négatives. Les anomalies de températures positives sont interprétées comme des venues de fluide géothermal chaud. Elles n'avaient pas été observées dans les autres puits du Fossé rhénan (section 6.2). L'orientation et le pendage des fractures perméables ne semblent pas en lien avec la polarité de l'anomalie de température. La représentation géométrique des zones de fractures à l'échelle du puits apporte une première visualisation 3D des zones de fractures le long des puits et suggère des circulations hydrothermales complexes. Le puits GRT-1 montre un contrôle mono-structure de ces circulations dans la zone de fractures principale à la base du granite altéré. Elle est composée d'une fracture ouverte de 24 cm d'épaisseur acoustique à 2368 m Measured Depth (MD) (i.e. 2352 m True Vertical Depth (TVD)). Elle est orientée N170°E avec un pendage 55°W et est associée à une large anomalie de température négative et des pertes de boue. Elle marque la base d'une zone altérée et poreuse de 40 m d'épaisseur. Le puits GRT-2 montre un contrôle pluri-structure des circulations. La zone de fractures principale est localisée dans le granite altéré également. Elle est composée d'une fracture ouverte de 17 cm d'épaisseur acoustique à 2774 m MD (i.e. 2393 m TVD). Elle est orientée N170°E avec un pendage 65°W et est associée à une double anomalie de température positive-négative et des pertes de boue. Elle marque le toit d'une zone altérée et poreuse de 35 m d'épaisseur. Cette asymétrie dans l'organisation de la perméabilité au sein des zones de fractures n'était pas observée dans les puits de Soultz.

La perméabilité du puits GRT-2 est bien supérieure à celle de GRT-1. Les deux fractures perméables principales présentent des orientations et des pendages similaires à ceux de la faille de Rittershoffen. Contrairement aux observations faites dans les puits de Soultz [*Valley and Evans*, 2007], l'étude des fractures induites en tensions dans le granite du puits GRT-1 ne montre pas d'hétérogénéité de la contrainte horizontale maximale autour de la fracture

perméable majeure [*Hehn et al.*, 2016]. La contrainte horizontale maximale est orientée N150°E à N170°E dans le granite profond d'après les mesures de fractures induites en tension [*Hehn et al.*, 2016]. La perméabilité de ces fractures semble être influencée par la quantité et la nature des dépôts secondaires. La cristallisation incomplète des remplissages secondaires au cœur des fractures perméables crée des chenaux résiduels de perméabilité. Les fractures perméables sont associées à des veines de quartz visibles sur les imageries de paroi acoustiques. Autour de ces fractures, les zones altérées et poreuses semblent être très argilisées. Cette hypothèse sera développée dans le chapitre suivant avec l'étude pétro-minéralogique des cuttings (chapitre 8). La trajectoire très inclinée du puits GRT-2 pourraient également augmenter les connexions entre le puits et le réseau de fracture vertical associé à la faille de Rittershoffen. La zone de fractures perméables principale dans le puits GRT-2 est composée de plusieurs fractures ouvertes aux orientations sécantes qui pourraient favoriser les circulations au sein de la zone. Cependant, l'extension des fractures est difficilement appréciable et le domaine inter-puits n'est pas imagé. Les relations entre les fractures à l'échelle du puits et les structures de plus grandes échelles seront discutées dans la troisième partie de la thèse.

La caractérisation hydraulique et thermique des deux puits est détaillée dans l'article consultable dans l'Annexe 3. L'étude du champ de contrainte à partir des fractures induites en tension est détaillée dans le résumé étendu consultable dans l'Annexe 4.

7.2 Structure des fractures naturelles dans les puits de Rittershoffen

7.2.1 Abstract

A geothermal doublet was drilled at Rittershoffen (Alsace, France) in order to exploit the local geothermal anomaly. Geothermal resource is trapped into fracture network at the sediments-basement interface. Acoustic image logs were analyzed in open-hole section of the wells GRT-1 and GRT-2 and correlated with permeability indication such as temperature anomalies and/or mud losses during drilling operations. The main fracture orientation in GRT-1 is N10°E to N20°E dipping westward. In GRT-2, the main fracture orientation is N160°E to N-S dipping eastward or westward. Less than 5% of fractures present natural permeable indication at borehole scale. Permeable fracture zones present complex cluster indication with major permeable drains surrounded by damage zone.

Keywords: Natural fractures and faults, permeability, downhole logging methods, acoustic image logs, Enhanced Geothermal System, Rhine Graben, Rittershoffen.

7.2.2 Introduction

The Upper Rhine Graben (URG) is characterized by several local thermal anomalies associated to hydrothermal convective cells circulating inside a nearly vertical fracture network in the granite basement and in the Triassic fractured sediments above it [*Schellschmidt and Clauser*, 1996; *Pribnow and Clauser*, 2000].

A deep geothermal project located at Rittershoffen (Alsace, France) was initiated in 2011 by the company ECOGI, a partnership between the companies Groupe Electricité de Strasbourg and Roquette Frères and the French public financial institution La Caisse des Dépôts et Consignation. The project is based on a geothermal doublet that produces geothermal heat from the reservoir at the sediment-basement interface [*Baujard et al.*, 2015]. The heat will be used for industrial processes at the Roquette Frères bio-refinery at Beinheim, located 15 km west of the drill site. A doublet of deep geothermal wells has been drilled to a

depth of approximately 2.6 km between 2012 and 2014. It is expected a flowrate of 70kg/s and a surface temperature higher than 160°C [*Baujard et al.*, 2015]. The ECOGI project is in commissioning phase and will be operated commercially from summer 2016.

In Enhanced Geothermal Systems (EGS), multi-scale fracture network acting as fluid pathways is an important component to understand and deal with hard rock reservoirs. Therefore, characterization of natural permeable fracture system at the borehole scale is an important milestone for industrial project.

Standard geophysical logging data, mud logging data and high resolution borehole acoustic image logs have been collected in the deep fractured open-hole sections as well as temperature logs. This work details structural analysis of image logs combined with temperature data and shows the occurrence of permeable local-scale fractured zones or faulted zones developing hydrothermally altered granite called damage zone in both wells. An preliminary attempt to represent the permeable fracture system in 3D is proposed in this study in order to estimate geometrical correlation between the two geothermal wells in their open-hole section.

7.2.3 Geological settings

The project is based on EGS technology and takes advantage of the lessons learned from the Soultz-sous-Forêts geothermal project located less than 10 km to the north-west of Rittershoffen (Figure 7.1). The doublet was drilled above the so-called Rittershoffen fault. This normal fault is located approximately 15 km east of the Western Rhenane border fault and is oriented N45°E from surface geological data [*Baujard et al., 2017*]. The open-hole sections penetrated fractured Triassic sandstones, Paleozoic hydrothermally altered granite and fresh granite. The fracture network at the sediment-basement interface was geothermal target of the doublet and showed residual permeability indication. The first well GRT-1 is nearly vertical and its open-hole section is composed by 300 m of sandstones and 350 m of granite. The second well GRT-2 is deviated and its open-hole is composed by 350 m of sandstones and 700 m of granite.

The sandstones are typical medium-grained to conglomeratic continental sandstones with clay formations called Vosgian sandstones deposited during

early Triassic ages. The bottom of the sedimentary cover are argillaceous red sandstones and Permian aged [*Aichholzer et al.*, 2015].

The Paleozoic granitic basement, encountered at a depth of approximately 2200 m, is divided into three units: the oxidized granite, the hydrothermally altered granite and the fine-grained fresh granite. The Paleozoic granitic basement was affected by pre-Cenozoic tectonics, particularly the Hercynian orogeny. The top of the granitic basement was affected by post-orogenic exhumation and subsequent paleo-weathering. Uplift of the top basement involved an uploading of the rock mass and the formation of low dipping angle fractures called jointing. Residual permeability in the granite is intimately linked to Hydrothermally Altered Fractured Zones (HAFZ) showing a cluster organization deeper in the granitic basement [*Genter et al.*, 2000].

In GRT-1, a preliminary analysis of the natural fracture network and the rock petrography was done from 1400 m to 2600 m [*Dezayes et al.*, 2014]. The main fracture orientation is N160°E to N30°E with a main westward dip.

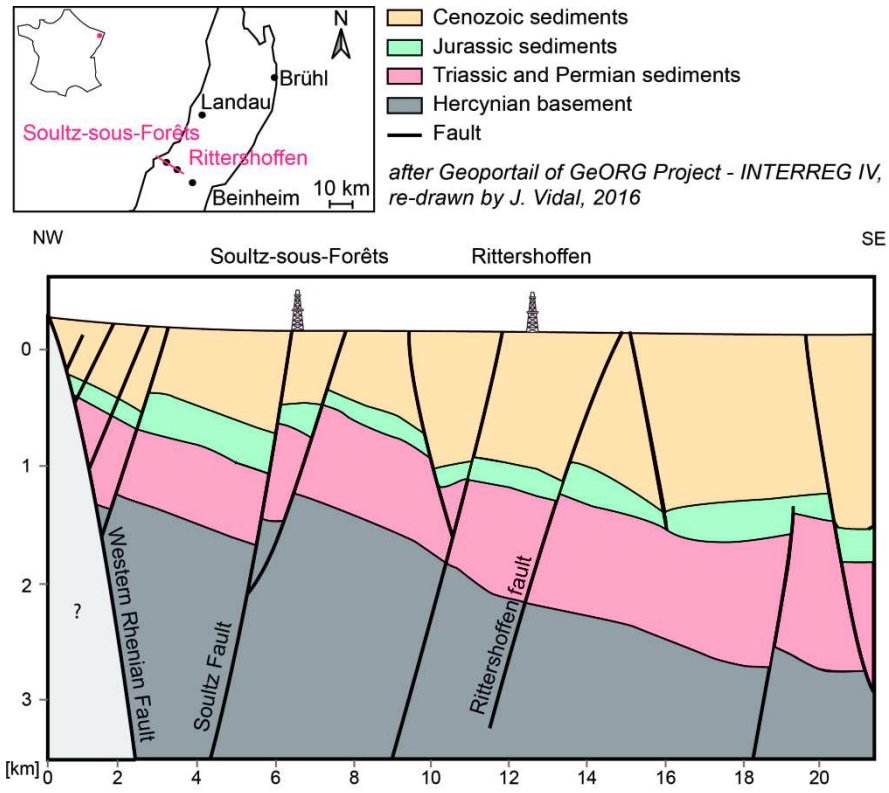

Figure 7.1 Geological cross-section through Soultz-sous-Forêts and Rittershoffen after *GeORG Team* [2017]

7.2.4 Materials and methods

7.2.4.1 Description of acoustic image logs

The present study is based on these acoustic image logs, which were produced by Schlumberger and are referred as Ultrasonic Borehole Images (UBIs). This logging was performed using a transducer that emits an ultrasonic pulse towards the borehole wall and records the first echo [*Zemaneck et al.*, 1970]. The amplitude and transit time of the reflected signal generate two unwrapped borehole images (Figure 7.2). The amplitude data correspond to the energy of the reflected signal, i.e., the reflectivity of the borehole wall. The transit time of the pulse from the transducer to the wall and its return is related to the geometry of the borehole and the acoustic velocity in the wellbore mud. The transducer is rotated as it advances, which allows it to create a complete map of the wall as the tool travels a spiral trajectory. An orientation tool consisting of a three-axis inclinometer and a three-axis magnetometer is added to the probe to orient the images with respect to magnetic north [*Serra*, 2008]. It is thereby possible to map the fracture orientations along the well [*Davatzes and Hickman*, 2005b].

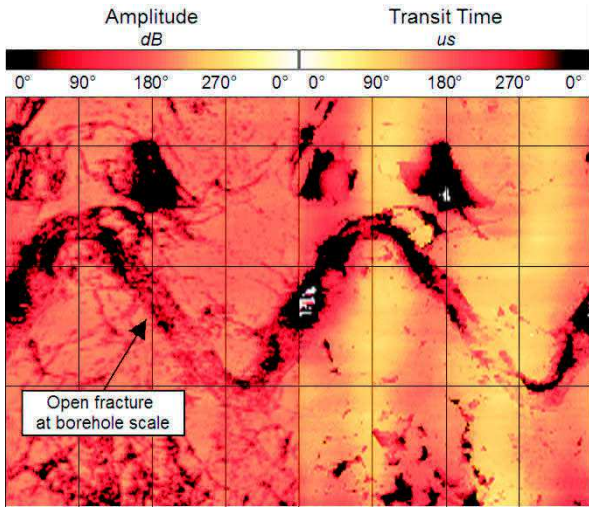

Figure 7.2 Example of natural fractures from acoustic image logs of the granitic basement in GRT-1.

Natural fractures intersecting the well appear as continuous sinusoidal traces. The amplitude and phase of these traces provide quantitative estimates of their orientations (Figure 7.2). If this sine wave is also visible in the transit time image (free aperture), then the fracture is interpreted as an open structure at least at the

borehole scale. If not, then the fracture is assumed to be completely or partly filled with secondary mineral deposits.

The acoustic image logs of wells GRT-1 and GRT-2 were acquired at a vertical resolution of 1 cm and an azimuthal resolution of 2°. Due to the deviation of the well GRT-2, image log acquisition was affected by “stick and slip” and eccentering effects, especially in the granite when the tool encountered fracture zone cavities (Figure 7.3). Data quality is lower and 120 m of the open-hole section was not imaged. The bottom hole was not imaged because the well was to hot and the internal temperature tool was critical.

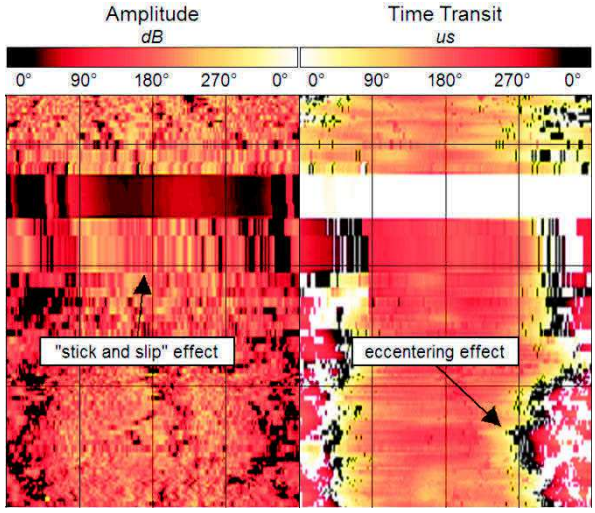

Figure 7.3 Example of "stick and slip" effect eccentering affecting the acoustic image logs in GRT-2.

7.2.4.2 Fracture characterization

First image log were oriented to the North thanks to the orientation data recorded by the orientation tool. As structural dips picked from image were created in inclined borehole, they were corrected for the inclination and azimuth of borehole trajectories. These corrections provide the true azimuth and dip of fractures.

In order to summarize the structural orientation information (dip and dip direction) of natural fractures a polar projection diagram (Schmidt diagram, lower hemisphere) is used. Rose diagrams can also be used to represent strikes of the fracture population. In this study, all diagrams represent true dips and dip directions of fractures.

Structural analysis was performed reflecting the lithology (sandstones, oxidized granite, hydrothermally altered granite and fresh granite). Only continuous sine waves were considered in this analysis. The fracture is considered as “major” if its thickness is higher than 1 cm and if transit time data present an aperture (Figure 7.4). Otherwise the fracture is considered as “minor”. The thickness is the difference of altitude between the depth of the hanging wall and the depth of the foot wall of the fracture. On transit time data, an “acoustic” aperture may be observed. The free aperture of the fracture may be localized on a small section only along the fracture because of presence of secondary minerals.

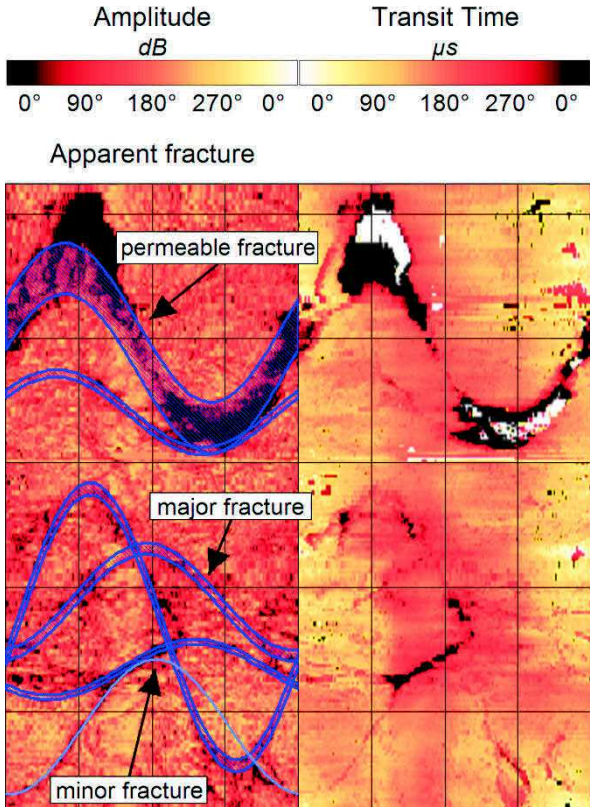

Figure 7.4 Example of an individual permeable fracture occurring into a fracture cluster affecting the granitic basement in GRT-2.

The permeability of a fracture is assessed if temperature logs present anomalies and/or mud losses are recorded during drilling operations. Negative anomalies on the temperature logs are the thermal signature of permeable fractures that were cooled by the drilling and massive hydraulic injections [*Genter et al.*, 2010]. Positive anomalies indicate circulation of hot geothermal fluid through a permeable fracture zone.

7.2.5 Results

7.2.5.1 Natural fractures in GRT-1

346 natural fractures were observed in GRT-1 among which 19 are considered as major (Table 7.1). In sandstones, the fracture density is 0.24 fract/m (Figure 7.5). The main set is oriented N15°E-N20°E with a dip of 80°W (Figure 7.6). 8 fractures are considered as major but only 1 fracture cluster located in Triassic sandstones is considered as permeable (Table 7.1). This cluster is composed by 16 fractures belonging to the main fracture set (N20°E, 85°W) and spreading on a 20 m-wide vertical section [*Vidal et al.*, 2016a].

Table 7.1 Natural fractures observed in GRT-1 open-hole section from acoustic image logs. Permeable fracture zones are characterized by anomalies on temperature logs and mud losses during drilling operations.

GRT-1		Number of natural fractures	Permeable fracture zones
Sandstones	300 m	68	1
Oxidized granite	50 m	90	0
Deep granite	300 m	188	1
Total	350 m	346	2

At the top of the granitic basement, polar projection is more scattered with two principal directions (Figure 7.6). One is oriented N15°E-N20°E and dips 50°W-60°W and the other is oriented N160°E-N170°E and dips 55°W-65°W. The highest fracture density of the open-hole section is observed at the top of the granite (2.51 fract/m). They are steeply dipping fractures. Despite of the high fracture density, any fracture presents permeability indication (Figure 7.5). Only one fracture is considered as major.

The deep granite is divided into two sections: the hydrothermally altered granite and the fresh granite. The fracture density is 0.90 fract/m in the hydrothermally altered granite and decreases in the fresh granite (Figure 7.5). 9 out of 112 fractures are considered as major in the hydrothermally altered granite whereas only one out of 76 fractures is considered as major in the fresh granite. Polar projections of fractures in the hydrothermally altered granite and the fresh granite are superimposed. The main fracture orientation is N-S with a dip of 60°W. The

set presents an azimuthal scattering from N10°W to N30°E (Figure 7.6). A minority of fractures are dipping eastward. One permeable fracture zone is observed at the base of the hydrothermally granite (Table 7.1). The main permeable fracture strikes N175°E, dips 65°W and present a thickness of 24 cm [*Vidal et al.*, 2016a]. Above this main permeable fracture, from 2325 to 2365 m depth, a 40 m-wide altered and fractured section called damage zone is present.

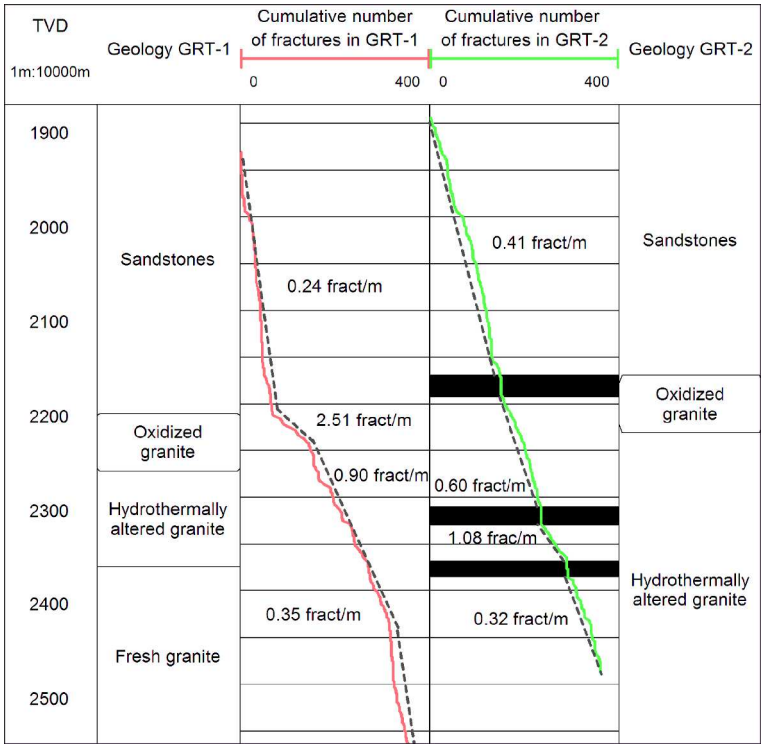

Figure 7.5 Fracture density in the open-hole section of GRT-1 and GRT-2. Black sections indicate major zones were acoustic images where not acquired. TVD=True Vertical Depth

7.2.5.2 Natural fractures in GRT-2

367 natural fractures were observed in GRT-2 among which 64 are considered as major (Table 7.2). Fracture orientations are much more scattered in GRT-2 than in GRT-1 (Figure 7.6).

In sandstones, 142 fractures are observed and 23 are considered as major. The main set is oriented N155°E-N175°E and dips from 80°E to 90°E (Figure 7.6). This conjugate set presents westward dipping fractures which dip between 50°E and 60°E. Two fracture clusters show permeability indication in both Triassic and

Permian sandstones (Table 7.2). The fracture density is 0.41 fract/m in the sedimentary section of the open-hole.

At the top of the granitic basement, 34 fractures are observed and 7 are considered as major but any one shows permeability indication (Table 7.2). Fracture orientations are very scattered but the main pole strikes N150°E-N160°E and dips between 60°E and 70°E (Figure 7.6). In the deep granitic basement, 191 fractures are observed and 44 are considered as major. In the section of hydrothermally altered granite where data were acquired with no sampling artefact, the fracture density is 1.08 fract/m (Figure 7.5).

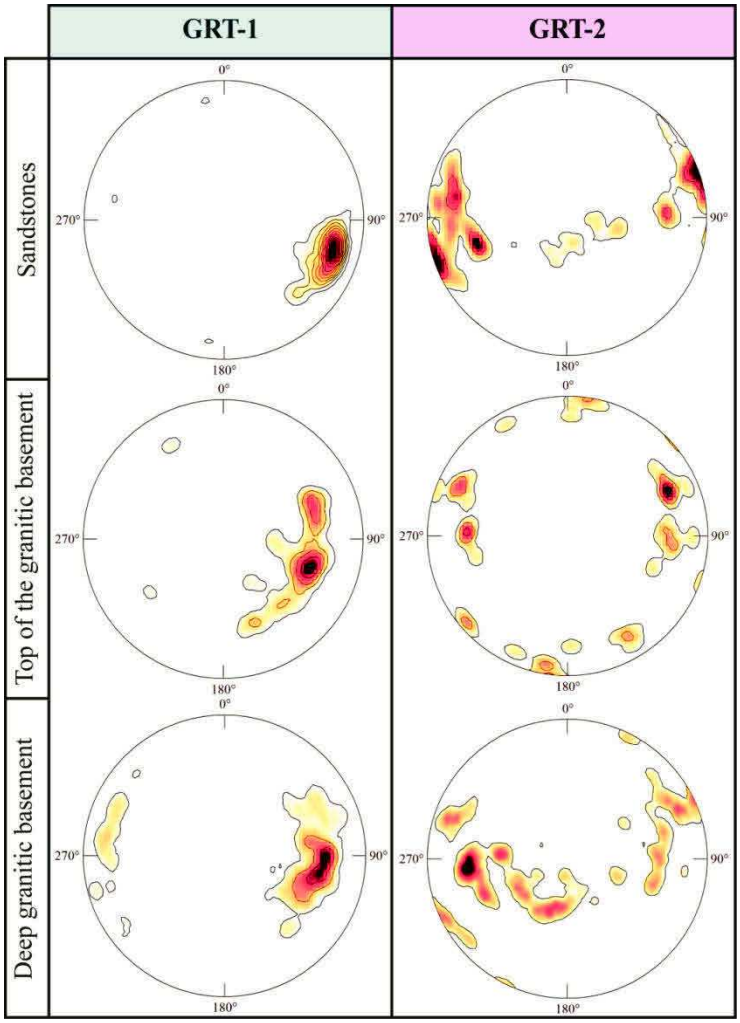

Figure 7.6 Schmidt diagrams (lower hemisphere) that display density contours of natural fractures in the open-hole section of GRT-1 and GRT-2.

Table 7.2 Natural fractures observed in GRT-2 open-hole section from acoustic image logs. Permeable fracture zones are characterized by anomalies on temperature logs and mud losses during drilling operations.

GRT-2		Number of natural fractures	Permeable fracture zones
Sandstones	450 m	142	2
Oxidized granite	50 m	34	0
Deep granite	650 m	191	4
Total	1150 m	367	6

The main fracture set strikes N160°E to N-S with dips between 55°E and 65°E (Figure 7.6). A secondary fracture set strikes N100°E and dips 30°N. Four zones in the hydrothermally altered granite present permeability indication observed in temperature profiles and drilling mud loss occurrences (Table 7.2). One fracture zone was imaged and correlates with open fracture clusters. It presents a complex structural organization with main permeable fractures surrounding by damage zones extending on several meters. For example, Figure 7.4 shows a part of a permeable fracture zone in the hydrothermally altered granite in GRT-2. A main permeable fracture strikes N155°E and dips 80°W and thus belong to the main fracture set. It presents a thickness of 6.5 cm with a partial acoustic aperture. It also correlates with a positive thermal anomaly and mud losses. This fracture intersects another oriented N140°E and dipping 75°W. Below, three major fractures and one minor fracture intersect each other. The major fractures present thickness up to 10 cm and all present acoustic apertures at borehole scale. One of them belongs to the second fracture set with a strike of N78°E and a dip of 27°N. The others belong to the main fracture set with a mean strike of N05°E and a mean dip of 70° W and 30°E.

7.2.5.3 Orientation along borehole trajectories

The Figure 7.7 shows rose diagrams along the open-hole trajectories of GRT-1 and GRT-2 every 150 m-length sections. The GRT-1 trajectory is slightly inclined westward at the bottom hole. At the top of the open-hole section the main direction is N10°E to N20°E associated to sandstone formation (rose diagrams 1.1 and 1.2 Figure 7.7). At the top of the granitic basement, the main direction is

oriented N-S to N10°E (rose diagram 1.3). In the deep basement (rose diagram 1.4), the main direction strikes N30°W to N10°W and a secondary one strikes N10°E. In conclusion, the direction N10°E to N20°E is the most present direction in the open-hole section of GRT-1.

The GRT-2 trajectory is oriented N-S but with a strong deviation of 40°. The top of the open-hole section is dominated by the direction N20°W to N10°W (rose diagram 2.1 Figure 7.7). The bottom of the sedimentary cover (rose diagram 2.2) presents three main directions very scattered: N20°W and N10°E-N20°E. Secondary directions are N10°W to N30°E.

At the top of the granitic basement (rose diagram 2.3), directions are scattered and strikes mainly N-S, N20°E and N160°E-N170°E. Minor fracture orientations are visble around N70E and N100E. The following 150 m-section (rose diagram 2.4) presents a main direction between N160°E-N170°E as the previous section and secondary directions N-S and N110°E. The deepest rose diagram (2.5) presents three mainorientations N-S, N20°E and N160°E-N170°E and two secondary orientations N10°E and N150°E. In conclusion, the angular sector ranging N20°W to N20°E is the most present fracture orientation in the open-hole section of GRT-2.

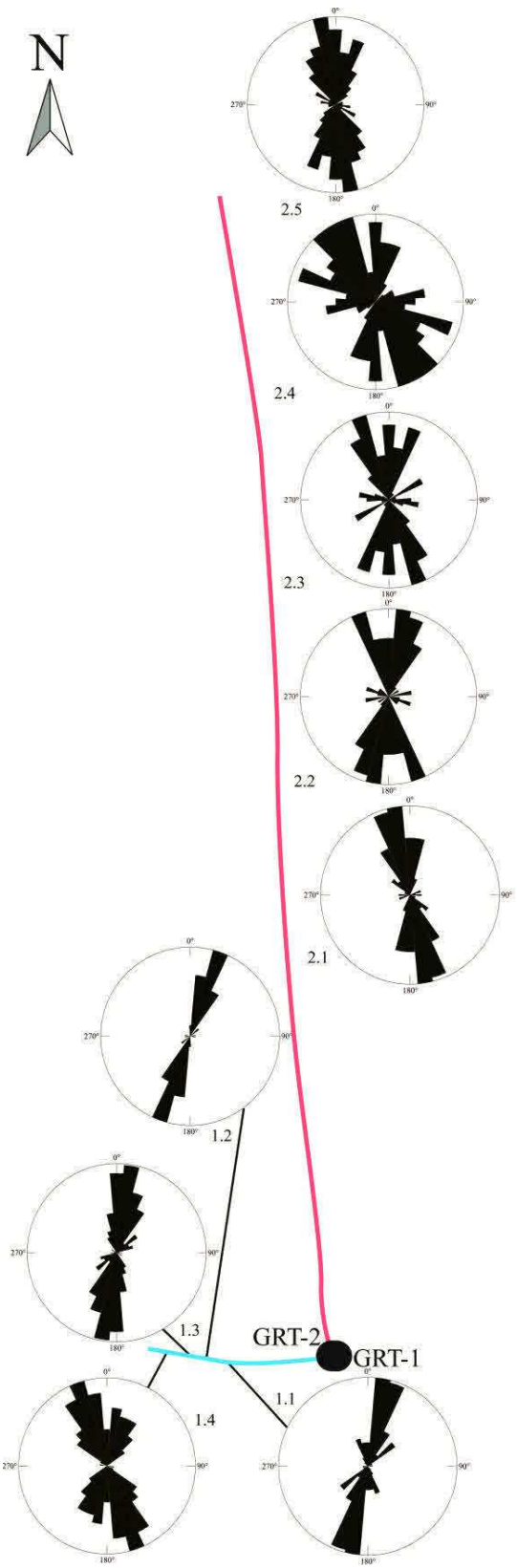

Figure 7.7 Map of rose diagrams representing natural fracture strikes every 150-m length sections along the open-holes of GRT-1 (in blue) and GRT-2 (in red). Positions of rose diagram are not on scale.

7.2.5.4 Raw fracture spacing

The raw fracture spacing is a consecutive distance between two fractures along the borehole. The highest spacing observed is 24 m and 33.6 m in GRT-1 and GRT-2 respectively (Figure 7.8). The Coefficient of variation (C_v) is an index of clustering of fractures which uses the point of intersection of fractures with a line sample. The spacing between adjacent fractures (S) are measured and the C_v is then the standard deviation of S divided by the mean of S.

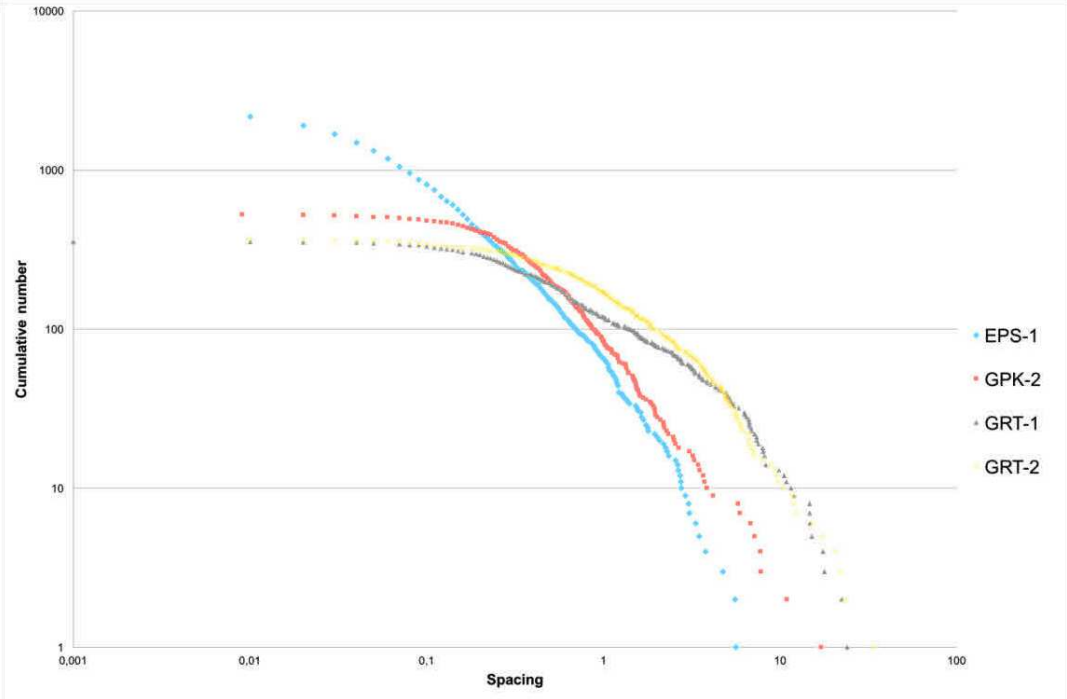

Figure 7.8 Cumulative distribution of fracture spacings from UBI in GRT-1 and GRT-2 compared to fracture spacings from core samples in EPS-1 and from UBI in GPK-2 at Soultz-sous-Forêts. Fracture spacings are calculated over the first 370 m of the granitic basement.

The wells GRT-1 and GRT-2 present the same spatial distribution of fractures with a C_v of 1.81 and 1.70 respectively. As the C_v is higher than 1, natural fractures are organized as cluster. At Soultz, in the well EPS-1, fracture-spacing distribution fits a negative power law from 0.1 to 2.6 m. The highest spacing in the well EPS-1 is 5.6 m, that is lower than in the Rittershoffen wells. Thus, core samples detected closely fractures than acoustic image logs [*Genter et al.*, 1997a]. The C_V (2.65) is also higher in EPS-1 than in Rittershoffen wells.

7.2.6 Discussion

7.2.6.1 Comparison with regional structural directions

During Variscan orogeny, in the URG area, the main structural trend strikes NE-SW to ENE-WSW. The major Variscan dislocation zone which delimited the Hercynian tectonic realms strikes in that direction [*Ziegler*, 1990; *Edel and Weber*, 1995]. A further important Variscan trend strikes NNE-SSW.

It is also related to sinistral strike-slip fault zones associated with Lower Carboniferous to Permian intrusive bodies and dyke swarms [*Edel and Weber*, 1995; *Edel et al.*, 2007]. The third regional trend strikes N-S to NNW-SSE is associated to these sinistral shear zones. During Eocene rifting phase, a N-S compression is created during the Pyrenean tectonic event and generate dextral shears oriented N160°E to N170°E and sinistral shears oriented N10°E to N20°E. Normal faults forming the URG were created during the Oligocene and strikes N-S to NNE-SSW [*Villemin and Bergerat*, 1987].

The trend NW-SE is observed in the surroundings of the URG and is associated to dextral faults [*Villemin and Bergerat*, 1987]. During the Cenozoic evolution of the URG, reactivation of a complex set of crustal discontinuities established during Permo-Carboniferous times plays an important role [*Villemin and Bergerat*, 1987; *Schumacher*, 2002]. Fracture sets in geothermal boreholes and geological outcrops in the URG are associated to the reactivation of old Hercynian structures [*Dezayes et al.*, 2013b, 2015]. In sediments, predominant orientations in GRT-1 and GRT-2 are consistent with the Oligocene Rhine rifting: NNE-SSW in GRT-1 and also NNW-SSE in GRT-2 (Figure 7.7). These directions are also present in the granitic basement.

7.2.6.2 Comparison with structural directions in Soultz boreholes

Natural fracture orientations where observed in the Soultz geothermal boreholes from core samples, electrical and acoustic image logs. In sandstones, NNW-SSE to N-S-striking and W-dipping fractures dominate [*Genter and Traineau*, 1996]. In the granitic basement, two major families strike N-S and NNW-SSE and dips 75° westward or eastward. Minor families are oriented NW-SE and NE-SW with subvertical dips [*Genter et al.*, 1997a; *Valley*, 2007]. In GPK-3 and GPK-4 wells,

less than 5% of fractures below 4 km depth strikes E-W and are subvertical or dip 45°S [*Valley*, 2007].

In sandstones, natural fractures are striking similarly in GRT-2 than in Soultz boreholes with a dip eastward or westward (Figure 7.6). In GRT-1, fractures strike NNE-SSW and dip westward. In general, fractures in sediments are parallel to the Rhenane direction. This orientation is also major in the granitic basement of Soultz and Rittershoffen.

Horizontal joints present at the top of the granite on core samples in Soultz exploration well called EPS-1 [*Genter et al.*, 1997a] are not observed on acoustic image logs in GRT-1 and GRT-2. Maybe, they are not well imaged with this well-logging method because of their low dip. Furthermore fractures at the top of the granitic basement are not associated to large thickness and small fractures below the acoustic image resolution are not detected. In EPS-1 well, the fracture density observed in sandstones on acoustic image logs is the same than in GRT-2. In the granitic basement, the fracture density is higher in Rittershoffen than in Soultz (0.64 fract/m) [*Genter et al.*, 1997a].

At Soultz, in the deep granitic basement, maximum horizontal stress is oriented N170°E [*Valley*, 2007]. Natural fractures including the major permeable fracture zones are critically stressed [*Evans*, 2005]. Some major permeable fractures could disturb locally the stress field orientation in the granitic basement [*Valley*, 2007].

7.2.6.3 Fracture network in Rittershoffen boreholes

346 fractures are observed at borehole scale in GRT-1 among which 2 fracture zones are associated to permeability indications. One permeable fracture zone affects Triassic sandstones and one affects granitic basement. 367 fractures are observed at borehole scale in GRT-2 among which 6 fracture zones are associated to permeability indications. Two permeable fracture zones affect Triassic and Permian sandstones, four zones affect granitic basement of which only two were imaged by acoustic image logs. Permeable zones present a complex cluster organization with permeable drains surrounded by altered, porous and fractured zones.

GRT-1 is nearly vertical with a slight deviation westward in the open-hole section. The borehole cross cuts perpendicularly the N-S oriented fracture network which dips westward (Figure 7.6). The open-hole section was thermally and chemically stimulated in order to improve the injectivity of the well [*Vidal et al.*, 2016a]. A low pressure hydraulic injection was also performed from the wellhead. The hydraulic behavior is mainly controlled by one originally permeable fault zone at the base of the hydrothermally altered granite. This structure is oriented N170°E. Drilling induced fractures provide an estimation of the maximum horizontal stress orientation in GRT-1 [*Hehn et al.*, 2016]. In GRT-1, the maximum horizontal stress is oriented N160-N170°E in the fractured granite section and rotates from N30°E to N160°E in the deep granitic basement. Variations of maximum horizontal stress orientation in the granitic basement are not clearly associated to the presence of major permeable structures. Analysis of stress field magnitude and orientation in GRT-2 is ongoing work.

GRT-2 trajectory is nearly N-S oriented and highly deviated. Structural analysis at borehole scale indicates that the borehole cross cuts a N160°E to N-S oriented fracture set. Fracture orientations are more scattered and fractures are highly dipping eastward. In the deep granitic basement a minor fracture set is oriented N100°E with low dips (Figure 7.6). Considering the northward trajectory of the borehole and the high density of N-S oriented fractures that it crosses cut, the borehole was probably drilled into a N-S oriented fracture zone parallel to the open-hole section. In the deep granitic basement, the E-W fracture set was cross cut perpendicularly. The natural flow regime of GRT-2 is controlled by several permeable fracture zones mainly in the granitic basement. Acoustic image logs show complex permeable fractures belonging to N-S oriented set and E-W oriented set that intersect each other. The well did not required stimulation to reach the expected industrial flowrate. The highly inclined open-hole section of GRT-2 samples more fractures and increases the probability to intersect permeable fracture clusters.

Fracture orientations ranging from N20°W to N20°E are predominant in GRT-1 and GRT-2 regardless of the lithology considered. 3D correlation between fracture zones between GRT-1 and GRT-2 and structural modeling of permeable fracture network will be investigated soon.

7.2.7 Conclusions

Acoustic image logs in open-hole sections of geothermal boreholes GRT-1 and GRT-2 were used to analyze natural fracture network at borehole scale. In GRT-1, fractures are oriented N10°E to N20°E dipping westward. A conjugated fracture system oriented N20°W and N20°E and dipping eastward or westward is observed in GRT-2. Fracture permeability controls fluid circulation through sedimentary and granitic formation. Only 1.2% of fractures are permeable at borehole scale in GRT-1 and 3% in GRT-2. The well GRT-2 intersects a number of permeable fractures more than two times higher than GRT-1. The deviated trajectory of the open-hole section is probably more adapted to geothermal project. The 3D interpretation of fracture network between the geothermal doublet will be investigated soon.

7.3 Zones de fractures perméables dans les puits de Rittershoffen (Article publié dans J. Geophys. Res. Solid Earth)

Permeable fracture zones in the hard rocks of the geothermal reservoir at Rittershoffen, France

Jeanne Vidal[1], Albert Genter[2] and Francis Chopin[1]

[1] IPGS, University of Strasbourg/CNRS, Strasbourg, France
[2] ES-Géothermie, Schiltigheim, France

Key Points:

- Structural characterization of normal faults and fracture zones from acoustic image logs in two recently drilled geothermal wells
- Better understanding of natural permeability in a deep hidden granitic basement from thermal profiles
- Improvement of a conceptual model of fracture zones and fluid circulations at the borehole scale in the Upper Rhine Graben

7.3.1 Abstract

Fluid circulations in zones of fractures is a key challenge to exploit deep geothermal heat from natural reservoir. At Rittershoffen (Upper Rhine Graben, France), two geothermal boreholes, GRT-1 and GRT-2, were drilled in 2012 and 2014 respectively. They targeted the local Rittershoffen normal fault, which strikes N-S and dips westward. In this study, major natural fractures were observed in the open-holes of both wells from acoustic image logs correlated with other standard geophysical logs (gamma ray, neutron porosity, and caliper). Their permeability was evaluated at the borehole scale from temperature logs, mud losses and gas surveys. One originally permeable (OP) fracture zone was observed in the granite of GRT-1. In GRT-2, four OP fracture zones were observed in the granite, and two in sandstones. In GRT-2, fracture zones are composed by several fluid pathways that could explain the higher natural permeability than in GRT-1. All OP fractures are associated with positive temperature anomaly, interpreted as circulation of hot geothermal water through

the permeable fracture, or negative one, interpreted as the cooling of a porous, altered and fractured zone around the permeable fracture after drilling operations. Permeability of natural fracture oriented N170° seems to be intimately linked to the secondary mineral deposits resulting from paleo-circulations. The geometrical fracture model along the wellbore suggests that the inclined trajectory of GRT-2 increases the connection between the borehole and the nearly vertical fracture network associated to the local fault. A good characterization of zones of fractures in a targeted natural reservoir allows an optimal exploitation of geothermal resource.

7.3.2 Introduction

The European Cenozoic Rift System hosts major thermal anomalies in Central Europe [*Ziegler*, 1992]. Its central segment, the Upper Rhine Graben (URG), extends over 300 km from Basel (Switzerland) to Mainz (Germany) in a NNE-SSW direction and is over 40 km wide [*Illies*, 1965]. The URG is characterized by several thermal anomalies associated with natural brine circulation through a nearly vertical multi-scale fracture system cross-cutting both deep-seated Triassic sediments and Paleozoic crystalline basement [*Benderitter and Elsass*, 1995; *Pribnow and Clauser*, 2000; *Pribnow and Schellschmidt*, 2000]. Over more than 30 years, fifteen deep wells were drilled in the URG to exploit geothermal anomalies [*Baumgärtner et al.*, 2005; *Hettkamp et al.*, 2013; *Genter et al.*, 2016]. In the 1980s, the Enhanced Geothermal System (EGS) pilot project located at Soultz-sous-Forêts was initiated to develop a deep fractured granite reservoir (Figure 7.9a and b) [*Gérard and Kappelmeyer*, 1987]. In crystalline rocks characterized by low matrix porosity, the main flow channeling occurs in permeable and connected fractures [*Evans et al.*, 2005a]. Thus, projects based on EGS technology require good knowledge of the fracture network to understand flow distribution at depth and to design borehole trajectories according to the geometrical properties of the fracture network [*Schulte et al.*, 2010]. In France, the first industrial geothermal project aiming to produce overheated water from a geothermal resource in a fracture network at the sediment-basement interface was initiated in 2004 at Rittershoffen (Figure 7.9b) [*Baujard et al.*, 2017]. The project was designed to produce geothermal energy with a capacity of 24 MWth and deliver it to the bio-refinery Roquette Frères

located 15 km to the east. The geothermal doublet was drilled between 2012 and 2014, and after well-testing operations, circulation tests and construction of the heat delivery loop, the geothermal plant was operational by mid-2016. The geothermal target was the local fault of Rittershoffen, which is oriented N-S and dips moderately westward (Figure 7.9b). Geological investigations based on borehole images collected in the GRT-1 and GRT-2 wells provide an exhaustive characterization of natural fractures in sedimentary formations and granitic basement along boreholes [*Vidal et al.*, 2016b].

The structural study was correlated with temperature log and permeability indications in order to identify and characterize preferential fluid pathways for the geothermal fluid into the two boreholes GRT-1 and GRT-2. First, the main permeable fractures or zones of fractures at the borehole scale are located via the correlation of acoustic borehole images, standard geophysical well-log data (temperature log, caliper, neutron porosity and spectral gamma ray) and mud log data (cuttings, mud losses and gas surveys) available from the two deep wells. The internal organization of permeable fracture zones is described in terms of strike, dip, primary mineral leaching, secondary mineral deposits, porosity and permeability indications observed during drilling operations and associated temperature anomalies. Then, the spatial organization of the main permeable fracture zones is assessed using a geometric model of the discrete permeable fracture network. The results provide the locations of permeable fractures and their organization along the borehole trajectories.

The goals of the present paper are to identify the factors that characterize natural permeability at the borehole scale, the organization of permeable zones with respect to non-permeable zones, the relationships between natural fracture networks at the borehole scale and the manner in which the geothermal boreholes penetrate the permeable fracture network. One of the main challenge will be to explain how the vertical well, GRT-1, intersecting a nearly vertical local fault is rather poorly permeable whereas, the second deviated well, GRT-2, which was drilled parallel to the same local fault, evidenced larger natural permeable conditions of a the same hydrothermal system.

7.3.3 Background

7.3.3.1 Rittershoffen geothermal site

The Rittershoffen site is located in the URG, approximately 15 km east of the Western Rhenian fault, which strikes N45°E in this part of the graben (Figure 7.9a). A geothermal doublet was drilled in the southeastern end of a horst to intersect the so-called Rittershoffen normal fault at the top of the basement (Figure 7.9) [*Baujard et al.*, 2017]. Based on a seismic reflection interpretation of the sedimentary cover, this fault strikes N-S, dips 45° westward and displays an apparent vertical offset of approximately 200 m (Figure 7.9) [*Baujard et al.*, 2017]. The wells penetrate the Cenozoic, Mesozoic and Permian sediments overlying the Paleozoic basement. They target the geothermal resource trapped in the fracture network at the sediment-basement interface. Based on cuttings observation from GRT-1 and GRT-2, [*Aichholzer et al.*, 2015] proposed a first detailed lithology of the sedimentary cover. The bottom of the sedimentary cover is composed of sandstones deposited during the early Triassic and Permian. They are 400m-thick in Northern Alsace. The Lower Triassic sandstones are called Vosgian sandstones and are typically medium-grained to conglomeratic continental sandstones with clay formations. The Permian sandstones are argillaceous red sandstones. Their thickness is variable but estimated to 10 m at Rittershoffen. The Paleozoic granitic basement, encountered at a depth of approximately 2200 m, is divided into three units: paleo weathered oxidized granite, hydrothermally altered granite and granitic protolith. Based on gravity data, it is assumed that the granitic basement penetrated at Rittershoffen is the same batholith as at the neighboring geothermal site of Soultz-sous-Forêts (Figure 7.9) [*Edel and Schulmann*, 2009] and is affected by the same alteration stages [*Genter*, 1989; *Traineau et al.*, 1992]. As was observed at Soultz, the pervasive alteration affects the rock mass on a large scale without visible modification of the granite texture. Then, a second type of hydrothermal alteration called vein alteration, due to several successive tectonic events, developed within the fracture zones and strongly affected the texture, mechanical properties and chemical composition of the granite. The upper part of the batholith shows a pronounced reddish color due to hematization related to weathering alteration and sub-horizontal joints after post-orogenic exhumation.

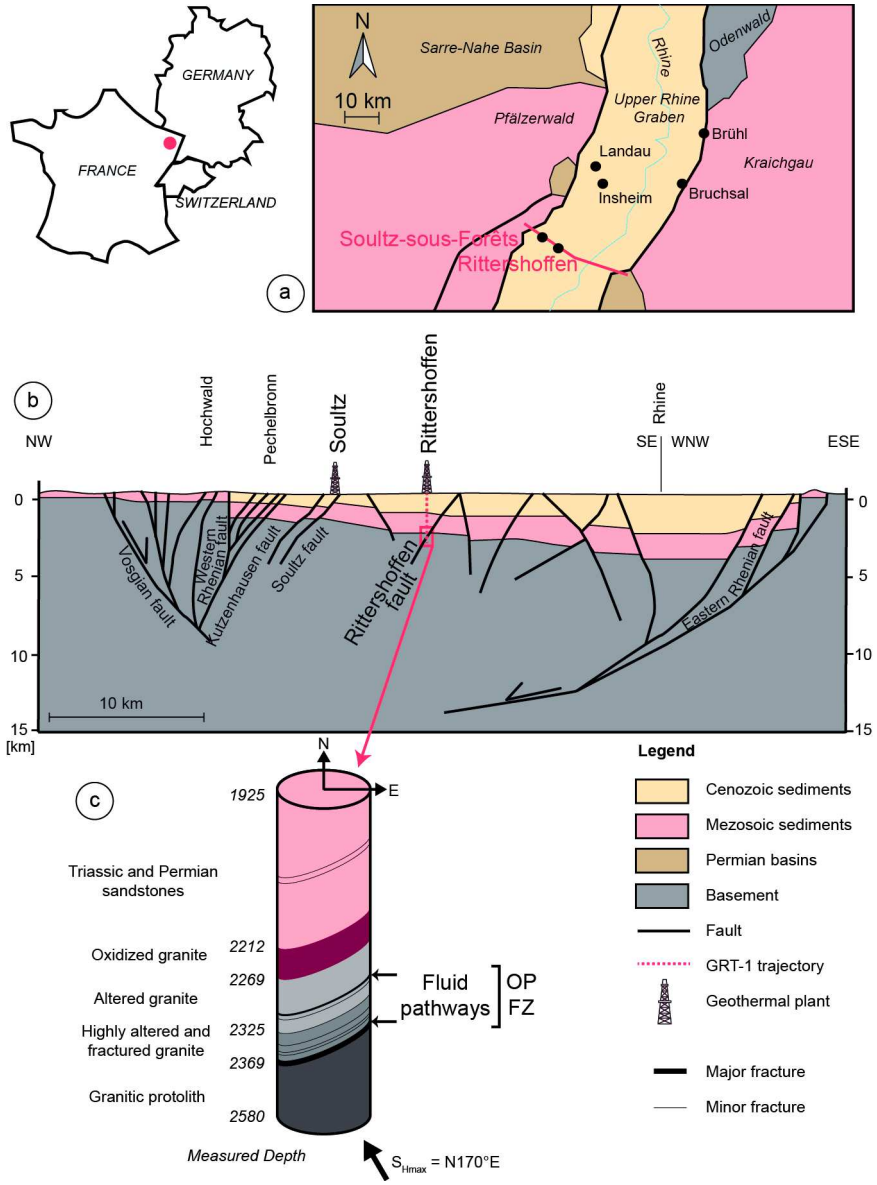

Figure 7.9 Location of the Rittershoffen geothermal site and geological cross section through the Upper Rhine Graben at the latitude of Rittershoffen. The cross section was modified after *Kappelmeyer et al.* [*Kappelmeyer et al.*, 1992] and the interpretation below 4 km depth is done by analogy to the cross section of *Brun et al.* [*Brun et al.*, 1992] and is highly speculative.

The first well, GRT-1, is nearly vertical, and the open-hole section is composed of 300 m of sandstones and 350 m of granite. Due to a lower initial productivity index of 0.50l/s/bar, the well was successively thermally, chemically and hydraulically (TCH) stimulated. It was considered as the future injection well and its injectivity index was enhanced to 2.5l/s/b [*Vidal et al.*, 2016a; *Baujard et al.*, 2017]. The main permeable fracture zone that controlled the hydraulic behavior of

the well is located in the granitic basement. At 2368 m MD, is located a main open permeable fracture, striking N170°E and dipping 55°W with a thickness of 24 cm (Figure 7.10) [*Vidal et al.*, 2016a]. This fracture is associated with a large amount of secondary quartz observed in cutting samples (Figure 7.10) [*Vidal et al.*, 2016a]. It marks an interface between a highly altered granitic basement above and the granitic protolith below. This fracture presented natural permeability without stimulations and thus, is qualified as Originally Permeable (OP). After TCH stimulation, a Newly Permeable (NP) fracture cluster is associated to a temperature anomaly in Triassic sandstones not observed after drilling operations. The second well, GRT-2, is deviated to the north, and the open-hole section is composed of 350 m of sandstones and 700 m of granite [*Baujard et al.*, 2017]. The second well was not stimulated due to its good productivity index higher than 3 l/s/bar [*Baujard et al.*, 2017]. A previous study of the acoustic image logs in the open-hole sections identified the main fracture orientation in GRT-1 and GRT-2 [*Vidal et al.*, 2016b]. In GRT-1, the main fracture set in sandstones strikes N20°E and dips 70°W and in the granite, the main fracture set strikes N-S and dips 65°W. In GRT-2, the main fracture set strikes N170°E and dips 80°E in sandstones and granite. As in Soultz wells, the major fracture network is oriented N-S on average, i.e., the predominant orientation of the URG [*Genter and Traineau*, 1996; *Genter et al.*, 1997a; *Valley*, 2007].

For Soultz, Rittershoffen and most of geothermal reservoirs in the URG, the permeability is supported by natural fractures and fault zones. As geothermal fluids are channelized into this network, the study of permeable fractures and fault zone structure is a key challenge for Rittershoffen geothermal project.

7.3.3.2 Hydrothermal circulations and fractured system

At Rittershoffen, the high-temperature anomaly is concentrated around the Rittershoffen fault, which probably hosts the main hydrothermal circulation [*Baillieux et al.*, 2014]. The Cenozoic and Mesozoic (Lower Jurassic and Upper Triassic) sediments are also associated with a high thermal gradient of 85-90°C/km whereas the Triassic and Permian sediments and the granitic basement are associated with a thermal gradient of 3°C/km in GRT-1 and 18°C/km in GRT-2 [*Baujard et al.*, 2017]. These low thermal gradients are quite low compared to a normal geothermal gradient observed in stable continental basin and interpreted

as the result of circulation of convective cells in a permeable fracture network [*Baujard et al.*, 2017]. The temperature profiles show either negative or positive anomalies at the bottom of the sedimentary cover and in the granitic basement.

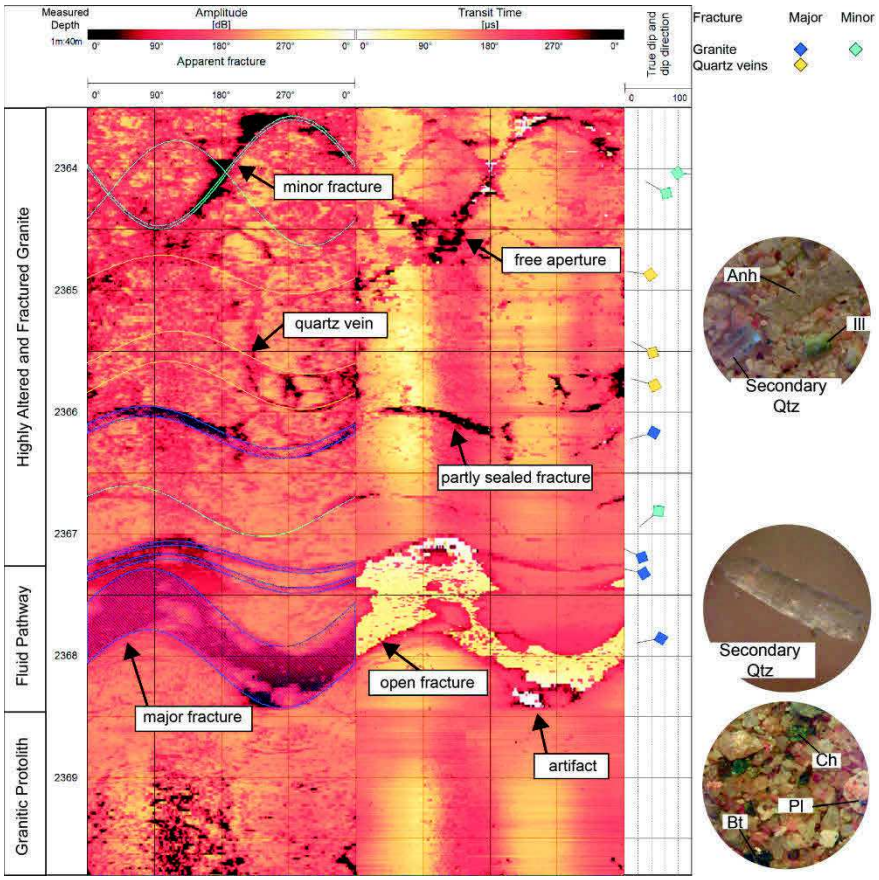

Figure 7.10 Major OP fracture zone affecting the hydrothermally altered granite in GRT-1. Typology used for the structural interpretation is indicated on the acoustic image (light blue = minor fracture, dark blue = major fracture, yellow = quartz veins). The permeable fracture at 2368 m MD characterizes the limit between the hydrothermally altered granite and the fresh granite.

In comparison the so-called Soultz anomaly is also concentrated around the local faults of Kutzenhausen and Soultz which fits with the Western rim of the local horst structure (Figure 7.9). This well-konwn is interpreted as circulation through the permeable fracture network connected to the fault zone [*Benderitter and Elsass*, 1995; *Pribnow and Clauser*, 2000; *Pribnow and Schellschmidt*, 2000; *Geiermann and Schill*, 2010]. The Cenozoic and Mesozoic (Lower Jurassic and Upper Triassic) sediments are associated with a geothermal gradient higher than 100°C/km such as at Rittershoffen. [*Pribnow and Schellschmidt*, 2000]and

[*Pribnow and Clauser*, 2000] suggest that they act as a cap rock formation that insulates the hydrothermal system active below. Convective cells circulate through permeable fracture zones in the Triassic and Permian sediments and the granitic basement and overheat the sedimentary cover above. In contrast to the overlying sediments, the Triassic and Permian sediments and the granitic basement are associated with a thermal gradient lower than 5°C/km. Permeable fracture zones in Soultz reservoirs present a typical thermal signature. They are associated to local negative anomaly on thermal profiles interpreted as cooling of hydrothermally altered and porous granite after drilling operations [*Genter et al.*, 2010]. Indeed fracture zones observed from continuous coring are organized in clusters with a brecciated granite in the core of the zone resulting from successive stages of brittle deformation and surrounded by a hydrothermally altered and porous granite (Figure 7.11) [*Genter*, 1989; *Genter et al.*, 1995, 2000]. In the core, fractures several centimeters thick are mainly filled by geodic quartz that we associate with high reflectivity in amplitude data of acoustic images (Figure 7.11) [*Genter et al.*, 1992]. Surrounding the core, the width of damage zone ranges from centimeters to tens meters. This altered and porous zone corresponds with the highest porosity value (reflecting mainly the leaching of plagioclase) and with a fracture density that is less intense than in the core. It is associated to a lower amplitude reflectivity than the granitic protolith and a darker mottled pattern in acoustic images (Figure 7.11). Primary minerals are partly dissolved and illite precipitation dominates the granite matrix [*Ledésert et al.*, 1999]. Despite the high porosity values in the alteration zone, well tests reveal that 95% of the flow entered the rock mass at only 10 discrete flow points that correspond to the cores of fracture zones where the high fracture density promoted fluid circulation [*Evans et al.*, 2005a]. At Soultz, natural fractures contributed to fluid flow, and the natural permeability of the reservoir probably produces channeling inside the partial fracture sealing with a rather complex 3D organization [*Genter et al.*, 2000; *Méheust and Schmittbuhl*, 2001; *Evans et al.*, 2005a; *Sausse et al.*, 2006, 2008; *Dezayes et al.*, 2010b; *Genter et al.*, 2010; *Sausse et al.*, 2010].

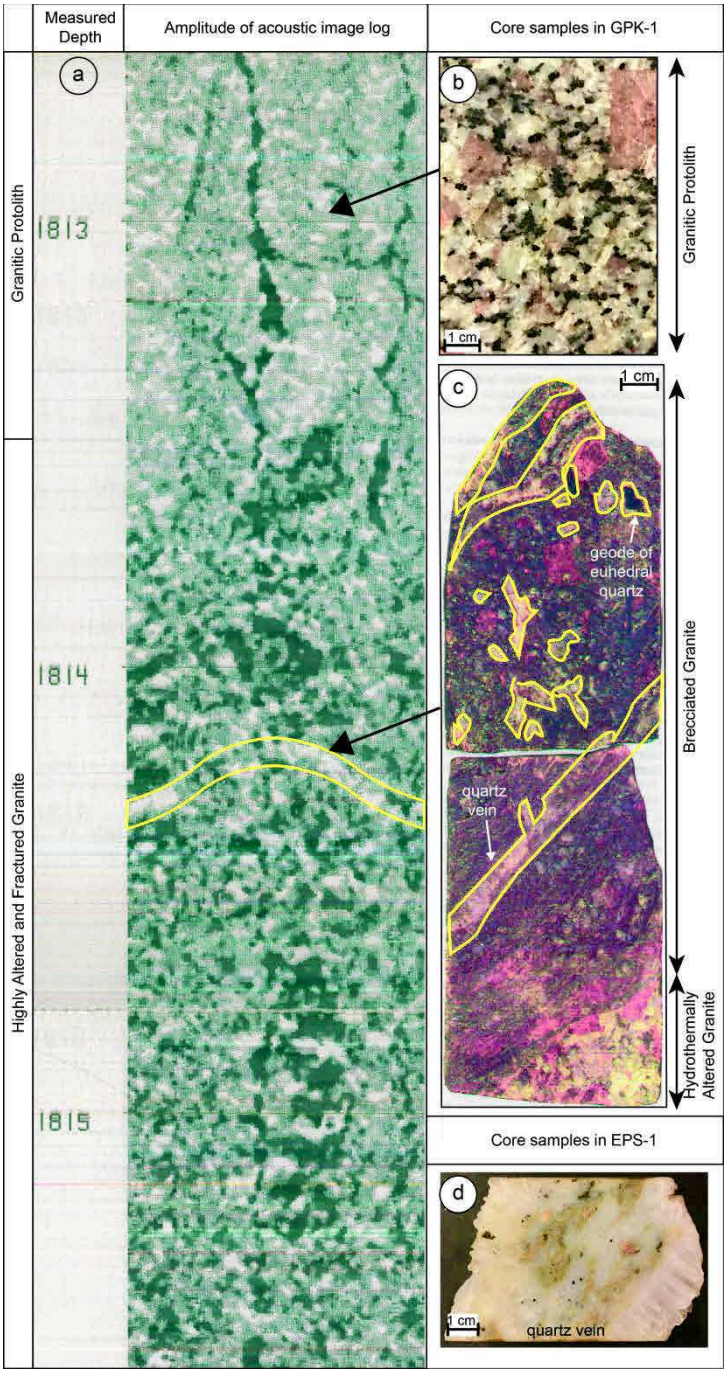

Figure 7.11 Top of an Hydrothermally Altered Fractured Zone at 1814 m MD in the geothermal Soultz well GPK-1 a) amplitude track of the acoustic image logs b) core sample of the granitic protolith c) core sample of a silicified zone affected by geodic quartz and transition to the hydrothermally altered granite and d) example of quartz vein in a deep permeable fracture zone in EPS-1 Soultz well.

This conceptual model of Hydrothermally Altered Fractured Zones (HAFZs) [*Genter*, 1989] is observed in other reservoirs and on field in the URG. It present similarities with the conceptual model proposed by [*Caine et al.*, 1996]. The fault

core that may consist of a single slip surface and a cataclastic zone is surrounded by a fracture-dominated, altered, porous damage zone [*Caine et al.*, 1996; *Davatzes and Hickman*, 2005a; *Wibberley et al.*, 2008; *Caine et al.*, 2010]. In high-porosity rocks as sandstones, the damage zone may be associated with cataclastic deformation bands [*Chambon et al.*, 2006; *Fossen et al.*, 2007] and a transition zone composed of deformed and mixed sediments [*Rawling and Goodwin*, 2006].

7.3.4 Materials and Methods

7.3.4.1 Fracture zones based on well-logging data

Fracture geometry can be evaluated using acoustic image logs. In this present study, acoustic image logs were produced by Schlumberger and are referred to as Ultrasonic Borehole Images (UBIs). This logging was performed using a transducer that emits an ultrasonic pulse towards the borehole wall and records the first echo [*Zemaneck et al.*, 1970]. The amplitude and transit time of the reflected signal generate two unwrapped but oriented borehole images (Figure 7.10).

Natural fractures are planes intersecting the cylindrical well. On unwrapped amplitude images, they appear as darker sinusoidal traces because the signal reflectivity is lower for the altered structure than the surrounding rock. Images are oriented to magnetic north using the orientation tool attached to the probe. Thus, the amplitude and phase of these sine waves provide quantitative estimates of their orientations [*Davatzes and Hickman*, 2005b]. The fracture has an orientation, a dip and a thickness. To calculate the thickness, the depth of the hanging wall and the footwall of a given fracture are measured. The thickness is the elevation difference between the two depths and corresponds to the space which is partly or totally filled by hydrothermal minerals. In case of partial fracture filling, a free aperture could take place. Otherwise, the fracture is totally sealed by a mineral assemblage of hydrothermal deposits which has a physical contrast completely different that the surrounding rock mass (Figure 7.12). Fractures are generally completely or partly filled with secondary deposits. In the Soultz cores, all the fractures are sealed with hydrothermal fill (quartz, carbonates, barite, clays, hematite, etc.), but only 20% of them are visible on the acoustic borehole

images [*Genter et al.*, 1997a]. When a fracture has a higher transit time than the host rock on the transit time track, it is interpreted as a “free” aperture fracture (Figure 7.10). Fractures with a low amplitude and a high transit time are qualified as opened at least at the borehole scale (Figure 7.10). For example, in the GRT-1well, only the fracture located at 2368 m MD is visible on the transit time track. It has a severe negative impact on the temperature log and is characterized by an exceptional free aperture of 24 cm. In contrast, a fracture with a different amplitude but no transit time delay by comparison with the host rock, is qualified as sealed. The fracture may also be partly sealed and thus, the fracture trace is not continuous on the amplitude and the transit time track. The free aperture observed on transit time track is often exacerbated by the mechanical erosion of fractures intersected by boreholes because of tools trips and fluid circulation. Thus the free aperture measured on transit time track is a relative geometrical aperture that is often higher than the true hydraulic aperture. Fractures sealed with geodic quartz are associated to a high amplitude reflectivity (Figure 7.10 and Figure 7.11) [*Genter et al.*, 1992].

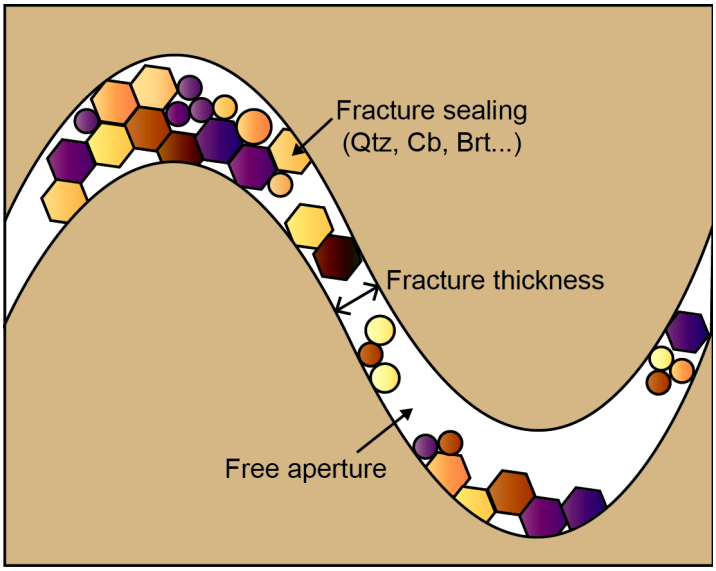

Figure 7.12 Sketch of partly sealed fracture at borehole scale (Qtz=quartz, Cb=carbonates, Brt=barite)

The acoustic image logs of wells GRT-1 and GRT-2 were acquired at a vertical resolution of 1 cm and an azimuthal resolution of 2°. The structural dips identified in the images were corrected for the inclination and azimuth of the GRT-1 and

GRT-2 borehole trajectories. These corrections provide the true azimuth and dip of the fractures.

For this study, only continuous or nearly continuous sinusoidal traces were considered. Thus, we measured the most dominating fracture network visible at borehole scale. Minor fractures, having a trace below the half of the borehole diameter, i.e. 10 cm, were not considered. A fracture is considered major when its thickness is greater than 1 cm and more than 50% of its trace on the borehole wall is visible (Figure 7.10).

Some acoustic image data within fractures may be contaminated by bright spots within fractures of apparent low travel time values and associated low amplitude values. This spurious travel time is an artifact that occurs when there is no returned reflection from the borehole wall within the data acquisition sampling window (Figure 7.10).

Due to the inclination of the well GRT-2, the image log acquisition was affected by stick-slip and eccentering effects, especially in the granite when the tool encountered fracture zone cavities (Figure 7.13). The stick-slip effect is due to the considerable inclination of the well. The sonde is slowed by the roughness of the borehole and then moves rapidly. The sonde is supposed to be centered in the wellbore; thus, its distance to the wellbore should be identical for 360 degrees. However, when the well is highly inclined, the sonde is not centered, and the transit time data are noisy because they are affected by the eccentering effect. Stick-slip and eccentering effects affect the data quality and approximately 120 m of the open-hole section were not imaged properly. The bottom of the hole was not imaged because the well was too hot, and the internal temperature of the tool was too high. In addition to borehole images, fracture zones can be characterized by standard geophysical logs, such as caliper, spectral gamma ray and neutron porosity [*Traineau et al.*, 1992; *Dezayes et al.*, 2010b]. The caliper measures the borehole diameter. At a fracture zone, the wellbore is not circular because it is affected by fracture branches. Caliper data show several peaks associated with fracture branches and presenting a cave-like shape. A 6-arm caliper was acquired with an orientation tool that indicates the position of the first arm to the north. Thus, it was possible to derive the orientation of fractures having a significant thermal anomaly from the 6-arms caliper log. It was

especially useful in the borehole sections where the borehole image acoustic log was missing or with a poor quality. Spectral gamma ray data involve measuring the potassium, thorium and uranium contents to detect the leaching of radioactive primary minerals (negative anomaly) or concentration of secondary radioactive elements in clay minerals (illite) due to the hydrothermal alteration of fracture zones (positive anomaly). The neutron porosity log is based on the effects of the formation of fast neutrons emitted by a source. In granite, the neutron porosity log is strongly affected by the presence of fractures, clays and hydrated minerals, The decrease of the gamma ray, the increase of the neutron porosity and a cave shape observed on the caliper which could be associated with thermal anomalie. are indicators of a permeable fracture zones [*Traineau et al.*, 1992; *Dezayes et al.*, 2010b].

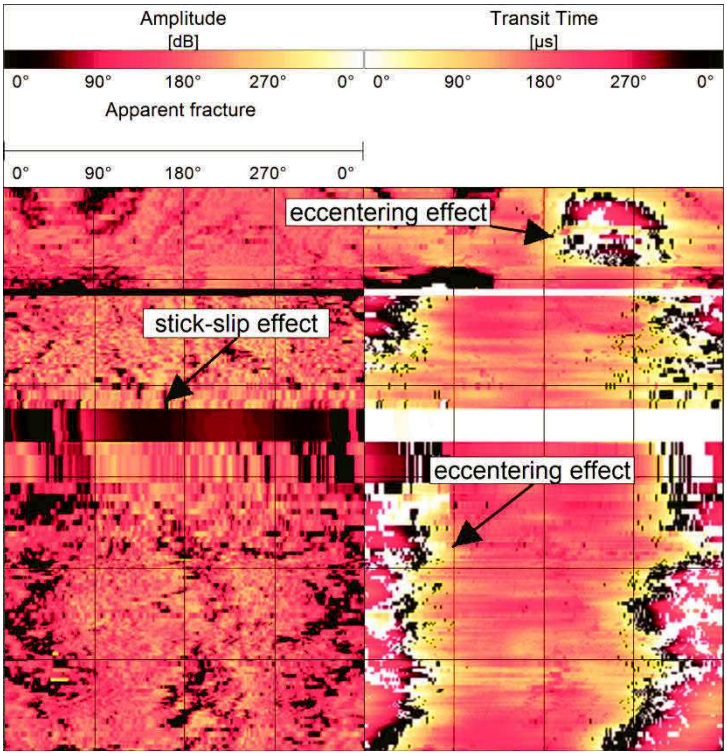

Figure 7.13 Example of stick-slip and eccentering effects affecting acoustic images in geothermal well GRT-2

7.3.4.2 Present-day permeability indicators

In the neighboring geothermal site, Soultz-sous-Forêts, which was extensively investigated based on 810 m length of core section in granite, the natural permeable indicators such as drilling mud losses or brine outflow are intimately

linked to the HAFZs [*Genter et al.*, 2000; *Evans et al.*, 2005a; *Mas et al.*, 2006; *Sausse et al.*, 2006, 2008; *Dezayes et al.*, 2010b; *Genter et al.*, 2010; *Sausse et al.*, 2010]. To investigate the permeable structures, mud logging data (mud losses, gas occurrences and cuttings) and geophysical logs (spectral gamma ray, neutron porosity and temperature logs) are used. Mud losses or geothermal fluid inflows observed during drilling operations indicate a permeable fracture zone [*Davatzes and Hickman*, 2005a; *Dezayes et al.*, 2010b]. Alkanes occurrences, as well as other gases, such as helium, CO_2 and radon, are associated with permeable fracture zones, as evidenced in the Soultz granite [*Vuataz et al.*, 1990; *Aquilina et al.*, 1993]. Mineralogical investigation of the rock cuttings was also an efficient method for identifying hydrothermally altered zones in the granite [*Dezayes et al.*, 2014; *Meller et al.*, 2014]. Brine circulation through a permeable fracture zone leads to partial sealing by secondary geodic quartz and clay mineral deposits, which are easily detectable in cuttings by visual inspection combined with X-ray diffraction.

However, the temperature anomalies observed in a temperature profile are considered the most reliable permeability indicator [*Evans et al.*, 2005a; *Bradford et al.*, 2013]. In the Soultz boreholes, the depths of anomalies observed in the temperature logs spatially match the depths of fracture zones observed in the image logs or on the core samples and are thus interpreted as the thermal expression of permeable fracture zones [*Evans et al.*, 2005a; *Dezayes et al.*, 2010b]. Negative anomalies in the temperature logs indicate remnant cooling of the alteration zone of the fracture zone due to mud losses during drilling operations and/or water injections during stimulation [*Genter et al.*, 2010]. Because the HAFZs show a secondary connected porosity which could locally exceed several percent, drilling fluids tend to cool preferentially those complex interconnected structures than the massive granite which is poorly fractured, tight and depleted in secondary porosity [*Sardini et al.*, 1997; *Ledésert et al.*, 1999; *Genter et al.*, 2000].

7.3.4.3 Geometrical modeling of permeable fractures

The geometrical modeling of the permeable fracture network along the well trajectories was performed with the MOVE™ software package from Midland Valley Exploration Ltd. The main goal of this model is to analyze the geometrical

organization of fracture networks intersected by the well trajectories and correlate the fracture directions and dips between the two geothermal wells. All permeable fractures observed from the well logging and mud logging data are incorporated into the model. They are represented as discs centered on the well at the measured depth. The acoustic borehole images provide information on fracture geometry at the borehole scale but not on their extents. The evaluation of the fracture extent, shape and orientation in the far field requires the correlation of geophysical data such as vertical seismic profile (VSP), seismic reflection interpretation, and microseismicity [*Michelet and Toksöz*, 2007; *Soma et al.*, 2007; *Sausse et al.*, 2010]. This is beyond the scope of this article, which focuses on the fracture network along the well trajectories. Even though there is an extensive literature that links fracture properties (thickness, length, off-set, horizontal trace, aperture) and fracture size (shape, height, length, diameter), we considered as a first approach, that the fracture extent was defined according to the magnitude of mud losses observed during drilling operations. Permeable fractures associated with mud losses of ≥10 m^3/h are geometrically modeled with a 100-m diameter. Permeable zones associated with mud losses of <10 m^3/h are modeled with a 70-m diameter. Permeable zones without mud losses but associated with a temperature anomaly are modeled with a 50-m diameter. With these three classes of fracture size, connections between fracture zones and wells that are not directly observed, are geometrically constrained.

7.3.5 Results

7.3.5.1 Internal organization of permeable fracture zones in the well GRT-1

All well-logging data and mud-logging data are correlated on Figure 7.14 with a single depth reference that is the depth of the casing shoe at 1924.5 m measured depth (MD). The well GRT-1 presents two permeable fracture zones affecting the open-hole section. One fracture zone is considered newly permeable (NP) and one is considered originally permeable (OP). These have already been discussed by [*Vidal et al.*, 2016a].

A NP fracture zone affects the Triassic sandstones between 1988 and 2008 m MD. The cluster is composed of 16 individual natural fractures, 7 of which are major fractures with an average orientation of N20°E and a mean dip of 70°W

(Figure 7.14a). However this cluster does not present mud losses during drilling operations or temperature anomaly in thermal profile in post-drilling temperature profile. After stimulation operations, this cluster is associated with a temperature anomaly on the post-stimulation temperature profile and thus is qualified as NP. As it is not an OP fracture zone, it will not be discussed further in this study

An OP fracture zone affects the hydrothermally altered granite between 2325 and 2368 m MD. The fracture zone is composed of 51 individual fractures, including nine major fractures and 12 filled with geodic quartz (Figure 7.14b). The dominant set of fractures is oriented N-S with a dip of 48°W, and the second set is oriented N-S with an average dip of 66°E. In detail the top of the fracture zone is characterized by 9 minor fractures dipping eastward and westward and one major fracture (N20°E, 50°W) at 2326 m MD (Figure 7.15). Below this major fracture, a thick partly sealed fracture is observed. Over 1 m thick, the amplitude track is affected by a mottled dark pattern with a partial opening observed on the transit time track. This sinusoidal trace is underlain by 5 fractures filled with quartz and a major fracture zone (N13°E, 56°W) at 2328 m MD. This major fracture is 23 cm wide and presents a large free aperture in the transit time data. It is spatially associated with a strong positive neutron porosity anomaly (41%) and a large gamma ray anomaly (269 gAPI) between 2328 and 2338 m MD (Figure 7.14). Mud losses started at 2325 m MD with a flowrate of 8 m^3/h; thus, the fracture is considered to be OP. Surprisingly, there is no temperature anomaly at 2328 m MD.

Figure 7.14 (next page) Composite log in the open-hole section of GRT-1. Well-logging and mud-logging data are indicated (mud losses, spectral gamma ray, neutron porosity, post-simulation temperature profile at equilibrium). The cumulative number of fractures and the cumulative width of fractures from acoustic image logs along the open-hole section are represented. Schmidt diagrams (lower hemisphere) associated to major permeable fracture zones from acoustic image logs are also represented a) 1988 to 2008 m MD and b) 2326 to 2369 m MD. Depth is Measured Depth, NP = Newly Permeable, OP = Originally Permeable.

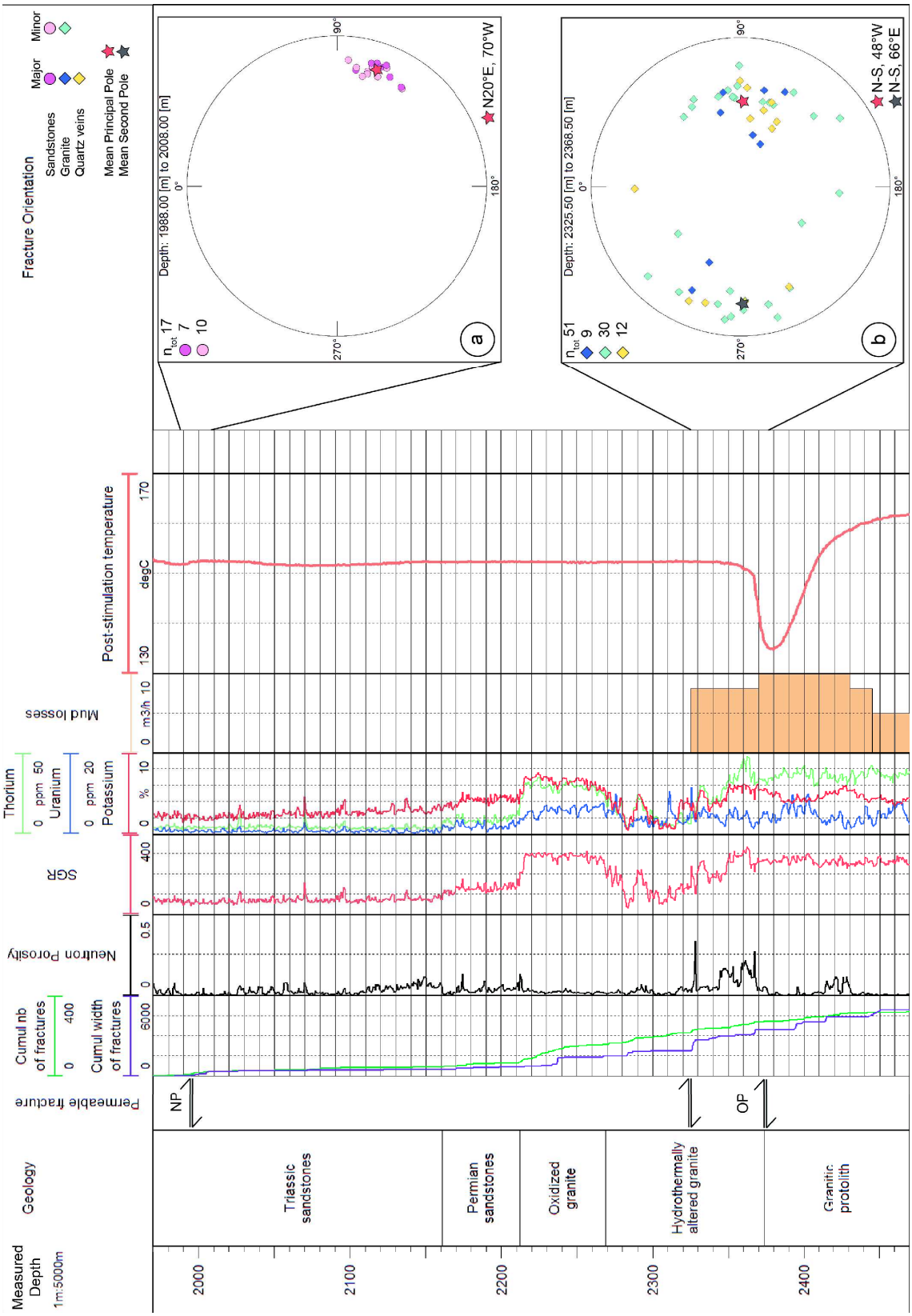
Fracture Orientation
Major
Minor
Sandstones
Granite
Quartz veins
Mean Principal Pole
Mean Second Pole
Depth: 1988.00 [m] to 2008.00 [m]
N20°E, 70°W
Depth: 2325.50 [m] to 2368.50 [m]
N-S, 48°W
N-S, 66°E
a
b
Post-stimulation temperature
degC
Mud losses
m3/h
Thorium
Uranium
Potassium
ppm
%
SGR
Neutron Porosity
Cumul nb of fractures
Cumul width of fractures
Permeable fracture
NP
OP
Geology
Triassic sandstones
Permian sandstones
Oxidized granite
Hydrothermally altered granite
Granitic protolith
Measured Depth
1m:5000m

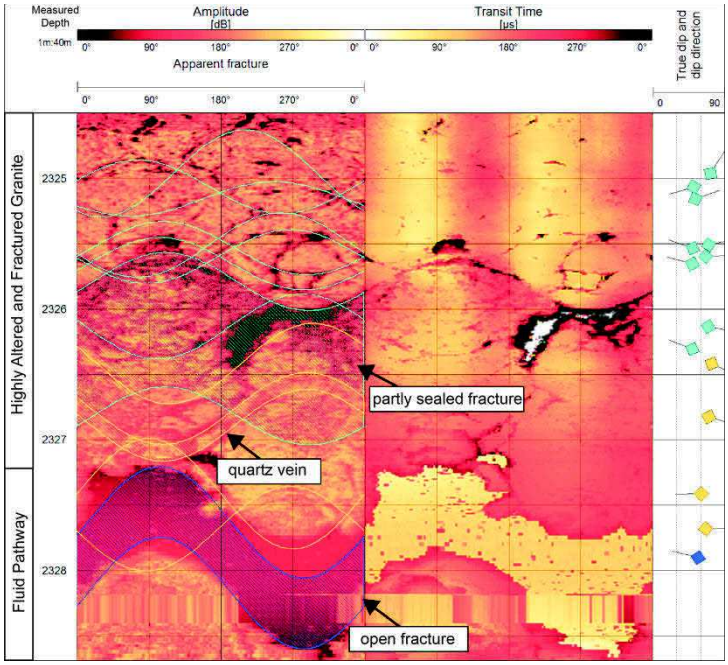

Figure 7.15 Top of the major OP fracture zone affecting the hydrothermally altered granite in GRT-1. Colors used for structural interpretation are similar to the legend of Figure 7.14.

Below this permeable fracture, the neutron porosity and the spectral gamma ray data are very disturbed (Figure 7.14) and cutting sample observations indicate a highly altered granite (Figure 7.10). The acoustic image at the same depth indicates a lower amplitude reflectivity than in the granitic protolith associated with several fractures and quartz veins (Figure 7.10). The bottom of the fracture zone is characterized by a major OP structure associated with an increase in mud losses (10 m^3/h) and a large negative temperature anomaly (Figure 7.14). The temperature decreases from 152°C at 2352 m MD to 134°C at 2380 m MD. This local-scale structure is composed of three major fractures (Figure 7.10). The first two ones strike N20°E, dip 30°W and present a thickness of 3 cm. At 2368 m MD, the third one strikes N170°E and dips 55°W. This fracture is 24 cm thick and presents a large free aperture in the transit time data. It is associated with a positive neutron porosity anomaly (16%) and a negative gamma ray anomaly (-50 gAPI). This fracture is considered a major permeable drain controlling the hydraulic behavior of the well [*Vidal et al.*, 2016a; *Baujard et al.*, 2017]. It also marks sharply the limit between the hydrothermally altered granite acting as the hanging wall and the fresh granite acting as the footwall located at 2369 MD

(Figure 7.10). It is quite surprising that a major permeable fracture limits the hydrothermally altered granite and the non-altered granite.

At local scale, the Rittershoffen fault is oriented N-S that is slightly different from major permeable drains observed in GRT-1. The fault is also dipping westward.

7.3.5.2 Internal organization of permeable fracture zones in the GRT-2 well

All well-logging data and mud-logging data are correlated on Figure 7.16 with a single depth reference that is the depth of the casing shoe at 2120 m MD. The well GRT-2 presents two permeable fracture zones in the sandstones and four in the granite. The three deepest fracture zones in the granite were not imaged properly during acoustic image log acquisition.

A fracture cluster affects the Triassic sandstones from 2245 to 2264 m MD (Figure 7.16). It is composed of 23 fractures, 4 of which are interpreted as major fractures. A first set of fractures is oriented N155°E with an average dip of 72°W dip (Figure 7.16a). A second set of fractures is oriented N05°E with an average dip of 75°E dip. This fracture cluster is precisely described in Supporting Information S1 and Figure S1. At the top of the cluster, two major fractures intersect each other at 2248 m MD (Figure S1a). The first one strikes N10°E, dips 72°E, and has a thickness of 3.2 cm. The second one strikes N147°E and dips 80°E with a thickness of 3 cm. The bottom of the cluster is also marked by two major fractures intersecting each other at 2263 m MD (Figure S1b). The first one strikes N05°W, dips 67°E, and has a thickness of 2 cm. The second one strikes N145°E, dips 81°W, and has a thickness of 1.8 cm. These major fractures are associated with large positive temperature anomaly (+2°C at 2263 m MD) and thus are considered OP (Figure 7.16).

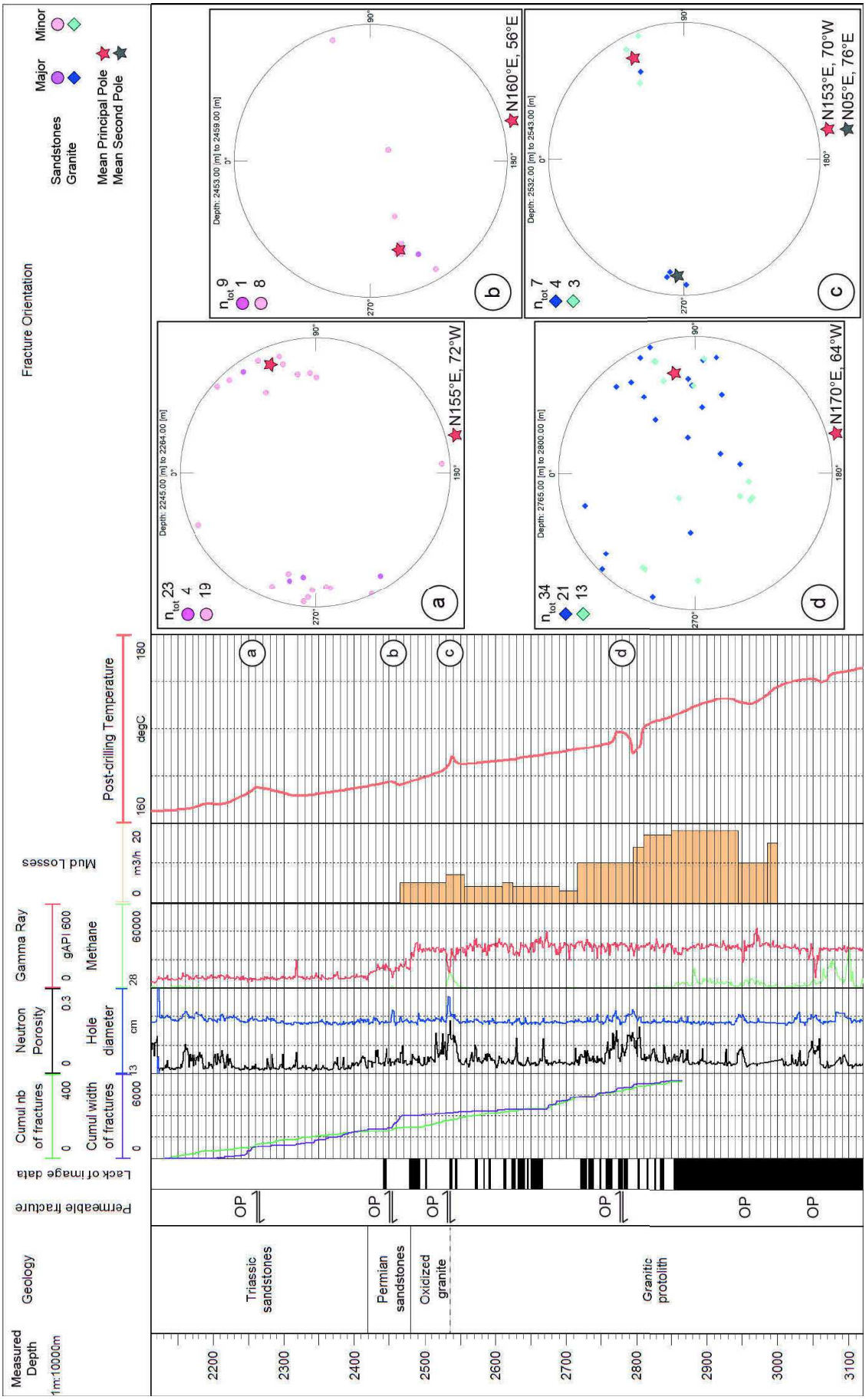
Measured Depth
1m:1000m
Geology
Triassic sandstones
Permian sandstones
Oxidized granite
Granitic protolith
Permeable fracture
OP
Lack of image data
Cumul nb of fractures
Cumul width of fractures
Neutron Porosity
Hole diameter
Gamma Ray
Methane
Mud Losses
Post-drilling Temperature
degC
Fracture Orientation
Sandstones
Granite
Major
Minor
Mean Principal Pole
Mean Second Pole
N155°E, 72°W
N160°E, 56°E
N170°E, 64°W
N153°E, 70°W
N05°E, 76°E

Figure 7.16 (previous page) Composite log in the open-hole section of GRT-2. Well-logging and mud-logging data are indicated (mud losses, neutron porosity, post-drilling temperature profile at equilibrium). The cumulative number of fractures and the cumulative width of fractures from acoustic image logs along the open-hole section are represented. Schmidt diagrams (lower hemisphere) associated to major permeable fracture zones from acoustic image logs are also represented (2245 to 2264 m MD, 2453 to 2459 m MD, 2610 to 2612 m MD and 2766 to 2800 m MD). Black sections indicate depths where acoustic image logs where not acquired. Depth is Measured Depth, OP = Originally Permeable.

The Permian sandstones are affected by a fracture cluster from 2453 to 2459 m MD (Figure 7.16). The main fracture set strikes N160°E and dips 56°E on average (Figure 7.16b). It is composed of 8 minor fractures and one major permeable fracture. The major fracture is located at 2455 m MD, strikes N152°E, dips 66°E, and has a thickness of 1.1 cm (Figure 7.17). In the transit time data, the fracture presents an almost total free aperture. It is considered OP because mud losses started at 2465 m MD (5 m^3/h) and a negative temperature anomaly was observed at 2464 m MD (-0.05°C). At the top of the major fracture, four tiny minor fractures intersect each other. At the lowest part of the fracture trace on the borehole wall, two minor fractures present large thickness (5.4 cm for the shallowest one and 18.8 cm for the deepest one). They are associated with a higher amplitude than the major permeable fracture but a lower one than the host rock and a high transit time. They are interpreted as thick partly sealed fractures and cutting observations at this depth indicate presence of geodic quartz, calcite and barite. They strike N160°E and dips 60°E.

The detailed petrographic log from cutting observations in the granitic basement is not yet available even though hydrothermal mineralogical investigations in terms of clay minerals have been analyzed with XRD characterization of 40 samples (Vidal et al., 2017). However the top of the granite present the gamma ray signature of the oxidized granite between 2480 and 2535 m MD (Figure 7.16). The gamma ray curve shifts from 144 to 300 gAPI at the sediment-basement interface and does not present major variations in the uppermost oxidized granite section (average gamma ray = 259 gAPI +/-40). This gamma ray signature is already observed in Soultz wells and GRT-1 well [*Vidal et al.*, 2016c]. At 2535 m

MD, the gamma ray signal decreases to 130 gAPI and the neutron porosity increases to 16%., that indicates the presence of a permeable fracture zone at the base of the oxidized granite. These variations are correlated with a methane concentration of 13,141 ppm at 2536 m MD (Figure 7.16). At 2537 m MD, the temperature profile presents a positive anomaly of +2°C in conjunction with mud losses of 7 m^3/h (Figure 7.16). Acoustic data are rather difficult to interpret at this depth but are described in Supporting Information S2 and Figure S2. The first fracture set of the cluster is oriented N153°E with a 70°W dip on average. The second fracture set of the cluster is oriented N05°E with a 76°E dip on average (Figure 7.16c). Two major fractures present a free aperture and are qualified as OP. At 2534 m MD, the first OP fracture strikes N-S, dips 80°E and present a thickness of 6.2 m (Figure S2a & b). At 2540 m MD, the second OP fracture strikes N10°E, dips 72°E with a thickness of 1.5 cm (Figure S2c).

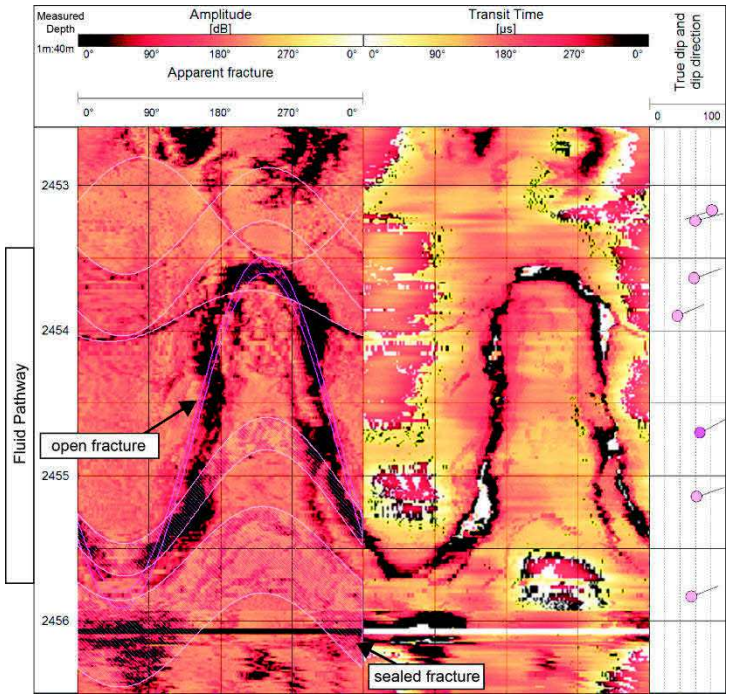

Figure 7.17 Major OP fracture at 2455 m MD affecting Permian sandstones in GRT-2

The main permeable fracture cluster is located between 2766 and 2800 m MD in the granitic protolith (Figure 7.16). At these depths, occurrences of secondary clay minerals are associated with hydrothermal alteration [*Ledésert et al.*, 1999; *Vidal et al.*, 2017]. Thirty-four individual natural fractures affect the granitic batholith and 21 are considered major. The orientations of the fractures are very

scattered. The main set strikes N170°E and dips 64°W on average (Figure 7.16d). The first major fracture is present at 2767 m MD (Figure 7.18a). It strikes N154°E and dips 83°W with a thickness of 6.6 cm.

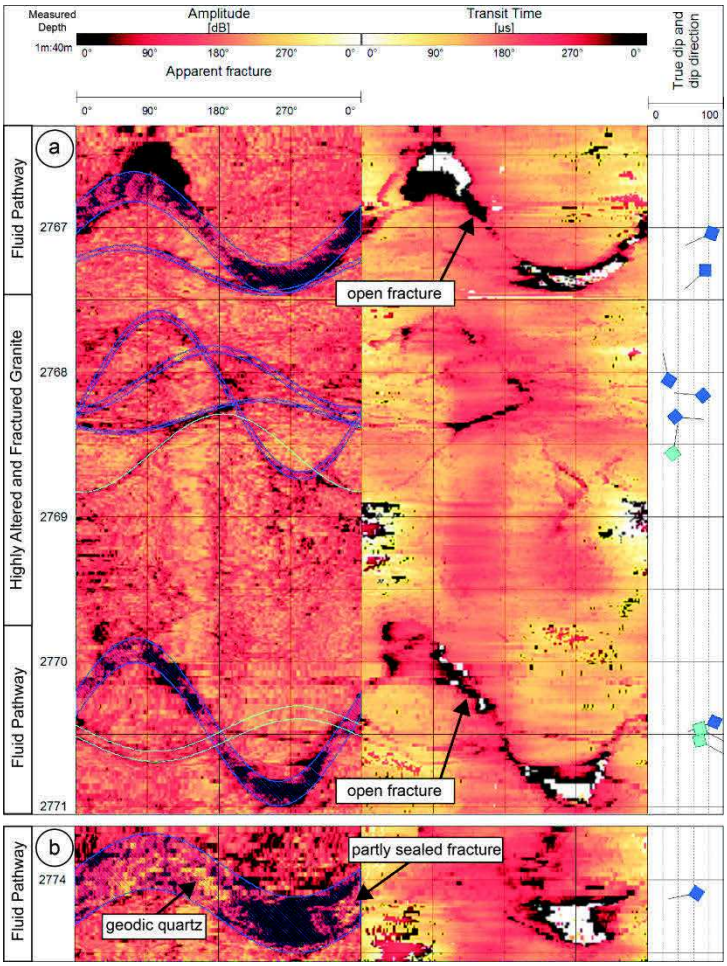

Figure 7.18 Major OP fracture zone affecting the granitic protolith in GRT-2 a) major fractures at 2767 and 2770.5 m MD b) fracture core at 2774 m MD that characterizes the top of the alteration zone. Colors used for structural interpretation are similar to the legend Figure 7.16.

At 2766 m MD, a positive neutron porosity peak of 15% is observed. At 2770.5 m MD, another fracture is observed with a thickness of 3.6 cm. It strikes N160°E and dips 87°W. It is associated with a positive neutron porosity peak of 15% at 2771 m MD and also with an increase in mud losses to 10 m^3/h (Figure 7.16). At 2774 m MD, a 17-cm-thick fracture strikes N170°E and dips 64°W (Figure 7.18b). Although the acoustic image is noisy at this depth, the fracture does not present a total free aperture in transit time scale and geodic quartz associated to high reflectivity is suspected from the amplitude track and confirmed from cuttings

observations. At 2787 m MD, a major fracture strikes N45°E and dips 87°E, with a thickness of 4 cm (Figure 7.19). This section is also affected by a fracture parallel to the borehole trajectory. Its trace is arch-shaped or oval-shaped and is observed at 2786.7 m MD and from 2788.2 m MD to 2789.5 m MD. This fracture strikes approximately N-S with a dip of approximately 55°W. These fractures are considered OP because they are associated with a positive temperature anomaly (+2°C) that extends from 2770 to 2790 m MD (Figure 7.16). From 2790 m MD to 2800 m MD, the neutron porosity and the spectral gamma ray are very disturbed (Figure 7.16). The granitic batholith is affected by natural fractures and presents a lower amplitude reflectivity with a mottled dark pattern in acoustic image logs. This section is associated with a negative temperature anomaly (-3°C) that extends from 2795 to 2805 m MD, and mud losses increase to 17 m^3/h (Figure 7.16).

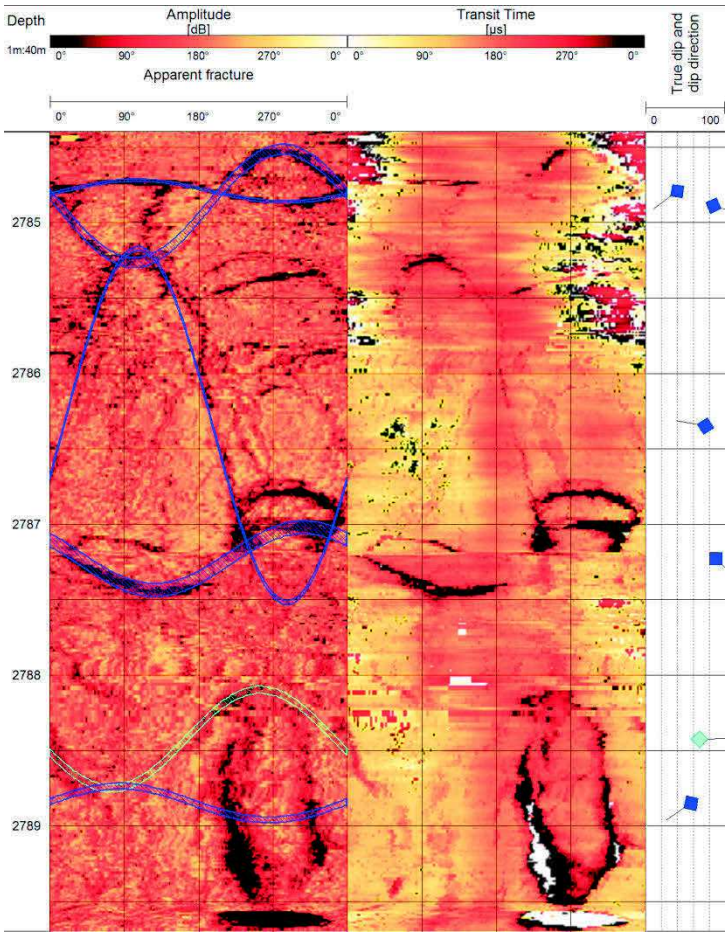

Figure 7.19 Major OP fracture zone from 2786.6 to 2789.5 m MD affecting the granitic protolith in GRT-2. Colors used for structural interpretation are similar to the legend Figure 7.16.

In the deep granitic basement, methane occurrences are observed below 2800 m MD. Two permeable zones are observed in the deep granite but are not imaged by the acoustic image data (Figure 7.16). The 6-arm oriented caliper data were not acquired at this depth, but the simple caliper data present many individual peaks associated with the presence of fracture clusters and reach 23.5 cm at 2950 m MD. At 2950 m MD, the gamma ray signal decreases to 173 gAPI, and the neutron porosity increases to 10%. These variations indicate the presence of a fracture zone. It is associated with a negative temperature anomaly (-0.5°C) over approximately 50 m. From 3000 m MD, hot geothermal water inflows are observed locally. At 3050 m MD, a negative gamma ray anomaly (-220 gAPI) is associated with neutron porosity variations (12% at 3050 m and 3060 m MD). The caliper values reach 23.5 cm at 3050 m MD. A negative temperature anomaly (-1°C) extends from 3050 to 3070 m MD, with a minimum of 175°C at 3060 m MD. Methane concentrations increase below 3050 m MD, with a maximum of 11,500 ppm at 3100 m MD. There is no evidence of additional permeable fractures between 3100 m and the bottom of the hole at 3196 m MD.

7.3.5.3 Spatial organization of permeable fracture zones

GRT-1 is nearly vertical and intersects one OP fracture zone in the granite protolith (Figure 7.14 and Table 7.3). GRT-2 is inclined and intersects four OP fracture zones in the granite and two in the overlying clastic sediments (Figure 7.16 and Table 7.3). The permeable fractures are roughly oriented N170°E-N175°E and dip 85°E and 65°W in both wells (Figure 7.20) and mimic the main fracture set observed in the open-hole sections [*Vidal et al.*, 2016b]. The orientation and dip of permeable fractures are not linked to the polarity of the temperature anomaly.

In the granitic basement, two main major permeable fractures intersect the boreholes: one along GRT-1 at 2368 m MD (GRT1-FZ2368), i.e., 2352 m True Vertical Depth (TVD), and one GRT-2 at 2774 m MD (GRT2-FZ2774), i.e., at 2393 m TVD (Table 7.3 and Figure 7.21a). They both strike N170°E and dip moderately westward. On Figure 7.21c, they appear as two parallel planar structures in the granitic formation with roughly the same dip direction.

Table 7.3 Major OP fractures observed from borehole data in GRT-1 and GRT-2

Geology	Name	Measured Depth	True Vertical Depth	Strike	Dip	Thickness	Temperature anomaly
		m	m	deg	deg	cm	
			GRT-1				
Highly Altered and fractured Granite	GRT1-FZ2328	2328	2312.5	N20°E	50°W	23	Negative
Highly Altered and fractured Granite	GRT1-FZ2368	2368	2352	N170°E	55°W	24	
			GRT-2				
Triassic sandstones	GRT2-FZ2248	2248	1974.5	N10°E	72°E	3.2	Positive
Triassic sandstones	GRT2-FZ2248.5	2248.5	1974.5	N147°E	80°E	3	
Triassic sandstones	GRT2-FZ1.2263	2263	1986	N05°E	67°E	2	
Triassic sandstones	GRT2-FZ2.2263	2263	1986	N145°E	81°W	1.8	
Permian sandstones	GRT2-FZ2455	2455	2141	N152°E	66°E	1.1	Negative
Highly Altered and fractured Granite	GRT2-FZ2534	2534	2207	N0°E	80°E	6.2	Positive
Highly Altered and fractured Granite	GRT2-FZ2540	2540	2209.5	N10°E	72°E	1.5	
Highly Altered and fractured Granite	GRT2-FZ2770.5	2770.5	2390	N160°E	87°W	3.6	Positive
Highly Altered and fractured Granite	GRT2-FZ2774	2774	2393	N170°E	64°W	17	
Highly Altered and fractured Granite	GRT2-FZ2787	2787	2404	N45°E	87°E	4	
Highly Altered and fractured Granite	GRT2-FZ2788	2788	2404.5	N0°E	55°W	3	

In GRT-1, the main major permeable fracture GRT1-FZ2368 is a thermohydraulic interface located below a highly altered, porous and fractured granite with an apparent thickness of 40 m. At the top of the alteration zone, there is a second but less pronounced major permeable fracture GRT1-FZ2328 (Table 7.3 and Figure 7.21). These two fractures present a similar orientation and dip. GRT1-FZ2328 does not match in depth with the temperature anomaly but it is probably associated to the large negative anomaly below.

In GRT-2, the main major permeable fracture GRT2-FZ2774 is surrounded by a porous and highly fractured granite with an apparent thickness of 45 m. Several other majors fractures are affecting this granitic section whose four are permeable (Table 7.3 and Figure 7.21d): GRT2-FZ2770.5 and GRT2-FZ2788 which are collinear to the mean of the fracture set (N170°E, Figure 7.16d) with a primarily westward dip; and GRT2-FZ2767 and GRT2-FZ2787 which are roughly

perpendicular to the mean fracture set (Figure 7.16d) with a primarily westward dip.

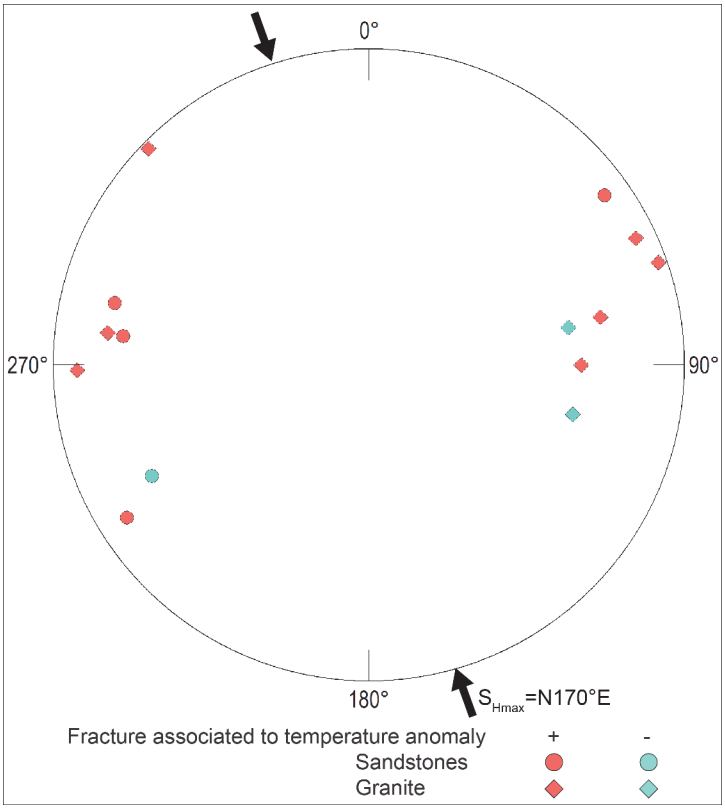

Figure 7.20 Schmidt diagram lower hemisphere of permeable fractures affecting granite and sandstone in GRT-1 and GRT-2. Data are from Table 7.3. Disks are for fractures in sandstones, diamonds for granite, blue for fractures associated to negative temperature anomaly and red for positive one.

Figure 7.21 (next page) 3D geometrical modeling of permeable fractures observed in GRT-1 and GRT-2 a) N-S cross section through GRT-1 and GRT-2, fractures are represented as disc with their strike (white horizontal bar) and dip direction (white vertical bar) on it b) Zoom of N-S cross section in the open-hole section of GRT-2 c) map view of permeable fractures in GRT-1 and GRT-2, fracture strike is the high bar and fracture dip is the perpendicular small bar d) zoom of permeable fractures in GRT-2 open-hole section. Symbol sizes are according to mud losses observed during drilling operation (see section 7.3.5.2). Data are from Table 7.3.

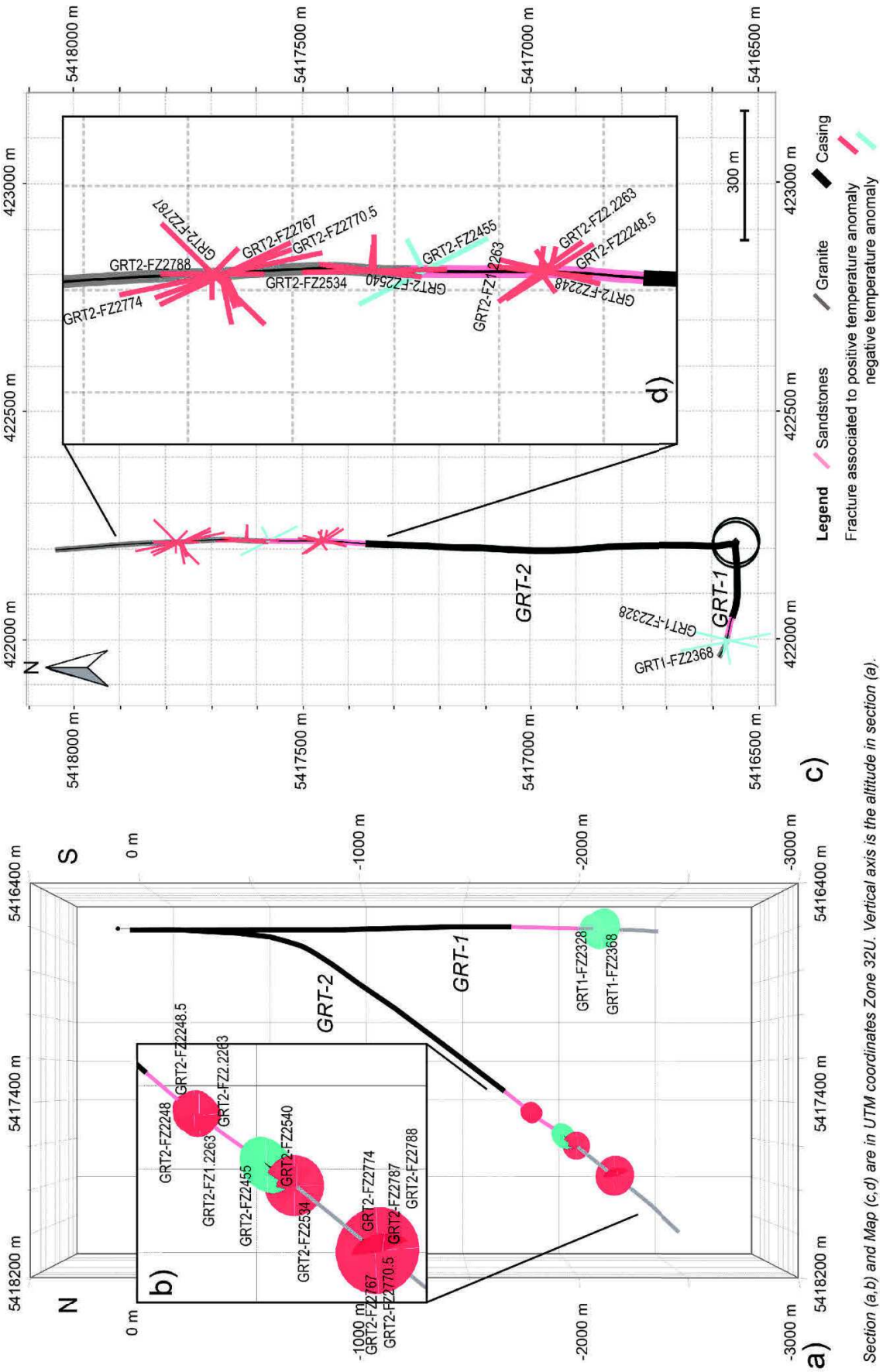

Section (a,b) and Map (c,d) are in UTM coordinates Zone 32U. Vertical axis is the altitude in section (a).

At the top of the granitic basement, two eastward-dipping major permeable fractures (GRT2-FZ2534 and GRT2-FZ2540) are nearly conjugated to the main fracture set striking N170°E. They delimit a porous and highly fractured granitic section. Also, the geometrical model suggests that they probably intersect the GRT2-FZ2774 fracture (Figure 7.21b). However, their spatial extents could be overestimated. In the sandstones, two intersecting striking directions (N10°E and N150°E) are observed. In the Permian sandstones, one isolated major permeable fracture GRT2-FZ2455 located at 2141 m TVD, dips eastward (Figure 7.21d). Above it, in the Triassic sandstones, the fracture zone is composed of two closely spaced major permeable fracture couples located at the base of highly fractured section of sandstones (GRT2-FZ1.2263 and GRT2-FZ2.2263) and at its top (GRT2-FZ2248 and GRT2-FZ2248.5). In both couples, one major permeable fracture strikes N10°E (GRT2-FZ1.2263 and GRT2-FZ2248) and the other strikes N150°E (GRT2-FZ2.2263 and GRT2-FZ2248.5). In the bottom couple, they are antithetic fractures that intersect each other. The highly fractured section of sandstones is also composed of thick sealed fracture.

7.3.6 Discussion

7.3.6.1 Permeable fracture zones in the Rittershoffen wells

The geothermal target was the Rittershoffen normal fault known at seismic scale from geophysical data that host the main hydrothermal circulation system (Figure 7.22a) [*Baillieux et al.*, 2014; *Baujard et al.*, 2017]. The local Rittershoffen fault is oriented N-S and dips westward. The granitic basement is highly fractured at all scales, from large faults to small-scale fractures to micro-cracks at the grain scale. Hydrothermal circulations occur at several fracture scales. Both geothermal wells intersect permeable fracture zones in the sandstones and granitic basement (Table 7.3 and Figure 7.21a). The maximum horizontal stress S_{Hmax} is oriented N170°E (Figure 7.20) [*Hehn et al.*, 2016].

GRT-1 is nearly vertical and the natural permeability is localized in a single permeable fracture zone between 2326 and 2369 m MD in the granitic basement (Figure 7.14). First-order permeability indicators indicate that the main fluid pathway is located at 2368 m MD. It correspond to an open thick fracture (GRT1-FZ2368) at the interface between a highly hydrothermally altered granitic section

above and a poorly altered and fractured granite below (Figure 7.10). This petrographic contrast suggests that the main fluid pathway could be a slip surface with a significant displacement and thus, the highly hydrothermally altered granitic section could be the hanging wall of the fracture zone. Observations of quartz veins associated to first-order permeability in the core zone coincide with conceptual models [*Caine et al.*, 1996; *Genter et al.*, 2000]. This fracture zone presents an asymmetrical structure with a 40-m thick of highly hydrothermally altered granite located above the main fluid pathway. This asymmetric structure slightly differed from fracture zones observed on core samples at Soultz. This highly hydrothermally altered granitic section is characterized by high porosity and occurrences of clay minerals. The presence of clay minerals tend to reduce the permeability of the fracture zone [*Caine et al.*, 1996]. First-order permeability is not observed at the borehole scale. Another fluid pathway (GRT1-FZ2328) is located at the top of the permeable fracture zone (Figure 7.15) but its permeability is probably reduced by secondary hydrothermal sealing.

GRT-2 is highly inclined to the north, and the natural permeability is localized in several permeable fracture zones in both the sandstones and the granite. The major permeable fracture zone is located between 2766 and 2800 m MD in the granite. First-order permeability indicators indicate that the main fluid pathway is located at 2774 m MD. It corresponds to an open thick fracture (GRT2-FZ2774). This main fluid pathway is surrounded by 35-m thick of highly fractured and porous granite as suggested by geophysical logs (neutron porosity, gamma ray, acoustic images). In contrast with GRT-1, this fracture zone is composed of 4 other fluid pathways (GRT2-FZ2767, -2770.5, -2787, 2788) (Figure 7.22c). As described by [*Faulkner et al.*, 2010], the presence of large-scale fractures with secant orientations favors the formation of intersections and is associated with higher permeability values. The illitization of the major permeable fracture zone is less intense than in GRT-1 [*Vidal et al.*, 2017]. The first-order permeability is supported by a more complex hydraulic network of channels than observed at Soultz. Other fracture zones contribute to the natural permeability of the well. A permeable fracture zone is located between 2532 and 2543 m MD. This zone is located 55 m below the sediment-basement interface, at the limit between the oxidized granite and the granitic protolith (Figure 7.16). Two permeable fractures

(GRT2-2534 and GRT2-2542) are surrounded by a highly fractured and porous granitic section (Figure S2). The top of the granitic basement is a porous and clay-rich zone with a high fracture density [*Vidal et al.*, 2016b, 2016c]. A 11-cm-thick open fracture was observed at 2236 m MD in GRT-1. This fracture did not behave as a permeable structure during drilling operations. This paleo weathered granitic formation is not considered as a permeable matrix or fractured aquifer. At the base of the sedimentary cover, an isolated permeable fracture zone (GRT2-FZ2455) is located at 2455 m MD and surrounded by thick sealed fractures (Figure 7.17). The Triassic sandstones also present a permeable cluster from 2245 to 2264 m MD (Figure S1). The presence of thick sealed fractures spatially closed to opened fracture at the borehole scale and the occurrences of geodic quartz, calcite and anhydrite suggest paleo-circulations that lead to fracture plug. At Soultz, fractures in sandstones are filled by barite, carbonates, secondary quartz and galena [*Vernoux et al.*, 1995; *Griffiths et al.*, 2016]. Permeable fracture zones in the Triassic and Permian sediments do not support the conceptual model proposed [*Chambon et al.*, 2006; *Rawling and Goodwin*, 2006; *Fossen et al.*, 2007].

Major permeable fracture zones intersected in both wells are a combined conduit-barrier case from the conceptual model for fault-related fluid flow in [*Caine et al.*, 1996]. They act as a short-lived conduit that then sealed to form a barrier to flow. Their permeability mainly depends on the secondary mineral deposits (quartz or clay minerals) and the secant orientation of fractures that channelized circulations favoring hydraulic connections [*Caine et al.*, 1996; *Faulkner et al.*, 2010]. Major permeable fracture zones in the granitic basement (between 2326 and 2369 m MD in GRT-1 and between 2766 and 2800 m MD in GRT-2) are heterogeneously affected by illitization due to fluid circulations [*Vidal et al.*, 2017]. In GRT-1, intense illitization observed at the top of the fracture zone suggests paleo-circulations that could plug fractures and reduce the natural permeability. In GRT-2, the fracture zone is probably less mature with a less intense illitization. The natural permeability of the well was high enough at the borehole scale for industrial exploitation and the well was not stimulated unlike GRT-1 [*Baujard et al.*, 2017].

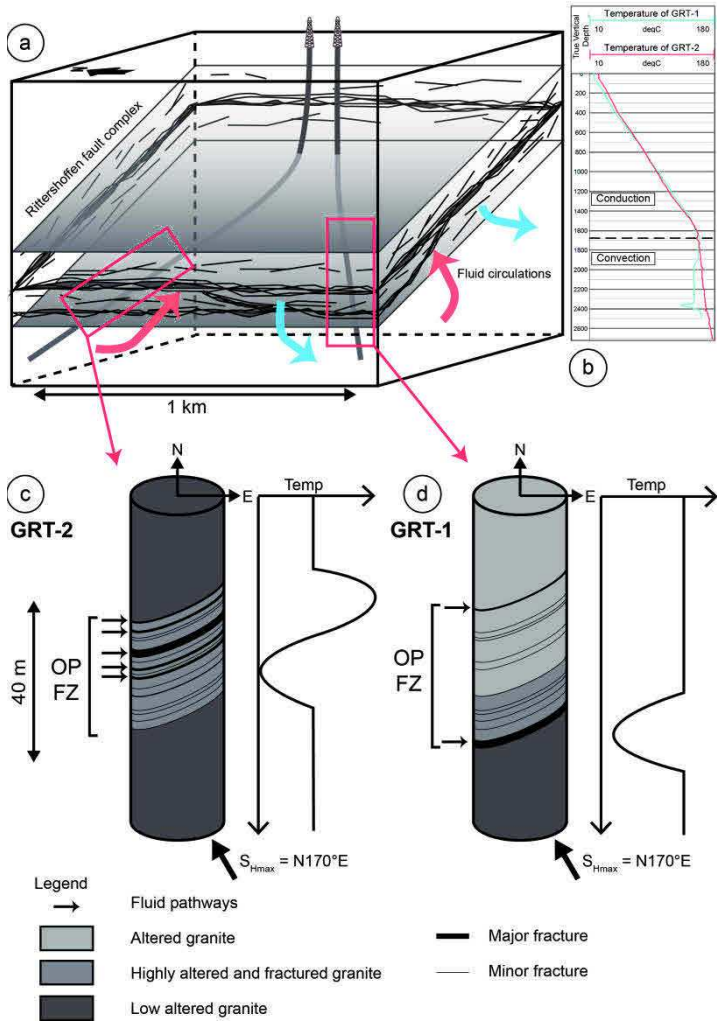

Figure 7.22 Conceptual model of permeable fracture zones in Rittershoffen wells a) geothermal wells targeted the Rittershoffen fault zone whose the major seismic plane is oriented N-S and dip moderately westward b) temperature profiles indicate a convection zone below the Triassic sediments and in the granitic basement c) schematic section of the major permeable fracture zone in the granite of GRT-2 d) schematic section of the major permeable fracture zone in the granite of GRT-1.

7.3.6.2 Thermal signature of permeable fracture zone in Rittershoffen wells

In the Triassic and Permian sediments and the granitic basement, the temperature profiles show either a null thermal gradient in GRT-1 (Figure 7.14) or a low one in GRT-2 (Figure 7.16), indicating both hydrothermal nearly-vertical circulation (Figure 7.22b) [*Baujard et al.*, 2017]. Similarly to the Soultz site, sediments above the Triassic units are associated with a very high thermal gradient of 95°C/km (Figure 7.22b) because they are heated by the hydrothermal

circulation below [*Pribnow and Clauser*, 2000; *Pribnow and Schellschmidt*, 2000]. The first-order permeability at the borehole scale is characterized by temperature anomalies on temperature profiles at thermal equilibrium, mud losses and methane emissions [*Davatzes and Hickman*, 2005a; *Mas et al.*, 2006; *Dezayes et al.*, 2010b; *Genter et al.*, 2010; *Bradford et al.*, 2013] which are dynamic information additional to the static information given by the acoustic image logs. In sandstones and granite, temperature anomalies are either positive or negative with a sharp shape or wider shape.

GRT-1 is characterized by a null geothermal gradient in the open-hole section indicative of a convective regime (Figure 7.22b). It is disturbed by one major negative anomaly of 18°C located 5 m below 2368 m MD and extending vertically for over 30 m (Figure 7.14). The maximum of the anomaly is located below the major permeable fracture (GRT1-FZ2368) in the fresh granite. The high fracture dip could also explain why the thermal profile is perturbed vertically in the borehole. The drilling mud could have invaded laterally but also vertically into the fracture zone and thus the temperature decrease could be visible deeper in the well beyond the borehole. The wide negative shape of the anomaly is attributed to remnant cooling of the highly hydrothermally altered granitic section from 2325 to 2370 m MD by mud losses during drilling (Figure 7.22d). The amplitude of the anomaly was increased after the TCH stimulation due to remnant cooling associated with the 7700 m^3 of geothermal fluids injected during TCH stimulation . In the granitic basement, the temperature profile of the GRT-1 well is similar to that of the Soultz wells [*Pribnow and Schellschmidt*, 2000; *Baujard et al.*, 2017].

GRT-2 is characterized in the open-hole section by a 18°C/km geothermal gradient and 6 localized temperature anomalies (2 in the sandstones and 4 in the granite) (Figure 7.16). In the granitic basement, the temperature profile is disturbed by one major dual positive-negative anomaly which is interpreted as the thermal signature of the major permeable fracture zone between 2766 and 2800 m MD (Figure 7.22d). The positive part, with a maximum located at 2770 m MD, corresponds to the localized hot brine inflow through fluid pathways from 2766 to 2795 m MD (GRT2-FZ2767, -FZ2770.5, -FZ2774, -FZ2787, -FZ2788). The negative part below, with a minima located at 2795 m MD, is interpreted as a more disseminated zone corresponding to the remnant cooling of the fractured

and porous zone until 2800 m MD. Moreover, the temperature profile in GRT-2 is disturbed by three other temperature anomalies in the granitic basement and two others in the sandstones that, in terms of depth, correlate with permeable fracture zones observed at the borehole scale. At the top of the granitic basement, a sharp positive anomaly is attributed to local fractures (GRT2-FZ2534 and GRT2-FZ2540). Deeper, two large negative anomalies are observed in the granitic basement: minimums are observed at 2960 m MD and at 3060 m MD, whereas standard geophysical logs indicate fractures at 2950 m MD and 3050 m MD. Upward in sandstones, the amplitudes of the thermal anomalies are smaller in term of amplitude: (1) in the Triassic sandstones, the wide positive anomaly, with a maximum located at 2263 m MD, is associated with two fracture couples separated by 20 m width of highly fractured and low-porosity matrix; (2) in the Permian sandstones, the wide negative anomaly peaks at 2464 m MD and is situated below an open fracture (GRT2-FZ2455) surrounded by sealed fractures in the low-porosity matrix. In GRT-2, the higher geothermal granite and the several temperature anomalies suggests consequently more complex circulation at the borehole scale.

Several negative anomalies are shifted downward compared to fractures observed in boreholes images in GRT-1 (at 2380 m MD) and in GRT-2 (at 2464 m, 2795 m 2960 m and 3060 m MD) whereas the depths of the positive anomalies in GRT-2 (at 2263 m, 2537 m and 2770 m MD) correspond to the depths of open fractures at the borehole scale. Inflow probably occurs through the main fluid pathway in GRT-1 (at 2368 m MD) but its thermal impact is likely hidden by the superimposed cooling effect of the highly hydrothermally altered granite.

7.3.6.3 Scale of permeability into Rittershoffen reservoir

The geothermal wells GRT-1 and GRT-2 targeted the local normal Rittershoffen fault zone (Figure 7.22a). At seismic scale, the local normal fault of Rittershoffen presents a main fault plane, which strikes nearly N-S, dips 45°W and has a 200-m apparent vertical offset (Figure 7.9) [*Baujard et al.*, 2017]. The Rittershoffen fault zone is connected to a dense vertical network of natural individual fractures. A complex convective system could circulate through this natural fracture network. In the nearby Soultz wells, *Sausse and Genter* [2005] proposed that two

types of permeable fractures are superimposed in the geothermal granitic batholith reservoir: (1) a wide and regular primary network of thin fractures and (2) thick local secondary permeable fractures which are studied in the present Rittershofen wells. The latter is a first-order permeability that responds quickly whereas the small-scale fracture network is related to a long-term permeability.

The probability that the vertical trajectory of GRT-1 intersects a vertical fracture network is low. The unique thermal anomaly in the granitic basement of GRT-1 suggests that the well intersects once the natural fracture network connected to the Rittershoffen fault zone. The initial productivity of the well is low with a productivity index of 0.60l/s/bar [*Baujard et al.*, 2017]. Although the GRT-2 trajectory is parallel to northern branch of the Rittershoffen fault, the inclined trajectory provides a higher probability of intersecting permeable fractures and could contribute to the higher productivity of the well. The various thermal anomalies in the granitic basement and the sandstones of GRT-2 suggest that the well intersects the natural fracture network connected to the fault zone several times. The initial productivity of the well is characterized with a productivity index higher than 3 l/s/bar [*Baujard et al.*, 2017]. The well inclination has a very important role in the probability to intersect permeable fractures and could explain the difference of productivity between both wells.

At the borehole scale, permeable fracture zones are composed of several fluid pathways with a complex and asymmetric organization. The thicker fluid pathways are located at 2368 m MD, i.e., 2352 m TVD, and at 2774 m MD, i.e., 2393 m TVD, in GRT-1 and GRT-2, respectively. In both wells, they are roughly parallel structures that are oriented N170°E and dip westward (Figure 7.21c). They are both collinear to the direction of the Rittershoffen fault, known at the base of the Triassic sediments from seismic scale. A fault zone is too complex to simply link the Rittershoffen fault plane to the fracture zones observed at the borehole scale. One hypothesis could be that the Rittershoffen fault plane is winding and has a variable dip. It was intersected in GRT-1 at 2352 m TVD with a 55°W dip and in GRT-2 at 2393 m TVD with a 64°W dip. If both of these structures represent the same Rittershoffen plane, the fault would need to exhibit a small twist eastward, not observed at seismic scale, between GRT-1 and GRT-2 trajectories. The fault zone would present a better connection to the fracture

network and thus more permeability in the area of GRT-2. The second hypothesis is that the Rittershoffen fault zone is composed of several nearly parallel planes oriented N-S and dipping westward. The GRT-1 well could intersect one plane dipping 55°W at 2352 m TVD, and the GRT-2 well could intersect a second plane dipping 64°W at 2393 m TVD located to the east of the plane intersected by GRT-1 and presenting a better connection to the fracture network and thus higher permeability. Nevertheless, the hydraulic data during low-pressure injection of water of the TCH stimulation raise the question if this well really intersects the main fault plane [*Baujard et al.*, 2017].

At larger scale, during the low-pressure injection of water of the TCH stimulation, induced seismicity activity was monitored [*Maurer et al.*, 2015]. A 2D approach reveals a microseismic cloud oriented N25°E and dipping westward [*Lengliné et al.*, 2017]. The cloud intersects GRT-1 trajectory but not GRT-2. The relative location of microseismic events is uncertain in the three space directions. Shifts of several tens of meters may exist. Focal mechanisms of the two biggest events were calculated and correspond to this orientation N25°E. However, it is challenging from two focal mechanism values to extrapolate at 3D reservoir scale that it is the dominant orientation. Moreover, it was demonstrated at Soultz, that the larger magnitude events are not representative to the background microseismicity cloud [*Cuenot et al.*, 2008]. The N25°E orientation is mainly observed at the borehole scale, especially at 2000 m MD in GRT-1 within the sandstone (Figure 7.14a). Deeper, this direction exists in the granite even the fracture orientations are more scattered (Figure 7.14b). In GRT-2 this N25E direction is not dominant where fracture geometry presents a relative stability [*Vidal et al.*, 2016b] or at the seismic scale [*Baujard et al.*, 2017]. At Soultz, several kilometer lengths of borehole log analysis in the Soultz granite recorded with the same acoustic borehole tool clearly illustrate a dominating fracture orientation in the basement around N160°E [*Genter and Traineau*, 1996; *Genter et al.*, 1997a; *Valley*, 2007]. However, the focal mechanisms present a high variability and are not representative of the fracture orientations at the borehole scale [*Horálek et al.*, 2010; *Schoenball et al.*, 2012]. Without a more representative panel of focal mechanisms, a theory would be a growth of a seismic cloud oriented N25°E induced on roughly NS- and EW-trending

structures that are ordered in an echelon like arrangement as proposed after development of Basel geothermal reservoir [*Häring et al.*, 2008]

Therefore, high-precision mapping of the induced seismicity is a good method highlighting structures in the granitic basement, however it does not necessarily correspond to the primarily permeable structures into the reservoir.

7.3.7 Conclusions

Several hundred natural fractures intersect the respective open-hole sections of two recently drilled geothermal wells, GRT-1 and GRT-2, at Rittershoffen in the Upper Rhine Graben (France). Their structural analysis shows a nearly-conjugated pattern of sub-vertical fracture oriented N170E and dipping eastward and westward. The natural fracture location correlated with various geophysical logs and mud logging data, reveals that a few of them show evidence of natural permeability during and after drilling operations. Temperature anomalies, mud losses and gas emissions are good indicators of permeable structures at the borehole scale when they are spatially correlated to fractures observed in acoustic image logs or caliper logs. Positive temperature anomalies are associated with geothermal water inflow through the main permeable fractures. Negative temperature anomalies are associated with the cooling of the porous and fractured alteration zones which are invaded by drilling mud during drilling operations and/or water injections. One major permeable fracture zone was intersected in the granitic basement of GRT-1. In GRT-2, two permeable fracture zones were observed in sandstones, and four permeable fracture zones were observed in the granitic basement. The permeable fractures are mainly striking N170°E and dip steeply westward or eastward. Main fracture zones in GRT-1 at 2368 m MD (2352 m TVD) and in GRT-2 at 2774 m MD (2393 m TVD) are N170°E-oriented and dip westward. The geometrical modeling shows that they are parallel to the local Rittershoffen fault initially targeted. However, the geometrical modeling is limited to the immediate vicinity of the boreholes, and the 3D organization of fracture in the far-field is not evaluated in this study. Other permeable fractures are observed at the borehole scale with secant directions. These fractures may form a dense network of natural fractures that are connected to the fault zone and host the main hydrothermal circulation. The

nearly vertical trajectory of GRT-1 probably intersects the dense network of natural nearly-vertical fractures connected to the fault zone only once. The inclined trajectory of GRT-2, which is parallel to the fault zone, probably intersects the dense network of natural fractures connected to the fault zone several times, enhancing its productivity. In Rittershoffen wells, permeable fracture zones are composed by several fluid pathways. The permeability is closely linked to occurrences of secondary minerals deposited during paleocirculations, particularly clay minerals that plug the fracture system. Furthermore, the inclined borehole trajectory increases the connection to intersect permeable fractures of the vertical fracture system.

7.3.8 Acknowledgments and Data

This work was based on data from the ECOGI geothermal project at Rittershoffen, France. The data for this paper are available by contacting the corresponding author at j.vidal@unistra.fr. A part of the work was performed in the framework of the LabEx G-Eau-Thermie Profonde, which is co-funded by the French government under the program “Investissements d’Avenir”. The manuscript was prepared as a contribution to the PhD thesis of Jeanne Vidal, co-funded by ADEME (French Agency for Environment and Energy). A part of this work was done in the framework of the EGS Alsace project co-funded by ADEME and Electricité de Strasbourg. A part of this work was done by ES-Géothermie in the framework of the H2020 DESTRESS Eu project which has received funding from the European Union Framework programme for Research and Innovation under grant agreement No. 691728. The authors acknowledge Midland Valley Exploration Ltd. for the use of MOVE™ modelling software under the Academic Software Initiative. The authors acknowledge the GEIE EMC for providing Soultz borehole data and core samples. Finally, the authors would like to kindly thank the two reviewers, Colleen Barton and Nick Hayman, the associated editor, Robert Lowell, and the editor, André Revil, for their contributions and manuscript improvement.

7.3.9 Supporting Information

This supporting information provides detailed descriptions of a permeable fracture zones in the Triassic sandstones in the granitic basement of the

geothermal well GRT-2 at Rittershoffen. It presents the acoustic image logs and their structural interpretation.

7.3.9.1 Text S1: Description of the major OP fracture zones affecting Triassic sandstones in GRT-2

In the Triassic sandstones of GRT-2, an OP cluster is observed. Associated variations of standard geophysical logs and mud logging data are described in section 4.2 and Figure 7.16. The cluster is considered as OP because it is associated with a large positive temperature anomaly (+2°C at 2263 m MD). The structural interpretation of the permeable cluster is based on acoustic image logs. At the top of the cluster, two major fractures intersect each other at 2248 m MD (Figure S1a). The first OP strikes N10°E, dips 72°E, and has a thickness of 3.2 cm. It is surrounded by a large sinusoidal trace, approximately 13 cm above and 7 cm below, with a higher amplitude than the major fracture but a lower than the host rock. The sinusoidal trace is not continuous on the transit time track. It is interpreted as a thick partly sealed fracture zone. Above, another sealed fracture, striking N172°E and dipping 75°E, is observed with a thickness of 2.7 cm. Cutting observations at this depth indicate presence of geodic quartz, calcite and barite. The hydrothermal sealing of fracture probably reflects paleo-circulations into these fractures. The OP fracture strikes N147°E and dips 80°E with a thickness of 3 cm. The bottom of the cluster is also marked by two major fractures intersecting each other at 2263 m MD (Figure S1b). The first OP strikes N05°E, dips 67°E, and has a thickness of 2 cm. The second OP strikes N145°E, dips 81°W, and has a thickness of 1.8 cm. Fracture traces are hardly distinguished on transit time track but acoustic image logs are affected by eccentering effect in this section.

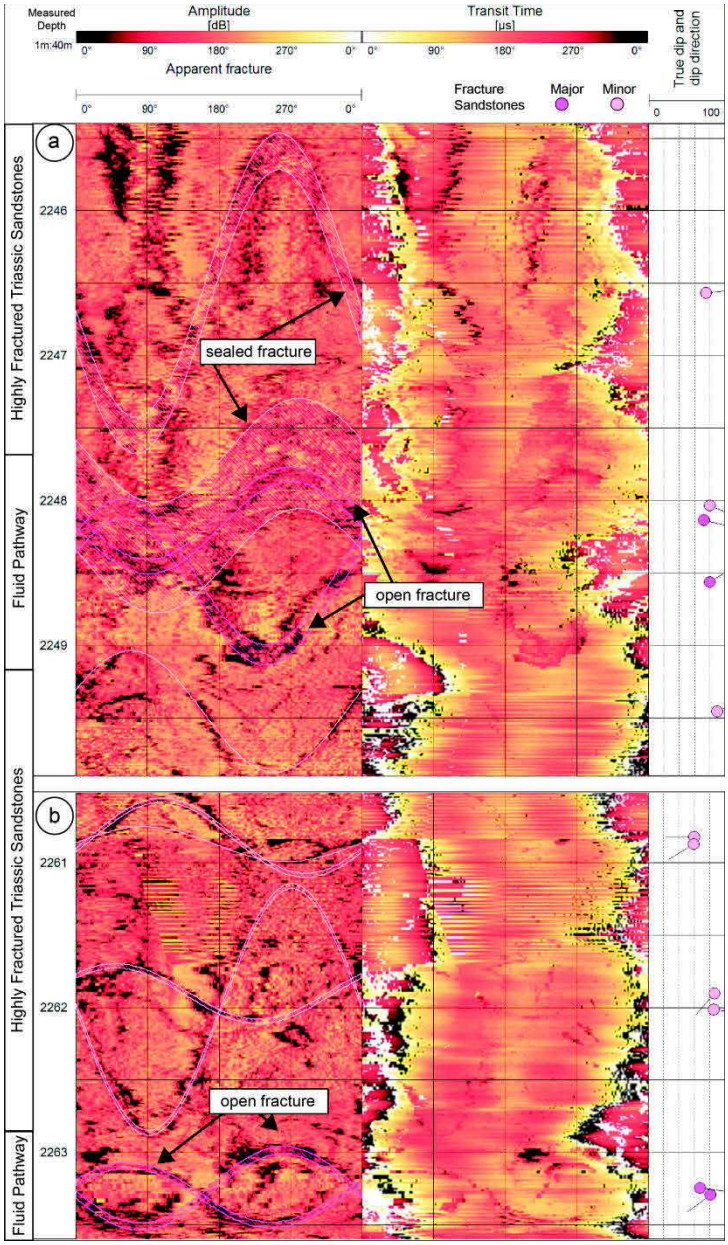

Figure S1. Major OP fracture zones affecting Triassic sandstones in GRT-2 a) major fractures at 2248 m MD b) major fractures at 2263 m MD. Colors used for structural interpretation are similar to the legend Figure 7.16 (light pink = minor fracture and dark pink = major fracture)

7.3.9.2 Text S2: Description of the major OP fractures affecting the top of the granitic basement in GRT-2.

At the top of the granitic basement, an OP fracture zone is observed. Associated variations of standard geophysical logs and mud logging data are described in section 4.2 andFigure 7.16. The fracture zone is considered as OP because it is associated to a methane occurrence, mud losses and a positive temperature

anomaly of +2°C at 2537 m MD (Figure 7.16). The acoustic data were only partially acquired at this depth (Figure S2b and c). To obtain an accurate strike and dip for the structure, the oriented 6-arm caliper data are used (Figure S2a). In this highly deviated well, the caliper data present a peak of 27 cm at 2535.7 MD on the first arm, 7.5 cm at 2535.2 MD on the third arm and 17 cm at 2535.5 MD. This indicates a fracture striking N-S and dipping 80°E. The acoustic data, which are rather difficult to interpret as this depth, show a sinusoidal trace of the top of a structure that could match the strike and dip of the fracture plane derived from the caliper data (Figure S2b). The structure presents a thickness of 6.2 cm and a free aperture. Even if the fracture trace is not continuous on the amplitude and the transit time track, the fracture is partly sealed at the borehole scale. In amplitude track, geodic quartz with high reflectivity is observed in the fracture trace as well as on cuttings observations at this depth. A second structure is observed at 2542 MD that strikes N10°E and dips 72°E (Figure S2c). It is also visible on caliper data. It presents a thickness of 1.5 cm and a free aperture (Figure S2c). The fracture trace is again not continuous on the amplitude and transit time track and the fracture is probably partly sealed at the borehole scale. Both structures are considered OP fractures.

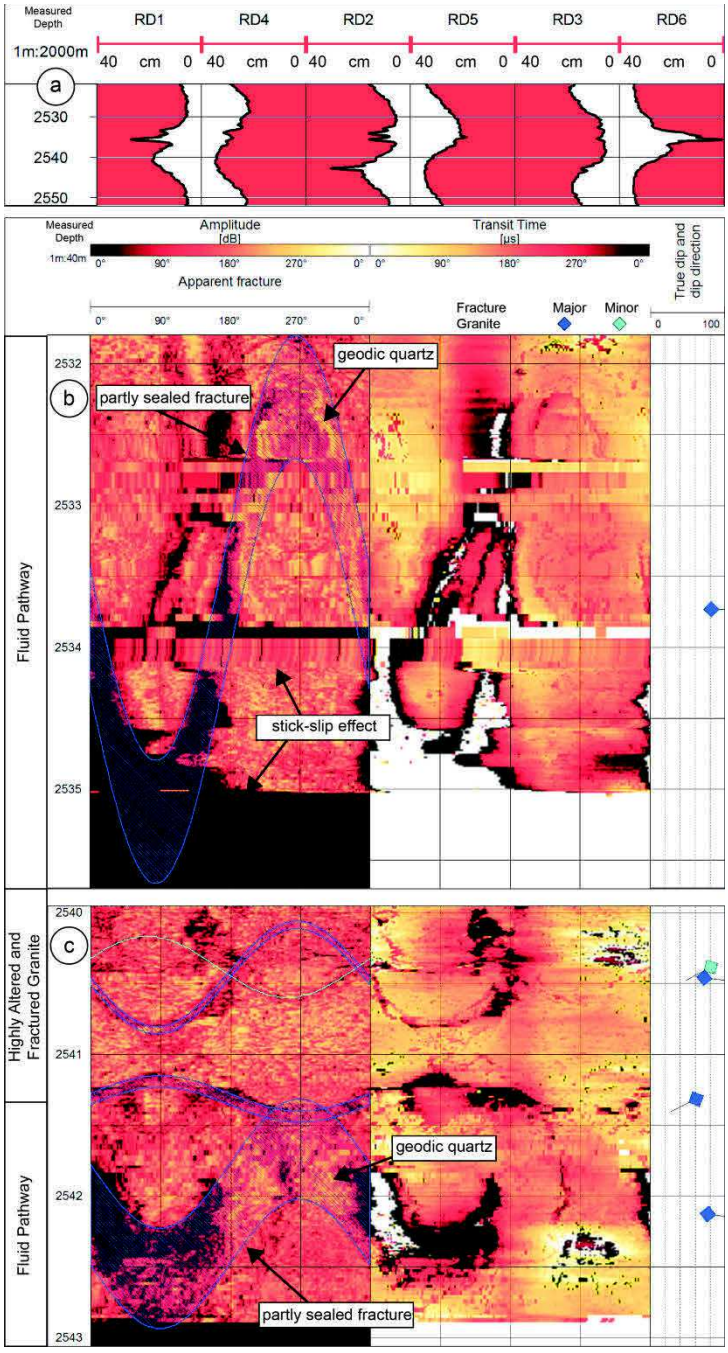

Figure S2. Major OP fractures affecting the base of the oxidized granite in GRT-2 a) 6-arm caliper data presenting hole diameter b) major fracture at 2534 m MD c) major fracture at 2542 m MD. Colors used for structural interpretation are similar to the legend Figure 7.16 (light blue = minor fracture and dark blue = major fracture).

8 Signature argileuse des zones de fractures perméables

8.1 Résumé

Ce chapitre s'appuie sur les données pétro-minéralogiques des cuttings échantillonnés autour des zones de fractures perméables des puits GRT-1 et GRT-2. L'objectif est d'évaluer l'altération hydrothermale liée à ces zones de fractures perméables identifiées dans le chapitre 7. Le chapitre se focalise sur les minéraux argileux. Il se décompose en trois parties.

La première partie du chapitre s'appuie sur un résumé étendu présenté aux 41st Workshops on Geothermal Reservoir Engineering à l'Université de Stanford en Californie en février 2016. Il est disponible sous la référence : Vidal J., Ulrich, R., Whitechurch H., Genter A., Schmittbuhl J., Dalmais E., Girard-Berthet V. (2016). Hydrothermal alteration of the hidden granite in the geothermal context of the Upper Rhine Graben, *41st Workshop on Geothermal Reservoir Engineering*, February 22 - 24 2016, Stanford University, California, USA. La section 8.2 est légèrement modifiée par rapport à au résumé étendu publié.

L'étude du profil de température de Soultz a montré une transition de la conduction à la convection au toit du socle (section 6.3). L'interface de la couverture sédimentaire et du socle granitique est attractive pour l'exploitation géothermale car elle coïncide avec la partie sommitale des cellules de convection. La ressource géothermale est donc accessible à faible profondeur. La température augmente très peu avec la profondeur dans le granite avec un gradient de 5°C/km, or le prix du forage est exponentiel avec la longueur forée. Les 100 premiers mètres du socle granitique pourraient donc être une cible attractive. Cependant, les forages du Fossé rhénan supérieur ont révélé que cet horizon n'était pas un aquifère perméable. Le toit du socle granitique correspond à un granite oxydé affecté par une paléo-altération supergène. Son émersion au Permien a entraîné une forte hématisation. Bien que la fracturation soit intense au toit du granite dans les puits de Soultz [*Genter and Traineau*, 1996] et de Rittershoffen (section 7.2), les fractures recoupées par les puits ne montrent pas

d'indice de perméabilité dans le toit rubéfié du granite. L'étude suivante cherche à comprendre l'absence de perméabilité et la production radiogénique élevée dans le granite oxydé à partir d'observations minéralogiques sur des carottes du puits d'exploration EPS-1 de Soultz. Une lame mince issue d'une fracture scellée a été analysée par Microscopie à Balayage Electronique (MEB) et spectrométrie (LA-ICP-MS). Des cartographies minérales ont été réalisées à partir des données de MEB et ont révélé un lien très proche entre les quartz, les carbonates et les illites au sein de la fracture. Au cœur de cette fracture, les feldspaths potassiques sont dissous. Les quartz et les carbonates ont probablement été déposés dans conditions géochimiques différentes. L'illite semble sceller l'ensemble des minéraux secondaires dans les fractures. Elle pourrait jouer un rôle central dans la perte de porosité au sein de la fracture. Cependant, la quantification de cette perte de porosité reste à évaluer. La chronologie des évènements de dissolution et de précipitation qui sont à l'origine de l'absence de perméabilité de la fracture n'est également pas établie. Ces résultats préliminaires mériteraient d'être approfondis et étendus à plusieurs zones de fractures du granite rubéfié afin de généraliser les résultats.

Le rôle des argiles secondaires issues des évènements hydrothermaux successifs dans les zones de fractures perméables des puits de Rittershoffen est présenté dans la seconde partie du chapitre. La signature argileuse des zones de fractures dans le socle granitique est présentée sous forme d'un article soumis dans la revue Journal of Volcanology and Geothermal Research.

Dans la première partie de cette étude, les cuttings ont été analysés dans les sections en trou ouvert des puits GRT-1 et GRT-2 pour évaluer l'altération hydrothermale dans le socle granitique à l'échelle du puits. Le degré d'altération du granite est déterminé à partir de l'abondance d'argiles observées dans les cuttings. Les degrés d'altération les plus intenses se distribuent autour des zones de fractures perméables identifiées dans le chapitre 7. Le socle granitique du puits GRT-1 montre un degré d'altération plus élevé que dans le puits GRT-2. Les zones de fractures perméables sont aussi associées à une décharge du fluide avec une abondance de quartz secondaires. Cependant, l'étude se focalise sur la fraction argileuse (<5 µm). Une cinquantaine d'échantillons sélectionnés autour des zones de fractures perméables est analysée par Diffraction aux

Rayons X (DRX) et par MEB. Les résultats issus de ces analyses montrent trois populations de minéraux illitiques distinguées par leur taille de domaine chohérent : des illites bien cristallisées avec un domaine cohérent plus grand que les illites dites mal cristallisées. Parmi ces illites mal cristallisées, on observe des interstratifiés de type illite-smectite (avec ~10% de smectite). La proportion d'illites bien cristallisées augmente avec la profondeur tandis que les illites mal cristallisées diminue. Localement, la présence d'interstratifiés illite-smectite est corrélée à la présence des zones de fractures perméables dans les deux puits. Deux populations de chlorite sont également observées : une chlorite ferro-magnésienne issue de l'altération des biotites primaires dans le protolithe granitique et une chlorite riche en fer présente sous forme de fines cristallites au sein des fractures. La chorite riche en fer est très peu présente dans les zones de fractures du puits GRT-1 en comparaison au puits GRT-2.

Ces minéraux argileux sont le résultat de plusieurs évènements hydrothermaux superposés. Une altération propylitique ancienne affecte l'ensemble du socle granitique et est à l'origine de la séricitisation des minéraux primaires, de la transformation des biotites primaires en chlorite ferromagnésienne et de la précipitation d'épidote. Elle est associée à des températures élevées entre 200° et 400°C [*Reyes*, 1990]. Une altération hydrothermale liée aux zones de fractures affecte de manière plus localisée le socle granitique. Trois paragenèses différentes sont observées :

- Illite + quartz + hématite +/- calcite
- Illite + chlorite ferreuse +/- pyrite
- Illite + interstratifiés illite-smectite + hématite +/- calcite

Ces trois paragenèses sont superposées au sein des fractures mais sont déconnectées dans le temps en raison des conditions de cristallisation physico-chimiques différentes. La précipitation de la chlorite ferreuse et de pyrite est possible dans des conditions réductrices à des températures plus élevées que les températures actuelles. La précipitation d'illite et d'hématite est possible dans des conditions oxydantes. Seuls les interstratifiés illite-smectite précipitent aux températures observées actuellement (environ 160°C). Leur présence conjointe

semble être un bon indicateur pour localiser les zones de circulations actuelles et anciennes dans les forages de Rittershoffen. L'abondance des interstratifiés illite-smectite peut entraîner un colmatage de la zone de fracture et une réduction partielle ou totale de sa perméabilité.

Dans le puits GRT-1, la présence d'interstratifiés illite smectite du haut de la zone de fractures perméables principale jusqu'au toit du socle, de 2340 à 2212 m MD, est associée une perméabilité très faible. Dans le puits GRT-2, les interstratifiés illite-smectite sont également observés dans les zones de fractures perméables du socle granitique. En revanche, la chlorite ferreuse est encore observée ce qui suggère une illitisation moins intense. Les paléo-circulations ont probablement conduit à une illitisation plus faible dans le puits GRT-2 ce qui expliquerait en partie une perméabilité naturelle plus élevée.

L'étude des minéraux argileux dans les grès n'a été réalisée que dans GRT-2. La signature argileuse des zones de fractures perméables dans les grès semble différente de celle du granite. Cependant, la signature hydrothermale est compliquée à identifier car elle est superposée à la signature de la diagenèse encore mal connue. La présence de la chlorite ferreuse, communément observée au sein des zones de fractures dans les grès triasiques et permiens, témoigne des évènements hydrothermaux. Des études complémentaires sont nécessaires pour appréhender la signature hydrothermal et celle de la diagrenèse.

8.2 Altération hydrothermale au toit du socle rubéfié dans le puits EPS-1 de Soultz

8.2.1 Abstract

The sedimentary cover of the Upper Rhine Graben (URG) is locally characterized by a thermal gradient up to 100 K/km like in Soultz-sous-Forêts or Rittershoffen (France). This high thermal gradient decreases to 5 K/km at the sediment-basement interface due to hydrothermal convective cells that circulate inside a nearly vertical fracture network affecting both the granite basement and the Triassic sediments above it. Therefore the sediment-basement interface is very challenging because the high thermal flux is attractive for geothermal exploitation. However natural permeability, evidenced by brine circulation, was only observed when the well cross-cuts a Hydrothermally Altered Fractured Zone in the deep Paleozoic granite. The uppermost top section of the granite was affected by a paleo-weathering superimposed alteration and is highly fractured but permeability evidence of this section was never clearly observed during drilling operations. In order to explain the permeability behaviour of fracture at the top of the basement, a detailed mineralogical investigation was carried out. Thin sections from a fully core Soultz well, EPS-1, were observed and analysed by several in situ technics including electron microprobe, SEM and LA-ICP-MS. Chemical maps were also acquired by SEM and treated based on a new routine, specially developed Matlab©-based code, in order to identify mineral phase relationships. The results show that secondary quartz, carbonates and illite observed in the fracture network in the granite derive from multiple processes of dissolution-precipitation after hydrothermal fluid events linked to the granitic basement geological history. The formation of secondary phyllosilicates and carbonates leads to a significant gain in volume that may reduce the porosity. Based on the mineralogical observations, it is proposed that the successive hydrothermal and paleo-weathering events characterized with dissolution-precipitation cycles tend to reduce fracture/matrix permeability of the uppermost granitic basement.

Keywords: hydrothermal alteration, sediment-basement interface, Soultz-sous-Forêts, Upper Rhine Graben

8.2.2 Introduction

The thermal regime of the Upper Rhine Graben (URG) is characterized by a series of geothermal anomalies near Soultz-sous-Forêts (Alsace, France), Rittershoffen (Alsace, France) and Landau (Rhine-Palatinate, Germany). These areas reveal local thermal gradients up to 100 K/km in the uppermost part of the sedimentary cover attributed to hydrothermal convective cells circulating inside a nearly vertical fracture network in the granite basement and in the Triassic fractured sediments above it [*Schellschmidt and Clauser*, 1996; *Pribnow and Schellschmidt*, 2000]. The thermal gradient decreases slowly to 5 K/km at the sediment-basement interface. The top of the basement is thermally attractive but its hydraulic behaviour is fracture dependent. Detailed structural studies on 800 m length of continuous EPS-1 core (Soultz) on Paleozoic monzogranite showed a higher average fracture density at the top of the granite due to the superimposition of sub-vertical fractures with nearly horizontal joints [*Genter and Traineau*, 1996]. About six Soultz wells penetrated the uppermost granite section but any of them clearly shown some evidences of residual permeability during drilling operations. Residual permeability in the granite is intimately linked to Hydrothermally Altered Fractured Zones (HAFZ) showing a cluster organization deeper in the granitic basement.

In the framework of the geothermal exploration, the study of alteration at the top of the granitic basement could aim to better understand its hydraulic behaviour characterized with permeability variations. It also contributes to identify the geological factors that could impact the thermal profile such as the natural radioactivity distribution in the top basement.

For that, the study presents accurate investigations of the minerals that fill fractures at the top of the basement in EPS-1. Multiple technics include Scanning Electron Microscope (SEM) acquisition, electron microprobe and LA-ICP-MS measurements have been performed on thin sections of fractures. Results about secondary mineral phases fill fractures and their spatial relationships are correlated with geophysical well logging data interpretation and expanded to the Rittershoffen geothermal site. Final goal is to link the mineralogy of the fractures and their relative chronology of crystallization to the major tectonic events and fluid circulations in this part of the Upper Rhine Graben.

8.2.3 Geological settings

8.2.3.1 Alteration of the Soultz granite

In 1990, the old petroleum well EPS-1 is deepened to 2227 m depth MD and full cored for seismic purpose. The well penetrates the granitic basement at 1418 m depth. The deep granite is considered as an Mg-K monzogranite (Figure 8.1) [*Stussi et al.*, 2002]. The granite is composed by quartz, biotite, hornblende, K-feldspar, plagioclase and accessory minerals (magnetite, titanite and apatite). It is a very radioactive granite with U content of 10 ppm vs 4 ppm for a standard granite of the Vosges area and Th content of 27 ppm vs 15 ppm for a standard granite. The granite batholith was affected by a pervasive alteration during its emplacement that involves the alteration of plagioclase and biotite and subsequent formations of corrensite and chlorite [*Genter*, 1989, p.198]. Then the batholith has been affected by fracture event, which caused the formation of large sets of fractured zones. They represent the main pathways for circulating fluids. The subsequent hydrothermal alteration superimposes the pervasive one and significantly changed the granite mineralogy. In the matrix, corrensite and chlorite are transformed into illite [*Genter*, 1989]. K-feldspars are also transformed into illite when brittle deformation is developed. Primary plagioclases react with rich CO_2 fluid circulating into the fractured granite and carbonates crystallize into matrix and fractured zone. All these reactions are accompanied by the formation of secondary quartz.

From 1418 to 1550 m depth, the granite is affected by paleo-weathering responsible for the whole reddish color (Fe-oxides) of the top of the granitic basement. The paleo-weathering is a consequence of the paleo-emersion of the top of the granitic basement. During this period, magnetic minerals as magnetite are altered into Fe-oxides or Fe-hydroxides minerals. The matrix of the granite is highly transformed into illite with some rare K-feldspars. The uplift of the top basement involves a decompression of the rock masse and the formation of horizontal fractures called jointing. Fractures at the top basement are filled by quartz, illite, carbonates and iron oxides as hematite.

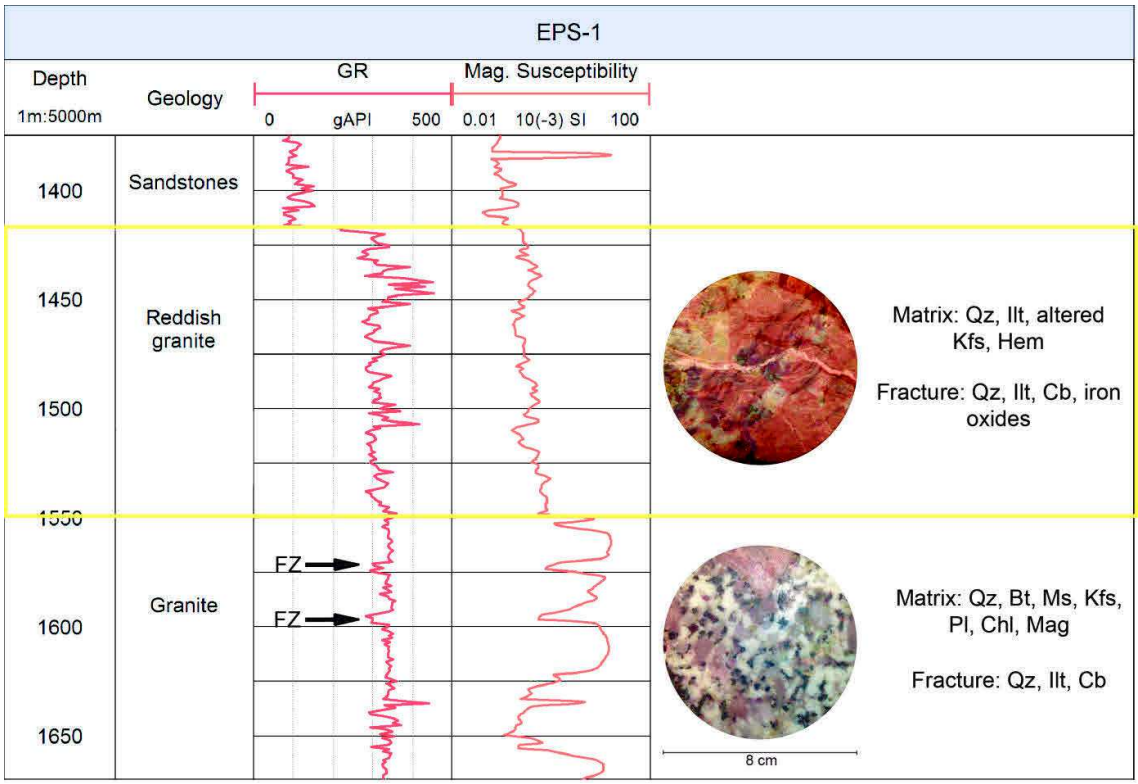

Figure 8.1 Gamma Ray and magnetic susceptibility in the well EPS-1 with core pictures of reddish granite and Mg-K granite (FZ = fractured zone, yellow frame = zone of the study, Qz=Quartz, Bt=Biotite, Ms=Muscovite, Kfs=K-feldspars, Pl=Plagioclase, Chl=Chlorite, Mag=Magnetite)

The post-Variscan tectonic events of the Upper Rhine Graben such as diagenesis, subsidence, extension or reactivation of Hercynian structures are characterized by successive hydrothermal fluid circulations. During these more recent circulations (Permian, Jurassic, Cretaceous and even younger times), illite crystallise in both veins and matrix [*Schleicher et al.*, 2006]. Ferromagnesian mineral and feldspars transformations occurred after fluid circulations. Carbonates and quartz veins precipitate and grow. The relative chronology of alteration and mineralogical transformation is not trivial because several hydrothermal circulation events took place in during the geological and tectonic history of this Paleozoic granite, which emplaces 333 M years ago [*Cocherie et al.*, 2004]. This study is focused on the major vein alteration at the top of the granite.

The granite alterations are observed macroscopically on core samples with the mineralogy but also with well-logging data. The Gamma Ray (GR) is the study of

the natural radioactivity into the well. The sediment-basement interface is evidenced by a large positive variation (from 70 to 225 gAPI) that indicates the transition to the radioactive granite. In the reddish granite section, the natural radioactivity varies from 225 to 450 gAPI while in the deep granite amplitudes of variations are more restrained (from 300 to 350 gAPI) excepted for sharp positive peaks that can reach more than 600 gAPI. The magnetic susceptibility is about 12.5 SI in the granite. In the reddish granite, it decreases to 0.4 SI that indicates the leaching of primary magnetic and ferromagnesian minerals (magnetite, biotite and hornblende) due to the superimposition of hydrothermal fluid alteration events. The important radioactivity at the top of the basement could influence the thermal flux.

8.2.3.2 Fractures in EPS-1 well

The borehole locally cross cuts fractured zones. They are evidenced by well-logging variations like the a negative anomaly of GR and magnetic susceptibility that correlate at 1570 m depth and 1670 m depth. These fractured zones could be pathways for paleo-circulation and primary minerals were dissolved (Figure 8.1). These fractures zones are also seen on core samples. Some of the fractures cross-cutting by the borehole showed a natural permeability during drilling operations and are called HAFZ. These zones combined a high fracture density and a strong hydrothermal alteration with successive dissolution-precipitation of primary minerals. At Soultz, HAFZ occurred in the deep granite where the fracture density is 3.2 fract/m whereas it is 7.6 fract/m at the top of the granite [*Genter and Traineau*, 1996].

The fracture fillings present the same mineralogy in the whole granitic basement but the proportion of minerals varies according to the granite petrography (Figure 8.2) [*Genter and Traineau*, 1996].

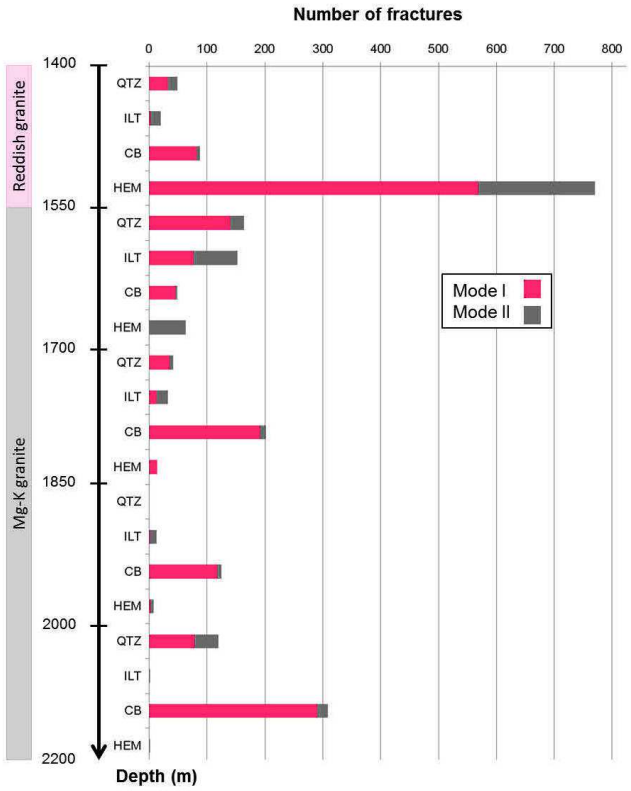

Figure 8.2 Mineral distribution in fractures of EPS-1 by section of 150-m. Fractures in Mode I and Mode II are differentiated for each mineral.

Hematite is mainly concentrated at the top granitic basement into fractures in Mode I (jointing and tension fractures), whereas illite is more concentrated into fractures in Mode II (shearing) from Mg-K monzogranite. The fracture fillings present the same mineralogy in the whole granitic basement but the proportion of minerals varies according to the granite petrography (Figure 8.2) [*Genter and Traineau*, 1996]. Hematite is mainly concentrated at the top granitic basement into fractures in Mode I (jointing and tension fractures), whereas illite is more concentrated into fractures in Mode II (shearing) from Mg-K monzogranite. Carbonates are almost exclusively present into fractures in Mode I and the number of fractures filled by carbonates increases with depth. Quartz is present in the whole granite in fractures in both Mode I and Mode II. Study of quartz vein into EPS-1 show at least seven generations of quartz [*Smith et al.*, 1998]. Primary quartz occurs as clasts and angular fragments while secondary quartz is microcrystalline. Fluid inclusion analyses indicate that they precipitate after several pulse of hot water whose the salinity and the chemical composition vary. Recent generations of quartz crystallize at the modern fluid temperature (150°C)

and pressure (20 bar) suggesting that quartz veins growth may be still active at the present day. Carbonates crystallized at 130°C [*Dubois et al.*, 2000] that corresponds more to fluids associated to early generations of quartz. The variations of fluid chemistry and temperature strongly influence the nature of the dissolution-precipitation process and minerals affected.

The relative chronology of fracture fillings is not trivial to define because several fracture and hydrothermal events are superimposed. Outcrop studies on the shoulders of the Upper Rhine Graben shows two successive stages of fillings; a sheared/cataclased phase associated with illite and quartz and a later precipitation of carbonates in tension fractures [*Dezayes et al.*, 2013b].

8.2.4 Materials and methods

40 core samples from EPS-1 well located on the first 200 meters of highly altered granite were studied. The results will be described for one sample at 1428 m depth. Into the reddish granite matrix (pink), K-felspars are highly microfractured and transformed into illite and primary quartz is visible (Figure 8.3). A fracture of ~1 cm large is filled by millimetric to micrometric grain-sized minerals, making difficult their identification only by using optical microscopy. Carbonate (in green) and secondary quartz (in blue) sometimes occur as large grains, but most of them are disseminated as a fine-grained mix with illite, iron oxides and plagioclase relics (brown area).

SEM and electron microprobe analyses were performed at IMPMC (Paris, France) on a 30 µm-thick thin section. SEM analyses were done on a ZEISS ULTRA55 equipped with a FEG-Schottky X-ray source operating at 30 nA with an acceleration voltage of 15 kV. Chemical maps were recorded with a matrix of 1024x758 pixels, a 3 µm step interval in both directions. For each map, the gray scale corresponds to the intensity of the Kα-lines of the different elements (O, Na, Mg, Al, Si, P, S, K, Ca, Ti, Cr, Mn, Fe, Ba, Th, U) calculated from the integration of a specified region of interest (ROI) of the energy range of XRF spectra. Then, ROI maps are used to calculate phase maps thanks to a new routine, specially developed Matlab©-based code, following the same approach than that previously published in Ulrich et al. (2014). The phase map calculation consists first of determining pure mineral phases that are expected to be present in the

sample, in order to create standard spectra (or ‘‘pure’’ spectra). Then, for each pixel of the map, a linear combination of the different standard spectra is performed in order to fit each single spectrum. Results provide quantitative phase maps showing the distribution of minerals previously identified in the sample.

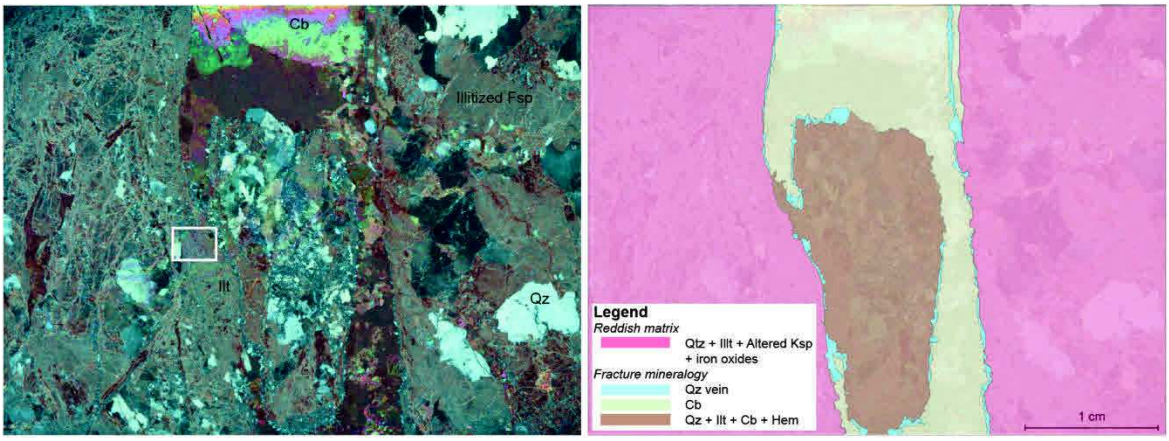

Figure 8.3 Picture of the thin section studied at the top granitic basement (left) and its schematic representation associated drawing of mineralogy observed microscopically (right). The white frame is the studied zone shown Figure 8.4.

A Cameca SX Five electron microprobe was used to determine the major element concentrations of minerals. Operating conditions were 15 kV accelerating voltage, sample current of 30 nA and count time of 3 s/element. Standards used were albite (Na), orthose (K, Al), wollastonite (Mg, Ca and Si), $MnTiO_3$ (Ti and Mn), Cr_2O_3 (Cr), Fe_2O_3 (Fe), P (Apatite), $BaSO_4$ (Ba and S), zircon (Zr), Th (monazite), U (U metal). The analyses have a spatial resolution of 1 micron. The total Fe is presented as FeO.

Trace element analyses in illite were carried out using a LA-ICP-MS at the GeoRessources laboratory (Vandoeuvre-lès-Nancy, France) composed of a 193 nm MicroLas Pro ArF Excimer coupled with the Agilent 7500c quadrupole ICP-MS. Laser ablations were performed with a constant 5 Hz pulse rate, with an ablation crater of 160 µm in diameter. The number of pulses was 200 pulses, sufficient to form a long and stable signal for integration. The ablated material is transported using a constant He flow and mixed with Ar in a cyclone coaxial mixer prior to entering the ICP torch and being ionized. The ions are then sampled, accelerated and focussed before being separated and analysed in the quadrupole mass spectrometer. The following isotopes were monitored: ^{29}Si, ^{39}K,

^{51}V, ^{53}Cr, ^{55}Mn, ^{59}Co, ^{60}Ni, ^{63}Cu, ^{66}Zn, ^{88}Sr, ^{89}Y, ^{137}Ba, ^{232}Th, ^{238}U. Data reduction was carried out using SILLS software [*Guillong et al.*, 2008] and following the standard methods of [*Longerich et al.*, 1996], and using Mg content – known from prior EMPA analyses – as an internal standard. External standard calibration was performed with the synthetic glass (NIST 610) [*Pearce et al.*, 1997].

In order to compare EPS-1 results to another geothermal well in the Upper Rhine Graben, well-logging data from GRT-1 well at Rittershoffen were analyzed. Only cuttings were available in the well and thus laboratory measurements like in EPS-1 were not possible. Data used for comparison are the spectral gamma ray that measures the natural radioactivity and indicates the variations of U, K and Th content in the well. The large variation of the spectral gamma ray on several meters indicates a variation of granite petrography. A sharp negative variation indicates paleo-circulations into a fractured zone and a leaching of primary magnetic and ferromagnesian minerals. The neutron porosity (NPHI) might be an additional indication of fractured zone if a sharp positive peak correlates with a sharp negative peak of GR. The measurement of neutron porosity is influenced by hydrogen atoms. Thus, the presence of clay minerals highly increases the value of the porosity. Finally, a structural analysis was done from acoustic image logs. Dip value, dip direction, thickness and aperture of fractures were measured on image logs. With structural analysis based on acoustic image logs, the fracture fillings cannot be define and the number and the width of fractures are underestimated compared to structural analysis based on core samples [*Genter et al.*, 1997a].

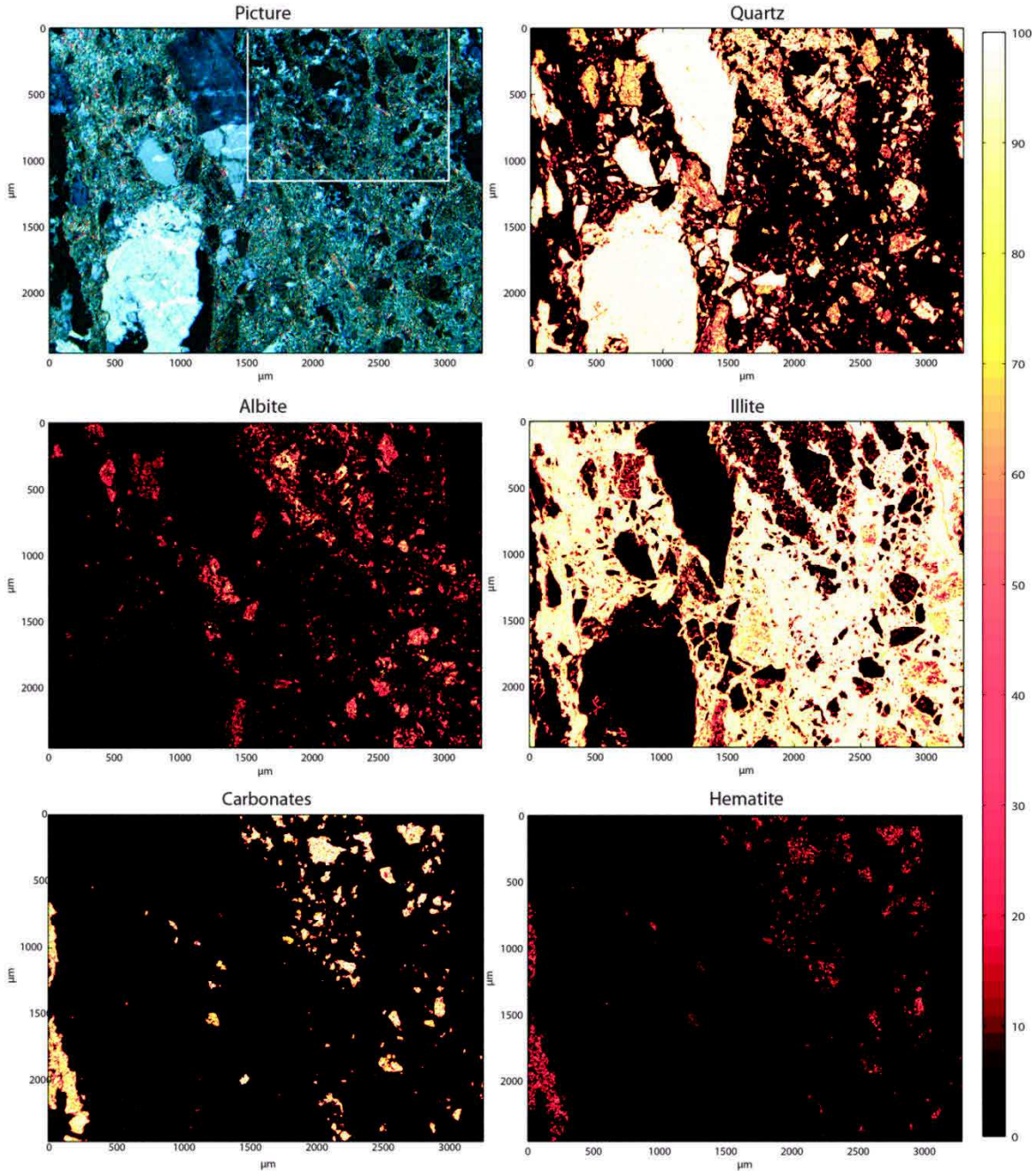

Figure 8.4 Picture of the focused zone at the edge of the fracture and associated phase mineral maps for quartz, illite, albite, carbonates and iron oxides. The colour bar is in percent of pixel. The white frame on the picture is the zoom into the vein shown Figure 8.5.

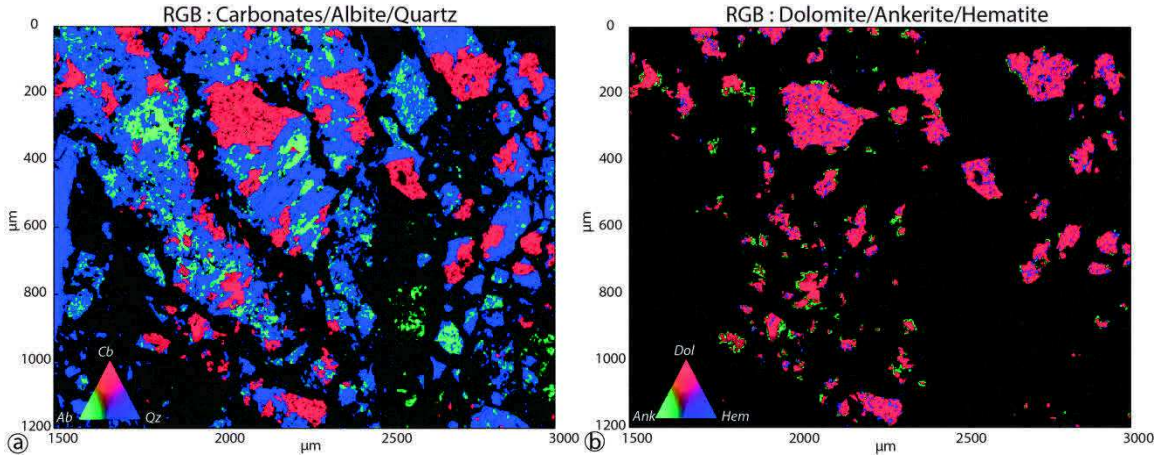

Figure 8.5 Chemical maps of relationships between carbonates (red), albite (green) and quartz (blue) (left) and between dolomite (red), ankerite (green) and hematite (blue) (rigth) calculated on the basis of SEM measurements into the vein

8.2.5 Results

8.2.5.1 Mineralogy and mineral relations in fracture fillings

Phase maps presented in Figure 8.4 and Figure 8.5 focus on the contact between the reddish granite and the fracture fillings and aim to highlight the mineral phase relationship at µm-scale. The mineralogy of fracture fillings includes quartz as large angular clasts (up to 1 mm width and 1.5 mm length) and more diffuse microcrystals (typically on the left-side of the map), albite, illite, carbonates (ankerite and dolomite) and iron oxides. Illite is ubiquitous, surrounding all other mineral phases. Albite is mainly present as small relics, this mineral being replaced by an assemblage of µ-quartz and carbonates. The close relation between albite, carbonate, and µ-quartz is clearly highlighted in RGB maps (Figure 8.5a). As illustrated in Figure 8.5b, dolomite is the dominant carbonate phase. Ankerite only occurs as small grains surrounding large aggregates of dolomite. In addition, both carbonates are systematically associated with small grains of iron oxides.

8.2.5.2 GRT-1 well

In GRT-1 well, temperature gradient has the same shape than in EPS-1 well. The uppermost part of the sedimentary cover is controlled by the conduction regime

with a thermal gradient up to 110 K/km. The brittle sediments at the base of the sedimentary cover and the granitic basement are controlled by the convective regime with a thermal gradient lower than 10 K/km. The average GR is 290 gAPI from 2212 to 2259 m depth with an increase of U, Th and K_2O (Figure 8.6). Below 2259 m depth, the average value of GR decreases to190 gAPI. The rock mass of the top basement, from cuttings description, present a reddish colour and are composed by quartz, illite, K-feldspars and hematite. The porosity measurement does not present significant variations at the top basement with an average value of 2%. The fracture density is about 1.9 fract/m [*Vidal et al.*, 2016b].

Below the reddish granite, the GR curve which is highly disturbed, trends with a overall decrease of Th and K_2O content at 2285 m depth (-160 gAPI), 2328 m depth (-180 gAPI) and 2368 m depth (-100 gAPI). These negative anomalies correlate to an increase of the neutron porosity that reaches 35% at 2328 m depth and 23% at 2368 m depth. Natural fractures are systematically filled by various hydrothermal minerals. Their cumulative width with depth presents steps from 1520 to 1860 mm at 2328 m depth, from 1895 to 2740 mm at 2328 m depth and from 3085 to 3455 mm at 2368 m depth (Figure 8.6). The linear fracture density is about 1.1 fract/m. Corresponding cuttings of this depth section are composed by euhedral quartz, anhydrite, illite and carbonates. Total mud losses were recorded around 2365 m depth during drilling operations.

After 2370 m depth, the GR is more stable with an average value of 260 gAPI and no individual peaks. Cumulative width of fractures does not present major steps and the fracture density is 0.4 fract/m. Mineralogy from cuttings is essentially composed by quartz, biotite, muscovite, K-feldspars, chlorite and illite.

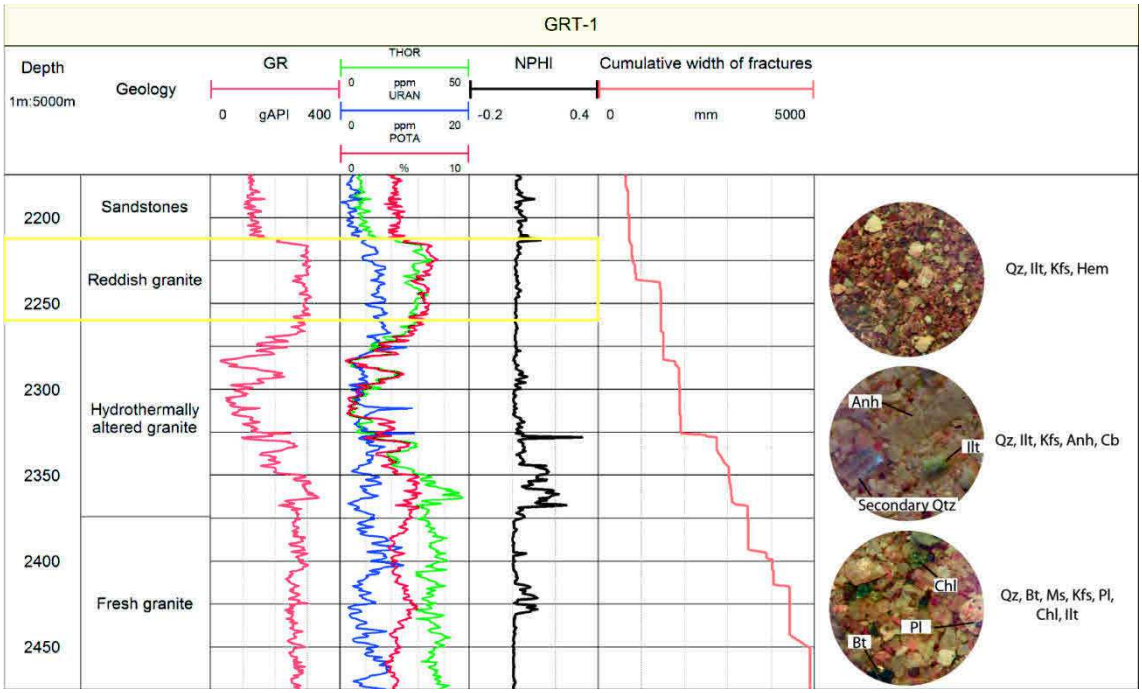

Figure 8.6 Spectral gamma ray, neutron porosity log and cumulative width of sealed fractures in GRT-1 with associated cuttings

8.2.6 Discussion

8.2.6.1 Dissolution-Precipitation processes and impact on the permeability

On the basis of the mineralogical phase maps and regarding the study of quartz veins by *Smith et al.* [*Smith et al.*, 1998], we infer that there is at least 2 different generations of quartz: Large clasts correspond to the early generation while µ-quartz has crystallized as a consequence of albite imbalance due to fluid circulations. This reaction is accompanied by the precipitation of ankerite: Mg and Fe required to form ankerite are assumed to result from the earlier destabilization of biotite and subsequent chlorite, while Ca results from the alteration of the plagioclase in the deep monzogranite [*Aquilina et al.*, 1997]. Ankerite is itself replaced by dolomite, as highlighted by Figure 8.5b. Reasons for this transition from ankerite to dolomite remain unclear. However RGB maps show that this reaction is accompanied by the release of iron that precipitates into hematite. Simultaneous precipitations of dolomite, which occurs in reducing conditions, and hematite, which supposes oxidizing conditions, indicate that changes of redox conditions may occur at grain scale. Finally, illite map indicate that this clay mineral has precipitated directly from the fluid, plugging the system (Figure 8.4).

The precipitation of illite probably prevents further fluid circulations and thus stopes all processes of dissolution-precipitation previously described.

At the fracture scale, carbonates and quartz veins are the last minerals to precipitate (Figure 8.3). These preliminary results show that each reaction associated to successive hydrothermal events form secondary minerals characterized by higher molar volume than the primary ones. This significant gain of volume reduces the connected porosity and consequently the fracture permeability.

At the basement scale, the neutron porosity measurements in the well also indicate a decrease of the porosity at the top basement (Figure 8.6). Some fractured zones are observed from well-logging variations in the underlying altered granite. They may be sealed at the borehole scale acting as a barrier for fluid circulation. Alternatively, they may present a residual permeability and be connected to a larger fracture network through the granitic basement.

8.2.6.2 Conceptual model

The early stage of alteration is pervasive, when plagioclase is altered into corrensite and biotite into chlorite during the granite batholith emplacement. The quartz remains stable. Then successive hydrothermal alterations correlated to tectonic and fracturing events through the geological history of this area. In both fractured zones and matrix, corrensite and chlorite are transformed into illite, which is also the case for K-feldspars when shearing occurs. Secondary quartz and carbonates precipitate into fractured zones. Paleo-emersion of the top of the granite leads to a decompression involving nearly horizontal jointing and a subsequent episode of paleo-weathering. Ankerite is replaced by dolomite and hematite crystallise at the edge of carbonates. Finally, subsidence related to the extension of the Upper Rhine Graben causes the burying of the granitic basement under a stack of thick sediments. Mesozoic and Cenozoic tectonic events such as reactivation of Hercynian structures and creation of new one affect the granitic basement. The P-T conditions increase to reach modern temperature and pressure conditions.

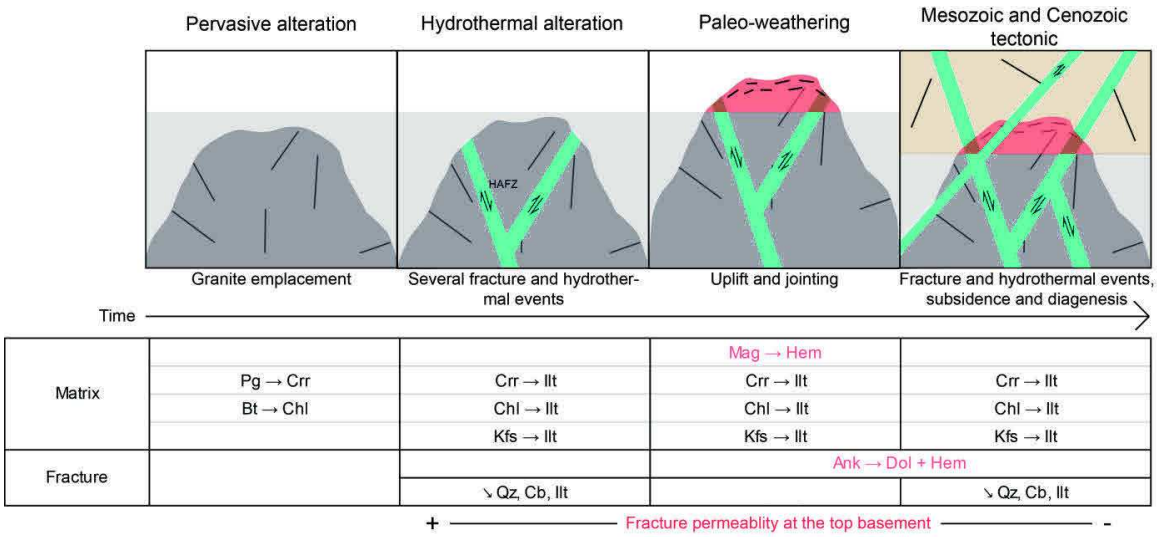

Figure 8.7 Conceptual model of alteration and mineral transformation of hidden granite in geothermal granite. Specific mineral transformations observed at the top basement are indicated in red.

During post-Variscan events, the mineral transformations such as ankerite destabilisation to dolomite continue until illite precipitation plugs the system. Quartz and carbonates crystallise into fractured zone as veins. Quartz is the only mineral considered as actively growing. The chain reaction of dissolution-precipitation processes lead to reduce the connected porosity. Fractures that are critically stressed might present residual permeability [*Evans*, 2005].

8.2.7 Conclusion

In conclusion, fractures mineralogy in the reddish granite were analysed by several laboratory methods. Results reveal complex zone into the fracture where precipitation of secondary quartz and ankerite takes place. These precipitations are assumed to occur after albite destabilisation reacting with Mg- Fe- and Ca-rich fluid circulating through deep granite. Ankerite, dolomite and hematite are closely associated and suggest ankerite replacement by dolomite accompanied by the release of iron that precipitates into hematite. The precipitation of illite probably prevents further fluid circulations and thus all processes of dissolution-precipitation. Carbonates are also observed around complex zones into the fracture with quartz vein crystallising at the edge. Successive precipitations of secondary minerals associated to hydrothermal events and fluid circulation decrease the fracture permeability. The lower porosity of the reddish granite is

correlated to an increase of the natural radioactivity observed in several geothermal well of the Northern Upper Rhine Graben thanks to well-logging data. The preliminary results do not allow defining which mineral bears radio-elements that are concentrated into the reddish granite located at the top basement.

8.2.8 Acknowledgments

The authors are grateful to the GEIE Exploitation Minière de la Chaleur for providing Soultz core samples and geophysical data and ECOGI company for the Rittershoffen geophysical logs. A part of this work was done in the framework of the LabEx G-Eau-Thermie Profonde which is co-funded by the French government under the program “Investissements d’Avenir”. The extended abstract was performed as a contribution to the PhD thesis of Jeanne Vidal co-founded by ADEME (French Agency for Environment and Energy). The authors thank M. Amann and O. Boudouma for helping during laboratory analysis.

8.3 Minéraux argileux liés à l'altération hydrothermale dans les fractures des sédiments gréseux

Cette section devait initialement faire partie de l'article soumis à la revue Journal of Volcanology and Geothermal Research présenté dans la section suivante (section 8.4). Cependant, afin focaliser l'article sur le socle granitique, l'étude des argiles dans les fractures perméables des grès du puits GRT-2 a été retirée de la version soumise. Elle est donc présentée dans cette section en anglais.

8.3.1 Introduction

Well GRT-2 intersects two Originally Permeable (OP) fracture zones within the Triassic and Permian sandstones (Figure 8.8). These OP fracture zones channelize brine circulations that lead to hydrothermal alteration. Brine circulations are complex and polyphase, and they likely occur in a pulsated mode [*Smith et al.*, 1998; *Dubois et al.*, 2000]. The secondary minerals are a record of several hydrothermal events because they are dependent on the chemistry of the fluid, fluid/rock ratio and temperature [*Reyes*, 1990; *Beaufort et al.*, 1992, 1996; *Ledésert et al.*, 1999]. This section focuses on the argillic alteration of permeable fracture zones in the sandstones of well GRT-2. First, observations of the sampled cuttings around the permeable fracture zones are presented. Then, X-ray Diffraction (XRD) and scanning Electron Microscope (SEM) coupled with EDS results are detailed. The XRD results detail the properties of the crystal structures of the clays, whereas the SEM results detail the chemical compositions of the clay minerals. Finally, the results for the sandstones are discussed and compared to those from Soultz.

8.3.2 Methodology

The crystal structure of clay minerals was analyzed with XRD performed on oriented powders of untreated and ethylene–glycol (EG) saturated samples of the fine-grained fraction (<5 μm). XRD was carried out on a Bruker D8 Advance diffractometer (CuKα radiation, 40 kV, 40 mA). Analytical conditions used for the acquisition of XRD data were as follows: angular domain: 2θ=between 2.5 and 30; step increment: 2θ=0.025; counting time per step: 3s.

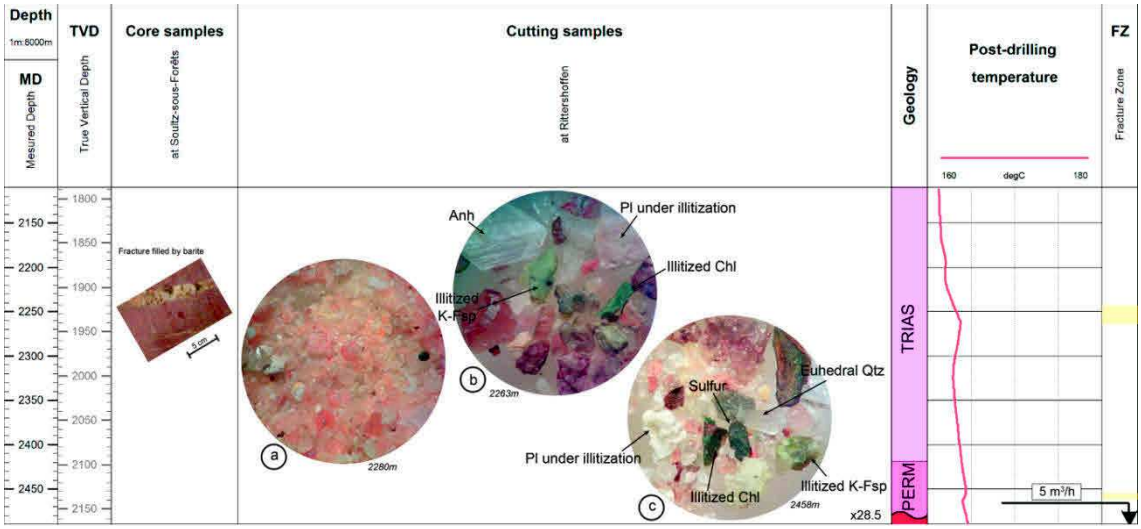

Figure 8.8 Cutting samples observations in Permian and Triassic sandstones from GRT-2 a) at 2280 m MD, b) at 2263 m MD in the OP fracture zone and c) at 2458 m MD in the OP fracture zone. Light yellow intervals are OP fracture zones from the structural analysis [*Vidal et al.*, 2017]. Core sample from Soultz-sous-Forêts indicates a fracture filled by barite. Qtz=quartz, anh=anhydrite, chl=chlorite, ill=illite, hem=hematite, bte=biotite, pg=plagioclase feldspar, K-Fsp=potassic feldspar.

Illite coherent scattering domain (CSD) size was estimated from crystallinity along c axis and thus, the full width at half maximum (FWHM) intensity of the typical (001) reflection at 10 Å. Chlorite CSD was estimated from the FWHM intensity of the (002) reflection at 7 Å.

The chemical compositions of clay minerals which were analyzed with SEM JEOL 5600 LV equipped with a BRUKER XFlash 4030 SSD (associated with SPIRIT software). Analytical conditions were 15 kV, 1 nA, counting time 60 s, working distance 16.5 mm. Elements analyzed were Si, Al, Fe, Mg, Mn, Ti, Ca, Na and K. The system was calibrated with a variety of synthetic oxide and natural silicate standards. The reproducibility of standard analyses was close to 1% except for Na, which was 1.5%.

8.3.3 Cuttings observations

The Triassic sandstones are typically medium-grained to conglomeratic continental sandstones with argillaceous layers. The cuttings exhibit a pink color (Figure 8.8a). Microscopic observations reveal quartz-feldspar sandstones with

an ilitic or carbonate matrix (Figure 8.9a and b). From 2263 to 2250 m MD, the samples are localized in an OP fracture zone and are bleached compared to the unfractured sandstones (Figure 8.8b). Plagioclase and potassic feldspars are highly transformed into illite. Illite presents as small-sized crystallites. Chlorite is locally observed as transformed into illite, and anhydrite is abundant. Microscopic observations indicate that the primary minerals are completely or partially transformed into illite (Figure 8.9c). Fragments of quartz are surrounded by small-sized crystallites of illite and carbonates, and calcite is also frequently observed.

The Permian sandstones intersected by GRT-2 are argillaceous red sandstones [*Aichholzer et al.*, 2015]. The cuttings exhibit a reddish color. From 2461 to 2452 m MD, the samples are localized in the OP fracture zone and show plagioclase and potassic feldspars that are transformed into illite or are completely transformed locally (Figure 8.8c). Chorite is transformed into illite locally. Sulfides with metallic lusters are observed as well as some euhedral quartz. Microscopic observations at the same depths reveal primary minerals that are completely transformed into illite (Figure 8.9i). Iron-rich chlorite is clearly identified, and anhydrite is observed locally (Figure 8.9d, g and h).

Figure 8.9 (next page) Microscopic observations of cuttings samples in GRT-2; a) and b) samples from unfractured Triassic sandstones at 2281 m; c) sample from OP fracture zone in Triassic sandstones at 2263; d) sample from OP fracture zone in Permian sandstones at 2452 m MD; e) sample from OP fracture zone in Permian sandstones at 2455 m MD; f), g) and h) samples from OP fracture zone in Permian sandstones at 2458 m MD; i) sample from OP fracture zone in Permian sandstones at 2452 m MD. Qtz=quartz, Chl=chlorite, Ill=illite, Cb=carbonates.

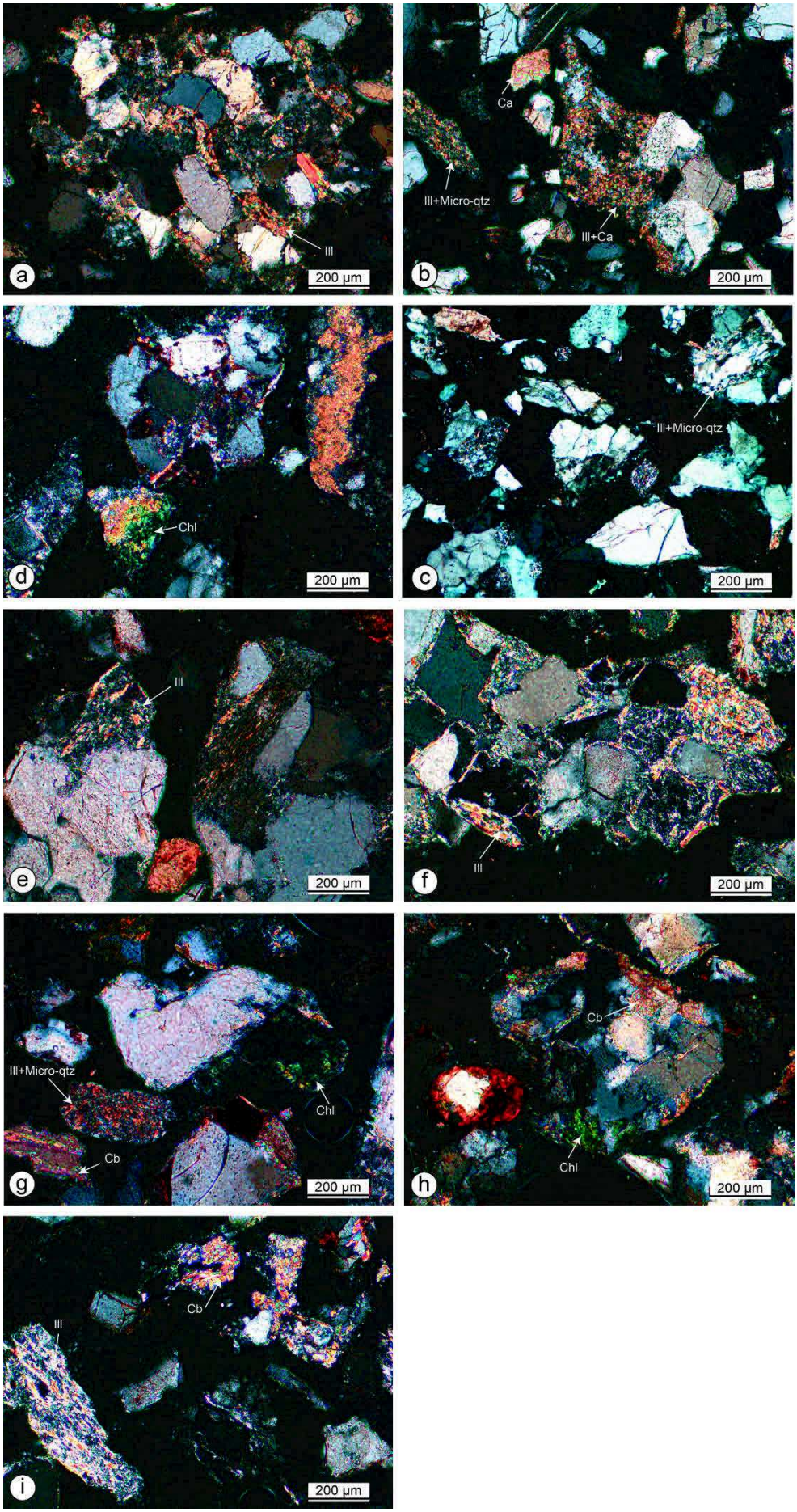
a
Ill
200 µm
b
Ca
Ill+Micro-qtz
Ill+Ca
200 µm
d
Chl
200 µm
c
Ill+Micro-qtz
200 µm
e
Ill
200 µm
f
Ill
200 µm
g
Ill+Micro-qtz
Chl
Cb
200 µm
h
Cb
Chl
200 µm
i
Cb
Ill
200 µm

8.3.4 XRD results

The X-ray diffractograms indicate that clay alteration products are dominated by illite and chlorite in Rittershoffen wells (Figure 8.10).

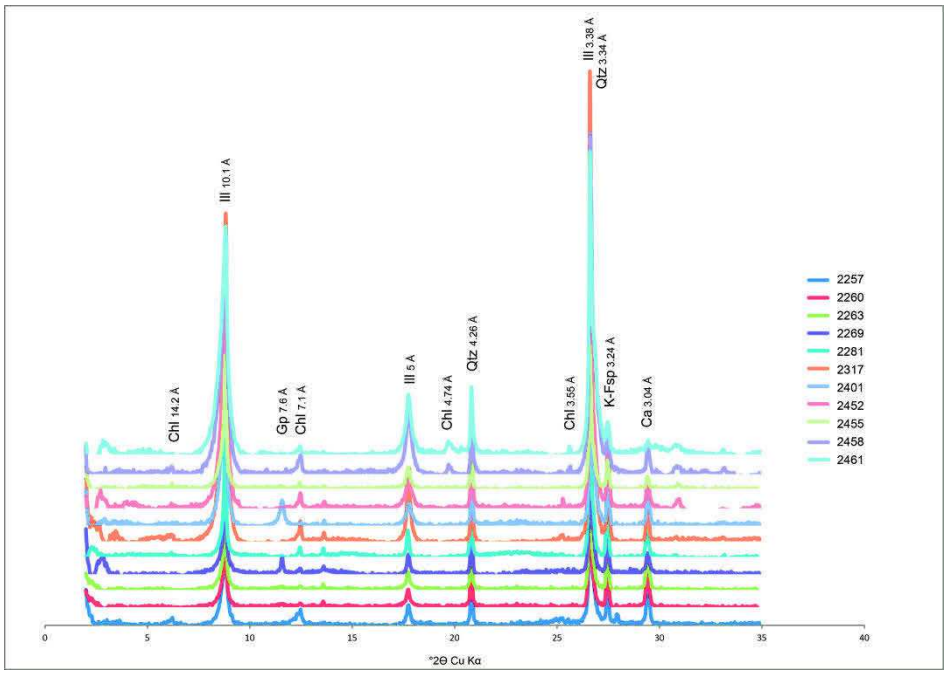

Figure 8.10 X Ray diffractograms of the clay fraction (<5 µm) as observed in major originally permeable fracture zone a) in GRT-1 (samples 2377, 2368, 2362 and 2359) and b) in GRT-2 (samples 2785, 2773, 2770 and 2767). Ill=illite, chl=chlorite, qtz=quartz, pg=plagioclase feldspars, K-Fsp=potassic feldspars, ca=calcite.

The (001) reflections of the illitic peak at 10 Å are complex. They were deconvoluted into two or three Gaussian peaks (Figure 8.11). Microscopic observations indicate two illitic populations with different sizes. The well-crystallized illite (WCI) is associated to large sheets whereas the poorly crystallized illite (PCI) is associated to small flakes The WCI peak corresponds to a 10 Å d-spacing and is characterized by a narrow FWHM that ranges between 0.09 and 0.16 °2Θ (Figure 8.11a and b). The PCI peak corresponds to a 10.2 Å d-spacing and is characterized by a broader FWHM that ranges between 0.26 and 0.40 °2Θ. Mixed layers illite-smectite (~10% of smectite) were identified in some of the samples. They are characterized in the air-dried samples by a broad peak near 10.3 Å that splits into two peak near 10.5 Å and at 9.7 Å after EG

saturation (Figure 8.11c). The WCI and PCI peaks do not shift after EG saturation. Chlorite was identified from their non-expandability and their harmonic peaks at 14 Å and 7 Å. The FWHM of the peak at 7 Å varies between 0.08 and 0.18 °2Θ.

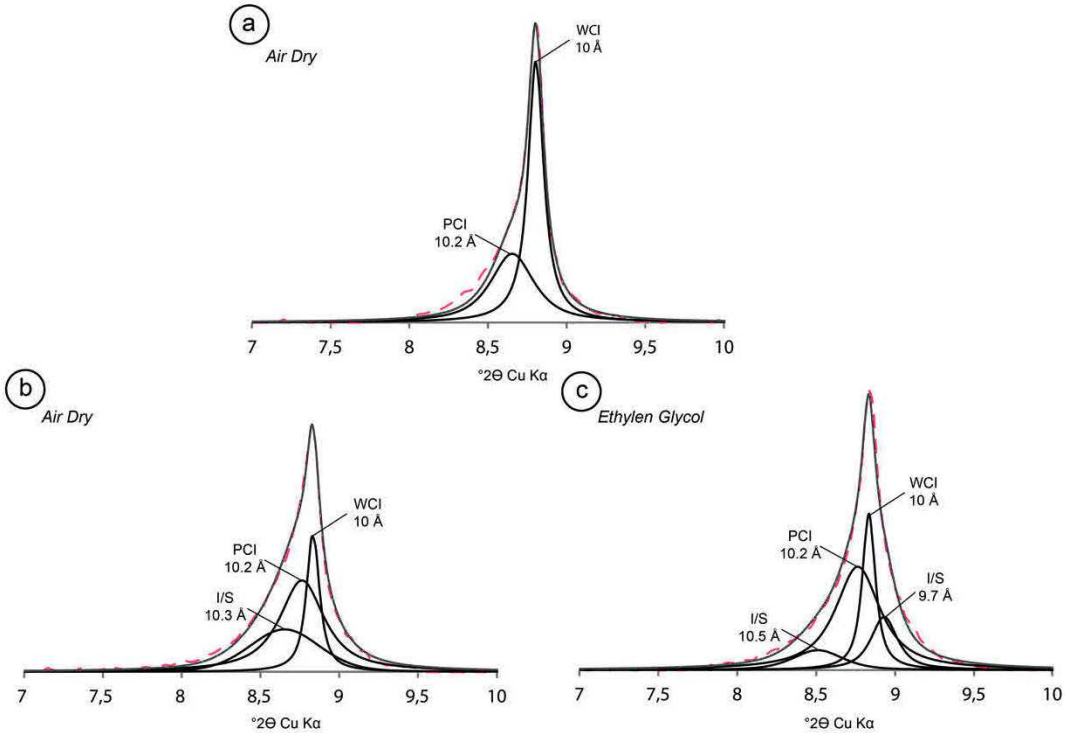

Figure 8.11 Deconvolution in the 7-10°2Θ CuKa domain of the X Ray diffractograms (<5 µm clay fraction) of a) air dried oriented powder of sample 2455, b) air dried oriented powder of sample 2452 and c) EG-saturated oriented powder of sample GRT-1 2452. I/S: mixed layers illite/smectite; WCI: well-crystallized illite, PCI: poorly crystallized illite. Dashed red lines are data.

In sandstones, the presence of the PCI and the WCI was observed in all diffraction patterns (Figure 8.12). The proportion of WCI is between 0.50 and 0.89 with an average value of 0.68. The average FWHM is 0.12 °2Θ. The average proportion of WCI increases in samples at 2257, 2260, 2263, 2269, 2281 and 2455 m MD wherein the proportion of WCI is between 0.78 and 0.90. They correspond to samples in the OP fracture zones of sandstones. Mixed layers illite-smectite are observed in samples at 2401, 2452, 2458 and 2461 m MD. The average proportion of PCI is 0.24 with the maximum of 0.44 at 2317 m MD and the minimum of 0.10 at 2281 m MD. The average FWHM of 0.34 °2Θ with the

minimum of 0.26 °2Θ at 2281 m MD and the maximum of 0.40 °2Θ at 2317 m MD.

The average proportion of chlorite is 0.05 in sandstones with the maximum of 0.02 at 2461 m MD and the maximum of 0.06 at 2458 m MD. The FWHM is quite similar in all samples with the average value of 0.14 °2Θ.

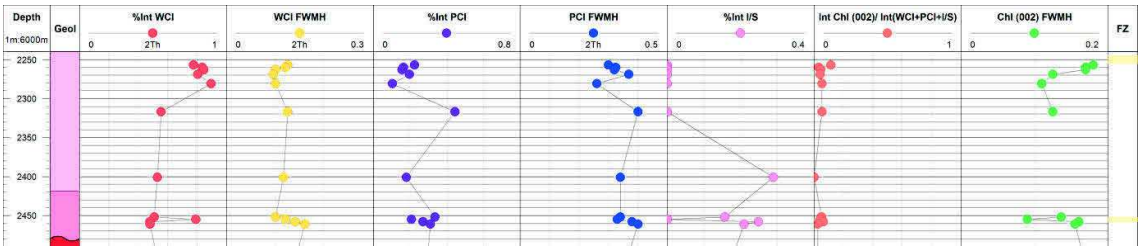

Figure 8.12 Crystal structure properties of illitic minerals and chlorite measured using XRD of the <5 µm clay fraction versus depth in sandstones within well GRT-2. The proportion of WCI is defined as %Int WCI = WCI int/(PCI int + WCI int + I/S int), where WCI int = the intensity of the peak deconvolved from the (001) reflection of the illitic minerals. The proportion of chlorite is defined as %Int Chl = Chl int/(PCI int + WCI int + I/S int + Chl int), where Chl int = the intensity of the peak of the (002) reflection of the chlorite. Light yellow intervals are originally permeable (OP) fracture zones from the structural analysis [*Vidal et al.*, 2017].

8.3.5 SEM results

The structural formulas of the illitic minerals are calculated relative to 11 oxygens while assuming the total iron content was Fe^{3+} (Table 8.1). In sandstones of GRT-2, chemical analyses of illitic mineral (WCI+PCI +I/S ml) do not present major variations. The interlayer charge is between 0.85 and 0.91 and the average octahedral Al content is 1.62+/-0.08 per $O_{10}(OH)$. The average Fe and Mg contents are 0.15+/-0.05 and 0.18+/-0.04 in sandstones.

The structural formulas of chlorite are calculated relative to 14 oxygens while assuming the total iron content was Fe^{2+} (Table 8.2). In sandstones, the octahedral occupancy is 5.95. Iron-rich chlorites (XFe>0.80) are observed in samples at 2452 and 2458 m MD in OP fracture zones in Permian sandstones (Table 8.2). Although chlorites were observed in cutting samples by macroscopic observations and XRD in the OP fracture zones in the Triassic sandstones, no one was observed in thin sections.

Table 8.1 Calculations of structural formulae of some illitic minerals in sandstones of GRT-2 wells. n.a.: number of analyses; An. Av.: analytical average; s.d.: standard deviation; OCT: octahedral occupancy; INTCH: interlayer charge.

Samples	GRT-2 2260		GRT-2 2263		GRT-2 2445		GRT-2 2452		GRT-2 2455		GRT-2 2458		GRT-2 2461	
n. a.	9		23		16		19		28		49		49	
	An. Av.	s.d.	An. Av.	s.d.	An. Av.	s.d.	An. Av.	s.d.	An. Av.	s.d.	An. Av.	s.d.	An. Av.	s.d.
Si	3,49	*0,19*	3,36	*0,17*	3,33	*0,21*	3,48	*0,17*	3,46	*0,21*	3,34	*0,14*	3,37	*0,10*
Al IV	0,51	*0,19*	0,64	*0,17*	0,67	*0,21*	0,52	*0,17*	0,54	*0,21*	0,66	*0,14*	0,63	*0,10*
Al VI	1,60	*0,04*	1,67	*0,07*	1,63	*0,10*	1,59	*0,07*	1,59	*0,08*	1,66	*0,10*	1,60	*0,10*
Fe 3+	0,14	*0,04*	0,13	*0,04*	0,15	*0,07*	0,15	*0,04*	0,16	*0,06*	0,14	*0,06*	0,17	*0,06*
Mg	0,18	*0,03*	0,18	*0,03*	0,15	*0,04*	0,21	*0,03*	0,17	*0,06*	0,19	*0,05*	0,21	*0,04*
Ti	0,01	*0,02*	0,01	*0,01*	0,03	*0,07*	0,01	*0,01*	0,01	*0,01*	0,00	*0,01*	0,01	*0,04*
Mn	0,00	*0,00*	0,00	*0,00*	0,00	*0,00*	0,00	*0,00*	0,00	*0,00*	0,00	*0,00*	0,00	*0,00*
OCT	1,93	*0,07*	1,99	*0,04*	1,96	*0,08*	1,96	*0,07*	1,93	*0,11*	1,99	*0,04*	1,99	*0,03*
Ca	0,01	*0,01*	0,01	*0,02*	0,04	*0,07*	0,02	*0,03*	0,01	*0,01*	0,02	*0,03*	0,01	*0,02*
Na	0,01	*0,03*	0,00	*0,00*	0,00	*0,00*	0,00	*0,00*	0,00	*0,00*	0,00	*0,00*	0,00	*0,00*
K	0,84	*0,12*	0,84	*0,07*	0,86	*0,12*	0,81	*0,10*	0,90	*0,13*	0,84	*0,05*	0,83	*0,05*
INTCH	0,88	*0,13*	0,85	*0,07*	0,91	*0,09*	0,84	*0,09*	0,91	*0,13*	0,86	*0,05*	0,85	*0,05*

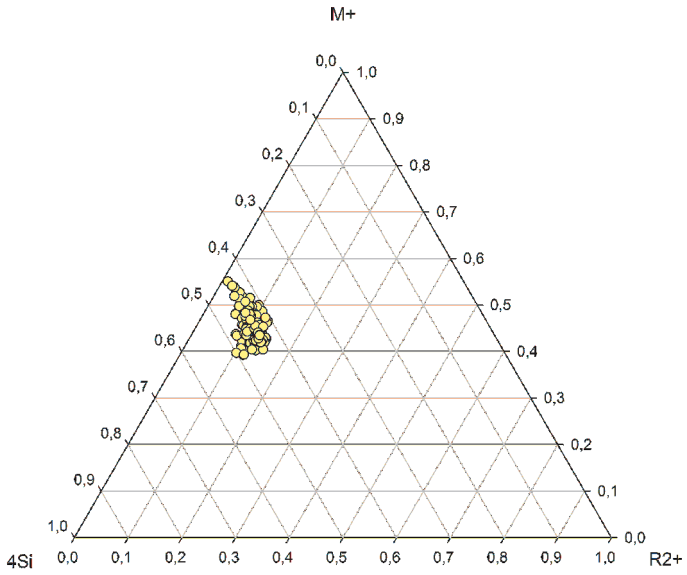

Figure 8.13 Plot of structural formulas of illitic minerals from sandstones in GRT-2 well in a M+-R2+-4Si ternary diagram.

Table 8.2 Calculations of structural formulae of iron-rich chlorite observed in OP fracture zone in Permian sandstones of GRT-2 wells. n.a.: number of analyses; An Av: analytical average; s.d.: standard deviation; OCT: octahedral occupancy; INTCH: interlayer charge; XFe= Fe/(Fe+Mg).

Samples	GRT-2 2452		GRT-2 2458	
an. loc.	FZ		FZ	
n. a.	3		9	
	An. Av.	s.d.	An. Av.	s.d.
Si	2,83	*0,00*	2,84	*0,05*
Al IV	1,17	*0,00*	1,16	*0,05*
Al VI	1,22	*0,01*	1,20	*0,05*
Ti	0,00	*0,00*	0,00	*0,00*
Fe 2+	4,12	*0,06*	4,00	*0,20*
Mn 2+	0,00	*0,00*	0,00	*0,00*
Mg 2+	0,61	*0,08*	0,74	*0,17*
OCT	5,95	*0,01*	5,95	*0,02*
Ca	0,01	*0,00*	0,02	*0,01*
Na	0,00	*0,00*	0,00	*0,00*
K	0,01	*0,00*	0,01	*0,02*
INTCH	0,03	*0,00*	0,06	*0,04*
XFe	0,87	*0,02*	0,84	*0,04*

8.3.6 Discussion

In the sandstones of GRT-2, an illitic signature in the background (with a high proportion of PCI and the presence of mixed layers illite-smectite) is associated with diagenesis. In the OP fracture zones, the illitic signature is represented by a high proportion of WCI and the absence of mixed layers illite-smectite. The OP fracture zones in the sandstones of GRT-2 are associated with iron-rich chlorite and are observed in the thin sections from the OP fracture zone of the Permian sandstones but not in the OP fracture zone of the Triassic sandstones. In the acoustic image logs, the OP fracture zones of the Permian sandstones show open fractures of more than 1 cm, whereas the OP fracture zone in the Triassic sandstones shows sealed fractures [*Vidal et al.*, 2017]. The intense precipitation of illitic minerals in the OP fracture zone of the Triassic sandstones probably prevents further fluid circulation and decreases the natural permeability of the zone. The persistence of iron-rich chlorite in the OP fracture zones in the Permian sandstones indicates that the illitic minerals do not replace all of the other minerals or seal all of the fractures. Iron-rich chlorite was probably

crystallized with a reducing fluid. Small-sized crystallites of illite and mixed layers illite-smectite can crystallize at temperatures lower than 200°C. Several populations of illite that were deposited during different hydrothermal events are probably superimposed within the OP fracture zones. However, the fluids did not significantly change; this is indicated by the chemical compositions of the illitic minerals that remained stable (Figure 8.13).

Secondary minerals in the OP fracture zones of GRT-2 (i.e., euhedral quartz, illite, carbonates, anhydrite, and sulfur) are quite similar to those observed at Soultz except for anhydrite, which was not detected at Soultz [*Vernoux et al.*, 1995; *Genter and Traineau*, 1996]. At Soultz, barite was observed in the fracture zones of the sandstones. The higher barium concentrations in the Rittershoffen fluids relative to those at Soultz raises some questions (Table 8.3). Since the barite solubility increases and the anhydrite solubility decreases with increasing temperatures [*Sanjuan et al.*, 2010], it is probable that the fluids circulating in the Rittershoffen fractured areas are hotter than those at Soultz. This could explain why anhydrite and not barite was precipitated in the Rittershoffen fractured zones, which is in contrast to the mineralogies in the Soultz observations. The relative chronologies between the secondary minerals deduced from the cuttings samples are very uncertain because the sandstones were destroyed. Observations of the core samples of EPS-1 at Soultz indicate that the illite with epitaxial growth crystallized prior to the small-sized crystallites of illite that are associated with microquartz [*Dezayes et al.*, 2011]. Subsequently, barite crystallized in the central part of the fracture during a different hydrothermal event. Finally, the carbonates cemented the barite, illite and hydrothermal quartz together [*Dezayes et al.*, 2011]. Absolute dates of the illites in the sandstones at Soultz reveal ages between 95 and 70 Ma [*Clauer et al.*, 2008].

Table 8.3 Chemical compositions of geothermal fluid sampled in the Paleozoic granite at Soultz-sous-Forêts in the well GPK-2 at 5000 m depth and at Rittershoffen in the well GRT-1 at 2580 m depth (Sanjuan et al., 2010; 2016).

Location	T_{Bottom} °C	pH	TDS g/L	Na mg/L	K mg/L	Ca mg/L	Mg mg/L	Cl mg/L	SO_4 mg/L	SiO_2 mg/L
Soultz-sous-Forêts	200	4.98	99	28 140	3195	7225	131	58 559	157	201
Rittershoffen	160	6.27	101	28 451	3789	7200	138	59 900	220	146

Location	Br mg/L	Li mg/L	Sr mg/L	Ba µg/L	Gas
Soultz-sous-Forêts	216	173	455	5070	CO_2 N_2 CH_4
Rittershoffen	251	190	498	17 638	unknown

8.4 Minéraux argileux liés à l'altération hydrothermale dans les fractures du socle granitique (Article soumis à Journal of Volcanology and Geothermal Research)

Clay minerals related to the circulation of geothermal fluids in boreholes at Rittershoffen (Alsace, France)

Jeanne VIDAL[1], Patricia PATRIER[2], Albert GENTER[3], Daniel BEAUFORT[2], Chrystel DEZAYES[4], Carole GLAAS[3], Catherine LEROUGE[4], Bernard SANJUAN[4]

[1] University of Strasbourg, CNRS UMR 7516 IPGS, 1 rue Blessig, F-67084 Strasbourg Cedex

[2] University of Poitiers, CNRS UMR 7285 IC2MP, HydrASA, Bat B8, Rue Albert Turpain, TSA51106 F-86073 Poitiers Cedex 9

[3] ES-Géothermie, 5 rue Lisbonne, 67300 Schiltigheim, France

[4] BRGM - 3, Av. Claude Guillemin / BP6009 - 45060 Orléans Cedex 02, France

8.4.1 Abstract

Two geothermal wells, GRT-1 and GRT-2, were drilled into the granite at Rittershoffen (Alsace, France) in the Upper Rhine Graben to exploit geothermal resources at the sediment-basement interface. Brine circulation occurs in a permeable fracture network and leads to hydrothermal alteration of the host rocks. The goal of the study was to characterize the petrography and mineralogy of the altered rocks with respect to the permeable fracture zones in the granitic basement. As clay minerals are highly reactive to hydrothermal alteration, they can be used as indicators of present-day and paleo-circulation systems. Special attention has been paid to the textural, structural and chemical properties of these minerals. The fine-grained clay fraction (<5 µm) was analyzed around the originally permeable fracture zones to observe the crystal structure of clay minerals using X-ray diffraction. Chemical microanalysis of the clay minerals was performed using scanning electron microscopy coupled with energy dispersive X-ray spectroscopy. The occurrences of mixed layers illite-smectite (~10% smectite) provide a promising guide for identifying the fracture zones that control the present-day circulation of geothermal fluids in the Rittershoffen wells. However, multistage paleo-circulation systems could lead to an abundance of

heterogeneous and fine-grained illitic minerals that could plug the fracture system. The permeability of fracture zones in the GRT-1 well was likely reduced because of an intense illitization, and the well was stimulated. The occurrence of chlorite in the permeable fracture zones of GRT-2 is indicative of less intense illitization, and the natural permeability is much higher in GRT-2 than in GRT-1.

Keywords: clay minerals; hydrothermal parageneses; chemical composition; geothermal field; Rittershoffen; Upper Rhine Graben

8.4.2 Introduction

In geothermal systems, alteration minerals provide useful information about the physico-chemical conditions of both past and present hydrothermal activity. This is particularly the case with clay minerals, which have been investigated as markers of circulation zones based on their reactivity to changes in physico-chemical conditions [*Beaufort et al*., 1992, 1996; *Browne and Ellis*, 1970; *Flexser*, 1991; *Mas et al*., 2006; *Patrier et al*., 1996; *Reyes*, 1990]. The properties of clay minerals are affected by temperature in addition to several other factors, such as rock and fluid chemistries, time and the fluid/rock ratio. This study focused on the argillic alteration of permeable fracture zones related to a hydrothermal system located in the Upper Rhine Graben at Rittershoffen in France (Figure 8.14). Two deep geothermal wells - GRT-1, which has a vertical trajectory, and GRT-2, which has a deviated trajectory - intersect natural, permeable fracture zones in the sandstones and granitic basement beneath Rittershoffen [*Baujard et al*., 2017; *Vidal et al*., 2017]. The influence of argillic alteration on the permeability of fracture zones at the borehole scale is an important milestone for an industrial project because fracture zones channel hot geothermal fluids that are exploited for high-temperature (>160°C) heat applications at the surface.

Geothermal systems are dynamic systems that are constantly evolving; thus, the observed secondary minerals potentially consist of several superimposed alteration assemblages. In Rittershoffen boreholes, the mineral products of the existing hydrothermal circulation system (160°C) appear to be superimposed upon previous secondary minerals formed during earlier circulations events. Abundance of secondary minerals may lead to plugging and the transformation of fracture zones from conduits into barriers to fluid flow. As the nature of fracture

permeability is an important aspect of this geothermal project, most of the cutting samples were collected along the open-hole sections of wells around the originally permeable (OP) fracture zones in both wells. Cutting samples from both GRT-1 and GRT-2 were investigated to identify the alteration mineralogies, and special attention was paid to the clay fraction. The fine-grained fraction of cuttings (<5 µm) was analyzed using X-ray Diffraction (XRD) to identify well-crystallized illite, poorly crystallized illite and mixed layers illite-smectite. Then, scanning electron microscopy (SEM) coupled with energy-dispersive X-ray spectroscopy (EDS) was used to analyze the chemical compositions of the clay minerals.

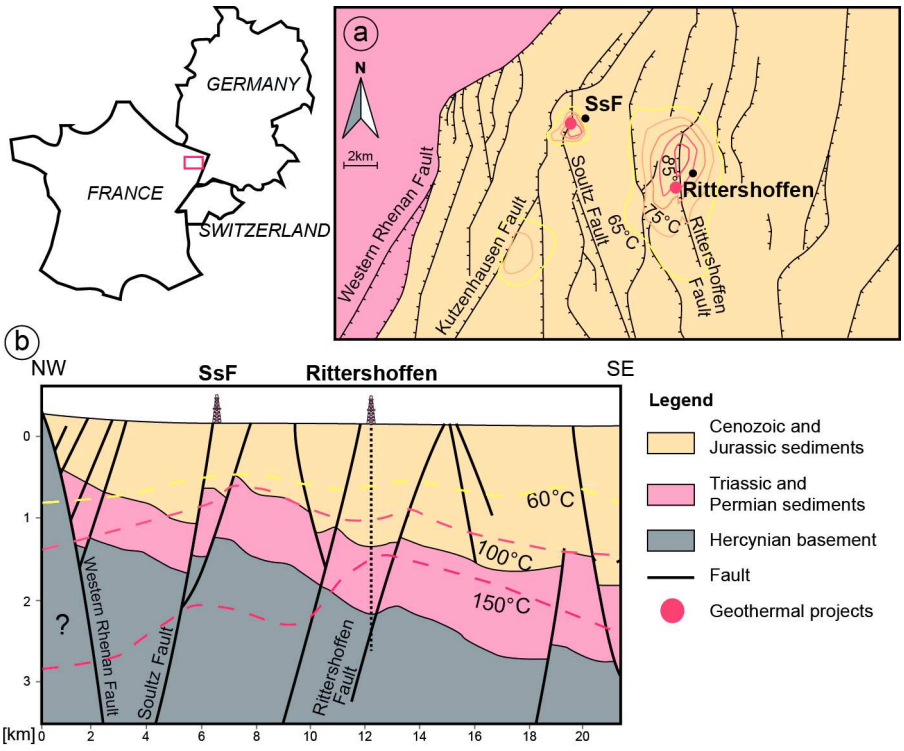

Figure 8.14 Location of the Rittershoffen geothermal site. a) Geological and structural map of the Rittershoffen and Soultz-sous-Forêts (SsF) area. Isotherms at the top of the basement are from *Baillieux et al* [2014]. b) Geological cross section through the Rittershoffen and Soultz-sous-Forêts geothermal sites after *GeORG* [2017]. The dashed line is an interpreted trajectory of the geothermal well GRT-1.

8.4.3 Geological context

The geothermal site at Rittershoffen is located in the Upper Rhine Graben (URG), approximately 15 km east of the Western Rhenan fault and less than 10 km from

the well-known Soultz-sous-Forêts geothermal site (Alsace, France) (Figure 8.14a). In the URG, the underground temperature distribution is spatially heterogeneous, and several geothermal anomalies are concentrated throughout the western side of the URG in the areas of Soultz-sous-Forêts and Rittershoffen [*Baillieux et al.*, 2013; *Pribnow and Schellschmidt*, 2000; *Schellschmidt and Clauser*, 1996). Temperature anomalies at the top of the granitic basement indicated by several temperature measurements are concentrated along the Soultz and Kutzenhausen normal faults that dip toward the west (Figure 8.14a) [*Baillieux et al.*, 2014]. These zones are attributed to the upwelling of hot geothermal fluids through fault zones within the crystalline basement and Triassic and Permian sandstones (Figure 8.14b) [*Benderitter et al*., 1995; *Pribnow and Clauser*, 2000; *Pribnow and Schellschmidt*, 2000]. Geothermal reservoirs in the granitic basement at Rittershoffen are quite similar to the reservoir at Soultz. Both deep fluids are of the NaCl type with total dissolved solids (TDS) values close to 100 g/L (Table 8.3) [*Sanjuan et al*., 2014, 2016]. The pH values of the fluids in both reservoirs are close to 5.0. The fluids are interpreted as having originated from the mixing of primary marine brine with water of meteoric origin [*Sanjuan et al*., 2010, 2016]. The estimated temperature of the deep reservoir calculated by primary cationic geothermometers (Na-K, Na-K-Ca, Na-K-Ca-Mg, K-Mg, Na-Li and Mg-Li) and by a δ^{18}OH2O-SO4 isotope geothermometer was 225 ± 25°C at Soultz and at Rittershoffen [*Sanjuan et al*., 2016].

Alteration episodes of the granitic reservoir are well known to have occurred in deep wells at Soultz [*Gente*r, 1989; *Hooijkaas et al.*, 2006; *Ledésert et al.*, 1999; *Traineau et al.*, 1992]. Early propylitic alteration of the whole granitic batholith is characterized by the formation of epidote, the partial transformation of primary biotite into Fe,Mg-chlorite and the partial replacement of primary potassic feldspar with small crystallites of illite. Then, hydrothermal alterations dominated by illite, quartz and calcite occur around fracture zones after fluid circulations. Several alteration facies were identified by Hooijkaas et al. [2006]. The same granitic batholith was encountered at Rittershoffen. As geothermal fluids are similar, alterations observed at Soultz could be a reasonable reference for petrographical studies at Rittershoffen.

8.4.4 OP fracture zones, thermal profile and hydraulic yield of the geothermal wells at Rittershoffen

At Rittershoffen, two wells, GRT-1 and GRT-2, penetrate the Cenozoic, Mesozoic and Permian sediments overlying the Paleozoic basement. The wells were drilled to a true vertical depth of 2.6 km in the southeastern end of a horst and targeted the so-called Rittershoffen normal fault at the top of the basement [*Baujard et al*., 2017]. Based on a seismic reflection interpretation of the sedimentary cover, this fault strikes N-S, dips 45° westward and displays an apparent vertical offset of approximately 200 m (Figure 8.14b) [*Baujard et al*., 2017]. Wells intersect the fracture network associated with the Rittershoffen fault in Buntsandstein and Permian sandstones (from ~245 Ma to ~255 Ma) and in the Carboniferous granite (~340 Ma) [*Baujard et al*., 2017]. The fracture network was investigated in the open-hole sections using acoustic image logs correlated with standard geophysical logs (e.g., gamma ray, neutron porosity), cutting observations and permeability indicators (i.e., mud losses, gas occurrences), and temperature logs [*Vidal et al.,* 2017]. If fracture zones present indications of permeability or temperature anomalies at the borehole scale after drilling operations without any stimulation operations, they are qualified as OP fracture zones [*Vidal et al*., 2017]. In GRT-1, one main OP fracture zone was observed in the granitic basement from measured depths (MD) of 2325 to 2368 m (Figure 8.15) [*Vidal et al.*, 2016a, 2017]. In GRT-2, four OP fractures zones were observed in the granitic basement (Figure 8.16) [*Baujard et al.,* 2017; *Vidal et al*., 2017]. The main OP fracture zone is located at 2766-2800 m MD (Figure 8.16). Others OP fracture zones are located at approximately 2535 m MD, approximately 2950 m MD and approximately 3050 m MD [*Vidal et al.*, 2017].

The thermal profiles of two wells are divided into two parts [*Baujard et al*., 2017].

- The uppermost part is associated with a linear geothermal gradient of 95°C/km indicative of conductive heat transfer [*Baujard et al*., 2017]. The sedimentary formations from the Cenozoic and Mesozoic (Lower Jurassic and Upper Triassic) may serve as cap rocks that insulate the active hydrothermal system below.

• The deepest part exhibits a null geothermal gradient in GRT-1 (Figure 8.15) and a low geothermal gradient of 18°C/km in GRT-2 (Figure 8.16) [*Baujard et al*., 2017]. Heat and matter transfer in these hard, fractured sandstones (of the Buntsandstein and the Permian formations) and the fractured granitic basement are dominated by convective processes. This section has positive and negative deviations from the geothermal gradient, which are positive or negative anomalies interpreted as the thermal signature of the OP fracture zones [*Baujard et al*., 2017; *Vidal et al.,* 2017]. Each OP fracture zone is associated with thermal anomalies that may be caused by the outflow of hot geothermal fluids (positive anomalies) or by remnant cooling of porous damage zones after mud invasion during drilling operations and the massive injection of water during stimulation operations (negative anomalies) [*Barton et al*., 1995; *Bradford et al*., 2013; *Davatzes and Hickman*, 2005; *Genter et al*., 2010; Vidal et al., 2017].

The bottom-hole temperatures are 166°C in GRT-1 and 177°C in GRT-2 [*Baujard et al*., 2017]. The hydraulic behavior of the vertical well GRT-1 is controlled by the main OP fracture zone in the granitic basement from 2325 to 2368 m MD (Figure 8.15), and its natural permeability was deemed too low for industrial exploitation [*Baujard et al*., 2017; *Vidal et al,* 2016a]. The well was thermally, chemically and hydraulically (TCH) stimulated with success, and its hydraulic yield was enhanced from 0.5 L/s/bar to 2.5 L/s/bar [*Baujard et al*., 2017]. The hydraulic behavior of the deviated well GRT-2 is controlled by several OP fracture zones. The natural permeability of the well was high enough for industrial exploitation and presented a good hydraulic yield (higher than 3 L/s/bar) and therefore was not stimulated [*Baujard et al*., 2017]. These OP fracture zones in the granitic basement host the fracture-controlled circulation of fluids that generate the observed hydrothermal alterations. The study focused on the hydrothermal alteration in the granitic basement inferred from observations of clay minerals. Associated minerals such as silicates (i.e., quartz and other forms of silica) and carbonates also provide information about the hydrothermal alteration, but they were not part of the study.

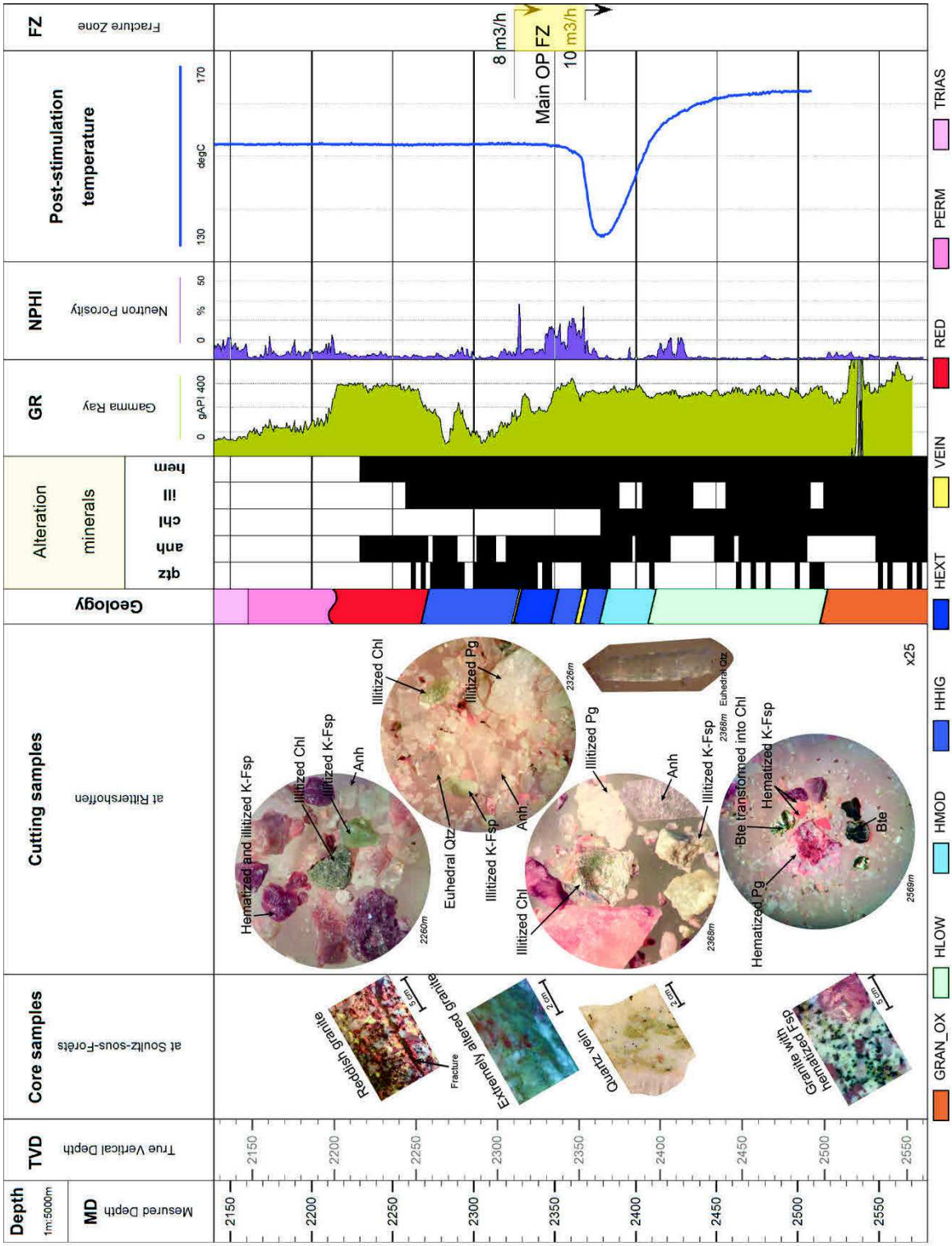
FZ
Fracture Zone
Post-stimulation temperature
170
degC
130
8 m3/h
Main OP FZ
10 m3/h
NPHI
Neutron Porosity
50
%
0
GR
Gamma Ray
gAPI 400
0
Alteration minerals
hem
ill
chl
anh
qtz
Geology
Cutting samples
at Rittershoffen
Hematized and illitized K-Fsp
Illitized Chl
Illitized K-Fsp
Anh
2260m
Illitized Chl
Illitized Pg
Euhedral Qtz
Illitized K-Fsp
Anh
2326m
Euhedral Qtz
Illitized Pg
Anh
Illitized K-Fsp
Illitized Chl
2368m
Bte transformed into Chl
Hematized K-Fsp
Bte
Hematized Pg
2569m
x25
Core samples
at Soultz-sous-Forêts
Redish granite
Fracture
5 cm
Extremely altered granite
2 cm
Quartz vein
5 cm
Granite with hematized Fsp
5 cm
Depth
1m:5000m
MD
Measured Depth
TVD
True Vertical Depth
2150
2200
2250
2300
2350
2400
2450
2500
2550
GRAN_OX
HLOW
HMOD
HHIG
HEXT
VEIN
RED
PERM
TRIAS

Figure 8.15 (previous page) Temperature profile in the granitic basement of GRT-1 correlated with cutting samples observations, occurrences of alteration minerals, and gamma ray (GR) and neutron porosity (NPHI) data. The light yellow interval is an originally permeable (OP) fracture zone from a structural analysis [*Vidal et al.*, 2016a, 2017]. Core samples from Soultz-sous-Forêts are indicated as potential analogs of the alteration grades observed in the cuttings. Black colors in the alteration mineral columns indicate the presence of the minerals. Cuttings observed with a hand lens are magnified 25x. Qtz=quartz, anh=anhydrite, chl=chlorite, ill=illite, hem=hematite, bte=biotite, pg=plagioclase feldspar, K-Fsp=potassic feldspar. GRAN_OX = propylitic alteration and hematite precipitation, HLOW = low degree of argilization, HMOD = moderate degree of argilization, HHIG = high degree of argilization, HEXT = extreme degree of argilization, VEIN = quartz vein, RED = reddish granite affected by paleoweathering, PERM = Permian sediments, TRIAS = Triassic sediments

Figure 8.16 (next page) Temperature profile in the granitic basement of GRT-2 correlated wwith cutting samples observations, occurrences of alteration minerals, and gamma ray (GR) and neutron porosity (NPHI) data. Light yellow intervals are originally permeable (OP) fracture zones from a structural analysis [*Vidal et al.*, 2017]. Core samples from Soultz-sous-Forêts are indicated as potential analogs of the alteration grades observed in the cuttings. Black colors in the alteration mineral columns indicate the presence of the minerals. Cuttings observed with a hand lens are magnified 25x. Qtz=quartz, anh=anhydrite, chl=chlorite, ill=illite, hem=hematite, bte=biotite, pg=plagioclase feldspar, K-Fsp=potassic feldspar, ms=muscovite.

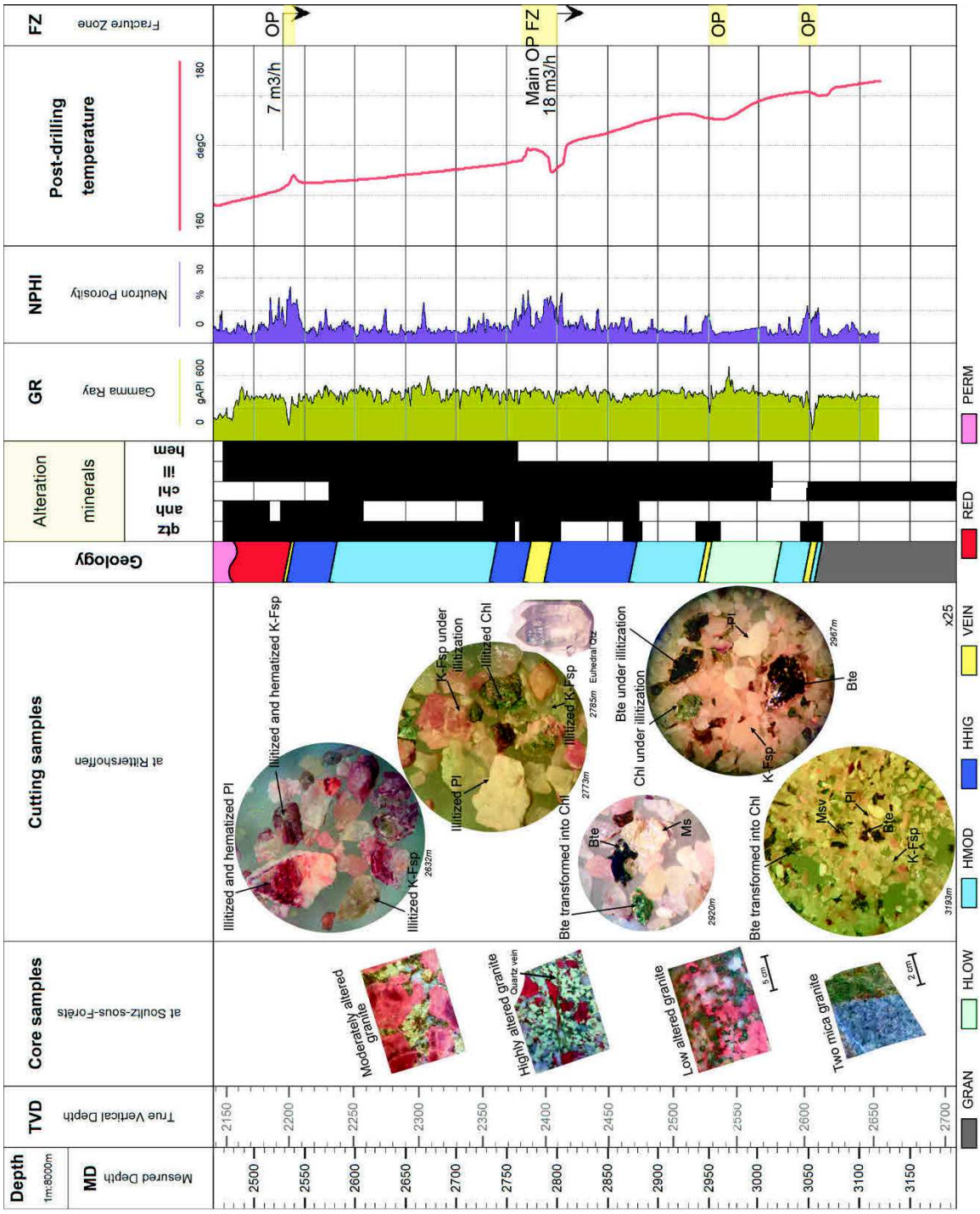
FZ
Fracture Zone
OP
7 m3/h
Main OP FZ
18 m3/h
OP
OP
Post-drilling temperature
degC
180
160
NPHI
Neutron Porosity
%
30
0
GR
Gamma Ray
gAPI
600
0
Alteration minerals
qtz
anh
chl
ill
hem
Geology
Cutting samples
at Rittershoffen
Illitized and hematized Pl
Illitized and hematized K-Fsp
Illitized K-Fsp
2632m
K-Fsp under illitization
Illitized Chl
Illitized Pl
Illitized K-Fsp
2785m
Euhedral Qtz
2773m
Bte transformed into Chl
Bte
Ms
2920m
Bte under illitization
Chl under illitization
Pl
Bte
K-Fsp
2967m
Bte transformed into Chl
Msv
Pl
Bte
K-Fsp
3193m
x25
Core samples
at Soultz-sous-Forêts
Moderately altered granite
Highly altered granite
Quartz vein
5 cm
Low altered granite
Two mica granite
2 cm
TVD
True Vertical Depth
2150
2200
2250
2300
2350
2400
2450
2500
2550
2600
2650
2700
Depth
1m:8000m
MD
Measured Depth
2500
2550
2600
2650
2700
2750
2800
2850
2900
2950
3000
3050
3100
3150
GRAN
HLOW
HMOD
HHIG
VEIN
RED
PERM

8.4.5 Methodology

8.4.5.1 Evaluation of argilization from observations of cutting

The first part of the study involved the investigation of the alteration petrography of the cutting samples by hand-lens examination at 3-m depth intervals. With cutting samples, spatial resolution is low and textural relations between minerals are not studied. Moreover, minerals from the fractures and the surrounding granitic protolith are commonly mixed within each cutting sample. The degree of argilization of the primary minerals and the occurrence of chlorite were investigated by hand-lens examination of the granitic samples. The degrees of alteration of the granitic cuttings was determined based on observations of analogue core samples from Soultz (core samples in Figures 8.15 and 8.16) [*Genter and Traineau*, 1992; *Hooijkaas et al.,* 2006]. The whole granitic basement affected by propylitic alteration is designated GRAN (core sample in Figure 8.16). The top of the granitic basement is affected by paleo-weathering related to Permian exhumation of the basement. This facies is associated with hematization and designated reddish granite (RED) (core sample in Figure 8.15). Moreover, four types of granitic facies were determined to show increasing levels of argilization of the primary minerals:

- A facies with a low degree of argilization (HLOW) is characterized by the persistence of weakly argilized biotite and chlorite and by unaltered plagioclase and potassic feldspars. The texture of the granitic protolith is preserved (core sample in Figure 8.16);
- A facies with a moderate degree of argilization (HMOD) is characterized by the total argilization of biotite and the preservation of unaltered plagioclase and potassic feldspars (core sample in Figure 8.16);
- A facies with a high degree of argilization (HHIG) is characterized by the total argilization of biotite and the partial to total replacement of plagioclase and potassic feldspars with clay minerals (core samples in Figure 8.16);
- A facies with an extremely high degree of argilization (HEXT) is characterized by the total argilization of primary minerals (i.e., biotite and the plagioclase and potassic feldspars). The overall texture of the core sample is

completely modified compared with that of the granitic protolith (core samples in Figure 8.15).

The macroscopic observations were correlated with the geophysical logs (i.e., gamma ray and neutron porosity) to provide supplementary information about the vertical distribution of the clay minerals identified in the cuttings. The gamma ray log involves the measurement of the potassium, thorium and uranium contents used to detect the leaching of radioactive primary minerals (negative anomaly) or the presence of clay minerals that incorporate radioactive chemical elements within the fracture zones (positive anomaly). The neutron porosity log is based on the response of a formation to the emission of fast neutrons by a given source; in granite, that response is positive if there is a fracture or if clays and hydrated minerals occur in the formation.

Then, thin sections made from mount cuttings in epoxy were observed by microscopy in approximately fifty cutting samples from both wells. The degree of illitization of the primary minerals was estimated from microscopic observations of the replacement rate of the K-feldspars by illite in thin sections.

8.4.5.2 Identification of clay minerals

The second part of the study focused on the identification of clay minerals. Twenty-one and thirty-eight cuttings samples were collected from GRT-1 and GRT-2, respectively. The sampling was concentrated in the permeable and altered fracture zones, which were identified within the granitic basement using acoustic image and temperature logs. Some of the samples were located in lightly altered zones and were used as reference materials, as they are believed to be representative of rocks preserved from present-day fluid circulation properties. Samples were not ground; they were dispersed in distilled water by ultrasonic vibration to disintegrate the particles. Oriented powders on glass slides were prepared with a <5 µm clay suspension, obtained by sedimentation. Clay minerals were identified by XRD of air-dried and ethylene–glycol (EG)-saturated oriented powders carried out on a Bruker D8 Advance diffractometer (CuKα radiation, 40 kV, 40 mA). The analytical conditions were as follows: angular domain: 2.5-30° 2θ; step increment: 0.025 2θ; and counting time per step: 3 s. XRD data acquisition and treatment were conducted using the X'Pert HighScore

software (PANalytical B.V.). The clay minerals were identified according to the literature (Brindley and Brown, 1980) (Figure 8.17). When present, the (001) reflection from the illitic minerals was deconvolved into poorly crystallized illite (PCI), well-crystallized illite (WCI) and ordered illite-rich mixed layered illite/smectite (I/S) using the Fityk software (Figure 8.17c). The full width at half maximum (FWHM) intensity of the typical (001) reflections of WCI and PCI at 10 Å is a good indicator of the crystallinity along the c axis (Kubler, 1968). The crystallinity along the c axis of the chlorite was estimated from the FWHM intensity of the (002) reflection at 7 Å.

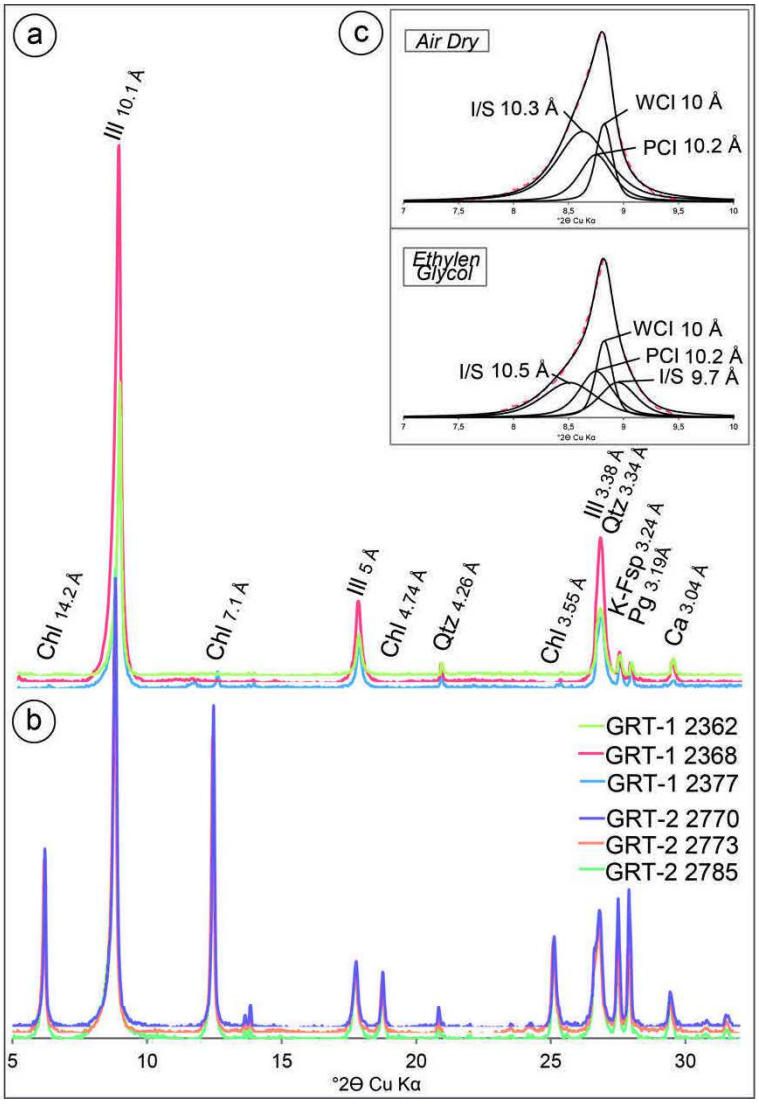

Figure 8.17 X-ray diffractograms of the clay fraction as observed in the main OP FZ a) in GRT-1 (samples 2362, 2368 and 2377) and b) in GRT-2 (samples 2770, 2773 and 2785). Ill=illite, Chl=chlorite, Qtz=quartz, Pg=plagioclase feldspar, K-Fsp=potassic feldspar, Ca=calcite. c) deconvolution of the 7-10° 2Θ CuKa

domain of the X-ray diffractograms (<5 µm clay fraction) of air-dried and EG-saturated oriented powder of an example sample. I/S: ordered illite/smectite mixed layer; WCI: well-crystallized illite, PCI: poorly crystallized illite. Dashed red line represents the data.

8.4.5.3 Analysis of chemical composition of clay minerals

Finally, the third part of the study involved the investigation of the chemical compositions of clay minerals using a JEOL 5600LV SEM, which was equipped with a BRUKER XFlash 4030 Silicon Drift Detector (accompanied by the SPIRIT software). The analytical conditions were as follows: 15 kV; 1 nA; counting time: 60 s; and working distance: 16.5 mm. The analyzed elements were Si, Al, Fe, Mg, Mn, Ti, Ca, Na and K. The system was calibrated with a variety of synthetic oxide and natural silicate standards. The reproducibilities of the standard analyses were approximately 1%, except for Na, which had a reproducibility of 1.5%.

8.4.6 Alteration petrography in the geothermal wells at Rittershoffen

Observations in GRT-1

The top of the granitic basement is encountered at 2212 m MD in GRT-1. The first granitic facies intersected is the RED facies down to 2270 m MD (Figure 8.15). Cuttings near the contact with the overlying sediments are reddish because of the intense precipitation of hematite (cuttings in Figure 8.15). Fractures into reddish granite contain a large amount of illitic minerals associated with micro-quartz (Figure 8.18a). Carbonates such as calcite and dolomite as well as sulfate are prevalent in fractures. Some green chlorite minerals are observed (Figure 8.18a). More microscopy images of the cutting samples in GRT-1 are provided in the supporting information S1. SEM observations indicate epitaxial growth of the large chlorite (>50 µm) that likely crystallized from hydrothermal circulations (Figure 8.18b). The RED facies is correlated with a well-known pattern of gamma rays that is characteristic of the reddish granite in the area (Figure 8.15) [*Vidal et al*., 2016b]. At the top of the granitic basement, the gamma ray intensity decreases abruptly in the sedimentary cover.

Below the RED facies, an HHIG facies is intersected down to 2326 m MD (cuttings in Figure 8.16).

The main OP fracture zone presents abundant euhedral quartz from 2326 to 2329 m MD and from 2365 to 2368 m MD that could indicate the presence of quartz veins (cuttings in Figure 8.15). These quartz veins are associated with a sharply negative anomaly of gamma ray radiation (Figure 8.15) and have already been observed in acoustic image logs [*Vidal et al.,* 2017]. Small crystallites of illitic minerals occur as grain coatings of quartz (Figure 8.18c). At the top of the main OP fracture zone, a HEXT facies is observed from 2329 to 2350 m MD (Figure 8.15) in which cuttings are highly bleached in response to intense hydrothermal alteration (cuttings in Figure 8.15). Anhydrite and pyrite are abundant in the main OP fracture zone of GRT-1. Chlorite is seldom observed within the main OP fracture zone of GRT-1. At the bottom of the main OP fracture zone, an HHIG facies is observed down to 2380 m MD (cuttings in Figure 8.15), and primary biotite and local feldspars are completely replaced by small crystallites of illitic minerals (Figure 8.18d). Neutron porosity values confirm the significant argilization of the main OP fracture zone, with values between 10 and 20% from 2340 to 2370 m MD and maxima of nearly 40% at 2325 and 2370 m MD.

Below the main OP fracture zone, from 2380 to 2410 m MD, an HMOD facies is encountered, and then from 2410 to 2516 m MD, an HLOW facies is observed (Figure 8.15). The deep granitic samples from 2516 to 2580 m MD are affected by propylitic alteration with the partial transformation of primary biotite into chlorite and the partial replacement of primary potassic feldspar or muscovite with small crystallites of illitic minerals (Figure 8.18e). Cuttings exhibit a reddish color, and this facies is designated GRAN_OX (Figure 8.15).

Figure 8.18 (next page) Microscopic observations of thin sections of cuttings fixed in epoxy in GRT-1 at a) 2236 m MD (PPL), b) 2212 m MD (SEM observations), c) 2326 m MD (PPL), d) 2368 m MD (PPL), and e) 2503 m MD (plane polarized light, PPL); and in GRT-2 at f) 2773 m MD (PPL), g) 2773 m MD (crossed polarized light, XPL), h) 2273 m MD (SEM), i) 2950 m MD (PPL) and j) 2977 m MD (PPL) Qtz=quartz, Bte=biotite, Chl=chlorite, Ill=illite, Py=pyrite, Anh=anhydrite, Dol=dolomite, Ca=calcite, Fe-ox=iron oxides.

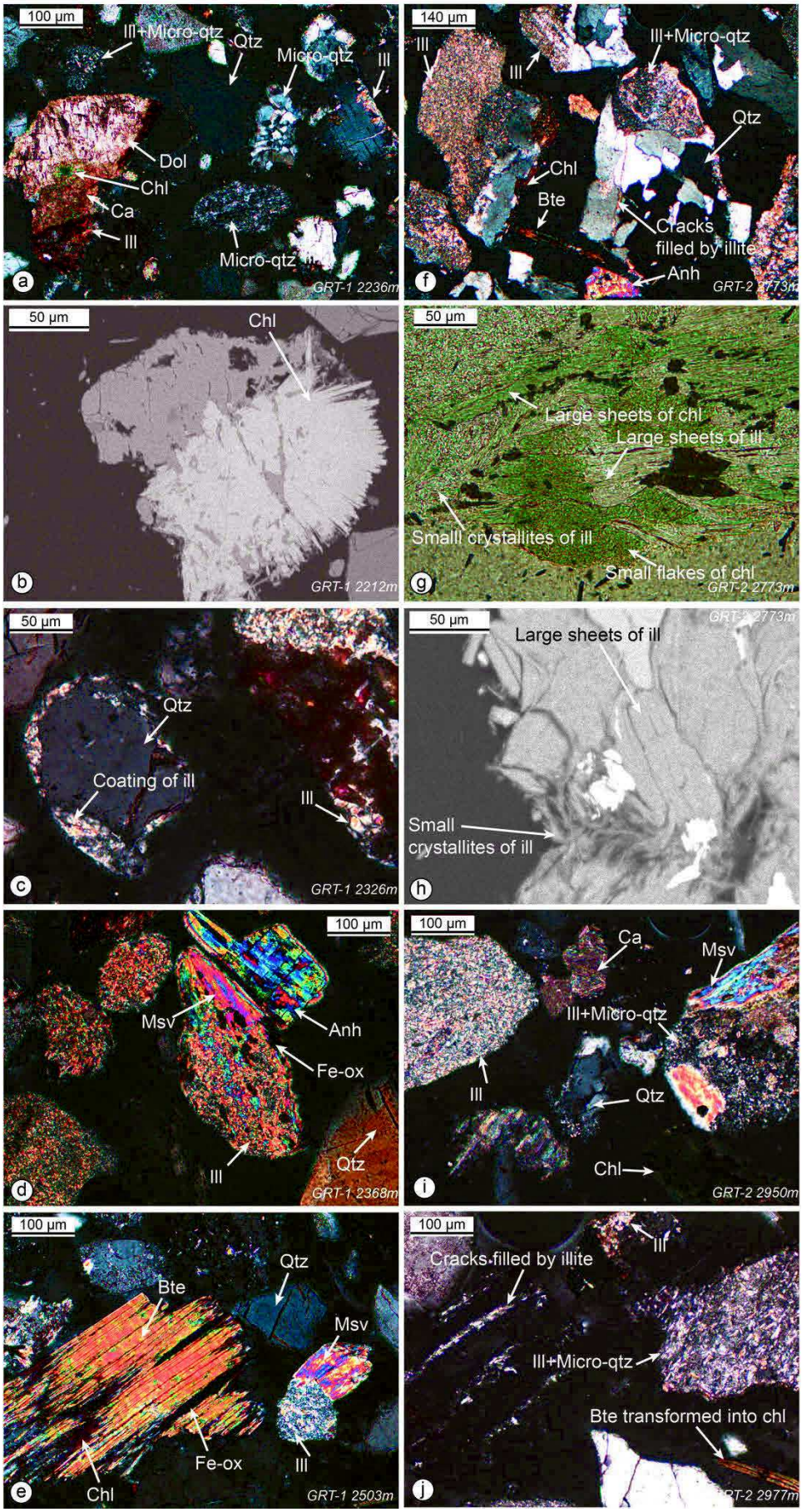
100 µm
Ill+Micro-qtz
Qtz
Micro-qtz
Ill
Dol
Chl
Ca
Ill
Micro-qtz
a
GRT-1 2236m
140 µm
Ill
Ill
Ill+Micro-qtz
Qtz
Chl
Bte
Cracks filled by illite
Anh
f
GRT-2 2773m
50 µm
Chl
b
GRT-1 2212m
50 µm
Large sheets of chl
Large sheets of ill
Small crystallites of ill
Small flakes of chl
g
GRT-2 2773m
50 µm
Qtz
Coating of ill
Ill
c
GRT-1 2326m
GRT-2 2773m
50 µm
Large sheets of ill
Small crystallites of ill
h
100 µm
Msv
Anh
Fe-ox
Ill
Qtz
d
GRT-1 2368m
100 µm
Ca
Msv
Ill+Micro-qtz
Ill
Qtz
Chl
i
GRT-2 2950m
100 µm
Qtz
Bte
Msv
Fe-ox
Ill
Chl
e
GRT-1 2503m
100 µm
Ill
Cracks filled by illite
Ill+Micro-qtz
Bte transformed into chl
j
GRT-2 2977m

Observations in GRT-2

The top of the granitic basement is encountered at 2480 m MD in GRT-2. The first granitic facies is RED down to 2533 m MD (Figure 8.16). At the base of the RED facies, the abundance of euhedral quartz from 2533 to 2536 m MD suggests the presence of quartz veins associated with the presence of an OP fracture zone at the same depth. Then, an HHIG facies is observed from 2536 to 2578 m MD, and an HMOD facies is observed from 2578 m MD to 2737 m MD (Figure 8.16).

The main OP fracture zone in GRT-2 is associated with an HHIG facies observed from 2737 to 2875 m MD. The top of the main OP fracture zone is associated with neutron porosity values between 10% and 20% from 2760 to 2810 m MD, which are correlated with the significant argilization of the cuttings (Figure 8.16). In thin sections, primary minerals are replaced by illitic minerals but are still identifiable compared with the main OP fracture zone in GRT-1 (Figure 8.18f). The microscopic observations indicate at least two different sizes of illitic minerals that are likely associated with different hydrothermal events. Illitic minerals are present as large sheets (>50 µm) as well as small crystallites (<5 µm) and are sometimes present as the infill of cracks (Figure 8.18f, g and h). At least two sizes of chlorite are also observed. Chlorite derived from the transformation of biotite is observed as large sheets (>50 µm), and another population of chlorite in the form of small flakes (<5 µm) is also observed (Figure 8.18h). More microscopy images of the cutting samples in GRT-2 are provided in the supporting information S2. In the main OP fracture zone, cuttings from 2770 to 2791 m MD indicate euhedral quartz, which is interpreted as the occurrence of quartz veins (Figure 8.16). These cuttings correlate with quartz veins observed in acoustic image logs [*Vidal et al*., 2017].

Below the main OP fracture zone, an HMOD facies is observed until the OP fracture zone at 2944 m MD. Locally, primary minerals are completely transformed into small crystallites of illitic minerals, while primary muscovite could be preserved (Figure 8.18i). Green chlorite and calcite are also found at these depths. The OP fracture zone is associated with an abundance of euhedral quartz from 2944 to 2950 m MD correlated with a sharply negative anomaly of gamma ray radiation (Figure 8.16). Below the OP fracture zone, from 2950 to

3020 m MD, an HLOW facies is associated with primary quartz minerals intersected by microcracks filled with illitic minerals or with an assemblage of microquartz and illitic minerals (Figure 8.18j). Then, the increase in neutron porosity until 13% suggests an increase in the argilization of cuttings. Cuttings from 3020 to 3046 m MD confirm this increase in argilization and are associated with an HMOD facies (Figure 8.16). The deepest OP fracture zone is associated with an abundance of euhedral quartz from 3046 to 3061 m MD correlated with a sharp negative anomaly of gamma ray radiation (Figure 8.16). The deepest cuttings, from 3061 to 3196 m MD, are light gray (Figure 8.16). They are associated with the propylitic alteration and are designated GRAN.

In conclusion, four main facies of argilization were observed in GRT-1, and three were observed in GRT-2 (Figures 8.15 and 8.16 and supporting information S3). An HEXT facies is not observed in the main OP fracture zones of GRT-2, the primary minerals are not completely transformed into illitic minerals in the OP fracture zones of GRT-1, and Fe-rich chlorite is much more abundant. The highest levels of alteration (HHIG and HEXT) are observed in the main OP fractures zones of GRT-1 and GRT-2 (Figures 8.15 and 8.16 and supporting information S3). Euhedral quartz is always observed in abundance within the OP fracture zones.

8.4.7 Identification of clay minerals

X-ray diffractograms indicate that the clay alteration products are dominated by illite and chlorite in the Rittershoffen wells (Figure 8.17). The (001) reflections of the illitic minerals at 10 Å are complex. The (001) reflections were deconvolved into two or three Gaussian peaks (Figure 8.17c). Two peaks that correspond to the index peaks of WCI and PCI are consistently observed at approximately 10 Å and 10.2 Å, respectively (Figure 8.17c). The WCI peak corresponds to a d-value of 10 Å and is characterized by a narrow FWMH that ranges from 0.08 to 0.24 °2θ in GRT-1 and from 0.09 to 0.18 °2θ in GRT-2. The PCI peak corresponds to a d-value of 10.2 Å and is characterized by a broader FWMH (between 0.26 and 0.48 °2θ in GRT-1 and between 0.18 and 0.44 °2θ in GRT-2). Microscopic observations reveal that illitic minerals occur as large sheets and as small crystallites. Deconvolution is therefore based on a first-order approximation with

well-crystallized illitic minerals and poorly crystallized illitic minerals. However, there are likely more illitic populations.

Mixed layers I/S (~10% smectite) were identified in some of the samples. In air-dried samples, the layers are characterized by a broad peak near 10.3 Å that splits into two peaks near 10.5 Å and 9.7 Å after EG saturation (Figure 8.17c) (Lanson et al., 1995). The WCI and PCI peaks do not shift after EG saturation. Chloritic minerals were identified by their non-expandability and their harmonic peaks at 14 Å and 7 Å. The FWHM of the peak at 7 Å varies between 0.08 and 0.12 °2θ in GRT-1 and between 0.09 and 0.18 °2θ in GRT-2. Chlorite is less abundant in the diffractograms of GRT-1 than in those of GRT-2 (Figure 8.17).

Observations in GRT-1

Based on the crystallographic properties of the illitic minerals, two zones can be observed in the granite (Figure 8.19a).

The shallowest zone is composed of samples from 2212 to 2338 m MD that are associated with the first three alteration facies intersected by the well GRT-1, RED, HHIG and HEXT. In this zone, the average proportion of WCI (%Int WCI) is 0.43, and the average FWHM of WCI is 0.15 °2θ. The average proportion of PCI (%Int PCI) is 0.31, and the average FWMH of PCI is 0.34 °2θ. Mixed layers I/S are systematically present in this section, with an average %Int I/S of 0.26.

The deepest zone is composed of samples from 2347 to 2503 m MD that are associated with the last three alteration facies intersected by the well GRT-1, HHIG, HMOD and HLOW. In this zone, the %Int WCI is 0.72, and the average FWHM of WCI is 0.15 °2θ. The average %Int PCI is 0.40, and the average FWMH of PCI is 0.28 °2θ. Mixed layers I/S layers are no longer present in this section.

The crystallographic properties of chlorite are more strongly influenced by the main OP fracture zone than by the limits of alteration facies, as observed for illitic minerals (Figure 8.19a).

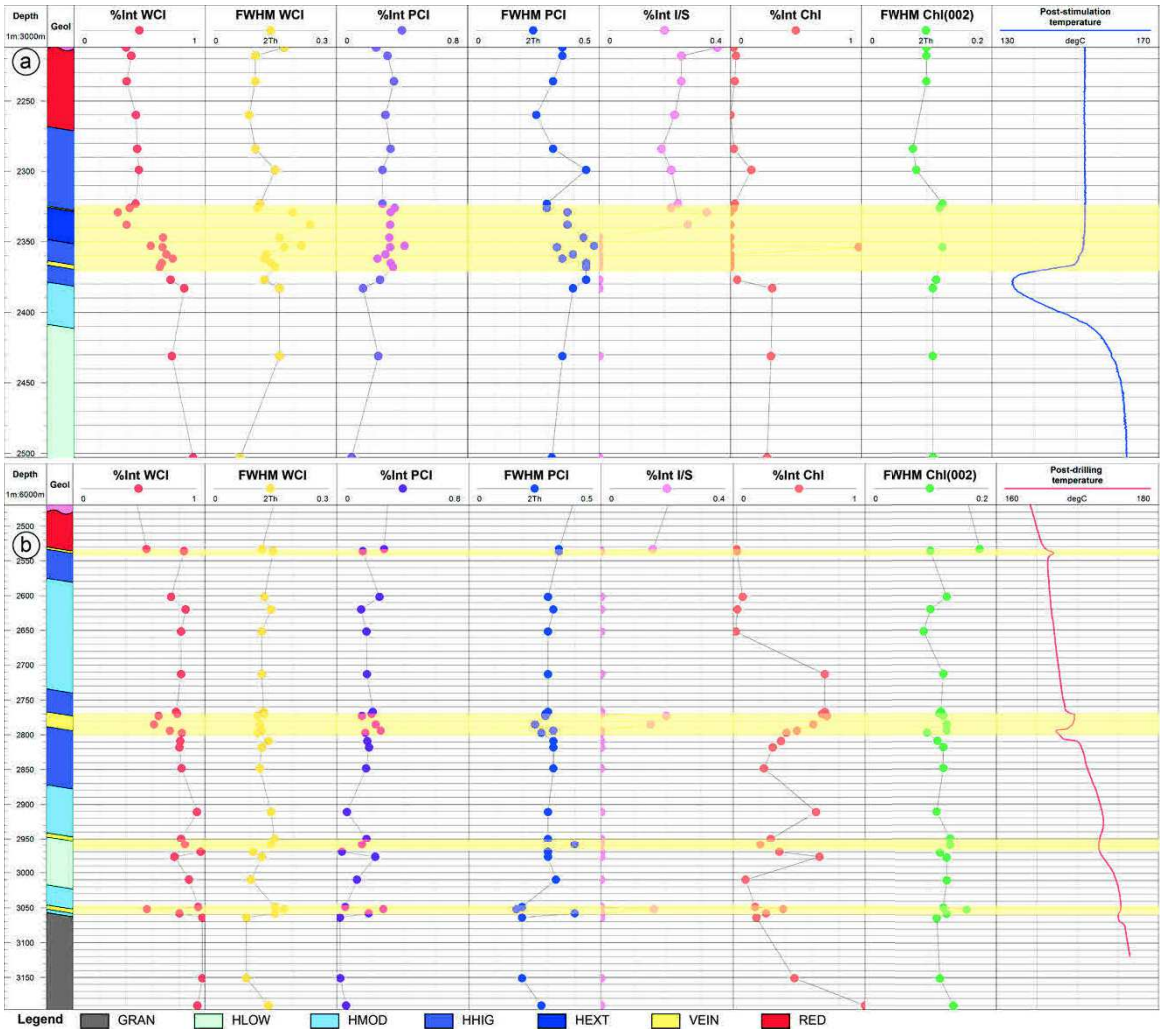

Figure 8.19 Crystal structure properties of the illitic minerals and chlorite measured using XRD of the <5 µm clay fraction versus depth a) in GRT-1 and b) in GRT-1. Relative proportion of WCI: %Int WCI = WCI int/(WCI int + PCI int + I/S int), where WCI int = the intensity of the peak deconvolved from the (001) reflection of the illitic minerals. Relative proportion of Chl: %Int Chl = (Chl int/(Chl int + WCI int + PCI int + I/S int), where Chl int = the intensity of the peak of the (002) reflection of the chlorite. Light-yellow intervals represent originally permeable (OP) fracture zones from a structural analysis [*Vidal et al.*, 2016a, 2017].

From the top of the granitic basement (2212 m MD) to the top of the main OP fracture zone (2326 m MD), the average proportion of chlorite (%Int Chl) is 0.05 (Figure 8.19a). Chlorite is only observed in one sample of the main OP fracture zone at 2354 m MD, wherein the highest proportion of chlorite in GRT-1 (0.97) is observed. From the base of the main OP fracture zone (2377 m MD) to the

bottom of the granitic basement (2503 m MD), chlorite is observed with an average %Int Chl of 0.24. With an average value of 0.10 °2θ, the FWHM values of chlorite do not vary significantly with depth.

Observations in GRT-2

The crystallographic properties of illitic minerals are more strongly influenced by the occurrence of the OP fracture zone than by limits of alteration facies, as observed for GRT-1 (Figure 8.19b).

From the top of the granitic basement (2480 m MD) to the bottom of the granitic basement (3196 m MD), %Int WCI tends to increase with depth (Figure 8.19b). The average %Int WCI is 0.78, with an average FWMH of 0.13 °2θ. Locally, the %Int WCI decreases in OP fracture zones:

- %Int WCI is 0.56 for the sample at 2533 m MD;
- %Int WCI is 0.65 and 0.61 for samples at 2773 and 2785 m MD;
- %Int WCI is 0.56 for the sample at 3052 m MD.

From the top of the granitic basement (2480 m MD) to the bottom of the granitic basement (3196 m MD), %Int PCI tends to decrease with depth (Figure 8.19b). The average %Int PCI is 0.16, with an average FWMH of 0.30 °2θ. Locally, %Int PCI increases at each OP fracture zones:

- %Int PCI is 0.29 for the sample at 2533 m MD;
- %Int PCI is 0.23 and 0.27 for samples at 2785 and 2794 m MD;
- %Int PCI is 0.18 and 0.15 for samples at 2950 and 2959 m MD;
- %Int WCI is 0.28 for the sample at 3052 m MD.

Mixed layers I/S are observed in samples at 2533, 2773, 2785 and 3052 m MD and are associated with OP fracture zones (Figure 8.19b). Outside OP fracture zones, mixed layers I/S are no longer observed.

Chlorite is observed in all samples from the granitic basement of GRT-2 (Figure 8.19b). The average %Int Chl is 0.38, and the FWHM is relatively constant, with an average value of 0.12 °2θ (Figure 8.19b). In the main OP fracture zone, the %Int Chl decreases from 0.71 at 2773 m MD to 0.23 at 2848 m MD.

In conclusion, the granitic basement is characterized by a general increase in %Int WCI and a decrease in %Int PCI with depth. However, local variations are associated with OP fracture zones in both wells. Each OP fracture zone is associated with a decrease in %Int WCI, an increase in %Int PCI and the occurrences of mixed layers I/S. These variations are more strongly correlated with the alteration facies limit in GRT-1 than in GRT-2. In GRT-1, the main OP fracture zone appears to act as an interface between two zones that are quite distinct, with occurrences of mixed layers I/S above and no longer mixed layers I/S below.

8.4.8 Chemical compositions of clay minerals

The structural formulae of the illitic minerals were calculated relative to a structure containing 11 oxygen atoms and assuming that the total iron content was composed of Fe3+ (Supporting information S4). The structural formulae of the chlorite were calculated relative to a structure containing 14 oxygen atoms and assuming the total iron content was composed of Fe2+ (Supporting information S4).

Observations in GRT-1

The chemical analyses of the illitic minerals (WCI+PCI+ml I/S) in GRT-1 do not demonstrate major variations with depth (Figure 8.20a). The interlayer charge is between 0.83 and 0.90, and the average octahedral Al content is 1.67+/-0.05 per O10(OH) (Supporting information S4). Samples above the main OP fracture zone (i.e. from 2212 to 2329 m MD) present an XFe ratio<0.5, whereas samples in the main OP fracture zone and below (i.e. from 2329 to 2503 m MD) present an XFe ratio>0.5.

Two types of chlorite were distinguished based on their structural formulae. Samples associated to sealed fracture zone at the top of the granitic basement, at 2218 m MD, and in the main OP fracture zone, at 2368 m MD, contain Fe-rich chlorite with XFe>0.80 (Figure 8.20a). The deepest sample in GRT-1 associated to granitic protolith, at 2503 m MD, contains ferromagnesian chlorite with XFe=0.38.

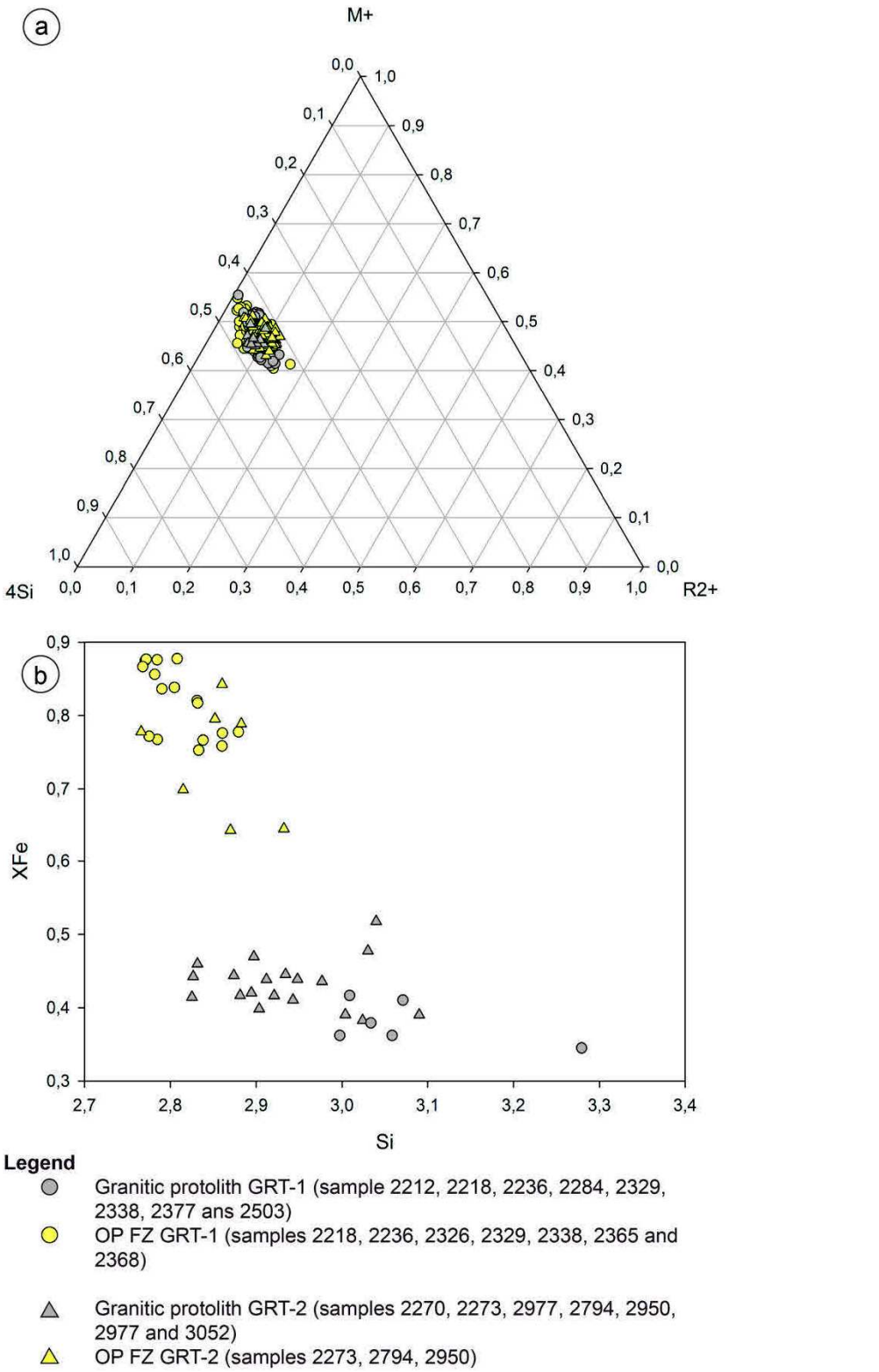

Figure 8.20 Plot of the structural formulae of a) the illitic minerals in a M+-R2+-4Si ternary diagram and b) chlorite in a diagram of XFe versus Si for wells GRT-1 and GRT-2. XFe = Fe/(Fe+Mg). The average structural formula for each sample is presented in supporting information 4.

Observations in GRT-2

The chemical analyses of the illitic minerals (WCI+PCI+ml I/S) in GRT-2 do not demonstrate major variations with depth (Figure 8.20b). The interlayer charge varies between 0.85 and 0.91, and the average octahedral Al content is 1.63+/-0.07 per O10(OH) (Supporting information S4). Samples in OP fracture zones, i.e. at 2270, 2773, 2950, and 3052 m MD, present an XFe ratio (~0.5) similar to that of samples associated to the granitic protolith, i.e. at 2794 and 2977 m MD.

Two types of chlorite were distinguished based on their structural formulae. Samples in OP fracture zones, i.e. at 2773, 2794 and 2950 m MD, contain Fe-rich chlorites with XFe>0.60 (Figure 8.20b). Ferromagnesian chlorite with XFe<0.5 is observed in samples in OP fracture zones, i.e. at 2770, 2773, 2950, and 3052 m MD, as well as in the sample at 2977 m MD associated to the granitic protolith (Figure 8.20b).

In conclusion, the illitic minerals in both wells exhibit similar compositions regardless of the size of the illitic minerals, the occurrences of OP fracture zones or the alteration facies of the granitic basement (Figure 8.20a). Chlorite occurs as two distinct populations: Fe,Mg-chlorite, which corresponds to the large sheets observed by microscopy, resulting from the alteration of biotite (Figure 8.18g); and Fe-chlorite, which forms aggregates of small flakes or epitaxial growths along pore walls, formed during later hydrothermal events (Figure 8.18g and b). Fe-chlorite is associated with OP fracture zones, whereas Fe,Mg-chlorite is observed regardless of the occurrence of OP fracture zones and the alteration facies of the granitic basement.

8.4.9 Discussion

8.4.9.1 Interpretation of the alteration assemblages in the granitic basement

The characterizations of the alteration petrography and of the secondary mineralogies of the cuttings collected from the two wells investigated in this study help to refine the hydrothermal history of the granitic basement at Rittershoffen (Figure 8.21).

Early alteration stage in the poorly fractured granitic basement

Petrographic observations of the basement rocks from the parts of the wells that preserve the characteristics of strong fracture-controlled alteration features reveal that the entire granitic batholith has been affected by an earlier alteration stage consisting of the pervasive replacement of biotite and primary calc-silicate minerals with an assemblage of Fe,Mg-chlorite, epidote and illite (Figure 8.21). This type of alteration and its consequent mineral assemblage correspond to the propylitic alteration facies reported in the literature [*Lowell and Guilbert*, 1970]. Propylitic alteration is very common in magmatic intrusive bodies. This alteration occurs during the cooling of an igneous intrusion, and results from interactions, at moderate to high temperatures (200 to 400°C), of the most reactive igneous minerals with fluids of diverse origins that are stagnant in pores or microcracks ([*Thomasson and Kristmannsdottir*, 1972; *Reyes*, 1990]. Consequently, propylitic alteration can affect large volumes of intrusive rocks, and it is representative of hydrothermal alteration in inactive flow regimes [*Beaufort et al.*, 1990].

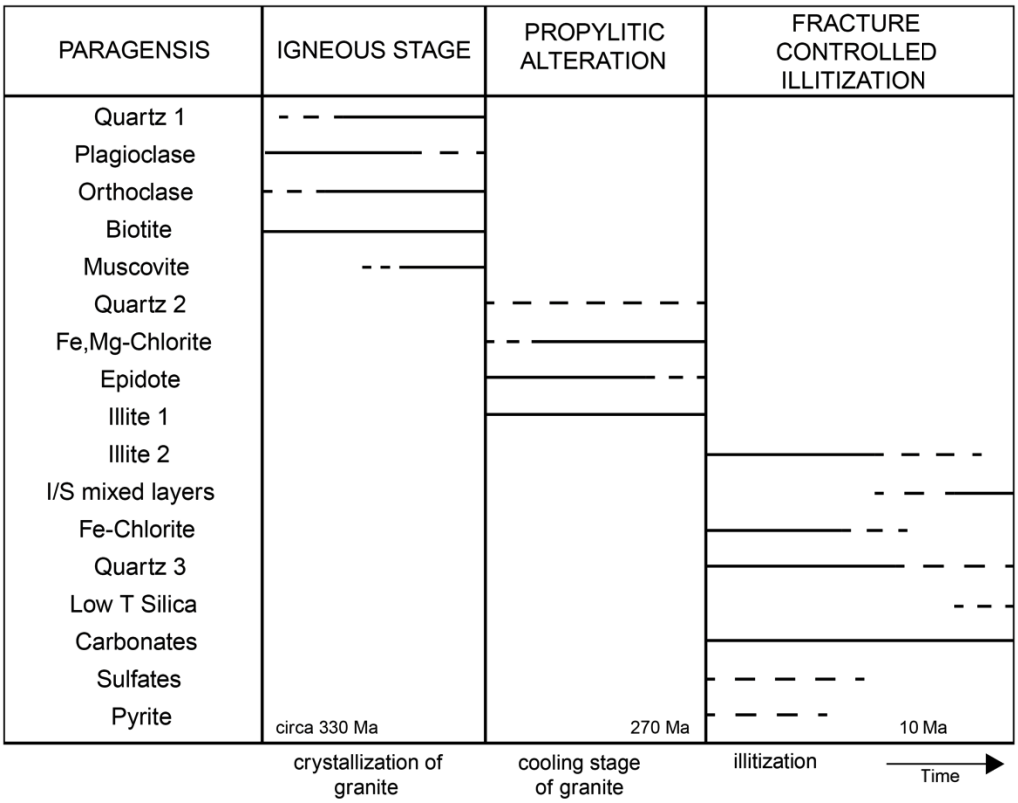

Figure 8.21 Paragenesis sequence and alteration history of the granitic basement at Rittershoffen.

Subsequent alteration stages in the highly fractured granitic basement

The OP fracture zones identified within the two boreholes during the drilling operations and from the subsequent geophysical monitoring were characterized. In the well GRT-1, OP fracture zones correlate with HEXT and HHIG facies, whereas in the well GRT-2, they correlate with HHIG and HMOD facies (Figures 8.15 and 8.16 and supporting information S3). According to petrographic observations of cuttings from these facies, three different mineral assemblages can be distinguished based on the following parageneses:

- Illite + quartz + hematite ± calcite
- Illite + Fe-chlorite ± pyrite
- Illite + ml I/S + hematite ± calcite

These three parageneses crystallized under different physico-chemical conditions and reveal typical multistage hydrothermal crystallization (Figure 8.21). The strong illitization of the wall rock in these facies could completely obliterate the features of the earlier propylitic alteration, and in some cases, strong illitization dominated by mixed layers I/S could even obliterate minerals from earlier hydrothermal parageneses (Figure 8.21). For example, in HEXT facies in the well GRT-1, chlorite is no longer observed and was likely replaced completely by illite and mixed layers I/S. The relative timing of the hydrothermal events that promoted these mineral assemblages is not strictly constrained due to the absence of core samples.

It is important to note that similar mineral parageneses have been observed in the geothermal wells of Soultz [*Genter*, 1989; *Genter and Traineau*, 1993; *Ledésert et al.*, 1999; *Jacquemont*, 2002], in which the occurrence of illitic minerals in fractures of core samples has been dated to more than five different geological ages from the Permian to the Eocene [*Schleicher et al.*, 2006; *Bartier et al.*, 2008]. Moreover, these clay minerals were not found at isotopic equilibrium within the currently circulating fluids at either Soultz or Rittershoffen (Table 8.3). Only calcite was found to be in isotopic equilibrium with the existing fluids [*Fouillac and Genter*, 1992]. Nevertheless, the isotopic composition of the mixed layers I/S has not yet been determined because of the difficulty in separating

these phases from other illitic minerals and because their relationship with the subsurface geothermal fluids is still questionable.

8.4.9.2 Illitic signature paleo-circulation systems and OP fracture zones

Illitic minerals are known to be potential indicators of fluid circulation and paleo-circulation systems [*Flexser*, 1991; *Harvey and Browne*, 1991; *Patrier et al.,* 1996; *Teklemariam et al*., 1996; *Mas et al.,* 2003, 2006].

Observations of cuttings, macroscopically by a hand lens and microscopically in thin sections, reveal that the highest illitization occurs above 2380 m TVD in the well GRT-1 (HEXT and HHIG) and above 2470 m TVD in the well GRT-2 (HHIG and HMOD). These sections of strong illitization suggest that intense paleo-circulation systems were concentrated in the first 200 m of the granitic basement in GRT-1 and in the first 300 m of the granitic basement in GRT-2. Both sections of strong illitization are delimited at the base by main OP fracture zones in both wells.

XRD results obtained for the well GRT-1 confirm the observations of cuttings. The main OP fracture zone acts as an interface between two highly distinct sections. The uppermost section is associated with a low proportion of WCI correlated with the occurrence of mixed layers I/S that suggest intense paleo-circulations. This uppermost section correlates with HEXT and HHIG facies. The deepest section is associated with a high proportion of WCI correlated with the absence of mixed layers I/S. This deepest section correlates with HHIG, HMOD and HLOW facies.

The XRD results obtained for the well GRT-2 do not indicate two sections delimited by the main OP fracture zone, as observed for cuttings and GRT-1. XRD results reveal local variations that correlate with the three OP fracture zones in the granitic basement. The three OP fracture zones are associated with a local decrease in WCI, a local increase in PCI and occurrences of mixed layers I/S regardless of the alteration facies. These variations in the XRD results could be linked to local variations in the physico-chemical conditions in OP fracture zones. In an OP fracture zone that channels ascending geothermal fluids that are strongly oversaturated with respect to the surrounding clay minerals, abrupt

changes in the flow regime, including the mixing of geothermal fluids, can lead to the explosive nucleation of small clay crystallites and promote the occurrence of heterogeneous mineral assemblages, such as mixed layers I/S [*Beaufort et al.,* 1996; *Patrier et al.,* 1996].

The chemical analyses of the illitic minerals in the Rittershoffen wells are quite consistent, and thus, we can suppose that the fluid did not evolve over time (Figure 8.20a).

Even if mixed layers I/S can result from both past and present-day hydrothermal events, the occurrence of mixed layers I/S appears to be the signature of the OP fracture zones in the Rittershoffen wells (Figure 8.22). Mixed layers I/S occur in the main OP fracture zone in the well GRT-1 and in three OP fracture zones in the well GRT-2. However, extensive precipitations of mixed layers I/S could lead to plugging of the OP fracture zones, thereby decreasing their natural permeability. In the well GRT-1, for example, primary and earlier secondary minerals are completely replaced by mixed layers I/S in the main OP fracture zone, and the permeability is reduced to the point that the well needs to be stimulated to bring it into production.

8.4.9.3 Chlorite signature in OP fracture zones

Two populations of chlorite were observed in the wells GRT-1 and GRT-2 (Figure 20b). Ferromagnesian chloritic minerals associated with propylitic alteration occur throughout the granitic batholith. These minerals originate from the alteration of biotite under oxidizing conditions. It has been demonstrated that the chemistries of chloritic minerals are rock-dominated during propylitic alteration [*Beaufort et al.*, 1992; *López-Munguira et al.*, 2002; *Mas et al.,* 2006] and that the incorporation of magnesium is promoted within the structure of chlorite, which crystallizes with iron oxides such as hematite under oxidizing conditions [*Beaufort et al.*, 1992]. It has also been demonstrated that the chemistry of Fe-chlorite is likely controlled by fluids circulating in the permeable fracture zones under reducing conditions [*Beaufort et al.,* 2015; *Mas et al.,* 2006; *Patrier et al.,* 1996]. Both of these chlorites are associated with higher temperatures than those in the present-day wells, and they do not represent current hydrothermal circulation. However, the persistence of Fe-chlorite in the OP fracture zones of GRT-2

indicates that these minerals have yet to be completely destabilized by oxidizing fluids, which are currently crystallizing mixed layers I/S (Figure 8.22). The OP fracture zones of GRT-2 show higher natural permeabilities than the main OP fracture zone in GRT-1.

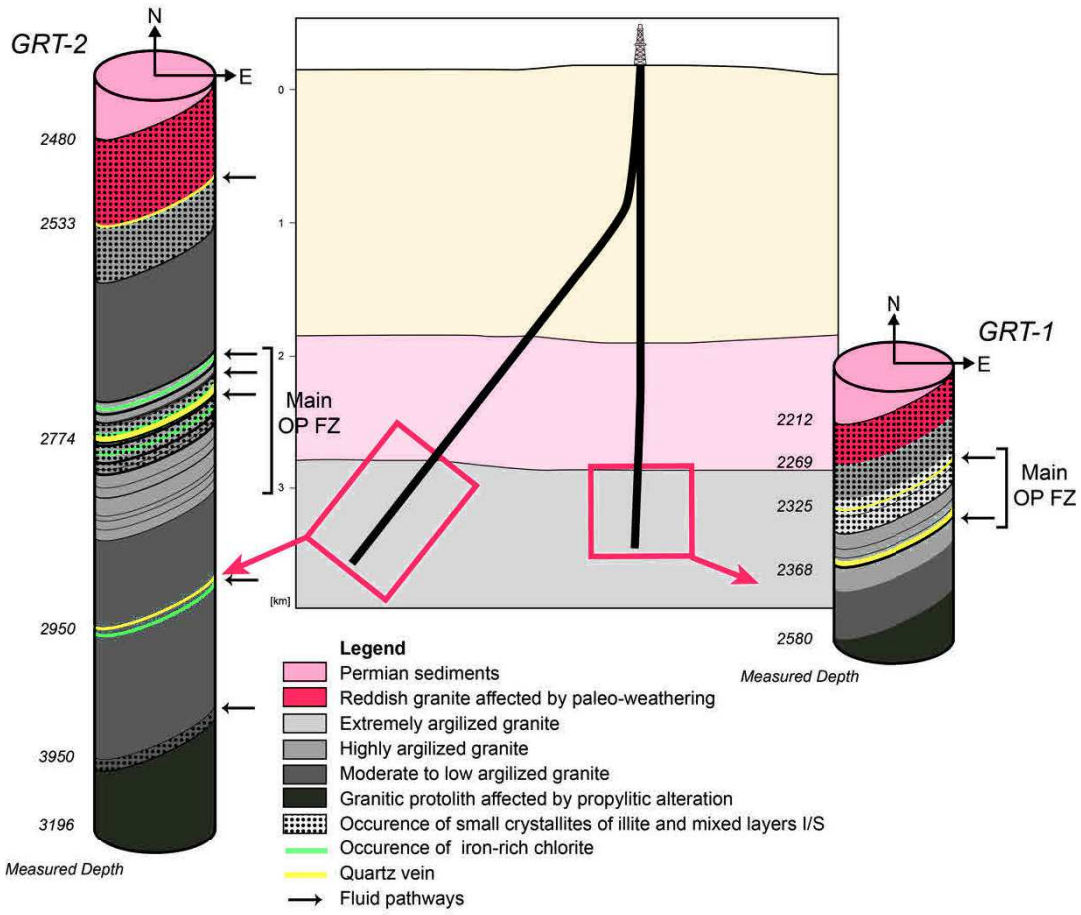

Figure 8.22 Conceptual model of alteration from the clay minerals along open-hole sections in wells GRT-1 and GRT-2.

8.4.10 Conclusions

The alteration petrography within the granitic basement of two deep geothermal wells at Rittershoffen, GRT-1 and GRT-2, was investigated with a special focus on the clay minerals and their influence on permeability. The whole granitic basement was affected by a pervasive early stage of propylitic alteration, with the crystallization of Fe,Mg-chlorite, illite and epidote. Several stages of fluid circulation occurred later within OP fracture zones and led to subsequent alteration of the granite. These stages can be identified based on several mineral

assemblages dominated by illitic minerals that formed successively. OP fracture zones in both wells are associated with occurrences of small crystallites of illite and mixed layers I/S (~10% smectite) that are the clay signatures of zones of circulation at Rittershoffen. However, the abundance of small crystallites of illite and mixed layers I/S could lead to plugging of the fracture network. When small crystallites of illite and mixed layers I/S do not completely obliterate minerals from previous hydrothermal parageneses, as observed for the well GRT-2, the natural permeability of OP fracture zones is higher and the corresponding well does not require stimulation.

8.4.11 Acknowledgments

This work was based on data from the geothermal project at Rittershoffen, France. The authors acknowledge the ECOGI project, the ES-Géothermie company and the owners of the geological and geophysical log data and the cutting samples. The authors also acknowledge GEIE EMC for providing the Soultz core samples. This work was performed under the framework of the LabEx G-Eau-Thermie Profonde, which is overseen by the French National Research Agency (ANR) under the program “Investissements d’Avenir”. This manuscript was prepared as a contribution to the PhD thesis of Jeanne Vidal and was co-funded by the ADEME (French Agency for Environment and Energy Management) and the LabEx G-Eau-Thermie Profonde. The research leading to these findings received funding from the ANR Programme under the grant agreement ANR-15-CE06-0014 (Project CANTARE-Alsace) and was also supported by the EGS Alsace project co-funded by the ADEME and Electricité de Strasbourg company. The authors acknowledge the use of the Move Software Suite granted by Midland Valley's Academic Software Initiative.

8.4.12 Supporting Information

8.4.12.1 Supporting information S1

This supporting information provides microscopic observations of cutting samples in the granitic basement of the well GRT-1.

Cuttings samples in the well GRT-1

1: Cutting samples in the granitic basement at 2536 m MD (GRAN_OX)

2: Cutting samples in the granitic basement at 2503 m MD (HLOW)

3: Cutting samples in the granitic basement at 2407 m MD (HMOD)

4: Cutting samples in the granitic basement at 2407 m MD (HMOD)

5: Cutting samples in the granitic basement at 2377 m MD (HHIG)

6: Cutting samples in the granitic basement at 2371 m MD (HHIG)

7: Cutting samples into the main OP fracture zone in the granitic basement at 2368 m MD (HHIG)

8: Cutting samples into the main OP fracture zone in the granitic basement at 2368 m MD (HHIG)

9: Cutting samples into the main OP fracture zone in the granitic basement at 2368 m MD (HHIG)

10: Cutting samples into the main OP fracture zone in the granitic basement at 2368 m MD (HHIG)

11: Cutting samples into the main OP fracture zone in the granitic basement at 2368 m MD (HHIG)

12: Cutting samples into the main OP fracture zone in the granitic basement at 2347 m MD (HEXT)

13: Cutting samples into the main OP fracture zone in the granitic basement at 2338 m MD (HEXT)

14: Cutting samples into the main OP fracture zone in the granitic basement at 2326 m MD (HEXT)

15: Cutting samples into the main OP fracture zone in the granitic basement at 2326 m MD (HEXT)

16: Cutting samples in the granitic basement at 2284 m MD (HHIG)

17: Cutting samples in the granitic basement at 2284 m MD (HHIG)

18: Cutting samples in the granitic basement at 2284 m MD (HHIG)

19: Cutting samples in the granitic basement at 2284 m MD (HHIG)

20: Cutting samples in the paleo-altered granitic basement at 2218 m MD (RED)

21: Cutting samples in the paleo-altered granitic basement at 2212 m MD (RED)

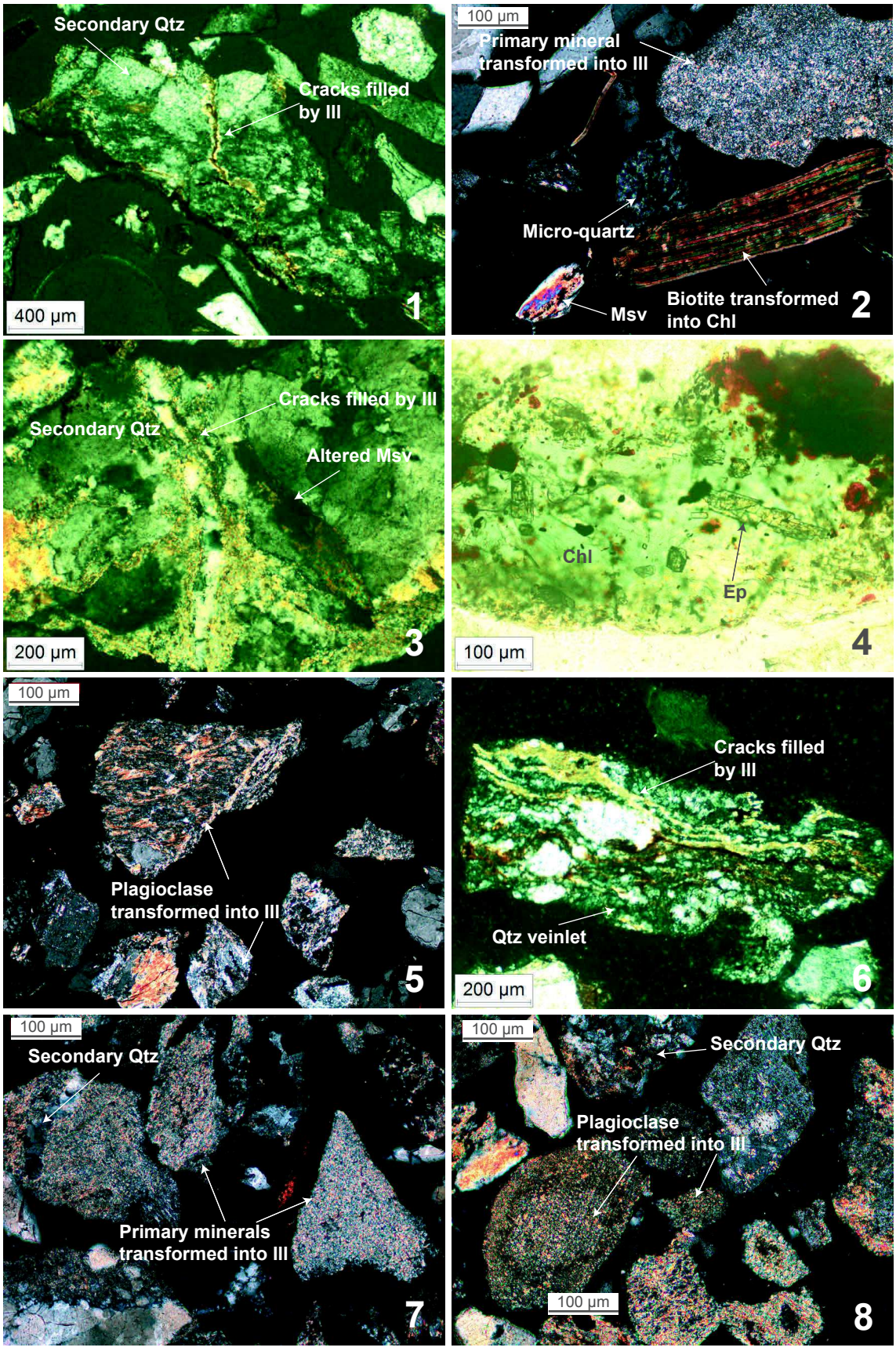

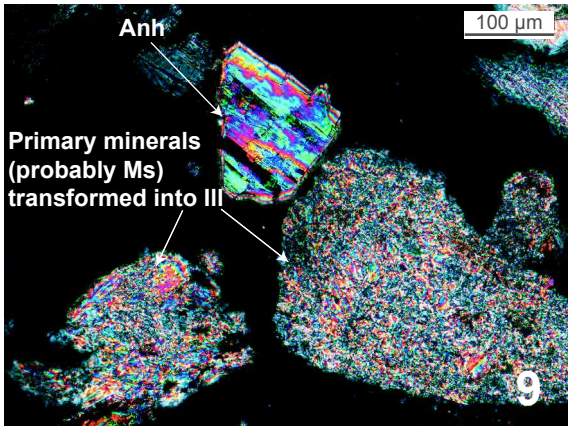
Anh
100 µm
Primary minerals
(probably Ms)
transformed into Ill
9

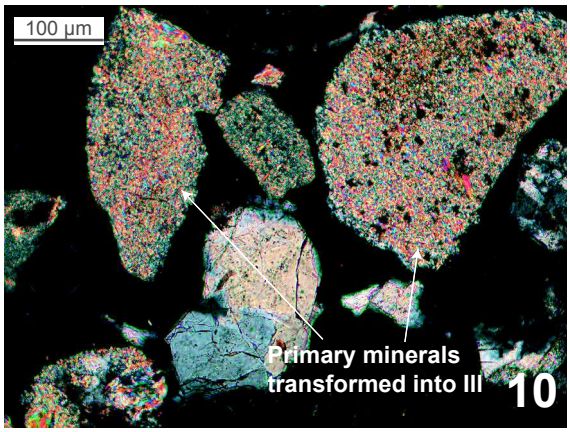
100 µm
Primary minerals
transformed into Ill
10

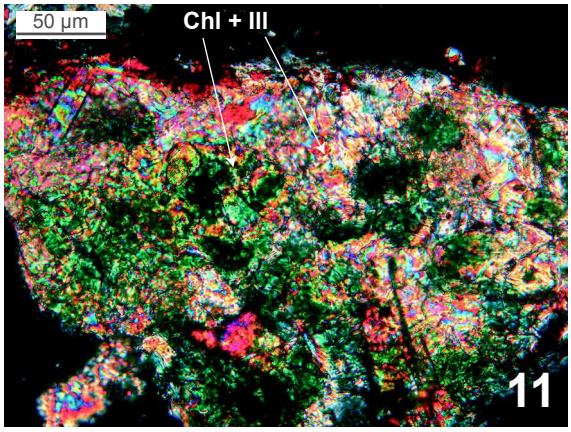
50 µm
Chl + Ill
11

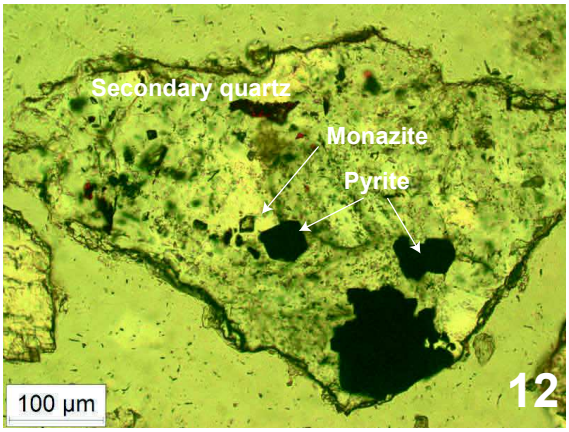
Secondary quartz
Monazite
Pyrite
100 µm
12

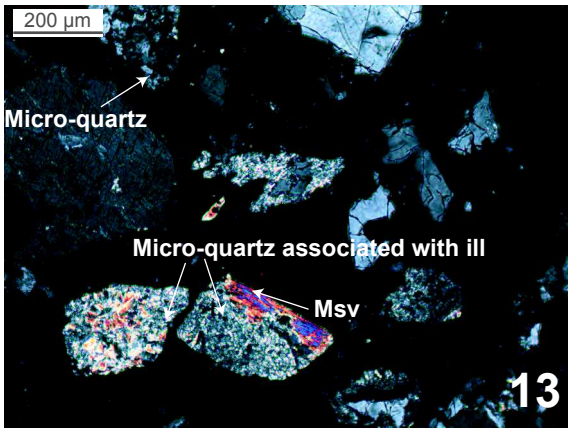
200 µm
Micro-quartz
Micro-quartz associated with ill
Msv
13

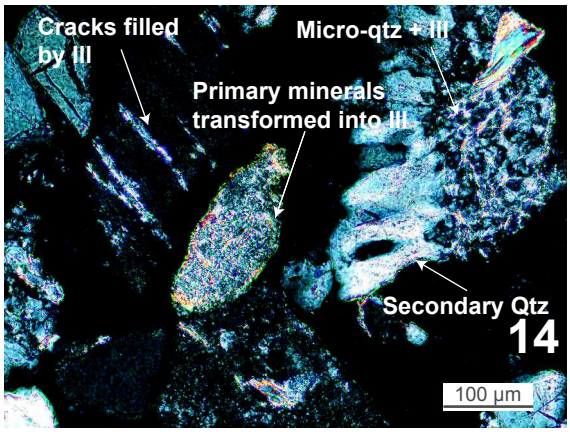
Cracks filled
by Ill
Micro-qtz + Ill
Primary minerals
transformed into Ill
Secondary Qtz
14
100 µm

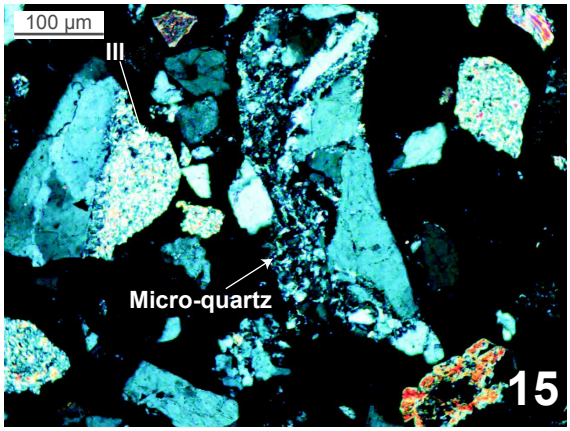
100 µm
Ill
Micro-quartz
15

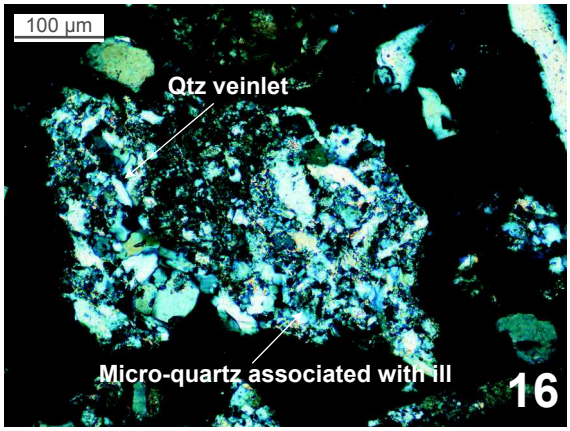
100 µm
Qtz veinlet
Micro-quartz associated with ill
16

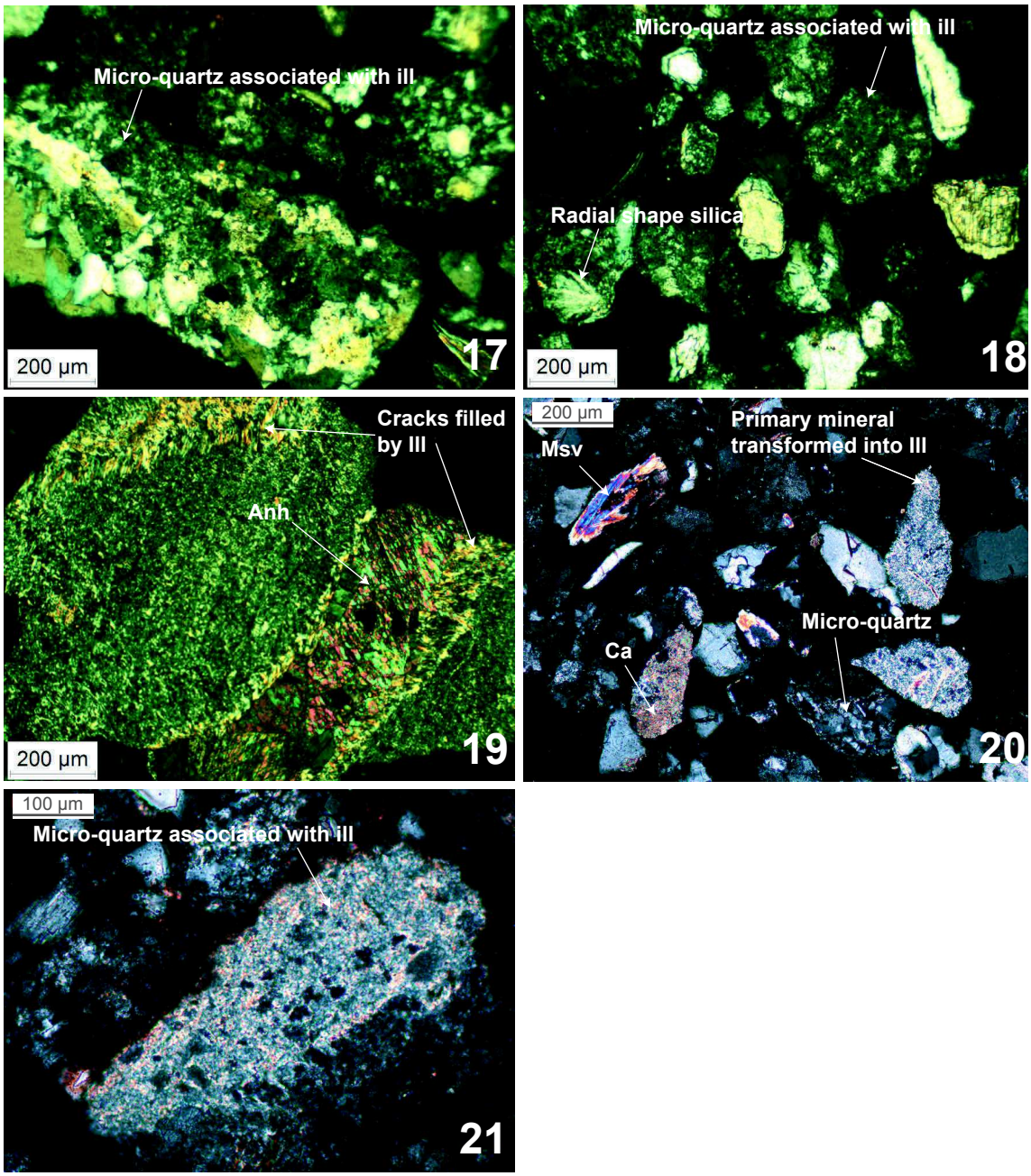

8.4.12.2 Supporting information S2

This supporting information provides microscopic observations of cutting samples in the granitic basement of the well GRT-2.

Cutting samples in the well GRT-2

1: Cutting samples into the deep OP fracture zone in the granitic basement at 3052 m MD (HMOD)

2: Cutting samples into the deep OP fracture zone in the granitic basement at 3052 m MD (HMOD)

3: Cutting samples in the granitic basement at 2977 m MD (HLOW)

4: Cutting samples into the deep OP fracture zone in the granitic basement at 2950 m MD (HMOD)

5: Cutting samples into the main OP fracture zone in the granitic basement at 2794 m MD (HHIG)

8: Cutting samples into the main OP fracture zone in the granitic basement at 2773 m MD (HHIG)

9: Cutting samples into the main OP fracture zone in the granitic basement at 2773 m MD (HHIG)

10: Cutting samples into the main OP fracture zone in the granitic basement at 2773 m MD (HHIG)

11: Cutting samples into the main OP fracture zone in the granitic basement at 2368 m MD (HHIG)

12: Cutting samples into the main OP fracture zone in the granitic basement at 2770 m MD (HHIG)

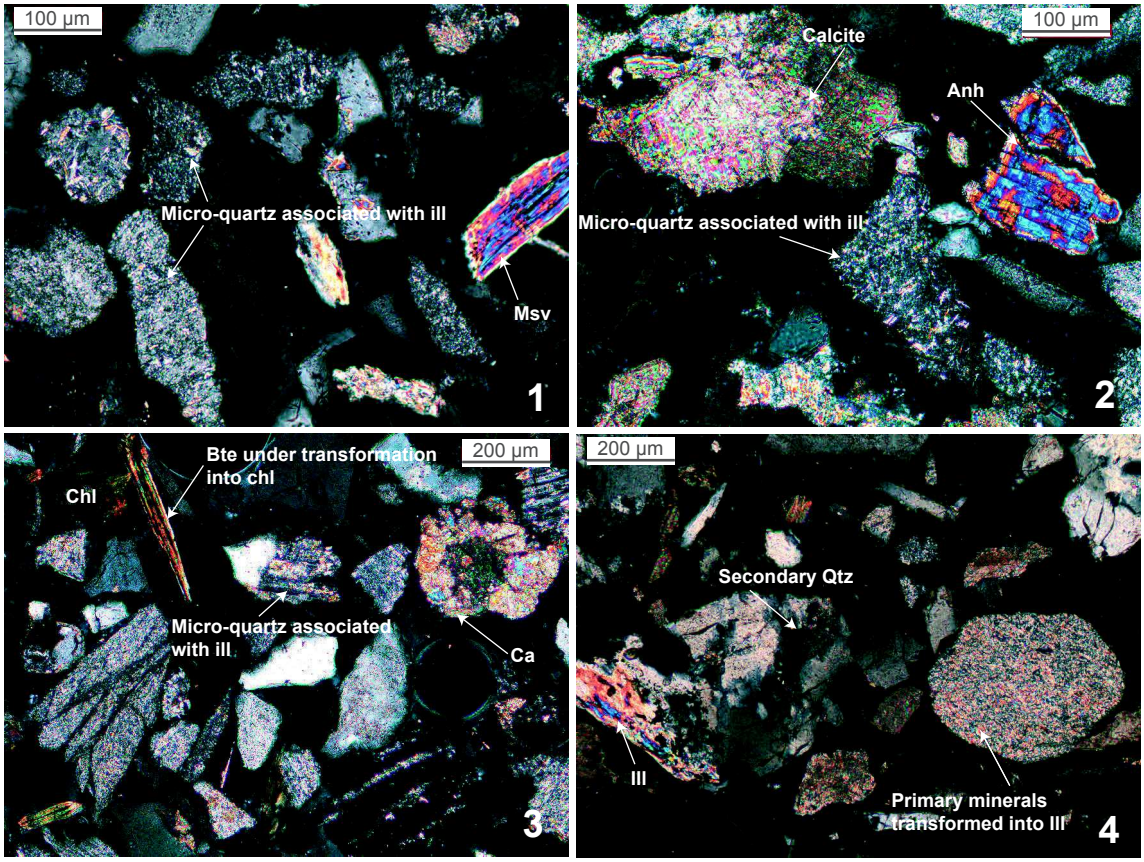

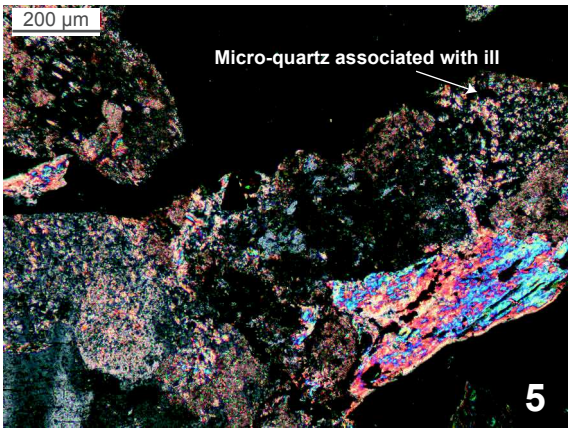
200 µm
Micro-quartz associated with ill
5

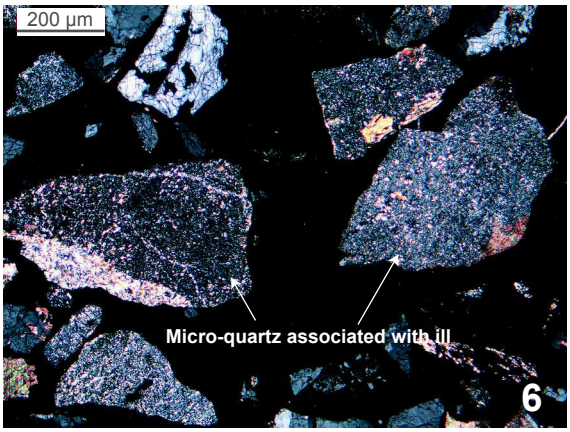
200 µm
Micro-quartz associated with ill
6

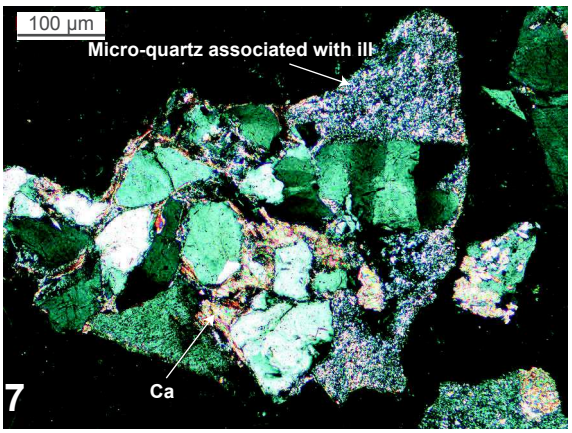
100 µm
Micro-quartz associated with ill
Ca
7

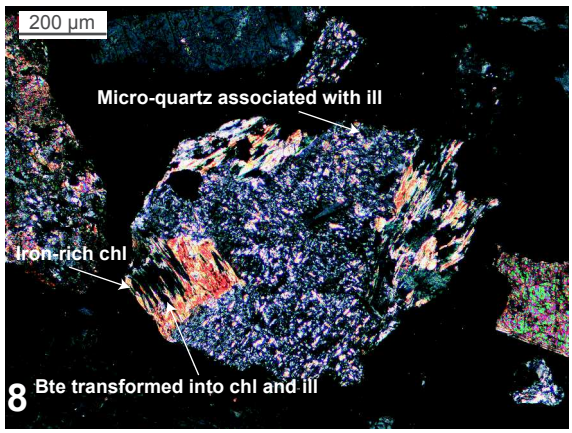
200 µm
Micro-quartz associated with ill
Iron-rich chl
Bte transformed into chl and ill
8

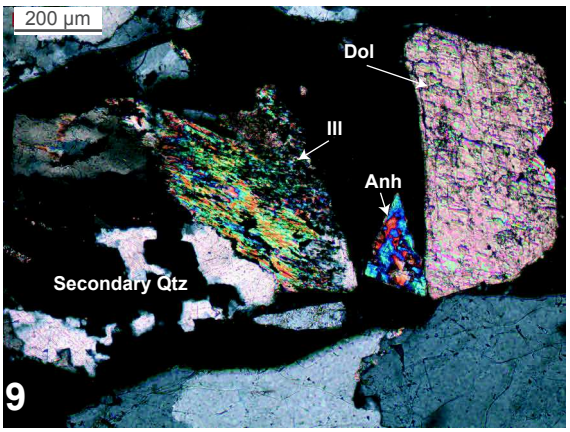
200 µm
Dol
Ill
Anh
Secondary Qtz
9

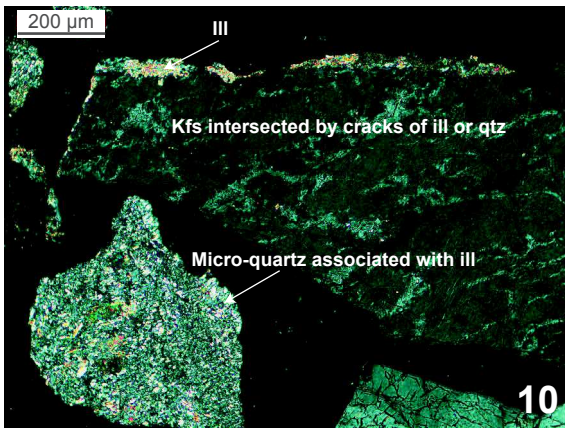
200 µm
Ill
Kfs intersected by cracks of ill or qtz
Micro-quartz associated with ill
10

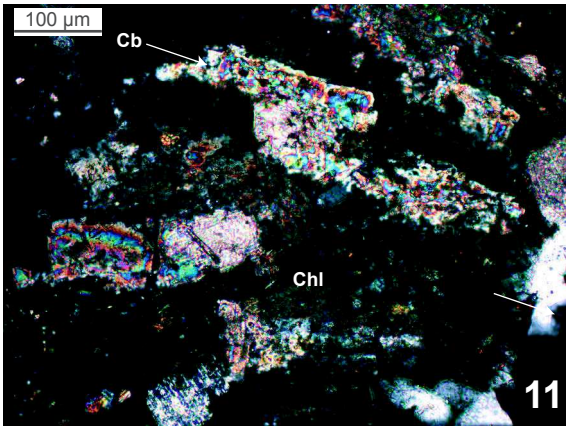
100 µm
Cb
Chl
11

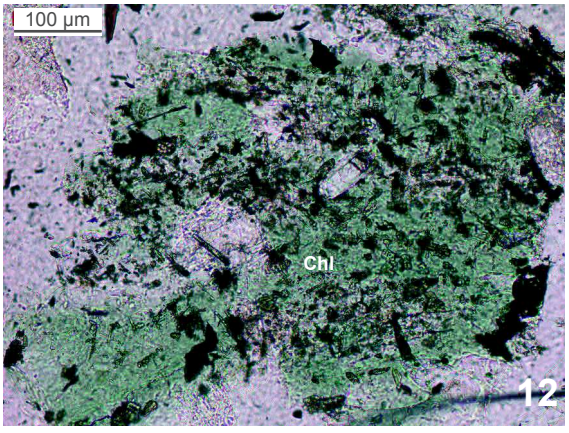
100 µm
Chl
12

8.4.12.3 Supporting information 3

This supporting information provides a geometrical representation of degrees of alteration in the granitic basement in the wells GRT-1 and GRT-2.

Degrees of alteration are based on argilization of cuttings described in section 5 of the article. Limits of each facies intersected by wells are detailed in the table below.

Figure

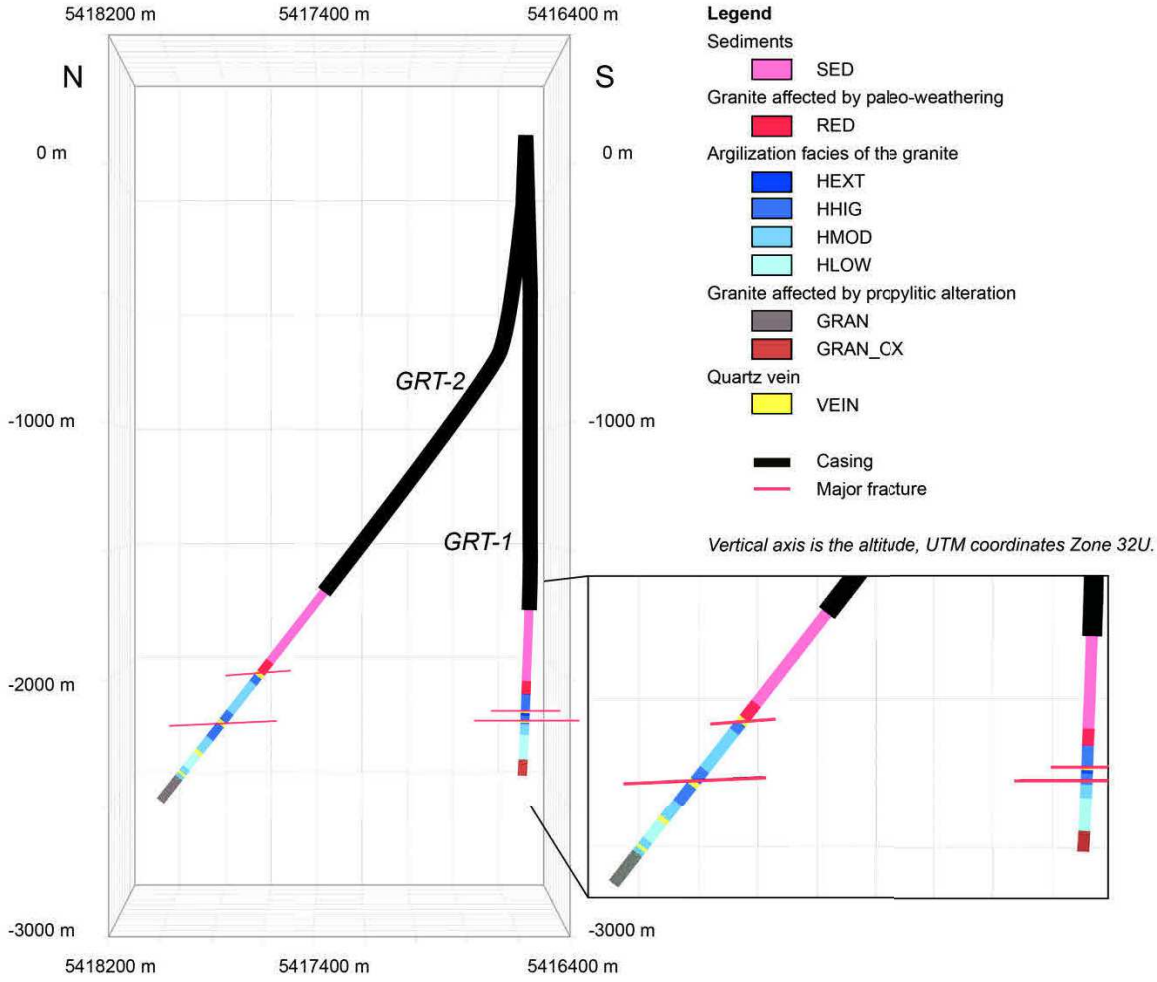

Caption

N-S cross section through the wells GRT-1 and GRT-2 (from MOVE 3D geometrical modeling) with the degrees of alteration indicated along the open-hole sections. A magnification of the open-holes is presented. Red lines are major fractures that act as fluid pathways in the main OP fracture zones of both wells. They were identified from acoustic image logs reported by Vidal et al. (2017).

RED: reddish granite

GRAN: granitic protolith

HLOW: low degree of argilization

HMOD: moderate degree of argilization

HHIG: high degree of argilization

HEXT: extreme degree of argilization

Table Facies of alteration encountered in wells GRT-1 and GRT-2 from the top to the deepest granitic basement. The top of the granitic basement is located at 2212 m MD (i.e., 2198 m TVD) in GRT-1 and at 2480 m MD (i.e., 2156 m TVD) in GRT-2.

Facies intersected by wells from the shallowest to the deepest	GRT-1			GRT-2		
	Name of the facies	Measured depth (m)	True vertical depth (m)	Name of the facies	Measured depth (m)	True vertical depth (m)
Facies 1	RED	2270	2057	RED	2533	2204
Facies 2	HHIG	2326	2310	VEIN	2536	2206
Facies 3	VEIN	2329	2314	HHIG	2578	2239
Facies 4	HEXT	2350	2334	HMOD	2737	2363
Facies 5	HHIG	2365	2349	HHIG	2770	2390
Facies 6	VEIN	2368	2352	VEIN	2791	2407
Facies 7	HHIG	2380	2364	HHIG	2875	2470
Facies 8	HMOD	2410	2393	HMOD	2944	2523
Facies 9	HLOW	2516	2498	VEIN	2950	2528
Facies 10	GRAN_OX	2580	2562	HLOW	3020	2579
Facies 11				HMOD	3046	2600
Facies 12				VEIN	3061	2610
Facies 13				GRAN	3196	2708

8.4.12.4 Supporting information 4

This supporting information provides detailed calculations of structural formulae of illitic minerals (Tables 1 and 2) and chlorite (Table 3). Results are represented in Figure 8.20 of the article.

Table 1 Calculations of structural formulae of some illitic minerals at various depths in GRT-1 well. n.a.: number of analyses; An. Av.: analytical average; s.d.: standard deviation; OCT: octahedral occupancy; INTCH: interlayer charge; XFe: Fe/(Fe+Mg).

Samples	GRT-1 2212		GRT-1 2218		GRT-1 2236		GRT-1 2284		GRT-1 2326		GRT-1 2329	
n. a.	13		18		15		14		29		22	
	An. Av.	s.d.	An. Av.	s.d.	An. Av.	s.d.	An. Av.	s.d.	An. Av.	s.d.	An. Av.	s.d.
Si	3,35	*0,25*	3,28	*0,20*	3,36	*0,02*	3,40	*0,04*	3,31	*0,19*	3,38	*0,12*
Al IV	0,65	*0,25*	0,72	*0,20*	0,64	*0,02*	0,60	*0,04*	0,69	*0,19*	0,62	*0,12*

Al VI	1,66	*0,18*	1,73	*0,11*	1,61	*0,13*	1,63	*0,06*	1,71	*0,21*	1,66	*0,07*
Fe 3+	0,13	*0,08*	0,11	*0,03*	0,18	*0,09*	0,16	*0,04*	0,13	*0,07*	0,14	*0,00*
Mg	0,21	*0,10*	0,16	*0,06*	0,19	*0,02*	0,19	*0,04*	0,15	*0,14*	0,18	*0,06*
Ti	0,01	*0,01*	0,01	*0,01*	0,00	*0,00*	0,00	*0,00*	0,00	*0,00*	0,00	*0,00*
Mn	0,00	*0,00*	0,00	*0,00*	0,00	*0,00*	0,00	*0,00*	0,00	*0,00*	0,00	*0,00*
OCT	2,00	*0,02*	2,01	*0,03*	1,99	*0,01*	1,98	*0,02*	1,99	*0,00*	1,99	*0,02*
Ca	0,01	*0,00*	0,01	*0,02*	0,00	*0,00*	0,00	*0,00*	0,00	*0,00*	0,00	*0,00*
Na	0,00	*0,01*	0,00	*0,01*	0,00	*0,00*	0,00	*0,00*	0,00	*0,00*	0,00	*0,00*
K	0,83	*0,08*	0,84	*0,04*	0,86	*0,04*	0,85	*0,03*	0,86	*0,06*	0,82	*0,01*
INTCH	0,85	*0,08*	0,85	*0,05*	0,87	*0,04*	0,85	*0,03*	0,86	*0,06*	0,83	*0,01*
XFe	0,38	*0,44*	0,41	*0,33*	0,49	*0,33*	0,46	*0,50*	0,46	*0,33*	0,44	*0,00*

Samples	GRT-1 2338		GRT-1 2365		GRT-1 2368		GRT-1 2377		GRT-1 2503	
n. a.	21		46		52		19		22	
	An. Av.	s.d.	An. Av.	s.d.	An. Av.	s.d.	An. Av.	s.d.	An. Av.	s.d.
Si	3,44	*0,29*	3,30	*0,06*	3,34	*0,12*	3,31	*0,08*	3,33	*0,06*
Al IV	0,56	*0,29*	0,70	*0,06*	0,66	*0,12*	0,69	*0,08*	0,67	*0,06*
Al VI	1,67	*0,07*	1,68	*0,04*	1,65	*0,09*	1,72	*0,07*	1,74	*0,06*
Fe 3+	0,14	*0,06*	0,16	*0,04*	0,17	*0,05*	0,14	*0,03*	0,11	*0,04*
Mg	0,14	*0,04*	0,14	*0,01*	0,16	*0,05*	0,12	*0,04*	0,11	*0,05*
Ti	0,00	*0,00*	0,00	*0,00*	0,00	*0,00*	0,00	*0,00*	0,00	*0,00*
Mn	0,00	*0,00*	0,00	*0,00*	0,00	*0,00*	0,00	*0,00*	0,00	*0,00*
OCT	1,95	*0,11*	1,98	*0,02*	1,98	*0,05*	1,99	*0,01*	1,96	*0,02*
Ca	0,00	*0,00*	0,00	*0,00*	0,01	*0,03*	0,00	*0,00*	0,04	*0,04*
Na	0,00	*0,00*	0,00	*0,02*	0,00	*0,00*	0,00	*0,00*	0,00	*0,00*
K	0,84	*0,14*	0,89	*0,05*	0,86	*0,05*	0,85	*0,05*	0,86	*0,04*
INTCH	0,84	*0,14*	0,90	*0,02*	0,87	*0,05*	0,85	*0,04*	0,90	*0,07*
XFe	0,50	*0,60*	0,53	*0,80*	0,52	*0,50*	0,54	*0,43*	0,50	*0,44*

Table 2 Calculations of structural formulae of some illitic minerals at various depths in GRT-2 well. n.a.: number of analyses; An. Av.: analytical average; s.d.: standard deviation; OCT: octahedral occupancy; INTCH: interlayer charge; XFe: Fe/(Fe+Mg).

Samples	GRT-2 2770		GRT-2 2773		GRT-2 2794		GRT-2 2950		GRT-2 2977		GRT-2 3052	
n. a.	21		15		18		29		24		20	
	An. Av.	s.d.	An. Av.	s.d.	An. Av.	s.d.	An. Av.	s.d.	An. Av.	s.d.	An. Av.	s.d.
Si	3,32	*0,15*	3,31	*0,09*	3,35	*0,03*	3,32	*0,01*	3,33	*0,02*	3,35	*0,00*
Al IV	0,68	*0,15*	0,69	*0,09*	0,65	*0,03*	0,68	*0,01*	0,67	*0,02*	0,65	*0,00*
Al VI	1,62	*0,20*	1,64	*0,05*	1,59	*0,07*	1,68	*0,03*	1,68	*0,04*	1,60	*0,02*
Fe 3+	0,17	*0,08*	0,17	*0,01*	0,19	*0,02*	0,15	*0,03*	0,15	*0,05*	0,19	*0,02*
Mg	0,18	*0,11*	0,18	*0,04*	0,20	*0,06*	0,15	*0,01*	0,15	*0,01*	0,19	*0,04*
Ti	0,00	*0,01*	0,01	*0,00*	0,00	*0,00*	0,00	*0,00*	0,00	*0,00*	0,00	*0,00*
Mn	0,00	*0,00*	0,00	*0,00*	0,00	*0,00*	0,00	*0,00*	0,00	*0,00*	0,00	*0,00*
OCT	1,99	*0,01*	1,99	*0,00*	1,98	*0,01*	1,99	*0,01*	1,99	*0,00*	1,98	*0,00*
Ca	0,00	*0,00*	0,00	*0,00*	0,00	*0,00*	0,00	*0,00*	0,00	*0,00*	0,01	*0,00*
Na	0,00	*0,00*	0,00	*0,00*	0,00	*0,00*	0,00	*0,00*	0,00	*0,00*	0,00	*0,00*
K	0,90	*0,02*	0,89	*0,04*	0,89	*0,01*	0,86	*0,00*	0,84	*0,02*	0,87	*0,03*
INTCH	0,91	*0,02*	0,89	*0,04*	0,90	*0,01*	0,87	*0,00*	0,85	*0,01*	0,88	*0,04*
XFe	0,49	0,42	0,49	0,20	0,49	0,25	0,50	0,75	0,50	0,83	0,50	0,33

Table 3 Calculations of structural formulae of some chlorite at various depths in GRT-1 and GRT-2 wells. n.a.: number of analyses; An Av: analytical average; s.d.: standard deviation; OCT: octahedral occupancy; INTCH: interlayer charge; XFe: Fe/(Fe+Mg); an. loc.: microsite of crystallization; Fe–Mg: chlorite in replacement of primary ferromagnesian minerals; FZ: chlorite crystallized in fracture zone.

Samples	GRT-1 2212		GRT-1 2368		GRT-1 2503		GRT-2 2770		GRT-2 2773		GRT-2 2773	
an. loc.	FZ		FZ		FeMg		FeMg		FeMg		FZ	
n. a.	7		10		6		2		3		4	
	An. Av.	s.d.	An. Av.	s.d.	An. Av.	s.d.	An. Av.	s.d.	An. Av.	s.d.	An. Av.	s.d.
Si	2,81	*0,03*	2,81	*0,04*	3,07	*0,10*	2,88	*0,01*	2,88	*0,05*	2,84	*0,07*
Al IV	1,19	*0,03*	1,19	*0,04*	0,93	*0,10*	1,12	*0,01*	1,12	*0,05*	1,16	*0,07*
Al VI	1,24	*0,04*	1,28	*0,04*	1,22	*0,06*	1,22	*0,01*	1,76	*0,10*	1,68	*0,13*
Ti	0,00	*0,00*	0,01	*0,01*	0,03	*0,05*	0,01	*0,00*	0,00	*0,00*	0,00	*0,01*
Fe 2+	3,77	*0,24*	3,81	*0,25*	1,70	*0,16*	2,01	*0,12*	2,18	*0,12*	3,67	*0,32*
Mn 2+	0,01	*0,00*	0,01	*0,00*	0,07	*0,04*	0,04	*0,04*	0,04	*0,02*	0,01	*0,01*
Mg 2+	0,92	*0,20*	0,79	*0,23*	2,78	*0,09*	2,65	*0,05*	2,39	*0,15*	0,91	*0,18*
OCT	5,94	*0,04*	5,90	*0,05*	5,80	*0,08*	5,93	*0,01*	5,90	*0,03*	5,90	*0,03*
Ca	0,02	*0,02*	0,04	*0,07*	0,01	*0,01*	0,00	*0,01*	0,00	*0,00*	0,01	*0,02*
Na	0,00	*0,00*	0,00	*0,00*	0,00	*0,00*	0,00	*0,00*	0,00	*0,00*	0,00	*0,00*
K	0,01	*0,01*	0,02	*0,01*	0,04	*0,04*	0,01	*0,00*	0,00	*0,00*	0,01	*0,01*
INTCH	0,05	*0,04*	0,11	*0,14*	0,05	*0,04*	0,01	*0,01*	0,01	*0,00*	0,04	*0,02*
XFe	0,80	*0,04*	0,83	*0,05*	0,38	*0,03*	0,43	*0,02*	0,48	*0,03*	0,80	*0,05*

Samples	GRT2 2794	GRT-2 2950		GRT-2 2950		GRT-2 2977		GRT-2 3052	
an. loc.	FZ	FeMg		FZ		FeMg		FeMg	
n. a.	1	2		2		5		7	
		An. Av.	s.d.	An. Av.	s.d.	An. Av.	s.d.	An. Av.	s.d.
Si	2,81	2,97	*0,05*	2,90	*0,04*	3,00	*0,09*	2,90	*0,01*
Al IV	1,19	1,03	*0,05*	1,10	*0,04*	1,00	*0,09*	1,10	*0,01*
Al VI	1,37	1,15	*0,07*	1,30	*0,07*	1,21	*0,02*	1,20	*0,05*
Ti	0,01	0,01	*0,00*	0,01	*0,00*	0,01	*0,01*	0,01	*0,00*
Fe 2+	3,13	1,97	*0,16*	2,92	*0,08*	1,92	*0,07*	2,01	*0,11*
Mn 2+	0,01	0,05	*0,03*	0,01	*0,00*	0,07	*0,00*	0,05	*0,04*
Mg 2+	1,35	2,74	*0,22*	1,62	*0,05*	2,65	*0,02*	2,67	*0,01*
OCT	5,87	5,92	*0,02*	5,86	*0,07*	5,87	*0,07*	5,93	*0,03*
Ca	0,03	0,01	*0,00*	0,02	*0,01*	0,01	*0,00*	0,01	*0,01*
Na	0,00	0,00	*0,00*	0,00	*0,00*	0,00	*0,00*	0,00	*0,00*
K	0,00	0,00	*0,00*	0,02	*0,02*	0,03	*0,04*	0,01	*0,00*
INTCH	0,06	0,02	*0,00*	0,06	*0,04*	0,04	*0,05*	0,02	*0,01*
XFe	0,70	0,42	*0,04*	0,64	*0,00*	0,42	*0,01*	0,43	*0,01*

PARTIE 3 : CONCLUSION ET PERSPECTIVES

Sommaire de la Partie 3

9 Conclusion générale

Les travaux de thèse ont permis de comprendre la structure du réseau de fractures naturelles et les altérations hydrothermales associées dans les puits géothermiques GRT-1 et GRT-2 de Rittershoffen. Ce réseau de fractures chenalise les circulations de fluide au sein des puits à l'interface de la couverture sédimentaire et du socle granitique et contrôle la perméabilité à l'échelle du puits.

9.1 Perméabilité à l'échelle des puits de Rittershoffen

La cible géothermique était la faille normale de Rittershoffen, orientée N-S avec un pendage ouest et un fort rejet de plus de 200 m. Les données de sismique réflexion imagent très peu cette faille dans le socle granitique mais les données thermiques des anciens puits pétroliers suggèrent que cette zone pourrait être le siège des circulations hydrothermales [*Munck et al.*, 1979; *Baillieux et al.*, 2014].

Le premier forage GRT-1 est un puits quasi-vertical, légèrement dévié vers l'ouest, qui recoupe la zone de faille de Rittershoffen dans le socle granitique altéré (Figure 9.1). La zone de faille recoupée est associée à une large anomalie négative perturbant le gradient nul qui marque un régime convectif dominant à l'interface de la couverture sédimentaire et du socle granitique. Le drain perméable majeur à 2368 m MD situé à la base de la zone de fractures fait l'interface entre une zone d'altération hydrothermale intense et le protolithe granitique sous-jacent peu altéré et peu fracturé (Figure 9.1). Cette zone de fractures concentre les circulations actuelles à l'échelle du puits. Les dépôts hydrothermaux au sein de cette zone sont dominés par des minéraux illitiques hétérogènes de type interstratifiés illite-smectite (~10% de smectite). Les processus d'illitisation intenses des minéraux primaires tendent à colmater la zone de fractures et réduire sa perméabilité naturelle. Les minéraux illitiques de type interstratifiés illite-smectite sont observés sur une hauteur d'environ 150 m, de 2328 m MD jusqu'à 2212 m MD. Ils suggèrent des paléo-circulations qui ont mené à une réduction de la perméabilité de ce niveau par des précipitations d'interstratifiés illite-smectite. La perméabilité est aujourd'hui restreinte à 40 m au-dessus de la fracture ouverte, de 2328 à 2368 m MD.

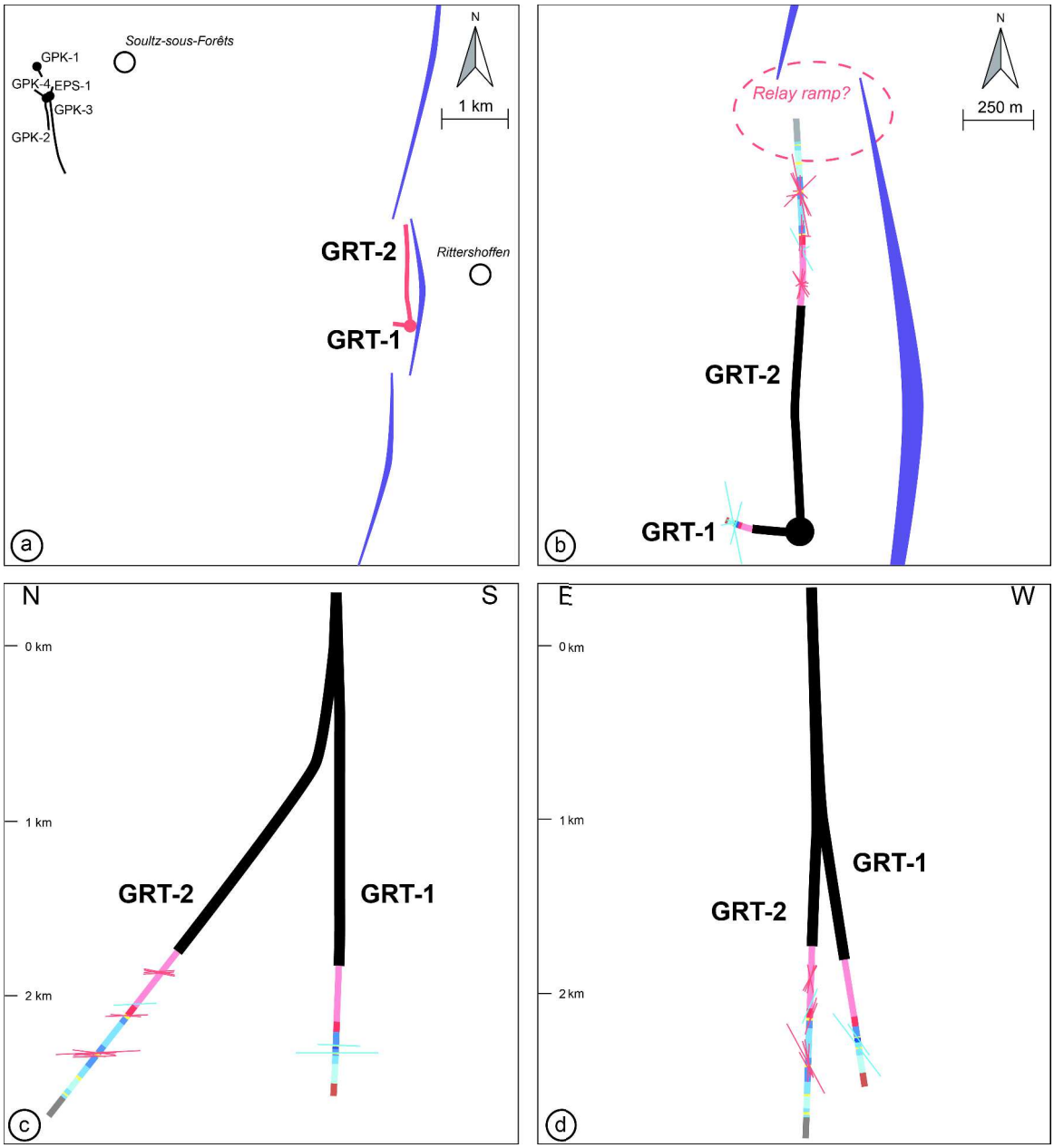

Figure 9.1 Etat des connaissances structurales et pétrographiques le long des puits GRT-1 et GRT-2 après les travaux de thèse. Les segments rouges et bleus sur la carte (b) et les coupes N-S (c) et E-W (d) représentent les fractures associées à des anomalies de températures positives et négatives d'après la corrélation des imageries de paroi acoustiques et des profils de température. Les couleurs dans la section en trou ouvert sont associées au degré d'altération. Les traces de failles locales à l'échelle sismique sur les cartes (a) et (b) sont spéculatives.

La perméabilité naturelle du puits GRT-1 étant trop faible à la fin des opérations de foration, il a nécessité une stimulation thermique, chimique et hydraulique afin d'augmenter les connexions avec le réservoir (Figure 9.2). Cette stimulation a contribué à améliorer la perméabilité naturelle des zones de fractures.

Le deuxième puits GRT-2 est fortement dévié de 37°N (Figure 9.1). Bien que la trajectoire du puits soit parallèle à la trace de la faille imagée en sismique, le puits recoupe plusieurs fois le réseau de fractures associé à la zone de faille. Deux zones de fractures perméables ont été recoupées dans les grès permiens et triasiques et quatre dans le socle granitique altéré (Figure 9.1). Contrairement à GRT-1, le comportement hydraulique du puits est contrôlé par plusieurs structures. Une autre différence est le gradient thermique plus élevé de 18°C/km affecté par plusieurs anomalies de température aux profondeurs des zones de fractures perméables. La zone de fractures perméables majeure est également située dans le socle granitique altéré. Le drain majeur est situé à 2774 m MD au toit de la zone de fractures. D'autres fractures ouvertes sont observées dans la zone de fractures favorisant les connexions hydrauliques au sein de la zone. Cette zone altérée est également marquée par des minéraux illitiques hétérogènes de type interstratifiés illite-smectite. Cependant, la présence de chlorite ferreuse suggère une illitisation moins intense des minéraux primaires et un colmatage partiel de la zone. Cette signature argileuse est observée dans les autres zones de fractures perméables du puits. Les paléo-circulations semblent avoir moins affecté les zones de fractures du puits GRT-2 dont la perméabilité naturelle est sept fois supérieure à celle du puits GRT-1 (Figure 9.2). La trajectoire déviée du puits favorise également les connexions entre le puits et le réseau de fractures naturelles verticales.

Le site de Rittershoffen présentent donc deux cas très différents. Le puits GRT-1 est marqué par une zone de factures majeure où le drain perméable est situé à la base. Ce drain fait l'interface entre deux domaines ; un domaine très hydrothermalisé au-dessus et moins hydrothermalisé en-dessous. Dans un contexte de faille normale, cette structure perméable pourrait être une zone de mouvement avec un toit très affecté par l'altération et un mur plus sain. Le puits GRT-2, quant à lui, est marqué par une zone de fracture majeure où le drain

perméable est situé au toit de la zone de fracture. Contrairement à GRT-1, l'altération hydrothermale semble moins hétérogène de part et d'autre du drain. Ceci ne signifie pas forcément qu'il n'y a pas eu de déplacement au sein de cette zone. Le puits GRT-2 pourrait traverser la zone de faille de Rittershoffen vers le Nord et recouper le réseau de fractures naturelles associé plusieurs fois tandis que le puits GRT-1 pourrait recouper la zone de faille de Rittershoffen de part en part une seule fois.

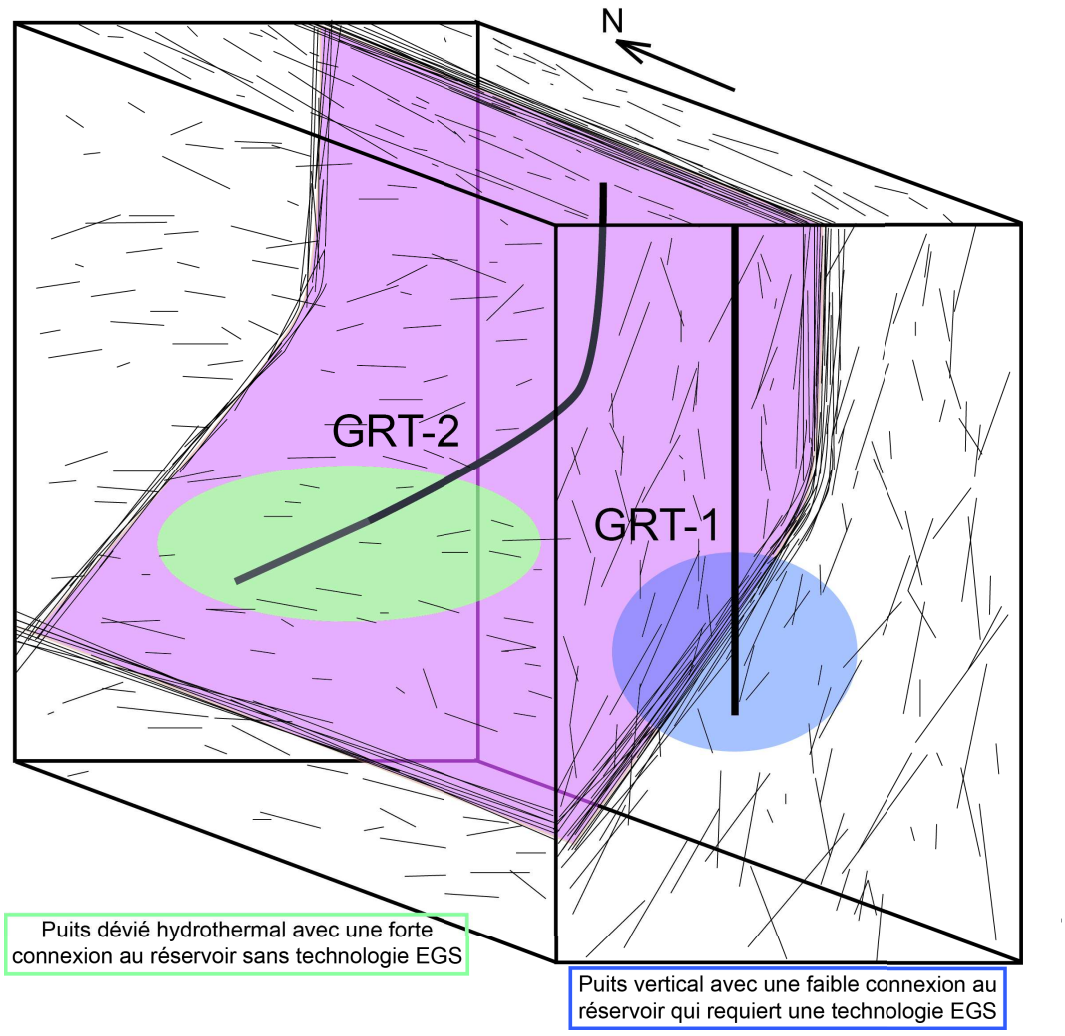

Figure 9.2 Modèle conceptuel du réservoir de Rittershoffen

9.2 Organisation asymétrique de la perméabilité à l'échelle de la zone de fractures

La perméabilité du réservoir est contrôlée par un réseau de fractures majeures organisé en cluster. Ces fractures orientées N-S +/-20° sont colinéaires à la contrainte horizontale maximale orientée entre N150°E et N170°E dans le granite altéré profond [*Hehn et al.*, 2016]. Dans le granite, d'après l'étude des fractures induites en tension de *Hehn et al*. [2017], les zones de fractures majeures ne perturbent pas localement ce champ de contraintes contrairement aux observations faites dans les puits de Soultz [*Valley and Evans*, 2007].

Les imageries de paroi acoustiques corrélées aux diagraphies différées standard imagent l'organisation de ces zones de fractures perméables avec une bonne résolution. Dans le socle granitique de Rittershoffen, les deux zones de fractures perméables majeures sont composées de fractures ouvertes qui sont probablement des drains pour le fluide géothermal. Elles sont localisées au sein d'un granite très poreux et affectées par l'altération hydrothermale. Les drains majeurs sont situés à la base de la zone altérée dans GRT-1 et au toit de la zone altérée dans GRT-2. Ils sont associés à des veines de quartz secondaires identifiables par leur forte réflectivité sur les imageries acoustiques de paroi. Les quartz secondaires sont également abondants dans les échantillons de cuttings à ces profondeurs.

Dans le puits GRT-2, la zone de fractures majeure est associée à une double anomalie de température. La partie positive supérieure est interprétée comme la venue de fluide géothermal chaud au sein des fractures ouvertes tandis que la partie négative inférieure est interprétée comme le refroidissement de la zone poreuse altérée plusieurs moins après le forage. Dans le puits GRT-1, la zone de fractures majeure est associée à une anomalie de température négative interprétée comme le refroidissement de la zone poreuse altérée plusieurs moins après le forage et les stimulations. Le drain perméable situé à la base de la zone de fracture n'est pas associé à une anomalie de température positive, ce qui ne signifie pas que le fluide géothermal chaud ne circule pas. L'anomalie négative associée à la zone poreuse altérée sus-jacente pourrait masquer la venue de fluide chaud.

L'organisation des zones de fractures observées dans les sédiments gréseux est un peu différente de celle dans le granite. Elles sont composées de fractures ouvertes pouvant agir comme des drains perméables et des fractures scellées suggérant des paléo-circulations. En revanche, autour de ces fractures, les matrices poreuses et altérées par les circulations hydrothermales ne sont pas clairement identifiées.

Les perméabilités les plus fortes sont observées dans le socle granitique altéré à Rittershoffen comme dans les autres puits géothermiques du Fossé rhénan supérieur. Les zones de fractures présentent un plus fort potentiel géothermique dans les 500 premiers mètres du socle granitique.

9.3 Influence des minéraux argileux sur la perméabilité

La présence des minéraux illitiques hétérogènes de type interstratifiés illite-smectite est un guide prometteur pour prospecter les zones de circulations actuelles et passées au sein des puits de Rittershoffen. Ils se déposent dans les zones de fractures suite à des perturbations abruptes des propriétés physico-chimiques du fluide géothermal chaud tel qu'un mélange avec un fluide plus froid. L'abondance des petites cristallites de minéraux illitiques colmatent les zones de fractures et tendent à diminuer fortement leur perméabilité.

Cependant bien que les argiles réduisent la perméabilité des zones de failles, la présence d'argiles au sein d'une zone de faille peut également favoriser les glissements appelés *clay smearing* [*Caine et al.*, 1996]. La présence d'argiles dans le socle granitique altéré de Soultz semble également influencer les mouvements asismiques contrairement aux zones plus cassantes situées dans le protolithe granitique profond [*Meller and Kohl*, 2014]. Les connaissances actuelles ne permettent pas de généraliser ces résultats au réservoir de Rittershoffen et le lien entre les argiles et les mouvements asismiques ne semble pas trivial [*Saffer & Marone*, 2003; *Zoback et al*., 2012].

10 Proposition de pistes futures

10.1 Modèle structural à l'échelle du réservoir

Les méthodes pour imager le réseau de fractures naturelles dans le réservoir sont restreintes à l'échelle du puits. L'extension des fractures loin des puits reste incertaine. L'interaction entre le puits et le réseau naturel de la zone de faille ne peut être évaluée loin du puits. L'interprétation sismique 2D du plan de faille de Rittershoffen pourrait être reconsidérée suite aux travaux à l'échelle du puits. Les données de Vertical Seismic Profile (VSP) dans le puits GRT-1 pourrait également permettre d'affiner l'interprétation. La résolution de ces méthodes géophysiques diminue avec la pénétration dans les formations et seules les structures hectométriques à kilométriques sont imagées. L'acquisition de données sismiques 3D apporterait une image plus précise des structures perméables au toit du socle granitique.

L'interprétation actuelle du plan de faille de Rittershoffen montre à l'extrémité nord, une forme légèrement concave vers l'Est avec un pendage ouest. Cette configuration semble géométriquement peu compatible avec des mouvements de faille normale. Le puits GRT-2 pourrait recouper une zone de relai entre deux segments de failles normales à pendage ouest (Figure 9.2). Ces zones de relai et de terminaison de failles sont des zones avec un fort potentiel géothermique [*Faulds and Hinz*, 2015]. Le puits GRT-2 pourrait également recouper des structures sans déplacement mais qui concentrent les écoulements de type *fracture corridors* avec une forte perméabilité. L'absence de rejet de ces structures ne permet pas de les imager avec les méthodes de sismique réflexion. L'étude d'analogues de terrain permettrait de faire évoluer les modèles conceptuels des zones perméables dans le socle granitique altéré du Fossé rhénan.

La sismicité induite semble prometteuse pour imager le réservoir granitique profond suite à la stimulation du puits GRT-1. Cependant en l'absence de modèle de vitesse 3D, de relocalisation absolue des évènements et de connaissance des mécanismes au foyer, cette méthode est incertaine.

La prise en compte de tous les résultats aux différentes échelles (fracturation à l'échelle du puits, microsismicité, sismique réflexion 2D voire 3D, VSP) permettrait d'établir un modèle géologique 3D contraint par les puits comme celui construit pour le réservoir de Soultz [*Sausse et al.*, 2010].

10.2 Altérations hydrothermales

Les études précédentes dans les réservoirs fracturés du Fossé rhénan supérieur, notamment à Soultz, ont montré un système hydrothermal complexe avec des phases de circulations pulsées [*Smith et al.*, 1998; *Dubois et al.*, 2000]. La superposition de plusieurs évènements hydrothermaux avec des fluides dont la composition peut évoluer dans le temps est à l'origine de plusieurs générations de minéraux secondaires dans les fractures. La résolution des cuttings ne permet pas d'établir une chronologie relative entre les minéraux secondaires. Les relations entre les minéraux sont détruites lors du broyage de la roche. Les outils actuels ne permettent pas de séparer des minéraux de même nature mais de générations différentes dans un même échantillon. Les datations absolues des minéraux illitiques de Soultz indiquent donc plusieurs âges qui s'étendent sur environ 250 Ma sans pouvoir distinguer les évènements hydrothermaux individuels [*Schleicher et al.*, 2006; *Bartier et al.*, 2008]. Enfin, les proportions en éléments chimiques du fluide géothermal de Rittershoffen peuvent varier de celui de Soultz. Un modèle géochimique adapté serait nécessaire pour évaluer précisément les équilibres entre le fluide et les minéraux observés en termes de sursaturation ou de sous-saturation.

Enfin, la compréhension du système convectif pourrait être améliorée grâce à une meilleure connaissance des vitesses de circulations naturelles, de leur évolution thermique et de leur mouvement per ascensum ou per descensum dans le réseau chenalisé et multi-échelle des fractures.

Références bibliographiques

Abdelfettah, Y., P. Sailhac, J.-F. Girard, E. Dalmais, and V. Maurer (2016), Magnetotelluric profile crossing the GRT1-2 geothermal doublet of the Rittershoffen EGS project, northern Alsace, in *Proceedings of European Geothermal Congress 2016*, Strasbourg, France.

Agemar, T., R. Schellschmidt, and R. Schulz (2012), Subsurface temperature distribution in Germany, *Geothermics*, *44*, 65–77, doi:10.1016/j.geothermics.2012.07.002.

Aichholzer, C., P. Duringer, S. Orciani, and A. Genter (2015), New stratigraphic interpretation of the twenty-eight-year old GPK-1 geothermal well of Soultz-sous-Forêts (Upper Rhine Graben, France), in *Proceedings of the Fourth European Geothermal Workshop*, Strasbourg, France.

Aichholzer, C., P. Duringer, S. Orciani, and A. Genter (2016), New stratigraphic interpretation of the Soultz-sous-Forêts 30-year-old geothermal wells calibrated on the recent one from Rittershoffen (Upper Rhine Graben, France), *Geotherm. Energy*, *4*(13), doi:10.1186/s40517-016-0055-7.

Altherr, R., U. Henes-Klaiber, E. Hegner, M. Satir, and C. Langer (1999), Plutonism in the Variscan Odenwald (Germany): from subduction to collision, *Int. J. Earth Sci.*, *88*(3), 422–443, doi:10.1007/s005310050276.

Altherr, R., A. Holl, E. Hegner, C. Langer, and H. Kreuzer (2000), High-potassium, calc-alkaline I-type plutonism in the European Variscides: Northern Vosges (France) and Northern Schwarzwald (Germany), *Lithos*, *50*(1–3), 51–73, doi:10.1016/S0024-4937(99)00052-3.

Aquilina, L., M. Brach, J. C. Foucher, A. De Las Heras, and G. Braibant (1993), *Deepening of GPK-1 HDR borehole 2000-3600m (Soultz-sous-Forêts, France), Geochemical monitoring of drilling fluids*, R26619, Open file, BRGM, Orléans, France.

Aquilina, L., H. Pauwels, A. Genter, and C. Fouillac (1997), Water-rock interaction processes in the Triassic sandstone and the granitic basement of the Rhine Graben: Geochemical investigation of a geothermal reservoir,

Geochim. Cosmochim. Acta, *61*(20), 4281–4295, doi:10.1016/S0016-7037(97)00243-3.

Arnórsson, S. (1995), Geothermal systems in Iceland: Structure and conceptual models—I. High-temperature areas, *Geothermics*, *24*(5–6), 561–602, doi:10.1016/0375-6505(95)00025-9.

Axelsson, G., S. Thorhallsson, and G. Björnsson (2006), Stimulation of geothermal wells in basaltic rock in Iceland, in *Proceedings of ENGINE Workshop 3, Stimulation of reservoir and microseismicity*, Zurich, Switzerland.

Bächler, D., T. Kohl, and L. Rybach (2003), Impact of graben-parallel faults on hydrothermal convection-Rhine Graben case study, *Phys. Chem. Earth*, *28*(9-11), 341–441, doi: 10.1016/s1474-7065(03)00063-9.

Baillieux, P., E. Schill, J.-B. Edel, and G. Mauri (2013), Localization of temperature anomalies in the Upper Rhine Graben: insights from geophysics and neotectonic activity, *Int. Geol. Rev.*, *55*(14), 1744–1762, doi:10.1080/00206814.2013.794914.

Baillieux, P., E. Schill, Y. Abdelfettah, and C. Dezayes (2014), Possible natural fluid pathways from gravity pseudo-tomography in the geothermal fields of Northern Alsace (Upper Rhine Graben), *Geotherm. Energy*, *2*(16), doi:10.1186/s40517-014-0016-y.

Baldeyrou, A., O. Vidal, and B. Fritz (2003), Étude expérimentale des transformations de phase dans un gradient thermique : application au granite de Soultz-sous-Forêts, France, *Comptes Rendus Geosci.*, *335*(4), 371–380, doi:10.1016/S1631-0713(03)00056-7.

Bartier, D., B. Ledésert, N. Clauer, A. Meunier, N. Liewig, G. Morvan, and A. Addad (2008), Hydrothermal alteration of the Soultz-sous-Forêts granite (Hot Fractured Rock geothermal exchanger) into a tosudite and illite assemblage, *Eur. J. Mineral.*, *20*(1), 131–142, doi:10.1127/0935-1221/2008/0020-1787.

Barton, C. A., M. D. Zoback, and D. Moos (1995), Fluid flow along potentially active faults in crystalline rock, *Geology*, *23*(8), 683–686, doi:10.1130/0091-7613(1995)023<0683:FFAPAF>2.3.CO;2.

Baujard, C., A. Genter, J.-J. Graff, V. Maurer, and E. Dalmais (2015), ECOGI, a New Deep EGS Project in Alsace, Rhine Graben, France, in *Proceedings of World Geothermal Congress 2015*, Melbourne, Australia.

Baujard, C., A. Genter, E. Dalmais, V. Maurer, R. Hehn, R. Rosillette, J. Vidal, and J. Schmittbuhl (2017), Hydrothermal characterization of wells GRT-1 and GRT-2 in Rittershoffen, France: Implications on the understanding of natural flow systems in the rhine graben, *Geothermics*, *65*, 255–268, doi:10.1016/j.geothermics.2016.11.001.

Baujard, C., R. Hehn, A. Genter, D. Teza, J. Baumgärtner, F. Guinot, A. Martin, and S. Steinlechner (2017), Rate of penetration of geothermal wells: a key challenge in hard rocks, in *Proceedings of 42nd Workshop on Geothermal Reservoir Engineering*, Stanford University, California.

Baumgärtner, J., P. L. Moore, and A. Gérard (1995), Drilling of hot and fractured granite at Soultz-sous-Forêts, in *Proceedings of World Geothermal Congress 1995*, Florence, Italy.

Baumgärtner, J., A. Gérard, and R. Baria (2000), Soultz-sous-Forêts: main technical aspects of deepening the well GPK2, in *Proceedings of World Geothermal Congress 2000*, Kyushu - Tohoku, Japan.

Baumgärtner, J., D. Teza, T. Hettkamp, G. Homeier, R. Baria, and S. Michelet (2005), Electricity production from hot rocks, in *Proceedings of World Geothermal Congress 2005*, Antalya, Turkey.

Baumgärtner, J. (2007), The geox GmbH project in Landau – The first geothermal power project in Palatinate/Upper Rhine Valley, in *Proceedings of First European Geothermal Review*, Mainz, Germany.

Baumgärtner, J., D. Teza, and G. Wahl (2013), *Gewinnung geothermischer Energie durch Entwicklung und Zirkulation eines Störungssystems im Kristallin und deren mikroseismische Überwachung am Beispiel des Geothermieprojektes Insheim*, 0325158, Bestec GmbH, Landau, Germany

Baumgärtner, J., and C. Lerch (2013), Geothermal 2.0: The Insheim Geothermal Power Plant. The second generation of geothermal power plants in the Upper

Rhine Graben, in *Proceedings of Third European Geothermal Review*, Mainz, Germany.

Baumann, H. (1981), Regional stress field and rifting in Western Europe, *Tectonophysics*, *73*(1), 105–111, doi:10.1016/0040-1951(81)90177-3.

Beaufort, D., D. Westercamp, O. Legendre, and A. Meunier (1990), The fossil hydrothermal system of Saint Martin, Lesser Antilles: geology and lateral distribution of alterations, *J. Volcanol. Geotherm. Res.*, *40*(3), 219–243, doi:10.1016/0377-0273(90)90122-V.

Beaufort, D., P. Patrier, A. Meunier, and M. M. Ottaviani (1992), Chemical variations in assemblages including epidote and/or chlorite in the fossil hydrothermal system of Saint Martin (Lesser Antilles), *J. Volcanol. Geotherm. Res.*, *51*(1–2), 95–114, doi:10.1016/0377-0273(92)90062-I.

Beaufort, D., P. Papapanagiotou, P. Patrier Mas, A. M. Fouillac, and H. Traineau (1996), I/S and C/S mixed layers, some indicators of recent physical-chemical changes in active geothermal systems: The case study of Chipilapa (El Salvador), in *Proceedings of Seventeenth Workshop on Geothermal Reservoir Engineering*, Stanford University, California, USA.

Beaufort, D., C. Rigault, S. Billon, V. Billault, A. Inoue, S. Inoue, and P. Patrier (2015), Chlorite and chloritization processes through mixed-layer mineral series in low-temperature geological systems – a review, *Clay Miner.*, *50*(4), 497–523, doi:10.1180/claymin.2015.050.4.06.

Behrmann, J. H., O. Hermann, M. Horstmann, D. C. Tanner, and G. Bertrand (2003), Anatomy and kinematics of oblique continental rifting revealed: A three-dimensional case study of the southeast Upper Rhine Graben (Germany), *AAPG Bull.*, *87*(7), 1105–1121, doi:10.1306/02180300153.

Benderitter, Y., and P. Elsass (1995), Structural control of deep fluid circulation at the Soultz HDR site, France, *Geotherm. Sci. Technol.*, *4*(4), 227–237.

Benderitter, Y., A. Tabbagh, and P. Elsass (1995), Calcul de l'effet thermique d'une remontée hydrothermale dans le socle fracturé. Application à l'anomalie géothermique de Soultz-sous-Forêts (Nord Alsace), *Bull. Société Géologique Fr.*, *1*, 37–48.

Berger, J.-P., B. Reichenbacher, D. Becker, M. Grimm, K. Grimm, L. Picot, A. Storni, C. Pirkenseer, and A. Schaefer (2005a), Eocene-Pliocene time scale and stratigraphy of the Upper Rhine Graben (URG) and the Swiss Molasse Basin (SMB), *Int. J. Earth Sci.*, *94*(4), 711–731, doi:10.1007/s00531-005-0479-y.

Berger, J.-P., B. Reichenbacher, D. Becker, M. Grimm, K. Grimm, L. Picot, A. Storni, C. Pirkenseer, C. Derer, and A. Schaefer (2005b), Paleogeography of the Upper Rhine Graben (URG) and the Swiss Molasse Basin (SMB) from Eocene to Pliocene, *Int. J. Earth Sci.*, *94*(4), 697–710, doi:10.1007/s00531-005-0475-2.

Bergerat, F. (1985), Déformations cassantes et champs de contrainte tertiaires dans la plate-forme européenne, Habilitation à Diriger la Recherche, Université Pierre et Marie Curie-Paris VI, France.

Bertani, R. (2015), Geothermal power generation in the world 2010-2014 - Update report, in *Proceedings of World Geothermal Congress 2015*, Melbourne, Australia.

Boissier, F., A. Desplan, and P. Laplaige (2010), France – country update, in *Proceedings of World Geothermal Congress 2010*, Bali, Indonesia.

Bourgeois, O., M. Ford, M. Diraison, C. L. C. de Veslud, M. Gerbault, R. Pik, N. Ruby, and S. Bonnet (2007), Separation of rifting and lithospheric folding signatures in the NW-Alpine foreland, *Int. J. Earth Sci.*, *96*(6), 1003–1031, doi:10.1007/s00531-007-0202-2.

Bradford, J., J. McLennan, J. Moore, D. Glasby, D. Waters, R. Kruwells, A. Bailey, W. Rickard, K. Bloomfield, and D. King (2013), Recent developments at the Raft River geothermal field, in *Proceedings of Thirty-Eighth Workshop on Geothermal Reservoir Engineering*, Stanford University, California, USA.

BRGM (1971), *Forage d'eau thermominérale 1266bis - Rapport SGAL*, 71-SGN-244-SGA, Open file, BRGM, Orléans, France.

BRGM (1993), *Recherche de nouvelles ressources en eaux thermales à Merkwiller-Pechelbronn (67). Compte rendu des travaux de réalisation du forage HELION III*, N-0549-STR-4S-93 Open file, BRGM, Orléans, France.

Brindley, G. W., and G. Brown (1980), X-ray Diffraction procedures for clay mineral identification, in *Crystal structures of clay minerals and their X-ray identification.*, vol. 5, pp. 305-360, Brindley G.W. and Brown G, Mineralogical Society of Great Britain and Ireland, London, Great Britain, doi:10.1180/mono-5 .

Bromley, C. J., and E. L. Majer (2012), Geothermal Induced Seismicity - Risks and Rewards, in *Proceedings of New Zealand Geothermal Workshop*, Auckland, New Zealand.

Browne, P. R. L., and A. J. Ellis (1970), The Ohaki-Broadlands hydrothermal area, New Zealand; mineralogy and related geochemistry, *Am. J. Sci.*, *269*(2), 97–131, doi:10.2475/ajs.269.2.97.

Browne, P. R. L. (1978), Hydrothermal alteration in active geothermal fields., *Ann Rev Earth Planet Sci*, *6*, 3693–3696.

Brudy, M., and M. D. Zoback (1999), Drilling-induced tensile wall-fractures: implications for determination of in-situ stress orientation and magnitude, *Int. J. Rock Mech. Min. Sci.*, *36*(2), 191–215, doi:10.1016/S0148-9062(98)00182-X.

Brun, J. P., M.-A. Gutscher, and DEKORP-ECORS teams (1992), Deep crustal structure of the Rhine Graben from dekorp-ecors seismic reflection data: A summary, *Tectonophysics*, *208*(1–3), 139–147, doi:10.1016/0040-1951(92)90340-C.

Burg, J.-P., J. Van Den Driesche, and J.-P. Brun (1994), Syn- to post-thickening extension: mode and consequences, *Comptes Rendus Académie Sci.*, *319*(2), 1019–1032.

Caine, J. S., J. P. Evans, and C. B. Forster (1996), Fault zone architecture and permeability structure, *Geology*, *24*(11), 1025–1028, doi:10.1130/0091-7613(1996)024<1025:FZAAPS>2.3.CO;2.

Caine, J. S., R. L. Bruhn, and C. B. Forster (2010), Internal structure, fault rocks, and inferences regarding deformation, fluid flow, and mineralization in the seismogenic Stillwater normal fault, Dixie Valley, Nevada, *J. Struct. Geol.*, *32*(11), 1576–1589, doi:10.1016/j.jsg.2010.03.004.

Caner, L. (2011), Phyllosilicates des sols: de l'identification à la quantification., Université de Poitiers.

Cathelineau, M., and M.-C. Boiron (2010), Downward penetration and mixing of sedimentary brines and dilute hot waters at 5km depth in the granite basement at Soultz-sous-Forêts (Rhine graben, France), *Comptes Rendus Geosci.*, *342*(7), 560–565, doi:10.1016/j.crte.2009.08.010.

Cautru, J.-P. (1988), *Coupe géologique passant par le forage GPK-1 calée sur la sismique réflexion*, Technical report, BRGM, Institut Mixte de Recherches Géothermiques, France.

Chambon, G., J. Schmittbuhl, A. Corfdir, N. Orellana, M. Diraison, and Y. Géraud (2006), The thickness of faults: From laboratory experiments to field scale observations, *Tectonophysics*, *426*(1–2), 77–94, doi:10.1016/j.tecto.2006.02.014.

Chorowicz, J., and B. Deffontaines (1993), Transfer faults and pull-apart model in the Rhinegraben from analysis of multisource data, *J. Geophys. Res. Solid Earth*, *98*(B8), 14339–14351, doi:10.1029/93jb00190.

Clauer, N., N. Liewig, B. Ledesert, and H. Zwingmann (2008), Thermal history of Triassic sandstones from the Vosges Mountains-Rhine Graben rifting area, NE France, based on K-Ar illite dating, *Clay Miner.*, *43*(3), 363–379, doi:10.1180/claymin.2008.043.3.03.

Cocherie, A., C. Guerrot, M. C. Fanning, and A. Genter (2004), Datation U-PB des deux faciès du granite de Soultz (Fossé Rhénan, France), *Comptes Rendus Geosci.*, *336*(9), 775–787, doi :10.1016/j.crte.2004.01.009.

Cornet, F. H. (1987), Results from Le Mayet de Montagne project, *Geothermics*, *16*(4), 355–374, doi:10.10016/0375-6505(87)90016-2.

Cornet, F. H., J. Helm, H. Poitrenaud, and A. Etchecopar (1997), Seismic and aseismic slips induced by large-scale fluid injections, *Pure Appl. Geophys.*, *150*(3-4), 563–583, doi:10.1007/s000240050093.

Cornet, F., T. Berard, and S. Bourouis (2007), How close to failure is a granite rock mass at a 5 km depth, *Int J Rock Mech Min Sci*, *44*(1), 47–66.

CREGE c/o CHYN, Laboratoire de Géothermie - CREGE, Available from: https://crege.ch/ (Accessed 19 June 2017)

Cuenot, N., C. Dorbath, and L. Dorbath (2008), Analysis of the microseismicity induced by fluid injections at the EGS site of Soultz-sous-Forêts (Alsace, France): Implications for the characterization of the geothermal reservoir properties, *Pure Appl. Geophys.*, *165*(5), 797–828, doi:10.1007/s00024-008-0335-7.

Dalmais, E., A. Genter, J. Vidal, C. Baujard, and F.-D. Vuataz (2015), Permeability assessment based on drilling data in EGS projects: Case study of Muschelkalk fracture in GRT-1 well for ECOGI Project (Rittershoffen, Alsace, France), in *Proceedings of the Fourth European Geothermal Workshop,* Strasbourg, France.

Davatzes, N. C., and S. H. Hickman (2005a), Controls on fault-hosted fluid flow; Preliminary results from the Coso Geothermal Field, CA, in *Geothermal Resources Council Transactions*, vol. 29, pp. 343–348, Geothermal Resources Council, Davis, California.

Davatzes, N. C., and S. H. Hickman (2005b), Comparison of Acoustic and Electrical image logs from the Coso Geothermal Field, CA, in *Proceedings of Thirtieth Workshop on Geothermal Reservoir Engineering*, Stanford University, California, USA.

Degouy, M., B. Villeneuve, and R. Weber (1992), *Logistical support and development of the Soultz hot dry rock site: seismic observation wells and well EPS-1, Final drilling report*, RR-41179-FR, Open file, BRGM, Commission of European Communities, Bruxelles, Belgique.

Deiller, P. (2013), *Log pétrographique du granite recoupé par le puits géothermique GRT-1*, Confidential report, ECOGI, Strasbourg, France.

Dempsey, D., S. Kelkar, N. C. Davatzes, S. Hickman, D. Moos, and E. Zemach (2014), Evaluating the roles of thermoelastic and poroelastic stress changes in the Desert Peak EGS stimulation, in *Proceedings of Thirty-Ninth Workshop on Geothermal Reservoir Engineering*, Stanford University, California, USA.

Dezayes, C. (1995), Caractérisation et interprétation d'un volume rocheux fracturé à partir de données de forages, les forages géothermiques de Soultz-sous-Forêts, PhD thesis, 246 pp., Université de Savoie, Chambéry, France.

Dezayes, C., A. Genter, and S. Gentier (2005), *Deep geothermal energy in Western Europe: the Soultz Project, Final report*, RP-54227-FR, Open file, BRGM, Orléans, France.

Dezayes, C., A. Gérard, J.-J. Graff, F. Hanot, and I. Thinon (2009), *Projet géothermique Hatten-Rittershoffen: retraitement et interprétation des données sismiques régionales et locales.*, 09-021RT, Confidential Report, ES-Géothermie, Strasbourg, France.

Dezayes, C., G. Courrioux, P. Calcagno, B. Tourlière, P. Chèvremont, J. Sausse, and J. Place (2010a), *Des données géologiques aux modèles 3D du site EGS de Soultz-sous-Forêts (Alsace, France), Rapport final*, RP-57927-FR, Open file, BRGM, Orléans, France.

Dezayes, C., A. Genter, and B. Valley (2010b), Structure of the low permeable naturally fractured geothermal reservoir at Soultz, *Comptes Rendus Geosci.*, *342*(7-8), 517–530, doi:10.1016/j.crte.2009.10.002.

Dezayes, C., L. Capar, L. Beccaletto, and C. Lerouge (2011), *Etude de la partir Trias-Permien-toit du socle dans le Fossé rhénan pour des applications de géothermie profonde, Rapport final*, RP-60387-FR, Open file, BRGM, Orléans, France.

Dezayes, C., B. Sanjuan, F. Gal, C. Lerouge, and M. Brach (2013a), *Forage d'exploration géothermique GRT1 : suivi géochimique des fluides et caractérisation des zones fracturées*, RP-62546-FR, Open file, BRGM, Orléans, France.

Dezayes, C., C. Lerouge, C. Ramboz, and G. Wille (2013b), Relative chronology of deep circulations within the fractured basement of the Upper Rhine Graben, in *Proceedings of World Geothermal Congress 2013*, Pisa, Italy.

Dezayes, C., B. Sanjuan, F. Gal, and C. Lerouge (2014), Fluid geochemistry monitoring and fractured zones characterization in the GRT1 borehole

(ECOGI project, Rittershoffen, Alsace, France), in *Proceedings of Deep Geothermal Days*, Paris, France.

Dezayes, C., C. Lerouge, B. Sanjuan, C. Ramboz, and M. Brach (2015), Toward a better understanding of the fluid circulation in the Rhine Graben for a better geothermal exploration of the deep basins, in *Proceedings of World Geothermal Congress 2015*, Melbourne, Australia.

Dèzes, P., S. M. Schmid, and P. A. Ziegler (2004), Evolution of the European Cenozoic Rift System: interaction of the Alpine and Pyrenean orogens with their foreland lithosphere, *Tectonophysics*, *389*(1–2), 1–33, doi:10.1016/j.tecto.2004.06.011.

Doebl, F. (1967), The tertiary and pleistocene sediments of the Northern and Central part of the upper Rhinegraben, *Mém. Serv. Carte Géologique Alsace Lorraine*, 48–54.

Dubois, M., B. Ledésert, J.-L. Potdevin, and S. Vançon (2000), Détermination des conditions de précipitation des carbonates dans une zone d'altération du granite de Soultz (soubassement du fossé Rhénan, France) : l'enregistrement des inclusions fluides, *Comptes Rendus Académie Sci. - Ser. IIA - Earth Planet. Sci.*, *331*(4), 303–309, doi:10.1016/S1251-8050(00)01429-4.

Economides, M. J., and K. G. Nolte (1989), *Reservoir Stimulation*, 440 pp., Second Edition., Prentice Hall, Upper Saddle River, NY, USA.

Edel, J. B., and K. Weber (1995), Cadomian terranes, wrench faulting and thrusting in the central Europe Variscides: geophysical and geological evidence, *Geol. Rundsch.*, *84*(2), 412–432, doi:10.1007/BF00260450.

Edel, J.-B., H. Whitechurch, and M. Diraison (2006), Seismicity wedge beneath the Upper Rhine Graben due to the backwards Alpine push?, *Tectonophysics*, *428*(1-4), 49–64, doi:0.1016/j.tecto.2006.08.009.

Edel, J.-B., K. Schulmann, and Y. Rotstein (2007), The Variscan tectonic inheritance of the Upper Rhine Graben: evidence of reactivations in the Lias, Late Eocene–Oligocene up to the recent, *Int. J. Earth Sci.*, *96*(2), 305–325, doi:10.1007/s00531-006-0092-8.

Edel, J.-B., and K. Schulmann (2009), Geophysical constraints and model of the “Saxothuringian and Rhenohercynian subductions – magmatic arc system” in NE France and SW Germany, *Bull. Société Géologique Fr.*, *180*(6), 545–558, doi:10.2113/gssgfbull.180.6.545.

Eisbacher, G. H., and W. Fielitz (2010), *Karlsruhe und seine Region. Nordschwarzwald, Kraichgau, Neckartal, südlicher Odenwald, Oberrhein-Graben, Pfälzerwald und westliche Schwäbische Alb*, Borntraeger Science Publishers, Stuttgart, Germany.

Equipe du projet GeORG (2013), *Potentiel géologique profond du Fossé rhénan supérieur. Rapport final du projet GeORG – INTERREG IV – Partie 2 : géologie et potentiel*, Open file, Available from : http://www.geopotenziale.org/ (Accessed June 2017)

Evans, K., A. Genter, and J. Sausse (2005a), Permeability creation and damage due to massive fluid injections into granite at 3.5km at Soultz: 1. Borehole observations, *J. Geophys. Res.*, *110*(B4), doi:10.1029/2004JB003168.

Evans, K., H. Moriya, H. Niitsuma, R. H. Jones, W. S. Phillips, A. Genter, J. Sausse, R. Jung, and R. Baria (2005b), Microseismicity and permeability enhancement of hydrogeologic structures during massive fluid injections into granite at 3 km depth at the Soultz HDR site, *Geophys. J. Int.*, *160*(1), 389–412, doi:10.1111/j.1365-246x.2004.02474.x.

Evans, K. F. (2005), Permeability creation and damage due to massive fluid injections into granite at 3.5 km at Soultz: 2. Critical stress and fracture strength, *J. Geophys. Res.*, *110*(B4), doi:10.1029/2004JB003169.

Faulkner, D. R., C. A. L. Jackson, R. J. Lunn, R. W. Schlische, Z. K. Shipton, C. A. J. Wibberley, and M. O. Withjack (2010), A review of recent developments concerning the structure, mechanics and fluid flow properties of fault zones, *J. Struct. Geol.*, *32*(11), 1557–1575, doi:10.1016/j.jsg.2010.06.009.

Flexser, S. (1991), Hydrothermal alteration and past and present thermal regimes in the western moat of Long Valley caldera, *J. Volcanol. Geotherm. Res.*, *48*(3–4), 303–318, doi:10.1016/0377-0273(91)90048-5.

Fouillac, A. M., and A. Genter (1992), An O, D, C isotopic study of water/rock interactions in the sSoultz-sous-Forêts granite. Drillhole GPK-1, HDR Site, Alsace., in *Geothermal Energy in Europe - The Soultz Hot Dry Rock Project*, pp. 105–117, James C. Bresee, Montreux, Switzerland.

Fossen, H., R. A. Schultz, Z. K. Shipton, and K. Mair (2007), Deformation bands in sandstone: a review, *J. Geol. Soc.*, *164*(4), 755–769, doi:10.1144/0016-76492006-036.

Fuchs, K., K. . Bonjer, D. Gajewski, E. Lüschen, C. Prodehl, K. . Sandmeier, F. Wenzel, and H. Wilhelm (1987), Crustal evolution of the Rhinegraben area. 1. Exploring the lower crust in the Rhinegraben rift by unified geophysical experiments, *Tectonophysics*, *141*(1), 261–275.

Franke, W. (2000), The mid-European segment of the Variscides: tectonostratigraphic units, terrane boundaries and plate tectonic evolution, *Geol. Soc. Lond. Spec. Publ.*, *179*(1), 35–61, doi:10.1144/GSL.SP.2000.179.01.05.

Geiermann, J., and E. Schill (2010), 2-D Magnetotellurics at the geothermal site at Soultz-sous-Forêts: Resistivity distribution to about 3000 m depth, *Comptes Rendus Geosci.*, *342*(7–8), 587–599, doi:10.1016/j.crte.2010.04.001.

Genter, A. (1989), Géothermie roches chaudes sèches: le granite de Soultz-sous-Forêts (Bas-Rhin, France). Fracturation naturelle, altérations hydrothermales et interaction eau-roche, PhD thesis, 201 pp., Université d'Orléans, France.

Genter, A., and H. Traineau (1992), Borehole EPS1, Alsace, France: preliminary geological results from granite core analyses for Hot Dry Rock research, *International Journal of Rock Mechanics and Mining Sciences & Geomechanics Abstracts*, *30*(3), 205–214, doi:10.1016/0148-9062(93)92984-x.

Genter, A., P. Martin, and P. Montaggioni (1992), Application of FMS and BHTV toolsfor evaluation of natural fractures in the Soultz geothermal borehole GPK-1, in *Geothermal Energy in Europe - The Soultz Hot Dry Rock Project*, pp. 69–82, James C. Bresee, Montreux, Switzerland.

Genter, A., H. Traineau, C. Dezayes, P. Elsass, B. Ledésert, A. Meunier, and T. Villemin (1995), Fracture analysis and reservoir characterization of the granitic basement in the HDR Soultz project (France), *Geotherm. Sci. Technol.*, *4*(3), 189–214.

Genter, A., and H. Traineau (1996), Analysis of macroscopic fractures in granite in the HDR geothermal well EPS-1, Soultz-sous-Forêts, France, *J. Volcanol. Geotherm. Res.*, *72*(1–2), 121–141, doi:10.1016/0377-0273(95)00070-4.

Genter, A., C. Castaing, C. Dezayes, H. Tenzer, H. Traineau, and Villemin (1997a), Comparative analysis of direct (core) and indirect (borehole imaging tools) collection of fracture data in the Hot Dry Rock Soultz reservoir (France), *J. Geophys. Res.*, *102*(B7), 15,419–15,431, doi:10.1029/97JB00626.

Genter, A., H. Traineau, and D. Artignan (1997b), *Synthesis of geological and geophysical data at Soultz-sous-Forêts(France)*, R 39440, Open file report, BRGM.

Genter, A., H. Traineau, B. Ledésert, B. Bourgine, and S. Gentier (2000), Over 10 years of geological investigations within the HDR Soultz project, France, in *Proceedings of World Geothermal Congress 2000*, Kyushu - Tohoku, Japan.

Genter, A., K. Evans, N. Cuenot, D. Fritsch, and B. Sanjuan (2010), Contribution of the exploration of deep crystalline fractured reservoir of Soultz to the knowledge of enhanced geothermal systems (EGS), *Comptes Rendus Geosci.*, *342*(7), 502–516, doi:10.1016/j.crte.2010.01.006.

Genter, A., N. Cuenot, B. Melchert, W. Moeckes, G. Ravier, B. Sanjuan, R. Sanjuan, J. Scheiber, E. Schill, and J. Schmittbuhl (2013), Main achievements from the multi-well EGS Soultz project during geothermal exploitation from 2010 and 2012, in *Proceedings of European Geothermal Congress 2013*, Pisa, Italy.

Genter, A., J. Vidal, C. Baujard, E. Dalmais, and J. Schmittbuhl (2015), Permeability in deep-seated granitic rocks: lessons learnt from deep geothermal boreholes in the Upper Rhine Graben, in *Vingtièmes journées techniques du Comité Français d'Hydrogéologie de l'Association*

Internationale des Hydrogéologues - Aquifères de socle : le point sur les concepts et les applications opérationnelles, La-Roche-sur-Yon, France.

Genter, A. et al. (2016), Geology, Geophysics and Geochemistry in the Upper Rhine Graben: the frame for geothermal energy use, in *Proceedings of European Geothermal Congress 2016*, Strasbourg, France.

Geoportail Minergies, Espace cartographique | Bureau des ressources énergétiques du sous-sol, Available from: http://www.minergies.fr/fr/cartographie (Accessed 19 June 2017)

GeORG Team (2017), EU-Projekt GeORG - Geoportal, Available from: http://www.geopotenziale.org/home?lang=3 (Accessed 17 June 2017)

Gérard, A., and O. Kappelmeyer (1987), Le projet géothermique européen de Soutz-sous-Forêts : situation au 1er janvier 1988, *Geothermics.*, *16*(4), 393-399, doi :10.1016/0375-6505(87)90018-6.

Gérard, A., A. Genter, T. Kohl, P. Lutz, P. Rose, and R. Fritz (2006), The deep EGS (Enhanced Geothermal System) project at Soultz-sous-Forêts (Alsace, France), *Geothermics*, *35*(5-6), 473–483., doi:0.1016/j.geothermics.2006.12.001

Géraud, Y., M. Rosener, F. Surma, J. Place, É. Le Garzic, and M. Diraison (2010), Physical properties of fault zones within a granite body: Example of the Soultz-sous-Forêts geothermal site, *Comptes Rendus Geosci.*, *342*(7–8), 566–574, doi:10.1016/j.crte.2010.02.002.

Grant, A. M., J. Clearwater, J. Quinão, F. P. Bixley, and M. Le Brun (2013), Thermal stimulation of geothermal wells: a review of field data, in *Proceedings of Thirty-Eighth Workshop on Geothermal Reservoir Engineering*, Stanford University, California, USA.

Grecksch, G., A. Ortiz, and R. Schellschmidt (2003), *Thermophysical Study of GPK2 and GPK3 Granite Samples: HDR Project Soultz Report*, GGA-Bericht, Hannover, Germany.

Griffiths, L., M. J. Heap, T. Reuschlé, P. Baud, and J. Schmittbuhl (2015), Permeability enhancement by shock cooling, in *Proceedings of European*

Geosciences Union, Geophysical Research Abstracts, vol. 17, Vienna, Austria.

Griffiths, L., M. J. Heap, F. Wang, D. Daval, H. A. Gilg, P. Baud, J. Schmittbuhl, and A. Genter (2016), Geothermal implications for fracture-filling hydrothermal precipitation, *Geothermics*, *64*, 235–245, doi:10.1016/j.geothermics.2016.06.006.

Guillong, M., D. . Meier, M. . Allan, C. . Heinrich, and B. W. D. Yardley (2008), Appendix A6: SILLS: a MatLab-based program for the reduction of Laser Ablation ICP-MS data of homogeneous materials and inclusions, *Mineral. Assoc. Can. Short Course*, *40*, 328–333.

Guillou-Frottier, L., and C. Jaupard (1995), On the effect of continents on mantle convection, *J. Geophys. Res.*, *110*(B12), 24217–24238, doi: 10.1029/95JB02518.

Guillou-Frottier, L. (2003), *Compilation et analyse des données thermiques sur le champ géothermique de Bouillante*, *Rapport final.*, RP-52452-FR, BRGM, Orléans, France.

Guillou-Frottier, L., C. Carre, B. Bourgine, V. Bouchot, and A. Genter (2013), Structure of hydrothermal convection in the Upper Rhine Graben as inferred from corrected temperature data and basin-scale numerical models, *J Volcanol. Geotherm. Res*, *256*, 29–49, doi:10.1016/j.jvolgeores.2013.02.008.

Haas, I. O., and C. R. Hoffmann (1929), Temperature gradient in Pechelbronn Oil-Bearing Region, Lower Alsace: its determination and relation to oil reserves, *AAPG Bull*, *13*.

Haffen, S., Y. Géraud, M. Diraison, and C. Dezayes (2013), Determining fluid-flow zones in a geothermal sandstone reservoir from thermal conductivity and temperature logs, *Geothermics*, *46*, 32–41, doi: 10.1016/j.geothermics.2012.11.001.

Häring, M. O., U. Schanz, F. Ladner, and B. C. Dyer (2008), Characterisation of the Basel 1 enhanced geothermal system, *Geothermics*, *37*(5), 469–495, doi:10.1016/j.geothermics.2008.06.002.

Harvey, C. C., and P. R. L. Browne (1991), Mixed-layer clay geothermometry in the Wairakei geothermal field, New Zealand, *Clays Clay Miner.*, *39*(6), 614–621, doi:10.1346/ccmn.1991.0390607.

Hehn, R., A. Genter, J. Vidal, and C. Baujard (2016), Stress field rotation in the EGS well GRT-1 (Rittershoffen, France), in *Proceedings of European Geothermal Congress 2016*, Strasbourg, France.

Herbrich, B. (1988), *Le forage géothermique de Soultz-sous-Forêts (GPK1), Rapport de fin de sondage*, 29421, CFG, Orléans, France.

Herzberger, P. et al. (2010), The geothermal power plant Bruchsal, in *Proceedings of World Geothermal Congress 2010*, Bali, Indonesia.

Hettkamp, T., J. Baumgärtner, R. Baria, A. Gérard, T. Gandy, S. Michelet, and D. Teza (2004), Electricity production from hot rocks., in *Proceedings of Twenty-Ninth Workshop on Geothermal Reservoir Engineering*, University of Stanford, California, USA.

Hettkamp, T., D. Teza, J. Baumgärtner, T. Gandy, and G. Homeier (2007), A multi-horizon approach for the exploration and exploitation of a fractured geothermal reservoir in Landau/Palatine, in *Proceedings of First European Geothermal Review*, Mainz, Germany.

Hettkamp, T., J. Baumgärtner, D. Teza, and C. Lerch (2013), Experiences from 5 years operation in Landau, in *Proceedings of Third European Geothermal Review*, Mainz, Germany.

Hooijkaas, G. R., A. Genter, and C. Dezayes (2006), Deep-seated geology of the granite intrusions at the Soultz EGS site based on data from 5km-deep boreholes, *Geothermics*, *35*(5-6), 484–506, doi:10.1016/j.geothermics.2006.03.003.

Horálek, J., Z. Jechumtálová, L. Dorbath, and J. Šílený (2010), Source mechanisms of micro-earthquakes induced in a fluid injection experiment at the HDR site Soultz-sous-Forêts (Alsace) in 2003 and their temporal and spatial variations, *Geophys. J. Int.*, *181*(3), 1547–1565, doi:10.1111/j.1365-246X.2010.04506.x.

Hosni, A., S. Gentier, A. Genter, J. Riss, D. Billaux, and F. Dedecker (2003), Coupled THM modeling of stimulated permeable fractures in the near well at the Soultz-sous-Forêts site (France), in *Proceedings of GeoProc 2003: International Conference on Coupled T-H-M-C Processes in Geosystems*, Stockholm, Sweden.

Housse, B.-A. (1984), Reconnaissance du potentiel géothermique du Buntsandstein à Strasbourg-Cronenbourg, *Géotherm. Actual.*, *1*.

Huenges, E., H.-G. Holl, D. Bruhn, W. Brandt, A. Saadat, I. Moeck, and G. Zimmermann (2007), Current state of the EGS project Gross Schönebeck - Drilling into deep sedimentary geothermal reservoirs., in *Proceedings of European Geothermal Congress*, Szeged, Hungary.

Ikeuchi, K., N. Doi, Y. Sakagawa, H. Kamenosono, and T. Uchida (1998), High-temperature measurements in well WD-1A and the thermal structure of the kakkonda geothermal system, Japan, *Geothermics*, *27*(5–6), 591–607, doi:10.1016/S0375-6505(98)00035-2.

Illies, H. J. (1965), Bauplan und Baugeschichte des Oberrheingrabens, *Oberrheinische Geol. Abh.*, *14*, 1–54.

Illies, H. J. (1972), The Rhine graben rift system-plate tectonics and transform faulting, *Geophys. Surv.*, *1*(1), 27–60, doi:10.1007/bf01449550.

Illies, H. J. (1975), Recent and paleo-intraplate tectonics in stable Europe and the Rhinegraben rift system, *Tectonophysics*, *29*(1–4), 251–264, doi:10.1016/0040-1951(75)90149-3.

Illies, H. J. (1977), Ancient and recent rifting in the Rhinegraben, *Geol. Mijnb.*, *56*(4), 329–350.

Illies, H. J., and G. Greiner (1979), Holocene movements and state of stress in the rhinegraben rift system, *Tectonophysics*, *52*(1–4), 349–359, doi:10.1016/0040-1951(79)90245-2.

Inoue, A., M. Utada, and M. Shimizu (1999), Mineral-fluid interactions in the Sumikawa geothermal system, Northeast Japan., *Resour. Geol. Spec. Issue*, *20*, 79–98.

Jacquemont, B. (2002), Etude des intéractions eaux-roches dans le granite de Soultz-sous-Forêts; Quantification et modélisation des transferts de matière par les fluides., PhD thesis, 182 pp., Université de Strasbourg, France.

Jung, R. (1992), Hydraulic fracturing and hydraulic testing in the granitic section of borehole GPK-1, Soultz-sous-Forêts., in *Geothermal Energy in Europe - The Soultz Hot Dry Rock Project*, pp. 149–198, James C. Bresee, Montreux, Switzerland.

Jung, R., and R. Weidler (2000), A conceptual model for the stimulation process of the HDR-system at Soultz, in *Geothermal Resources Council Transactions*, vol. 24, pp. 143-147, Geothermal Resources Council, Davis, California.

Kappelmeyer, O., A. Gérard, R. Schloemer, F. Ferrandes, F. Rummel, and Y. Benderitter (1992), European HDR Project at Soultz-sous-Forêts: General Presentation, in *Geothermal Energy in Europe - The Soultz Hot Dry Rock Project*, pp. xvii-xliii, James C. Bresee, Montreux, Switzerland.

Käser, B., A. Kalt, and J. Borel (2007), *The crystalline basement drilled at the Basel-1 geothermal site. A preliminary petrological-geochemical study. Report to Geopower Basel AG for Swiss Deep Heat Mining Project Basel.*, Institut de Géologie et d'Hydrogéologie, Université de Neuchâtel, Switzerland.

Kölbel, T. (2010), Geothermal power plant Bruchsal: construction and initial operating experiences, in *Proceedings of Third European Geothermal Review*, Mainz, Germany.

Kohl, T., D. Baechler, and L. Rybach (2000), Steps towards a comprehensive thermo-hydraulic analysis of the HDR test site Soultz-sous-Forêts, in *Proceedings of World Geothermal Congress 2000*, Kyushu - Tohoku, Japan.

Kreuter, H., N. Harthill, M. Judt, and B. Lehmann (2003), Geothermal power generation in the Upper Rhine Valley, the project Offenbach/Pfalz, in *Proceedings of International Geothermal Conference 2003*, Reykjavik, Island.

Krohe, A., and P. Willner (1995), *The Odenwald crystalline complex, in pre-Permian geology of Central and Eastern Europe.*, Springer., R. D. Dallemeyer, W. Franke and K. Weber.

Kubler, B. (1968), Evaluation quantitative du métamorphisme par la cristallinité de l'illite: Etat des progrès réalisés ces dernières années., *Bull. Cent. Rech. Pau-SNPA*, *2*(2), 385–397.

Ladner, F., and M. O. Häring (2009), Hydraulic characteristics of the Basel 1 Enhanced Geothermal system, in *Geothermal Resources Council Transactions*, vol. 33, pp. 199-204, Geothermal Resources Council, Davis, California.

Lagarde, J. L., R. Capdevila, and S. Fourcade (1992), Granites et collision continentale; l'exemple des granitoides carbonifères dans la chaine hercynienne ouest-européenne, *Bull. Sociéte Géologique Fr.*, *163*(5), 597–610.

Le Carlier, C., J. . Royer, and E. . Flores (1994), Convective heat transfer at the Soultz-sous-Forets geothermal site: Implications for oil potential, *First Break*, *12*(1285), doi:10.3997/1365-2397.1994033.

Ledésert, B., J. Joffre, A. Amblès, P. Sardini, and A. Genter (1996), Organic matter in the Soultz HDR granitic thermal exchanger (France): natural tracer of fluid circulations between the basement and its sedimentary cover, *J. Volcanol. Geotherm. Res.*, *70*(3-4), 235–253, doi:10.1016/0377-0273(95)00058-5.

Ledésert, B., G. Berger, A. Meunier, A. Genter, and A. Bouchet (1999), Diagenetic-type reactions related to hydrothermal alteration in the Soultz-sous-Forêts Granite, France, *Eur. J. Mineral.*, *11*(4), 731–741, doi:10.1127/ejm/11/4/0731.

Ledru, P., and L. Guillou-Frottier (2010), Reservoir definition, in *Geothermal Energy Systems - Exploration, Development, and Utilization*, pp. 1–36, Ernst Huenges, Weinheim, Germany.

Lengliné, O., M. Boubacar, and J. Schmittbuhl (2017), Seismicity related to the hydraulic stimulation of GRT1, Rittershoffen, France, *Geophys. J. Int.*, *208*(3), 1704–1715, doi:10.1093/gji/ggw490.

Longerich, H., S. Jackson, and D. Günther (1996), Laser ablation inductively coupled plasma mass spectrometric transient signal data acquisition and analyte concentration calculation, *J. Anal. At. Spectrom.*, *11*, 899–904.

Lopes Cardozo, G. G. O., and J. H. Behrmann (2006), Kinematic analysis of the Upper Rhine Graben boundary fault system, *J. Struct. Geol.*, *28*(6), 1028–1039, doi:10.1016/j.jsg.2006.03.010.

López-Munguira, A., F. Nieto, and D. Morata (2002), Chlorite composition and geothermometry: a comparative HRTEM/AEM-EMPA-XRD study of Cambrian basic lavas from the Ossa Morena Zone, SW Spain, *Clay Miner.*, *37*(2), 267–281, doi:10.1180/0009855023720033.

Lorenz, V., and I. . A. Nicholls (1976), The Permocarboniferous Basin and Range province of Europe. An application of plate tectonics, in *The Continental Permian in Central, West, and South Europe: Proceedings of the NATO Advanced Study Institute*, vol. 22, pp. 313–342, H. Falke, Dordrecht, Holland, doi:10.1007/978-94-010-1461-8_22.

Lotz, U. (2013), Specific challenges for geothermal projects in Baden-Württemberg - Geothermal Project Brühl, in *Proceedings of Third European Geothermal Review*, Mainz, Germany.

Lowell, J. D., and J. M. Guilbert (1970), Lateral and vertical alteration-mineralization zoning in porphyry ore deposits, *Econ. Geol.*, *65*(4), 373–408, doi:10.2113/gsecongeo.65.4.373.

Magnenet, V., C. Fond, A. Genter, and J. Schmittbuhl (2014), Two-dimensional THM modelling of the large scale natural hydrothermal circulation at Soultz-sous-Forêts, *Geotherm. Energy*, *2*(1), doi:10.1186/s40517-014-0017-x.

Majer, E. L., R. Baria, M. Stark, S. Oates, J. Bommer, B. Smith, and H. Asanuma (2007), Induced seismicity associated with Enhanced Geothermal Systems, *Geothermics*, *36*(3), 185–222, doi:10.1016/j.geothermics.2007.03.003.

Mas, A., P. Patrier, D. Beaufort, and A. Genter (2003), Clay-mineral signatures of fossil and active hydrothermal circulations in the geothermal system of the Lamentin Plain, Martinique, *J. Volcanol. Geotherm. Res.*, *124*(3–4), 195–218, doi:10.1016/S0377-0273(03)00044-1.

Mas, A., D. Guisseau, P. Patrier Mas, D. Beaufort, A. Genter, B. Sanjuan, and J. P. Girard (2006), Clay minerals related to the hydrothermal activity of the Bouillante geothermal field (Guadeloupe), *J. Volcanol. Geotherm. Res.*, *158*(3–4), 380–400, doi:10.1016/j.jvolgeores.2006.07.010.

Matte, P. (1986), Tectonics and plate tectonics model for the Variscan belt of Europe, *Tectonophysics*, *126*(2–4), 329–374, doi:10.1016/0040-1951(86)90237-4.

Matte, P. (2001), The Variscan collage and orogeny (480–290 Ma) and the tectonic definition of the Armorica microplate: a review, *Terra Nova*, *13*(2), 122–128, doi:10.1046/j.1365-3121.2001.00327.x.

Maurer, V., N. Cuenot, E. Gaucher, M. Grunberg, J. Vergne, H. Wodling, M. Lehujeur, and J. Schmittbuhl (2015), Seismic monitoring of the Rittershoffen EGS project (Alsace, France), in *Proceedings of World Geothermal Congress 2015*, Melbourne, Australia.

McCann, T., C. Pascal, M. J. Timmerman, P. Krzywiec, J. López-Gómez, L. Wetzel, C. M. Krawczyk, H. Rieke, and J. Lamarche (2006), Post-Variscan (end Carboniferous-Early Permian) basin evolution in Western and Central Europe, *Geol. Soc. Lond. Mem.*, *32*(1), 355–388, doi:10.1144/GSL.MEM.2006.032.01.22.

Méheust, Y., and J. Schmittbuhl (2001), Geometrical heterogeneities and permeability anisotropy of rough fractures, *J. Geophys. Res. Solid Earth*, *106*(B2), 2089–2102, doi:10.1029/2000JB900306.

Meixner, J., E. Schill, E. Gaucher, and T. Kohl (2014), Inferring the in situ stress regime in deep sediments: an example from the Bruchsal geothermal site, *Geotherm. Energy*, *2*(1), doi:10.1186/s40517-014-0007-z.

Meixner, J., E. Schill, J. C. Grimmer, E. Gaucher, T. Kohl, and P. Klingler (2016), Structural control of geothermal reservoirs in extensional tectonic settings: An

example from the Upper Rhine Graben, *J. Struct. Geol.*, *82*, 1–15, doi:10.1016/j.jsg.2015.11.003.

Melchert, B., I. Stober, and U. Lotz (2013), Erste Ergebnisse der hydraulischen Testmaßnahmen und geochemischen Analysen der Geothermie-Bohrung GT1 in Brühl/Baden-Württemberg, *Geothermiekongress 2013*, Bundesverband Geothermie, Essen, Germany.

Meller, C., and T. Kohl (2014), The significance of hydrothermal alteration zones for the mechanical behavior of a geothermal reservoir, *Geotherm. Energy*, *2*(1), 1–21, doi:10.1186/s40517-014-0012-2.

Meller, C., A. Kontny, and T. Kohl (2014), Identification and characterization of hydrothermally altered zones in granite by combining synthetic clay content logs with magnetic mineralogical investigations of drilled rock cuttings, *Geophys. J. Int.*, *199*(1), 465–479, doi:10.1093/gji/ggu278.

Ménillet, F., M. Durand, A. Genter, and J.-P. Party (2015), Notice explicative, Carte géologique de la France (1/50000), feuille Haguenau, 345 pp., BRGM, Orléans, France.

Michelet, S., and M. N. Toksöz (2007), Fracture mapping in the Soultz-sous-Forêts geothermal field using microearthquake locations, *J. Geophys. Res. Solid Earth*, *112*(B7), doi:10.1029/2006JB004442.

Michon, L., and O. Merle (2005), Discussion on “Evolution of the European Cenozoic Rift System: interaction of the Alpine and Pyrenean orogens with their foreland lithosphere” by P. Dèzes, S.M. Schmid and P.A. Ziegler, Tectonophysics 389 (2004) 1–33, *Tectonophysics*, *401*(3–4), 251–256, doi:10.1016/j.tecto.2005.01.006.

Mukuhira, Y., H. Asanuma, H. Niitsuma, and M. O. Häring (2013), Characteristics of large-magnitude microseismic events recorded during and after stimulation of a geothermal reservoir at Basel, Switzerland, *Geothermics*, *45*, 1–17, doi:10.1016/j.geothermics.2012.07.005.

Munck, F., F. Walgenwitz, P. Maget, K. Sauer, and R. Tietze (1979), *Synthèse géothermique du Fossé rhénan supérieur.*, BRGM Service Géologique

Régional d'Alsace -Geologisches Landesamt Baden-Württemberg. Commission of the European Communities.

Nami, P., R. Schellschmidt, M. Schindler, and T. Tischner (2008), Chemical stimulation operations for reservoir development of the deep crystalline HDR/EGS system at Soultz-sous-Forêts (France), in *Proceedings of Thirty-Second Workshop on Geothermal Reservoir Engineering*, Stanford University, California, USA.

Neuville, A., R. Toussaint, and J. Schmittbuhl (2010), Fracture roughness and thermal exchange: A case study at Soultz-sous-Forêts., *Comptes Rendus Geosci.*, *342*, 616–625, doi:10.1016/j.crte.2009.03.006.

Papapanagiotou, P., D. Beaufort, P. Patrier, and H. Traineau (1993), Clay mineralogy of the >0.2 µm rock fraction of the M1 drill hole of the geothermal field of Milos (Greece)., *Bull Geol Soc Greece*, *28*(2), 575–586.

Patrier, P., P. Papapanagiotou, D. Beaufort, H. Traineau, H. Bril, and J. Rojas (1996), Role of permeability versus temperature in the distribution of the fine (< 0.2 µm) clay fraction in the Chipilapa geothermal system (El Salvador, Central America), *J. Volcanol. Geotherm. Res.*, *72*(1–2), 101–120, doi:10.1016/0377-0273(95)00078-X.

Pauwels, H., C. Fouillac, and A.-M. Fouillac (1993), Chemistry and isotopes of deep geothermal saline fluids in the Upper Rhine Graben: Origin of compounds and water-rock interactions, *Geochim. Cosmochim. Acta*, *57*(12), 2737–2749, doi:10.1016/0016-7037(93)90387-C.

Pearce, N., W. Perkins, J. Westgate, M. Gorton, S. Jackson, C. Neal, and S. Chenery (1997), A compilation of new and published major and trace element data for NIST SRM 610 and NIST SRM 612 glass reference materials., *Geostand. Geoanalytical Res.*, *21*(1), 115–144, doi:10.1111/j.1751-908x.1997.tb00538.x.

Person, M., and G. Garven (1992), Hydrologic constraints on petroleum generation within continental rift basins: theory and application to the Rhine graben (1), *AAPG Bull.*, *76*(4), 468–488, doi:10.1029/gm047p0035.

Pflug, R. (1982), *Bau und Entwicklung des Oberrheingrabens*, Erträge der Forschung, vol. 184, 145 pp., Wissenschaftliche Buchgesellschaft, Darmstadt, Germany.

Pine, R. J., and A. S. Batchelor (1984), Downward migration of shearing in jointed rock during hydraulic injections, *Int. J. Rock Mech. Min. Sci. Geomech. Abstr.*, *21*(5), 249–263, doi:10.1016/0148-9062(84)92681-0.

Portier, S., F.-D. Vuataz, P. Nami, B. Sanjuan, and A. Gérard (2009), Chemical stimulation techniques for geothermal wells: experiments on the three-well EGS system at Soultz-sous-Forêts, France, *Geothermics*, *38*(4), 349–359, doi: 10.1016/j.geothermics.2009.07.001.

Pribnow, D. (2000), *The deep thermal regime in Soultz and implications for fluid flow: HDR Project Soultz Report*, GGA-Bericht, Hannover, Germany.

Pribnow, D., and C. Clauser (2000), Heat and fluid flow at the Soultz Hot Dry Rock system in the Rhine Graben, in *Proceedings of World Geothermal Congress 2000*, Kyushu - Tohoku, Japan.

Pribnow, D., and R. Schellschmidt (2000), Thermal tracking of upper crustal fluid flow in the Rhine Graben, *Geophys. Res. Lett.*, *27*(13), 1957–1960, doi:10.1029/2000GL008494.

Ratouis, T. M. P., and S. J. Zarrouk (2016), Factors controlling large-scale hydrodynamic convection in the Taupo Volcanic Zone (TVZ), New Zealand, *Geothermics*, *59*, 236–251, doi:10.1016/j.geothermics.2015.09.003.

Rawling, G. C., and L. B. Goodwin (2006), Structural record of the mechanical evolution of mixed zones in faulted poorly lithified sediments, Rio Grande rift, New Mexico, USA, *J. Struct. Geol.*, *28*(9), 1623–1639, doi:10.1016/j.jsg.2006.06.008.

Recalde Lummer, N., O. Rauf, S. Gerdes, A. Genter, J. Scheiber, and G. Villadangos (2014), New biodegradable stimulation system - First field trial in granite/Bunter sandstone formation for a geothermal application in the Upper Rhine Valley, in *Proceedings of Deep Geothermal Days*, Paris, France.

Reinecker, J., J. Bauer, and S. L. Philipp (2014), Fault zones and associated fracture systems in geothermal exploration, *Tiefengeothermie –Forum*, Hessen, Germany.

Reyes, A. G. (1990), Petrology of Philippine geothermal systems and the application of alteration mineralogy to their assessment, *J. Volcanol. Geotherm. Res.*, *43*(1), 279–309, doi:10.1016/0377-0273(90)90057-M.

Ritter, J., M. Frietsch, L. Gassner, J. Groos, M. Grund, and J. Zeiss (2014), Mechanism of fluid-induced micro-earthquakes near Landau, Upper Rhine Graben, Germany, in *Proceedings of European Geosciences Union 2014*, Wien, Austria.

Rose, P., T. Xu, K. Kovac, M. Mella, and K. Pruess (2007), Chemical stimulation in near-wellbore geothermal formations: silica dissolution in the presence of calcite at high temperature and high pH, in *Proceedings of Thirty-Second Workshop on Geothermal Reservoir Engineering,* Stanford University, California, USA.

Rotstein, Y., and M. Schaming (2008), Tectonic implications of faulting styles along a rift margin: The boundary between the Rhine Graben and the Vosges Mountains, *Tectonics*, *27*(2), doi:10.1029/2007TC002149.

Rummel, F., U. Haack, and E. Gohn (1988), *Uranium, thorium and potassium content and derived heat production rate*, 6-9, Yellow report, Ruhr Universität, Bochum, Germany., Germany

Rummel, F. (1992), Physical properties of the rock in the granite section of borehole GPK-1, Soultz-sous-Forêts, in *Geothermal Energy in Europe - The Soultz Hot Dry Rock Project*, pp. 199–216, James C. Bresee, Montreux, Switzerland.

Saffer, D. M., & Marone, C. (2003), Comparison of smectite- and illite-rich gouge frictional properties: application to the updip limit of the seismogenic zone along subduction megathrusts, *Earth and Planetary Science Letters*, 215(1), 219–235, doi:10.1016/S0012-821X(03)00424-2

Sanjuan, B., R. Millot, C. Dezayes, and M. Brach (2010), Main characteristics of the deep geothermal brine (5 km) at Soultz-sous-Forêts (France) determined

using geochemical and tracer test data, *Comptes Rendus Geosci*, *342*(7-8), 546-559, doi:10.1016/j.crte.2009.10.009.

Sanjuan, B., R. Millot, R. Ásmundsson, M. Brach, and N. Giroud (2014), Use of two new Na/Li geothermometric relationships for geothermal fluids in volcanic environments, *Chem. Geol.*, *389*, 60–81, doi:10.1016/j.chemgeo.2014.09.011.

Sanjuan, B., R. Millot, C. Innocent, C. Dezayes, J. Scheiber, and M. Brach (2016a), Major geochemical characteristics of geothermal brines from the Upper Rhine Graben granitic basement with constraints on temperature and circulation, *Chem. Geol.*, *428*, 27–47, doi:10.1016/j.chemgeo.2016.02.021.

Sanjuan, B., J. Scheiber, F. Gal, S. Touzelet, A. Genter, and G. Villadangos (2016b), Interwell chemical tracer testing at the Rittershoffen site (Alsace, France)., in *Proceedings of European Geothermal Congress 2016*, Strasbourg, France.

Sardini, P., B. Ledésert, and G. Touchard (1997), Quantification of microscopic porous networks by image analysis and measurements of permeability in the Soultz-sous-Forêts granite (Alsace, France), in *Fluid Flow and Transport in Rocks—Mechanisms and Effects*, pp. 171–188, Jamtveit, B. and Yardley, B, London, Great Britain.

Sausse, J., and A. Genter (2005), Types of permeable fractures in granite, *Geol. Soc. Lond. Spec. Publ.*, *240*, 1–14, doi:doi:10.1144/GSL.SP.2005.240.01.01.

Sausse, J., M. Fourar, and A. Genter (2006), Permeability and alteration within Soultz granite inferred from geophysical and flow log analysis, *Geothermics*, (35), 544–560.

Sausse, J., C. Dezayes, A. Genter, and A. Bisset (2008), Characterization of fracture connectivity and fluid flow pathways derived from geological interpretation and 3D modelling of the deep seated EGS reservoir of Soultz (France), in *Proceedings of Thirty-Third Workshop on Geothermal Reservoir Engineering*, Stanford University, California, USA.

Sausse, J., C. Dezayes, L. Dorbath, A. Genter, and J. Place (2010), 3D model of fracture zones at Soultz-sous-Forets based on geological data, image logs,

induced microseismicity and vertical seismic profiles, *Comptes Rendus Geosci.*, *342*(7–8), 531–545, doi:10.1016/j.crte.2010.01.011.

Schad, A. (1962), Das Erdoelfeld Landau, *Abh Geol Baden-Würtemberg*, *4*, 81–101.

Schellschmidt, R., and C. Clauser (1996), The thermal regime of the Upper Rhine Graben and the anomaly at Soultz, *Z. Für Angew. Geol.*, *42*(1), 40–44.

Schellschmidt, R., B. Sanner, S. Pester, and R. Schulz (2010), Geothermal energy use in Germany, in *Proceedings of World Geothermal Congress 2010*, Bali, Indonesia.

Schill, E., T. Kohl, C. Baujard, and J.-F. Wellmann (2009), *Geothermische Ressourcen in Rheinland-Pfalz: Bereiche Süd- und Vorderpfalz*, Final report to the Ministry of Environment Rhineland-Palatine.

Schill, E., A. Genter, N. Cuenot, and T. Kohl (2017), Hydraulic performance history at the Soultz EGS reservoirs from stimulation and long-term circulation tests, *Geothermics*, *70*, 110–124, doi:10.1016/j.geothermics.2017.06.003.

Schindler, M., J. Baumgärtner, T. Gandy, P. Hauffe, T. Hettkamp, H. Menzek, P. Penzkofer, D. Teza, G. Wahl, and T. Tischner (2010), Successful hydraulic stimulation techniques for electric power production in the Upper Rhine Graben, Central Europe, in *Proceedings of World Geothermal Congress 2010*, Bali, Indonesia.

Schleicher, A. M., L. N. Warr, B. Kober, E. Laverret, and N. Clauer (2006), Episodic mineralization of hydrothermal illite in the Soultz-sous-Forêts granite (Upper Rhine Graben, France), *Contrib. Mineral. Petrol.*, *152*(3), 349–364, doi:10.1007/s00410-006-0110-7.

Schlumberger (2002), *Ultrasonic Imaging*, Marketing Communications, Schlumberger, Houston, Texas.

Schmittbuhl, J., O. Lengline, F. Cornet, N. Cuenot, and A. Genter (2014), Induced seismicity in EGS reservoir: the creep route, *Geotherm. Energy*, *2*(1), doi:10.1186/s40517-014-0014-0.

Schnaebele, R., J.-O. Haas, and C. R. Hoffmann (1948), Monographie Géologique du Champ Petrolifere de Pechelbronn, Strasbourg, *Mém. Carte Géologique Alsace Lorraine*, *7*(254).

Schneider, C. (1984), *Les granitoïdes de la partie Nord-Est des Vosges moldanubiennes: évolution magmatique et structural*, Master thesis, Université Louis Pasteur, Strasbourg, France.

Schoenball, M., C. Baujard, T. Kohl, and L. Dorbath (2012), The role of triggering by static stress transfer during geothermal reservoir stimulation, *J. Geophys. Res. Solid Earth*, *117*(B9), doi:10.1029/2012JB009304.

Schulmann, K., J. Jezek, and Z. Verena (1997), Perpendicular linear fabrics in granite: markers of combined simple shear and pure shear flows, in *Granite: from segregation of melt to emplacement fabrics*, J. L. Bouchez, D. H. W. Hutton, and W. E. Stephens, Dordrecht, Netherlands.

Schulmann, K., J. Konopásek, V. Janoušek, O. Lexa, J.-M. Lardeaux, J.-B. Edel, P. Štípská, and S. Ulrich (2009), An Andean type Palaeozoic convergence in the Bohemian Massif, *Comptes Rendus Geosci.*, *341*(2), 266–286, doi:10.1016/j.crte.2008.12.006.

Schulte, T., G. Zimmermann, F.-D. Vuataz, S. Portier, T. Tischner, R. Junker, R. Jatho, and E. Huenges (2010), Enhancing geothermal reservoirs, in *Geothermal Energy Systems - Exploration, Development, and Utilization*, pp. 173–243, Ernst Huenges, Weinheim, Germany.

Schumacher, M. E. (2002), Upper Rhine Graben: Role of preexisting structures during rift evolution, *Tectonics*, *21*(1), 6–1 to 6-17, doi:10.1029/2001tc900022.

Serra, O. (2008), *The Well Logging Handbook*, Editions Technip., Paris, France.

Serra, O., and L. Serra (2000), *Diagraphies, Acquisition et applications*, Editions Serralog.

Sissingh, W. (1998), Comparative Tertiary stratigraphy of the Rhine Graben, Bresse Graben and Molasse Basin: correlation of Alpine foreland events, *Tectonophysics*, *300*(1–4), 249–284, doi:10.1016/S0040-1951(98)00243-1.

Sittler, C. (1965), *Le Paléogene des fossés rhénan et rhodanien: Etudes sédimentologiques et paléoclimatiques*, Université de Strasbourg. Centre National de la Recherche Scientifique.

Sittler, C. (1985), Les hydrocarbures d'Alsace dans le contexte historique et géodynamique du fossé Rhénan, *Bull. Cent. Rech. Elf Explor. Prod.*, *9*(2), 335–371.

Sittler, C. (1992), Illustration de l'histoire géologique du Fossé rhénan et de l'Alsace, *N Jb Geol Paläont Abh*, *186*(3), 255–282.

Smith, M. P., V. Savary, B. W. D. Yardley, J. W. Valley, J. J. Royer, and M. Dubois (1998), The evolution of the deep flow regime at Soultz-sous-Forêts, Rhine Graben, eastern France: Evidence from a composite quartz vein, *J. Geophys. Res. Solid Earth*, *103*(B11), 27223–27237, doi:10.1029/98JB02528.

Soma, N., H. Niitsuma, and R. Baria (2007), Reflection imaging of deep reservoir structure based on three-dimensional hodogram analysis of multicomponent microseismic waveforms, *J. Geophys. Res. Solid Earth*, *112*(B11), doi:10.1029/2005JB004216.

Sosio, G. et al. (2016), Integrated Geological, Fluid Flow and Geomechanical Model of a Geothermal Field, in *Proceedings of European Geothermal Congress 2016*, Strasbourg, France.

Stober, I., and M. Jodocy (2009), Eigenschaften geothermischer Nutzhorizonte im abden-württembergischen und französischen Teil des Obberheingrabens, *Grundwasser - Z. Fachsekt. Hydrogeol.*, *14*, 127–137, doi:10.1007/s00767-009-0103-3.

Stober, I., and M. Jodocy (2011), Hydrochemical characteristic of deep seated waters in the Upper Rhine Graben. Basic information for geothermal energy, *Z. Für Geol. Wiss. Berl.*, *39*, 39–57.

Stussi, J.-M., A. Cheilletz, J.-J. Royer, P. Chèvremont, and F. Gilbert (2002), The hidden monzogranite of Soultz-sous-Forêts (Rhine Graben, France), mineralogy, petrology and genesis, *Géologie Fr.*, *1*, 45–64.

Teklemariam, M., S. Battaglia, G. Gianelli, and G. Ruggieri (1996), Hydrothermal alteration in the Aluto-Langano geothermal field, Ethiopia, *Geothermics*, *25*(6), 679–702, doi:10.1016/S0375-6505(96)00019-3.

Thomasson, J., and H. Kristmannsdottir (1972), High temperature alteration minerals and thermal brines, Reykjanes, Iceland., *Contrib. Mineral. Petrol.*, *36*(2), 123–134, doi:10.1007/bf00371183.

Tingay, M., J. Reinecker, and B. Müller (2008), Borehole breakout and drilling-induced fracture analysis from image logs., in *World Stress Map Proj. Stress Anal. Guidelines: Image logs.* Helmholtz Cent. Potsdam, GFZ German Research Centre for Geosciences, Potsdam, Germany.

Traineau, H., A. Genter, J.-P. Cautru, H. Fabriol, and P. Chèvremont (1992), Petrography of the granite massif from drill cutting analysis and well log interpretation in the geothermal HDR borehole GPK-1 (Soultz, Alsace, France), in *Geothermal Energy in Europe - The Soultz Hot Dry Rock Project*, pp. 1–29, James C. Bresee, Montreux, Switzerland.

Tulinius, H., H. Correia, and O. Sigurdsson (2000), Stimulating a high enthalpy well by thermal cracking, Kyushu - Tohoku, Japan.

Valley, B. (2007), The relation between natural fracturing and stress heterogeneities in deep-seated crystalline rocks at Soultz-sous-Forêts (France), PhD thesis, 243 pp., Swiss Federal Institute of Technology Zurich.

Valley, B. C., and K. F. Evans (2007), Stress state at Soultz-sous-Forêts to 5 km depth from wellbore failure and hydraulic observations, in *Proceedings of Thirty-Second Workshop on Geothermal Reservoir Engineering*, Stanford University, California, USA.

Vernoux, J.-F., A. Genter, P. Razin, and C. Vinchon (1995), *Geological and petrophysical parameters of a deep fractured sandstone formation as applied to geothermal exploitation: EPS1 borehole, Soultz-sous-Forêts, France*, R38622, Open file, BRGM, Orléans, France.

Vidal, J., A. Genter, and J. Schmittbuhl (2015), How do permeable fractures in the Triassic sediments of Northen Alsace characterize the top of

hydrothermal convective cells? Evidence from Soultz geothermal boreholes (France), *Geotherm. Energy*, *3*(1), doi:10.1186/s40517-015-0026-4.

Vidal, J., A. Genter, and J. Schmittbuhl (2016a), Pre- and post-stimulation characterization of geothermal well GRT-1, Rittershoffen, France: insights from acoustic image logs of hard fractured rock, *Geophys. J. Int.*, *206*(2), 845–860, doi:10.1093/gji/ggw181.

Vidal, J., A. Genter, F. Chopin, and E. Dalmais (2016b), Natural fractures and permeability at the geothermal site Rittershoffen, France, in *Proceedings of European Geothermal Congress 2016*, Strasbourg, France.

Vidal, J., M. Ulrich, H. Whitechurch, A. Genter, J. Schmittbuhl, E. Dalmais, and V. Girard-Berthet (2016c), Hydrothermal Alteration of the Hidden Granite in the Geothermal Context of the Upper Rhine Graben, in Proceedings of *Forty-First Workshop on Geothermal Reservoir Engineering*, Stanford University, California, USA.

Vidal, J., P. Patrier Mas, A. Genter, and D. Beaufort (2017), Occurrences of clay minerals in permeable fracture zones in the granitic basement of geothermal wells at Rittershoffen, France, in *Proceedings of Forty-Second Workshop on Geothermal Reservoir Engineering*, Stanford University, California, USA.

Vidal, J., A. Genter, and F. Chopin (2017), Permeable fracture zones in the hard rocks of the geothermal reservoir at Rittershoffen, France, *J. Geophys. Res. Solid Earth*, *122*, doi:10.1002/2017JB014331.

Villadangos, G. (2013), ECOGI, EGS Upper Rhine Geothermal project for the industry, first well and result, in *Proceedings of Third European Geothermal Review,* Mainz, Germany.

Villemin, T. (1986), Tectonique et extension, fracturation et subsidence: le Fossé rhénan et le bassin de Sarre-Nahé, PhD thesis, 270 pp., Université Paris VI, France.

Villemin, T., and F. Bergerat (1987), L'évolution structurale du Fosse rhénan au cours du Cénozoïque: un bilan de la déformation et des effets thermiques de l'extension, *Bull. Société Géologique Fr.*, *8*, 245–255.

Vuataz, F.-D., M. Brach, A. Criaud, and C. Fouillac (1990), Geochemical monitoring of drilling fluids: a powerful tool to forecast and detect formation waters, *SPE Form. Eval.*, *5*(2), 177–184, doi:10.2118/18734-PA.

Wibberley, C. A. J., G. Yielding, and G. D. Toro (2008), Recent advances in the understanding of fault zone internal structure: a review, *Geol. Soc. Lond. Spec. Publ.*, *299*(1), 5–33, doi:10.1144/SP299.2.

Wyns, R. (2012), *Etude géologique du cadre structural et des forages du bassin versant de recherche du Ringelbach (Soultzeren, Haut-Rhin), Rapport final*, RP-56540-FR, Open file, BRGM, Orléans, France.

Vuataz, F.-D., M. Brach, A. Criaud, and C. Fouillac (1990), Geochemical monitoring of drilling fluids: a powerful tool to forecast and detect formation waters, *SPE Form. Eval.*, *5*(2), 177–184, doi:10.2118/18734-PA.

Zemaneck, J., E. E. J. Glen, L. J. Norton, and R. L. Cardwell (1970), Formation evaluation by inspection with the borehole televiewer, *Geophysics*, *35*(2), 254–269, doi:10.1190/1.1440089.

Ziegler, P. A. (1990), *Geological Atlas of western and central Europe*, 2nd Edition., Shell International Petroleum Mij B V, London, Great Britain.

Ziegler, P. A. (1992), European Cenozoic rift system, *Tectonophysics*, *208*(1–3), 91–111, doi:10.1016/0040-1951(92)90338-7.

Ziegler, P. A. (1994), Cenozoic rift systems of Western and Central Europe: an overview, *Geol. Mijnb.*, *73*, 99–127.

Ziegler, P. A., M. E. Schumacher, P. Dèzes, J.-D. V. Wees, and S. Cloetingh (2006), Post-Variscan evolution of the lithosphere in the area of the European Cenozoic Rift System, *Geol. Soc. Lond. Mem.*, *32*(1), 97–112, doi:10.1144/GSL.MEM.2006.032.01.06.

Zoback, M. D., Kohli, A., Das, I., & Mcclure, M. W. (2012), The Importance of Slow Slip on Faults During Hydraulic Fracturing Stimulation of Shale Gas Reservoirs, *Society of Petroleum Engineers*, doi:10.2118/155476-MS

ANNEXES

ANNEXE 1

SOURCE THERMALE DES HELIONS

Données générales	*Compagnie :*	-		
	Position géographique :	*Pays* France		
		Région Alsace, Bas-Rhin		
		Ville Preuschdorf		
Données d'exploration	*Campagne d'exploration :*	Campagne de sismique réflexion réalisée par la Compagnie Générale de Géophysique pour la réalisation du troisième forage		
	Exploitation pétrolière :	Champ de Pechelbronn	Huile dans le Tertiaire (Couches de Pechelbronn) et dans le Trias inférieur (Buntsandstein)	
	Contexte géologique :	Le site est situé à moins de 5 km à l'Est de la faille bordière Ouest, dans le bassin compartimenté de Merkwiller-Pechelbronn		
	Cible :	Formations du Muschelkalk et du Trias		
	Concept :	Matriciel		
	Modèle 3D :	Non		
Données de production	*Production :*	Chaleur	*Nombre de puits :*	3
	Puissance installée planifiée :	-	*Débit de production planifié :*	-
	Système planifié :	-	*Température de pompage planifiée :*	-
	Statut actuel :	Abandon	*Température d'injection planifiée :*	-
Données de sous-sol	*Réservoir :*	Muschelkalk-Buntsandstein		
	Profondeur du réservoir (top) :	Autour de 900 m (variable selon les puits)		
Fluide géothermal	*Salinité :*	12 g/L (valeur mesurée en 1910 sur le premier forage)		
	Ions majeurs :	Cl Na K Ca SO_4		
	Gaz :	N_2 65,31% - CO_2 26,05% - He 1,09%		

Historique du projet

1909	Premier forage (1266, devenu les Hélions I) réalisé par la SAEM Pechelbronn pour la recherche d'huile
	Découverte d'eau salée dans les formations triasiques et utilisation pour réchauffer l'huile de la raffinerie puis pour alimenter un établissement de bains, en raison de la valeur thérapeutique attribuée aux eaux de forage renommée « Source des Hélions »
1967	Recherche d'eaux thermales dans le secteur de Preuschdorf pour alimenter des établissements thermaux sous la direction du Syndicat Intercommunal Merkwiller-Pechelbronn et étude hydrogéologique réalisée par la SGAL
1970	Deuxième forage (1266bis, devenu les Hélions II) dans le but de créer une station balnéaire et essais de débit entre les deux forages
	Les analyses physico-chimiques montrent la contamination des eaux superficielles par les eaux salées profondes (Tertiaire et Trias) en raison de la vétusté du forage les Hélions I
	Proposition d'aménager et de recimenter le forage les Hélions I rejetée
1993	Troisième forage (les Hélions III, indice national 198-3-45) réalisé sous la direction de la SEM « Les Cybéliades » dans l'objectif de créer un nouvel établissement thermal dans le secteur de Merkwiller-Pechelbronn et qui montre un fort caractère corrosif du fluide géothermal

	Proposition d’approfondir le puits pour augmenter la température en fond de puits et le débit, rejetée

SOURCE THERMALE DES HELIONS

Carte des failles à la surface du site

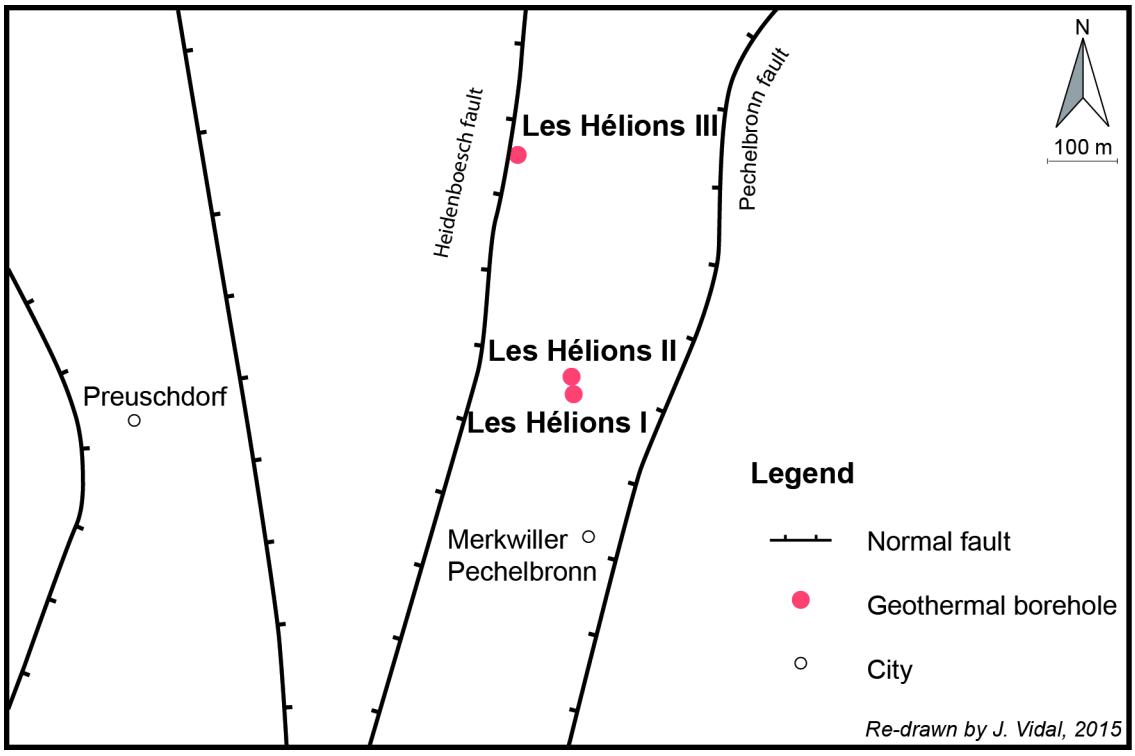

Coupe géologique interprétative du site

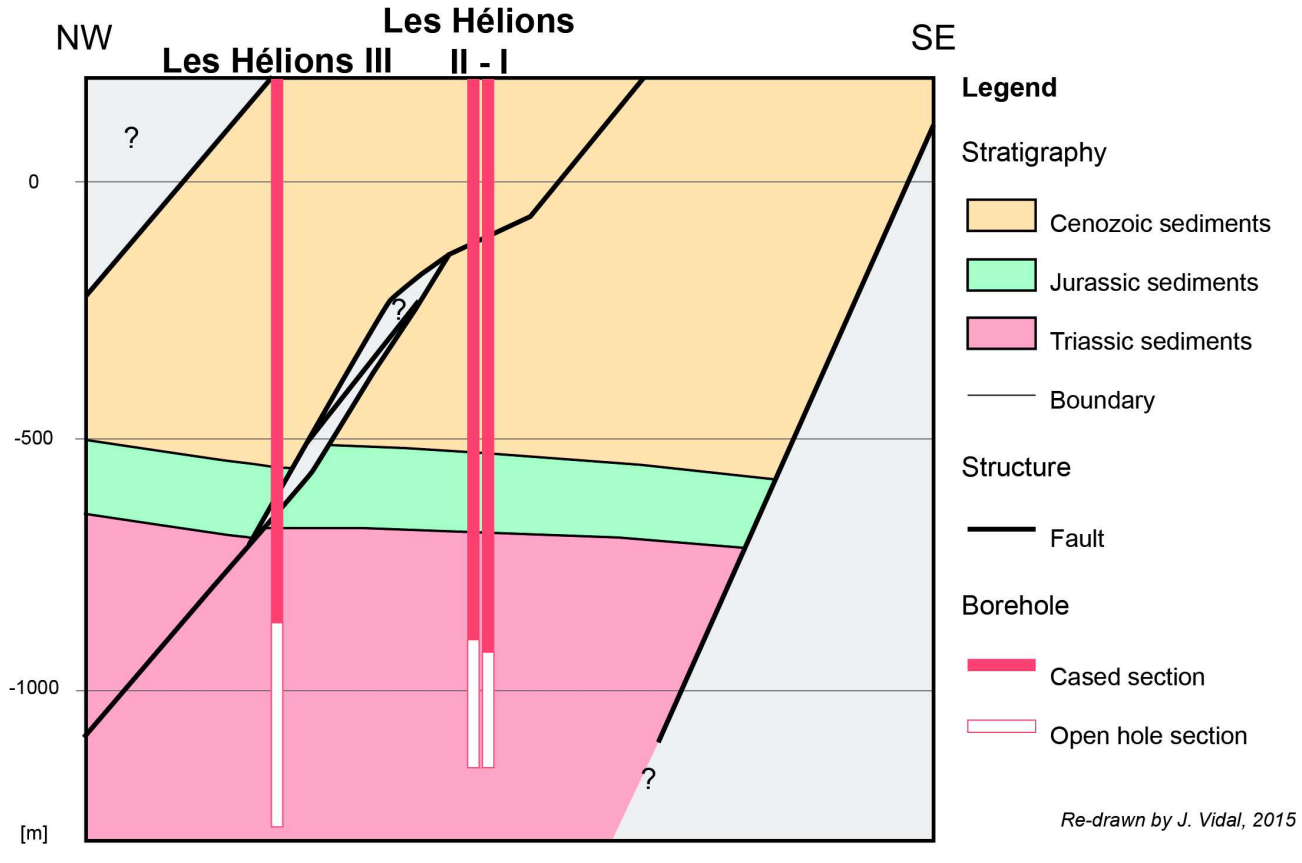

SOURCE THERMALE DES HELIONS

Données du puits les Hélions I	*Date de forage :*	01/02/1909 - 01/10/1910
	Coordonnées géographiques :	7° 49' 22" E 48° 56' 35" N
	Cible :	Formations tertiaires et triasiques riches en huile Forage situé entre les failles normales de Pechelbronn et de Hoesloch à plongement Ouest
	Trajectoire :	Verticale
	Fond de puits :	1157 m de profondeur - Buntsandstein
	Complétion :	Section en trou ouvert à partir de 933 m de profondeur
	Développement :	-
	Profil thermique :	-
	Température en fond de puits :	65°C
	Gradient de température :	-
	Toit de la convection :	-
	Débit :	3 L/s
	Indice de productivité :	-
	Zones productrices :	Venues d'eau chaude à 494 m (Zone Dolomitique), à 938 m (Lettenkohle) à un débit de 0.4 L/s et une température de 39°C, à 970 m (Muschelkalk) à un débit de 1.5 L/s et une température de 53°C, à 1051 m (Muschelkalk) à un débit de 3 L/s et une température de 65°C
	Fracturation naturelle :	Imageries de paroi non disponibles
	Orientation S_{Hmax} :	Champ de contrainte régional N145°E

SOURCE THERMALE DES HELIONS

Coupe géologique et technique du puits les Hélions I

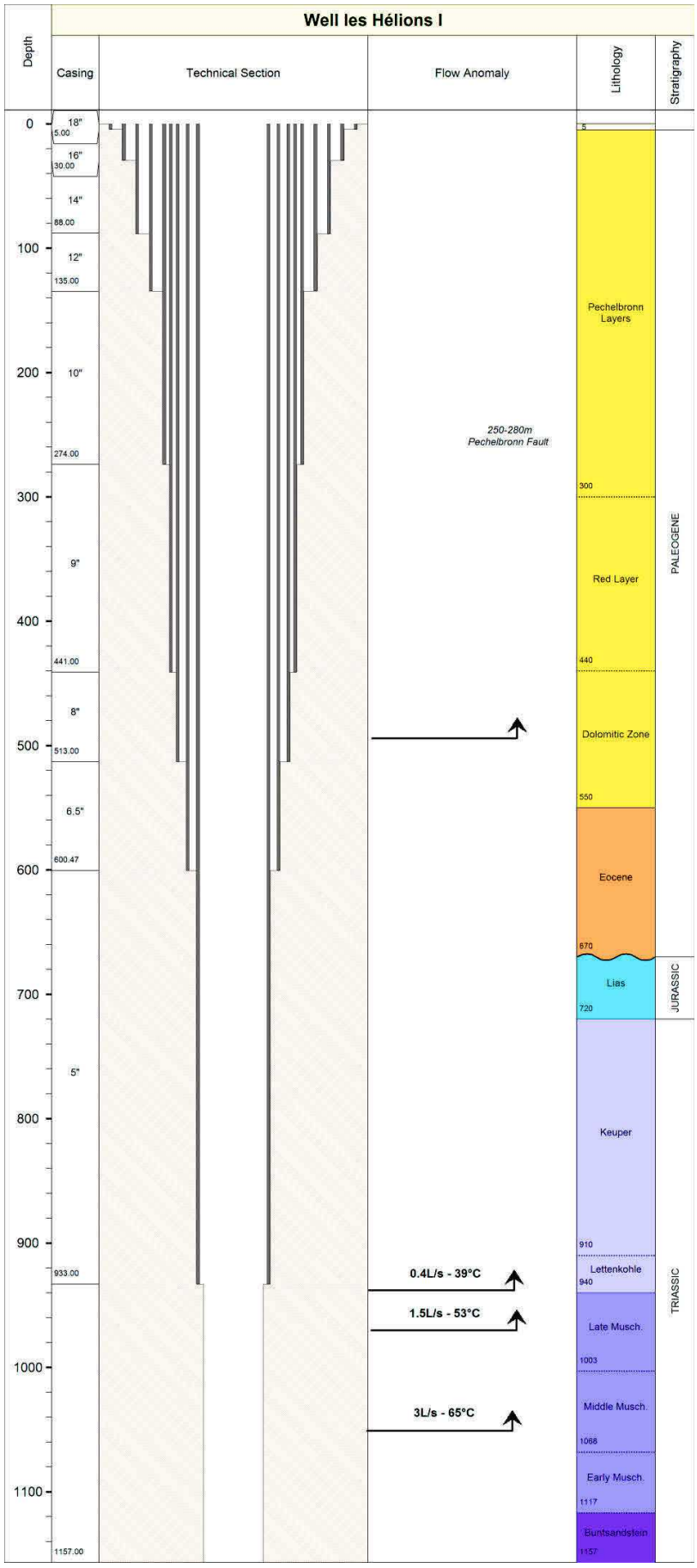

SOURCE THERMALE DES HELIONS

Données du puits les Hélions II

Date de forage :	19/11/1970 - 10/01/1971	
Coordonnées géographiques :	7° 49' 23" E 48° 56' 36" N	
Cible :	Aquifère des formations triasiques Forage situé entre les failles normales de Pechelbronn et de Hoesloch à plongement Ouest, à 35 m au N-NE du forage les Hélions I	
Trajectoire :	Verticale	
Fond de puits :	1146 m de profondeur - Buntsandstein	
Complétion :	Section 8”1/2 en trou ouvert à partir de 906 m de profondeur	
Développement :	1971	Acidification du forage avec 5 tonnes d’acide injecté Essais de débit qui montrent une interférence entre les deux forages qui captent le même aquifère dans les formations du Trias
Profil thermique :	Acquis à l’équilibre en octobre 1988	
Température en fond de puits :	80°C	
Gradient de température :	6 K/km	
Toit de la convection :	900 m (Lettenkohle)	
Débit :	5.5 L/s	
Indice de productivité :	-	
Zones productrices :	Venues d’eau chaude à 925 m (Lettenkohle) à un débit jusqu’à 0.7 L/s, puis de 2.5 L/s à partir de 1000 m (Muschelkalk) et qui augmente jusqu’à la fin du forage atteignant des valeurs > 5 L/s (Buntsandstein) Anomalies de température étroites à 988 m, 1000 m et 1025 m de profondeur	
Fracturation naturelle :	Imageries de paroi non disponibles	
Orientation S_{Hmax} :	Champ de contrainte régional N145°E	

SOURCE THERMALE DES HELIONS

Coupe géologique et technique du puits les Hélions II

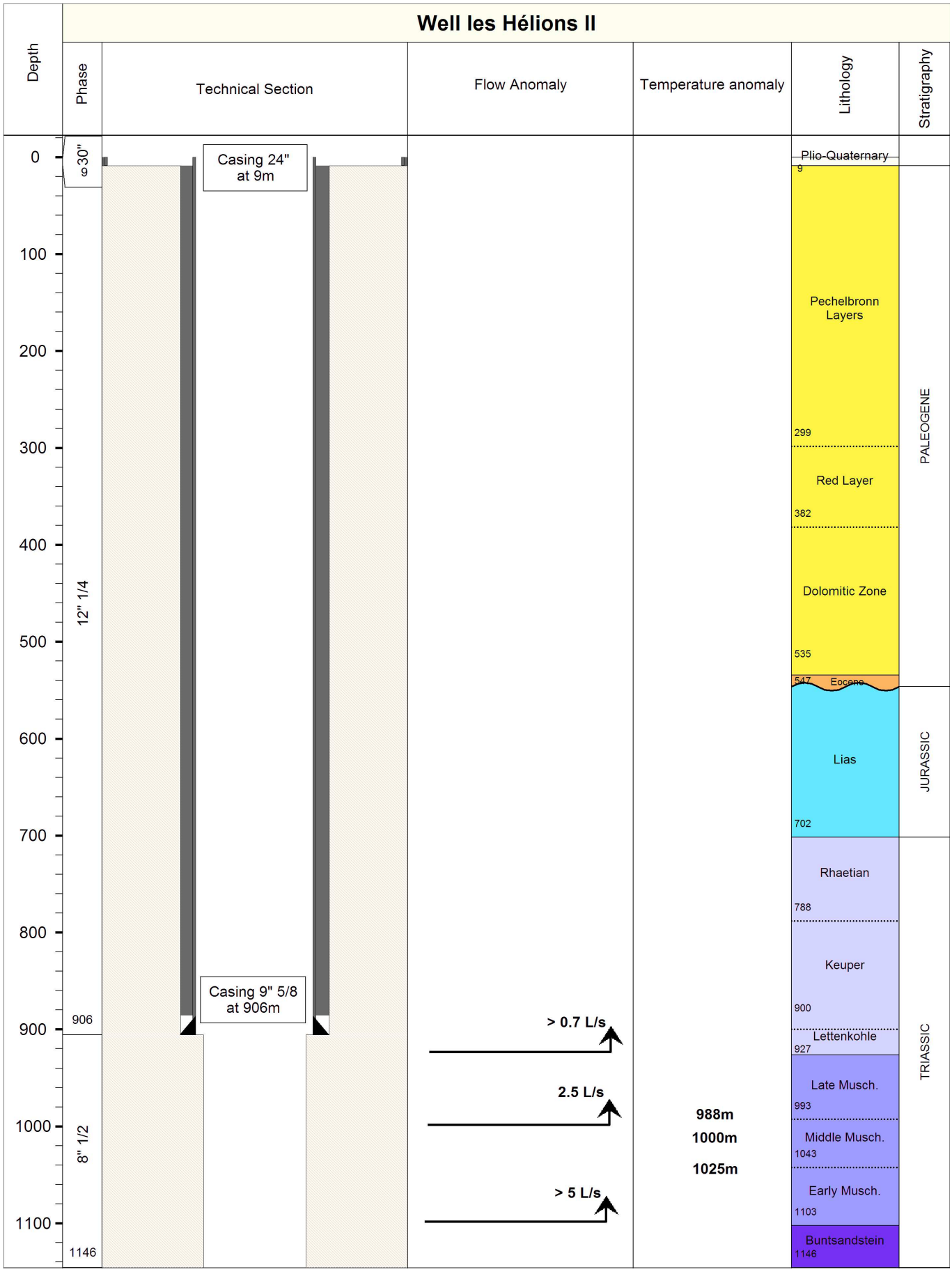

SOURCE THERMALE DES HELIONS

Données du puits les Hélions III

Date de forage :	17/08/1993 - 20/10/1993	
Coordonnées géographiques :	7° 49' 14" E 48° 56' 59" N	
Cible :	Aquifère des formations triasiques Forage situé au NO des premiers forages, dans la commune de Lampertsloch	
Trajectoire :	Verticale	
Fond de puits :	1295 m de profondeur - Buntsandstein	
Complétion :	Section 6” à partir de 880 m de profondeur avec Liner perforé 4”1/2	
Développement :	1993	Nettoyage du forage à l’eau javellisée puis pompage par « air-lift » Acidification des formations calcaires puis pompage par « air-lift »
Profil thermique :	-	
Température en fond de puits :	>70°C	
Gradients de température :	6 K/km	
Toit de la convection :	900 m (Lettenkohle)	
Débit :	>7 L/s	
Indice de productivité :	-	
Zones productrices :	Niveau producteur de 919-936 m (Muschelkalk) avec un débit de 2 L/s (1/3 du débit total) Niveaux producteurs de 1047 à 1274 m (Buntsandstein) produisant 4 L/s au total Zone productrice totale de 172 m d’épaisseur Anomalies de température positives à 931 m, à 1070 m et 1200 m de profondeur	
Fracturation naturelle :	Imageries de paroi non disponibles	
Orientation S_{Hmax} :	Champ de contrainte régional N145°E	

Coupe géologique et technique du puits les Hélions III

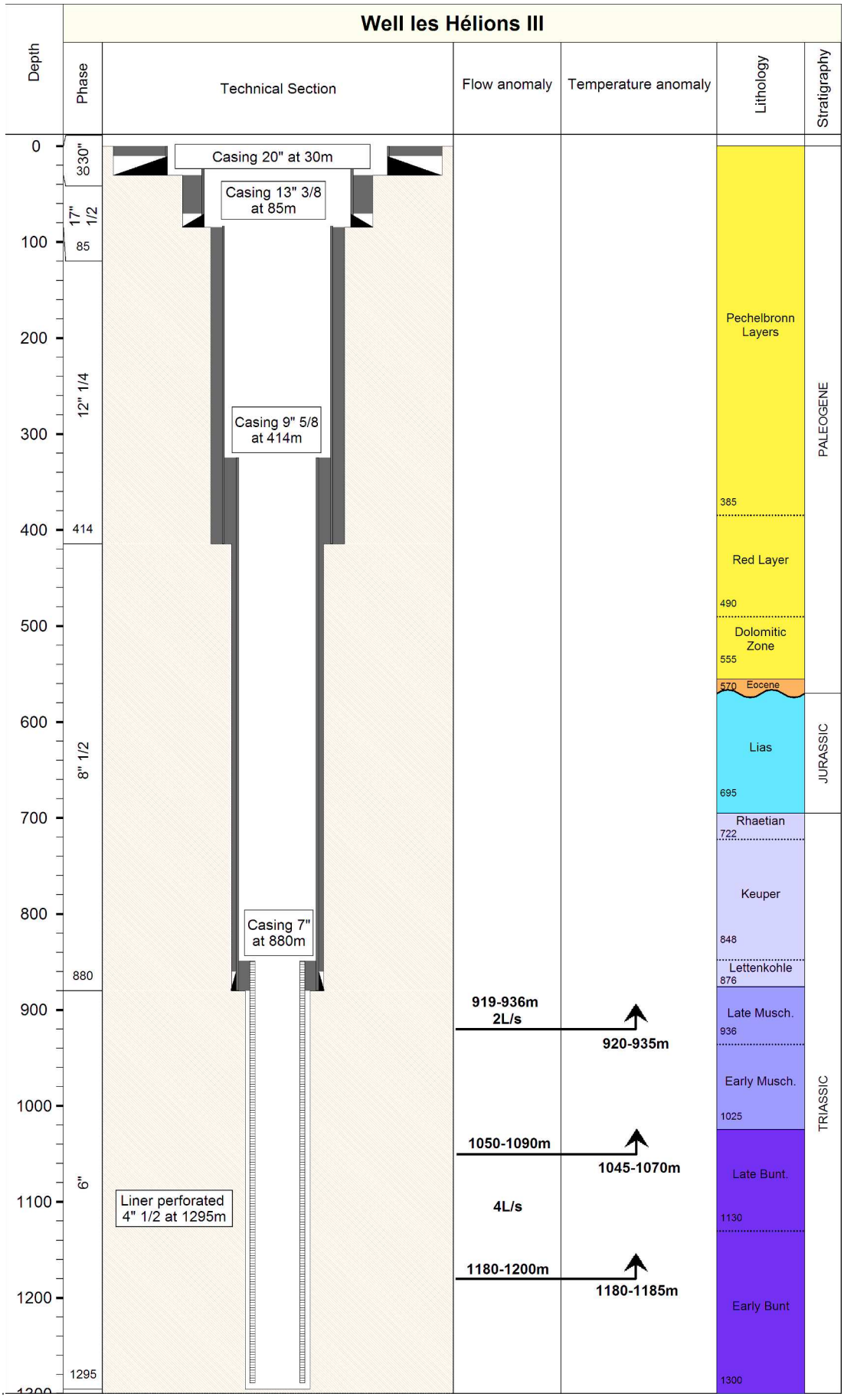

SOURCE THERMALE DES HELIONS

Profil thermique dans les puits les Hélions II et III

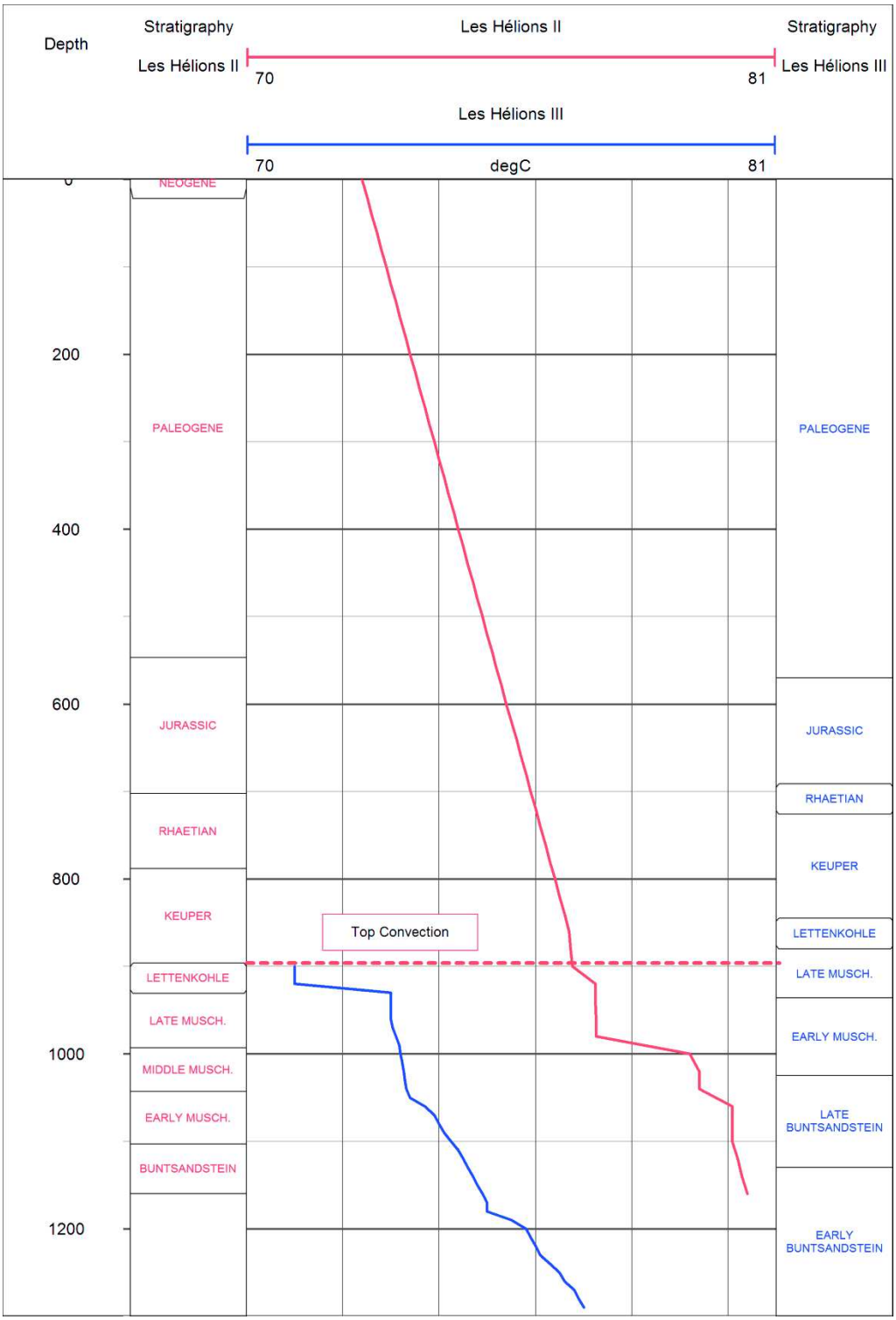

Les profils thermiques sont une approximation des données réelles acquises à l'équilibre thermique et dans le casing des puits géothermiques les Hélions II (en octobre 1988) et III.

SOURCE THERMALE DES HELIONS	
Références	Anonyme, 1958. *Fiche de description technique et géologique du forage 1266*, Document SAEM Pechelbronn Sartory, A. and Sartory, M.R., 1924. *Analyse de l'eau thermale de Pechelbronn*, Faculté de Pharmacie de Strasbourg SGAL, 1971. *Forage d'eau thermominérale 1266bis,* Rapport SGAL 71 SGN 244 SGA BRGM, 1993. *Recherche de nouvelles ressources en eaux thermales à Merkwiller-Pechelbronn (67). Compte rendu des travaux de réalisation du forage HELION III*, Rapport BRGM N 0549 STR 4S 93

GEOTHERMIEKRAFTWERKE BRUCHSAL

Données générales	*Compagnie :*	EnBW AG		
	Position géographique :	*Pays* Allemagne		
		Région Baden-Württemberg		
		Ville Bruchsal		
Données d'exploration	*Campagne d'exploration :*	Ré-interprétation de données sismiques et exploration géologique		1979
	Exploitation pétrolière :	Champ de Forst	Huile dans le Tertaire	
	Contexte géologique :	Le site est situé à moins de 5 km de la faille bordière Est, dans le bassin de Kraichgau, un système complexe de failles normales en échelon		
	Cible :	Formations gréseuses du Buntsandstein et du Permien		
	Concept :	Matriciel dans des compartiments faillés		
	Modèle 3D :	Oui		
Données de production	*Production :*	Electricité	*Nombre de puits :*	2
	Puissance installée :	550 kWe	*Débit de production :*	25 L/s
	Système :	Kalina	*Température de pompage :*	123°C
	Statut actuel :	Exploitation	*Température d'injection :*	60°C
Données de sous-sol	*Réservoir :*	Buntsandstein - Permien		
	Profondeur du réservoir (top) :	Variable suivant les compartiments faillés		
Fluide géothermal	*Salinité :*	130 g/L		
	Ions majeurs :	Cl Na Ca		
	Gaz :	CO_2 90% - CH_4 1% - He 0.1%		

Historique du projet

1983-1985	Projet initié par l'Union Européenne, du gouvernement fédéral du Land du Baden-Württemberg et de la société Energie- und Wasserversorgung Bruchsal GmbH avec les forages de deux puits géothermiques
1990	Utilisation de l'énergie géothermale pour le chauffage non rentable et abandon du projet
2001	Reprise du projet dans le cadre du German Renewable Energy Act
2002-2005	Rénovation de la centrale par la société Geothermie-Gesellschaft Bruchsal GmBH (consortium Stadtwerke Bruchsal GmbH et EnBW Kommunake Beteiligungen GmBH)
2012	EnBW AG devient majoritaire et en charge de la gestion opérationnelle

GEOTHERMIEKRAFTWERKE BRUCHSAL

Carte des failles à la surface du site

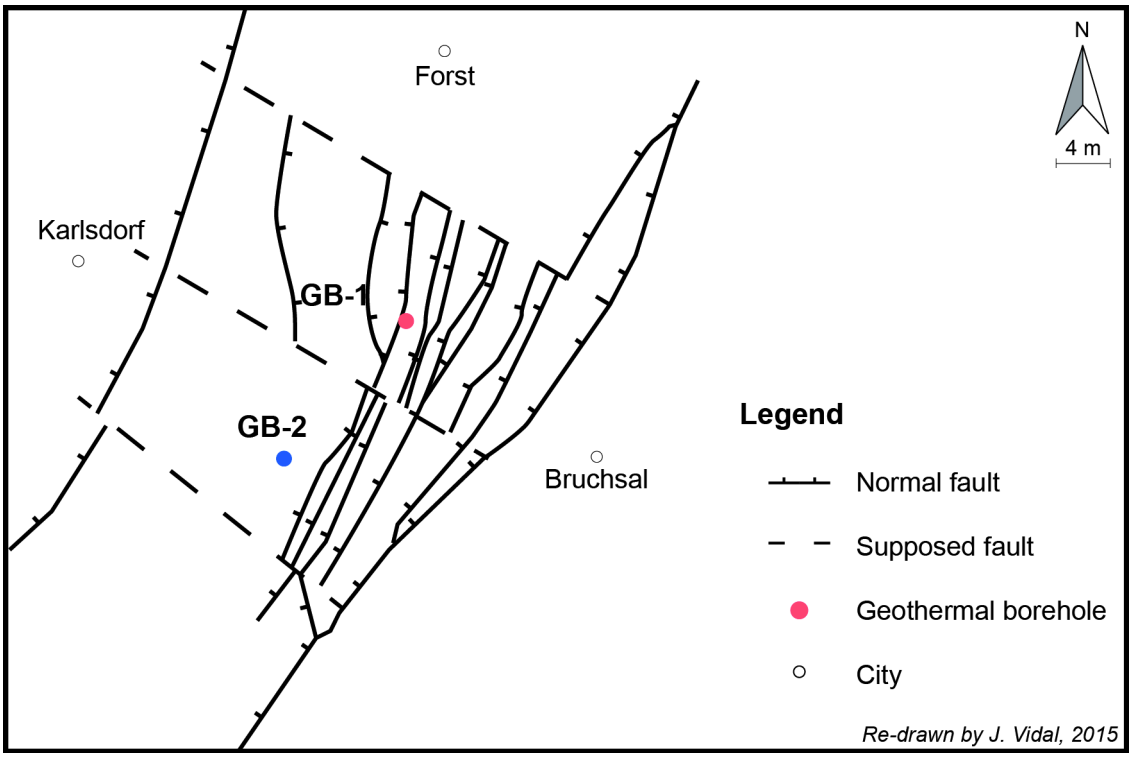

Coupe géologique du site

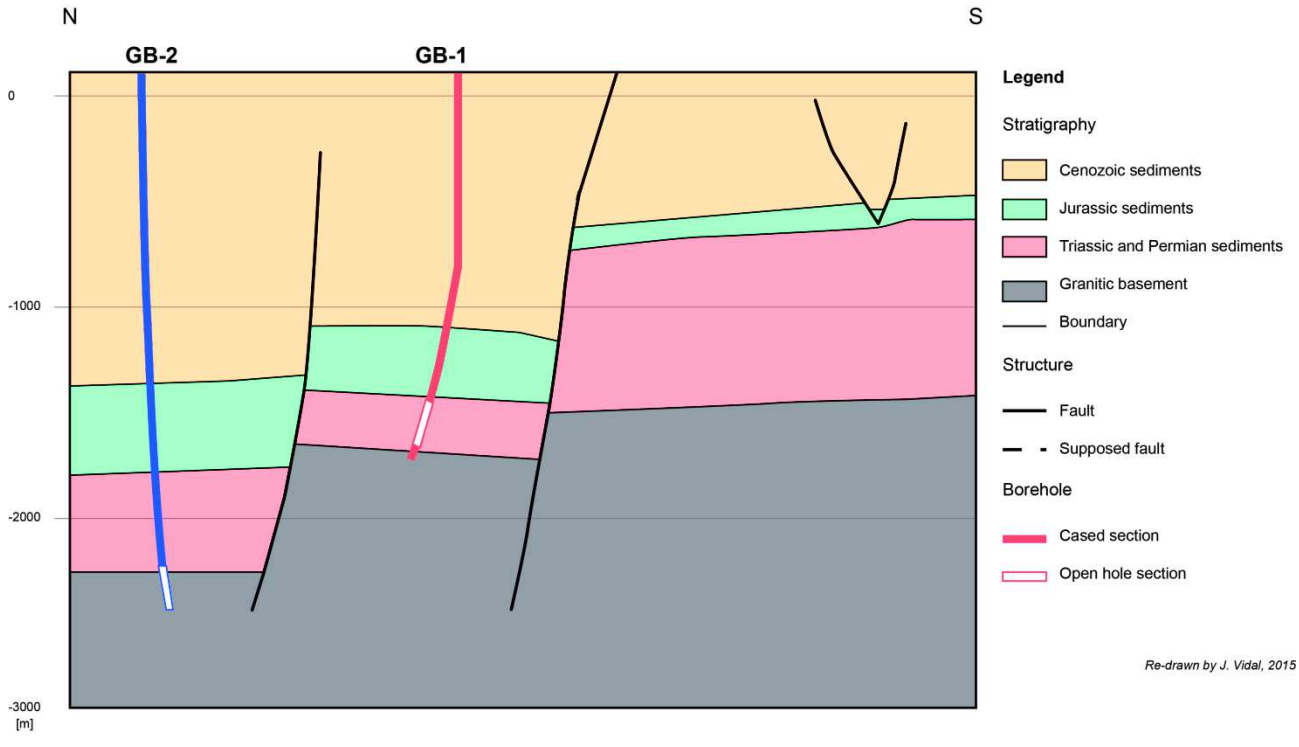

GEOTHERMIEKRAFTWERKE BRUCHSAL

Données du puits de production GB-1

Date de forage :	09/08/1983 - 18/11/1983	
Coordonnées géographiques :	08°35'00"E 49°10'00"N	
Cible :	Centre d'un compartiment du bassin de Kraichgau	
Trajectoire :	Quasi-verticale déviée à la fin vers l'Est	
Fond de puits :	1932 m de profondeur - Permien	
Complétion :	Section 8"1/2 à partir de 1573 m de profondeur avec Liner perforé 7" jusqu'à 1874 m et fond du puits cimenté	
Développement :	1983	Test d'injection à un débit de 11 L/s à 22 L/s et une température en surface de 112°C. La forte minéralisation et salinité du fluide géothermal rendent le puits de réinjection nécessaire.
Profil thermique :	Acquis de 1986 à 1987 dans des conditions d'équilibre thermique	
Température en fond de puits :	120°C	
Gradients de température :	57 K/km dans la partie en conduction Quasi-nul dans la partie en convection	
Toit de la convection :	1700 m de profondeur	
Indice de productivité :	-	
Zones productrices :	Zone de convection sous 1700 m (Buntsandstein) mais aucune d'anomalies de température discrète	
Fracturation naturelle :	Imageries de paroi non disponibles	
Orientation S_{Hmax} :	N141°E dans la partie en trou ouvert	

Coupe géologique et technique du puits de production GB-1

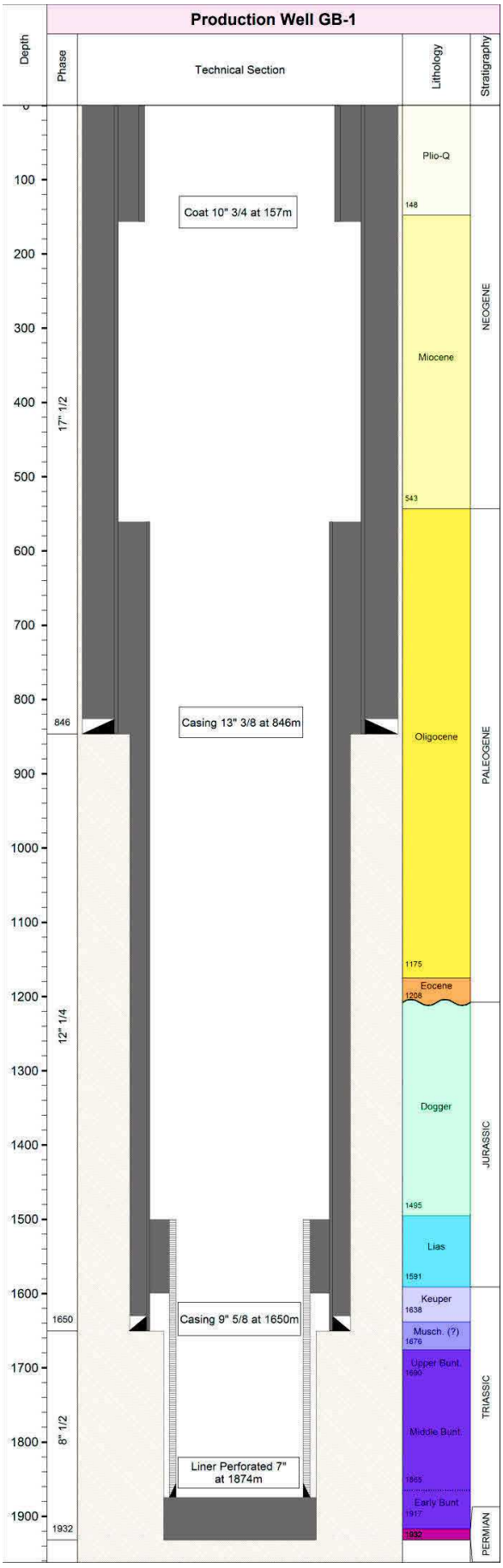

GEOTHERMIEKRAFTWERKE BRUCHSAL

Données du puits d'injection GB-2

Date de forage :	15/12/1984 - 26/08/1985	
Coordonnées géographiques :	08°37'00"E 49°11'00"N	
Cible :	Compartiment affaissé à l'Ouest de GB-1 Puits séparés par une distance d'environ 1.5 km et une faille normale à fort plongement Ouest et avec 500m de rejet	
Trajectoire :	Quasi-verticale déviée à la fin vers l'Ouest	
Fond de puits :	2542 m de profondeur - Permien	
Complétion :	Section 8"1/2 à partir de 2350 m de profondeur avec Liner perforé 5"	
Développement :	1987	4 tests d'injection à un débit de 15 L/s et une température en surface de 115°C durant 24h, 72h, 24h et 24h. Injection simultanée de HCl pour éviter les problèmes de scaling. Surpression de 0.5 bar dans le puits GB1 avec une réinjection de 12-17 L/s à 80°C.
	2002	Injection à 19 L/s à 110°C pour un volume produit de 90000 m^3
	2005	Injection à 28.5 L/s à 120°C durant 7 semaines
Profil thermique :	Acquis de 1986 à 1987 dans des conditions d'équilibre thermique	
Température en fond de puits :	130°C	
Gradients de température :	52 K/km dans la partie en conduction Quasi-nul dans la partie en convection	
Toit de la convection :	2200 m de profondeur	
Indice de productivité :	0.7 L/s/bar	
Zones productrices :	Zone de convection sous 2200 m (Buntsandstein) et une anomalie de température discrète entre 1250 et 1300 M MD	
Fracturation naturelle :	Imageries de paroi non disponibles	
Orientation S_{Hmax} :	N°132E dans la partie en trou ouvert	

Coupe géologique et technique du puits d'injection GB-2

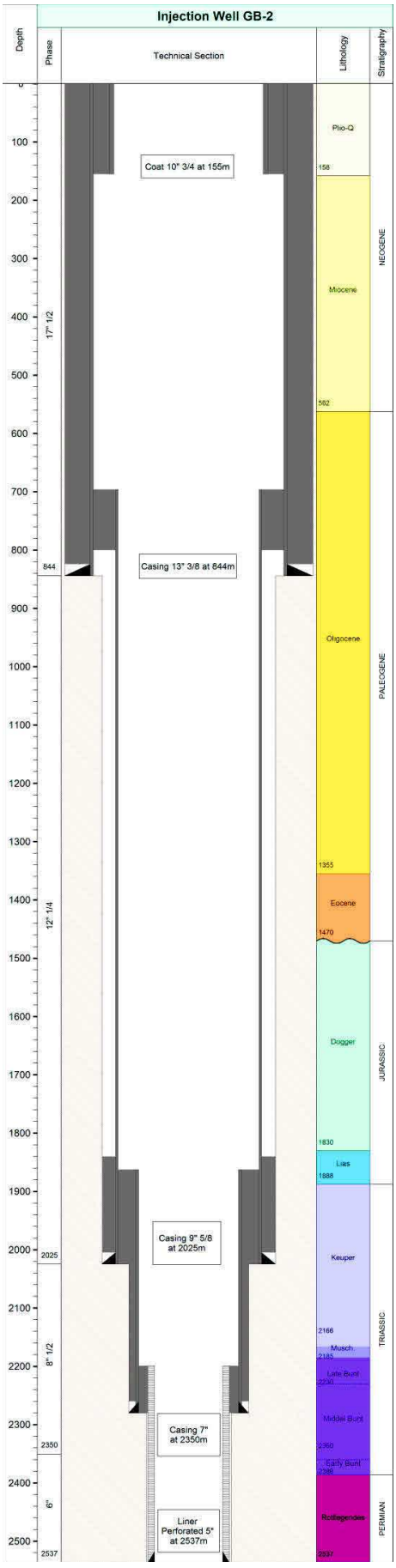

GEOTHERMIEKRAFTWERKE BRUCHSAL

Profils thermiques dans les puits

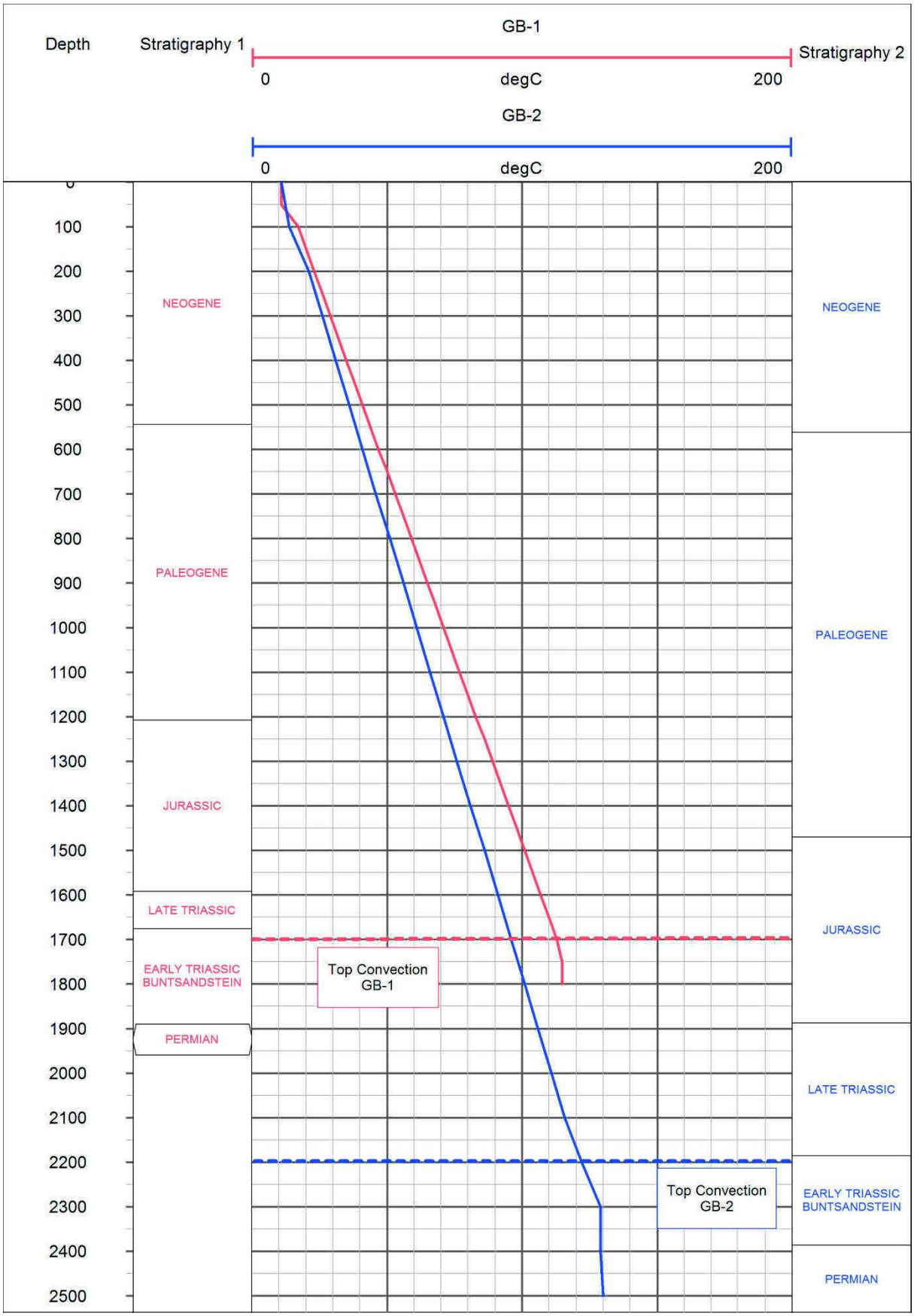

Les profils thermiques sont une approximation par régression linéaire des données réelles acquises à l'équilibre thermique et dans le casing des puits géothermiques GB-1 et GB-2 de Bruchsal en 1986 et 1987.

GEOTHERMIEKRAFTWERKE BRUCHSAL

Références

Kölbel, T., 2010. Geothermal power plant Bruchsal: construction and initial operating experiences*, Proceedings of Second European Geothermal Review*, Mainz, Germany

Herzberger, P., Münch, W., Kölbel, T., Bruchmann, U., Schalgermann, P., Hötzl, H., Wolf, L., Rettenmaier, D., Steger, H., Zorn, R., Seibt, P., Möllmann, G.-U., Sauter, M., Ghergut, J. & Ptak, T., 2010. The Geothermal Power Plant Bruchsal, *Proceedings to World Geothermal Congress,* Bali, Indonesia

Eggeling, L. & Kölbel, T., 2012. Power generation from geothermal energy in Bruchsal, *Proceedings of 8th International Geothermal Congress*, Freiburg, Germany

Eggeling, L., 2014. Two years operation of the geothermal power plant in Burchsal - experiences, development and research, *Proceedings of Deep Geo Days*, Paris, France

Meixner, J., Schill, E., Grimmer, J.C., Gaucher, E., Kohl, T. and Klingler, P. (2015). Structural control of geothermal reservoirs in extensional tectonic settings: an example from the Upper Rhine Graben, *Journal of Structural Geology*, doi: 10.1016/j.jsg.2015.11.003

PROJET DE DEMONSTRATION COMMUNAUTAIRE DE FORAGE GEOTHERMIQUE A STRASBOURG

Données générales	*Compagnie :*	SOCALMIG (Société Alsacienne Minière de Géothermie)			
	Position géographique :	*Pays*	France		
		Région	Alsace, Bas-Rhin		
		Ville	Strasbourg, Cronenbourg		
Données d'exploration	*Campagne d'exploration :*	Campagne vibrosismique avec 4 profils (32 km au total) réalisés par la SNEA (Société Nationale Elf Aquitaine) en prolongement des profils pétroliers déjà existants			1975
	Exploitation pétrolière :	Champ d'Eschau	Huile dans le Tertiaire (Grès de Niederroedern) et dans le Dogger (Calcaires de la Grande Oolithe)		
	Contexte géologique :	Le site est situé dans le bassin de Strasbourg, fortement compartimenté.			
	Cible :	Formation gréseuse du Buntsandstein			
	Concept :	Matriciel dans des compartiments faillés			
	Modèle 3D :	Non			
Données de production	*Production :*	Chaleur		*Nombre de puits :*	1
	Puissance installée planifiée :	-		*Nombre de puits planifiés pour la production :*	2
	Système planifié :	-		*Débit de production planifié :*	42 L/s
	Statut actuel :	Abandon		*Température de pompage planifiée :*	140°C
				Température d'injection planifiée :	-
Données de sous-sol	*Réservoir :*	Buntsandstein			
	Profondeur du réservoir (top) :	2700 m			
Fluide géothermal	*Salinité :*	104 g/L			
	Ions majeurs :	Cl Na K Ca			
	Gaz :	-			

Historique du projet

1974	Site de Cronenbourg retenu pour un projet de chauffage urbain dans l'agglomération de Strasbourg
1975	Campagne vibrosismique par la SNEA pour déterminer l'emplacement du forage
1980	Forage du puits d'exploration GCR-1 par la SOCALMIG (association de la Communauté locale, majoritaire et les sociétés pétrolières) dans le but d'évaluer le potentiel géothermique des grès du Buntsandstein ainsi que des calcaires de la Grande Oolithe et du Muschelkalk et essais de production sur les différents niveaux producteurs
	Abandon du forage pour manque de productivité

PROJET DE DEMONSTRATION COMMUNAUTAIRE DE FORAGE GEOTHERMIQUE A STRASBOURG

Carte des failles à la surface au toit du Buntsandstein

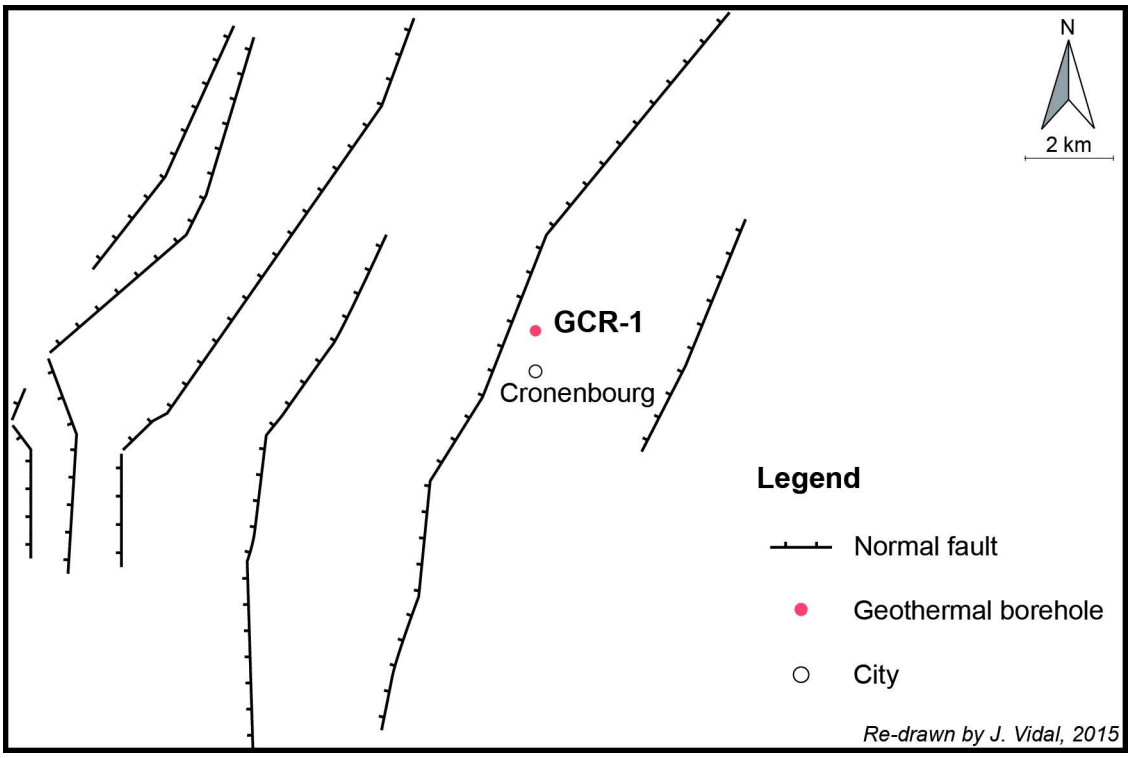

Coupe géologique du site

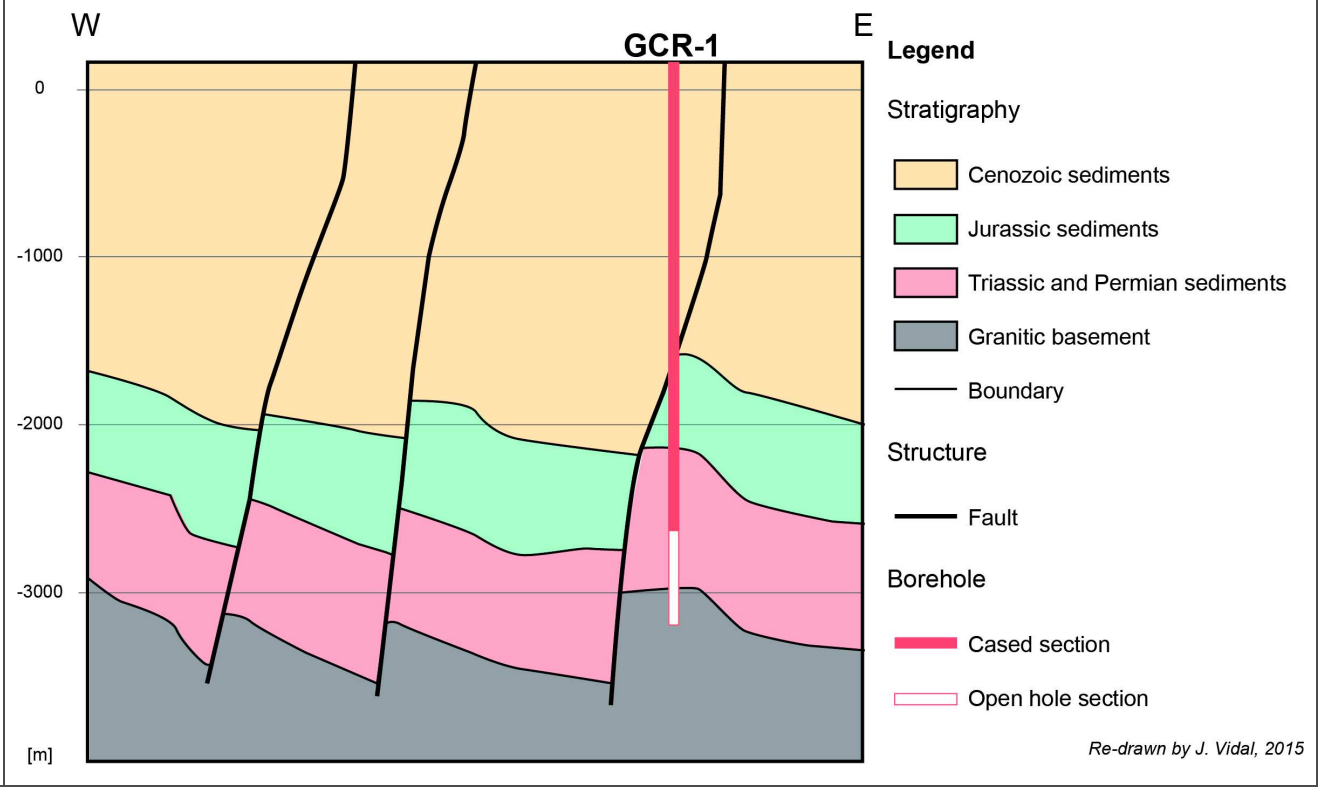

PROJET DE DEMONSTRATION COMMUNAUTAIRE DE FORAGE GEOTHERMIQUE A STRASBOURG

Données du puits de production GCR-1

Date de forage :	04/05/1980 - 07/08/1980	
Coordonnées géographiques :	7° 43' 28'' E 48° 36' 04'' N	
Cible :	Tête de puits située sur le compartiment Ouest affaissé pour atteindre la série du Buntsandstein dans le compartiment surélevé en recoupant dans la série de la Grande Oolithe la faille normale de direction SO-NE, avec un plongement Ouest de 45° et plus de 400 m de rejet	
Trajectoire :	Verticale	
Fond de puits :	3320 m de profondeur - Permien	
Complétion :	Section 6" à partir de 2664 m de profondeur avec Liner perforé 4"1/2	
Développement :	07/1980	Test de production qui montre une faible productivité provenant d'une zone fissurée ayant déjà montré des pertes lors du forage et une température de fond >130°C
	08/1980	Test de production par air lift qui montre une productivité un peu améliorée
		Acidification dans l'objectif d'un « lessivage des zones fissurées »
	10/1980	Test de production longue durée par air-lift de façon intermittente durant 5 jours
	11/1980	Test de production longue durée par air-lift puis par débit artésien avec une productivité légèrement améliorée après l'acidification mais un débit et la perméabilité qui restent très faibles
Profil thermique :	Acquis avant et après l'acidification en 1980 puis en 1981 à l'équilibre thermique du puits	
Température en fond de puits :	144°C à 2670 m, extrapolée à 148°C en fond de puits	
Gradient de température :	50 K/km dans la partie en conduction	
Toit de la convection :	Effet de la convection non visible sur le profil allant jusqu'à 2670 m	
Débit :	7 L/s	
Indice de productivité :	0.12 L/s/bar	
Zones productrices :	Zones de pertes à 1972-1987m (0,5-4 m^3/h au total 18 m^3/h), pertes totales à 2844 m puis partielles jusqu'à la fin du sondage (8-16 m^3/h puis 1 m^3/h) Anomalies de température à 2850-2857 m après acidification, à 2875-2880 m avant acidification, à 2933 m après acidification Mesures de débit (diagraphie) à l'interprétation très douteuse : 20% du débit acquis à 2980-2905 m, 40% à 2880-2875 m et 40% à 2780-2775 m	
Fracturation naturelle :	Imageries de paroi non disponibles	
Orientation S_{Hmax} :	Champ de contrainte régional N145°E	
Résultats majeurs :	Les carottes prélevées ont mis en évidence des grès homogènes poreux mais peu perméables et des grès affectés par des fractures et/ou fissures isolées qui semblent être les niveaux les plus producteurs Mise en évidence du Permien jusqu'alors inconnu dans cette partie du bassin	

Coupe géologique et technique du puits d'exploration GCR-1

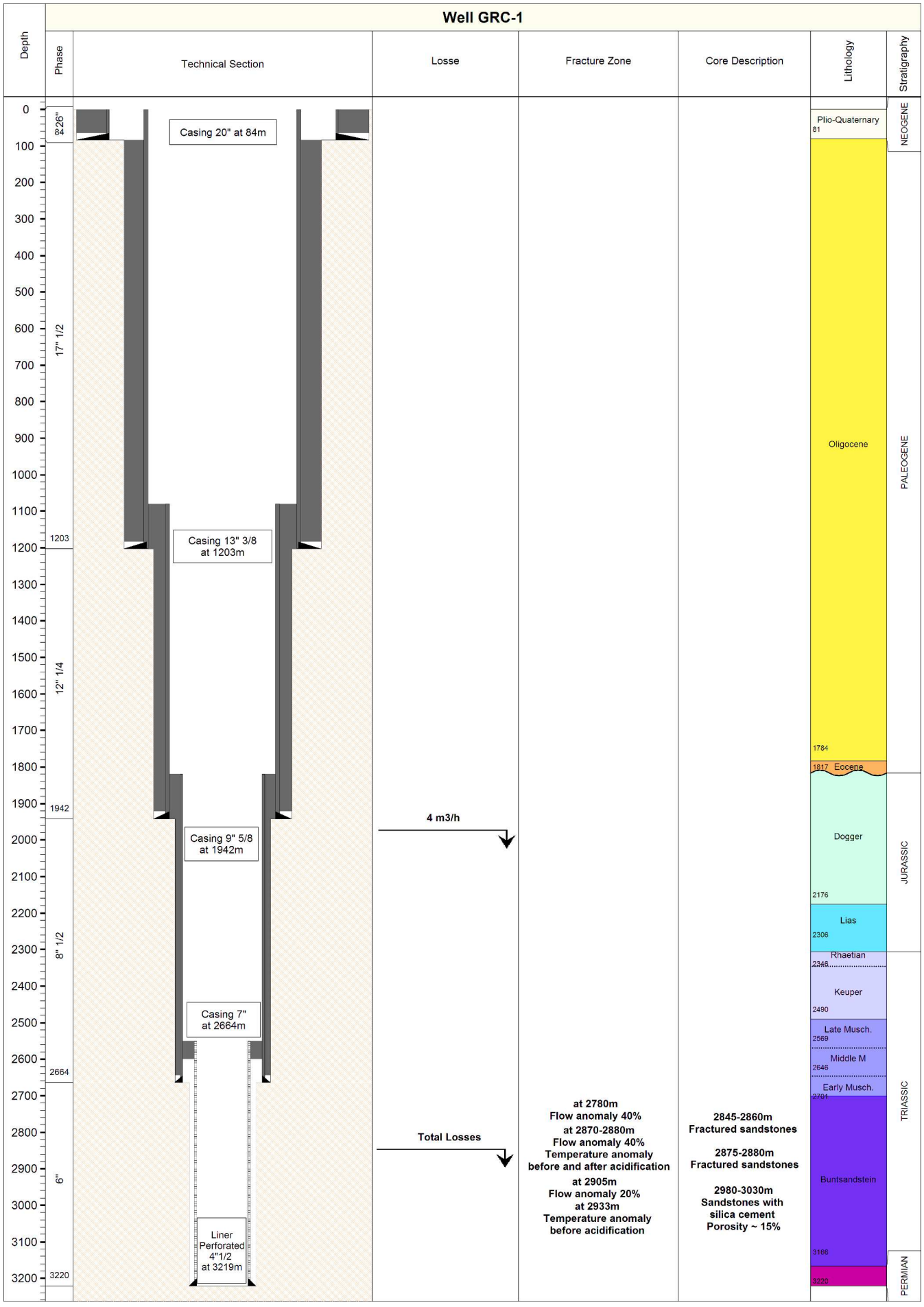

PROJET DE DEMONSTRATION COMMUNAUTAIRE DE FORAGE GEOTHERMIQUE A STRASBOURG

Profil thermique dans le puits

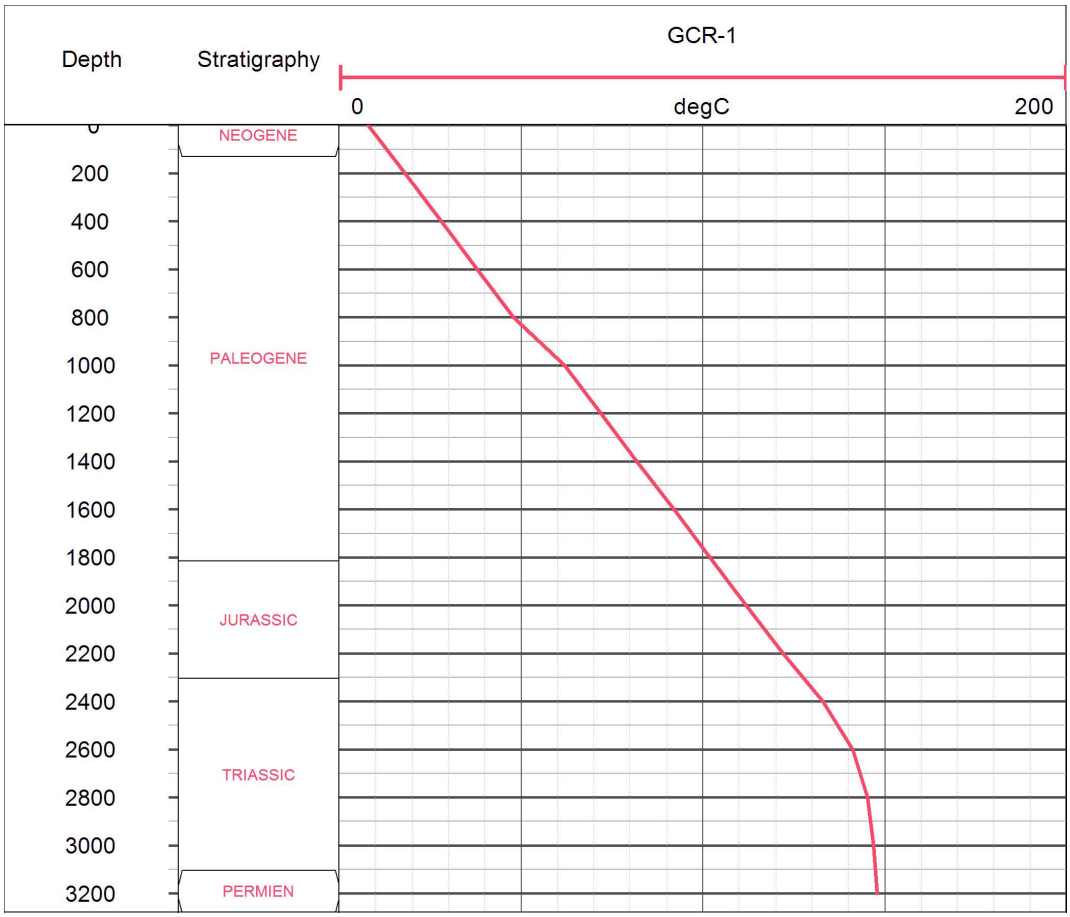

Le profil thermique est une approximation par régression linéaire des données réelles acquises à l'équilibre thermique et dans le casing du puits géothermique GCR-1 jusqu'à 2670 m de profondeur en décembre 1981 puis extrapolé jusqu'au fond du puits.

PROJET DE DEMONSTRATION COMMUNAUTAIRE DE FORAGE GEOTHERMIQUE A STRASBOURG	
Références	SOCALMIG, 1980. *Proceedings of second international seminar on the results of Geothermal Energuy Research*, document publié par D. Reidel Publishing Compagny SOCALMIG, 1980. *Rapport de fin de sondage, Géothermie Cronenbourg 1 (GCR-1),* document établi par la SNEA SNEA, 1983. *Projet de démonstration communautaire de forage géothermique à Strasbourg*. Rapport final de forage EUR 8720 FR, document publié par la Commission des Communautés Européennes Housse, B.-A., 1984. Reconnaissance du potential géothermique du Buntsandstein à Strasbourg-Cronenbourg, *Géothermie Actualités n°1*

PROJET PILOTE DE GEOTHERMIE DE SOULTZ-SOUS-FORETS

Données générales	*Compagnie :*	GEIE, Exploitation Minière de la Chaleur (création en 1997)			
	Position géographique :	*Pays*	France		
		Région	Alsace, Bas Rhin		
		Ville	Soultz-sous-Forêts		
Données d'exploration	*Campagne d'exploration :*	Ré-interprétation de données sismiques pétrolières et de données de puits des 5000 puits pétroliers alentours		Début des années 80	
		Forage d'un puits d'exploration		1988	
		Approfondissement d'anciens puits pétroliers		1990 – 1991	
		Acquisition de données de VSP		1995	
	Exploitation pétrolière :	Champ de Merkwiller-Pechelbronn	Huile dans le Tertiaire (Couches de Pechelbronn) et dans le Trias inférieur (Buntsandstein)		
	Contexte géologique :	Le site est situé à moins de 5 km à l'Ouest de la faille bordière Est, au centre de la structure du horst de Soultz.			
	Cible :	Socle granitique chaud à stimuler par fracturation hydraulique			
	Concept :	HDR, HFR, HWR puis EGS			
	Modèle 3D :	Oui			
Données de production	*Production :*	Electricité	*Nombre de puits :*	5	
	Puissance installée :	1.7 MWe	*Débit de production :*	20 L/s	
	Système :	ORC	*Température de pompage :*	>150°C	
	Statut actuel :	Reconstruction de la centrale en surface	*Température d'injection :*	50-60°C	
Données de sous-sol	*Réservoir :*	Granite			
	Profondeur du réservoir (top) :	1400 m			
Fluide géothermal	*Salinité :*	100 g/L			
	Ions majeurs :	Cl Na Ca			
	Gaz :	CO_2 84% - CH_4 2.5% - He 0.7%			

Historique du projet

1984	Première phase d'exploration avec ré-interprétation d'anciennes données sismiques pétrolières et choix du site de Soultz-sous-Forêts pour une forte anomalie thermique connue grâce aux nombreux forages pétroliers
1987 - 1988	Forage du premier puits d'exploration GPK-1 jusqu'à 2000 m de profondeur avec acquisition de plusieurs mesures de diagraphies et stimulation hydraulique
1990 - 1991	Approfondissement d'anciens puits pétroliers dont des puits pour la surveillance sismique et le puits d'exploration EPS-1 carotté sur 1.3 km
1992	Développement d'un réservoir granitique supérieur R2 entre 1.4 km et 2.2 km avec EPS-1 et GPK-1 puis approfondissement de GPK-1 jusqu'à 3.59 km de profondeur
1994-1995	Forage du second puits du doublet géothermique GPK-2 jusqu'à 3.9 km de profondeur avec acquisition de plusieurs mesures de diagraphies et stimulation hydraulique

1995-1999	Développement d'un réservoir granitique intermédiaire R3 entre 3 et 3.9 km de profondeur avec de nombreux tests de production et d'injection pour déterminer la perméabilité des puits du doublet géothermique, une stimulation hydraulique dans GPK-1 en 1994 et deux stimulations hydrauliques dans GPK-2 en 1995 et 1996. Trois tests de circulation ont été réalisés avec injection de tracer : - Trois circulations avec GPK-1 = P et GPK-2 = I, 15 L/s pendant 15 jours, 22 L/s pendant 10 jours et 15 L/s pendant 3 jours ; - Deux circulations avec GPK-1 = I et GPK-2 = P, 12 L/s pendant 3.4 jours et 24 L/s pendant 1 jours ; - Une circulation longue avec GPK-1 = I et GPK-2 = P, 24 L/s pendant 4 mois durant lesquels seuls 30% du tracer a été récupéré ce qui indique que le système est ouvert et connecté à un réservoir plus large
1999	Approfondissement de GPK-2 jusqu'à 5.08 km de profondeur afin de développer un réservoir granitique profond au-delà de 4.5 km de profondeur avec un triplet géothermique
2001	Début de la construction de la centrale
2002	Forage du troisième puits GPK-3 jusqu'à 5.1 km de profondeur stimulation chimique et hydraulique du puits GPK-2
2003-2004	Stimulation hydraulique et chimique du puits GPK-2 et test de circulation avec GPK-3 = P et GPK-2 = I, 15 à 20 L/s pendant 20 jours puis forage du quatrième puits GPK-4 jusqu'à 5.24 km de profondeur
2004-2006	Stimulation hydraulique et chimique de GPK-3 et GPK-4 durant lesquelles de nombreux séismes induits sont enregistrés ainsi que plusieurs tests d'injection et de production des puits du triplet puis un test de circulation avec GPK-2 et -4 = P et GPK-3 = I, 15 L/s de juillet à décembre 2005 avec injection de tracer. Développement d'un réservoir granitique profond R5 entre 4 km et 5.4 km
2008	Mise en service de la centrale

2008-2013

Well	Type of operation	Flow rate ($L\ s^{-1}$)	Temperature (°C)	Well-head Pressure (MPa)
Test 2008-1: 27th July to 17th August 2008				
GPK2		25	163	
GPK3		23	60	7.3
Test 2008-2: 03th to 16th December 2008				
GPK2		17	160	
GPK3	IP	27.5	68	8.6
GPK4	ESP	12	153	
Test 2009: March to October 2009 (240 days)				
GPK1	gravity	2	70	≤ 1
GPK2	LSP	20	156	2
GPK3	IP	10	73	2 - 6
GPK4	ESP	8	147	≤ 2
Test 2009/2010: December 2009 to November 2010 (323 days)				
GPK1	gravity	2	50	0.3
GPK2	LSP	18	164	1.8
GPK3	IP	15	66	4.7
GPK4	not in operation			1.3
Test 2010/2011: December 2010 to April 2011 (90 days)				
GPK1	gravity	11	75	0.5
GPK2	LSP	22	159.3	1.9
GPK3	IP not in operation	9	75	1.8
GPK4	not in operation			
Test 2011-2: August to October 2011 (70 days)				
GPK1	gravity	12	75	0.4
GPK2	LSP	23	157.5	2
GPK3	IP not in operation	9	75	1.6
GPK4	not in operation			
Test 2012: 20-23rd April 2012 (3 days)				
GPK1	gravity	6	55	0.1
GPK2	LSP	21	156	2
GPK3	IP not in operation	15	55	0.8
GPK4	not in operation			
Test 2013: April to June 2013 (78 days)				
GPK1	not in operation			
GPK2	LSP	15	157.5	2
GPK3 / GPK4	IP not in operation	12	60	0.25

2014-2015 Evolution du projet pilote à vocation scientifique vers un projet industriel avec la re-construction des installations de surface

09/2016 Inauguration de la nouvelle centrale

Carte et coupe N-S de la trajectoire des puits

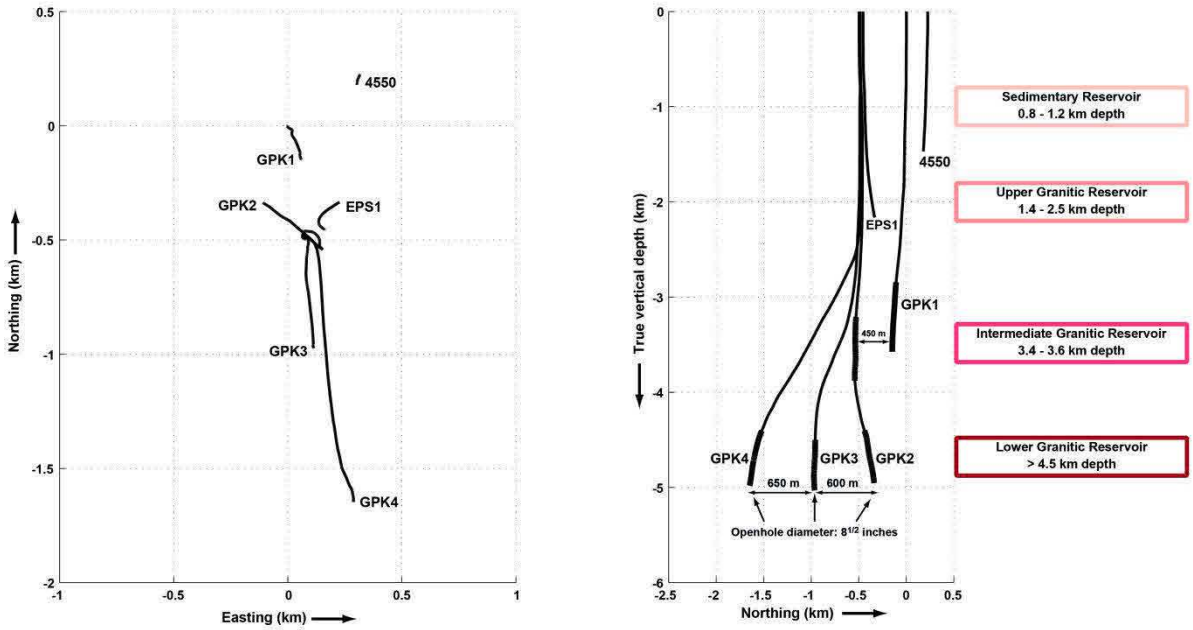

PROJET PILOTE DE GEOTHERMIE DE SOULTZ-SOUS-FORETS

Carte des failles à l'interface sédiments-socle

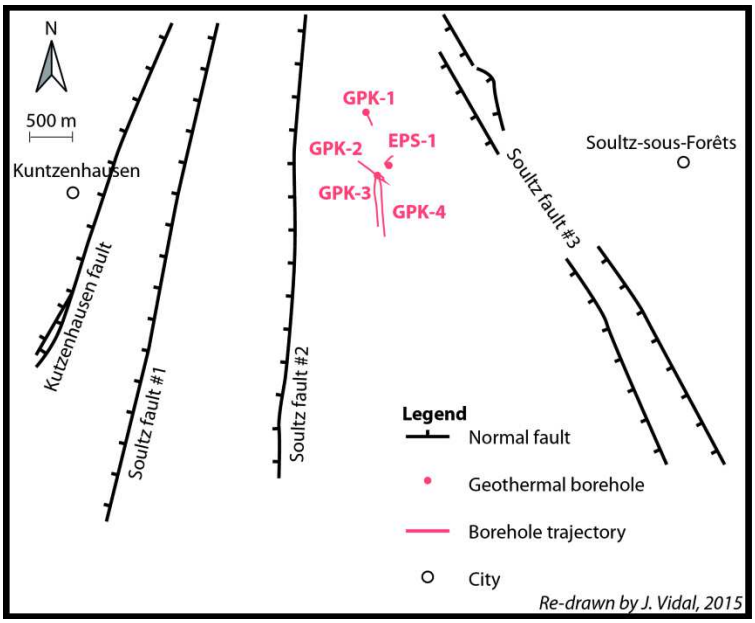

Carte des failles à 1400 m de profondeur. Dans le granite, l'interprétation des imageries de paroi et des données VSP montrent que les puits GPK-2 et GPK-3 interceptent la branche de la faille de Soultz #3 à 4500 m de profondeur (Sausse et al., 2010)

Coupe géologique du site

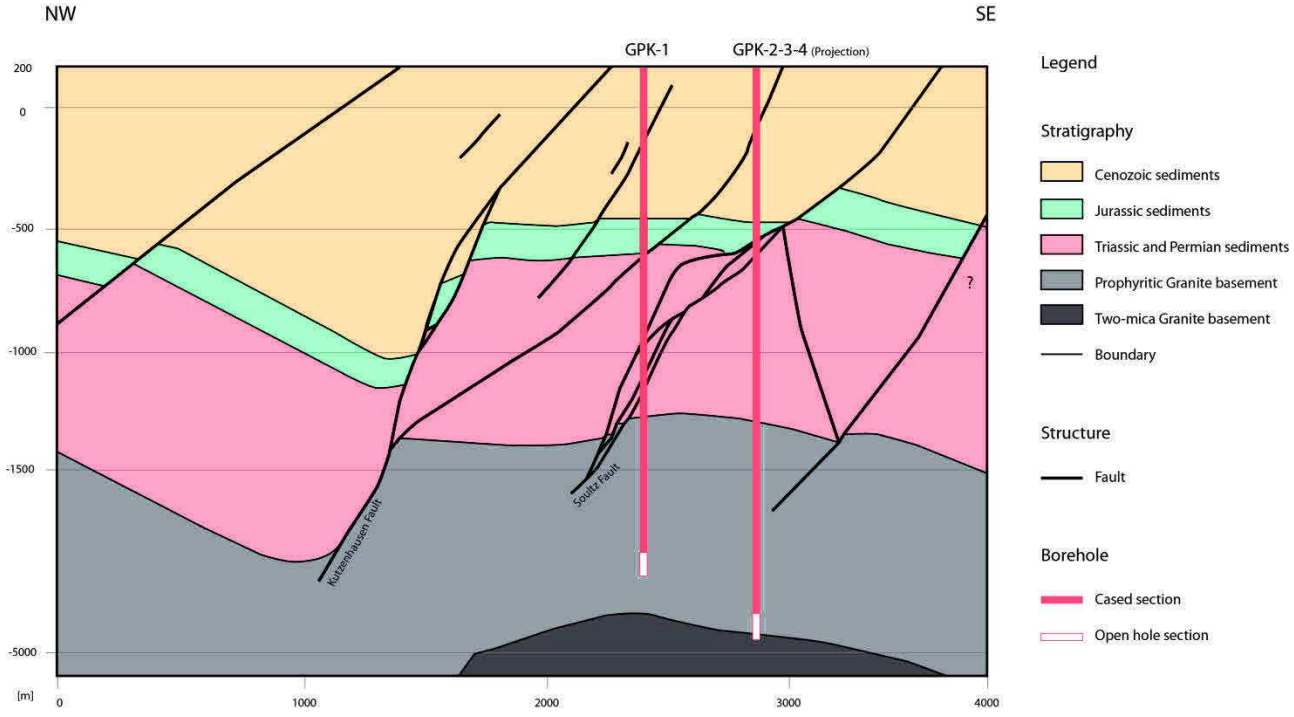

PROJET PILOTE DE GEOTHERMIE DE SOULTZ-SOUS-FORETS

Données du puits d'exploration EPS-1

Date de forage :	25/07/1990 - 14/02/1991
Coordonnées géographiques :	7°52'3"E 48°55'52"N
Cible :	Ancien puits pétrolier 4589 foré en mars 1950 jusqu'à 830 m approfondi jusqu'au toit du granite comme puits d'exploration et entièrement carotté de 930 à 2227 m de profondeur (78 mm de diamètre jusqu'à 2000 m puis 58 mm)
Trajectoire :	Déviée de 23°
Fond de puits :	2227 m de profondeur – Toit du granite
Complétion :	Section 3.78 " en trou ouvert à partir de 1994.5 m de profondeur
Développement :	-
Profil thermique :	Acquis en novembre 1991 à l'équilibre thermique
Température en fond de puits :	146°C
Gradient de température :	110 K/km dans la partie en conduction 35°K/km dans la partie au toit de la convection
Toit de la convection :	1000 m
Indice de productivité :	-
Zones productrices :	à 1198 m (direction de pendage 247°, pendage 74° et épaisseur 30 m), pertes à un débit de 34 m^3/h (Buntsandstein) à 2180 m (275°, 53° et 15 m), pertes totales (toit du granite – trou ouvert)
Fracturation naturelle :	Dans la série du Buntsandstein : - D'après le relevé sur carottes, une famille de direction N0° et pendage 75°W et une famille N165° et pendage 75°E - D'après les imageries de paroi, une famille de direction N170° et pendage 75°W et une famille N0° et pendage 70°E Dans le socle granitique : - D'après le relevé sur carottes, une famille de direction N40° et pendage 80°W et une famille N170° et pendage 70°E - D'après les imageries de paroi, une famille de direction N45° et pendage 80°W
Orientation S_{Hmax} :	N175°E

Coupe géologique et technique du puits d'exploration EPS-1

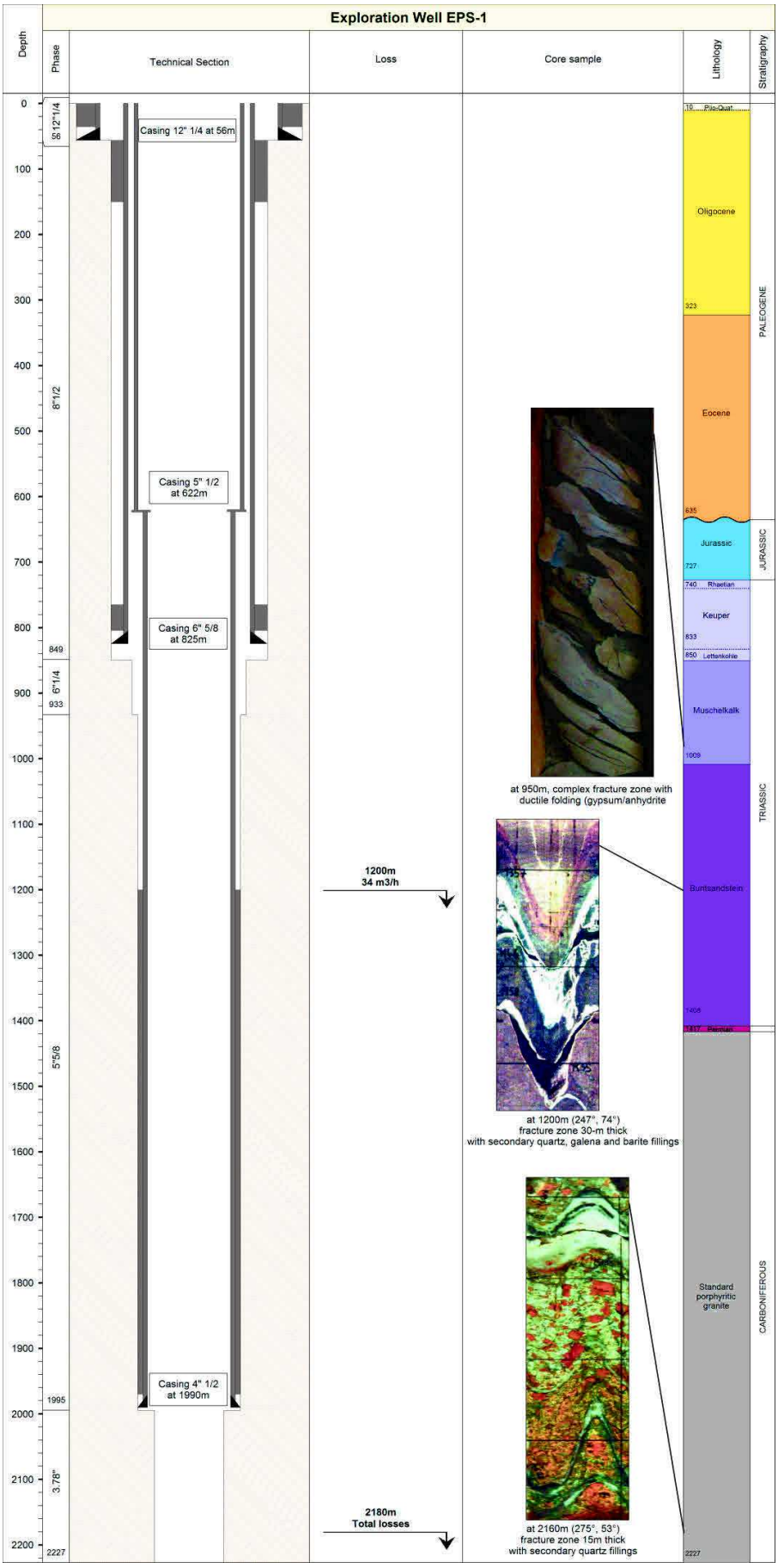

PROJET PILOTE DE GEOTHERMIE DE SOULTZ-SOUS-FORETS

Données du puits géothermique GPK-1

Date de forage :	29/07/1987 - 12/12/1987 06/10/1992 - 06/12/1992 : Approfondissement de 2000 à 3590 m de profondeur	
Coordonnées géographiques :	7°51'55''E 48°56'6''N	
Cible :	Socle granitique au centre du Horst situé entre la faille de Kutzenhausen et d'Hemmerswiller et qui recoupe la faille de Soultz	
Trajectoire :	Déviée de 6° à partir de 2650 m puis de 2° à la fin du puits	
Fond de puits :	3590 m de profondeur – Granite porphyrique	
Complétion :	Section 6"1/4 en trou ouvert à partir de 2850 m de profondeur	
Développement :	1988	8 tests basés sur la méthode Hydraulic Tests on Pre-existing Fracture (HTPF) réalisés entre 1458 et 2000 m de profondeur dans l'objectif de tester les conditions hydro-mécaniques du site Les injections à l'aide de packers conventionnels ont montré des problèmes techniques en raison de la température élevée (140°C) et de la forte salinité du fluide géothermal (100 g/L)
	1991	4 tests basés sur la méthode HydroFracs (HF) en utilisant des packers en aluminium
	1993-1994	Stimulation hydraulique de GPK-1 après l'approfondissement avec surveillance de la sismicité induite
Profil thermique :	Acquis en mai 1995 à l'équilibre thermique	
Température en fond de puits :	160°C	
Gradient de température :	100 K/km dans la partie en conduction 5°K/km dans la partie en convection	
Toit de la convection :	1000 m	
Indice d'injectivité :	0.09 L/s/bar dans le réservoir R2 0.07 L/s/bar avant stimulation dans le reservoir R3 puis 0.1 L/s/bar après stimulation	
Zones productrices :	à 1220 m (247°, 75°) pertes totales et anomalie négative de température post-forage (Buntsandstein) à 1820 m (27°, 75°), pertes totales avec des quartz secondaire et des illites en abondance dans les cuttings à 2815 m (230°, 70° et 8m), zone perméable après stimulation (toit du granite) à 3492 m (257°, 63° et 8m), zone perméable après stimulation (toit du granite – trou ouvert)	
Fracturation naturelle :	Dans le socle granitique : - Fracturation naturelle de direction N170° et pendage 70°E et 70°W de 1420 à 2000 m d'après les imageries FMS - Fracturation naturelle de direction N10° et pendage 75°E et 75°W de 2000 à 3600 m d'après les imageries FMI	
Orientation S_{Hmax} :	N169 +/- 11°E entre 1450-2000 m (Granite) N181 +/- 22°E entre 2000-3590 m (Granite)	

Coupe géologique et technique du puits géothermique GPK-1

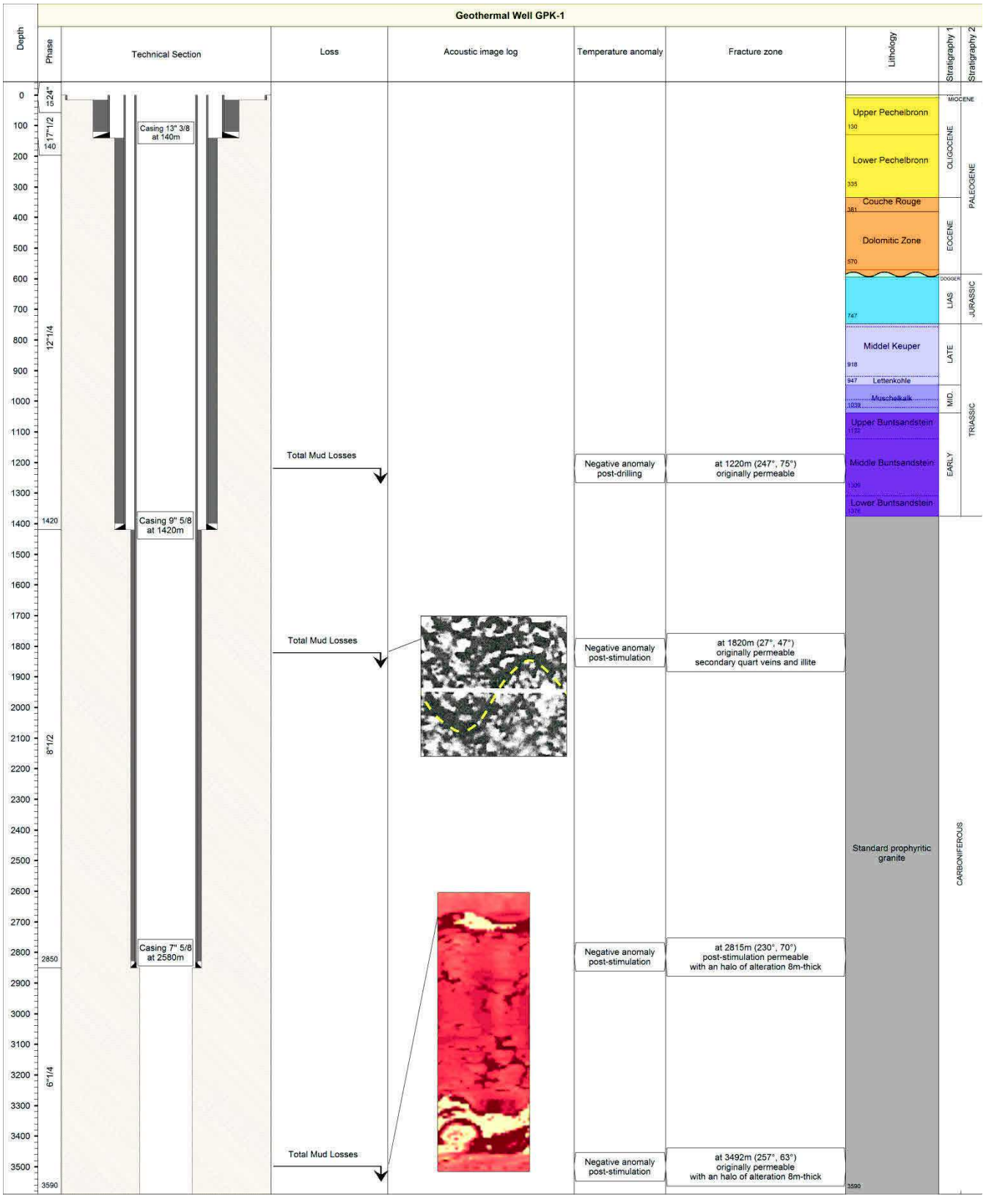

PROJET PILOTE DE GEOTHERMIE DE SOULTZ-SOUS-FORETS

Données du puits de production GPK-2

Date de forage :	03/11/1994 - 28/01/1995 02/1999 - 05/1999 : Approfondissement de 3887 à 5000 m de profondeur	
Coordonnées géographiques :	7°51'59"E 48°55'51"N	
Cible :	Socle granitique au centre du Horst situé entre la faille de Kutzenhausen et d'Hemmerswiller Le second puits du doublet est situé dans le nuage de sismicité des opérations de stimulation de GPK-1, au Sud du puits (zone également plus chaude) et séparé du premier puits par une distance d'environ 450 m à 3000 m de profondeur	
Trajectoire :	Déviée de 8° à partir de 3900 m, de 26° à partir de 4550 m puis de 16° à la fin du puits	
Fond de puits :	5093 m de profondeur – Granite à 2 micas	
Complétion :	Section 8"1/2 en trou ouvert à partir de 4440 m puis 6" à partir de 5057 m de profondeur	
Développement :	1995	Stimulation hydraulique jusqu'à 56 L/s
	1996	Stimulation hydraulique jusqu'à 78 L/s
	02/2003	Stimulation chimique avec une solution d'acide chlorhydrique à 0.09% puis 0.18%
Profil thermique :	Acquis en janvier 1999 à l'équilibre thermique	
Température en fond de puits :	200°C	
Gradient de température :	100 K/km dans la partie en conduction 5°K/km dans la partie en convection	
Toit de la convection :	1000 m	
Indice d'injectivité :	0.1 L/s/bar dans le reservoir R3 avant stimulation et 1.5 L/s/bar après 0.02 L/s/bar dans le reservoir R5 avant stimulation puis 0.5 L/s/bar après	
Zones productrices :	à 2123 (65°, 70° et 15m), pertes totales et anomalie négative de température post-forage, zone qui contrôle 95% du débit avant l'approfondissement (toit du granite) à 3900 m, 4766 m et 5060 m, zones qui contrôlent le débit lors des tests de stimulation mais où les imageries UBI n'ont pas pu être acquises (granite à 2 micas – trou ouvert)	
Fracturation naturelle :	Fracturation naturelle de direction N170° et pendage presque vertical d'après les imageries UBI dans le socle granitique	
Orientation S_{Hmax} :	N169 +/- 14°E (Granite)	

Coupe géologique et technique du puits de production GPK-2

PROJET PILOTE DE GEOTHERMIE DE SOULTZ-SOUS-FORETS

Données du puits d'injection GPK-3

Date de forage :	06/2002 – 11/2002	
Coordonnées géographiques :	7° 51' 59" E 48° 55' 51" N	
Cible :	Socle granitique au centre du Horst situé entre la faille de Kutzenhausen et d'Hemmerswiller Le second puits du triplet est situé au Sud de GPK-2 dans un alignement N170°E (direction de la fracturation naturelle) et séparé de GPK-2 par une distance d'environ 6 m en surface et 600 m à 5000 m de profondeur	
Trajectoire :	Déviée de 25.5° vers N180°E à partir de 2680 m puis redevient vertical dans la partie en trou ouvert	
Fond de puits :	5111 m de profondeur – Granite à 2 micas	
Complétion :	Section 8"1/2 en trou ouvert à partir de 4592 m de profondeur	
Développement :	2003	Stimulation hydraulique jusqu'à 30 L/s
	06/2003	Stimulation chimique avec une solution d'acide chlorydrique à 0.45%
	02/2007	Stimulation chimique avec une solution d'OCA HT (organic clay acid high temperature)
Profil thermique :	Acquis en janvier 2003 à l'équilibre thermique	
Température en fond de puits :	200°C	
Gradient de température :	100 K/km dans la partie en conduction 5°K/km dans la partie en convection	
Toit de la convection :	1000 m	
Indice d'injectivité :	0.2 L/s/bar dans le réservoir R5 avant stimulation puis 0.4 L/s/bar après	
Zones productrices :	à 2100 m, pertes totales (toit du granite) à 2970 m (77°, 82° et 9m) et à 3271m (345°, 85° et 15m), zones qui montrent des halos d'altération sur les UBI et qui sont perméables après les stimulations (granite profond) à 4775m (345, 85° et 15m), pertes totales pendant le forage et anomalie négative de température post-forage, zone qui contrôle 70% du débit (granite à deux micas – trou ouvert)	
Fracturation naturelle :	1420 m – 2950 m : N5°E, 75°E 2950 m – 4560 m : N30°E, 75°W 4560 m – 5110 m : N5°E, 70°W	
Orientation S_{Hmax} :	N169 +/- 14°E (Granite)	

Coupe géologique et technique du puits d'injection GPK-3

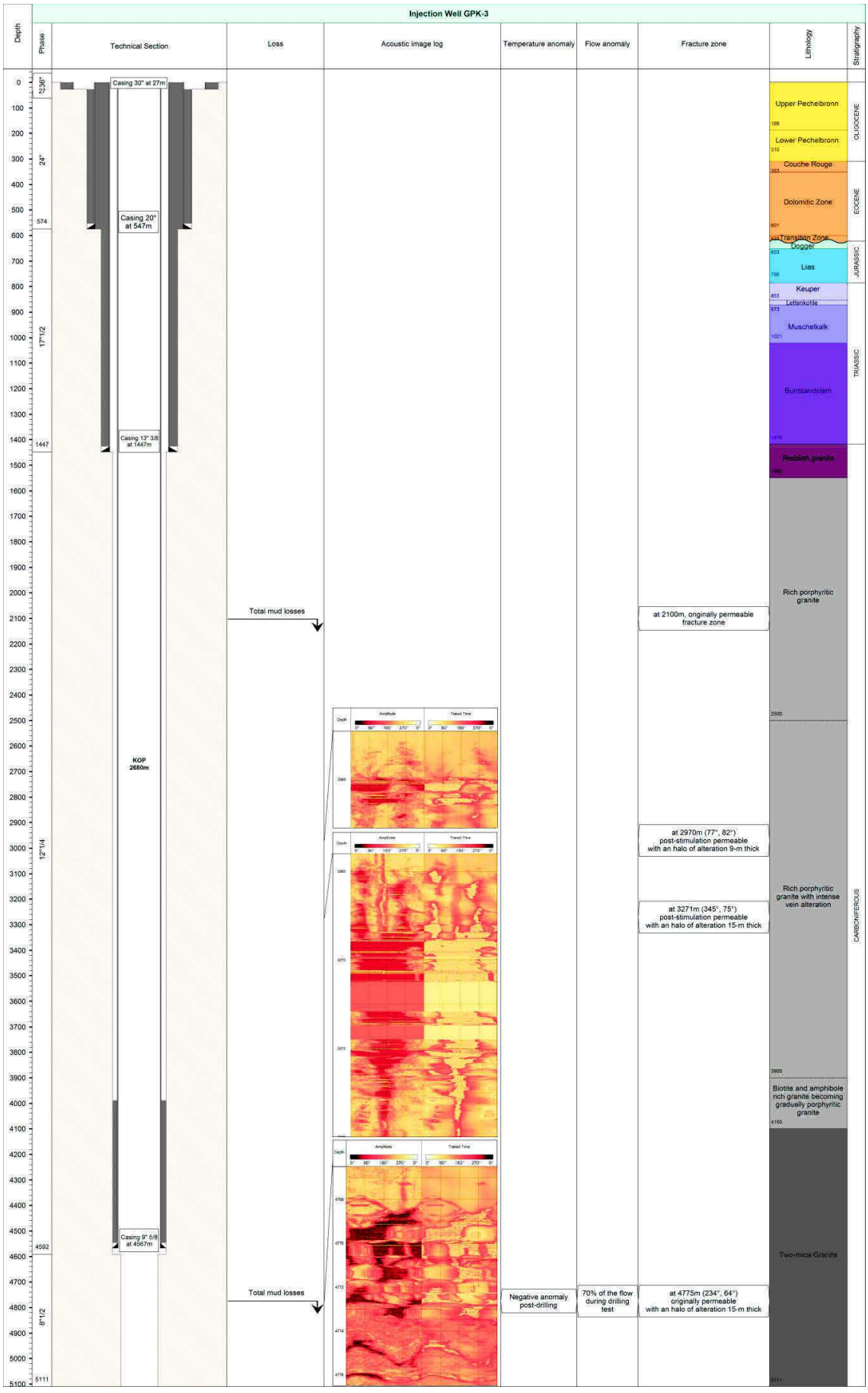

PROJET PILOTE DE GEOTHERMIE DE SOULTZ-SOUS-FORETS

Données du puits d'injection GPK-4

Date de forage :	08/2003 – 04/2004	
Coordonnées géographiques :	7° 51' 59" E 48° 55' 50" N	
Cible :	Socle granitique au centre du Horst situé entre la faille de Kutzenhausen et d'Hemmerswiller	
	Le dernier puits du triplet est situé au Sud de GPK-2 et GPK-4 dans un alignement N170°E (direction de la fracturation naturelle) et séparé de GPK-3 par une distance d'environ 6 m en surface et 650 m à 5000 m de profondeur	
Trajectoire :	Déviée de 34° vers N170°E à partir de 2100 m puis redevient vertical dans la partie en trou ouvert	
Fond de puits :	5270 m de profondeur – Granite à 2 micas	
Complétion :	Section 8"1/2 en trou ouvert à partir de 4767 m de profondeur	
Développement :	2005	Stimulation hydraulique jusqu'à 45 L/s
	02/2005	Stimulation chimique avec une solution d'acide chlorydrique à 0.2%
	01/2006	Stimulation chimique avec une pre-acidification (HCl 15%) puis une solution RMA (regular mud acid) (HCL 12% - HF 3%)
	10/2006	Stimulation chimique avec une solution NTA à 19% (nitrilotriacetic acid)
	03/2007	Stimulation chimique avec une solution d'OCA HT
Profil thermique :	Acquis en janvier 2006 à l'équilibre thermique	
Température en fond de puits :	200°C	
Gradient de température :	100 K/km dans la partie en conduction	
	5°K/km dans la partie en convection	
Toit de la convection :	1000 m	
Indice d'injectivité :	0.01 L/s/bar dans le réservoir R5 avant stimulation puis 0.4-0.5 L/s/bar après	
Zones productrices :	à 2100 m, pertes totales (toit du granite)	
	à 4361 m (280°, 77° et 4m) et à 4712m (221°, 50° et 1m), zones qui montrent des halos d'altération sur les UBI et qui sont perméables après les stimulations (granite à 2 micas – trou ouvert)	
Fracturation naturelle :	1420 m – 2950 m : N5°E, 75°E 2950 m – 4560 m : N30°E, 75°W 4560 m – 5110 m : N5°E, 70°W	
Orientation S_{Hmax} :	N169 +/- 14°E (Granite)	

Coupe géologique et technique du puits d'injection GPK-4

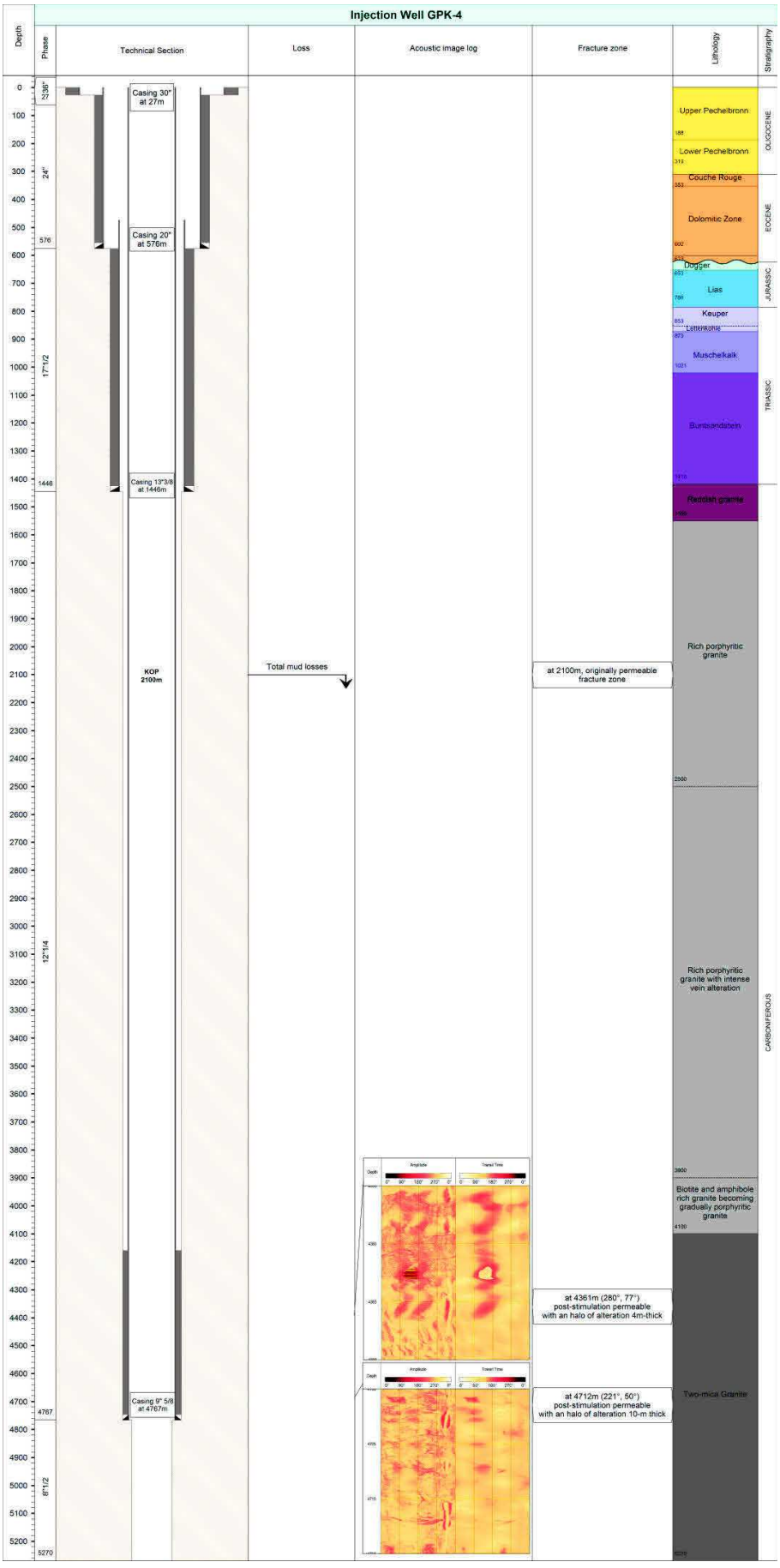

Fracturation naturelle dans les puits

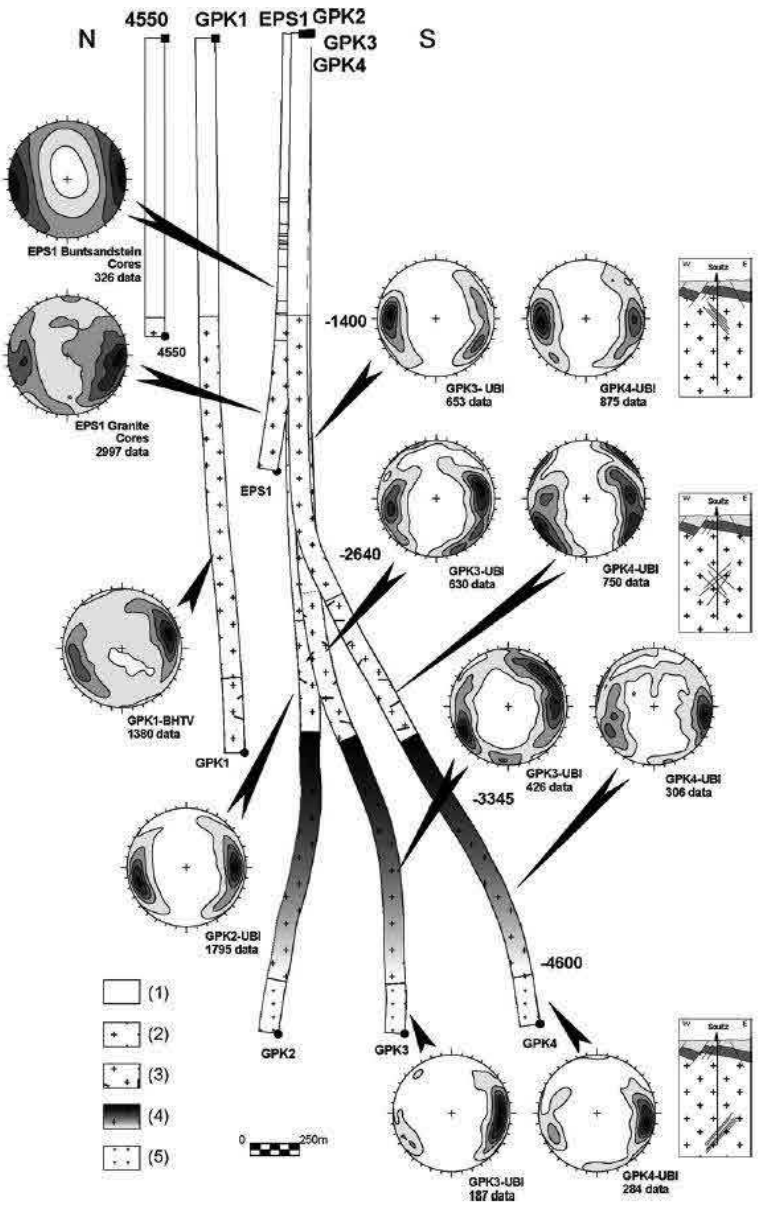

Orientation des fractures dans les puits de Soultz à partir de l'analyse des carottes et des images de paroi. Pour les puits GPK3 et GPK4, les données sont regroupées par faciès pétrographique majeur (Hooijkaas et al., 2006). La profondeur le long des puits indique la limite supérieure et inférieure des sections pétrographiques (altitude à partir du niveau marin de l'IGN). Diagramme de densité en projection de Schmidt, hémisphère inférieur, courbes à 10 %, 30 %, 50 %, 70 %, 90 % de la fréquence maximale. Géologie : (1) couverture sédimentaire, (2) granite standard, (3) granite standard avec une altération filonienne intensive, (4) granite riche en amphibole et en biotite évoluant progressivement vers un granite standard. (5) granite à deux micas et granite riche en biotite.

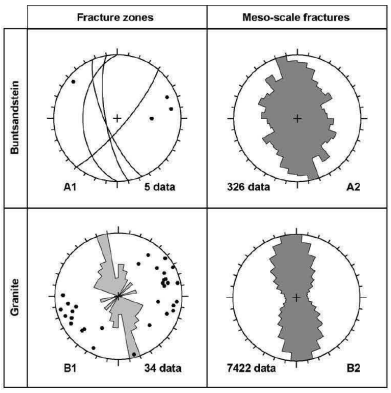

Zones de fractures
Set 1 : N165°E +/-10°
Set 2 : N40°E

Mésofractures : N0°E +/-20° à pendage ouest majoritairement

Zones de fractures
Set 1 : N160°E +/-15°
Set 2 : N20°E +/-10° et N130°E +/- 15°

Mésofractures : N175°E +/-20° à pendage ouest majoritairement

Orientation des zones de fractures et des mésofractures dans les sédiments du Buntsandstein (A) et dans le granite (B). (A1) Traces et pôles des zones de fracture dans le Buntsandstein ; (A2) rosace de direction (classes de 10°) des mésofractures mesurées sur les carottes de Buntsandstein du forage EPS1 ; (B1) pôles et rosace de direction (classes de 10°) des zones de fractures dans le granite ; (B2) rosace de direction (classes de 10°) des mésofractures mesurées sur les images de paroi de tous les forages dans le granite.

- Pas de découplage entre les grès du Buntsandstein et le granite
- Légère rotation dans le sens des aiguilles d'une montre entre l'orientation des zones de fractures et des mésofractures

Profils thermiques dans les puits

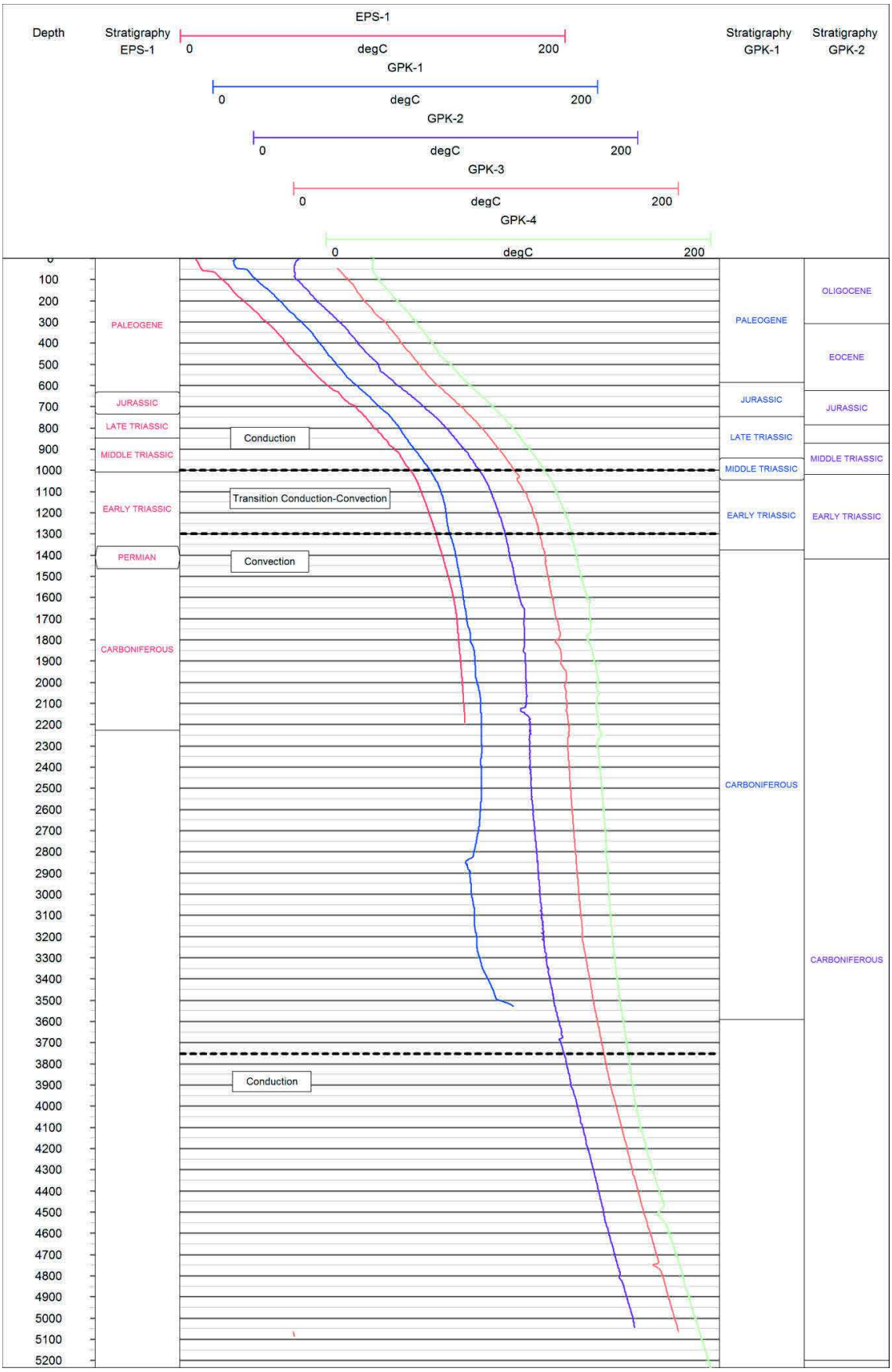

Les profils thermiques ont été acquis à l'équilibre thermique et dans le casing des puits géothermiques ESP-1 en novembre 1991, GPK-1 en mai 1995 et GPK-2, -3 et -4.

PROJET PILOTE DE GEOTHERMIE DE SOULTZ-SOUS-FORETS

Références

Gérard, A., Menjoz, A. and Schwoerer, P. (1984) L'anomalie thermique de Soultz-sous-Forêts, *Géothermie actualités n°3*

Baria, R., Baumgärtner, J., Gérard, A. and Moore, P. (1992). GPK1, Preliminary results obtained during the drilling operations at Soultz, *Rapport Socomine*

Baumgärtner, J., Jung, R., Gerard, A., Baria, R. and Garnish, J. (1996). The European HDR project at Soultz-sous-Forêts; stimulation of the second deep well and first circulation experiments, *Proceedings of 21st Workshop on Geothermal reservoir Engineering,* Stanford University, California

Baumgärtner, J., Gerard, A. and Baria, R. (1999). GPK-2 Re-entry and deepening, *Rapport technique Socomine*

Datalog Technology LTD (1995). Socomine GPK-2, *Rapport de fin de sondage*

Degouy, M., Villeneuve, B. and Weber, R. (1992). Seismic observation wells and EPS-1 well, Soultz-sous-Forêts, *Rapport de fin de sondage, 92CFG09*

Dezayes, C., Gentier, S. and Genter, A. (2005). Deep Geothermal energy in western Europe: the Soultz project, *Rapport BRGM RP-54227-FR*

Dezayes, C., Genter, A. and Valley, B. (2010). Structure of the low permeable naturally fractured geothermal reservoir at Soultz, *Comptes Rendus Geoscience*, 342, 517-530

Genter, A. and Traineau, H. (1996). Analysis of macroscopic fractures in granite in the HDR geothermal well EPS-1, Soultz-sous-Forêts, France, *Journal of Volcanology and Geothermal Research*, 72, 121-141

Genter, A., Castaing, C., Dezayes, C., Tenzer, H., Traineau, H. and Villemin T. (1997). Comparative analmysis of direct (core) and indirect (borehole imaging tools) collection of fracture data in the Hot Dry Rock Soultz reservoir (France), *Journal of Geophysical Research*, 102(B7), 15419-15431

Genter, A., Evans, K., Cuenot, N., Fritsch, D. and Sanjuan, B. (2010). Contribution of the exploration of deep crystalline fractured reservoir of Soultz to the knowledge of enhanced geothermal systems (EGS), *Comptes Rendus Geoscience*, 342, 502-516

Genter, A., Cuenot, N., Melchert, B., Moeckes, W., Ravier, G., Sanjuan, B., Sanjuan, R., Scheiber, J., Schill, E. and Schmittbuhl, J. (2013). Main achievements from the multi-well EGS Soultz project during geothermal exploitation from 2010 and 2012, *Proceedings of European Geothermal Congress,* Pisa, Italia

Herbirch, B. (1988). Forage géothermique de Soultz-sous-Forêts GPK-1, *Rapport de fin de sondage, 88CFG03*

Jung, R. (1991). Hydraulic fracturing and hydraulic testing in the granitic section of borehole GPK1, Soultz-sous-Forêts. In: *Geothermal Energy in Europe. The Soultz Hot Dry Rock Project* (edited by Bresee J.C) 3, Gordon and Breach Science Publishers, p 148-199

Jung, R., Willis-Richard J., Jicholls, J., Bertozzi, A. and Heinemann B. (1995) Evaluation of hydraulic tests at Soultz-sous-Forêts, European HDR-site, *Proceedings of Worl Geothermal Conférence,* Florence, Italy

Klee, G. and Rummel, F. (1993). Hydrofrac stress data fort he European HDR Research Project test site Soultz-sous-Forêts, *Int. J., Rock Mech. Min. Sci. & Geomech. Abtr.*, 30(7), p.973-976

Nami, P., Schellschmidt, R., Schindler, M. and Tischner, T. (2008). Chemical stimulation operations for reservoir development of the deep crystalline HDR/EGS system at Soultz-sous-Forêts (France), *Proceedings of 32nd Workshop on Geothermal reservoir Engineering,* Stanford University, California

Portier, S., Vuataz, F-D., Nami, P., Sanjuan, B. and Gérard, A. (2009). Chemical stimulation techniques for geothermal wells: experiments on the three-well EGS system at Soultz-sous-Forêts, France, *Geothermics*, 38, 349-359

Sausse, J., Dezayes, C., Dorbath, L., Genter, A. and Place, J. (2010). 3D model of fracture zones at Soultz-sous-Forêts based on geological data, image logs, induced microseismicity and vertical seismic profiles, *Comptes Rendus Geoscience*, 342, 531-545

Schill, E., Cuenot, N., Genter, A. and Kohl, T. (2015). Hydraulic performance history at the Soultz EGS reservoirs from stimulation and long-term circulation tests*, Geothermics*, 70, 110-124

Schindler, M., Nami, P., Schellschmidt, R., Teza, D. and Tischner, T. (2008). *Proceedings of 33rd Workshop on Geothermal reservoir Engineering,* Stanford University, California

Southern International Inc (2003). GEIE EMC GPK-3, *Rapport de fin de sondage*

Valley, B. (2007). *The relation between natural fracturing and stress heterogeneities in deep-seated crystalline rocks at Soultz-sous-Forêts (France)*, Rapport de thèse, Université de Neuchâtel, Suisses

DEEP HEAT MINING PROJECT

Données générales	*Compagnie :*	Geopower Basel AG			
	Position géographique :	*Pays* Suisse *Région* Bâle-Ville *Ville* Bâle			
Données d'exploration	*Campagne d'exploration :*	Etude de la sismicité régionale, des mécanismes au foyer et des contraintes in situ du réservoir			1998
	Exploitation pétrolière :	-			
	Contexte géologique :	Horst de Basel Ruecken situé à environ 5 km à l'Est de la faille bordière et à l'Ouest de la faille d'Allschwill			
	Cible :	Granite profond chaud fracturé à stimuler			
	Concept :	EGS			
	Modèle 3D :	Non			
Données de production	*Production :*	Cogénération	*Nombre de puits planifiés:*		3
	Puissance planifiée :	30 MWth	*Débit de production :*		100 L/s
	Système :	-	*Température de pompage :*		200°C
	Statut actuel :	Abandon	*Température d'injection :*		-
Données de sous-sol	*Réservoir :*	Granite			
	Profondeur du réservoir (top) :	2650 m			
Fluide géothermal	*Salinité :*	Non publiée			
	Ions majeurs :	Non publiés			
	Gaz :	98% N_2 et CO_2 90% - CH_4 en traces			

Historique du projet

1998	Etude du site et de la contrainte maximale dans les puits de la région
2001	Forage d'un puits d'exploration OT-2
05-10/2006	Forage du premier puits du triplet
12/2006	Stimulation hydraulique du puits, évènement sismique M=3.4, suspension du projet
2009	Abandon du projet

DEEP HEAT MINING PROJECT

Carte des failles à la surface du site

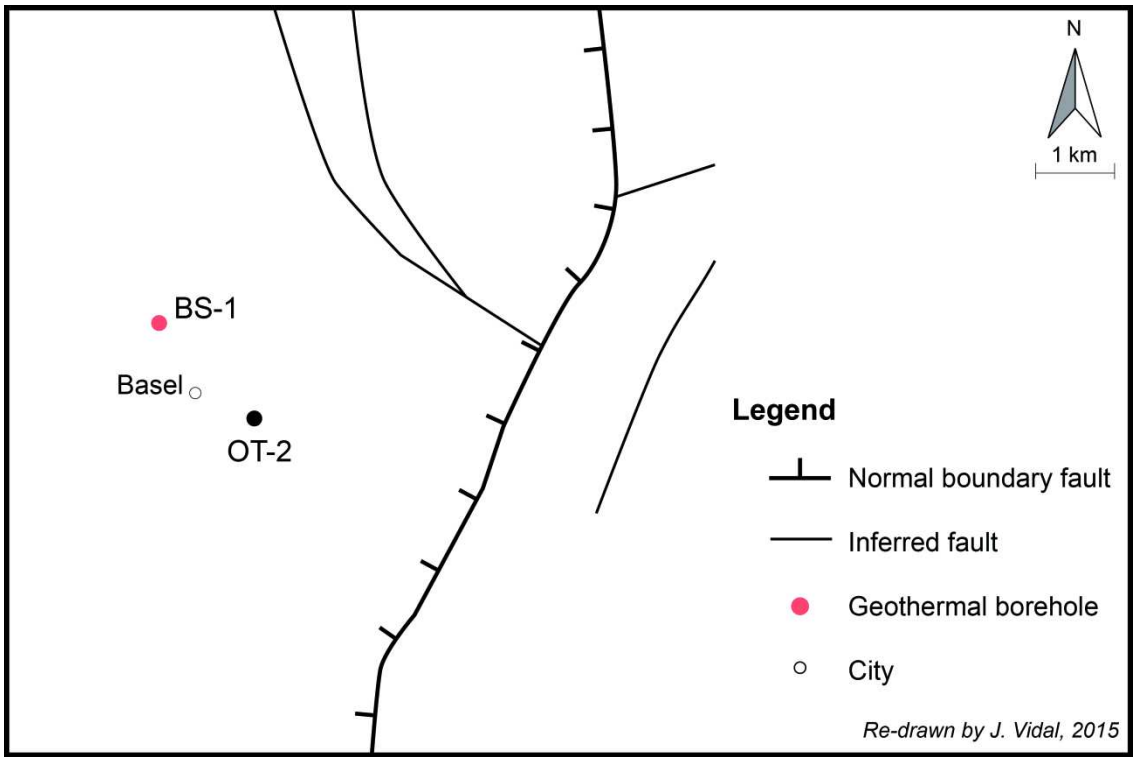

Coupe géologique du site

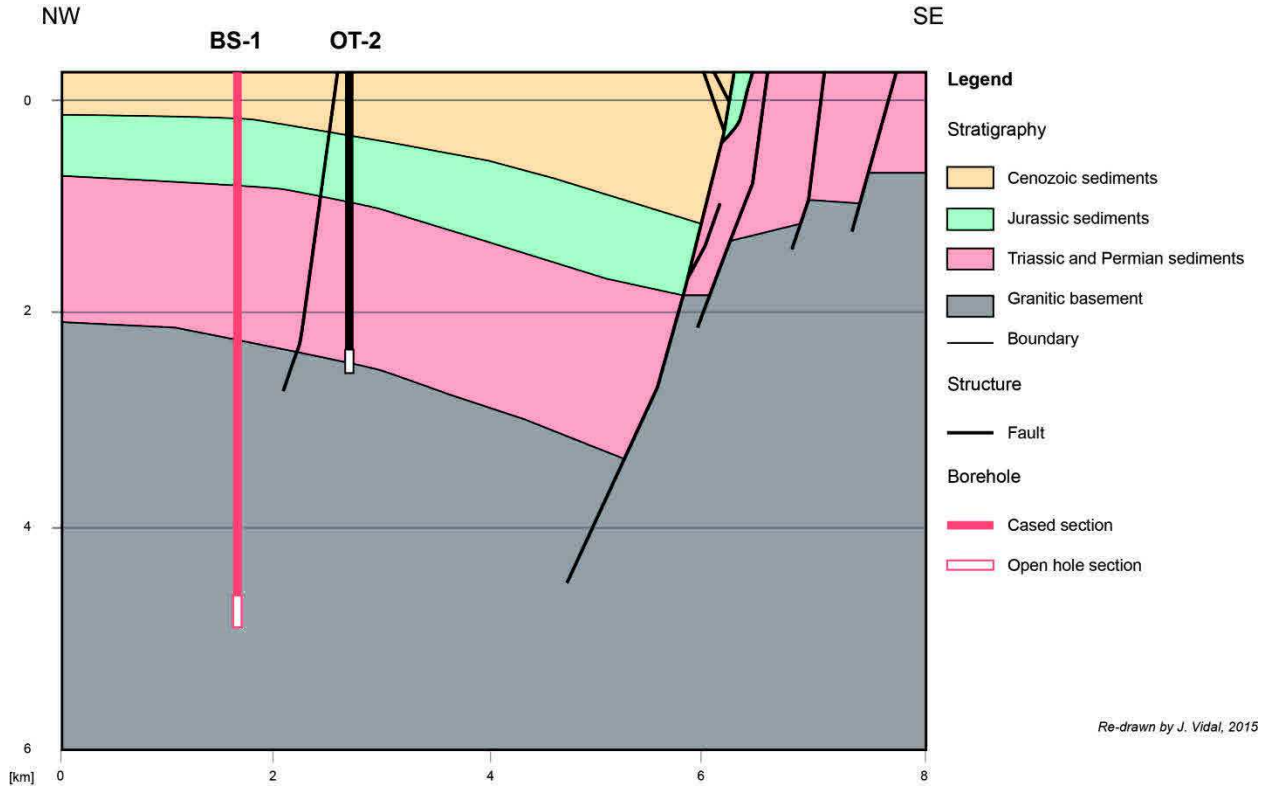

DEEP HEAT MINING PROJECT

Données du puits d'exploration OT-2	*Date de forage :*	2001
	Coordonnées géographiques :	-
	Cible :	Dans la dépression de S^{t} Jakob – Tuellinger Mulde, entre le horst de Basel Rueckel et la faille bordière
	Trajectoire :	Quasi-verticale
	Fond de puits :	2755 m de profondeur - Granite
	Complétion :	Section 6"1/4 à partir de 2550 m
	Développement :	-
	Profil thermique :	Non publié
	Température en fond de puits :	123°C
	Gradients de température :	40°C/km
	Toit de la convection :	-
	Indice de productivité :	-
	Zones productrices :	
	Fracturation naturelle :	Imageries de paroi non disponibles
	Orientation S_{Hmax} :	N115°E dans les sédiments et N140°+/-16° dans le socle
Coupe géologique et technique du puits d'exploration OT-2	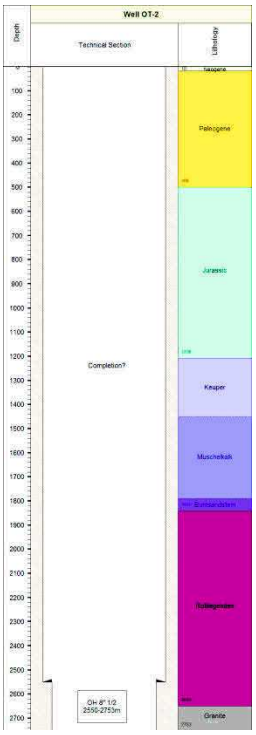	

DEEP HEAT MINING PROJECT

Données du puits géothermique BS-1

Date de forage :	05-10/2006	
Coordonnées géographiques :	-	
Cible :	Socle granitique profond, situé à 1 km au NO de OT-2	
Trajectoire :	Quasi-verticale	
Fond de puits :	5000 m de profondeur - Granite	
Complétion :	Section en trou ouvert 9”5/8 à partir de 4629 m de profondeur puis 8”1/2 à partir de 4834 m de profondeur	
Développement :	11/2006	Test hydraulique du réservoir avec injection à faible débit durant 75h : après la fermeture du puits, la pression en tête de puits est supérieure à 14bar et augmente pendant plus de 18h. Interprétation : un granite à la matrice peu perméable contenant des fractures à faible perméabilité.
	12/2006	Stimulation hydraulique : 11570m^3 injecté, palier de 0 à 100L/min durant les 16 premières heures avec une pression en tête de puits de 110bar, puis débit augmenté jusqu'à 3000 L/min avec une pression en tête de puits de 296bar. Après 6 jours d’injection, en raison des nombreux évènements sismiques, décision de réduire le débit mais des évènements > M=1 se produisent toujours donc décision de fermer le puits. 5h après la fermeture, un évènement M=3.4 se produit. Après la fermeture du puits, le niveau d'eau dans le puits se stabilise difficilement avec des retours d'eau de 20-40m3 en quelques heures, au total 3900m3 éjecté sur 14 mois.
	01-02/2009	Tests d'injection et de production à faible débit. Interprétation : les circulations sont contrôlées par quelques fractures majeures perméables et la perméabilité est augmentée de deux ordres.
Profil thermique :	Acquis en décembre 2008 et juin 2009 dans des conditions d’équilibre thermique	
Température en fond de puits :	174°C à 4862 m de profondeur, extrapolé à 190°C en fond de puits	
Gradients de température :	41 K/km dans la partie en conduction 27 K/km dans la partie le socle	
Toit de la convection :	2500 m de profondeur (peu visible)	
Indice d’injectivité:	2.5 x 10^{-3} L/s/bar avant stimulation	
Zones productrices :	Après les opérations de forage, zone de fractures majeures entre 4700 et 4835 m de profondeur avec une forte altération argileuse et une forte présence d’anhydrite. Après stimulation ; à 4671 m de profondeur, anomalie de débit de 50% associé à une anomalie de température.	
Fracturation naturelle :	NW-SE et NNW-SS avec un pendage de 60 à 90° Densité de fracture de 0.95 fract/m au toit du socle et 0.3 fract/m dans la partie inférieure	
Orientation S_{Hmax} :	N°144E au-delà de 2.5 km de profondeur (granite)	

Coupe géologique et technique du puits géothermique BS-1

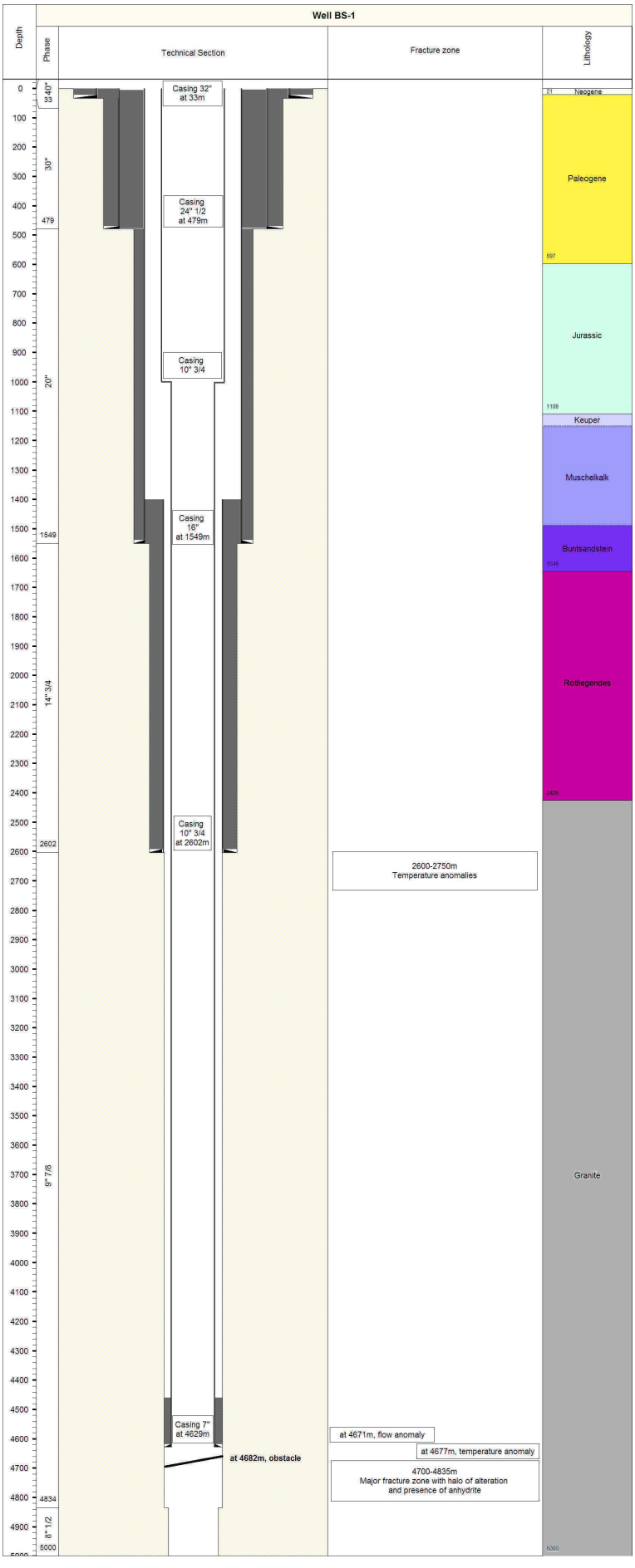

Profil thermique dans le puits BS-1

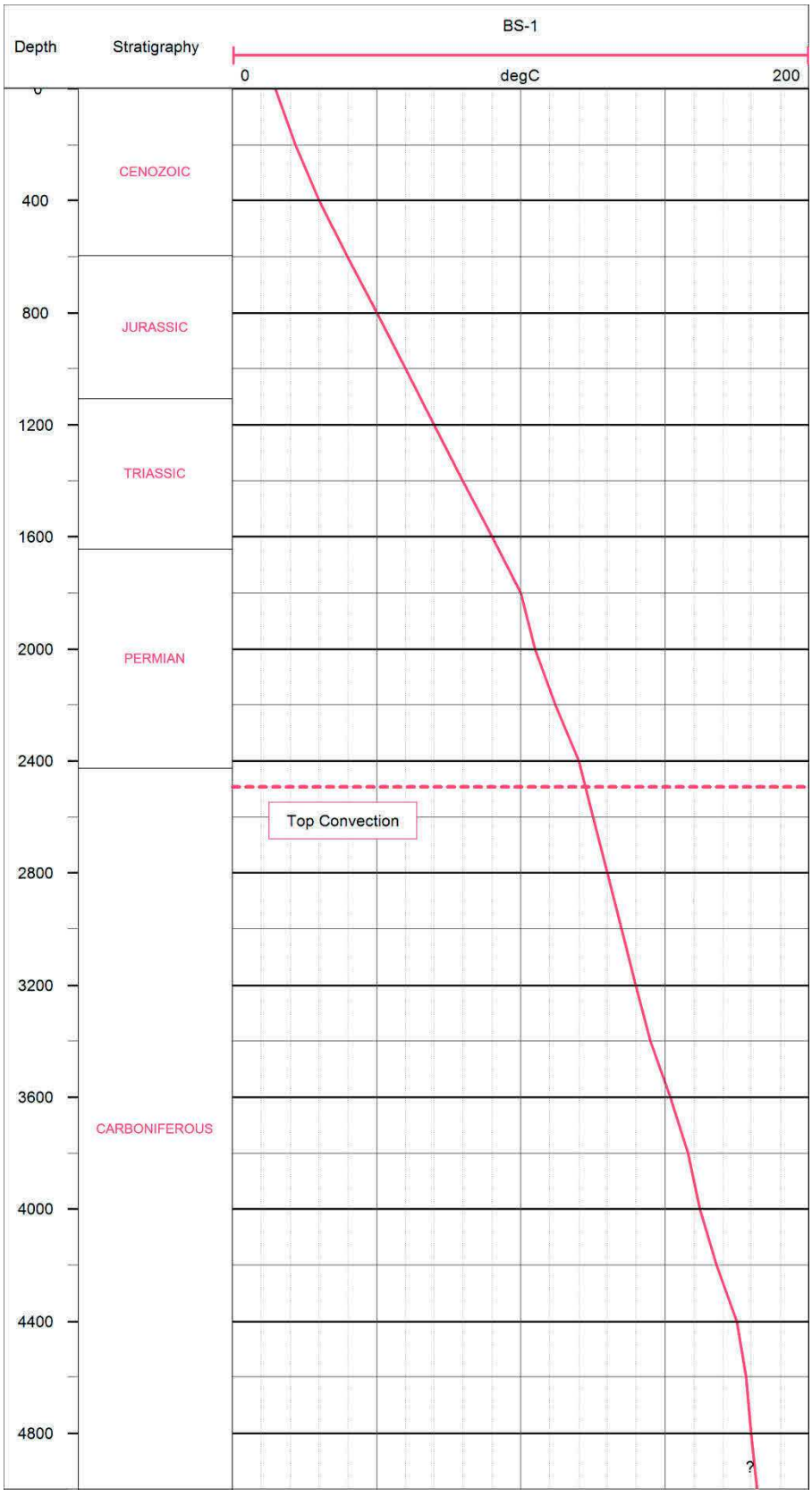

Le profil thermique est une approximation par régression linéaire des données réelles acquises à l'équilibre thermique et dans le casing du puits géothermique BS-1.

DEEP HEAT MINING PROJECT	
Références	Evans, K. F. and Roth, P., 1988. *The state of stress in northern Switzerland inferred from earthquake seismological data and in situ stress measurements,* Unpublished study for the Deep Heat Mining Hearing, M. O., 1999. The geology of Basle in view of Deep heat Mining, *Bulletin d'Hydrogéologie*, **17** Hearing, M. O., Schanz, U., Ladner, F. and Dyer B. C., 2008. Charactéerization of the Basel 1 enhanced geothermal system, *Géothermics*, **37**, 469-495 Ladner, F. and Haering, M. O., 2009. Hydraulic Characteristics of the Basel 1 Enhanced Geothermal System, *GRC Transactions*, **33** Valley, B. and Evans, K. F. 2009. Stress orientation to 5 km depth in the basement below Basel (Switzerland) from borehole failure analysis, *Swiss J. Geosci.,* **102**, 467-480, doi:10.1007/s00015-009-1335-z

GEOTHERMIEKRAFTWERK LANDAU

Données générales	*Compagnie :*	Geo x GmbH		
	Position géographique :	*Pays* Allemagne		
		Région Baden-Württemberg		
		Ville Landau in der Pfalz		
Données d'exploration	*Campagne d'exploration :*	Non communiquées		
	Exploitation pétrolière :	Champ de Landau	Huile dans le Tertiaire	
	Contexte géologique :	Le site est situé à moins de 5 km à l'Est la faille bordière Ouest		
	Cible :	Failles normales parallèles à fort plongement Est et visibles en sismique		
	Concept :	Hydrothermal/EGS		
	Modèle 3D :	Oui		
Données de production	*Production :*	Electricité / Chaleur	*Nombre de puits :*	2
	Puissance installée :	2.9 MWe / 3-4 MWth	*Débit de production :*	50-70 L/s
	Système :	ORC	*Température de pompage :*	160°C
	Statut actuel :	Expertise sous-sol	*Température d'injection :*	-
Données de sous-sol	*Réservoir :*	Granite		
	Profondeur du réservoir (top) :	3000 m		
Fluide géothermal	*Salinité :*	102 g/L		
	Ions majeurs :	Cl Na Ca		
	Gaz :	CO_2 dominant		

Historique du projet	
2000-2005	Phase préparatoire menée par la société HotRock GmbH
2005-2006	Opérations de forage des deux puits menées par la société GeoX GmbH
03-05/2007	Tests de circulation dont une injection de 25 à 15 L/s sans pompe pendant 5 semaines avec une chute de pression en surface de 10 bar
11/2007	Mise en service de la centrale géothermique
2009	Séisme de magnitude 2.7 le 15/08/2009 6 séismes entre le 13/09 et le 15/09/2009 dont un évènement de magnitude 2.4 le 14/09/2009
10/2010	Mise en service de la centrale
2014	Arrêt de la centrale et expertise sous-sol suite à des soulèvements de terrain autour du site géothermique

GEOTHERMIEKRAFTWERK LANDAU

Carte des failles à la surface du site

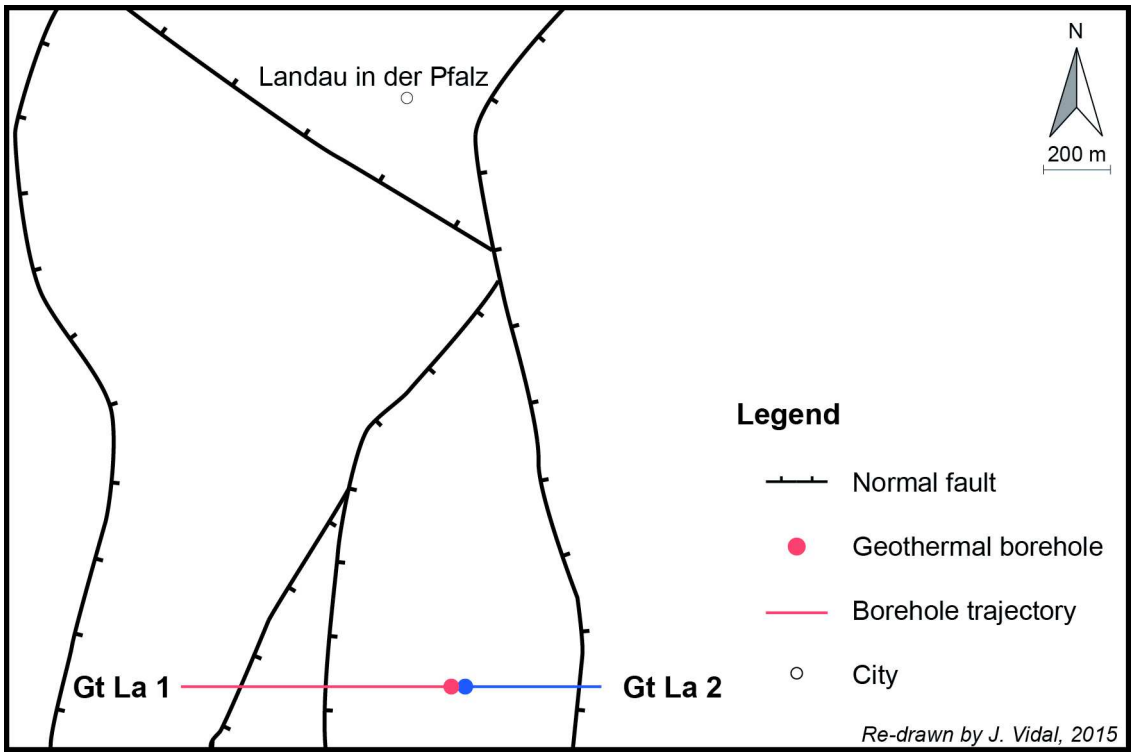

Coupe géologique interprétative du site

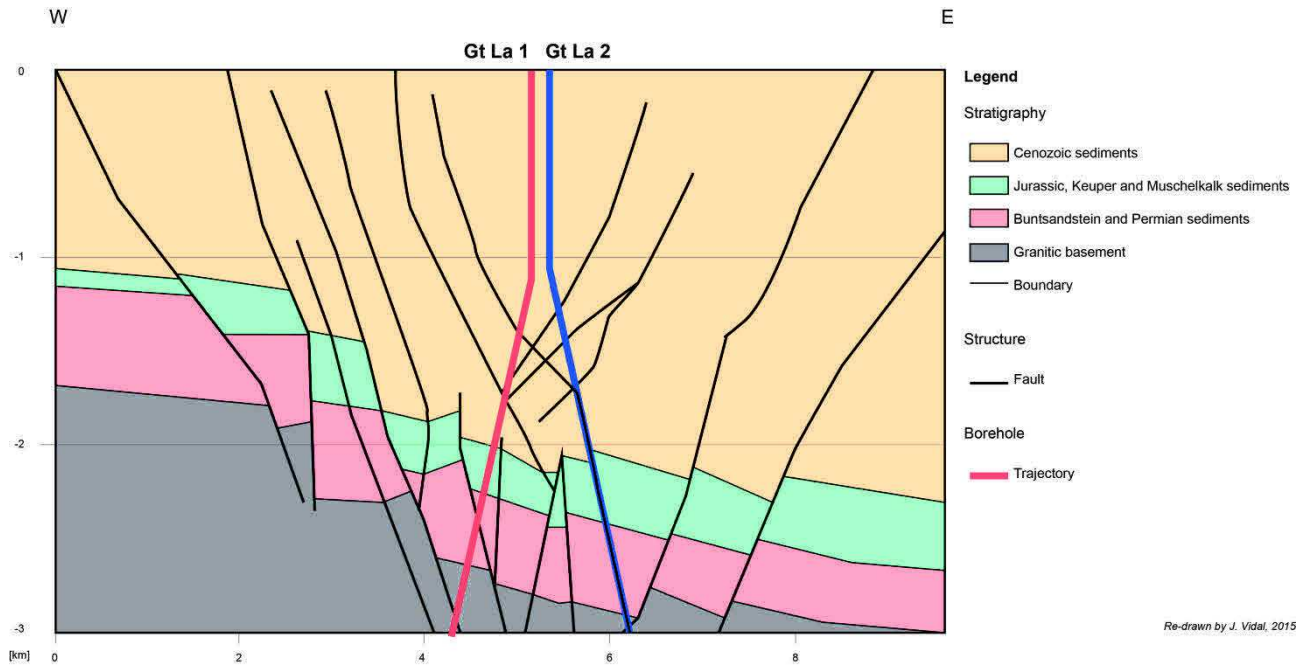

L'interprétation géologique et la trajectoire des puits sont très approximatives

GEOTHERMIEKRAFTWERK LANDAU

Données du puits de production Gt La1	*Date de forage :*	05/08/2005 - 07/10/2005
	Coordonnées géographiques :	Non communiquées
	Cible :	Faille normale à plongement Est qui recoupe le toit du socle
	Trajectoire :	Déviée de 33° vers l'Ouest
	Fond de puits :	3300 m de profondeur – Toit du Granite
	Complétion :	Liner perforé à partir de 2100 m de profondeur
	Développement :	-
	Profil thermique :	Acquis à l'équilibre thermique et tronqué à 2600 m de profondeur
	Température en fond de puits :	160°C
	Gradient de température :	80 K/km dans la partie en conduction 5 K/km dans la partie en convection
	Toit de la convection :	2100 m (Buntsandstein)
	Indice de productivité :	
	Zones productrices :	-
	Fracturation naturelle :	Imageries de paroi non publiées
	Orientation S_{Hmax} :	NNW-SSE

GEOTHERMIEKRAFTWERK LANDAU

Données du puits d'injection Gt La2

Date de forage :	22/01/2006 - 15/03/2006	
Coordonnées géographiques :	Non communiquées	
Cible :	Faille normale à plongement Est qui recoupe le toit du socle et située à l'Est de la faille recoupée par Gt La1 Puits séparés par une distance d'environ 1.2 km en profondeur	
Trajectoire :	Déviée de 25° vers l'Est	
Fond de puits :	3170 m de profondeur – Toit du Granite	
Complétion :	Liner perforé à partir de 2200 m de profondeur	
Développement :	2006	Stimulation hydraulique: injection >190 L/s et une pression en fdp >300 bar Stimulation chimique: injection de 95 m³ de solution à 33 % HCl injecté à un débit de 10 L/s par coiled tubing Multiplication de l'Indice de Productivité par 5 après les stimulations
Profil thermique :	Tronqué à 2750 m de profondeur	
Température en fond de puits :	170°C	
Gradients de température :	80 K/km dans la partie en conduction 5 K/km dans la partie en convection	
Toit de la convection :	2200 m (Buntsandstein)	
Indice de productivité :	0.25 L/s/bar avant stimulation puis 1 L/s/bar après	
Zones productrices :	Petites anomalies de température discrètes au toit du granite sur les profils de température avant la stimulation chimique	
Fracturation naturelle :	Imageries de paroi non publiées	
Orientation S_{Hmax} :	NNW-SSE	

GEOTHERMIEKRAFTWERK LANDAU

Profils thermiques dans le puits

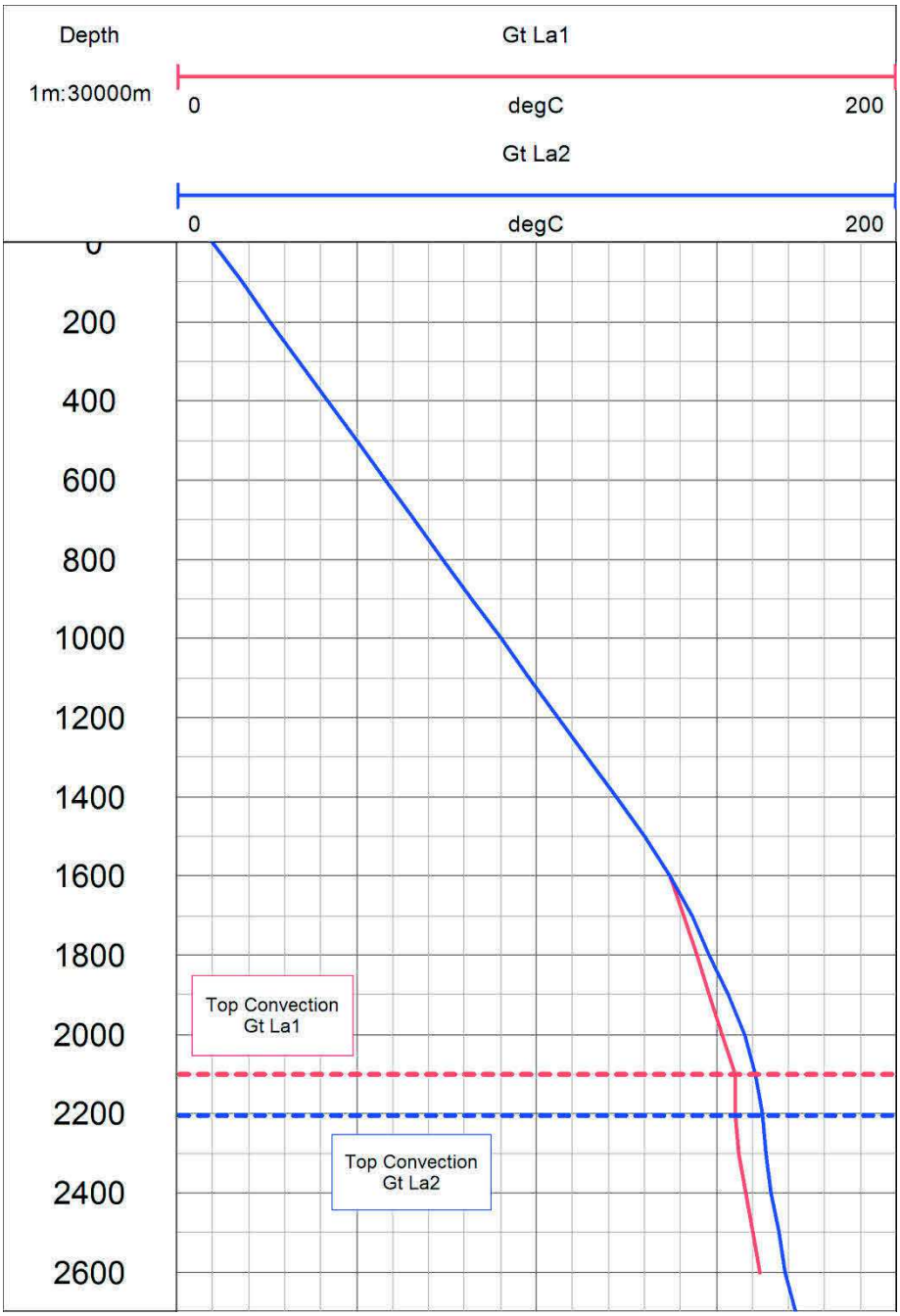

Les profils thermiques sont une approximation par régression linéaire des données réelles acquises à l'équilibre thermique et dans le casing des puits géothermiques Gt La1 et Gt La2.

GEOTHERMIEKRAFTWERK LANDAU

Références

Baumgärtner, J., 2007.The geox GmbH Project in Landau – The First Geothermal Power Project in Palatinate / Upper Rhine Valley*, Proceedings of First European Geothermal Review*, Mainz, Germany

Hettkamp, Th., 2007. A Multi-Horizon Approach for the Exploration and Exploitation of a Fractured Geothermal Reservoir in Landau/Palatinate*, Proceedings of First European Geothermal Review*, Mainz, Germany

Das seismische Ereignis bei Landau vom 15. August 2009*. Final Report from the expert group "Seismisches Risiko bei hydrothermaler Geothermie"*, Hannover, 2010

Schindler, M., Baumgärtner, J., Gandy, T., Hauffe, P., Hettkamp, Th., Menzel, H., Penzkofer, P., Teza, D., Tischner, T. and Wahl, G., 2010. Successful Hydraulic Stimulation Techniques for Electric Power Production in the Upper Rhine Graben, Central Europe. *Proceedings of World Geothermal Congress*, Bali, Indonesia

Hettkamp, Th., 2010. Experiences from 5 years operation in Landau, *Proceedings of Third European Geothermal Review*, Mainz, Germany

Ritter, J., Frietsch, M., Gassner, L., Groos, J., Grund, M., and Zeis, J., 2014. Mechanism of fluid-induced micro-earthquakes near Landau, Upper Rhine Graben, Germany, *Proceedings of European Geosciences Union*, Wien, Austria

GEOTHERMIEKRAFTWERK INSHEIM

Données générales	*Compagnie :*	Pfalzwerke geofuture GmbH		
	Position géographique :	*Pays* Allemagne		
		Région Baden-Württemberg		
		Ville Insheim		
Données d'exploration	*Campagne d'exploration :*	Non publiée		
	Exploitation pétrolière :	Champ de Landau	Huile dans le Tertiaire	
	Contexte géologique :	Le site se situe à moins de 5 km à l'Est de la faille bordière Ouest		
	Cible :	Système de failles normales parallèles à fort plongement (Est ?) visibles en sismique		
	Concept :	Hydrothermal/EGS		
	Modèle 3D :	Oui		
Données de production	*Production :*	Electricité	*Nombre de puits :*	2
	Puissance installée :	4.8 MWe	*Débit de production :*	70 L/s
	Système :	ORC	*Température de pompage :*	> 160°C
	Statut actuel :	Exploitation	*Température d'injection :*	-
Données de sous-sol	*Réservoir :*	Multi-horizons : Muschelkalk-Buntsandstein-Permien-Granite		
	Profondeur du réservoir (top) :	Toit du Muschelkalk à environ 2500 m de profondeur (variable selon les puits)		
Fluide géothermal	*Salinité :*	~100 g/L		
	Ions majeurs :	Cl Na Ca		
	Gaz :	CO_2 dominant		

Historique du projet	2005-2007	Phase préparatoire menée par la société Hot Rock Holding GmbH
	2008	Pfalzwerke geofuture GmbH devient majoritaire et en charge de la gestion du projet
	2008-2009	Opérations de forage des deux puits
	03-04/2010	Tests de circulation entre les deux puits
	08-10/2010	Réalisation d'un sidetrack dans le premier puits afin d'obtenir une meilleure perméabilité
	11/2010	Mise en service de la centrale

GEOTHERMIEKRAFTWERK INSHEIM

Carte schématique de la trajectoire des puits au toit des sédiments triassiques

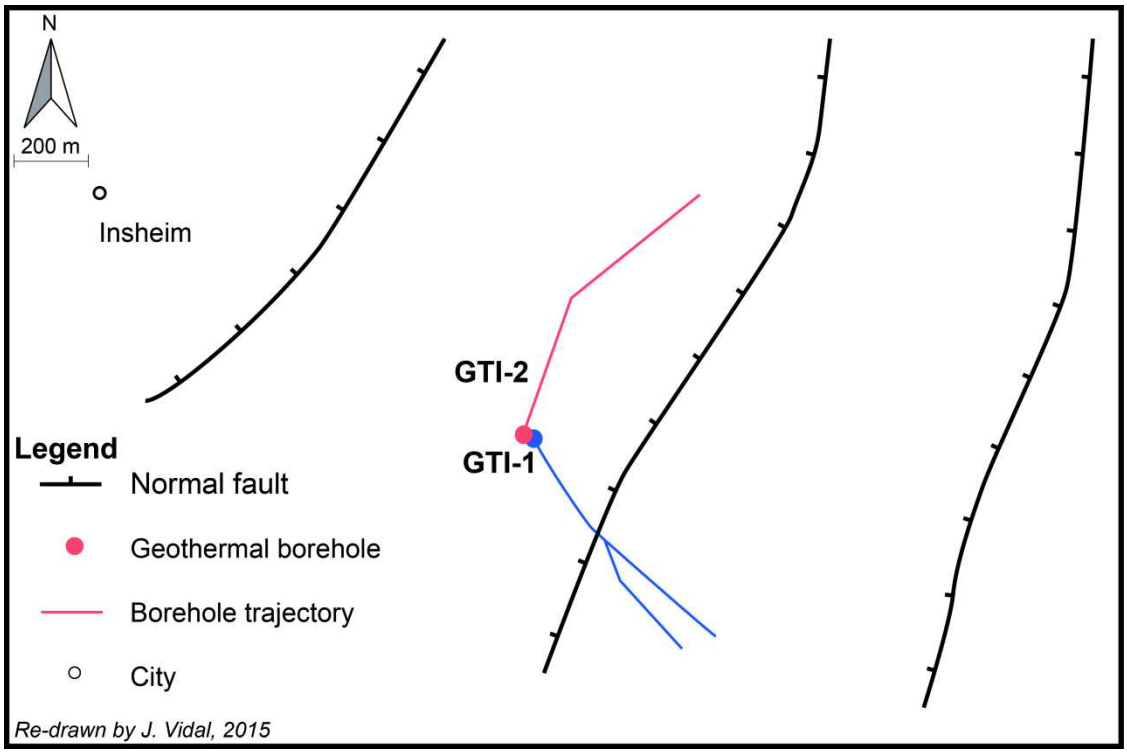

Modèle 3D du site

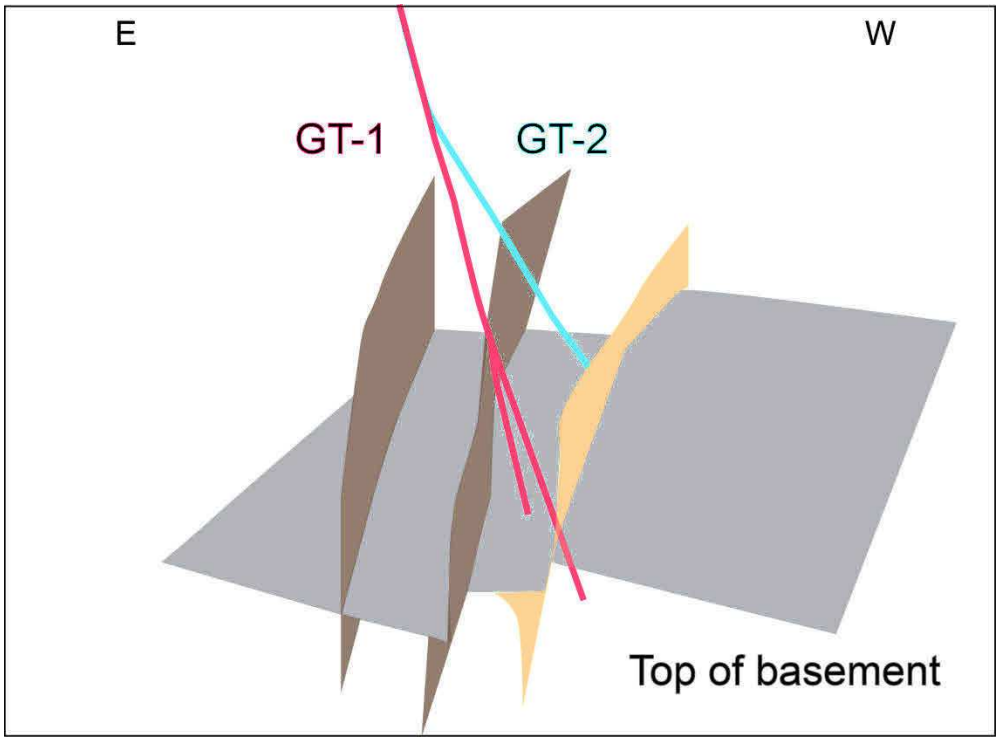

GEOTHERMIEKRAFTWERK INSHEIM

Données du puits d'injection GTI-1

Date de forage :	03/06/2008 - 12/09/2008
Coordonnées géographiques :	Non communiquées
Cible :	Faille avec une direction Nord-Sud (?) à fort plongement (vers l'Est ?) qui recoupe les sédiments triasiques profonds et le toit du socle
Trajectoire :	Déviée vers le Sud-Est
Fond de puits :	3654 m de profondeur puis 3856 m de profondeur après le sidetrack – Toit du Granite
Complétion :	Section 8"1/2 à partir de 2499 m avec Liner 7" jusqu'à 3340 m puis Liner perforé 7" jusqu'à 3618 m *(complétion avant le sidetrack)*
Développement :	2010 Opérations de forage pour réaliser un sidetrack puis stimulation hydraulique pour atteindre une perméabilité suffisante pour la viabilité économique du projet
Profil thermique :	Non communiqué
Température en fond de puits :	> 160°C
Gradient de température :	Non communiqué
Toit de la convection :	Non communiqué
Indice de productivité :	0.9 L/s/bar avant le sidetrack puis 1.3 L/s/bar après la stimulation hydraulique (pression non stabilisée sur le test de puits)
Zones productrices :	Zones de failles à environ 3362 m de profondeur (Rotliegendes), environ 3547-3562 m (toit du granite) et environ 3592-3600 m de profondeur (toit du granite)
Fracturation naturelle :	Imageries de paroi non publiées
Orientation S_{Hmax} :	N-S

GEOTHERMIEKRAFTWERK INSHEIM

Coupe géologique et technique du puits d'injection GTI-1

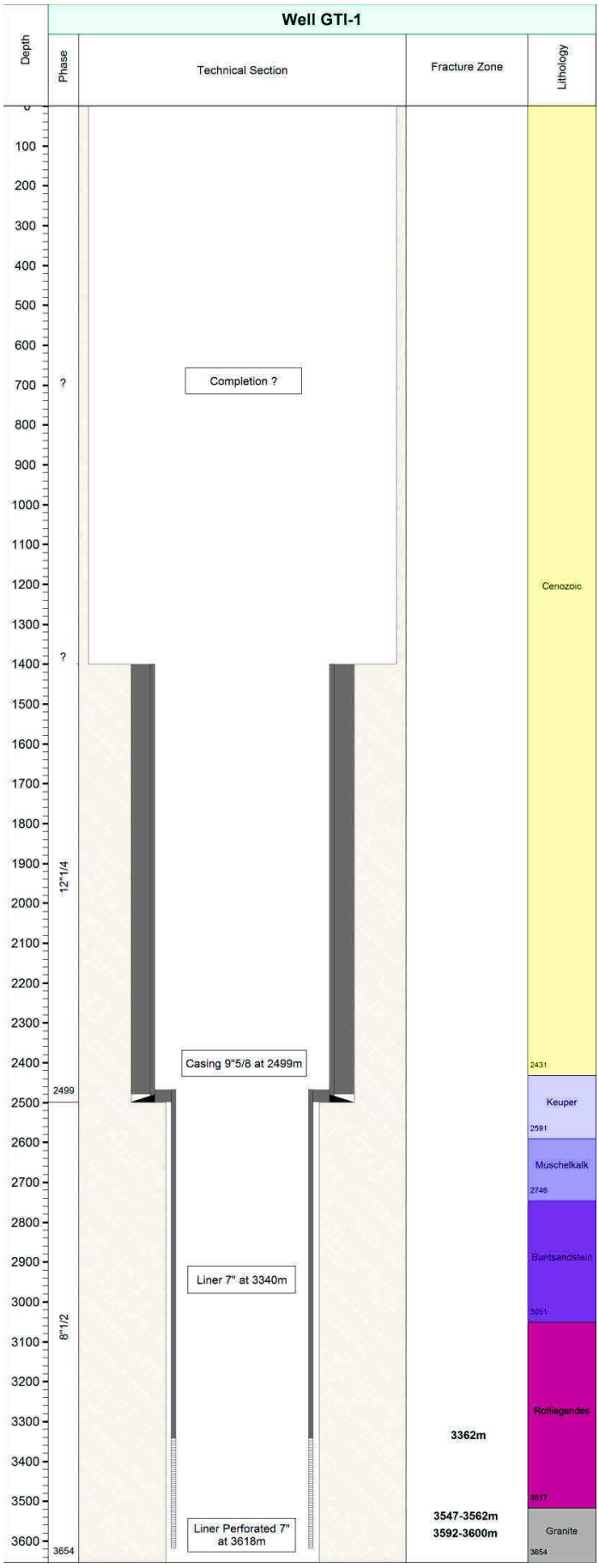

GEOTHERMIEKRAFTWERK INSHEIM

Données du puits de production GTI-2	*Date de forage :*	28/01/2009 - 20/04/2009
	Coordonnées géographiques :	Non communiquées
	Cible :	Partie Nord de la faille normale à fort plongement recoupée par GTI-1
	Trajectoire :	Déviée vers le Nord-Est
	Fond de puits :	3846 m de profondeur – Toit du Granite
	Complétion :	Section 8”1/2 à partir de 2515 m avec Liner 7” jusqu’à 2981 m puis Liner perforé 7”
	Développement :	-
	Profil thermique :	Non communiqué
	Température en fond de puits :	Non communiquée
	Gradient de température :	Non communiqué
	Toit de la convection :	Non communiqué
	Indice de productivité :	-
	Zones productrices :	Zones de failles à environ 2718-2736 m (Muschelkalk), zones productrices plus profondes non publiées
	Fracturation naturelle :	Imageries de paroi non publiées
	Orientation S_{Hmax} :	N-S

Coupe géologique et technique du puits de production GTI-2

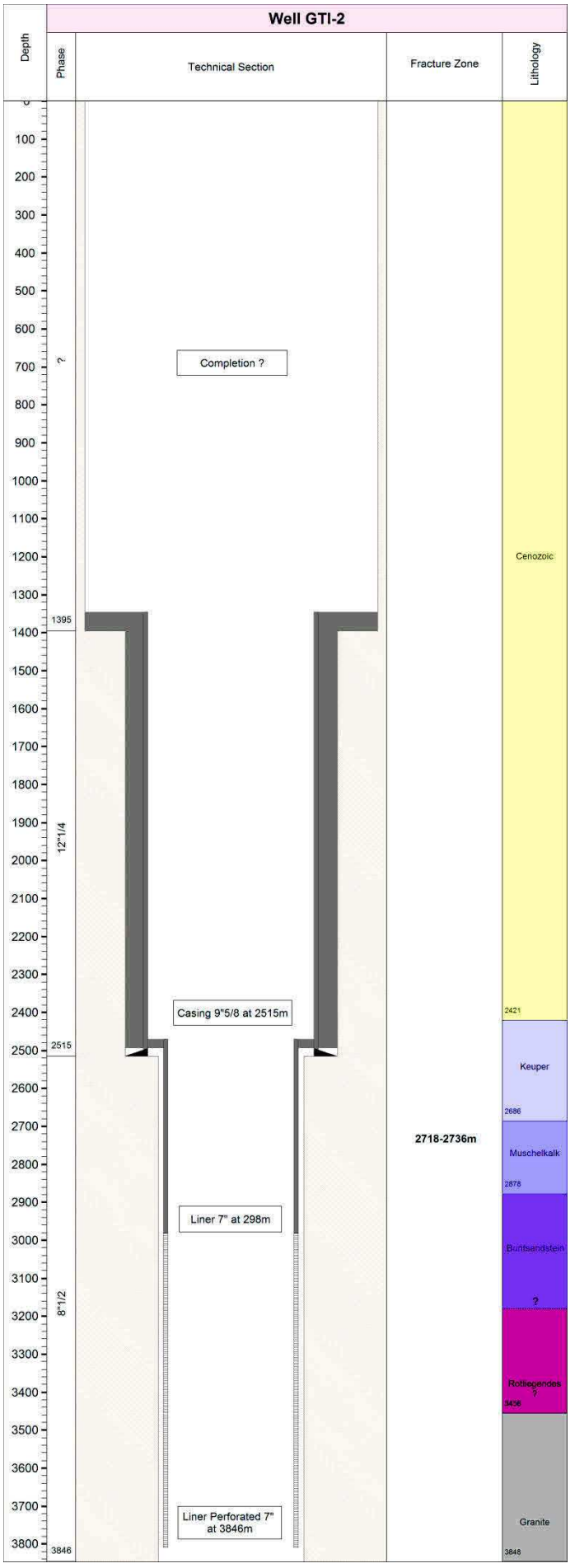

GEOTHERMIEKRAFTWERK INSHEIM

Références

Baumgärtner, J., Teza, D., Hettkamp, T., Gandy, T. and Schindler, M., 2010. Geothermal Reservoir Development in the Upper Rhine Graben “Concepts, Techniques and Experiences” The geothermal projects in Landau and Insheim*, Proceedings of Second European Geothermal Review*, Mainz, Germany

Baumgärtner, J., 2013. Geothermal 2.0: The Insheim Geothermal Power Plant. The second generation of geothermal power plants in the Upper Rhine Graben, *Proceedings of Third European Geothermal Review*, Mainz, Germany

Baumgärtner, J., Teza, D., Wahl, G., 2013. Gewinnung geothermischer Energie durch Entwicklung und Zirkulation eines Störungssystems im Kristallin und deren mikroseismische Überwachung am Beispiel des Geothermieprojektes Insheim, *Final Report Bestec No. 325158*, Germany

Baumgärtner, J., 2014. The Insheim Project – Geothermal from a German Point of View, *Proceedings of Deep Geo Day,* Paris, France

Baria, R., Baumgärtner, J., Teza, D., Bennett, T., Glass, H., Jupe, A., 2016. Development of geothermal technology to address the climate change issue in the densely populated areas of the world, *Proceedings of European Geothermal Congress 2016*, Strasbourg, France.

GEOTHERMIE-BOHRUNG IN BRÜHL

Données générales	*Compagnie :*	GeoEnergy GmbH		
	Position géographique :	*Pays* Allemagne		
		Région Baden-Württemberg		
		Ville Brühl		
Données d'exploration	*Campagne d'exploration :*	Ré-interprétation de données sismiques pétrolières Acquisition de données sismiques 2D et 3D Etude de faisabilité		2005-2008
		Etudes de risque sismique		2008-2011
	Exploitation pétrolière :	-		
	Contexte géologique :	Le site est situé à moins de 10 km à l'Ouest de la faille bordière Est, dans la zone d'accommodation du bassin d'Heidelberg de type « pull-apart ».		
	Cible :	Faille normale à fort plongement Ouest visible en sismique qui s'étend sur 3 km		
	Concept :	Hydrothermal		
	Modèle 3D :	Oui		
Données de production	*Production :*	Electricité	*Nombre de puits :*	1
	Puissance installée :	-	*Débit de production :*	-
	Système :	-	*Température de pompage :*	-
	Statut actuel :	Doublet en cours	*Température d'injection :*	-
Données de sous-sol	*Réservoir :*	Buntsandstein		
	Profondeur du réservoir (top) :	3000 m		
Fluide géothermal	*Salinité :*	98 g/L		
	Ions majeurs :	Cl Na Ca		
	Gaz :	CO_2 86% - CH_4 2.5% - He 0.4%		

Historique du projet	
2005-2008	Première phase d'exploration avec ré-interprétation et nouvelle acquisition de données sismiques
2008-2011	Deuxième phase d'exploration avec plusieurs études sismiques suite aux évènements sismiques sur les projets de géothermie voisins
2012-2013	Forage du premier puits dont le débit et la température sont suffisants pour un projet viable économiquement
2013-2015	Attente de financements pour le second puits
2016	Abandon du projet

GEOTHERMIE-BOHRUNG IN BRÜHL

Carte des failles au toit du Buntsandstein

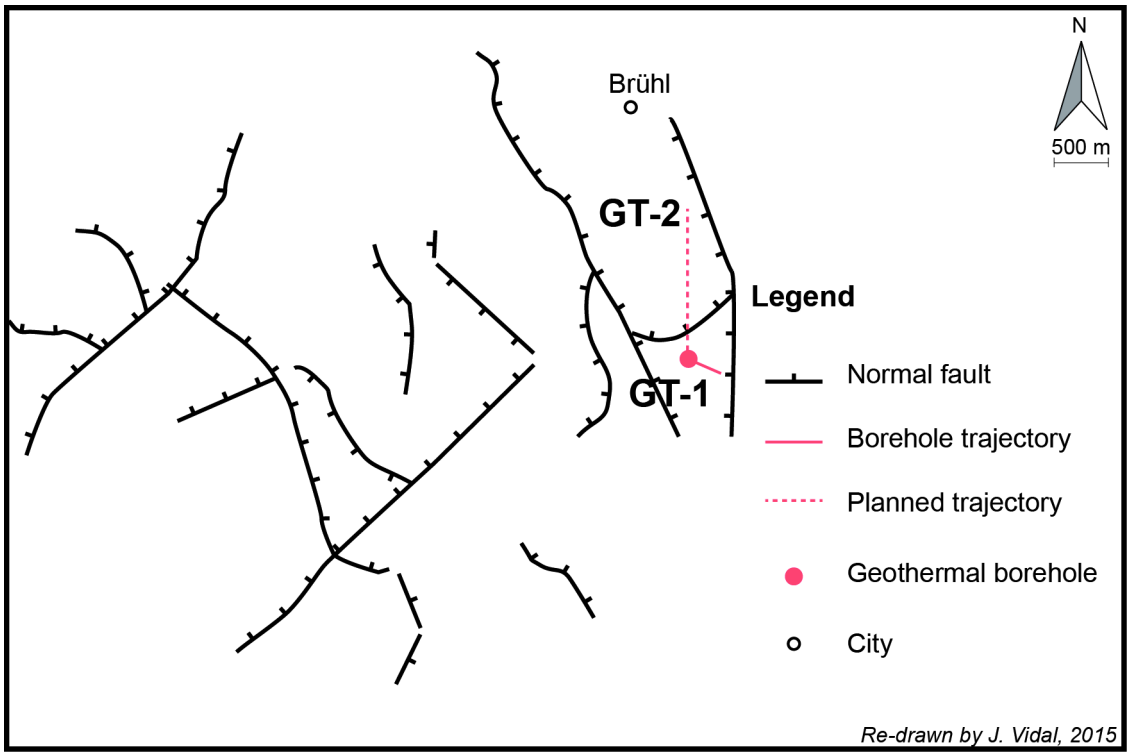

Coupe géologique du site

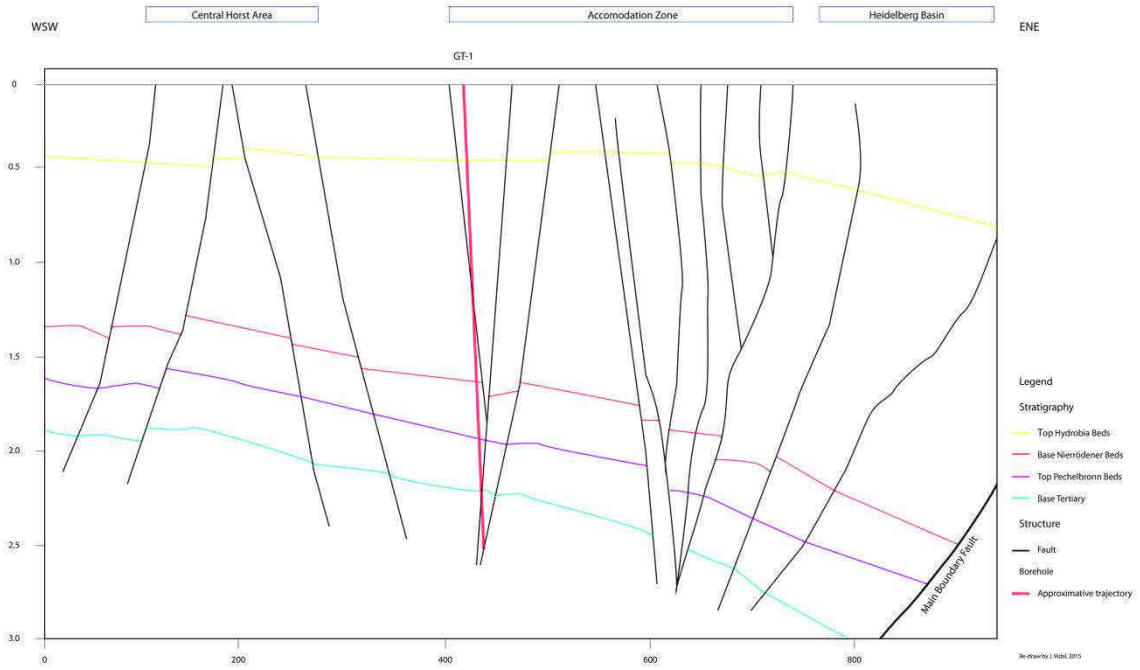

L'interprétation géologique est en temps et ne prend pas en compte le profil de vitesse du site

GEOTHERMIE-BOHRUNG IN BRÜHL

Données du puits de production GT-1	*Date de forage :*	14/07/2012 - 10/02/2013	
	Coordonnées géographiques :	Non communiquées	
	Cible :	Branche Sud d'une faille normale qui recoupe le Buntsandstein avec une direction Nord-Sud et un plongement Ouest de 75°	
	Trajectoire :	Déviée de moins de 30° vers le Sud-Est, KOP=2250 m	
	Fond de puits :	3319 m de profondeur - Buntsandstein	
	Complétion :	Section 7"5/8 à partir de 2903 m de profondeur avec Liner 6" 5/8 jusqu'à 3155 m	
	Développement :	2013	Test artésien 70 L/s pendant 12h avec une chute de 3 bar ds le réservoir Test d'injection de 3000 m^3 à 95 L/s avec une pression <30 bar en tête de puits et aucune sismicité ressentie
	Profil thermique :	Acquis en septembre 2013, 6 mois après la fin des opérations de forage et de développement (mars 2013)	
	Température en fond de puits :	158.5°C	
	Gradient de température :	45 K/km dans la partie en conduction	
	Toit de la convection :	Effet de la convection non visible	
	Indice de productivité :	3.5 L/s/bar	
	Zones productrices :	Zones de perte vers 3150 m à un débit de 0.6 L/s puis 2 L/s à partir de 3190 m et jusqu'à 3210 m, puis les pertes diminuent à 1.5 L/s. Les pertes totales s'élèvent à 250 m^3 après 2 jours de forage dans la section en trou ouvert.	
	Fracturation naturelle :	Famille principale orientée N170°E avec un pendage subvertical	
	Orientation S_{Hmax} :	N140°E entre 3160-3294 m (Buntsandstein)	
Emplacement prévisionnel pour le puits GT-2	*Cible prévisionnelle :*	Branche Nord de la faille recoupée par GT-1 dans le Buntsandstein avec une direction NO-SE et un plongement Ouest de 75°	
	Trajectoire prévisionnelle :	Séparation de 1.4 km en profondeur avec GT-1	

Coupe géologique et technique du puits de production GT-1

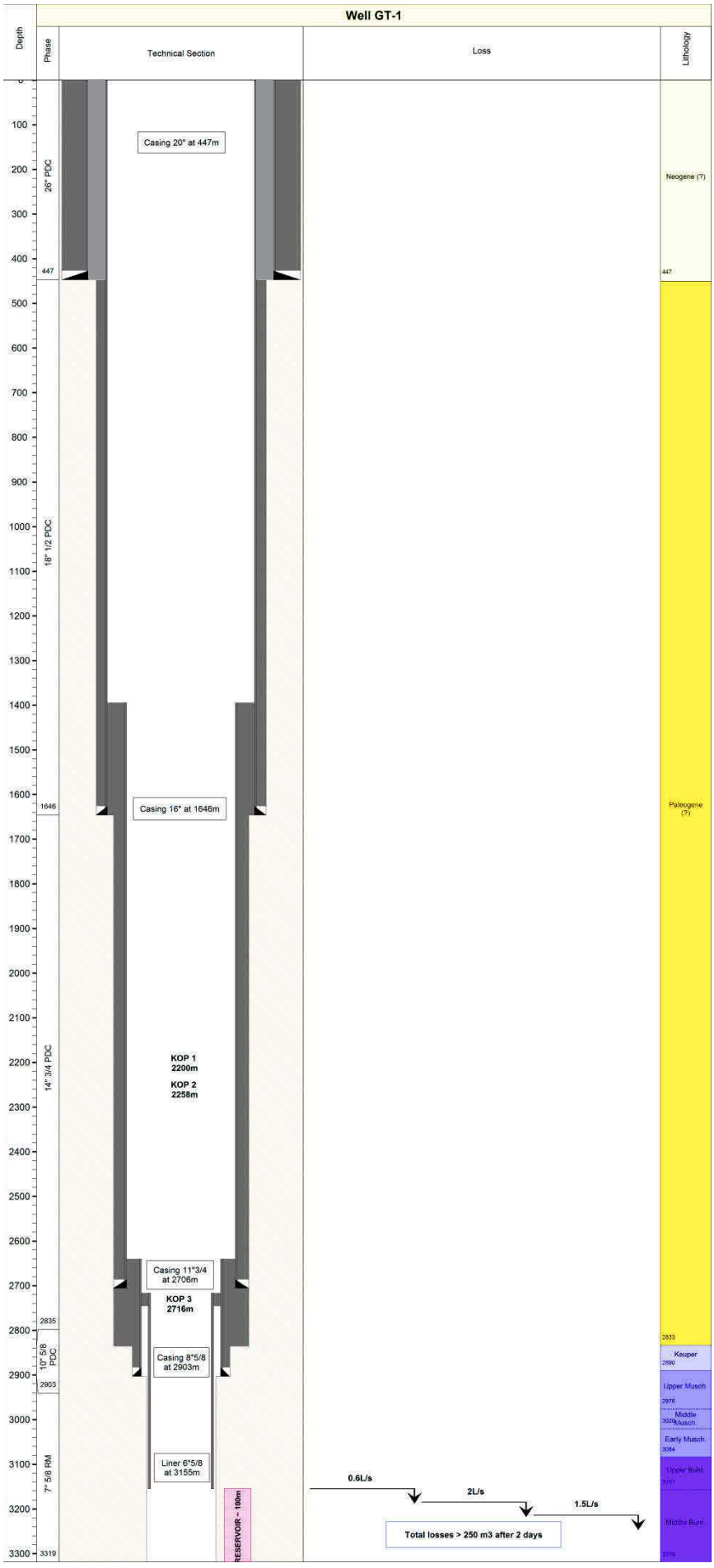

GEOTHERMIE-BOHRUNG IN BRÜHL

Profil thermique dans le puits

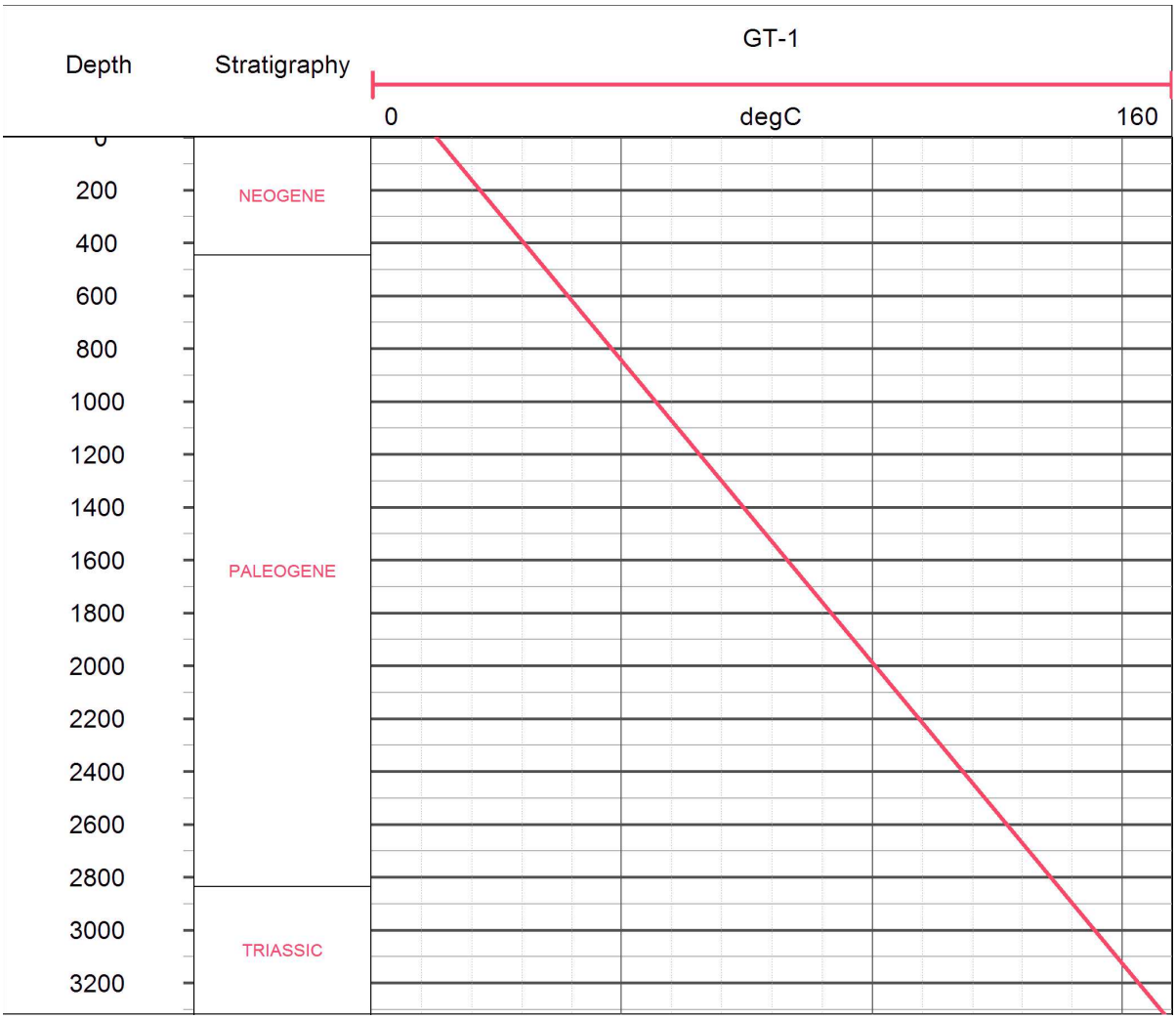

Le profil thermique est une approximation par régression linéaire des données réelles acquises à l'équilibre thermique et dans le casing du puits géothermique GT-1 en septembre 2013.

GEOTHERMIE-BOHRUNG IN BRÜHL

Références

Lotz, U., 2013. Geothermal Project Brühl – specific challenges for geothermal projects in Baden-Württemberg*, Proceedings of Third European Geothermal Review*, Mainz, Germany

Melchert, B., Stober, S., Lotz, U., 2013. Erste Ergebnisse der hydraulischen Testmaßnahmen und geochemischen Analysen der Geothermie-Bohrung GT1 in Brühl / Baden-Württemberg. *Proceedings of Geothermiekonferen*z, Essen , Germany

Reinecker, J., Bauer, J., Philipp, S.L., 2013. Fault zones and associated fracture systems in geothermal exploration. *AuGE Project*

PROJET INDUSTRIEL DE GEOTHERMIE DE RITTERSHOFFEN

Données générales	*Compagnie :*	ECOGI, Exploitation de la Chaleur d'Origine Géothermale pour l'Industrie		
	Position géographique :	*Pays* France *Région* Alsace, Bas Rhin *Ville* Rittershoffen		
Données d'exploration	*Campagne d'exploration :*	Ré-interprétation de données sismiques pétrolières et de données de puits pétroliers alentours 2006-2009		
	Exploitation pétrolière :	Les sondages pétroliers autour de Rittershoffen ont montré des indices très faibles d'hydrocarbures		
	Contexte géologique :	Le site est situé à environ15 km à l'Est de la faille bordière Est, et à 8 km à l'Est du site de Soultz au centre d'une structure de graben.		
	Cible :	Faille de Rittershoffen à l'interface sédiments-socle visible en sismique		
	Concept :	EGS/hydrothermal		
	Modèle 3D :	Oui		
Données de production	*Production :*	Chaleur	*Nombre de puits :*	2
	Puissance installée :	24 MWth	*Débit de production :*	70-80 L/s
	Système :	Chauffage de réseau de chaleur	*Température de pompage :*	166-168°C
	Statut actuel :	Exploitation	*Température d'injection :*	70°C
Données de sous-sol	*Réservoir :*	Interface sédiments-socle		
	Profondeur du réservoir (top) :	1900 m		
Fluide géothermal	*Salinité :*	100 g/L		
	Ions majeurs :	Cl Na		
	Gaz :	N_2 80% - O_2 18%		

Historique du projet

2006	Etude de préfaisabilité à partir des données d'anciens puits pétroliers de la région
2007-2008	Ré-interprétation des données de sismique réflexion. Création de la société ECOGI (Groupe ES, Roquette Frères, Caisse des dépôts et des consignations)
2012	Forage du premier puits GRT-1
2013	Stimulation du puits GRT-1 et campagne de sismique réflexion
2014	Forage du second puits du doublet géothermique GRT-2 et test de traçage et de production
2015-2016	Construction de 15 km de canalisation entre la centrale géothermique et la bioraffinerie Roquette Frères à Beinheim Mise en service en juin 2016

PROJET INDUSTRIEL DE GEOTHERMIE DE RITTERSHOFFEN

Carte des failles à l'interface sédiments-socle

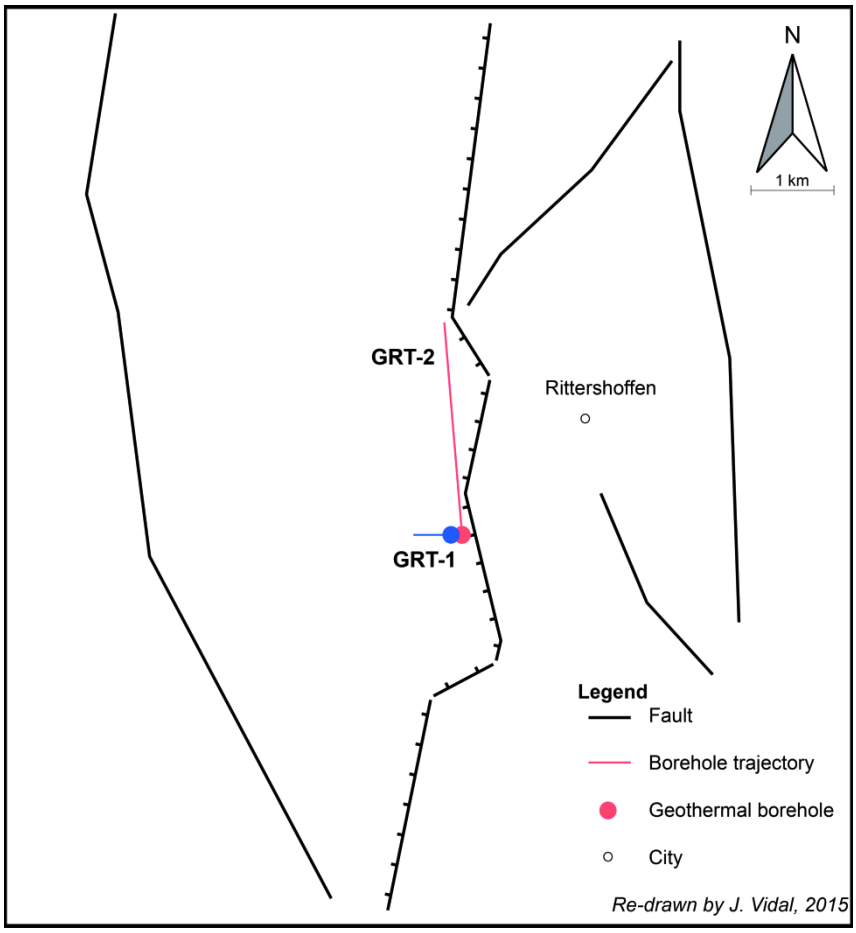

Modèle 3D du site

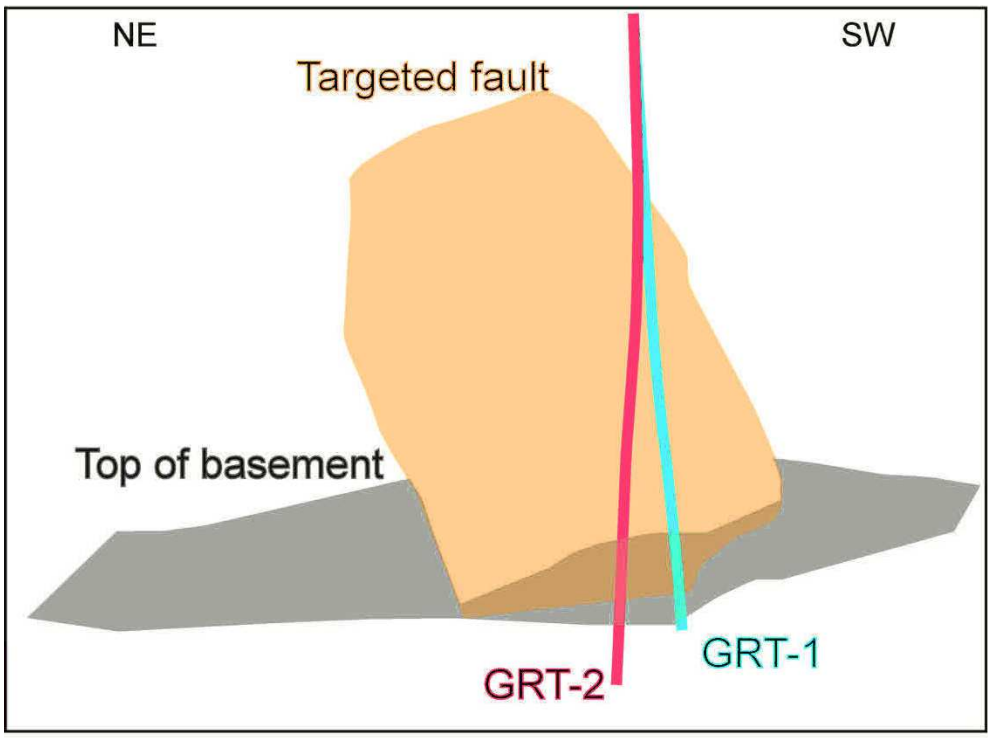

PROJET INDUSTRIEL DE GEOTHERMIE DE RITTERSHOFFEN

Données du puits d'injection GRT-1

Date de forage :	09/2012 - 12/2012	
Coordonnées géographiques :	7°56'19"E 48°53'49"N	
Cible :	Branche N-S de la faille de Rittershoffen à l'interface sédiment-socle	
Trajectoire :	Légèrement déviée de 8° vers l'Ouest	
Fond de puits :	2580 m de profondeur – Toit du granite	
Complétion :	Section 8.5 " en trou ouvert à partir de 1922 m de profondeur	
Développement :	04/2013	Stimulation thermique : injection de 4200 m^3 en tête de puits durant 60h
	06/2013	Stimulation chimique : injection d'un fluide biodégradable contenant des agents GLTA dans des zones localisées à l'aide de packer afin de dissoudre les carbonates et les sulphates dans les zones de fractures
		Injection hydraulique basse pression : injection de 3250 m^3 en tête de puits par palier de 10 l/s à 80 L/s
Profil thermique :	Acquis en décembre 2015 à l'équilibre thermique	
Température en fond de puits :	160°C	
Gradient de température :	90 K/km dans la partie en conduction > 5°K/km dans la partie au toit de la convection	
Toit de la convection :	1650 m TVD	
Indice d'injectivité :	0.5 L/s/bar avant stimulation et 2.5 L/s/bar après	
Zones productrices :	Cluster de fractures de 1995 à 2000 m de profondeur (Buntsandstein) perméables après stimulation Zone de faille perméable de 2325 à 2370 m de profondeur avec le drain majeur perméable (N170°E, 55°W) à 2368 m de profondeur (Granite altéré) qui contrôle les 2/3 du débit	
Fracturation naturelle :	N10°E, 60°W	
Orientation S_{Hmax} :	N166°E +/-11°	

Coupe géologique et technique du puits d'injection GRT-1

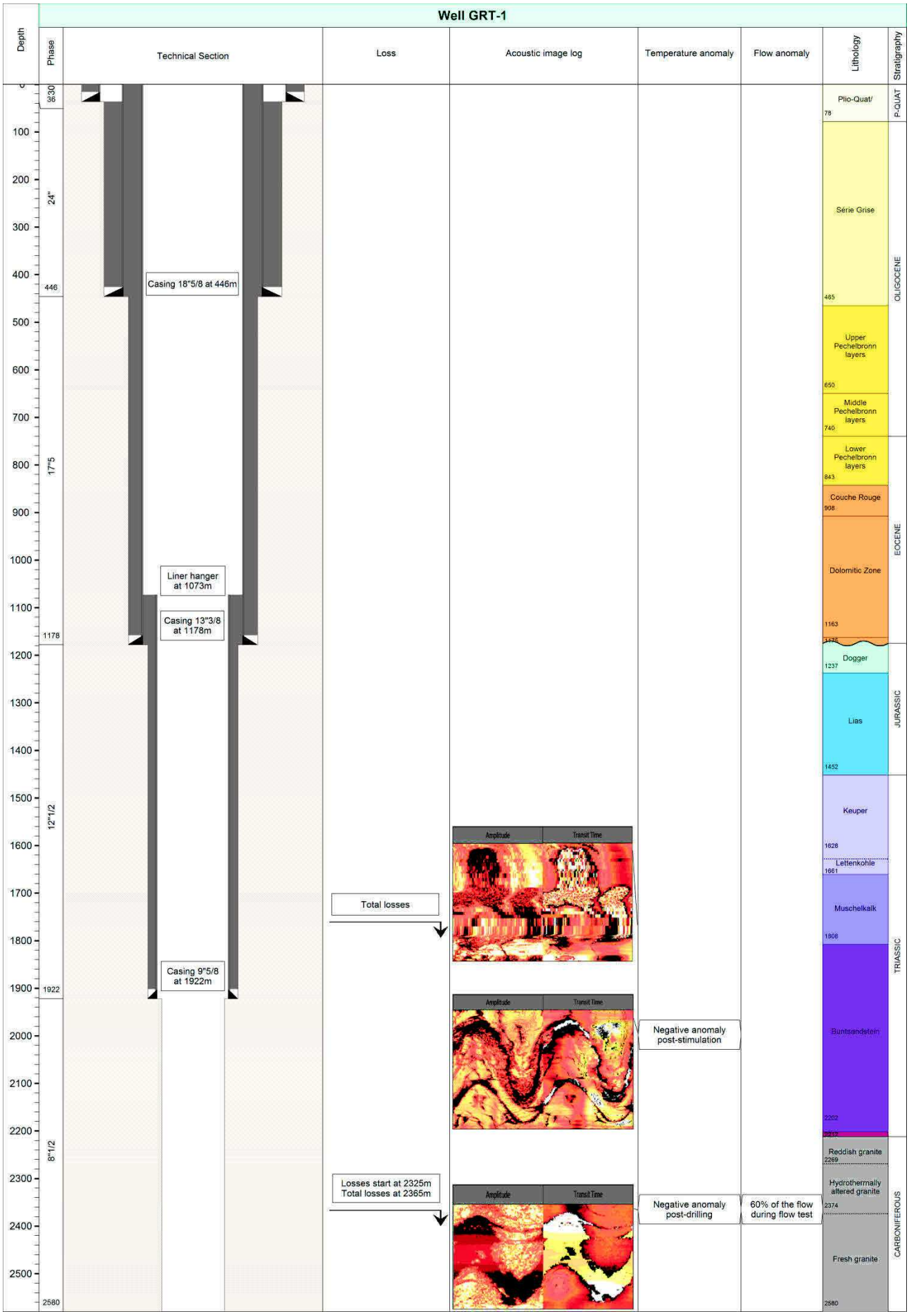

PROJET INDUSTRIEL DE GEOTHERMIE DE RITTERSHOFFEN

Données du puits de production GRT-2	*Date de forage :*	03/2014 – 07/2014
	Coordonnées géographiques :	7°56'19"E 48°53'49"N
	Cible :	Relai NNE-SSW entre deux branches N-S de la faille de Rittershoffen à l'interface sédiment-socle
	Trajectoire :	Déviée de 1°/10m° à partir de 663 m puis de 37° à la fin du puits vers le Nord
	Fond de puits :	3196 m de profondeur – Toit du granite
	Complétion :	Section 8"1/2 en trou ouvert à partir de 2120 m de profondeur
	Développement :	-
	Profil thermique :	Acquis en juillet 2015 à l'équilibre thermique
	Température en fond de puits :	180°C
	Gradient de température :	90 K/km dans la partie en conduction > 15°K/km dans la partie en convection
	Toit de la convection :	1650 m TVD
	Indice de productivité :	3.5 L/s/bar
	Zones productrices :	Cluster de fractures perméables de 2245 à 2264 m de profondeur (Buntsandstein) et 2453 à 2459 m MD (Permien) Cluster de fractures perméables de 2532 à 2543 m de profondeur (Toit du granite) Zone de faille perméable de 2765 à 2800 m MD avec un drain majeur perméable (N170°E, 65°W) à 2774 m de profondeur (Granite altéré) Cluster de fractures perméables à 2950 m et 3050 m de profondeur (Granite profond) mais non imagée
	Fracturation naturelle :	N170°E, 80°E
	Orientation S_{Hmax} :	N165 +/- 11°E

Coupe géologique et technique du puits de production GRT-2

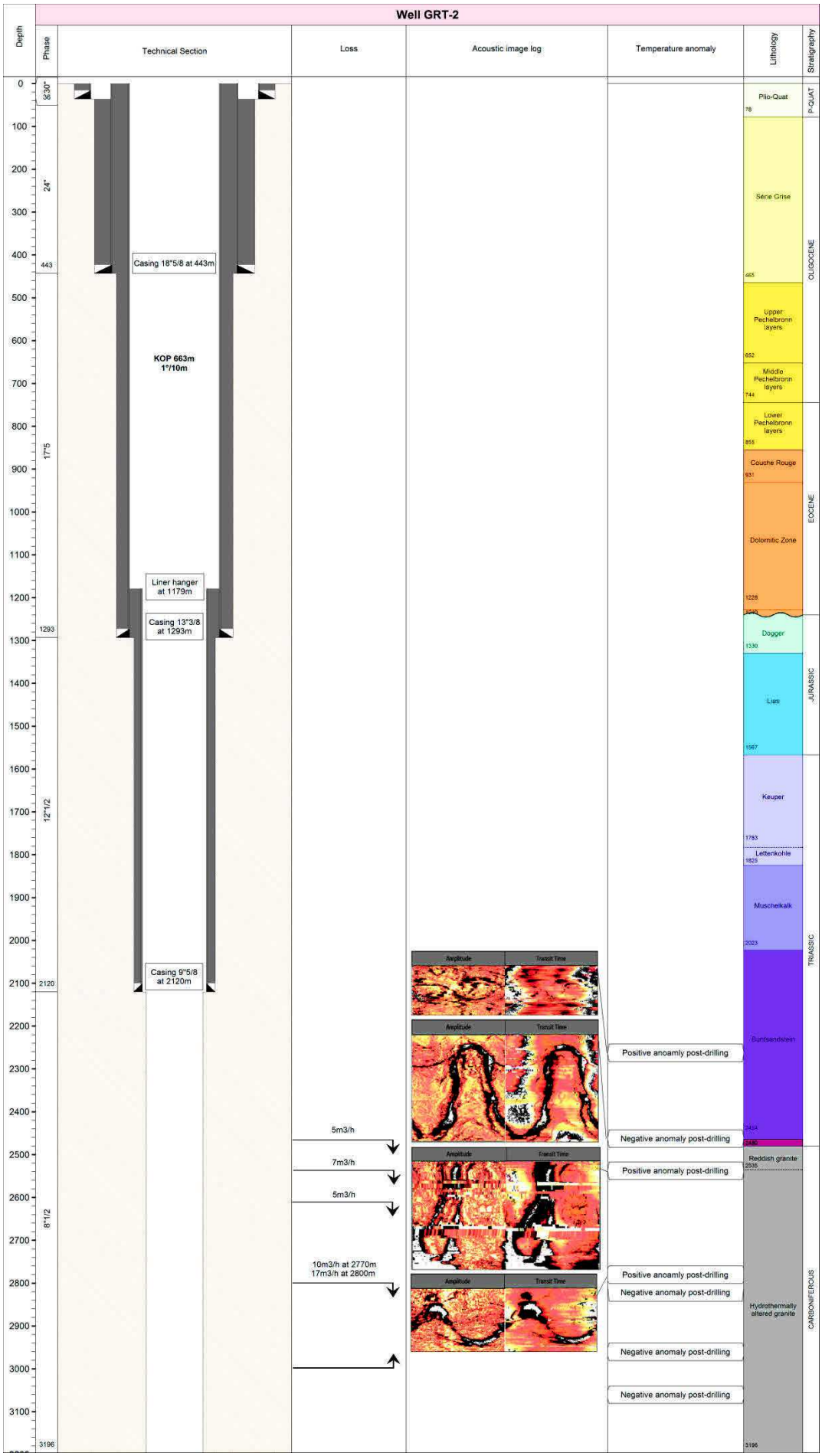

PROJET INDUSTRIEL DE GEOTHERMIE DE RITTERSHOFFEN

Profils thermiques dans les puits

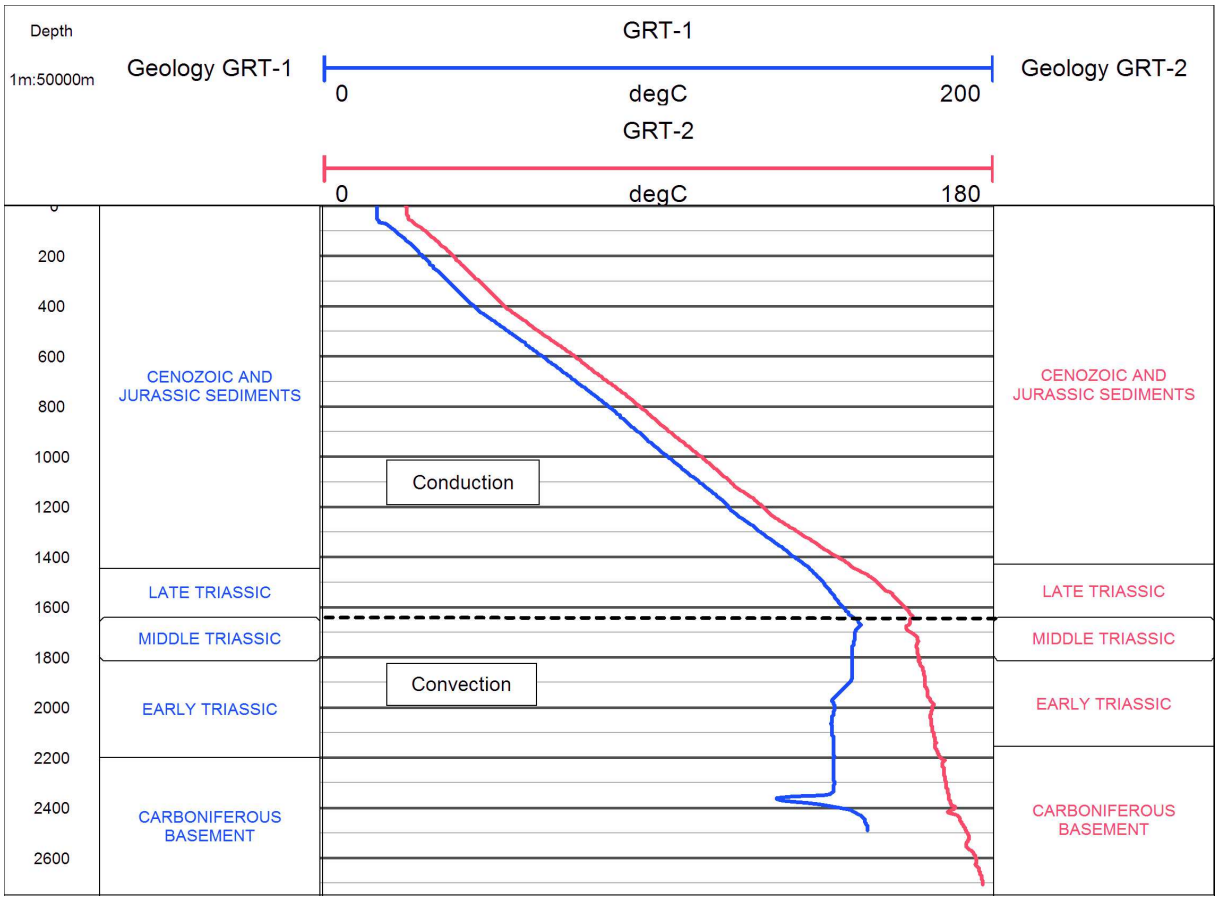

Les profils thermiques ont été acquis à l'équilibre thermique et dans le casing des puits géothermiques GRT-1 et GRT-2 en juillet 2015.La profondeur est en True Vertcal Depth.

Profils thermiques dans les puits

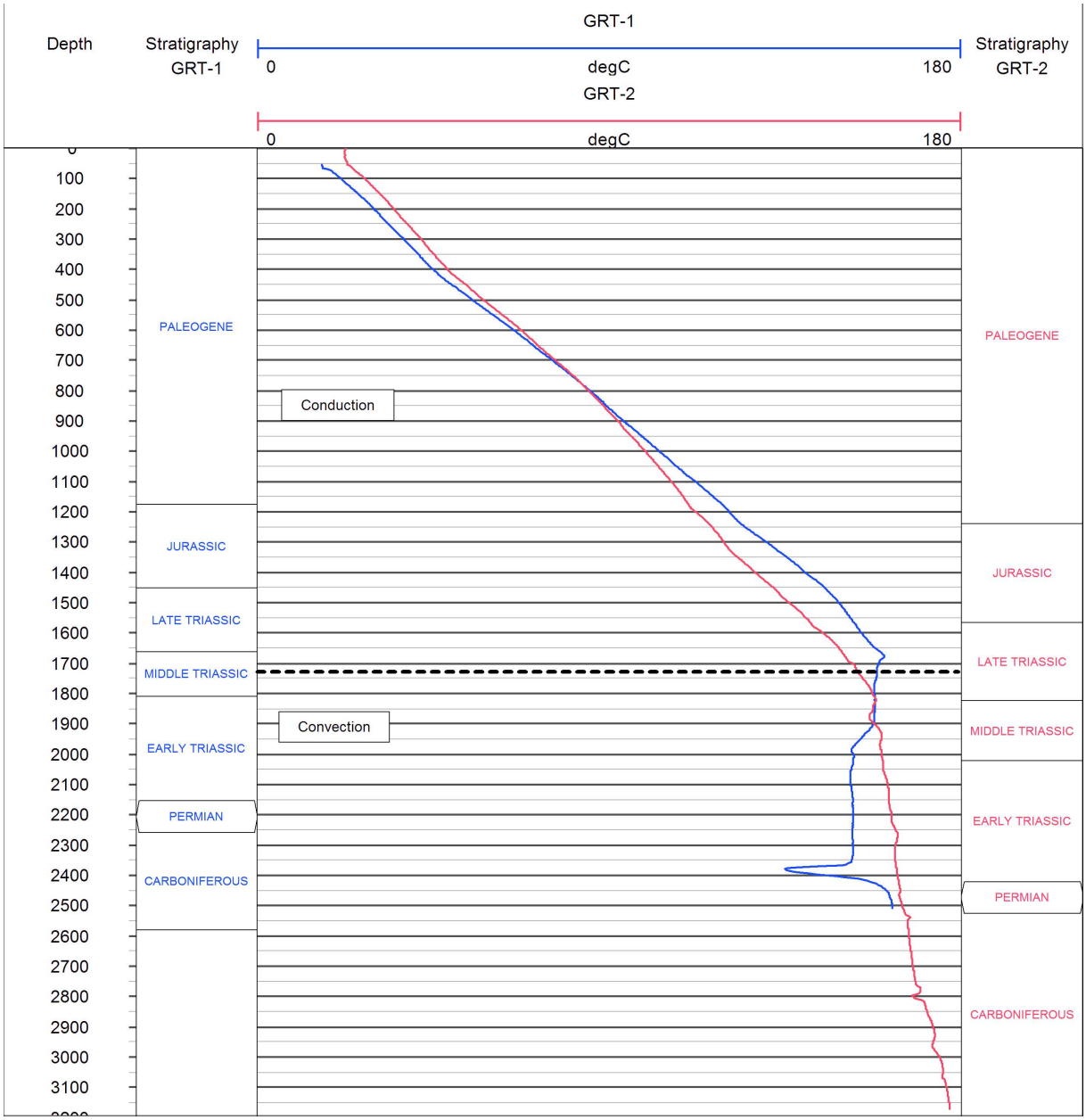

Les profils thermiques ont été acquis à l'équilibre thermique et dans le casing des puits géothermiques GRT-1 et GRT-2 en juillet 2015.La profondeur est en Measured Depth.

PROJET INDUSTRIEL DE GEOTHERMIE DE RITTERSHOFFEN

Références

Baujard, C., Genter, A., Graff, J.-J., Maurer, V., Dalmais, E., 2015. ECOGI, a New Deep EGS Project in Alsace, Rhine Graben, France, in *Proceedings of World Geothermal Congress 2015*, Melbourne, Australia.

Baujard, C., Genter, A., Dalmais, E., Maurer, V., Hehn, R., Rosillette, R., Vidal, J., Schmittbuhl, J., 2017. Hydrothermal characterization of wells GRT-1 and GRT-2 in Rittershoffen, France: Implications on the understanding of natural flow systems in the rhine graben. Geothermics, 65, 255–268

Hehn, R., Genter, A., Baujard, C., Vidal, J., 2016. Stress field rotation in the EGS well GRT-1 (Rittershoffen, France), in *Proceedings of European Geothermal Congress 2016*, Strasbourg, France.

Recalde Lummer, N., Rauf, O., Gerdes, S., Genter, A., Scheiber, J., Villadangos, G., 2014. New biodegradable stimulation system - First field trial in granite/Bunter sandstone formation for a geothermal application in the Upper Rhine Valley, in *Proceedings of Deep Geothermal Days,* Paris, France.

Vidal, J., Genter, A., Chopin, F., Dalmais, E., 2016. Natural fractures and permeability at the geothermal site Rittershoffen, France, in *Proceedings of European Geothermal Congress 2016*, Strasbourg, France.

Vidal, J., Genter, A., Schmittbuhl, J., 2016. Pre- and post-stimulation characterization of geothermal well GRT-1, Rittershoffen, France: insights from acoustic image logs of hard fractured rock, *Geophys. J. Int.*, *206*(2), 845–860, doi:10.1093/gji/ggw181.

Vidal J., Genter A., Chopin F. 2017. Permeable fracture zones in the hard rocks of the geothermal reservoir at Rittershoffen, France, *Journal of Geophysical Research: Solid Earth*, 122

ANNEXE 2

		Type Major	Type Minor
	TRIAS	#1	#2
	PERMIEN	#3	#4
	GRANITE RUBEFIE	#5	#6
	GRANITE ALTERE	#7	#8
	QUARTZ VEIN	#9	

FRACTURES DANS LE PUITS GRT-1					
Geol	Depth	Dip Direction	Dip	Thickness	Type
	m	deg	deg	mm	
TRIAS	1931.22	7.50	77.08	0.00	#2
	1938.41	170.77	75.58	18.76	#2
	1955.84	315.95	63.43	0.00	#2
	1955.99	285.29	74.66	0.00	#2
	1978.36	290.35	69.03	5.34	#2
	1979.68	282.86	73.64	0.00	#2
	1979.86	280.54	75.71	0.00	#2
	1987.85	298.34	71.94	7.43	#2
	1989.42	279.32	67.13	26.32	#1
	1992.07	286.51	71.90	10.49	#2
	1994.85	295.88	69.65	15.94	#1
	1995.08	284.91	68.10	0.00	#2
	1995.27	279.17	69.01	0.00	#2
	1995.42	290.34	66.80	0.00	#2
	1995.66	303.71	67.25	2.97	#2
	1996.07	303.03	67.60	23.25	#1
	1996.69	285.06	66.16	9.62	#2
	1999.99	285.68	73.99	59.35	#1
	2000.76	288.10	75.19	33.49	#1
	2002.98	283.01	64.22	0.00	#2
	2003.68	275.16	73.04	4.64	#2
	2004.75	292.37	74.28	0.00	#2
	2005.19	290.25	73.25	105.07	#1
	2005.83	292.86	74.16	11.80	#2
	2007.02	292.23	75.98	49.91	#1
	2008.64	293.30	72.10	16.93	#1
	2020.13	284.06	70.14	0.00	#2
	2022.18	287.01	72.57	9.12	#2
	2026.51	300.86	69.21	10.93	#2
	2032.98	290.11	77.23	24.88	#2
	2038.78	297.42	76.03	5.29	#2
	2053.93	292.46	72.27	1.65	#2
	2054.87	296.82	74.29	14.37	#2
	2069.57	280.49	71.66	5.29	#2
	2073.20	280.85	72.63	5.66	#2

	2073.96	274.04	70.09	7.58	#2
	2077.04	315.56	58.74	0.00	#2
	2077.13	274.89	63.33	0.00	#2
	2079.37	279.58	68.66	13.76	#2
	2083.71	296.16	65.83	2.63	#2
	2087.23	295.65	62.32	3.91	#2
	2088.21	289.69	46.26	4.20	#2
	2094.01	281.41	58.19	0.00	#2
	2108.81	275.48	65.14	4.05	#2
	2113.81	282.26	71.30	3.63	#2
	2128.47	275.70	69.36	24.66	#2
	2146.24	267.04	77.76	0.00	#2
	2156.08	301.75	72.85	0.00	#2
	2156.51	294.55	53.16	8.85	#2
PERMIEN	2161.54	284.42	63.70	0.00	#2
	2161.99	288.23	59.46	0.00	#2
	2170.13	287.11	67.15	17.78	#2
	2170.84	295.51	66.24	27.64	#2
	2171.38	295.66	58.74	0.00	#2
	2171.85	285.36	66.71	3.43	#2
	2175.14	315.53	66.85	22.66	#2
	2176.65	287.05	70.08	0.00	#2
	2177.19	286.27	68.59	7.57	#2
	2179.60	300.29	70.78	0.00	#2
	2179.97	275.91	70.51	0.00	#2
	2180.88	280.60	57.72	0.00	#2
	2182.61	284.99	70.71	20.34	#2
	2184.59	290.71	69.63	36.69	#2
	2189.09	284.46	75.46	0.00	#2
	2193.01	283.34	74.41	0.00	#2
	2200.41	311.52	65.61	15.54	#2
	2200.68	299.59	59.30	1.39	#2
	2208.21	100.98	69.12	0.00	#2
TOIT RUBEFIE	2212.27	281.14	29.67	0.00	#4
	2212.40	282.77	37.60	0.00	#4
	2212.71	289.45	44.86	0.00	#4
	2212.81	287.82	50.44	0.00	#4
	2212.97	289.59	47.68	0.00	#4
	2213.18	319.22	39.55	0.00	#4
	2213.20	285.25	58.30	7.52	#4
	2213.62	315.04	48.90	12.15	#4
	2213.96	292.92	44.59	0.00	#4
	2214.31	293.89	56.80	6.62	#4
	2214.40	293.94	47.99	0.00	#4
	2214.61	285.39	53.01	0.00	#4

	2214.85	283.91	60.43	6.54	#4
	2215.21	292.00	60.81	8.99	#4
	2215.31	101.33	40.39	0.00	#4
	2215.59	322.70	49.10	0.00	#4
	2216.05	305.40	52.61	14.18	#4
	2216.58	298.69	54.16	0.00	#4
	2217.15	272.42	31.14	0.00	#4
	2218.17	350.91	61.39	6.82	#4
	2219.09	318.64	57.53	0.00	#4
	2219.95	264.89	29.89	0.00	#4
	2220.15	293.48	58.92	7.42	#4
	2220.41	127.76	42.86	0.00	#4
	2220.94	152.86	66.43	0.00	#4
	2221.96	324.56	31.94	0.00	#4
	2222.07	244.38	56.90	0.00	#4
	2222.12	278.49	47.27	0.00	#4
	2222.38	274.53	51.23	0.00	#4
	2222.69	257.64	52.92	9.82	#4
	2222.82	241.24	56.36	0.00	#4
	2223.05	262.15	54.30	0.00	#4
	2223.68	297.66	56.64	0.00	#4
	2223.90	295.28	52.30	0.00	#4
TOIT RUBEFIE	2224.04	286.15	52.57	0.00	#4
	2224.25	281.23	50.98	0.00	#4
	2224.57	269.49	52.61	0.00	#4
	2225.26	270.33	52.88	12.34	#4
	2225.49	51.46	52.12	0.00	#4
	2225.53	284.26	57.38	9.44	#4
	2225.68	248.04	55.23	0.00	#4
	2226.18	280.30	40.01	0.00	#4
	2226.48	257.92	58.23	7.03	#4
	2226.66	247.37	60.86	0.00	#4
	2226.80	250.40	63.45	0.00	#4
	2227.08	245.81	62.97	23.23	#4
	2227.39	248.59	54.59	0.00	#4
	2227.49	252.64	55.01	3.99	#4
	2228.11	258.27	59.89	0.00	#4
	2229.03	1.04	78.29	0.00	#4
	2229.26	319.96	53.52	0.00	#4
	2230.29	247.15	62.19	5.24	#4
	2230.54	255.75	61.01	0.00	#4
	2231.91	247.24	58.29	8.75	#4
	2232.98	90.92	72.05	11.22	#4
	2233.59	331.48	29.02	0.00	#4
	2233.60	286.91	57.52	0.00	#4

	2233.96	282.45	55.31	8.91	#4
	2233.96	75.34	70.48	0.00	#4
	2234.31	259.53	57.56	0.00	#4
	2234.95	287.24	61.72	0.00	#4
	2235.27	309.46	62.33	0.00	#4
	2235.69	280.53	67.05	0.00	#4
	2235.85	261.35	60.63	0.00	#4
	2236.10	292.31	49.30	0.00	#4
	2236.68	276.65	59.90	109.03	#3
	2237.57	309.38	52.64	264.48	#4
	2237.95	7.14	48.46	0.00	#4
	2238.25	336.98	55.06	0.00	#4
	2238.51	56.08	58.27	0.00	#4
	2239.18	247.56	37.12	0.00	#4
	2240.72	324.41	54.75	0.00	#4
	2240.92	289.50	57.27	0.00	#4
	2241.01	281.18	62.93	0.00	#4
	2241.32	299.55	61.11	18.76	#4
	2241.62	291.40	55.63	0.00	#4
	2241.97	338.89	70.31	0.00	#4
	2242.55	272.46	59.91	0.00	#4
	2245.03	169.10	71.00	0.00	#4
	2245.31	148.26	65.93	5.73	#4
	2250.52	333.55	58.70	0.00	#4
	2250.74	343.95	55.07	0.00	#4
	2250.86	343.07	51.42	0.00	#4
	2251.30	334.03	50.60	0.00	#4
	2251.91	311.21	58.11	0.00	#4
	2253.50	283.67	55.62	5.44	#4
	2254.83	342.56	55.70	0.00	#4
	2265.64	300.14	52.99	0.00	#4
	2266.23	115.06	82.68	0.00	#4
	2266.50	135.10	77.00	30.45	#4
	2267.16	247.99	69.82	21.84	#4
GRANITE ALTERE	2270.27	283.87	68.55	0.00	#6
	2270.82	284.75	57.00	0.00	#6
	2271.02	286.76	60.37	0.00	#6
	2271.44	279.00	63.02	8.80	#6
	2271.60	276.59	63.91	6.34	#6
	2271.90	287.04	53.86	0.00	#6
	2278.55	292.74	44.28	0.00	#6
	2282.22	273.18	60.14	0.00	#6
	2282.37	284.34	55.73	0.00	#6
	2282.49	285.94	48.02	0.00	#6
	2282.82	301.46	44.68	0.00	#6

	2282.92	283.33	49.39	4.55	#6
	2283.07	287.91	56.63	37.30	#6
	2283.32	278.97	48.31	37.42	#6
	2283.66	272.76	49.10	28.25	#6
	2283.94	257.98	50.00	0.00	#6
	2284.20	324.04	62.41	0.00	#6
	2284.24	237.99	58.11	5.65	#6
	2285.56	320.77	57.43	0.00	#6
	2285.68	303.44	55.14	0.00	#6
	2285.99	310.51	65.36	34.04	#6
	2286.24	300.84	47.94	13.42	#6
	2286.43	303.42	44.59	0.00	#6
	2286.68	282.66	55.25	0.00	#6
	2286.95	257.80	46.59	0.00	#6
	2287.04	270.19	44.80	32.12	#6
	2287.55	299.75	55.04	0.00	#6
	2287.77	285.36	55.67	0.00	#6
	2287.92	282.83	58.14	0.00	#6
	2288.13	275.19	51.00	0.00	#6
	2288.72	282.95	66.31	0.00	#6
	2289.11	284.43	62.91	0.00	#6
	2291.58	295.04	61.47	4.20	#6
	2294.15	260.56	47.11	0.00	#9
	2294.20	315.81	59.95	0.00	#6
	2294.45	303.69	53.61	3.54	#6
	2297.08	286.77	68.66	5.29	#6
	2298.85	339.13	56.93	15.47	#9
	2305.53	268.97	62.12	0.00	#6
	2305.58	101.10	78.15	0.00	#6
	2305.63	264.91	61.09	0.00	#6
	2307.21	284.57	65.53	0.00	#9
GRANITE ALTERE	2308.01	283.10	62.93	0.00	#6
	2308.51	272.89	63.81	2.82	#6
	2308.60	277.13	59.84	0.00	#6
	2309.22	268.32	63.76	0.00	#6
	2309.62	273.98	57.21	0.00	#6
	2310.17	271.26	63.17	0.00	#6
	2311.33	270.79	64.68	0.00	#6
	2311.72	266.47	62.96	0.00	#6
	2311.86	271.46	64.16	0.00	#6
	2312.36	272.17	60.96	0.00	#6
	2313.06	274.07	66.75	0.00	#6
	2314.19	274.86	55.72	0.00	#6
	2315.05	271.08	64.90	4.87	#6
	2315.23	266.75	61.32	0.00	#6

	2315.91	278.46	54.46	0.00	#6
	2324.19	76.09	44.87	0.00	#6
	2324.96	33.05	72.18	0.00	#6
	2325.06	253.68	50.87	0.00	#6
	2325.16	70.45	52.99	0.00	#6
	2325.51	76.68	70.07	0.00	#6
	2325.53	288.93	49.76	0.00	#6
	2325.60	87.65	65.83	0.00	#6
	2325.65	284.60	49.18	0.00	#6
	2326.13	101.13	69.10	0.00	#6
	2326.30	291.58	49.48	551.42	#6
	2326.41	114.52	73.19	0.00	#9
	2326.82	107.11	70.20	59.96	#9
	2327.41	269.42	60.29	0.00	#9
	2327.68	87.64	65.89	0.00	#9
	2327.90	283.68	56.26	233.74	#5
	2328.97	290.03	50.42	0.00	#9
	2329.26	273.98	56.18	0.00	#9
	2330.26	267.87	57.29	0.00	#6
	2330.83	94.43	76.34	0.00	#6
	2332.74	269.04	70.27	3.11	#6
	2333.95	178.71	60.51	0.00	#9
	2335.82	3.83	56.05	9.54	#6
	2341.04	298.09	36.54	131.74	#9
GRANITE ALTERE	2341.57	316.07	57.63	0.00	#6
	2344.76	295.02	59.58	126.40	#5
	2349.90	325.47	70.12	0.00	#6
	2350.66	30.71	39.46	9.86	#6
	2351.45	63.93	64.68	0.00	#6
	2351.63	120.37	70.85	0.00	#6
	2352.22	115.43	65.72	29.03	#5
	2352.57	112.79	46.01	14.02	#5
	2353.36	74.14	80.12	0.00	#6
	2353.79	88.63	71.53	0.00	#6
	2354.64	136.07	75.78	0.00	#6
	2355.40	238.43	52.75	10.28	#6
	2355.69	241.51	56.36	4.80	#6
	2358.01	262.25	54.99	8.06	#6
	2358.21	96.10	59.70	10.87	#6
	2358.31	265.83	50.19	0.00	#6
	2358.76	255.88	52.42	8.84	#6
	2359.51	264.77	50.94	0.00	#6
	2359.95	64.05	63.63	0.00	#9
	2362.11	143.10	43.75	0.00	#6
	2364.04	96.92	78.76	9.09	#6

	2364.20	299.44	62.00	0.00	#6
	2364.87	278.09	38.08	0.00	#9
	2365.51	299.16	41.38	0.00	#9
	2365.78	286.74	44.47	0.00	#9
	2366.17	254.60	42.82	51.98	#5
	2366.81	230.47	50.71	0.00	#6
	2367.19	294.81	25.60	26.57	#5
	2367.32	283.22	29.09	35.15	#5
	2367.86	259.22	54.21	240.67	#5
	2372.80	280.97	62.19	10.34	#6
	2373.41	114.99	77.15	0.00	#6
	2376.91	282.75	32.20	10.54	#8
	2380.40	144.38	20.18	0.00	#8
	2381.28	94.58	75.46	0.00	#8
	2387.95	298.47	55.97	7.46	#8
	2388.67	266.68	51.04	0.00	#8
	2390.38	263.02	58.70	0.00	#8
	2390.58	236.95	43.26	0.00	#8
	2390.65	279.44	57.07	0.00	#8
	2390.99	300.26	53.86	0.00	#8
	2393.65	312.48	33.96	5.18	#8
	2395.13	125.20	61.21	405.03	#8
	2398.30	281.63	59.38	0.00	#8
	2398.54	295.15	54.70	0.00	#8
	2399.16	113.52	72.37	144.90	#8
	2399.78	302.26	49.02	0.00	#8
	2399.85	131.40	76.97	0.00	#8
	2399.93	294.65	52.39	0.00	#8
	2400.22	108.53	75.65	0.00	#8
	2401.29	103.96	71.55	0.00	#8
	2402.31	112.74	72.38	0.00	#8
	2403.79	285.61	43.73	0.00	#8
	2404.07	297.17	42.78	0.00	#8
	2405.47	237.94	67.41	9.29	#8
	2405.79	234.84	48.66	0.00	#8
	2407.78	233.10	71.88	7.47	#8
	2413.27	259.43	52.35	0.00	#8
	2413.36	276.51	58.19	0.00	#8
	2414.15	224.13	72.26	11.84	#8
	2414.74	235.65	62.33	357.55	#8
	2415.81	250.24	60.82	0.00	#8
	2416.15	248.20	62.30	0.00	#9
	2416.78	324.01	46.12	0.00	#9
GRANITE ALTER	2418.52	243.27	50.53	0.00	#8
	2419.44	239.97	63.85	0.00	#8

	2422.21	100.40	75.68	12.15	#8
	2423.04	86.11	72.74	0.00	#8
	2423.31	89.64	74.53	6.02	#8
	2423.82	97.17	77.89	0.00	#8
	2428.42	99.96	69.30	0.00	#8
	2428.75	112.09	54.45	0.00	#8
	2429.33	189.98	52.35	0.00	#8
	2430.05	80.92	56.17	0.00	#8
	2431.48	87.75	46.16	0.00	#8
	2438.29	270.01	63.25	0.00	#8
	2442.14	284.19	54.93	0.00	#8
	2442.67	319.09	56.63	0.00	#8
	2450.63	319.34	33.97	469.54	#8
	2462.60	297.35	71.53	1.40	#8
	2470.74	56.07	77.91	0.00	#8
	2471.24	60.45	75.12	0.00	#8
	2471.71	50.12	82.20	0.00	#8
	2495.65	249.01	54.35	0.00	#8
	2495.76	260.86	58.80	0.00	#8
	2502.66	32.83	69.06	0.00	#8
	2502.79	36.41	62.68	0.00	#8
	2504.45	130.57	71.46	0.00	#8
	2504.95	120.49	52.44	464.52	#8
	2505.79	263.09	59.62	34.67	#7
	2508.60	120.81	76.68	1.74	#8
	2519.12	73.42	68.99	0.00	#8
	2519.34	73.96	76.07	0.00	#8
	2519.53	55.35	70.80	0.00	#8
	2519.98	47.88	80.89	3.54	#8
	2522.98	217.23	60.98	0.00	#8
	2523.39	234.40	67.35	0.00	#8
	2529.66	223.83	48.94	0.00	#8
	2529.71	256.87	70.63	0.00	#8
	2529.82	224.15	54.63	0.00	#8
	2531.30	252.49	79.09	0.00	#8
	2532.88	251.21	77.12	108.34	#8
	2536.20	260.00	70.63	11.05	#8
	2542.51	306.65	36.69	0.00	#8
	2542.66	285.50	42.93	0.00	#8
	2543.15	76.27	86.68	32.50	#8
	2543.34	250.48	68.09	54.52	#8
	2550.67	242.17	65.28	0.00	#8
	2556.08	76.58	85.92	0.00	#8
	2556.32	241.86	73.46	0.00	#8
	2559.59	252.04	66.29	0.00	#8

	2559.84	245.89	68.25	0.00	#8
	2561.06	248.04	76.83	0.00	#8
	2562.71	266.85	69.55	0.00	#8
	2563.63	49.64	70.40	0.00	#8
	2566.10	71.38	87.70	3.97	#8

		Type Major	Type Minor
	TRIAS	#1	#2
	PERMIEN	#3	#4
	GRANITE RUBEFIE	#5	#6
	GRANITE ALTERE	#7	#8
	QUARTZ VEIN	#9	

FRACTURES DANS LE PUITS GRT-2					
Geol	Depth	Dip direction	Dip	Thickness	Type
	m	deg	deg	mm	
TRIAS	2129.98	75.64	81.01	0.13	#2
	2130.86	260.15	89.92	26.55	#1
	2131.83	68.29	87.96	0.00	#2
	2136.53	349.83	20.36	0.00	#2
	2137.45	57.94	34.94	0.00	#2
	2139.63	282.85	32.90	0.00	#2
	2140.35	81.61	58.12	1.08	#2
	2141.41	282.02	15.63	0.00	#2
	2141.63	255.49	89.96	0.00	#2
	2142.12	258.09	88.32	0.00	#2
	2142.68	251.18	81.41	0.00	#2
	2151.92	248.22	89.12	0.00	#2
	2152.32	230.98	87.04	0.00	#2
	2152.84	60.44	89.68	0.00	#2
	2155.45	247.22	88.94	0.00	#2
	2157.60	58.80	76.88	0.00	#2
	2159.56	246.82	84.94	0.00	#2
	2159.94	71.90	89.65	0.00	#2
	2160.61	63.44	78.01	0.00	#2
	2161.97	82.14	88.84	0.00	#2
	2165.20	258.78	88.94	0.00	#2
	2165.47	42.85	20.27	0.00	#2
	2172.55	72.38	79.09	11.82	#2
	2174.31	70.44	54.80	0.00	#2
	2175.20	99.92	66.14	11.22	#2
	2177.88	337.33	27.07	0.00	#2
	2180.47	86.09	67.86	0.00	#2
	2180.85	71.13	54.01	0.00	#2
	2181.11	77.50	57.63	0.00	#2
	2181.30	83.00	59.01	0.00	#2
	2181.48	87.46	63.47	0.00	#2
	2181.90	100.59	69.42	0.00	#2
	2185.77	2.99	16.11	0.00	#2
	2187.29	17.36	73.33	0.00	#2
	2189.82	79.67	59.60	1.06	#2

TRIAS	2196.61	267.54	89.41	7.51	#2
	2208.55	77.41	85.75	19.63	#1
	2209.66	70.64	82.06	8.79	#2
	2211.29	70.94	85.68	6.78	#2
	2216.92	262.14	89.96	22.52	#1
	2217.03	238.44	76.32	19.06	#2
	2222.46	269.03	65.47	12.76	#1
	2227.29	38.54	88.12	12.98	#1
	2229.57	42.81	78.55	6.08	#2
	2231.18	97.78	83.68	14.06	#2
	2236.08	77.48	71.64	10.74	#2
	2236.65	75.79	85.79	4.99	#1
	2239.99	106.00	57.82	35.59	#2
	2240.55	102.75	74.34	18.59	#2
	2246.57	82.69	75.42	27.56	#2
	2248.03	110.96	79.70	218.03	#2
	2248.14	103.60	71.83	32.07	#1
	2248.56	57.73	79.91	29.35	#1
	2249.46	65.08	89.57	0.00	#2
	2250.57	155.79	84.27	0.00	#2
	2251.30	355.78	83.24	0.00	#2
	2252.06	105.28	66.99	0.00	#2
	2254.68	84.79	74.40	198.65	#2
	2255.05	242.83	82.81	13.24	#2
	2256.91	227.15	83.07	0.00	#2
	2257.75	252.40	79.46	20.83	#2
	2258.08	253.15	72.95	12.24	#2
	2258.89	91.73	76.44	4.42	#2
	2259.68	93.57	82.17	0.00	#2
	2259.69	266.65	63.14	0.00	#2
	2260.06	259.57	63.46	12.54	#2
	2260.83	270.44	60.33	10.77	#2
	2260.87	238.34	59.58	0.00	#2
	2261.90	221.42	86.51	16.01	#2
	2262.02	95.38	85.99	4.51	#2
	2263.25	96.66	67.40	19.29	#1
	2263.30	234.39	81.30	17.58	#1
	2267.20	244.42	65.13	0.00	#2
	2269.33	211.22	76.65	0.00	#2
	2270.38	253.15	66.51	7.72	#2
	2275.81	270.02	62.51	0.00	#2
	2276.26	270.32	63.07	8.52	#2
	2276.55	276.26	78.59	12.94	#2
	2284.59	97.92	71.95	9.95	#2
	2285.48	87.59	63.79	0.00	#2

	2286.25	262.69	47.32	0.00	#2
	2287.31	302.55	22.19	0.00	#2
	2287.93	11.15	31.60	0.00	#2
	2288.95	282.78	89.23	10.73	#1
	2292.88	264.60	81.09	0.00	#2
	2293.33	290.06	56.75	0.00	#2
	2294.12	261.38	56.49	0.00	#2
	2294.47	307.51	86.83	0.00	#2
	2296.38	112.70	88.26	5.34	#2
	2298.74	295.34	81.72	13.53	#2
	2301.72	99.47	86.93	0.00	#2
	2308.78	65.90	86.09	0.00	#2
	2317.60	297.70	23.65	0.00	#2
	2318.64	15.96	24.93	37.93	#1
	2319.07	36.39	22.60	39.87	#1
	2320.54	251.26	88.73	0.00	#2
	2322.08	172.09	8.72	23.90	#1
	2323.29	250.16	84.17	0.00	#2
	2323.33	65.03	83.68	5.88	#2
	2330.05	95.03	80.03	43.73	#2
	2330.54	97.93	80.56	30.63	#1
	2331.53	72.87	55.11	12.52	#1
	2343.23	74.40	73.75	0.00	#2
	2345.75	354.58	12.76	162.12	#1
	2346.39	15.76	24.11	0.00	#2
	2346.88	328.91	18.62	0.00	#2
	2352.13	109.89	78.39	27.12	#1
	2353.37	108.85	75.03	0.00	#2
	2359.26	75.59	57.63	15.22	#1
	2360.75	67.03	56.06	7.12	#2
	2361.13	95.94	70.70	10.46	#2
	2361.45	90.57	70.60	90.87	#2
	2365.08	85.72	75.04	18.55	#1
	2365.11	104.89	74.30	20.89	#2
	2370.67	83.06	74.06	14.66	#1
	2376.86	272.13	17.49	0.00	#2
	2377.87	114.73	83.03	30.35	#1
	2382.11	272.26	73.55	9.27	#2
	2384.53	251.96	79.71	50.30	#2
	2384.60	96.56	71.74	85.44	#2
	2418.21	112.69	75.53	364.83	#2
PERMIEN	2421.78	105.71	76.36	34.21	#2
	2422.28	117.44	79.58	0.00	#2
	2422.93	120.21	82.72	0.00	#2
	2423.27	34.35	10.40	31.07	#2

	2446.33	269.37	57.68	0.00	#2
	2446.77	262.65	59.07	65.38	#2
	2451.89	247.84	77.20	0.00	#2
	2453.17	252.67	81.79	0.00	#2
	2453.24	74.36	59.83	0.00	#2
	2453.64	69.95	58.73	0.00	#2
	2453.90	66.58	36.77	0.00	#2
	2454.70	62.83	66.19	11.08	#1
	2455.14	71.62	61.31	53.90	#2
	2455.83	69.45	54.59	188.38	#2
	2457.64	58.86	82.08	15.82	#2
	2458.39	328.16	12.54	109.95	#2
	2459.61	279.94	29.61	0.00	#2
	2460.83	277.77	31.03	0.00	#2
	2466.76	269.79	18.12	426.78	#2
	2468.41	290.16	31.54	77.46	#2
	2472.20	272.37	7.45	0.00	#2
GRANITE RUBEFIE	2493.97	358.16	68.69	0.00	#4
	2495.20	51.74	84.07	0.00	#4
	2496.53	333.27	69.98	0.00	#4
	2496.81	325.90	72.23	14.35	#4
	2497.08	328.98	80.40	0.00	#4
	2498.52	263.36	61.67	0.00	#4
	2499.57	77.54	57.39	40.97	#3
	2504.50	109.67	65.32	0.00	#4
	2507.03	150.76	81.05	18.70	#3
	2507.96	119.59	70.69	0.00	#4
	2508.65	88.88	61.88	0.00	#4
	2509.55	24.38	80.81	0.00	#4
	2509.91	183.12	86.38	0.00	#4
	2512.78	46.82	86.26	0.00	#4
	2513.15	232.79	68.10	0.00	#4
	2514.69	181.58	75.25	0.00	#4
	2515.39	247.97	68.67	12.61	#3
	2515.69	247.33	80.98	9.90	#4
	2515.78	95.90	59.17	14.53	#3
	2516.68	114.71	76.48	11.93	#3
	2516.69	109.15	88.86	16.02	#3
	2518.40	8.69	86.22	0.00	#4
	2519.16	192.76	85.71	0.00	#4
	2521.02	91.51	63.50	0.00	#4
	2522.51	243.85	66.37	0.00	#4
	2523.64	112.09	75.70	0.00	#4
	2524.69	248.88	66.33	0.00	#4
	2525.05	269.99	56.34	0.00	#4

	2526.82	10.46	80.97	0.00	#4
	2527.37	270.80	78.58	0.00	#4
	2528.68	290.38	55.25	10.75	#3
	2529.33	278.12	63.42	13.32	#4
	2531.22	272.41	66.68	0.00	#4
	2531.66	242.37	71.50	0.00	#4
GRANITE ALTERE	2533.73	88.87	81.53	62.47	#5
	2537.80	249.30	86.01	7.08	#6
	2538.09	239.51	54.55	0.00	#6
	2540.38	241.72	80.12	0.00	#6
	2540.46	97.06	72.36	15.02	#5
	2541.32	243.16	61.06	50.46	#5
	2542.13	98.11	76.58	163.31	#5
	2545.34	84.69	58.94	7.65	#6
	2546.01	308.04	48.03	0.00	#6
	2546.03	80.45	65.36	0.00	#6
	2546.25	292.82	54.23	1.19	#6
	2547.02	50.84	52.99	4.53	#6
	2549.48	288.95	60.70	8.95	#6
	2550.58	249.05	78.65	11.20	#6
	2553.97	79.52	53.67	0.00	#6
	2557.68	33.98	70.91	11.37	#6
	2558.24	60.31	86.94	0.00	#6
	2558.35	292.25	32.39	10.80	#5
	2559.33	293.31	35.26	0.00	#6
	2561.29	280.16	53.53	0.00	#6
	2561.47	63.80	53.96	0.00	#6
	2566.07	266.59	58.11	0.00	#6
	2568.20	201.72	87.68	24.69	#5
	2569.22	251.00	57.34	0.00	#6
	2574.91	11.78	31.05	0.00	#6
	2577.98	169.53	89.35	0.00	#6
	2579.82	162.57	83.95	0.00	#6
	2580.40	180.69	87.76	0.00	#6
	2580.48	350.16	80.42	0.00	#6
	2580.91	161.94	83.84	0.00	#6
	2581.57	262.62	82.52	0.00	#6
	2586.23	67.66	87.70	0.00	#6
	2587.26	64.16	86.34	0.00	#6
	2593.89	52.21	80.11	0.00	#6
	2594.50	63.31	87.66	0.00	#6
	2598.71	93.38	38.27	0.00	#6
	2599.55	52.61	80.55	6.65	#6
	2606.19	18.62	67.62	42.75	#6
	2608.74	45.95	83.10	0.00	#6

	2610.59	20.78	84.96	16.08	#5
	2611.29	31.17	83.19	12.62	#5
	2615.05	59.23	84.85	4.91	#6
	2615.47	38.74	69.82	6.55	#6
	2617.54	197.55	77.32	0.00	#6
	2620.95	96.48	60.36	0.00	#6
	2621.23	88.64	55.68	0.00	#6
	2621.72	94.24	56.60	0.00	#6
	2631.50	120.38	47.96	0.00	#6
	2632.58	256.49	87.32	9.40	#6
	2634.84	242.50	76.42	24.61	#5
	2638.97	16.53	30.75	0.00	#6
	2639.26	52.29	30.32	0.00	#6
	2642.21	16.82	41.37	0.00	#6
	2642.22	124.28	68.60	0.00	#6
	2642.77	68.13	53.43	5.20	#6
	2643.31	52.93	49.79	0.00	#6
	2648.16	68.50	33.05	0.00	#6
	2648.27	72.36	34.48	0.00	#6
	2648.40	74.58	43.24	0.00	#6
	2648.72	59.69	39.98	0.00	#6
	2669.31	46.87	20.53	0.00	#6
GRANITE ALTERE	2670.97	18.80	74.70	0.00	#6
	2671.24	14.26	80.48	5.26	#6
	2671.86	35.38	38.55	0.00	#6
	2672.54	104.15	82.98	0.00	#6
	2673.44	84.28	62.43	0.00	#6
	2673.75	112.04	59.33	0.00	#6
	2675.49	30.41	28.68	47.23	#6
	2675.96	45.67	29.17	42.04	#6
	2676.89	7.59	31.64	0.00	#6
	2678.42	9.39	12.49	0.00	#6
	2678.49	350.00	20.82	0.00	#6
	2678.65	26.59	34.57	0.00	#6
	2678.73	335.07	17.33	0.00	#6
	2679.19	2.64	27.76	10.06	#6
	2680.43	62.32	51.59	5.14	#6
	2681.22	224.47	73.93	12.14	#6
	2682.42	24.98	26.11	13.62	#6
	2685.12	324.57	31.66	0.10	#6
	2686.09	327.65	25.35	221.64	#6
	2687.11	330.19	32.60	0.00	#6
	2687.51	352.79	26.73	0.00	#6
	2688.72	347.77	40.36	3.99	#6
	2690.17	287.71	53.67	0.00	#6

	2690.36	112.38	78.58	9.37	#6
	2692.17	2.03	6.91	0.00	#6
	2692.30	359.46	14.15	0.00	#6
	2693.72	348.67	68.67	0.00	#6
	2695.79	95.26	56.01	39.72	#5
	2696.12	86.70	61.65	11.21	#6
	2696.23	240.77	38.18	0.00	#6
	2696.35	238.91	40.91	0.00	#6
	2698.12	253.87	63.36	0.00	#6
	2701.66	215.85	60.79	0.00	#6
	2701.86	283.19	54.18	0.00	#5
	2701.94	275.15	56.59	0.00	#6
	2702.04	210.25	89.77	0.00	#6
	2704.35	224.08	74.14	82.02	#6
	2704.47	94.41	45.66	22.23	#9
	2705.08	50.67	81.33	23.63	#6
	2705.74	201.15	5.97	40.11	#9
	2705.82	49.72	35.23	17.73	#6
	2706.10	85.66	38.60	0.00	#6
	2706.63	109.37	21.79	0.00	#6
	2707.12	112.39	76.59	0.00	#6
	2708.33	97.52	42.00	0.00	#6
	2708.48	64.46	59.40	0.00	#6
	2708.60	68.51	33.40	12.86	#5
	2708.98	224.72	55.18	0.00	#6
	2709.80	90.37	64.66	14.12	#5
	2710.91	65.53	52.80	4.84	#6
	2711.05	70.93	57.20	0.00	#6
	2711.98	109.64	70.05	4.08	#6
	2712.73	90.81	60.19	0.00	#6
	2713.34	207.04	85.55	21.15	#6
	2718.17	207.73	85.79	11.44	#6
	2735.44	236.36	72.28	7.79	#6
	2740.07	84.11	53.45	0.00	#6
	2740.75	237.72	68.37	0.00	#6
	2740.76	291.69	29.17	0.00	#6
	2740.99	259.23	47.99	0.00	#6
	2741.57	246.57	70.61	0.00	#6
	2741.63	124.00	13.44	0.00	#6
	2741.98	26.63	8.15	98.25	#5
	2742.00	67.35	17.50	11.41	#9
	2742.95	61.02	20.31	15.95	#9
GRANITE ALTERE	2743.01	69.59	25.36	53.58	#5
	2743.62	58.60	32.69	0.00	#6
	2744.31	78.73	67.93	0.00	#6

	2747.60	241.39	73.58	81.87	#5
	2750.69	254.47	41.93	0.00	#6
	2750.76	93.13	47.40	0.00	#6
	2750.96	75.58	56.54	0.00	#6
	2751.05	39.64	35.86	0.00	#6
	2751.08	79.46	57.94	16.68	#5
	2751.29	50.80	36.56	0.00	#6
	2755.42	106.25	52.94	0.00	#6
	2756.57	258.29	61.72	16.18	#5
	2767.04	244.59	83.19	66.04	#5
	2767.30	227.62	75.14	18.20	#5
	2768.06	348.84	27.77	20.88	#5
	2768.16	274.13	71.91	10.01	#5
	2768.31	94.29	36.12	13.89	#5
	2768.56	9.35	32.96	0.00	#6
	2770.42	250.54	87.22	35.79	#5
	2770.46	117.59	68.14	0.00	#6
	2770.55	119.35	67.66	0.00	#6
	2774.09	258.21	64.20	169.48	#5
	2780.72	27.24	30.52	0.00	#6
	2781.13	26.17	37.19	0.00	#6
	2781.60	23.23	37.66	0.00	#6
	2781.87	138.30	77.19	34.71	#5
	2784.79	233.69	39.78	11.23	#5
	2784.89	108.57	85.21	18.85	#5
	2786.35	280.58	75.07	2.59	#5
	2787.23	134.39	87.64	40.60	#5
	2788.42	88.29	67.94	14.98	#6
	2788.85	236.20	57.05	30.12	#5
	2792.58	122.50	17.76	0.00	#6
	2792.92	234.93	70.56	10.95	#5
	2793.24	251.39	60.42	6.52	#6
	2793.47	250.37	76.02	0.00	#6
	2794.57	323.49	19.28	12.01	#5
	2794.65	163.74	73.23	12.60	#5
	2795.09	267.93	54.21	67.98	#5
	2795.29	276.38	39.84	11.43	#5
	2795.49	258.64	21.53	37.59	#5
	2795.81	268.71	53.96	0.00	#6
	2796.08	289.24	50.99	23.25	#5
	2797.53	265.85	58.50	27.44	#5
	2798.64	274.65	72.79	0.00	#6
	2799.20	250.87	75.22	5.67	#6
	2800.76	357.52	42.10	5.31	#6
	2806.48	9.86	22.91	0.00	#6

	2816.05	234.16	63.59	0.00	#6
	2816.95	300.24	89.98	5.05	#6
	2820.57	100.31	39.82	0.00	#6
	2821.27	133.39	74.34	10.26	#5
	2821.91	79.24	66.15	0.00	#6
	2822.34	78.41	48.59	0.00	#6
	2824.14	90.60	81.11	3.02	#6
	2825.52	83.10	63.86	17.05	#6
	2840.78	112.64	68.11	84.84	#5
	2841.50	307.68	88.79	18.77	#5
	2841.90	107.18	75.40	0.00	#6
	2842.32	281.56	31.44	11.58	#6
	2842.65	263.12	48.93	10.51	#6
	2844.12	105.47	85.59	9.64	#6
	2844.38	281.05	24.08	0.00	#6
	2844.73	278.68	60.35	7.53	#6
	2847.26	104.66	72.41	11.58	#5
	2847.39	109.26	79.64	7.30	#6
	2852.43	90.31	36.18	6.03	#6
	2864.78	293.98	83.36	16.53	#5

ANNEXE 3

Geothermics 65 (2017) 255–268

Contents lists available at ScienceDirect

Geothermics

journal homepage: www.elsevier.com/locate/geothermics

Hydrothermal characterization of wells GRT-1 and GRT-2 in Rittershoffen, France: Implications on the understanding of natural flow systems in the rhine graben

C. Baujard[a,*], A. Genter[a], E. Dalmais[a], V. Maurer[a], R. Hehn[a], R. Rosillette[a], J. Vidal[b], J. Schmittbuhl[b]

[a] ES-Geothermie, 26 Boulevard du Président Wilson, F-67000 Strasbourg, France
[b] EOST, 5 rue René Descartes, F-67084 Strasbourg Cedex, France

ARTICLE INFO

Article history:
Received 18 July 2016
Received in revised form 17 October 2016
Accepted 1 November 2016

Keywords:
EGS
ECOGI
Rittershoffen
Upper rhine graben
Stimulation
Hydro-thermal characterisation

ABSTRACT

An extended description of the implementation of the deep geothermal wells GRT-1 and GRT-2 respectively drilled in 2012 and 2014 in the framework of the ECOGI project is given. These wells located in Rittershoffen (France) offer a unique opportunity to gather high quality datasets on a deep geothermal system in the Upper Rhine Graben at the transition between the Buntsandstein sandstone and the Palaeozoic granite basement. We present the extensive logging and well testing program that was applied and focus on hydraulic and thermal characterization of the targeted deep reservoir. Well architectures of GRT-1 and GRT-2 are described. Temperature logs in both wells are discussed in details. In particular, temperature in the production well GRT-2 is shown to reach 177 °C at 3196 m MD at thermal equilibrium. Production tests of both wells, reservoir development strategy applied in well GRT-1 and circulation test realised between wells are analysed. Productivity and injectivity indexes of GRT-1 and GRT-2 are estimated: Post-stimulation injectivity of GRT-1 and productivity of GRT-2 are respectively estimated to 2.5 l/s/bar and 3.5 l/s/bar. Hydraulic properties of the reservoir are inferred from production tests. Implications for the characterization of the large scale natural hydro-thermal system are discussed.

1. Introduction

1.1. Project overview

ECOGI is the first industrial deep geothermal project in France aiming to produce overheated water from natural geothermal resource embedded at the interface between the Triassic sedimentary layers and the top crystalline fractured basement of the Upper Rhine Graben (Baujard et al., 2015) using an Enhanced Geothermal System (EGS).

In the framework of the ECOGI project, a geothermal doublet has been drilled, targeting a deep seated fault zone in the granitic basement. It is designed to produce hot water at 170 °C and to deliver a heat power of 24 MWth to the "Roquette Frères" bio-refinery located in Beinheim, in order to cover around 25% of the industrial heat needs. The heat is delivered using a 15 km transport loop.

The drilling site is located in Rittershoffen, a village located in the Upper Rhine Valley (Northern Alsace, France), 6 km east of Soultz-sous-Forêts, the well-known European EGS pilot site. The location of the project is shown in Fig. 1.

The project was initiated in 2004 thanks to the interest of Roquette Frères to supply its bio-refinery in Beinheim with renewable energy. A feasibility study concluded in 2011 that the geothermal potential of the area was significant. Furthermore, this study identified a potential geothermal target, constituted by a regional fault zone associated with high temperature gradients measured in pre-existing oil exploration wells. The first well GRT-1 was drilled as soon as the administrative authorizations could be gathered, from September 2012 to December 2012. Well testing and subsequent reservoir development operations were realised between January 2013 and June 2013. An additional seismic acquisition was achieved in August 2013, in order to secure the trajectory of second well GRT-2. This second well was drilled between May and July 2014. Well testing operations and a circulation test were carried out during August, September and October 2014. The construction of the 15 km long heat delivery loop and of the power

* Corresponding author.
E-mail address: clement.baujard@es.fr (C. Baujard).

http://dx.doi.org/10.1016/j.geothermics.2016.11.001

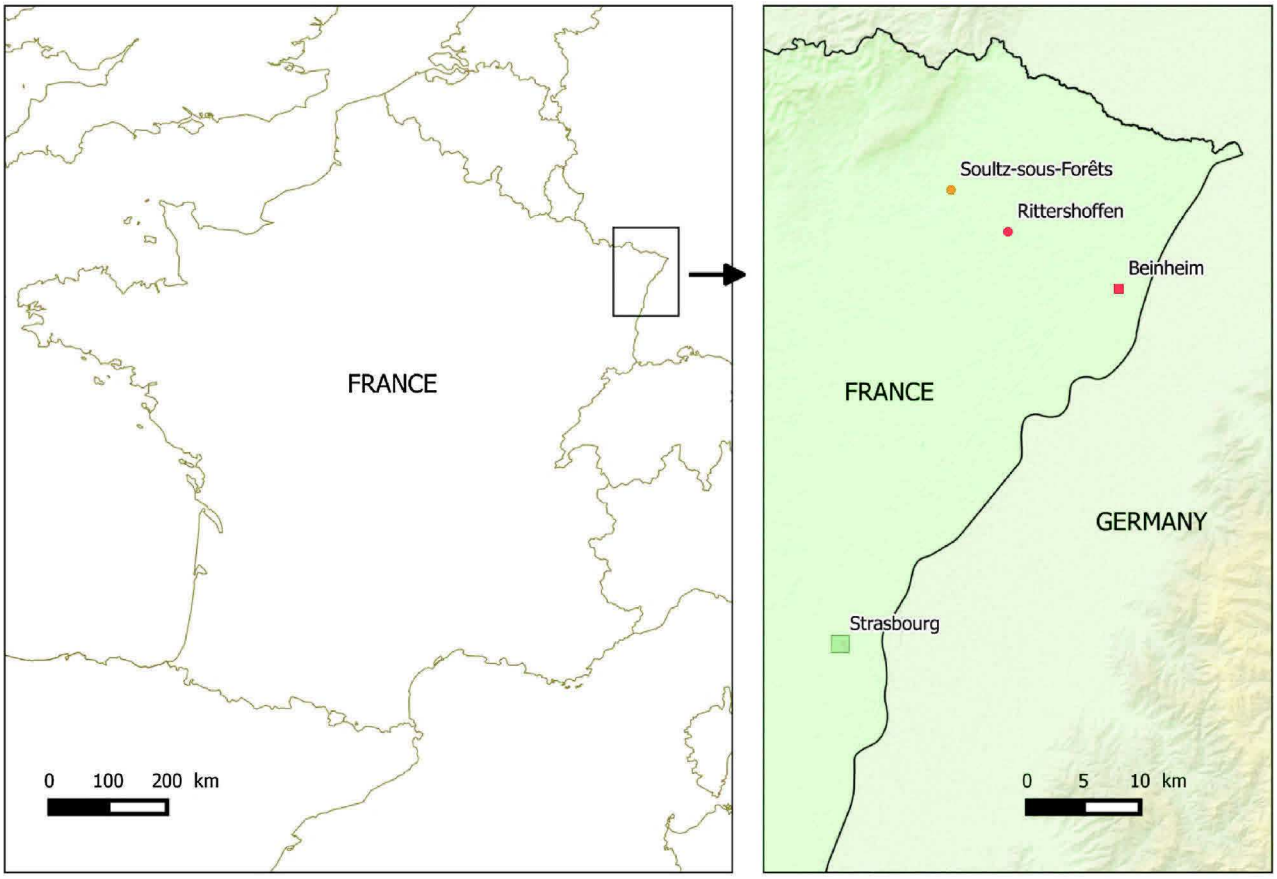

Fig. 1. Location of the ECOGI project: the deep geothermal reservoir for heat production is located in Rittershoffen (Northern Alsace, France), 6 km south-east of Soultz-sous-Forêts. The industrial site (Roquette Frères) where the heat will be used is in Benheim, 15 km. Heat will be transported between both site using a transport loop of overheated water.

plant started in February 2015. The geothermal plant went in operation by mid-2016.

1.2. Regional geological and geothermal settings

The Rittershoffen geothermal site is located 6 km south-east of the Soultz-sous-Forêts deep geothermal site where the overall geological, geophysical, geomechanical, geochemical features have been extensively studied (Kappelmeyer et al., 1992; Cornet et al., 2007; Dezayes et al., 2010; Genter et al., 2010; Bailleux et al., 2013, 2014). In summary, the site is within the Upper Rhine Graben (URG) which is part of the European Cenozoic rift system that extends from the Mediterranean to the North Sea coast. The site is located on the Western part of the URG at about 12 km form the major western Rhenane border fault. The URG's deep thermal structure, which is likely to be related to mantle uplift, shows an important rise up to 24 km depth in the southern URG (Edel et al., 2007). Extensive borehole data show that the temperature within the graben at depths of 1–2 km is highly variable, the thermal anomaly between Soultz and Rittershoffen being particularly high (Pribnow and Schellschmidt, 2000; Bailleux et al., 2013). Indeed, the shallow geothermal gradient in the graben ranges between 60 and 120 °C/km which corresponds to very high heat flow: up to 360 mW/m^2 assuming a typical thermal conductivity of 3 W/K/m and a purely conductive regime in the shallow crust (Pribnow and Schellschmidt, 2000).

The shallower geology of this area from 0 to 1500 m or 2200 m depth, respectively for Soultz and Rittershoffen (Georg Project Team, 2013), consists in Tertiary and Secondary sedimentary layers, overlaying a crystalline basement, constituted of altered and fractured granitic rocks from Carboniferous (Cocherie et al., 2004). Detailed geological analysis of the cuttings has shown that the top basement is located at about 2200 m MD (Measured Depth) in well GRT-1 (Aichholzer et al., 2015). The sedimentary layers are shifted by horst and graben structures with, in the vicinity of Rittershoffen, two horsts, Soultz in the west and Oberroedern in the East, enclosing a lower compartment in which the wells have been drilled (Georg Project Team, 2013).

Temperature, structural and stress conditions of the underground of the region are very well characterized thanks to numerous hydrocarbon exploration wells, to vintage seismic profiles and to extensive investigations that have been performed in the neighbouring geothermal site of Soultz-sous-Forêts (Genter et al., 2010; Dezayes et al., 2010; Place et al., 2010; Sausse et al., 2010; Valley, 2007).

During the 70′s and 80′s, several hydrocarbon exploration wells named R1–R4 and Oberroedern (OBR101) were drilled in this area (Fig. 3). They targeted deep-seated Triassic sedimentary layers, i.e. Muschelkalk limestone or Buntsandstein sandstone, or more shallowly tertiary layers, i.e. 'Couches de Pechelbronn' (Fig. 3). Most of these wells were unproductive for hydrocarbon but provided salty hot water (Munck et al., 1979). Temperatures derived mainly from drill stem tests show an overall geothermal linear gradient in the two first kilometers varying mainly between 7 and 9 °C/100 m (Fig. 4). Considering that these temperatures are often underestimated as they are acquired a few hours or days after drilling, the assumption of a gradient between 8.5 and 9 °C/100 m for Rittershoffen area was made before any geothermal drilling operations.

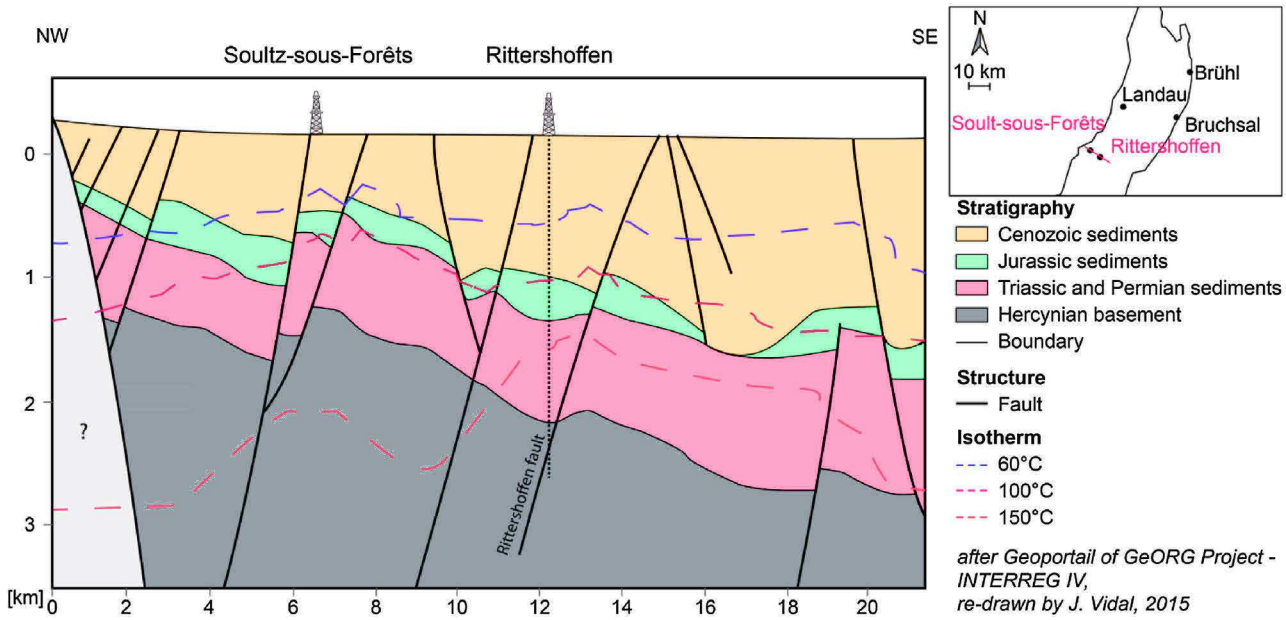

Fig. 2. NW-SE geological cross-section perpendicular to the graben axis between Soultz and Rittershoffen geothermal sites (Georg Project Team, 2013). The vertical dot line indicates an interpretative trajectory of GRT-1 that crosses the Rittershoffen fault.

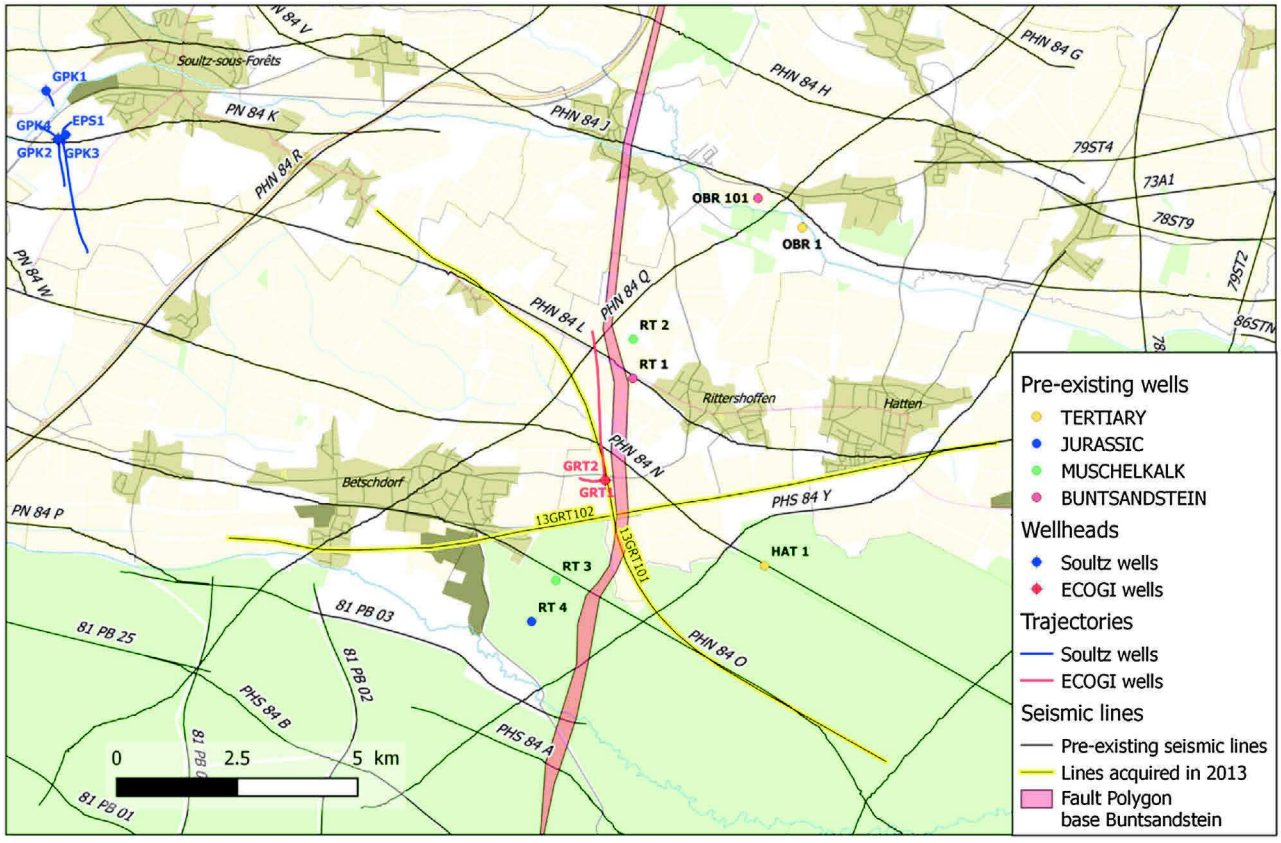

Fig. 3. Location and traces of pre-existing oil exploration wells, ECOGI and Soultz geothermal wells, pre-existing and recently acquired seismic data and target fault polygon at the base of the Buntsandstein (map background Open Street Maps).

Fig. 4 shows the measured temperatures of GRT1 and GRT2 at thermal equilibrium and confirms the relevance of the prediction (see Section 3 for an extended discussion).

The stress state to be found in the basement in this area is well known from various geophysical and mechanical measurements and interpretation derived from the area of Soultz (Valley, 2007; Cornet et al., 2007). Orientation of horizontal maximal stress S_H is approximately N169°E, whereas observations of focal mechanisms show a mix of normal and strike slip faulting suggesting that S_H is very closed to the vertical stress S_V (Dorbath, et al., 2010).

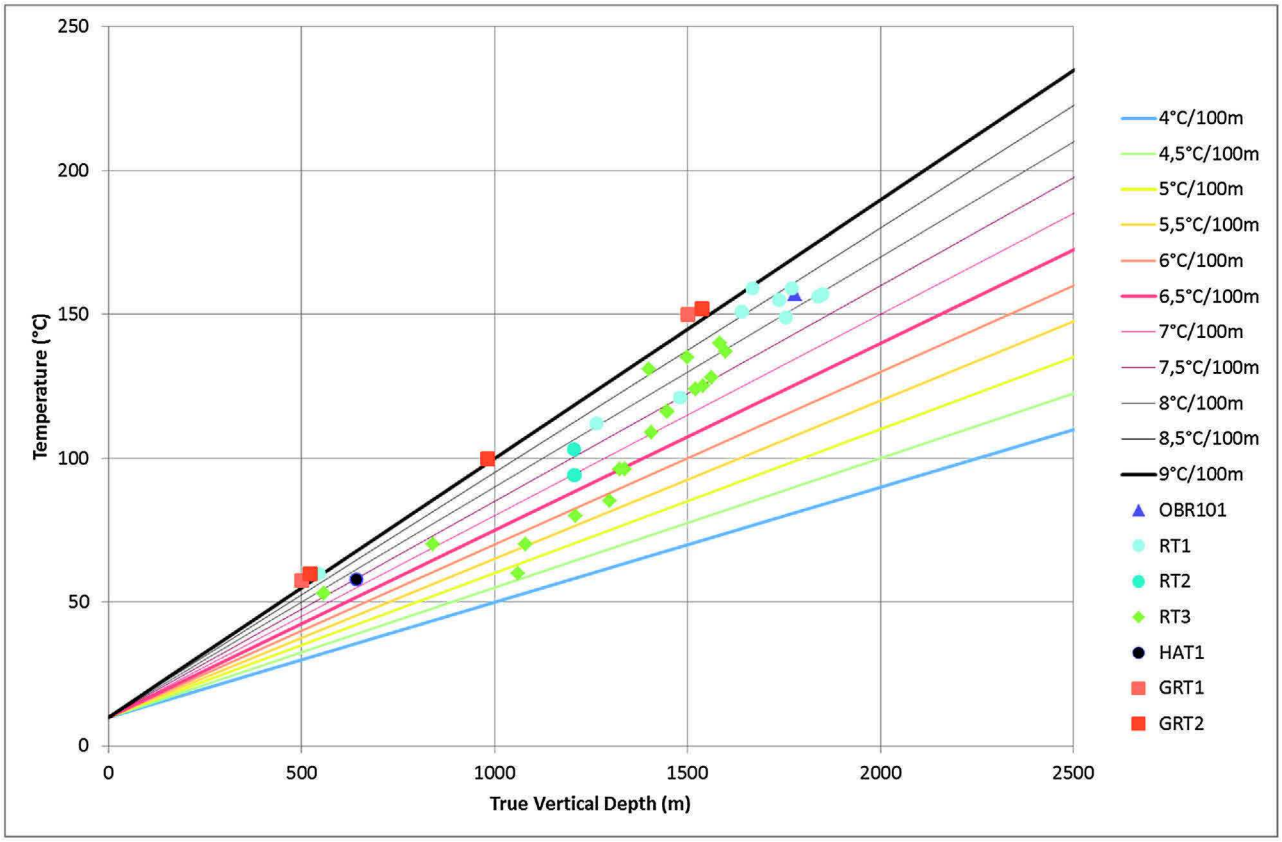

Fig. 4. Temperature versus depth from pre-existing oil wells drilled in Rittershoffen area (GRT-1 and GRT-2 temperatures are reported for comparison).

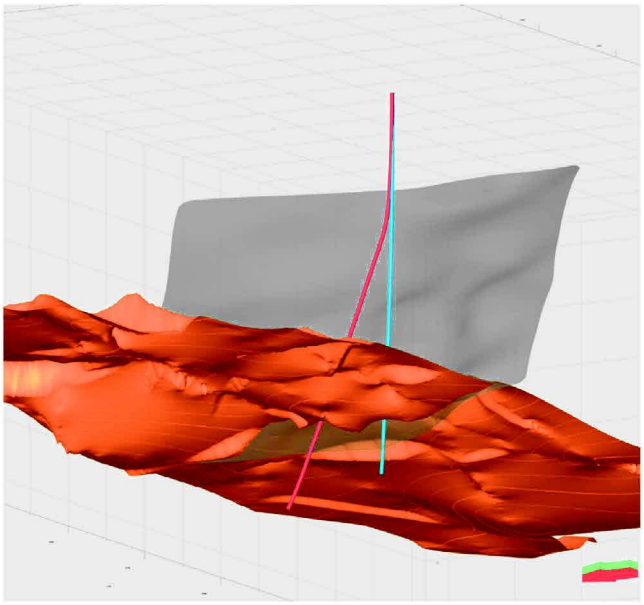

Fig. 5. 3D structural model based on seismic and well data showing GRT-1 (in blue – right side), GRT-2 (in red – left side), the Rittershoffen main fault structure (grey surface) and top granite basement (orange surface) at 2200 m TVD, viewed from below in the North/East direction. The red/green arrow indicates the north direction. (For interpretation of the references to colour in this figure legend, the reader is referred to the web version of this article.)

2. General description of wells GRT-1 and GRT-2

Both wells target the same fault zone, named Rittershoffen fault, in the crystalline basement (Fig. 2). This structure is relatively well known thanks to vintage seismic profiles from the 80′s available in the vicinity of the project (see also Figs. 3 and 4) which were reprocessed in 2009, leading to an updated lithostructural and stratigraphic interpretation of the Rittershoffen region. It is a N355°E fault zone (becoming North-South at the well site), dipping 45° to the West, and showing an apparent vertical offset of more than 250 m (Fig. 5).

In both wells, the open-hole section crosses Buntsandstein and Permian clastic sandstones which covers a Paleozoic crystalline basement made of hydrothermally altered and fractured granite and intact granite.

The drilling of the first vertical well GRT-1 started in September 2012 and ended in December 2012 when the well reached a depth 2580 m MD within the fractured granite basement (see Fig. 6). The drilling rig was a MR8000 (hook load capacity 200To). No deviation tool was used. The maximum deviation is 8° to the West (see Fig. 5). Thus, GRT-1 intersects the Rittershoffen fault just below the top basement, roughly around 2400 m MD.

The drilling rig was demobilized after the first well in order to be able to perform a series of extended hydraulic tests and apply a coherent reservoir development strategy. Two new seismic profiles were acquired during summer 2013 in order to produce a better structural image of the reservoir for targeting the second well, GRT-2. Several post processing strategies were applied to this newly acquired seismic data which improved the geometrical understanding of the major local faults. Combined with the numerous logs and hydraulic tests performed in GRT-1 well, GRT-2 target has been identified and the trajectory designed.

The drilling of well GRT-2 started mid-March 2014. The drilling rig was a HH300 (280To). The final depth of 3196 m MD was reached end of July 2014. The well was slightly deviated using a downhole

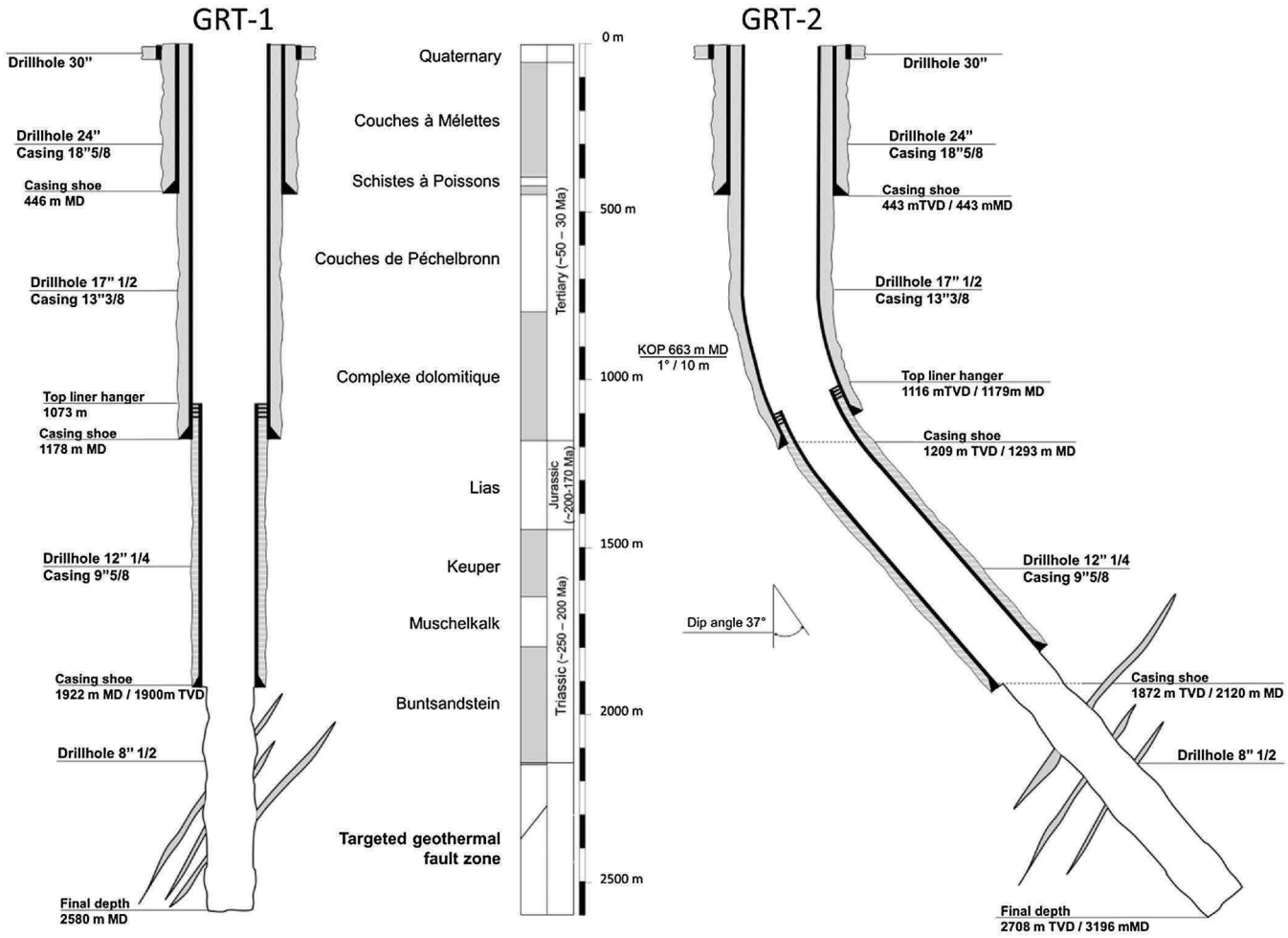

Fig. 6. GRT-1 and GRT-2 geothermal well completion and stratigraphic sequence. All depths are given from the surface.

mud motor. The inclination of the well reaches more than 37° and is directed to the north (Fig. 6).

The completion of both wells is very similar (Fig. 6). A conductor pipe was installed down to 40m depth prior to the drilling in order to avoid stability problems and protect groundwater from drilling mud losses. The first section (24″ hole diameter) was drilled in two stages (17″1/2 at first and the 24″ using a hole opener). The shoe of the 18″5/8 casing is set below the 'Schistes à Poisson' layer, known to be a regional aquifer. The 13″3/8 casing shoe is set at the base of the tertiary layers. The casing shoe of the 9/″58th liner is set at the base of the Muschelkalk. The hole diameter at target depth is 8″1/2; no perforated liner were used (the fully open section is in the Buntsandstein and granitic basement) in order to maximize well productivities.

3. Reservoir temperature

3.1. Measurement in well GRT-1

The most representative log of the thermal equilibrium profile was realised on April 22th 2013 (102 days after the well shut-in following the production tests in January 2013; the log was realised downwards). The maximum temperature at the bottom hole was measured at 163 °C at 2′526 m TVD (True Vertical Depth) (Fig. 7). From the surface approximately down to the top of the Muschelkalk, the temperature gradient is constant: 8.7 °C/100 m. It can be noted that this value is slightly lower than in Soultz-sous-Forêts where it reaches 11 °C/100 m (Genter et al., 2010; Vidal et al., 2015). At the top Muschelkalk, the temperature is about 160 °C (Fig. 7). Below the top Muschelkalk, the temperature profile changes very significantly despite a local small-scale positive anomaly. Indeed, the mean temperature gradient from the top Muschelkalk to the bottom of the well is very low: 0.3 °C/100 m which is about 30 times smaller than in the upper part of the well.

3.2. Measurement in well GRT-2

The most representative complete log of a thermal equilibrium profile in GRT-2 was measured in the cased well on September 08th 2014 (37 days after shut-in following the production sequence of the well; the log was performed downwards). The maximum temperature at the bottom hole in the granite section is 177.1 °C at 2′693 m TVD (Fig. 7). The thermal gradient shows very high values from the surface down to the top of the Muschelkalk with around 8.5 °C/100 m, very similarly to the temperature profile in GRT1, i.e. 8.7 °C/100 m. At the top of the Muschelkalk layers, the temperature reaches about 158 °C. Below the top Muschelkalk and down to the bottom hole, the thermal gradient is roughly constant despite several local perturbations and can be estimated to 1.8 °C/100 m. This value is significantly higher than for GRT-1, consistently with a higher bottom-hole temperature of the well. It must be emphasised that the well was probably not in a complete thermal steady-state when the temperature profile was acquired. Indeed, for GRT1, the waiting period before measuring the temperature log was

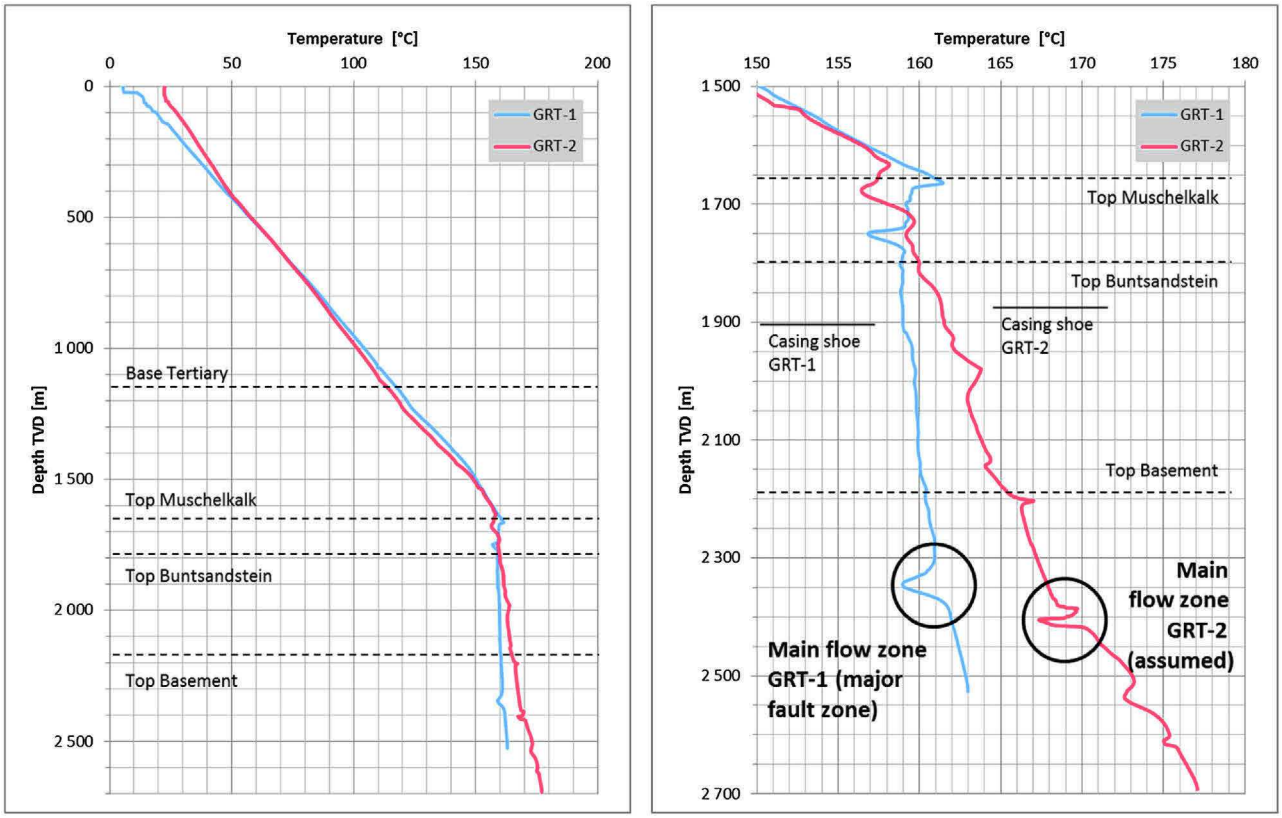

Fig. 7. Left: complete temperature profiles of GRT-1 and GRT-2; right: temperature profiles of GRT-1 and GRT-2 between the top Muschelkalk and the deep granite. Geological formation depths are indicative only as they may differ between the two geothermal wells (+/− 30 m).

comparable to the drilling period (about 3 months) which is typically a cooling period of the well owing to the drilling mud circulation. For GRT2, the waiting time is significantly shorter, only about 1/3 of the drilling period.

3.3. Temperature logs comparison and implication on natural flows

The general shape of both temperature profiles suggests a diffusive temperature regime from the ground surface to the top of the Muschelkalk formations and an advection-dominated temperature regime below the top Muschelkalk as proposed for the Soultz-sous-Forêts reservoir (Genter et al., 2010). This would suggest that the Keuper formations (mainly constituted of clays and dolomites), located directly above the Muschelkalk, act as a hydraulic barrier. The sharpness of the transition in the temperature profiles supports the existence of a barrier of caprock. The comparison between Soultz-sous-forêts and Rittershoffen where the Keuper formations are not at the same depth is of interest for addressing this question. At Soultz-sous-Forêts, the Keuper formations are at 860m and at 1650 m in GRT1. In both cases, it corresponds to the bottom end of the conductive regime. However, in Soultz-sous-Forêts, the transition to the convective regime is much smoother making it more difficult to associate specifically the correlation between the heat transport process change with the Keuper formations.

3.3.1. Muschelkalk and Buntsandstein

The temperature profile of GRT-1 shows two temperature anomalies in the Muschelkalk (a positive anomaly at the top of the formation, and a negative anomaly at the bottom). These anomalies could indicate that this formation host significant natural fluid circulations. This is supported by the fact that severe mud losses occurred in the Muschelkalk during drilling. This phenomenon is partly confirmed in GRT-2, where a negative temperature anomaly could be identified in the Muschelkalk. A high ROP (rate of penetration) was observed during the drilling operations of GRT-2 in the Muschelkalk, but no drilling mud losses were reported. This observation indicates that natural permeability in the Muschelkalk is very heterogeneous since wells are only separated in this formation by only a few hundred of meters.

In the Buntsandstein, a thermal positive anomaly can be identified in GRT-2 around 1980 m TVD, whereas no significant thermal anomaly could be seen in GRT-1.

3.3.2. Granitic basement

An important negative temperature anomaly is located in GRT-1 around 2350 m TVD in the granite section. The amplitude of the anomaly can be estimated to −2.5 °C (Fig. 7).

In GRT-2, five thermal anomalies with variable amplitudes were identified at 2200 m TVD, 2380 m TVD, 2400–2415 m TVD, 2530 m TVD and 2620 m TVD (Fig. 7). The most important temperature anomaly in the open-hole section of the well is observed in the granite section between 2′400 m TVD and 2′415 m TVD. The total amplitude of this negative anomaly is almost −3 °C. Interestingly, a positive anomaly is located directly above this negative anomaly, between 2′380 m TVD and 2′400 m TVD suggesting a strong lateral variability of the natural flows and subsequently significant channelling effects certainly related to large open fractures or faults.

The negative temperature anomaly located at 2′350 m TVD in the basement of GRT-1 is clearly correlated with a production zone according to spinner logs realised during a production test. Borehole image analysis also confirms the existence of a main fractured zone at that depth (Vidal et al., 2016). Unfortunately, no spinner log was performed in GRT-2, but the production temperature

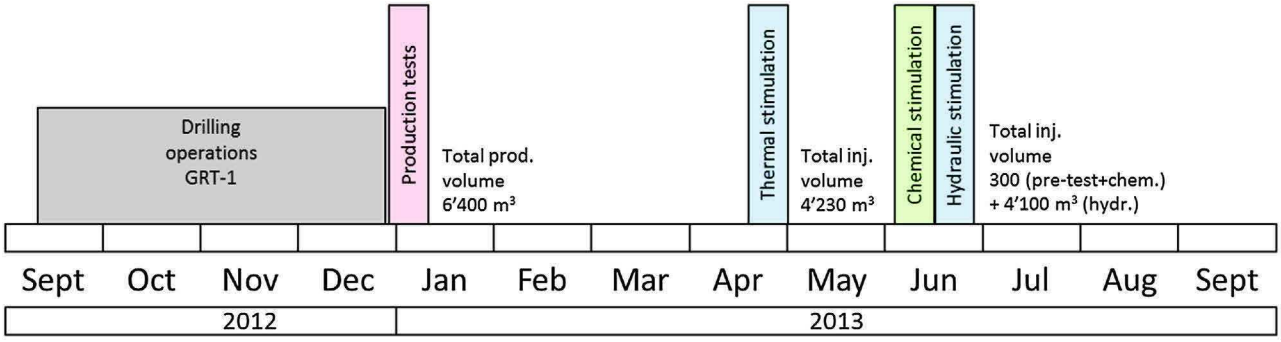

Fig. 8. GRT-1 well production tests and applied development strategy and total produced and injected volumes.

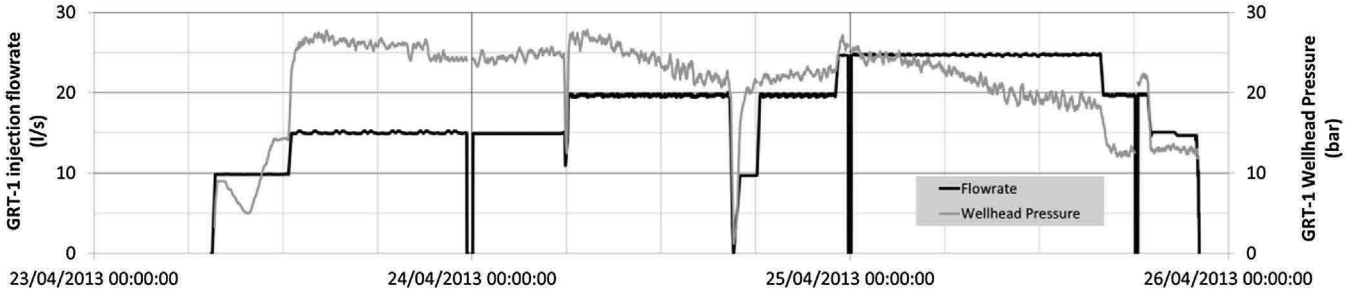

Fig. 9. Thermal stimulation of the geothermal well GRT-1 on April 2013.

during the circulation test (see below) reached 166 °C at the wellhead. This temperature value is compatible with a temperature of 168 °C at the production zone. Thus, it seems reasonable to assume that the temperature anomaly located around 2′400 m TVD in GRT-2 also corresponds to a main flow zone. These observations confirm that local fault zones of the Rhine Graben host natural fluid circulations.

The main difference between temperature profiles of both wells is the gradient value below the top Muschelkalk (see Fig. 7). The temperature gradient in GRT-1 is almost zero (0.3 °C/100 m) whereas it is significantly larger in GRT-2 (1.8 °C/100 m). This difference could be related to the difference in delay after the perturbations by the drilling fluid circulation, as the upper part of the 8″1/2 section was cooled down longer than the deeper part (which might already have reached thermal equilibrium, contrarily to the upper part). The difference could also be related to the lateral variability of the temperature field in the reservoir. The comparison between both temperature profiles also shows that the temperature profile of GRT-2 is characterized by several positive thermal anomalies, for example at 2′200 m TVD and 2′380 m TVD (Fig. 7), that are not observed in GRT-1 where only negative anomalies are observed. These anomalies could be linked with the previous production test (see Section 4).

4. Hydraulic testing of the reservoir

4.1. Well GRT-1

4.1.1. Production tests

The well clean-up operations were realised between December 30th, 2012 and January 1st, 2013. 3′000 m^3 were produced; the production started with an air-lift and continued with an artesian flow. No monitoring tool was installed in the well during this phase.

Following this well clean-up phase, a first air-lifted production test was performed between January 3rd and January 6th, 2013 (air injection at 300 m depth). A total of 3′000 m^3 were produced. The PT (Pressure Temperature) probe had been placed close to the casing shoe at 1′910 m MD during production. The production flowrate was extremely erratic. In order to try to stabilize it, the test started with a 24 h production sequence at a maximal flowrate (14 l/s) to heat-up the well. Three descending short step-rates were then imposed (14 l/s, 11 l/s and 9,7 l/s, 3 h each). The maximum recorded downhole temperature was 157 °C. Unfortunately, the downhole measurements had to be interrupted before and during the build-up due to the necessity to cool-down the pressure probe at the surface. The PT logging tool was put in the well again during the build-up phase at 1′907.5 m MD. After a 12 h build-up, the test was continued with a sequence of 32 h of artesian production (average flowrate 10 l/s), but the downhole sensors failed and no downhole PT could be recorded during this production phase.

In order to get better data, a second production test was performed on January 9th and 10th. A total of 400 m^3 were produced during this 12 h test. The production was air-lifted (air injection at 500 m depth, using a booster). Flowrate could be stabilised at 8 l/s and the downhole pressure during the build-up phase was fully recorded. The PT probe was positioned in the open-hole section at 2′298 m MD. The maximum recorded temperature at that depth was 158 °C.

Due to the erratic production flowrate and to a poor data quality, the interpretation of the pumping tests of GRT-1 is problematic. Nevertheless, the well productivity at this stage could be estimated to 0,45 l/s/bar.

4.1.2. GRT-1 well and reservoir development sequence

A reservoir development strategy was developed and applied. It consisted in three distinctive phases (Fig. 8). Firstly, a thermal stimulation (phase 1) of the well, with low-rate cold fluid injections was applied in April 2013. Then, a targeted chemical stimulation (phase 2) immediately followed by a hydraulic stimulation (phase 3) of the well were realised in June 2013.

The thermal stimulation (phase 1) of the well started on April 23rd 2013 at 07:40 and terminated on April 25th 2013 at 22:00 (Fig. 9). This stimulation consisted of a low-rate cold fluid injection into the well. A total fluid volume of 4′230 m^3 was injected,

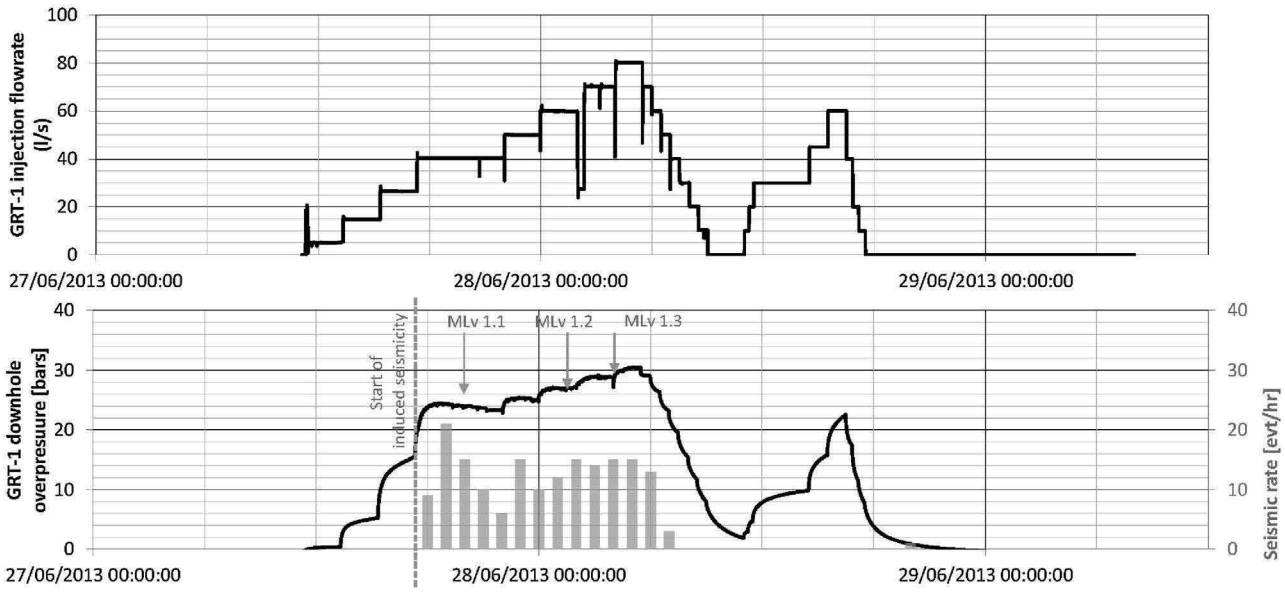

Fig. 10. Hydraulic stimulation sequence of GRT-1. The seismic rate is based on automatically detected events only. Main induced seismic events that occurred during injection are reported on the pressure curve (this figure does not show the post shut-in crisis).

at 6 different injection rates, ranging from 10 l/s to a maximum of 25 l/s. Injection temperature remained relatively constant to 12 °C. The maximum wellhead pressure recorded during this injection (no downhole tool was installed in the well) reached 28 bar. During this experiment, GRT-1 injectivity increased from an initial value of 0.6 l/s/bar to 1.3 l/s/bar at a flowrate of 20 l/s (see also Fig. 14). The injection generated 113 micro-earthquakes, with a maximum local magnitude (M_l) of 1.2 (Maurer, et al., 2015).

Phase 2 (chemical stimulation) and phase 3 (hydraulic stimulation) were realised consecutively. This stimulation experiment started on June 22nd 2013 and terminated on June 29th 2013. A total fluid volume of 4′400 m^3 was injected into the well. The sequence started with an injection test (3 constant flowrate steps of 5, 15 and 26.5 l/s) realised on June 22nd between 09:00 and 15:30. Downhole pressure was monitored using a logging tool at the casing shoe (1914 m MD).

Environmentally friendly acids were specifically designed for the chemical treatment of the well (phase 2), using drilling cuttings for laboratory testing (Recalde Lummer et al., 2014). The chemical stimulation was designed to dissolve the main hydrothermal minerals sealing the natural fractures. Clay minerals, secondary quartz, carbonates and sulphates were observed in the drilling cuttings from binocular observation, X-ray diffraction and thin sections. In order to avoid strong acids, it was decided to use glutamate-based chemicals able to dissolve calcite minerals (Recalde Lummer, et al., 2014). Mineralogical description and calcimetry based on cuttings were used for prioritizing the three main stimulated zones. The chemical injections were applied using open-hole packers at 5 l/s through 2“ coiled tubing, thus limiting the quantity of chemicals to be injected. No seismicity was detected during that sequence (Maurer, et al., 2015). Chemical injections were applied to three different depth intervals of the well, according to:

- From June 23rd – 16:00 to June 23rd – 23:00, 120 m^3 were injected to the first interval into the Basement (2′370–2′530 m MD).
- From June 24th 22:20 to June 24th 23:35, 42 m^3 were injected to the second interval into the Basement (2′300–2′335 m MD).
- From June 25th 14:00 to June 25th 19:00, 54 m^3 were injected to the third interval into the Buntsandstein (1′922–2′070 m MD).

The hydraulic stimulation (phase 3) was realised on June 27th and June 28th. In order to be able to quantify the effect of the chemical treatment, the three first injection steps were similar to the initial injection test realised on June 22nd. Maximum flowrates up to 80 l/s were applied during this stimulation sequence. The stepwise injection started on June 27th at 11:20 and terminated on June 28th at 09:00. It was consisted by 8 step rates injections, up to 80 l/s. The duration of the increasing steps was set up to a minimum of 2 h, and the decision to go to the next steps was based on the observed induced seismicity rate. The same injection steps were applied for the progressive shut-in, with a step length of one hour. On June 28th from 11:00 to 17:30, a short injection test was completed at the end of the stimulation to determine the final injectivity index (Fig. 10). The final injectivity index of the well could be estimated to 2,3–2,5 l/s/bar. An advanced seismological monitoring of the reservoir has been set up in collaboration with the University of Strasbourg (Maurer et al., 2015), allowing for real-time location of induced seismic events, thus offering the best support for decision makers during operation. In total, 212 induced events were automatically detected. The seismic activity started right after the flow rate exceeded 40 l/s meaning that the injection flow rate had to overtake the maximum injection flow rate of the thermal stimulation to generate a new micro-seismic activity. About 85 h after the last injection, while all activity was stopped on the platform, a sudden rise of seismic activity was observed during the shut-in period. A small crisis of 37 induced micro-seismic events was detected between the 2nd and the 4th of July. The largest micro-seismic event of the stimulation sequence occurred during this post-stimulation crisis and reached a magnitude M_l of 1.6 (Maurer, et al., 2015). The maximum magnitude threshold set (1.7 M_l) was never reached and no earthquake was felt by the local population.

The impacts of the thermal, chemical and hydraulic stimulations on the well are respectively estimated to factors 1.3, 2 and 1.5. The efficiency of the different stimulation sequences is discussed in Section 5.

4.2. Well GRT-2

The final depth of the well GRT-2 at 3196 m MD was reached on July 20th 2014. The first well cleaning operations were realised on July 25th and 26th using airlift (air injection at 300 m) and the total

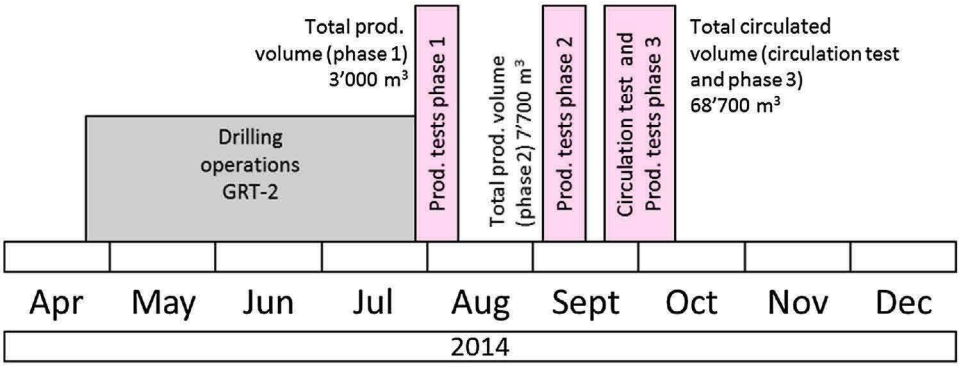

Fig. 11. GRT-2 well production tests and total produced and circulated volumes.

fluid volume produced reached 1′130 m^3, at a maximal flowrate of 54 l/s. During the logging operations, a well-logging tool could not reach the bottom of the well. Thus, it was decided to realise a well control by running a drill bit to the final depth in order to check the well integrity on July 27th and 28th. The operation run smoothly and final depth could be reached again. Then, standard acidizing (HCl) operations were realised on July 29th and July 30th. A total acid volume of 175 m^3 (KCl and HCl at 15% mixture) was injected and pushed in GRT-2 at 4 different depth intervals (Fig. 11).

4.2.1. Production test – phase 1

The first phase of production tests started on July 31st at 18:30. The well started to produce without any airlift. This testing phase was a step-rate test, aiming at reproducing the pumping test sequence applied for GRT-1. A total of 7 steps were performed at various flowrates. As for GRT-1, this sequence constitutes a stepwise procedure of decreasing flowrate. The objective was to characterize the near well reservoir and to derive a well productivity index. On the surface, the liquid flowrate was measured in a V-notch weir box, using an ultrasonic water level sensor. Pressure and temperature were measured at the wellhead, on the flow line and at the casing shoe (2110 m MD/1850 m TVD). The well was shut on August 1st 2014, at 17:00.

A total of 3′000 m^3 of geothermal fluid was produced during this test phase. Several problems were encountered during this production test:

- The downhole data are not consistent with the surface data (at least for pressure). The downhole pressure shows a constant decrease whereas the surface pressure and flowrate reach a steady state.
- The downhole pressure gauge stopped working after the step 7, implying that the build-up downhole data could not be recorded properly.

4.2.2. Production test – phase 2.1 (short production test)

New sensors were installed down to the casing shoe of GRT-2 (2′120 m MD), and a second step-rate test phase, denoted 2.1, was conducted. This time, it was decided to perform sequential steps of increasing flowrate (Fig. 12). The flow-line was modified in order to allow a better control of the flowrate and to eliminate vibrations. The downhole logging tool was located above the casing shoe (2091.3 m MD/1847.8 m TVD) and was equipped with two temperature and two pressure gauges in order to have a back-up in case of failure. Wellhead data are in agreement with downhole pressure data. A total of 1′670 m^3 of geothermal fluid (liquid phase only) was produced during this phase.

The initial downhole pressure value is 191.8 bar. After the test, the downhole pressure approximately stabilises at 190.1 bar. This difference can be explained by a change of density of the water column between reservoir depth and measurement depth. Indeed, the well is initially filled with a mix of geothermal brine and fresh water, as fresh water was injected into the well before the test in order to start production. The initial downhole temperature was 145 °C, whereas the wellwas filled with purely geothermal brine at the end of the test. Thus, assuming a 70% fresh water and 30% geothermal brine mixture at the beginning of the test (estimated resulting density at 145 °C: 942 kg/m^3 (Sharqawy et al., 2010) and a 100% geothermal brine at the end of the test (estimated density at 167 °C: 977 kg/m^3) leads to initial and final reservoir pressure estimations of respectively 242.8 bar and 243 bar at 2′400 m TVD.

4.3. Interference test – phase 2.2 (long production test)

This step-rate test was immediately followed by a 2.5 day production test, at approximately 28 l/s – liquid phase only (Fig. 12). The total liquid volume produced during this phase was 6′000 m^3. During this test, the downhole pressure/temperature was monitored in GRT-2 and in GRT-1. The well was very close to equilibrium as no production or injection had been realised in GRT-1 since the well was killed at the end of July 2014.

The downhole pressure in GRT-2 stabilises very quickly during production around 186.1 bar. At the end of the production, the pressure recovers to a level of 190 bar, very close to the initial pressure of 190.1 bar (still increasing when the logging tool was removed). The maximum recorded temperature during production is 169 °C at the casing shoe.

The downhole pressure recorded in GRT-1 shows a very clear tide signal. Thus, the signal was corrected using BETCO (Barometric Earth Tides Correction) software (Toll and Rasmussen, 2007). The input data were GRT-1 downhole pressure data, surface barometric pressure and earth tides values. The corrected pressure showed in Fig. 12 was obtained using a sampling interval of 15 mn and a maximum lag time of 8 h. After these corrections, it appears that recorded pressure in GRT-1 is clearly correlated with production in GRT-2 (see interpretation below).

4.4. Circulation test and production test – phase 3

Following phase 2, a three weeks circulation test has been conducted between wells GRT-1 and GRT-2. Injection in GRT-1 started on Sept. 16th at 8:35 and production from GRT-2 started on the same day at 10:00. Injection and production flowrates were kept relatively constant around 28 l/s until October 8th. Short breaks in production and injection for filter cleaning or production line cleaning occurred during this circulation test (Fig. 13).

Two different tracers were injected in GRT-1 on Sept. 18th: 200 kg of 2.7-naphthalene disulphonate (dissolved in 650 l of

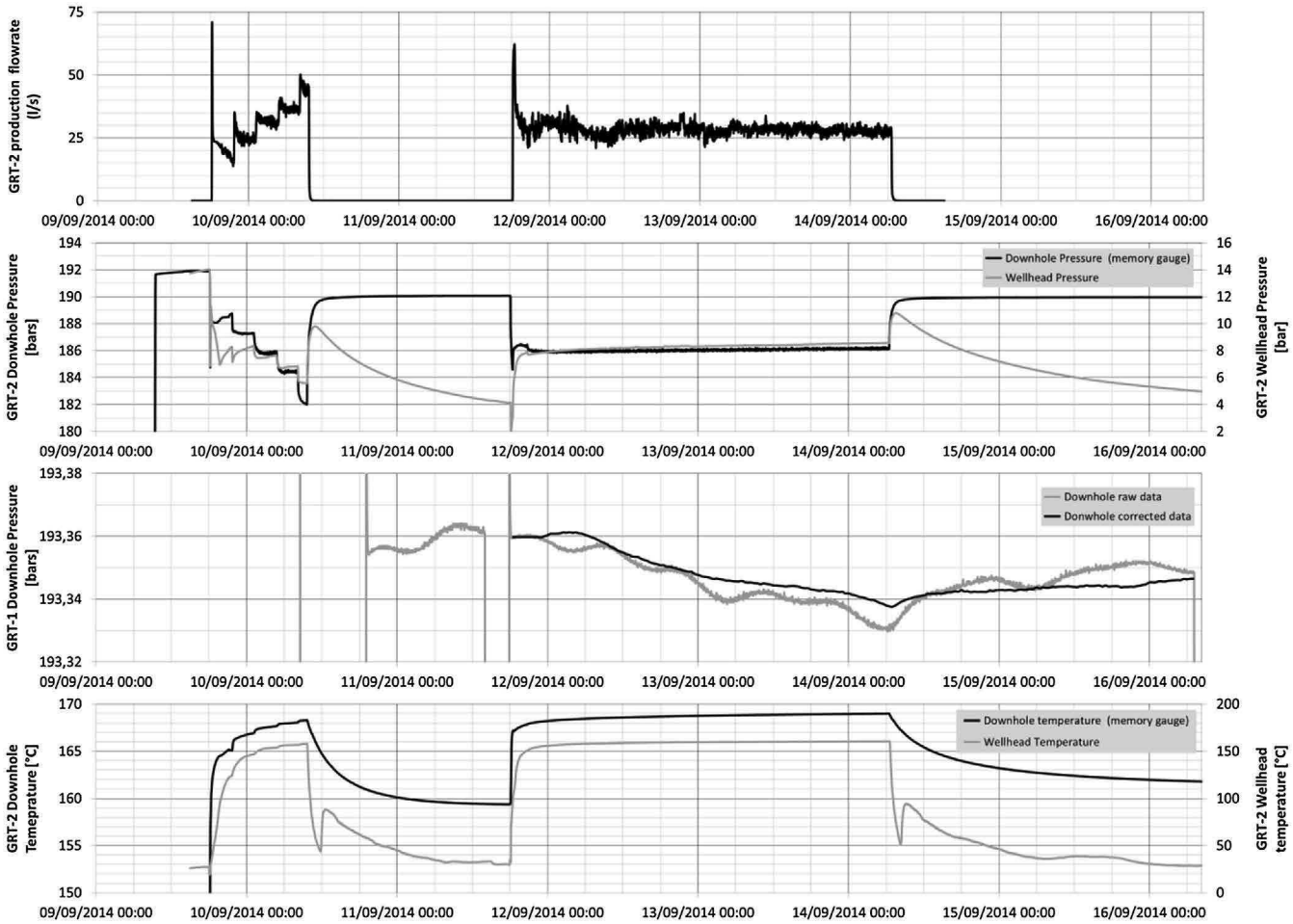

Fig. 12. GRT-2 production tests (phase 2.1 and phase 2.2).

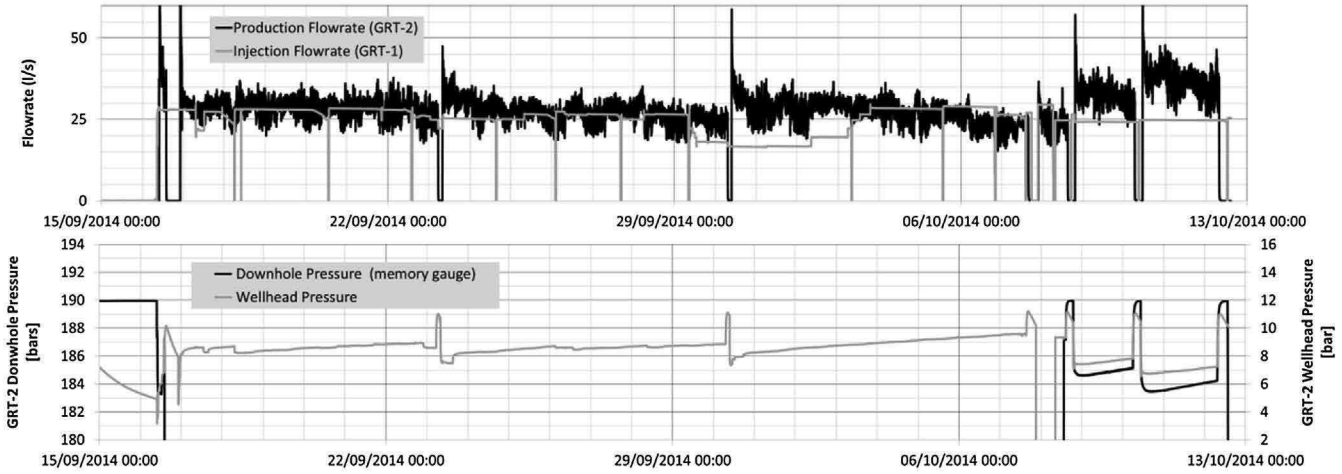

Fig. 13. Circulation test and production test – phase 3.

water) were injected at 9:00 am and 200 kg of fluorescein (dissolved in 700 l water) at 11:00 am The tracer breakthrough occurs on October 2nd, 14 days after injection, thus confirming the connection between GRT-1 and GRT-2 (Sanjuan, et al., 2016).

On October 8th, a downhole pressure gauge was set at the casing shoe GRT-2 at 2100 m MD, and a last GRT-2 production sequence (phase 3) was initiated. The purpose of this sequence was to confirm the well productivity after the three weeks circulation test. The initial pressure value measured is 189.96 bar (not stabilised). The injection in GRT-1 was continued at 25 l/s. A total of five production steps between 30 l/s and 42 l/s have been recorded during this phase. No induced seismicity was detected during this testing sequence (Maurer, et al., 2015)(Maurer, et al., 2015).

5. Inferred thermo-hydraulic properties and discussion

5.1. Injectivity and productivity indexes

The well development strategy applied on GRT-1 was successful. As a result, the injectivity of the well could be multiplied by a factor 5 to reach 2.5 l/s/bar at nominal flowrate of 70 l/s. The downhole overpressure versus the injection flowrate is showed in Fig. 14 for all injection phases. As no downhole pressure data were recorded during the thermal stimulation, a downhole pressure has been estimated using the fluid density measured at the surface (neglecting friction losses in the well as the flow-rate was quite low during this experiment). The final downhole differential pressure at nominal flowrate is estimated to 29 bar. The following observations can be made on this stimulation experiment:

- The thermal injection experiment clearly shows a well injectivity increase over time. The initial injectivity of the well using calculated downhole pressures is estimated to 0,6 l/s/bar, which is consistent with the measured initial productivity of the well (0,45 l/s/bar). The injectivity increase due to the thermal stimulation is almost permanent, as the pre-acidification step-rate test realised roughly 2 months later shows a similar injectivity.
- The chemical treatment had a clear impact on the well, as the low-rate steps realised at the beginning of the stimulation show lower injection pressure than the pre-acidification injections (see Fig. 14).
- Hydraulic stimulation had a big impact on the well, as the final injection tests show lower injection pressures than observed during the stimulation.

A clear change of the behaviour of the well can be observed during the hydraulic stimulation at flowrates above 40 l/s. Indeed, from that point, one can observe a linear increase of the downhole differential pressure with the flowrate. The question to know if this observation could be due to hydraulic fracturing processes in the reservoir has been investigated. It appears that this is not the case. Indeed, injection pressure at which this linear behaviour occurs is very low (between 23 bar and 31 bar overpressure during the stimulation and between 10 bar and 25 bar during the post stimulation injection test). The maximum absolute downhole pressure recorded during stimulation was 226.4 bar at 1′900 m TVD (corresponding to approximately 270 bar at 2′350 m TVD – assumed reservoir depth). In comparison, the minimal principal stress at that depth can be estimated to 316 bar, following the regional stress model based on experiments lead in Soultz-sous-Forêts (Cornet et al., 2007) or to 295 bar, considering only comparable depth values (Evans, 2005). Thus, the absolute reservoir pressure during injection remains below the minimal principal stress, confirming that hydraulic fracturing is not occurring during this stimulation phase. Moreover, the linear increase of pressure with injection flowrate could be reproduced during the final injection test and not only during stimulation. We would rather suggest that the stimulation sequence lead to the increase of near wellbore fracture aperture and permeability (in response to the reduced effective normal stress), resulting in connecting the well to a high-conductive feature (fractured reservoir).

Compared to the injectivity of GRT-1, the productivity of GRT-2 is very high. According to the different tests, the productivity index of GRT-2 is estimated to 2.8–3.5 l/s/bar at nominal flowrate. The downhole differential pressure at nominal flowrate (70 l/s) is estimated between 20 and 25 bar. Results obtained during all tests realised during the testing sequences 2.1, 2.2 and 3 are consistent with the fact that well GRT-2 is better connected to highly permeable features than GRT-1, through several drains (identified by the thermal anomalies in Fig. 4).

Table 1
Main hydraulic properties of the reservoir derived from pumping test interpretations based on Moench's model of double porosity with fracture skin effects (Moench, 1984). Fluid density is chosen as 970 kg/m^3 and reservoir thickness as 500 m (including a total fracture zone thickness of 40 m for GRT-2). Equivalent permeabilities are given in Table 2.

		GRT-1	GRT-2
Well	Dimensionless skin factor [–]	21.3	1.8
Fault	Hydraulic cond. [m s^{-1}]	–	$2.9{\cdot}10^{-06}$
	Specific storage [m^{-1}]	–	$7.2{\cdot}10^{-07}$
Matrix	Hydraulic cond. [m s^{-1}]	$6.1{\cdot}10^{-08}$	$5.3{\cdot}10^{-07}$
	Specific storage [m^{-1}]	$7.2{\cdot}10^{-07}$	$5.2{\cdot}10^{-07}$

5.2. Reservoir properties

In order to characterize hydraulic properties of the reservoir, classical pressure transient analysis interpretations have been carried out with pumping test data from each well using AQTESOLV software based on the direct use of analytical solutions (Baujard et al., 2016). For GRT-1, only downhole drawdown data of the 9/01/2013 and both recovery data of the 5/01/2013 (unfortunately incomplete) and of the 9/01/2013 have been interpreted. As the data quality is quite poor, the interpretation of GRT-1 production tests was realised using a single permeability confined aquifer model (Dougherty and Babu, 1984). For GRT-2, the step-drawdown test (phase 2.1) as well as drawdown and recovery data (phase 2.2) have been used for the interpretation. This time, the best results are obtained using a fractured confined aquifer model based on a double porosity approximation including a fracture skin effect (Moench, 1984). Observations realised in GRT-1 during GRT-2 test phase 2.2 have been taken into account (GRT-1 acting as an observation well) and measurements could be reproduced by the model. Main interpretation results are summarized in Table 1. Even though different models were applied to interpret these pumping tests, the following conclusions could be drawn from these works:

- GRT-1 is characterized by a high fracture skin coefficient (Horne, 1995) in comparison with GRT-2, meaning a low permeability in the near-well domain and a bad connection with the reservoir. These observations realised prior to the hydraulic stimulation of GRT-1, were largely confirmed by the stimulation results, leading to a drastic enhancement of near-well hydraulic properties and the development of a good connection with the reservoir.
- Reservoir properties derived from GRT-1 production tests are very different from values derived from GRT-2; GRT-1 seems so be badly connected to a medium permeability reservoir, whereas GRT-2 is connected to a highly permeable reservoir.
- No limit (no-flow or constant head boundary) could be identified in the data with the interpretations realised so far on GRT-1 or on GRT-2.

It must be underlined that GRT-1 production tests were quite short, and the production flowrates relatively low. Thus, the production tests are strongly influenced by near-well processes and head losses.

These tests also clearly demonstrate the existence of a hydraulic and of a mass (i.e. tracer) connection between GRT-1 and GRT-2 (see Fig. 12 and Section 4.d). On one hand, the hydraulic connection is quite fast, as, according to the pressure response recorded in GRT-1 during test phase 2.2, it seems that the pressure in GRT-1 starts to stop decreasing around 30 min after shut-in of GRT-2. On the other hand, the tracer breakthrough occurred 14 days after injection of the tracer. This period is very long in comparison with what has

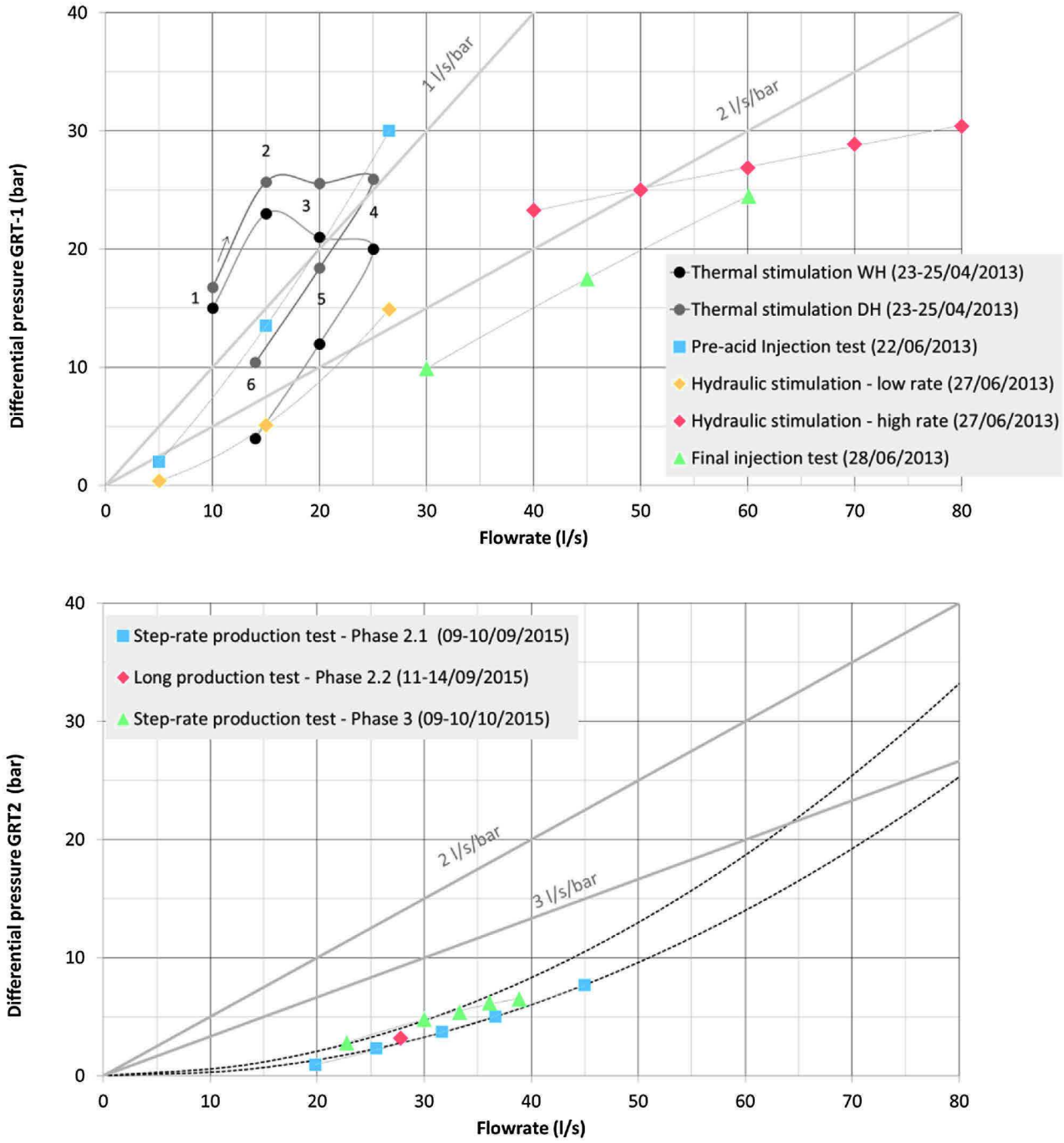

Fig. 14. GRT-1 injectivity index (top) and GRT-2 productivity index (bottom). Only liquid phase is considered in productivity index computation. All pressures are downhole differential pressures, except for the thermal stimulation experiment, for which a downhole overpressure is estimated ("Thermal stimulation DH") from the surface absolute pressure ("thermal stimulation WH"), using an estimation of the water column density.

been observed in Soultz-sous-Forêts between the best connected wells GPK-2 and GPK-3 (Sanjuan, et al., 2006).

5.3. Natural hydro-thermal convection

In order to investigate the possibility of occurrence of convection cells within the reservoir, the Rayleigh number has been calculated in the matrix and in the fault zone using the following formulation of the Rayleigh-Benard instability in a porous medium (Turcotte and Schubert, 2014):

$$Ra = \frac{\alpha_f g \rho_f^2 C_{pf} kb(T_1 - T_0)}{\mu \lambda_m}$$

With α_f [K^{-1}] the fluid thermal expansion coefficient, g [$m\,s^{-2}$] the gravity acceleration, ρ_f [$kg\,m^{-3}$] the fluid density, C_{pf} [$J\,kg^{-1}\,K^{-1}$] the fluid heat capacity, k [m^2] the reservoir permeability, b [m] the depth interval in which convection occurs, T_1 [K] the lower boundary initial temperature, T_0 [K] the upper boundary initial temperature, μ [Pa s] the fluid dynamic viscosity and λ_m [W/m/K] the reservoir thermal conductivity.

The values of the parameters used for the calculation and the resulting Rayleigh number are showed in Table 2. A lower boundary depth at 3000 m and a lower boundary temperature of 177 °C are assumed in the calculations. The upper boundary depth is set to

Table 2
Parameters used and resulting Rayleigh Number value. Hydraulic conductivity values are derived from pumping test interpretations of GRT-1 and GRT-2 (see Table 1).

			GRT1 Matrix	GRT2 Matrix	GRT2 Fracture
α	Fluid thermal expansion coefficient	[K^{-1}]	$1.50{\cdot}10^{-03}$		
g	Gravity acceleration	[m s^{-2}]	9,8		
ρ	Fluid Density	[kg m^{-3}]	970		
cp	Fluid heat capacity	[J kg^{-1} K^{-1}]	3800		
μ	Fluid dynamic viscosity	[Pa·s]	$1.75{\cdot}10^{-04}$		
λ	Matrix thermal conductivity	[W·m^{-1} K^{-1}]	3		
K	Hydraulic conductivity	m/s	$6.00{\cdot}10^{-08}$	$5.00{\cdot}10^{-07}$	$2.90{\cdot}10^{-06}$
k	Permeability	[m^2]	$1.10{\cdot}10^{-15}$	$9.20{\cdot}10^{-15}$	$5.34{\cdot}10^{-14}$
Z0	Upper boundary depth of convection zone	[m]	1650		
Z1	Lower boundary depth of convection zone	[m]	3000		
b	Depth interval of convection zone	[m]	1350		
T1	Lower boundary initial temperature	[°C]	177		
T surf	Mean surface temperature	[°C]	12		
∇T	Initial temperature gradient	[K/m]	0.055		
T0	Upper boundary initial temperature	[°C]	102.8		
DT	Delta temperature	[K]	74.25		
Ra	**Rayleigh number**	**[–]**	**11.1**	**92.4**	**535.7**

1650 m (top of the Muschelkalk formation) and the upper boundary temperature is calculated assuming a 12 °C mean surface temperature and a constant temperature gradient (calculated from the lower boundary depth and temperature). Three different cases have been calculated based on the hydraulic conductivity derived from the production tests of GRT-1 (matrix only) and GRT-2 (matrix and fracture zone).

According to (Turcotte and Schubert, 2014), the critical Rayleigh number value at which convection could occur is 39.5. Thus, the results show that convection is very likely to occur with a permeability value of the fault zone derived from GRT-2 production tests. Rayleigh number values calculated using permeability values of the matrix derived from GRT-1 and GRT-2 production test do not allow to draw clear conclusions as they are quite close to the critical value and because of the oversimplified model that is considered. A more precise estimate taking into account the fault geometry i.e. a porous medium between two narrow facing walls should be considered.

6. Conclusions and discussion

Several important conclusions can be drawn after the results observed in this EGS project in Rittershoffen:

- First of all, the two wells GRT-1 and GRT-2 show respectively high injectivity and productivity indexes, reaching the economic threshold for exploitation. The geothermal target identified (regional fault zone in the basement associated with high temperature gradients) could be confirmed.
- Furthermore, the well development strategy applied to GRT-1 was very successful, as the injectivity index was increased by a factor 5, and the induced seismicity was limited, as no event could be felt by inhabitants.
- The correlation between different observations (mostly UBI acoustic imaging logs, temperature logs, flow-logs) confirms that regional fault zones in the Rhine Graben are permeable structures and host natural fluid circulations.
- Temperature logs in both wells show a clear contrast between the upper part and the lower part of the reservoir. The transition at Rittershoffen corresponds to the Keuper formations. The upper part hosts a conductive regime with a very constant high gradient (85 °C/km). Below the top of the Muschelkalk formation, heat transport is dominated by advective and/or convective processes, in particular in the vicinity of the regional fault structure.
- This conclusion is confirmed by the Rayleigh Number calculated in the fracture zone using estimated hydraulic properties from hydraulic tests. It is higher than the critical Rayleigh Number, thus showing that convection is likely to occur in these fault zones.
- On a purely mechanical point of view, it is also clear that the successful stimulation of GRT-1 is only due to hydroshearing mechanisms and that no hydraulic fracturing was observed during the stimulation.
- A mass and hydraulic connection between wells GRT-1 and GRT-2 could be highlighted by the interference and circulation/tracer tests performed

The following observations would need further investigations:

- Even if no production test was carried out on well GRT-1 after the stimulation and no injection test was realised in GRT-2, the wells show quite different productivity/injectivity indexes. This difference tends to demonstrate that GRT-2 is better connected to highly permeable features. The pressure evolution in GRT-1 during stimulation raises the question to know if this well really hits the regional fault zone or only a secondary feature. In this case, the hydraulic stimulation would have developed the connection with the main feature.
- An interesting observation has been done on the temperature logs. Indeed, it appears that several thermal anomalies are constituted by a positive anomaly at the top and a negative anomaly at the bottom. For example, the most important thermal anomaly in GRT-2 at 2′400 m TVD shows a 1 °C temperature increase between 2′380 m and 2′400 m and a 2–3 °C temperature decrease between 2′400 and 2′420 m TVD. This would suggest the existence of convection cells within a 40 m wide fault zone with ascending hot fluids on the top of the fault zone and descending 'cold' fluids on the bottom of the zone. A possible small scale convection within the fault zone has not been investigated in this paper.
- It is interesting to observe that the temperature profile of GRT-1 is nearly vertical below the top of the Muschelkalk (the temperature gradient value is 0,3 °C/km). On the contrary, the temperature gradient in the same horizons in GRT-2 is significantly larger (1.8 °C/100 m). The implication of this observation (if not only due to non-equilibrium conditions) has not be investigated.
- The question to know if the fault zone could have been targeted at shallower depth of 1600m (in the Muschelkalk) is open. The temperature profile strongly suggests that the Muschelkalk formation host natural fluid flow and that it could show high permeabilities, as suggested by the mud losses met during GRT-1. That being said, one must keep in mind that the Muschelkalk is likely to show strong lateral heterogeneities, and that the layer

is quite thin in comparison with the Bundsandstein; thus constituting a challenging target.

Acknowledgements

The authors would like to thank ECOGI, which is a joint venture between “Electricité de Strasbourg”, “Roquette Frères”, and “Caisse des Dépôts et Consignation”. The authors also warmly acknowledge researchers of the EOST team in Strasbourg (“Ecole et Observatoire des Sciences de la Terre”), which is a main actor of the Labex (“Laboratoire d’Excellence”) G-Eau-Thermie Profonde for fruitful discussions and scientific support. The works described in this paper are supported by “ADEME” with the “Fonds Chaleur” as well as the “EGS Alsace” research program. A part of this work was done in the framework of the DESTRESS Eu project which has received funding from the European Union’s Horizon 2020 research and innovation program under grant agreement No 691728.

References

Aichholzer, C., Duringer, P., Orciani, S., Genter, A., 2015. New stratigraphic interpretation of the twenty-eight-year old GPK-1 geothermal well of Soultz-sous-Forêts (Upper Rhine Graben, France). 4th European Geothermal Workshop EGW. Strasbourg.

Bailleux, P., Schill, E., Edel, J., Mauri, G., 2013. Localization of temperature anomalies in the Upper Rhine Graben: insights from geophysics and neotectonic activity. Int. Geol. Rev. 55 (14), 1744–1762.

Bailleux, P., Schill, E., Abdelfettah, Y., Dezayes, C., 2014. Possible natural fluid pathways from gravity pseudo-tomography in the geothermal fields in Northern Alsace (Upper Rhine Graben). Geotherm. Energy 2 (1), 1–14.

Baujard, C., Genter, A., Maurer, V., Dalmais, E., Graff, J.-J., 2015. ECOGI a new deep EGS project in Alsace, Rhine graben, France. In: World Geothermal Congress, Melbourne, Australia, 19–25 April 2015.

Baujard, C., Genter, A., Dalmais, E., Maurer, V., Hehn, R., Rosillette, R., 2016. Temperature and hydraulic properties of the Rittershoffen EGS Reservoir. In: France European Geothermal Conference, 19–24 Sept. 2016 Strasbourg, France.

Cocherie, A., Guerrot, C., Fanning, M., Genter, A., 2004. Datation U-Pb des deux faciès du granite de soultz (Fossé Rhénan, France). C.R. Geosci. 336, 775–787.

Cornet, F., Bérard, T., Bourouis, S., 2007. How close to failure is a granite rock mass at a 5 km depth? Int. J. Rock Mech. Min. Sci. 44, 47–66.

Dezayes, C., Genter, A., Valley, B., 2010. Structure of the low permeable naturally fractured geothermal reservoir at Soultz. C.R. Geosci. 342, 517–530.

Dorbath, L., Evans, K., Cuenot, N., Valley, B., Charléty, J., Frogneux, M., 2010. The stress field at Soultz-sous-Forêts from focal mechanisms of induced seismic events: cases of the wells GPK2 and GPK3. C.R. Geosci. 342 (7), 600–606.

Dougherty, D., Babu, D., 1984. Flow to a partially penetrating well in a double-porosity reservoir. Water Resour. Res. 20 (8), 1116–1122.

Edel, J.-B., Schulmann, K., Rotstein, Y., 2007. The Variscan tectonic inheritance of the Upper Rhine Graben: evidence of reactivations in the Lias, Late Eocene-Oligocene up to the Recent. Int. J. Earth Sci. 96, 305–325.

Evans, K., 2005. Permeability creation and damage due to massive fluid injections into granite at 3.5 km at Soultz: 2. Critical stress and fracture strength. J. Geophys. Res. 110, 14, http://dx.doi.org/10.1029/2004JB003169.

Genter, A., Evans, K., Cuenot, N., Fritsch, D., Sanjuan, B., 2010. Contribution of the exploration of deep crystalline fractured reservoir of Soultz to the knowledge of Enhanced Geothermal Systems (EGS). C.R. Geosci. 342, 502–516.

Georg Project Team, 2013. Potentiel géologique profond du Fossé rhénan supérieur. In: Open File Report BRGM/RP-61945-FR. Georg Project Team http://www.geopotenziale.eu.

Horne, R., 1995. Modern Well Test Analysis: A Computer-Aided Approach, 2nd edition. Petroway.

Kappelmeyer, O., Gérard, A., Schloemer, R., Ferrandes, F., Rummel, F., Benderitter, Y., 1992. Geothermal Energy in Europe – The Soultz Hot Dry Rock Project. Grodon and Breach Science Pu.

Maurer, V., Cuenot, N., Gaucher, E., Grunberg, M., Vergne, J., Wodling, H., et al., 2015. Seismic Monitoring of the Rittershoffen EGS Project (Alsace, France). World Geothermal Congress, Melbourne, Australia.

Moench, A., 1984. Double-porosity models for a fissured groundwater reservoir with fracture skin. Water Resour. Res. 20 (7), 831–846.

Munck, F., Walgenwitz, F., Maget, P., Sauer, K., Tietze, R., 1979. Synthèse géothermique Du Fossé Rhénan Supérieur. BRGM Service Géologique Régional d'Alsace -Geologisches Landesamt Baden-Württemberg. Commission of the European Communities.

Place, J., Diraison, M., Naville, C., Géraud, Y., Schaming, M., Dezayes, C., 2010. Decoupling of deformation in the upper rhine graben sediments. seismic reflection and diffraction on 3-component vertical seismic profiling (Soultz-sous-Forêts area). C.R. Geosci., 575–586.

Pribnow, D., Schellschmidt, R., 2000. Thermal tracking of Upper crustal fluid flow in the Rhine Graben. Geophys. Res. Lett. 27, 1957–1960.

Recalde Lummer, N., Rauf, O., Gerdes, S., Genter, A., Scheiber, J., Villadangos, G., 2014. New biodegradable stimulation system – First field trial in granite/Bunter sandstone formation for a geothermal application in the Upper Rhine Valley. In: Deep Geothermal Days., Paris, France.

Sanjuan, B., Pinault, J., Rose, P., Gerard, A., Brach, M., Braibant, G., et al., 2006. Tracer testing of the geothermal heat exchanger at Soultz-sous-Forêts (France) between 2000 and 2005. Geothermics 35 (5–6), 622–653.

Sanjuan, B., Scheiber, J., Gal, F., Touzelet, S., Genter, A., Villadangos, G., 2016. Interwell chemical tracer testing at the Rittershoffen site (Alsace, France). In: European Geothermal Conference EGC, Strasbourg, France.

Sausse, J., Dezayes, C., Dorbath, L., Genter, A., Place, J., 2010. 3D fracture zone network at Soultz based on geological data, image logs: microseismic events and VSP results. C.R. Geoscience 342, 531–545.

Sharqawy, M., Lienhard, J., Zubair, S.M., 2010. Thermophysical properties of seawater: a review of existing correlations and data, desalination and water treatment. Desalin. Water Treat. 16, 354–380.

Toll, N., Rasmussen, T., 2007. Removal of barometric pressure effects and Earth tides from observed water levels. Ground Water 45 (1), 101–105.

Turcotte, D.L., Schubert, G., 2014. Geodynamics. University Press, Cambridge.

Valley, B., 2007. The Relation Between Natural Fracturing and Stress Heterogeneities in Deep-seated Crystalline Rocks at Soultz-sous-Forêts (France). ETH Zurich (Ph D. Thesis).

Vidal, J., Genter, A., Schmittbuhl, J., 2015. How permeable fractures in the Triassic sediments of Northern Alsace chracaterize the top of hydrothermal convective cells? Evidences from Soultz geothermal boreholes (France). Geotherm. Energy J. 3 (8), http://dx.doi.org/10.1186/s40517-015-0026-4, Special Issue: Characterization of Deep Geothermal Systems.

Vidal, J., Genter, A., Schmittbuhl, J., 2016. Pre- and post-stimulation characterization of geothermal well GRT-1, Rittershoffen, France: insights from acoustic image logs of hard fractured rock. Geophys. J. Int. 206 (2), 845–860, http://dx.doi.org/10.1093/gji/ggw181.

ANNEXE 4

Stress field rotation in the EGS well GRT-1 (Rittershoffen, France)

Régis Hehn[1], Albert Genter[1], Jeanne Vidal[2], Clément Baujard[1]

[1] ES-Géothermie, 3A chemin du gaz, F-67500 Haguenau, France

regis.hehn@es.fr

Keywords: Upper Rhine graben, Rittershoffen, geothermal well GRT-1, Stress field, stress orientation, drilling induced tensile fracture, Alsace.

ABSTRACT

The stress state in GRT-1, a recent deep geothermal well drilled in Northern Alsace (Upper Rhine Graben, France) has been investigated based on drilling-induced fractures (DIF) observed on borehole acoustic logs. Some of those fractures are compressive fractures, known as Breakouts, and others are tensile fractures, called DITFs in this study. They are used to estimate the orientation of the stress field because they occur respectively in the direction of Shmin and SHmax.

At a small scale, SHmax orientation follows a cyclic profile repeating every 50 m MD along the borehole. Those small cycles participate to a more global trend, where the orientation of SHmax tend to reach the regional orientation (N145°E) in weaker layers (as clays or marls), and turn clockwise toward N50°E in hard rock layers (as dolomite and sandstone).

Finally, this study shows that the entire stress state of the sedimentary layer is decoupled from the basement one: the orientation of SHmax is N155°E in the basement, but is globally N20°E in the sedimentary layer.

1. INTRODUCTION

Analysis of stress induced wellbore failure is a powerful method to characterize the state of stress of a rock mass (Zoback et al., 1985, 2003). Knowledge of the stress state in a recent deep geothermal well drilled in Northern Alsace (Upper Rhine Graben, France) has been investigated based on drilling-induced fractures observed on borehole acoustic logs. A new geothermal doublet located at Rittershoffen was drilled within deep fractured rocks lying at the interface between the Triassic clastic sediments from Buntsandstein and the Paleozoic granite (Baujard et al 2015, Genter et al 2015a, b). Many geological and geophysical data have acquired in the open-hole section of the well in order to characterize the natural fracture system as well as the present-day stress field. Based on borehole acoustic image logs, high quality datasets have been interpreted in terms of drilling-induced tension fractures.

Previous studies have characterized the regional stress field of the Upper Rhine Graben, with its magnitude and orientation (Heidbach et al 2008). At regional scale, in our area of interest, the orientation of the maximum horizontal stress component is NW-SE. In the nearby Soultz-sous-Forêts geothermal site, the stress field was characterized in the deep basement (1,5 to 5 km depth) by various methods such as hydraulic tests, borehole image logs and induced seismicity by Cornet et al (2007), Cornet (2013), Valley (2007) and Sahara et al (2014). In-situ stress orientation of the Soultz-sous-Forêts geothermal field were inferred from breakouts and drilling-induced tensile fractures (DITF) patterns observed I the deepest boreholes GPK3 and GPK4 (Valley, 2007, Valley and Evans, 2007). At Soultz, the mean maximum horizontal stress orientation values range between N164E and N185E. Stress heterogeneity have been also outlined from variations in stress orientation indicated by wellbore failure in two boreholes of the Soultz-sous-Forêts EGS site (Valley and Evans, 2007). Localized major stress orientation variations correlate with the occurrence of two most prominent fracture zones or faults, showing some evidence of natural permeability, observed at 2.0 and 4.7 km depth. The lowermost stress perturbation extends over several hundred metres and is characterised by SHmax rotations of up to 90° and changes in the mode of failure from compression (breakouts) to tension (DITFs) (Valley and Evans, 2007).

This study proposes an analysis of the evolution of the orientation of SHmax with depth, using the DITFs orientation, in the lower part of sedimentary Triassic

layers and the upper part of the granite Paleozoic basement (Brudy and Zoback, 1999).

Besides the study of the evolution of stress orientation with depth between the bottom of the basin and the top basement, we focused our analysis on stress heterogeneity, Thus, the goal of this study is to find any correlation between the rotation of the stress field and the presence of natural fractures or major changes in the geomechanical unit composition (lithology).

The structural analysis focuses on the vertical well GRT-1, owned by a company named ECOGI. This well has been drilled up to 2580 m Measured Depth (MD), in October-December 2012, in Rittershoffen, at 6 kilometers of the geothermal site of Soultz-sous-Forêts (Figure 1). GRT-1 is the first well of a doublet drilled for industrial thermal application. The second deviated well GRT-2 has been drilled in 2014 down to 3200 m MD and the geothermal power plant is now in activity.

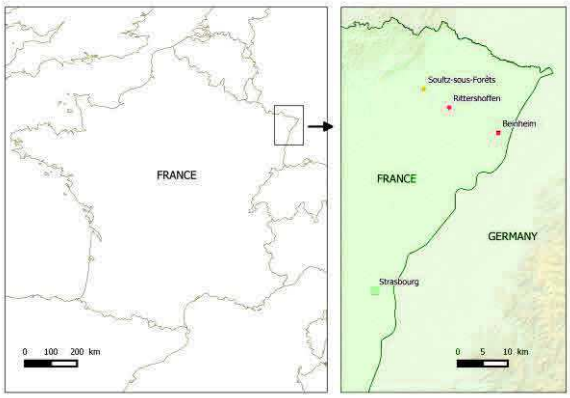

Figure 1: Location of Rittershoffen, (Northern Alsace, France).

The investigated depth interval corresponds to the section of the well GRT-1 which has been imaged by an Ultrasonic Borehole Imager (UBI): from 1460 m MD, in the Middle Keuper (Upper Trias), to 2550 m MD in the deep massive Paleozoic granite. The top basement has penetrated at 2200 m MD. The stress field characterization has been done in GRT-1 only inside the $12^{1/4}$ and $8^{1/2}$ inches borehole section.

2. PRINCIPLE – METHODOLOGY

2.1 Drilling Induced Tensile Fractures (DITFs)

The first step of this study is to get the orientation of SHmax at several depths in the well. To determine SHmax, the classical method is to use Drilling Induced Fracture (DIF) orientations (Davatzes and Hickmann 2005).

As this area has undergone a polyphasic tectonic history with many compressive and extensive structural events from the granite emplacement in Carboniferous to Recent times, the resulting natural fracture network intersected by the well is quite complex and not necessarily representative of the present-day stress field. For that reason, natural fractures are not used to determine the actual stress orientation. In the contrary, drilling a borehole into a rock mass creates a local modification of the actual stress state that usually induces the formation of tiny fractures at the surface of the borehole wall. Some of those fractures are compressive fractures, known as Breakouts, and others are tensile fractures, called DITFs in this study (Figure 2). The reason why DIFs are commonly used to get actual stress field orientation is that Breakouts occur in the direction of the actual minimal horizontal stress Shmin and the DITFs in the direction of the actual SHmax. At the studied depth (~2 km deep), Breakouts are much less present than DITFs, and DITFs are thinner, so their orientation is more accurate. For this reason, DIFTs are the only drilling induced borehole failure that has been investigated for this study.

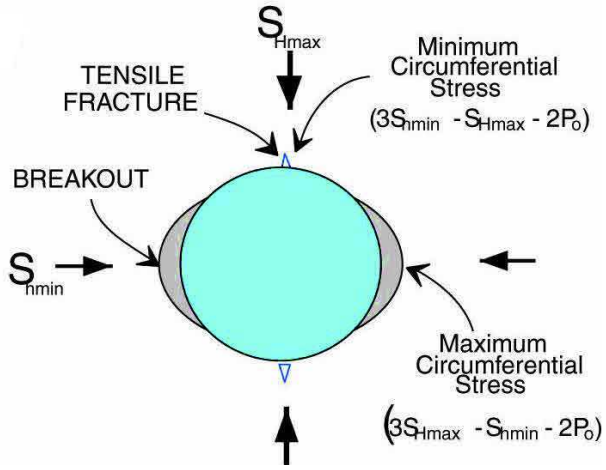

Figure 2: Schematic explanation of Breakouts and Drilling Induced Tensile Fractures formation principle. (Davatzes and Hickmann 2005).

Axial Drilling Induced Tensile Fractures (A DITFs):

There are different kinds of DITFs, some of them are called A DIFTs for "Axial" DITFs (Figure 3). They form vertical thin lines along the borehole surface, they occur symmetrically and they correspond to segments of the well where the stress field is well-aligned to the borehole: the two horizontal principal stresses Shmin and SHmax are in a plan orthogonal to the borehole and the vertical principal stress Sv is collinear to the borehole.

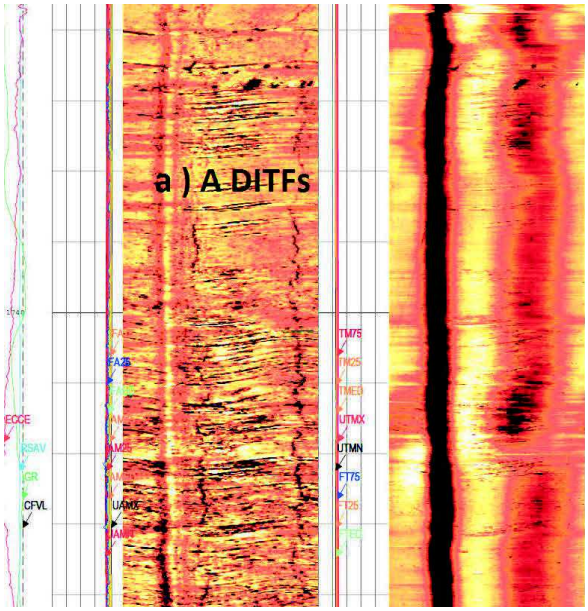

Figure 3: Example of A DITFs in GRT-1. The amplitude of the UBI is on the left, and the transit time on the right.

En Echelon Drilling Induced Tensile Fractures (E DITFs):

Another sort of DITF is called E DITFs for "en Echelon" DITFs. They form short inclined little fractures along the borehole (Figure 4). The middle of the fracture is still in the direction of SHmax and corresponds to segments of the well where the stress field is not well-aligned to the borehole: when Sv is not really collinear to the borehole. This orientation difference varies between 10° to 20°. As GRT-1 is mostly vertical (maximum deviation is 8.8°), E DITFs occur when Sv is not vertical anymore.

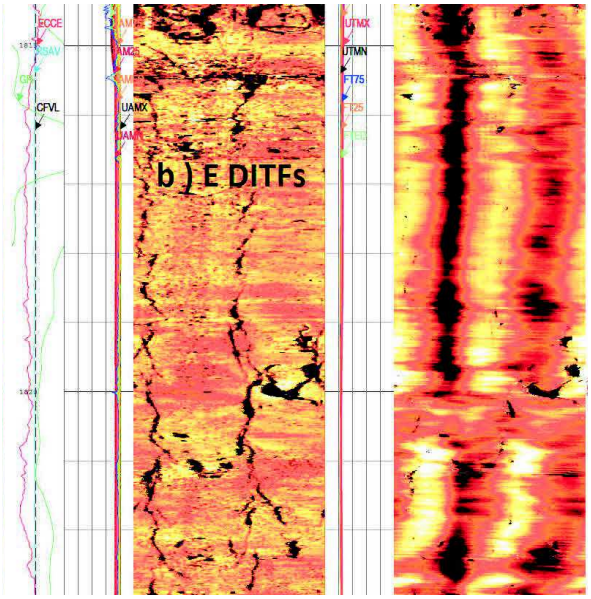

Figure 4: Example of E DITFs in GRT-1. The amplitude of the UBI is on the left, and the transit time on the right.

Petal Centerline Fracture:

The last sort of DITF is called Petal Centerline DITFs (Figure 5, Davatzes and Hickmann 2005). They are also formed during the drilling operation but some meters into the rock mass below the drill bit, due to the decompression of the rock, and are then crossed by borehole later. They are still aligned to SHmax, but the borehole doesn't always cross them in a manner that they appear symmetrically opposed in the borehole.

It is sometimes difficult to distinguish the DITFs from some natural fractures which have almost the same dip. It is also hard to distinguish Petal Centerline DITFs and A DITFs. For this reason, Petal Centerline DITFs are integrated in A DITFs in this study. Making this association still allows making the differentiation between the borehole sections where Sv is collinear to the borehole axis or not.

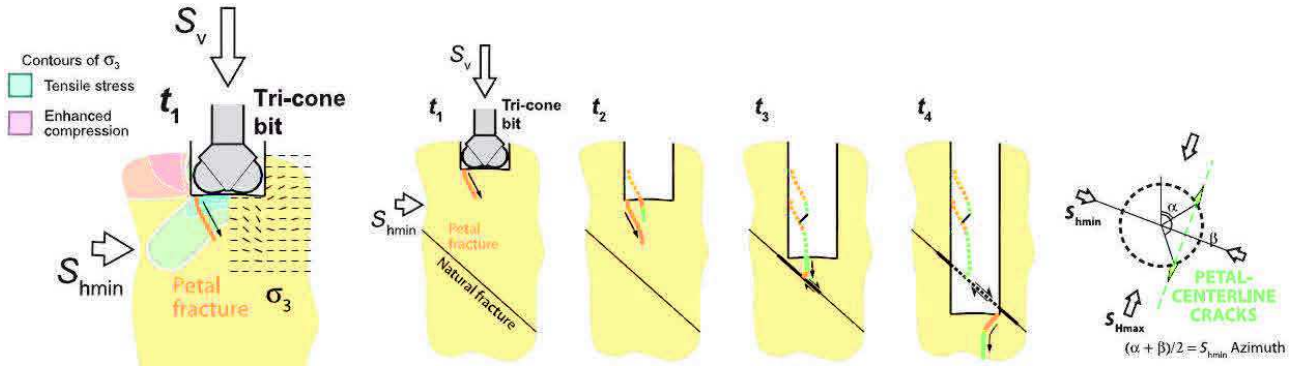

Figure 5: Schematic explanation of Petal Centerline Induced Fracture formation principle. (Davatzes and Hickman, 2006)

Picking strategy:

The DITFs have been picked visually by hand on a software, using available images of the GRT-1 from and Ultrasonic Borehole Imager (UBI). The acoustic image logs were acquired at a vertical resolution of 1 cm and an azimuthal resolution of 2°. A section of the UBI is missing between 1900 m MD and 1930 m MD because it corresponds to the depth of a change in drilling diameter: from 12.25 inches to 8.5 inches. This section is known to be naturally fractured but no UBI can visually attest it. Before the picking, the UBI has been corrected by the deviation of the well. DITFs have been picked and separated in 4 categories: Major and Minor A DITFs and E DITFs. As the qualification Major or Minor is only visual and qualitative, they have been grouped in A DITFs and E DITFs for this study. The DITFs database obtained has then been exported for a forthcoming treatment.

Natural fracture data were interpreted by Dezayes et al (2014) and Vidal et al (2016). Lithology and stratigraphy are given from Aichholzer et al (2015).

2.2 Treatment

The goal of this study is to find if there is a correlation between the rotation of the stress field and the presence of natural fractures or a change in the lithology (geomechanical unit). So the aim of the treatment was to compare the raw azimuth of DITFs, with the mean azimuth of DITFs for different lithological segmentation of the studied interval by taking into account the location of the major natural fractures crossed by the GRT-1 borehole.

Moving average:

First, the graphical representation of raw DITFs azimuths is too cloudy because the azimuths are too scattered. To solve this visualization issue, a moving average has been applied on the DITFs orientations. A moving window of 10 meters has been used, and each DITF has been weighted by its length. This moving average process is not optimal because it skews the distribution by artificially adding points at transitions between two clusters of strongly different DITF orientations. Nevertheless, it has only been used for visualization, and helps to see azimuthal trends or vertical evolutions where DITF orientations are smoothly rotating.

Depth interval segmentation:

Secondly, the studied interval has been discretized with three degrees of refinement related to lithology: ages, sub-ages, and formations. For each segment, a mean of DITF orientations has been calculated, weighted by the corresponding length of each individual DITF.

All the results are not presented here. It has been decided to focus on the global behaviour of all DITFs orientation (A and E) on the more refined depth interval discretization (Figure 6).

Natural Fracture selection:

Finally, the major natural fractures have been selected. It has been decided to keep only the larger fractures, because they could probably create stronger stress field perturbations. The picking of natural fractures has been done in a previous study (Dezayes et al 2014, Genter et al. 2015b, Vidal et al 2016). Due to their physical acoustic contrast with the surrounding rocks, natural fractures are detected on the UBI. Fractures visible on both transit time and amplitude, thus showing an apparent free aperture, are interpreted as locally opened fractured. However, it is again not optimal because when a fracture shows a free aperture in a UBI, it means that it is open in the direct vicinity of the borehole wall but it can be plugged or sealed in the far field. More detailed about fracture characterization is given by Vidal et al (2016).

A and E DITFs comparison:

The two major discriminating parameters are the orientation and the length of the DITFs. It has been decided not to treat differentially A and E DITFs orientation here, but to focus on length proportion of A or E DITFs among the same depth interval segments as for the All DITFs orientation study. For this purpose, the total length of A DITFs by depth interval has been compared with E DITFs length in the corresponding depth section. The ratio between A and E DITFs has been calculated, so that values of the ratio below 1 correspond to formations where there is more E DITFs than A DITFs and values above 1 correspond in the contrary to sections where A DITFs are more represented than E DITFs.

All the results are presented as graphs or tables in the next section.

3. RESULTS

3.1 All DITFs orientation

The Figure 6 summarise the resulting A DITFs orientation for one set of depths segmentation. It represents the azimuth of All DITFs corrected by a moving average, the mean azimuth of All DITFs for different the lithostratigraphic formations and the major natural fractures encountered in the well.

The Table 1 represent the ratio of A DTIFs length on E DITFs length for the more refined depth interval set: lithological formations.

From the bottom well section in the deep-seated granite to the sedimentary part in the Keuper formations, the main observations in terms of stress orientation derived from the DIFTs, can be done:

- At 2,500 m, in the unaltered granite, average SHmax is N20W;

- At 2,450 m, in the unaltered granite, SHmax is N10°W;
- At 2.390 m, in the unaltered granite, SHmax is N30°E. This zone is just below the largest and the most permeable fracture zone of GRT-1;
- From 2,980 m to 2210 m, within the highly hydrothermally altered and fractures granite as well as in the rubefied granite, SHmax is scattered but with an average orientation of N20°E±7°. This section contains the highly concentration of larger natural fractures;
- From the top basement, 2,210 m and 2,160 m, in the Annweiler sandstone, SHmax value is variable with N030°E in average. This interval is poorly fractured;
- From 2,160 m to 1,920 m in the Vosgian sandstone, SHmax value varies from N18°E to N25°E. This interval is poorly fractured except at 1,990 m where a fracture zone crosses the borehole;
- The borehole radius changes from $8^{1/2}$ to $12^{1/4}$ inches at 1,920 m depth. From 1,900 m to 1,800 m in the Upper Buntsandstein, the main SHmax orientation rotates anticlockwise form N40°E (1,900 m), N35°E (1,850m) and N27°E (1,810m). There is no large fracture in this depth section.
- From 1,810 m to 1,770 m depth in the Lower Muschelkalk layers (sandstone, dolomites), SHmax varies from N25°E to N18°E respectively.
- Around 1,760 m depth, severe mud losses related to the occurrence of a large fracture was observed during drilling operation. At that depth, SHmax is N20°W.
- From 1,700 m to 1,500 m depth, in the Upper Muschelkalk, and the Keuper formations, SHmax is quite stable and is oriented N10°E.

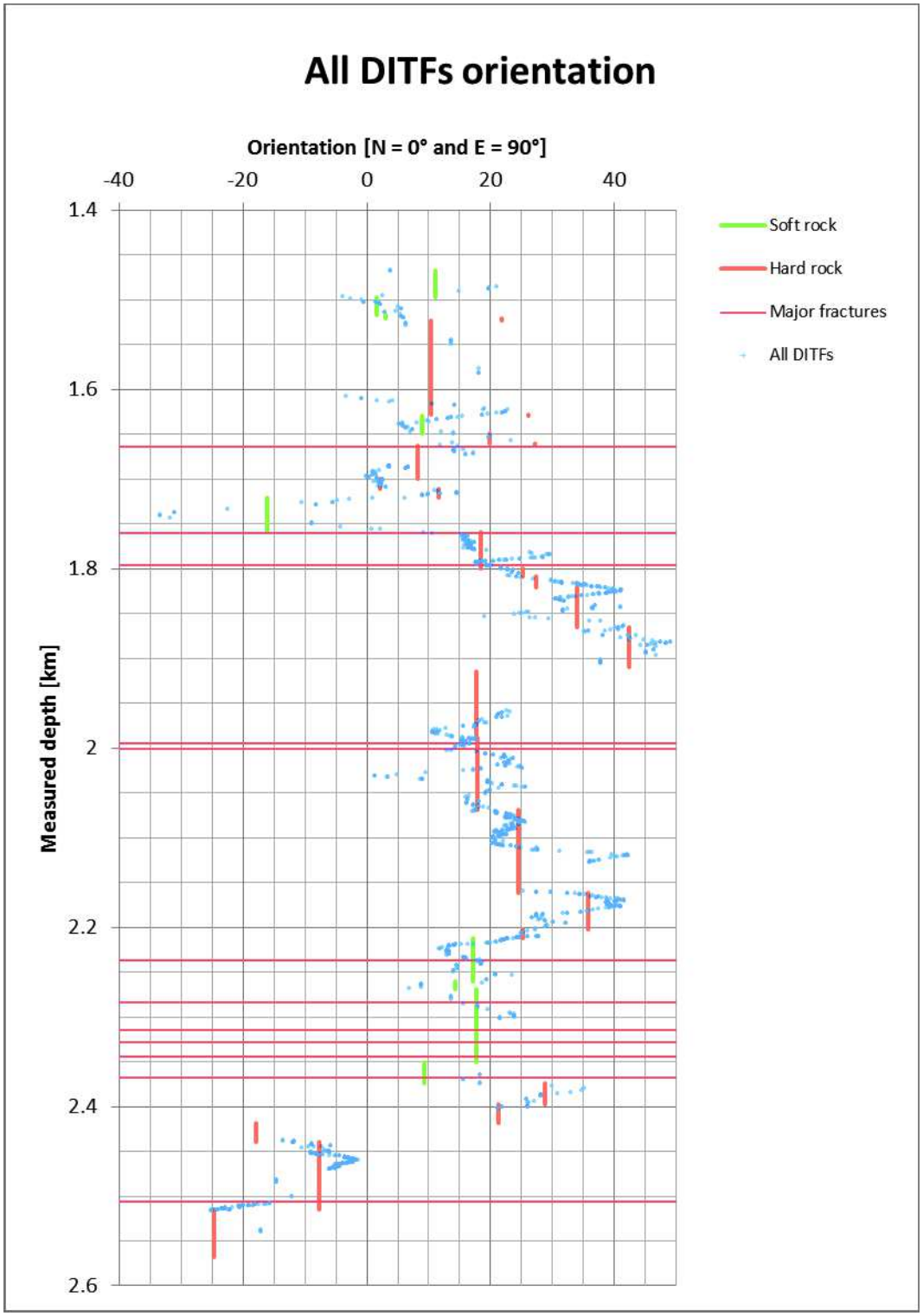

Figure 6: All DITFs orientation compared to the detailed lithostratigraphy units. DITF orientations are represented as blue crosses. Mean orientation are represented by vertical segments (green for soft rocks and orange for hard rocks) and major natural fractures are shown as horizontal red lines.

Table 1: Comparison between A and E DITFs cumulated length on depth intervals corresponding to lithological formations (bt: biotite, ms:muscovite).

Formations	Dominant lithology	All DITFs length	A DITFs length	E DITFs length	A/E DITFs length
Marnes Irisées supérieures	Marl	8.29	6.49	1.8	3.61
Argiles de Chanville	Clay	15.51	13.12	2.39	5.49
Marnes Irisées moyennes	Marl	5.39	3.91	1.48	2.64
Grès à Roseaux	Sandstone	0.98	0	0.98	0.00
Marnes Irisées inférieures	Marl	20.89	18.55	2.34	7.93
Dolomie Limite	Dolomite	0.37	0.37	0	+ infinity
Argile de la Lettenkohle	Clay	21.17	16.16	5.01	3.23
Dolomie Inférieure	Dolomite	2.39	0.91	1.48	0.61
Calcaire à Térébratules	Limestone	1.18	1.18	0	+ infinity
Couches à Cératites	Limestone	24.84	17.12	7.72	2.22
Calcaire à Entroques	Limestone	12.25	6.31	5.94	1.06
Dolomie à Lingules	Dolomite	9.37	2.5	6.87	0.36
Marnes Bariolées	Marl	31.24	29.09	2.15	13.53
Dolomies - Calcaires Ondulées - Couches à Myacites	Dolomite	36.93	13.04	23.89	0.55
Grès Coquillier	Sandstone	6.86	3.48	3.38	1.03
Grès à Voltzia	Sandstone	11.79	5.09	6.7	0.76
Couches intermédiaires	Sandstone	46.64	17.47	29.17	0.60
Couches de Karlstal 12.25	Sandstone	37.85	27.03	10.82	2.50
Couches de Karlstal 8.5	Sandstone	36.25	30.19	6.06	4.98
Couches de Rehberg	Sandstone	70.83	31.16	39.67	0.79
Couches de Trifels	Sandstone	55.04	8.76	46.28	0.19
Grès d'Annweiler	Sandstone	40.33	0	40.33	0.00
Permien anté - Annweiler	Sandstone	14.73	12.33	2.4	5.14
Rubefied granite	Granite	54.8	31.6	23.2	1.36
Weathered rubefied granite	Granite	4.97	3.44	1.53	2.25
White altered granite	Granite	18.48	15.22	3.26	4.67
Pink altered granite	Granite	8.2	8.2	0	+ infinity
Light grey bt/ms sound granite	Granite	45.32	44.26	1.06	41.75
Pink bt/ms sound granite	Granite	4.45	1.34	3.11	0.43
Pink-grey bt/ms sound granite	Granite	2.91	2.91	0	+ infinity
Light grey bt/ms sound granite	Granite	46.29	14.19	32.1	0.44
Pink-grey bt/ms sound granite	Granite	4.51	1.81	2.7	0.67
TOTAL		701.05	387.23	313.82	

4. INTERPRETATION

4.1 All DITFs orientation

One can notice that the global variations of SHmax orientation can be divided in cycles of fifty meters depth below 1,600 m MD. In those cycles, the orientation of SHmax by increasing depth rotates clockwise first and then anticlockwise. Similar cycles can be observed from 1,600 m to 2,500 m MD. The nature of lithostratical units and the natural fracture occurrences cannot clearly be related to this cycle frequency. The resulting global rotation of SHmax can be either clockwise or anticlockwise. The variations of these resulting global rotations are discussed in the following paragraphs.

Considering only the DITFs orientations represented as blue crosses in Figure 6, one can notice that there are many variations along the studied depth interval. The global orientation oscillates between N0°E and N20°E at 1,500 m MD. It can be noticed that this mean orientation is slightly different than the one measured in the basement at Soultz-sous-Forêts (Valley, 2007). In Figure 6 the variations of the orientations of SHmax are correlated with the lithology. Indeed, it appears that SHmax orientation rotates clockwise eastward until N30°E in hard rock formations, for example in Grès à Roseaux (sandstone [1,521 m MD; 1,523 m MD]) and Calcaire à Térébratules (limestone [1,659.5 m MD; 1,662 m MD]). Then, in weaker rocks, the orientation comes back anticlockwise to N0°E or N160°E, for example in Argiles de Chanville (clays [1,497 m MD; 1,517 m MD]) and Marnes Bariolées (marls [1,721 m MD; 1,758.5 m MD]).

From 1,750 m MD to casing shoe at 1,920 m MD (the end of the section in 12”1/4 inches), SHmax follows a global trend: the orientation of SHmax is rotating clockwise from N15°E at 1,750 m MD, to N50°E at 1,900 m MD in Couches de Karlstal (sandstone [1,865.5 m MD; 1,989 m MD]).

The Couches de Karlstal interval is cut in two parts by the casing shoe (1,920 m MD). Nevertheless, from the 12.25 to the 8.5 inches sections, SHmax has rotated anticlockwise from N50°E to N20°E. No reliable UBI are available for this diameter changing section (1,920 +/- 20 m MD), but the casing shoe has been placed at this depth because this interval is known for its high fracture density. So if the lithology can’t explain this stress rotation, maybe it can be related to this corresponding but not documented fracture zone.

Between 1,900 m to 2,275 m MD, another clockwise rotation of SHmax can be noticed. The global rotation is slower than the one between 1,750 m and 1,900 m MD, but it also goes from N20°E to N40°E.

At 2,200 m MD, the orientation is sharply turning anticlockwise again to N20°E. The pattern is similar than the rotation shown at 1,900 m MD. Here it corresponds precisely to the change between Grés d’Annweiler (unweathered and hard Sandstone [2,161 m MD; 2,202 m MD]) and the rubefied granite (weak and weathered crystalline rock mass). So the orientation of SHmax shows again a clockwise rotation Eastward in hard rocks, and the anticlockwise rotation Westward in weaker rocks.

This behaviour is reproduced once more between 2,200 m and 2,400 m MD: SHmax rotates clockwise from N15°E in weathered rubefied granite, to N30°E in unaltered granite.

Below 2,400 m MD where the unaltered granite basement is reached, the orientation of SHmax comes back anticlockwise from N30°E to N160°E: this latter value fits with the stress field orientation given between 1,500 to 5,000 m for the stress state in the basement at Soultz-sous-Forêts (Valley, 2007; Valley and Evans, 2007).

The explanation of those variations can be the following: the orientation of SHmax is known and stable in the basement. But the sedimentary layer is constrained by a slightly different stress state. When the lithology corresponds to hard rock, this stress state can’t be realised or accommodated. In this case, SHmax rotates from the global stress state to the sedimentary one. In weaker lithologies, clay-rich units, the sedimentary stress state has been accommodated or realised by the deformations of the rock itself. In this case, the sedimentary component of the stress state has been removed and the orientation of SHmax tends to reach the one observed in the basement.

At the top of the granite basement, the uppermost unaltered granite section has to support all the lithostatic stress due to the sedimentary pile, as well as its plastic deformation and its rotating pattern. For that reason, the uppermost part of the unaltered granite has a strongly rotated stress state. But as there is no plastic deformation anymore, all those variations are rapidly overprinted by the granite and the orientation of SHmax rotates with depth reaching the global and regional balanced stress state orientation.

Finally, the sedimentary part shows a totally different pattern for SHmax orientation. The stress state in the basement is decoupled from the sedimentary stress state. This decoupling of stress has already been outlined in Western Europe by Cornet and Roeckel (2012). They showed significant variations with depth of the maximum horizontal principal stress orientation, both in the Rhine Graben and in the North German Basin. They concluded that stress field observed at shallower depths in the sedimentary layers may be decoupled from that which prevails at greater depth in the basement.

No clear correspondence can be highlighted between the cyclic variation of SHmax orientation and the

presence of the bigger opened fractures. Maybe the fractures involved in this rotation phenomenon are not the largest ones.

4.2 A and E DITFs distribution ratio

The ration A/E DITFs varies a lot along the borehole for the different lithological intervals (Table 1). It can be noticed that values of the ratio between zero and one, representing intervals where there is more E DITFs than A DITFs, always correspond to hard rock intervals (e.g. ratio of 0.61 for Dolomie Inférieure, 0.60 for Grès à Voltzia, 0.43 for Pink biotite/muscovite massive granite, etc). On the other hand, the highest value of the ratio, representing intervals where there is more A DITFs than E DITFs, doesn't always correspond to weaker rock (e.g. ratio 5.49 for Argiles de Chanville, but ratio of 41.75 for Light grey biotite/muscovite massive granite).

These observations mean that E DITFs are more likely to occur in hard rocks than in weaker rocks. For A DITFs, there is no predominant rule: they can be found either in hard or weaker rocks.

This difference in the A/E DITFs ratio means that the so called "vertical principal stress Sv" is more likely to be really vertical in marls and clays. In other terms, only hard rocks can lead to a rotation of Sv.

This observation matches with the discussion made on global All DITFs orientation. In weaker rocks, the principal stresses orientations tend to reach the global and regional stress state of the Rhine Graben. In those lithological units, the shearing stresses are released because of the plastic deformation of marls and clays. In consequence, Sv tends to be more vertical in clay-rich formations and marls than in dolomite, sandstone, limestone or granite. In the contrary, in hard rocks, there is not enough plastic deformation to accommodate the shear stress. In consequence, the principal stresses rotate to compensate the differences between the upper sedimentary stress state and the basement one, making E DTFs more likely to occur.

CONCLUSIONS

On a global scale, this study shows that the entire stress state of the sedimentary layer is decoupled from the basement one. The first massive unaltered and poorly fractured granite sections between 2,400 m to 2,500 m MD make the interface between the two stress states.

On a larger scale, the orientation of SHmax in the Upper Rhine Graben is globally N145E, and at Soultz N170°E. But the study of the orientation of DITFs has shown that the orientation of SHmax varies a lot, from N150°E to N50°E in the sedimentary layers.

SHmax orientation follows a cyclic profile repeating every 50 m MD along the borehole. Those cycles are not well explained by the presence of major opened fractures or by any change in the geomechanical properties of the lithological units.

Those small cycles participate to a more global trend, where SHmax turn smoothly clockwise from N10°E to N40°E, and then comeback sharply anticlockwise to N0°E or N10°E. This global trend is repeated three times from 1,750 m MD to 2,450 m MD. Such behavior is also not explained by the presence of major opened fractures. But it has been shown that the orientation of SHmax tend to reach the regional orientation in weaker layers (as clays or marls), and turn clockwise toward N50°E in hard rock layers (as dolomite and sandstone).

This result is corroborated by the fact that E DITFs are less likely to occur in weak layers. It also shows that the stress state rotates more in hard rock layers, and is closer to the regional one weaker rock.

REFERENCES

Aichholzer, C., Duringer, P., Orciani, S. and Genter, A.: New stratigraphic interpretation of the twenty-eight-year old GPK-1 geothermal well of Soultz-sous-Forêts (Upper Rhine Graben, France), in: Proceedings of the *4th European Geothermal Workshop*, Strasbourg, France, (2015).

Baujard, C., Genter, A., Graff, J.-J., Maurer, V. and Dalmais, E.: ECOGI, a New Deep EGS Project in Alsace, Rhine Graben, France, in: *Proceedings of World Geothermal Congress* (2015), Melbourne, Australia.

Brudy, M. and Zoback, M.D.: Drilling-induced tensile wall fractures: implication for in-situ stress orientation and magnitude, *International Journal of Rock Mechanics & Mining Sciences*, **36** (1999), 199-215.

Cornet, F. H., Berard, T. and Bourouis S.: How close to failure is a granite rock mass at a 5 km depth? *International Journal of Rock Mechanics and Mining Sciences*, **44**, (2007), 47-66.

Cornet, F. H.: Seismic and aseismic motions generated by large scale fluid injections in a deep Granite massif, In Proceedings of *47th US Rocks Mechanics Symposium*, San Francisco, California, June 23-26, (2013), ARMA 13-222.

Cornet, F. H. and Roeckel, Th.: Vertical stress profiles and the significance of stress decoupling, *Tectonophysics*, **581**:13, (2012), doi:10.1016 /j.tecto. 2012.01.020.

Davatzes, N.C. and Hickman, S.H.: Comparison of Acoustic and Electrical image logs from the Coso Geothermal Field, CA, in: Proceedings of *Thirtieth Workshop on Geothermal Reservoir Engineering* (2005), Stanford University, California, USA.

Davatzes, N.C. and Hickman, S.H.: Stress and faulting in the Coso geothermal field: Update and recent

results from the east flank and Coso Wash, in: Proceedings of *Thirty-First Workshop on Geothermal Reservoir Engineering* (2006), Stanford University, California, USA.

Dezayes, C., Sanjuan, B., Gal, F. and Lerouge, C.: Fluid geochemistry monitoring and fractured zones characterization in the GRT1 borehole (ECOGI project, Rittershoffen, Alsace, France), in: Proceedings of *Deep Geothermal Days*. Paris, France, (2014).

Genter, A., Cuenot, N., Graff, J.J., Schmittbuhl, J. and Villadangos, G.: La géothermie profonde en France : quelles leçons tirer du projet pilote de Soultz-sous-Forêts pour la réalisation d'un projet industriel à Rittershoffen? *Revue Géologues*, **185**, (2015a), 97-101.

Genter, A., Vidal, J., Baujard, C., Dalmais, E. and Schmittbuhl, J.: Permeability in deep-seated granitic rocks: lessons learnt from deep geothermal boreholes in the Upper Rhine Graben, *20th International Association of Hydrogeologists*, (2015b), 09-10 June 2015, La Roche-sur-Yon, France.

Heidbach, O., Tingay, M., Barth, A., Reinecker, J., Kurfeß, D. and Müller, B.: The world stress map database release: 2008 10.1594/GFZ.WSM. Rel2008. (2008).

Sahara, D., Schoeball, M., Kohl, Th. and Mueller, B. I. R.: Impact of fracture networks on borehole breakout heterogeneities in crystalline rock, *International Journal of Rock Mechanics and Mining Science*, **71**, (2014), 301-309.

Valley, B. C. and Evans, K.F.: Stress state at Soultz-sous-Forêts to 5 km depth from wellbore failure and hydraulic observations, paper presented at *Thirty-Second Workshop on Geothermal Reservoir Engineering*, Stanford, California, US, (2007).

Valley, B. C.: The relation between natural fracturing and stress heterogeneities in deep-seated crystalline rocks at Soultz-sous-Forêts (France). Zurich: Swiss Federal Institute of Technology Zurich; (2007).

Zoback, M. D., Moos, D., Mastin, L. and Anderson R.N.: Wellbore breakouts and in situ stress, *Journal of Geophysical Research*, **90**, (1985), 5523-5530.

Zoback, M. D., Barton, C.A. Brudy, M.,, Castillo, D.A., Finkbeiner, T., Grollimund, B.R., Moos, D.B., Peska, P., Ward, C.D. and Wiprut, D.J.: Determination of stress orientation and magnitude in deep wells, *International Journal of Rock Mechanics and Mining Sciences*, **40**, (2003), 1049-1076.

Vidal, J., Genter, A., Chopin, F. and Dalmais, E.: Natural fractures and permeability at the geothermal site Rittershoffen, France, Proceeding of the *European Geothermal Congress*, Strasbourg, France (2016).

ACKNOWLEDGEMENTS

The authors are grateful to ECOGI for using geological and geophysical data from the Rittershoffen geothermal site. The authors are grateful to Ademe support in the framework of the EGS Alsace project. The authors are grateful to Chrystel Dezayes from BRGM, Guerric Villadangos from ES, and Jean Schmittbuhl and François Cornet from EOST for fruitful discussions about the preliminary interpretation of the stress field at Rittershoffen.

UNIVERSITÉ DE STRASBOURG

Jeanne Vidal

ECOST Ecole et Observatoire des Sciences de la Terre

Altérations hydrothermales associées aux zones de fractures à l'interface de la couverture sédimentaire et du socle cristallin dans le Fossé rhénan supérieur.

Application aux forages géothermiques de Rittershoffen (Alsace, France)

Résumé

La connaissance des réseaux de fractures est essentielle pour comprendre la circulation des fluides dans un réservoir. Cette thèse s'appuie sur la reconnaissance du réseau de fractures naturelles qui chenalisent les circulations à l'échelle des deux forages profonds GRT-1 et GRT-2 de Rittershoffen (Alsace, France) qui ont recoupé les sédiments gréseux triasiques et le socle granitique altéré dans le cadre d'un projet industriel de géothermie.

L'étude structurale de ce réseau de fractures a été réalisée à partir d'imageries de paroi acoustiques corrélées à des diagraphies géophysiques standard tandis que l'étude pétro-minéralogique se base sur les échantillons de cuttings. Les zones de fractures perméables des puits de Rittershoffen montrent une organisation asymétrique de la perméabilité. Des fractures ouvertes à l'échelle du puits semblent agir comme des drains perméables entourés de halos d'altération hydrothermale. Ces zones de fractures sont associées à des perturbations locales du profil de température dans le puits. La présence de minéraux illitiques hétérogènes pourrait être un indicateur pour prospecter les zones de circulations actuelles et passées à l'échelle des puits.

Cette étude géologique permet d'évoluer vers un modèle de forage hydrothermal possédant des connexions favorables avec le réservoir sans avoir recours à des opérations de stimulation.

Mots clés : fracturation naturelle, imageries de paroi acoustiques, altérations hydrothermales, géothermie profonde, Rittershoffen, Fossé rhénan supérieur

Abstract

The knowledge of the fracture network is a key challenge to understand the fluid circulation through a reservoir. The aim of this PhD project is to investigate the natural fracture network that channelized the hydrothermal circulations into two deep wells GRT-1 and GRT-2 at Rittershoffen (Alsace, France) that intersect Triassic sandstones and altered granitic basement in the framework of an industrial geothermal project.

The structural study of the fracture network was based on acoustic image logs correlated with standard geophysical logs, whereas the mineralogical study was based on cutting samples. Permeable fracture zones of wells at Rittershoffen present an asymmetrical organization of permeability. Open fractures at the borehole scale act as fluid pathways surrounded by halos of hydrothermal alteration. These fracture zones are associated with local thermal anomalies in the temperature profiles at the borehole scale. Occurrences of heterogeneous illitic minerals could be a good indicator to prospect zones of actual and past circulations at the borehole scale.

This geological study develops towards a model of hydrothermal well with favorable connections to the fractured reservoir without stimulation operations.

Keywords: natural fractures, acoustic image logs, hydrothermal alteration, deep geothermal site, Rittershoffen, Upper Rhine Graben.